UNIVERSIDADE DO PORTO

Inverse Scattering Techniques for the Synthesis of Microwave Structures

by

Mário Rui Silveira Pereira

A thesis submitted in candidature for the
degree of Doctor of Philosophy

in the
Faculdade de Engenharia
Departamento de Engenharia Electrotécnica e de Computadores

February 2014

Thesis Identification

Title:	Inverse Scattering Techniques for the Synthesis of Microwave Structures
Keywords:	Transmission Line, Inverse Scattering, Layer-Peeling, Group Delay, Wide-band, Microstrip, Directional Couplers, Filters, Impedance Transformers
Start:	October 2006
Candidate information:	
Name:	Mário Rui Silveira Pereira
e-Mail:	mario@fe.up.pt
Curriculum Vitae:	http://www.fe.up.pt/~dee06002/cv.pdf
Supervisor information:	
Name:	Henrique Manuel de Castro Faria Salgado
e-Mail:	hsalgado@fe.up.pt
Curriculum Vitae:	http://www.fe.up.pt/~hsalgado/cv.pdf
Educational Establishment:	Faculdade de Engenharia da Universidade do Porto
Research Institution:	INESC Porto
Co-Supervisor information:	
Name:	José Rocha Pereira
e-Mail:	jrp@ua.pt
Curriculum Vitae:	http://www.it.pt/~jrp/cv.pdf
Educational Establishment:	Universidade de Aveiro
Research Institution:	Instituto de Telecomunicações

Statement of Originality

The work presented in this thesis was carried out by the candidate. It has not been presented previously for any degree, nor is it at present under consideration by any other degree awarding body.

Candidate:

(Mário Rui Silveira Pereira)

Advisor:

(Henrique Manuel de Castro Faria Salgado)

Statement of Availability

I hereby give consent for my thesis, if accepted, to be available for photocopying and for interlibrary loan, and for the title and summary to be made available to outside organizations.

Candidate: _____

(Mário Rui Silveira Pereira)

Acknowledgements

First, I would like to express my sincere gratitude to my supervisor, Professor Henrique Salgado and co-supervisor Professor José Rocha Pereira for the continuous support of my research and for their patience, motivation and immense knowledge.

I am also grateful to Instituto de Engenharia de Sistemas e Computadores do Porto for providing me the technical conditions necessary to perform my research work.

I acknowledge the support from Fundação para a Ciência e a Tecnologia for the PhD scholarship.

I also would like to thank my friends Luís Pessoa, João Oliveira, and Qi Luo for their support and all fruitful discussions.

Last, but certainly not least, I am indebted to my family for their encouragement and constant support.

Summary

Today, due to the ever-increasing data-rate needs there is a high demand for faster, more reliable and ubiquitous microwave systems. Consequently, broad-band and multi-band applications are renewing the interest in the synthesis and design of novel planar ultra-wideband devices with enhanced capabilities. In this context, inverse scattering techniques for the synthesis of high performance passive microwave devices, emerge as a pertinent and timely subject.

Inverse scattering theory is widely used throughout many areas of physics and deals with determining the characteristics of a medium from the limited knowledge of the fields propagating through that medium. In the particular case of electromagnetic theory, the inverse scattering problem is concerned with finding the electrical properties of a medium from the associated scattering data such as, the reflection or transmission coefficients.

It is the objective of this thesis to present a solid working base regarding direct scattering and inverse scattering subjects and also to push the current boundary regarding the synthesis of high performance structures by introducing innovative methods/procedures, tools and novel microwave passive devices based on the inverse scattering theory.

This thesis addresses an in-depth analysis of numerical and analytical direct scattering methods as well as a complete analysis regarding inverse scattering procedures and methods. As a major contribution from this work, a new theoretical framework regarding the parallelism between discrete nonuniform transmission lines and digital filters is established opening new frontiers on the synthesis of microwave devices through inverse scattering.

Finally, several microwave passive devices have been designed employing the proposed inverse scattering techniques and validated through both numerical and electromagnetic simulations as well as by experimental measurements.

Sumário

Nos dias de hoje são cada vez maiores os requisitos de débito dos sistemas de comunicações sem fios exigindo o recurso a tecnologias de micro-ondas cada vez mais rápidas, fiáveis e disponíveis. Neste sentido, tem crescido o número de aplicações de banda-larga e multi-banda que exigem a síntese e projeto de novos dispositivos planares de banda muito larga contendo caraterísticas mais exigentes. É neste contexto que surge de forma pertinente o tópico da síntese de dispositivos passivos de micro-ondas de elevado desempenho recorrendo a técnicas de dispersão inversa.

A teoria da dispersão inversa é amplamente usada em diversas áreas da física e refere-se ao cálculo das caraterísticas de um determinado meio através do conhecimento limitado dos campos que se propagam nesse meio. No caso particular da teoria eletromagnética, a teoria da dispersão inversa dedica-se à determinação das propriedades elétricas de um meio através de informação de dispersão associada, seja através de parâmetros de reflexão ou transmissão.

Pretende-se nesta tese apresentar uma base de trabalho sólida sobre os assuntos de dispersão direta e inversa bem como fazer avançar o atual limite de conhecimento sobre a síntese de dispositivos micro-ondas de elevado desempenho, ao introduzir novos métodos, procedimentos, e ferramentas baseados na teoria da dispersão inversa. Em particular, realiza-se uma análise detalhada de métodos numéricos e analíticos de dispersão direta bem como uma análise completa sobre procedimentos e métodos de dispersão inversa.

Como contribuição destacada deste trabalho, refere-se a proposta de uma nova base teórica que permite um paralelismo entre a teoria de linhas de transmissão discretas não uniformes e filtros digitais, abrindo novas fronteiras no campo da síntese de dispositivos de micro-ondas através de dispersão inversa.

Finalmente, são projetados vários dispositivos passivos de micro-ondas recorrendo às técnicas de dispersão inversa propostas, e apresentada a sua validação através de simulações numéricas e electromagnéticas bem como através de medições experimentais.

Contents

List of Figures

List of Tables

Abbreviations

TL	Transmission Line
NTL	Nonuniform Transmission Line
CNTL	Continuous Nonuniform Transmission Line
DNTL	Discrete Nonuniform Transmission Line
TEM	Transverse Electro Magnetic
ADS	Advanced Design System
MoM	Method of Moments
FEM	Finite Element Method
CMT	Coupled Mode Theory
IS	Inverse Scattering
CLP	Continuous Layer-Peeling
DLP	Discrete Layer-Peeling
DSP	Digital Signal Processing
UWB	Ultra Wideband
TE	Transverse Electric
TM	Transverse Magnetic
TEM	Transverse Electromagnetic
EM	Electromagnetic
DC	Direct Current
EBG	Electronic Band Gap
GLM	Gel'fand-Levitan-Marchenko
ROC	Region Of Convergence
ZS	Zakharov-Shabat
LP	Layer-Peeling
TMM	Transmission Matrix Method
LHP	Left Hand Plane
RHP	Right Hand Plane
HFSS	High Frequency Structural Simulator
ADS	Advanced Design System
PLF	Power Loss Factor
VNA	Vectorial Network Analyzer

LTI	Linear Time-Invariant
MA	Moving Average
AR	Auto Regressive
ARMA	Auto Regressive Moving Average
FIR	Finite Impulse Response
IIR	Infinite Impulse Response
EF	Error Function

Chapter 1

Introduction

In many areas of physics the interest lies with determining the characteristics of a medium from the limited knowledge of the fields propagating through that medium. This is known as *inverse scattering theory*. Basically, the inverse scattering theory deals with the geometry reconstruction and material properties identification of a scatterer from its associated scattered data.

Inverse scattering theory finds application in several different areas such as, medical imaging, non-destructive evaluation, geophysical prospecting, underwater sound propagation, ionospheric profiling, microwave sensing and quantum physics to name a few. In the electromagnetic particular case, the inverse scattering problem is concerned with finding the electrical properties of a medium from the associated scattering data such as, the reflection or transmission coefficients.

The difficulty with electromagnetic inverse scattering and therefore inverse modeling lies with the complexity of the electromagnetic laws themselves which when translated into mathematical form give rise to complex differential and integral equations. In certain cases however, waves inherently propagate on a single direction, hence, writing the medium equations in the form of a two-component system describing the interaction of rightward and leftward propagating waves allows for the electromagnetic inverse problem to be reduced to the one-dimensional inverse scattering problem. Examples of such cases in the electromagnetic realm are fiber Bragg gratings and microwave transmission lines. In the particular case of microwave transmission lines, the solution for the one-dimensional inverse scattering problem results in the synthesis of a nonuniform transmission lines (NTLs) which realizes some previously specified frequency response. Because this is in fact the central problem of filter design, inverse scattering theory is

suitable to be used in the synthesis/design of microwave filters.

Most often and for many applications, there is the need to construct microwave structures [2] that meet certain scattering parameter specifications either in the frequency or time domains. Conventionally however, the synthesis/design procedure for such structures begins by first setting a lumped element prototype (usually an LC circuit) that approximates the prescribed characteristics, after which the Richard's transformation [3] and Kuroda's identities [4] are used to convert the lumped prototype elements into the appropriate structure of nonuniform transmission lines. Classical filters, *i.e.*, Butterworth, Chebyshev and elliptical filters are three examples of prototypes commonly used on microwave filter design [5].

The motivation for this work is to study the scattering characteristics of NTL structures (as they inherently result from inverse scattering procedures) as well as to identify and apply novel inverse scattering methods and techniques to the synthesis of innovative NTL based microwave structures with arbitrarily defined frequency domain responses.

Nonuniform transmission lines [6] have been widely studied for decades in both direct scattering and inverse scattering problems. Due to their inherent electrical and mechanical characteristics, NTL based devices are often desirable when compared to alternative solutions. As far as the electrical characteristics is concerned, NTLs based devices are usually desirable as they easily achieve ultra-wideband (UWB) performance [7], [8], [9] and due to their ability of achieving multi-band operation and suppressing fundamental frequency harmonics [10].

The ability to synthesize arbitrarily defined frequency responses when associated to the properties of NTL structures, proves that the synthesis of NTL based devices through inverse scattering theory is a pertinent and important subject. Moreover, in light of the present day context of ever-increasing data-rate requirements and the consequent need of ultra-wideband technology proves that the use of inverse scattering on the synthesis of NTL based devices is a current and hot topic, which as recently gained a renewed interest with the emergence of analog signal processing [11].

To the present day, the synthesis of NTL based microwave devices through inverse scattering has not yet been deeply explored, nevertheless we highlight the work of Arnedo *et.al.* [12] on the synthesis of waveguide band-stop filters, wideband couplers, pulse shapers and dispersive delay lines as well as the previous work of Roberts and Town [13], who to the best of our knowledge performed the first synthesis of a microwave filter in microstrip technology using a numerical inverse scattering procedure. On the other

hand, in the optic domain, inverse scattering methods/techniques are considerably more advanced due to the work of Skaar [14] and Fecced [15] on the synthesis of fiber Bragg gratings. A special note of attention to the work of Skaar, that has given a big push to the subject by applying more efficient, more simple and more accurate numerical algorithms to perform inverse scattering.

It is the objective of this thesis to present a solid working base regarding nonuniform transmission lines, direct scattering and inverse scattering subjects and also to slightly push the current boundary regarding the synthesis of NTL structures by introducing innovative methods/procedures, tools and novel NTL devices based on the inverse scattering theory.

1.1 Thesis organization

This thesis consists of this introduction followed by five main chapters and the concluding remarks.

In Chapter 2, an overview on transmission line theory and network analysis is presented. Here we address the basics of waveguide and transmission line theory necessary to a complete understanding of the following chapters. Also, we introduce the concepts of scattering parameters as well the wave-amplitude parameters.

In Chapter 3, the direct scattering problem of nonuniform transmission lines is considered. Here we address several methods that can be used to perform the analysis of nonuniform transmission lines and evaluate their efficiency and accuracy.

In Chapter 4, an in-depth analysis of inverse scattering techniques/methods and algorithms is performed. Here, we provide a complete mathematical analysis regarding the one-dimensional inverse scattering. Moreover, we describe and assess the performance and accuracy of several numerical inverse scattering methods.

In Chapter 5, we demonstrate the potential and versatility of the inverse scattering theory by performing the synthesis of several nonlinear transmission line based microwave devices. The inverse scattering synthesis of shuck devices is performed by using the layer-peeling algorithm.

In Chapter 6, we have introduced the concept of discrete nonuniform transmission line. Moreover, a new theoretical framework regarding the parallelism between discrete nonuniform transmission lines structures and digital filters is established and new inverse scattering based synthesis tools are developed.

Finally in Chapter 7, we present the concluding remarks as well as the future work guidelines.

1.2 Contributions

The primary goal of this research work is to propose innovative methods/procedures and tools for the synthesis of high performance structures employing inverse scattering theory.

The main contributions of this research work are summarized below:

- Detailed survey regarding the analytical and numeric direct scattering methods and procedures used in the analysis of nonuniform transmission lines.
- In-depth analysis of analytical and numerical inverse scattering methods for the synthesis of nonuniform transmission lines.
- The proposal of a novel layer-peeling algorithm to synthesis of nonuniform transmission lines.
- Proposal of procedures for the synthesis/design of band-stop filters, arbitrary group delay lines and wide-band couplers.
- Assessment of the truncation and windowing procedures impact on the synthesis of classical band-stop filters.
- Identification of the optimum windowing configurations in reducing the truncation error on the approximation to the ideal frequency response.
- Evaluation of the influence of the different classical filter parameters on the length and maximum characteristic impedance values of the synthesized filters.
- The proposal of a new theoretical framework regarding the parallelism between discrete nonuniform transmission lines and digital filters.
- Assessment of the minimum length synthesis conditions for discrete nonuniform transmission line structures.
- Proposal of a novel analog-to-digital transformation enabling the minimum length synthesis of discrete discrete nonuniform transmission line structures.

- Validation of the proposed design methods through a comparative study between numerical, analytical and EM simulations as well experimental measurements.
- Development of "software tools" implemented in MATLAB for the synthesis, analysis and simulation of nonuniform transmission line based passive devices.

The contributions of this research work have led to the following publications:

- M. R. Pereira, H. M. Salgado, and J. R. Pereira, "Synthesis of Nonuniform TEM-Mode Directional Couplers with Arbitrary Coupling Response, Proceedings of the IEEE International Conference on Electromagnetics in Advanced Applications (ICEAA) 2012, Cape Town, South Africa, September 2012.
- M. R. Pereira, H. M. Salgado, and J. R. Pereira, "Synthesis of Microstrip Filters with Arbitrary Reflective Group Delay Response, Proceedings of the IEEE International Conference on Electromagnetics in Advanced Applications (ICEAA) 2010, Sydney, Australia, September 2010.
- M. R. Pereira, H. M. Salgado, and J. R. Pereira, "A Novel Layer Peeling Algorithm for the Synthesis of Microwave Microstrip Filters, Proceedings of the IEEE International Conference on Electromagnetics in Advanced Applications (ICEAA) 2009, Turin, Italy, September 2009.
- M. R. Pereira, H. M. Salgado, J. R. Pereira, "Synthesis of Microstrip Electromagnetic Bandgap Structures, Proceedings of the VI Symposium On Enabling Optical Networks and Sensors (SEON) 2008, Porto, Portugal, June 2008.
- M. R. Pereira, H. M. Salgado, J. R. Pereira, "Analysis of Microstrip Electromagnetic Bandgap Structures Using the Couple-Mode Theory, Proceedings of the V Symposium On Enabling Optical Networks and Sensors (SEON) 2007, Aveiro, Portugal, June 2007.

Chapter 2

An overview on transmission line theory and network analysis

2.1 Introduction

In this chapter we introduce the basic concepts regarding transmission line theory and network analysis as these are essential to the understanding of the upcoming chapters.

We start by defining the Maxwell's equations which describe how electric and magnetic fields are generated and altered by each other and by charges and currents, thus forming the foundations for classical electrodynamics, optics.

From the Maxwell equations we demonstrate through the general guided wave solutions how energy can be transmitted in the form of guided waves both through waveguides and transmission lines. Moreover, we demonstrate how transmission lines are a special class of the more general definition of waveguide that are capable of guiding TEM waves.

We present and discuss the transmission line lumped element equivalent circuit and the corresponding circuit equations from which we derive the telegrapher equations and the corresponding wave equations.

Regarding the network analysis topic, we introduce the scattering parameters and the corresponding scattering matrix as well as the wave-amplitude transmission parameters and establish the corresponding relationships.

2.2 General solutions for electromagnetic waves

Transmission lines and waveguides may be defined as devices used to guide energy from one point to another. Transmission lines and waveguide consist of a set of conductors, dielectrics or a combination of both. In this section we will show using Maxwell equations that energy can be transmitted in the form of unguided waves (plane waves) through space and also that we can transmit energy in the form of guided waves both on waveguides and transmission lines. This chapter follows the mathematical derivation of [5].

2.2.1 Maxwell equations

The famous four equations known as the Maxwell's equations that describe the electric and magnetic phenomena at the macroscopic level are:

$$\nabla \times \vec{\mathcal{E}} = -\frac{\partial \vec{\mathcal{B}}}{\partial t} - \vec{\mathcal{M}}, \tag{2.1}$$

$$\nabla \times \vec{\mathcal{H}} = \frac{\partial \vec{\mathcal{D}}}{\partial t} + \vec{\mathcal{J}}, \tag{2.2}$$

$$\nabla \cdot \vec{\mathcal{B}} = 0, \tag{2.3}$$

$$\nabla \cdot \vec{\mathcal{D}} = \rho, \tag{2.4}$$

with constitutive relations,

$$\vec{\mathcal{B}} = \mu \vec{\mathcal{H}}, \tag{2.5}$$

$$\vec{\mathcal{D}} = \epsilon \vec{\mathcal{E}}. \tag{2.6}$$

The variables are defined as:

$\vec{\mathcal{E}}$ is the electric field intensity, in V/m.
$\vec{\mathcal{H}}$ is the magnetic field intensity, in A/m.
$\vec{\mathcal{D}}$ is the electric field intensity, in C/m^2.
$\vec{\mathcal{B}}$ is the magnetic field intensity, in Wb/m^2.
$\vec{\mathcal{M}}$ is the fictitius magnetic current density, in V/m.
$\vec{\mathcal{J}}$ is the electric current density, in A/m^2.
ρ is the electric charge density, in C/m^3.
ϵ is the medium permittivity, in F/m.

μ is the medium permeability, in H/m.

The foregoing differential equations can be converted through the use of various vector integral theorems, yielding the Maxwell's equations in integral form:

$$\oint_C \vec{\mathcal{E}} \cdot \vec{dl} = -\frac{\partial}{\partial t} \int_S \vec{\mathcal{B}} \cdot \vec{ds} - \int_S \vec{\mathcal{M}} \cdot \vec{ds}, \tag{2.7}$$

$$\oint_C \vec{\mathcal{H}} \cdot \vec{dl} = \frac{\partial}{\partial t} \int_S \vec{\mathcal{D}} \cdot \vec{ds} + \int_S \vec{\mathcal{J}} \cdot \vec{ds}, \tag{2.8}$$

$$\oint_S \vec{\mathcal{B}} \cdot \vec{ds} = 0, \tag{2.9}$$

$$\oint_S \vec{\mathcal{D}} \cdot \vec{ds} = \int_V \rho dv. \tag{2.10}$$

Assuming a steady state sinusoidal time dependence:

$$\vec{\mathcal{E}}(x, y, z, t) = \vec{E}(x, y, z)e^{j\omega t}, \tag{2.11}$$

$$\vec{\mathcal{H}}(x, y, z, t) = \vec{H}(x, y, z)e^{j\omega t}. \tag{2.12}$$

Considering an isotropic and homogeneous media and a $e^{j\omega t}$ time dependence as in (2.11) and (2.12), the time derivatives in (2.1) to (2.4) are replaced by $j\omega$. The phasor form of the well known Maxwell equations becomes[1]:

$$\nabla \times \vec{E} = -j\omega\vec{B}, \tag{2.13}$$

$$\nabla \times \vec{H} = \vec{J} + j\omega\vec{D}, \tag{2.14}$$

$$\nabla \cdot \vec{B} = 0, \tag{2.15}$$

$$\nabla \cdot \vec{D} = \rho. \tag{2.16}$$

2.2.2 Wave equation

Considering a source-free region ($\rho = 0$) and assuming no external current sources ($\vec{J} = 0$), equations (2.13) and (2.14) can be rewritten as:

$$\nabla \times \vec{E} = -j\omega\mu\vec{H}, \tag{2.17}$$

$$\nabla \times \vec{H} = j\omega\epsilon\vec{E}. \tag{2.18}$$

[1]For the sake of mathematical simplicity the spacial dependency of the fields is omitted.

We now have a system of two equations with two unknowns, $\vec{E}$ and $\vec{H}$. As such, both (2.17) and (2.18) can be combined to obtain a separate equation for each field. Thus, taking the curl of (2.17) gives:

$$\nabla \times \nabla \times \vec{E} = -j\omega\mu\nabla \times \vec{H} = \omega^2\mu\epsilon\vec{E}, \tag{2.19}$$

which is an equation for $\vec{E}$. This result can be simplified through the use of (2.18) and the vector identity $\nabla \times \nabla \times \vec{K} = \nabla(\nabla \cdot \vec{K}) - \nabla^2\vec{K}$, yielding:

$$\nabla(\nabla \cdot \vec{E}) - \nabla^2\vec{E} = \omega^2\mu\epsilon\vec{E}. \tag{2.20}$$

Because a source-free region is considered, ρ is assumed zero. This means that the divergence of the electric field is null ($\nabla \cdot \vec{E} = 0$) and so, equation (2.20) simplifies to:

$$\nabla^2\vec{E} + \omega^2\mu\epsilon\vec{E} = 0. \tag{2.21}$$

Equation (2.21) is known as the Helmholtz equation or the wave equation for $\vec{E}$. The same mathematical derivation can be performed for the $\vec{H}$ field, yielding the wave equation:

$$\nabla^2\vec{H} + \omega^2\mu\epsilon\vec{H} = 0. \tag{2.22}$$

Analyzing the wave equations (2.21) and (2.22), one can find the velocity of propagation to be $(\mu\epsilon)^{-1/2}$. In free space this velocity is equal to the speed of light. Another important property of propagating waves is the wavenumber, or propagation constant which is defined as $k = \omega\sqrt{\mu\epsilon}$.

2.2.3 Plane waves in lossless mediums

The simplest mathematical solutions to the Helmholtz equations, are basic plane waves traveling along one of the axles of the referential system. Considering an electric field with only $\hat{x}$ component and no variation in the x and y directions, then $\partial\vec{E}/\partial x = \partial\vec{E}/\partial y = 0$, and equation (2.21) reduces to:

$$\frac{\partial^2 E_x}{\partial z^2} + k^2 E_x = 0. \tag{2.23}$$

Equation (2.23) is a second-order linear differential equation and the solutions to this equation can be easily obtained in the form:

$$E_x(z) = E^+ e^{-jkz} + E^- e^{jkz}, \tag{2.24}$$

where E^+ and E^- are constant values and represent the amplitudes of the forward and backward propagating waves respectively. Applying (2.17) to the electric field (2.24) we obtain the magnetic field equations:

$$H_x(z) = 0, \tag{2.25}$$

$$H_z(z) = 0, \tag{2.26}$$

$$H_y(z) = \frac{1}{\eta}[E^+ e^{-jkz} - E^- e^{jkz}], \tag{2.27}$$

where, $\eta = \omega\mu/k = \sqrt{\mu/\epsilon}$ is the wave impedance, and is defined as the ration of the $\vec{E}$ and $\vec{H}$ fields. A more detailed explanation and mathematical derivation can be found in [5, 16].

2.2.4 Plane waves in lossy mediums

We now consider propagation in a lossy medium. A medium is considered lossy when it is conductive. In a medium with conductivity σ a conduction current density of the form $\vec{J} = \sigma\vec{E}$ will exist and the Maxwell's equations for a lossy medium then becomes:

$$\nabla \times \vec{E} = -j\omega\mu\vec{H}, \tag{2.28}$$

$$\nabla \times \vec{H} = j\omega\epsilon\vec{E} + \sigma\vec{E}. \tag{2.29}$$

Following the same mathematical derivation as for the lossless case, the wave equation for the electric field is now given by:

$$\nabla^2\vec{E} + \omega^2\mu\epsilon\left(1 - j\frac{\sigma}{\omega\epsilon}\right)\vec{E} = 0. \tag{2.30}$$

Comparing equation (2.30) with its lossless counterpart (2.21), we can see that the propagation constant $\omega^2\mu\epsilon$ is replaced by the complex expression $\omega^2\mu\epsilon[1-j\sigma/\omega\epsilon]$. The square root of this complex expression is referred to as the "complex propagation constant" of

the medium and is defined as

$$\gamma = \alpha + j\beta = j\omega\sqrt{\mu\epsilon}\sqrt{1 - j\frac{\sigma}{\omega\epsilon}}. \tag{2.31}$$

Assuming again an electric field with only $\hat{x}$ component and no variation in the x and y directions, equation (2.30) reduces to

$$\frac{\partial^2 E_x}{\partial z^2} - \gamma^2 E_x = 0. \tag{2.32}$$

with solutions

$$E_x(z) = E^+ e^{-\gamma z} + E^- e^{\gamma z}, \tag{2.33}$$

The forward propagating wave has a propagation factor of the form

$$e^{-\gamma z} = e^{-\alpha z} e^{-j\beta z} \tag{2.34}$$

which represents a wave traveling in the positive direction with phase velocity $v_p = \omega/\beta$ and an exponential damping factor due to the attenuation constant α. If there is no loss, $\sigma = 0$, and we end up with $\gamma = jk$, $\alpha = 0$ and $\beta = k$.

Similarly to the lossless case, the solutions for the magnetic field have given by

$$H_y(z) = \frac{1}{\eta}[E^+ e^{-\gamma z} - E^- e^{\gamma z}] \tag{2.35}$$

where η is the wave impedance, and for the lossy case is of the form

$$\eta = \frac{j\omega\mu}{\gamma}. \tag{2.36}$$

η is thus complex but reduces to the lossless case ($\eta = \sqrt{\mu/\epsilon}$) when $\sigma = 0$.

2.2.5 General guided wave solutions

So far we have solved Maxwell's equations for the particular case of electromagnetic plane waves propagating in a given medium in a given direction. This is called unguided wave propagation. We are now going to introduce the wave propagation on guiding structures, namely transmission lines and waveguides.

Waveguides structures are typically constituted by one enclosed conductor with a specific cross-section shape (usually rectangular or circular cross-sections). On the other

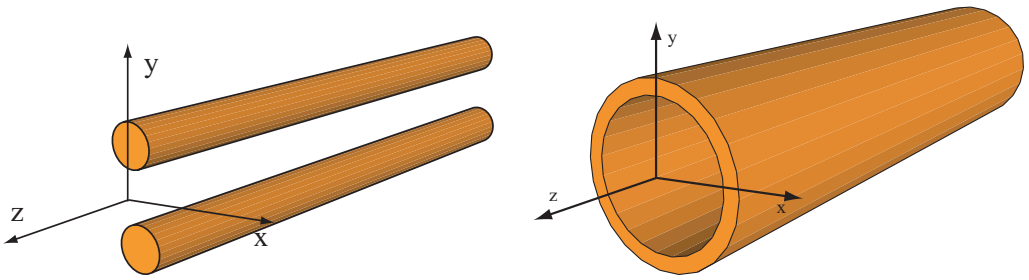

(a) Transmission line. (b) Circular waveguide.

FIGURE 2.1: EM wave guiding structures.

hand, transmission lines are composed by two or more conductors. In Figure 2.1 an example of both a transmission line and a waveguide are illustrated. Both structures are characterized by conductor boundaries that are parallel to the z-axis and are assumed to be uniform in the z direction.

Given a particular conductor geometry for a transmission line or waveguide, only certain patterns of electric and magnetic fields (modes) can exist for propagating waves. This modes must be solutions to the wave equation and at the same time they must satisfy the appropriate boundary conditions for the fields.

The propagating modes along a transmission line or waveguide are classified according to which field components are present in the propagating wave. The field components in the direction of wave propagation are called the longitudinal components and those perpendicular to the direction of propagation are defined as the transverse components.

Assuming a waveguide or transmission line with its longitudinal axis aligned with the z-axis (direction of propagation) as illustrated in Figure 2.1, we may classify the propagating modes as:

1. Transverse electric (TE) modes - The electric field is perpendicular to the direction of propagation, and so there is no electric field component in the longitudinal direction. The magnetic field has both transverse and longitudinal components ($E_z = 0, H_z \neq 0$).

2. Transverse magnetic (TM) modes - The magnetic field is perpendicular to the direction of propagation, and so there is no magnetic field component in the longitudinal direction. The electric field has both transverse and longitudinal components ($E_z \neq 0, H_z = 0$).

3. Hybrid modes - Both the electric and magnetic fields have longitudinal components ($E_z \neq 0, H_z \neq 0$). Hybrid modes are usually found in waveguides with inhomogeneous dielectrics and optical fibers.

4. Transverse electromagnetic (TEM) modes - Both the electric and magnetic field components are perpendicular to the direction of propagation, with no longitudinal components ($E_z = 0, H_z = 0$).

5. Quasi-TEM modes - Modes which approximate true TEM modes when the frequency is sufficiently small.

TE and TM modes are usually associated with waves propagating in waveguides. These modes are characterized by a cutoff frequency bellow which they do not propagate. On the other hand, TEM modes are usually related with waves propagating in transmission lines. Unlike TM and TE modes, TEM modes do not have a cutoff frequency. TE and TM modes can also exist on transmission lines but are generally undesirable.

As for the case of plane waves, the general solutions associated with waves propagating on a guiding structure can be derived from the Maxwell equations. For that, we are going to assume that the guiding structure is infinitely long , oriented along the z-axis, constructed from ideal materials and therefore lossless and uniform along its length. Assuming a steady-state sinusoidal time dependence of the fields, a source-free region for the transmission line or waveguide and no external current sources, Maxwell's equations reduce to equations (2.17) and (2.18). By expanding the curl operator in both equations in rectangular coordinates, the three components of both magnetic and electric are given by:

$$\frac{\partial E_z}{\partial y} - \frac{\partial E_y}{\partial z} = -jw\mu H_x, \tag{2.37}$$

$$\frac{\partial E_x}{\partial z} - \frac{\partial E_z}{\partial x} = -jw\mu H_y, \tag{2.38}$$

$$\frac{\partial E_y}{\partial x} - \frac{\partial E_x}{\partial y} = -jw\mu H_z, \tag{2.39}$$

$$\frac{\partial H_z}{\partial y} - \frac{\partial H_y}{\partial z} = jw\mu E_x, \tag{2.40}$$

$$\frac{\partial H_x}{\partial z} - \frac{\partial H_z}{\partial x} = jw\mu E_y, \tag{2.41}$$

$$\frac{\partial H_y}{\partial x} - \frac{\partial H_x}{\partial y} = jw\mu E_z. \tag{2.42}$$

Because we consider the guiding structure oriented along the z-axis, the waves within the structure shall propagate on the same direction, which means that both electric and magnetic fields have a z dependence of the form $e^{-j\beta z}$, yielding:

$$\vec{E}(x,y,z) = \hat{\vec{E}}(x,y)e^{-j\beta z}, \tag{2.43}$$

$$\vec{H}(x,y,z) = \hat{\vec{H}}(x,y)e^{-j\beta z}. \tag{2.44}$$

Substituting the previous couple of equations into equations (2.37) to (2.42), the expansion of Maxwell's equations (2.17) and (2.18) reduces to:

$$\frac{\partial E_z}{\partial y} + j\beta E_y = -jw\mu H_x, \tag{2.45}$$

$$-j\beta E_x - \frac{\partial E_z}{\partial x} = -jw\mu H_y, \tag{2.46}$$

$$\frac{\partial E_y}{\partial x} - \frac{\partial E_x}{\partial y} = -jw\mu H_z, \tag{2.47}$$

$$\frac{\partial H_z}{\partial y} + j\beta H_y = jw\mu E_x, \tag{2.48}$$

$$-j\beta H_x - \frac{\partial H_z}{\partial x} = jw\mu E_y, \tag{2.49}$$

$$\frac{\partial H_y}{\partial x} - \frac{\partial H_x}{\partial y} = jw\mu E_z. \tag{2.50}$$

The above six equations are very useful general equations that are valid for any wave (guided or unguided) propagating in the z-direction in a source-free region with a propagation constant of β. By re-arranging equations (2.45) to (2.50) they can be solved for the transverse fields components in terms of the longitudinal field components:

$$E_x = \frac{-j}{k_c^2}\left(\beta\frac{\partial E_z}{\partial x} + \omega\mu\frac{\partial H_z}{\partial y}\right), \tag{2.51}$$

$$E_y = \frac{j}{k_c^2}\left(-\beta\frac{\partial E_z}{\partial y} + \omega\mu\frac{\partial H_z}{\partial x}\right), \tag{2.52}$$

$$H_x = \frac{j}{k_c^2}\left(\omega\epsilon\frac{\partial E_z}{\partial y} - \beta\frac{\partial H_z}{\partial x}\right), \tag{2.53}$$

$$H_y = \frac{-j}{k_c^2}\left(\omega\epsilon\frac{\partial E_z}{\partial x} + \beta\frac{\partial H_z}{\partial y}\right), \tag{2.54}$$

where k_c is the cutoff wavenumber defined by:

$$k_c^2 = k^2 - \beta^2 \tag{2.55}$$

and

$$k = \omega\sqrt{\mu\epsilon} = \frac{2\pi}{\lambda} \tag{2.56}$$

is the wavenumber of the material filling the transmission line or waveguide.

2.2.5.1 TE waves

Recalling that TE waves are characterized by $E_z = 0$ and $H_z \neq 0$, equations (2.51) to (2.54) can be further simplified, yielding the expressions of the transverse fields for the TE modes in terms of the longitudinal magnetic field H_z:

$$E_x = \frac{-j\omega\mu}{k_c^2}\frac{\partial H_z}{\partial y}, \tag{2.57}$$

$$E_y = \frac{j\omega\mu}{k_c^2}\frac{\partial H_z}{\partial x}, \tag{2.58}$$

$$H_x = \frac{-j\beta}{k_c^2}\frac{\partial H_z}{\partial x}, \tag{2.59}$$

$$H_y = \frac{-j\beta}{k_c^2}\frac{\partial H_z}{\partial y}. \tag{2.60}$$

By inspection of the above equations, its easily seen that the cutoff wavenumber k_c must be non-zero in order to avoid an indeterminate result for the transverse field components of TE modes. This means that the guiding structure must be operated above a particular cutoff frequency in order for the corresponding TE mode to propagate.

In order to determine the transverse fields of the TE modes we first have to solve longitudinal component H_z from the Helmholtz wave equation:

$$\frac{\partial^2 H_z}{\partial^2 x^2} + \frac{\partial^2 H_z}{\partial^2 y^2} + \frac{\partial^2 H_z}{\partial^2 z^2} + k^2 H_z = 0, \tag{2.61}$$

but, because $\vec{H}(x, y, z) = \hat{\vec{H}}(x, y)e^{-j\beta z}$ it can be reduced to

$$\frac{\partial^2 \hat{H}_z}{\partial^2 x^2} + \frac{\partial^2 \hat{H}_z}{\partial^2 y^2} - \beta^2 \hat{H}_z + k^2 \hat{H}_z = 0, \tag{2.62}$$

and finally recalling that $k_c^2 = k^2 - \beta^2$, we end up with

$$\frac{\partial^2 \hat{H}_z}{\partial^2 x^2} + \frac{\partial^2 \hat{H}_z}{\partial^2 y^2} + k_c^2 \hat{H}_z = 0. \tag{2.63}$$

The above equation represents a reduced Helmholtz equation which can be solved for $\hat{H}_z(x, y)$ from the boundary conditions of the guiding structure geometry. Once $\hat{H}_z(x, y)$

is obtained, all of the transverse field components can be calculated by evaluating equations (2.57) to (2.60).

The wave impedance for TE modes is found from equations (2.57) to (2.60) as:

$$Z_{TE} = \frac{E_x}{H_y} = \frac{-E_y}{H_x} = \frac{\omega\mu}{\beta} = \frac{k\eta}{\beta}, \tag{2.64}$$

and it is frequency dependent.

2.2.5.2 TM waves

For the TM modes, the proceeding is the same as for TE case. TM waves are characterized by $E_z \neq 0$ and $H_z = 0$ and so, equations (2.51) to (2.54) can be further simplified, yielding the expressions of the transverse fields for the TM modes in terms of the longitudinal electric field E_z:

$$E_x = \frac{-j\beta}{k_c^2}\frac{\partial E_z}{\partial x}, \tag{2.65}$$

$$E_y = \frac{-j\beta}{k_c^2}\frac{\partial E_z}{\partial y}, \tag{2.66}$$

$$H_x = \frac{j\omega\epsilon}{k_c^2}\frac{\partial E_z}{\partial y}, \tag{2.67}$$

$$H_y = \frac{-j\omega\epsilon}{k_c^2}\frac{\partial E_z}{\partial x}. \tag{2.68}$$

By inspection of the above equations, its easily seen that the cutoff wavenumber k_c must be non-zero in order to avoid an indeterminate result for the transverse field components of TM modes. This means that the guiding structure must be operated above a particular cutoff frequency in order for the corresponding TM mode to propagate.

In order to determine the transverse fields of the TM modes we first have to solve longitudinal component E_z from the Helmholtz wave equation:

$$\frac{\partial^2 E_z}{\partial^2 x^2} + \frac{\partial^2 E_z}{\partial^2 y^2} + \frac{\partial^2 E_z}{\partial^2 z^2} + k^2 E_z = 0, \tag{2.69}$$

but, because $\vec{E}(x,y,z) = \hat{\vec{E}}(x,y)e^{-j\beta z}$ it can be reduced to

$$\frac{\partial^2 \hat{E}_z}{\partial^2 x^2} + \frac{\partial^2 \hat{E}_z}{\partial^2 y^2} - \beta^2 \hat{E}_z + k^2 \hat{E}_z = 0, \tag{2.70}$$

and finally recalling that $k_c^2 = k^2 - \beta^2$, we end up with

$$\frac{\partial^2 \hat{E}_z}{\partial^2 x^2} + \frac{\partial^2 \hat{E}_z}{\partial^2 y^2} + k_c^2 \hat{E}_z = 0. \tag{2.71}$$

The above equation represents a reduced Helmholtz equation which can be solved for $\hat{H}_z(x, y)$ from the boundary conditions of the guiding structure geometry. Once $\hat{E}_z(x, y)$ is obtained, all of the transverse field components can be calculated by evaluating equations (2.65) to (2.68).

The wave impedance for TM modes is determined from equations (2.65) to (2.68) as:

$$Z_{TM} = \frac{E_x}{H_y} = \frac{-E_y}{H_x} = \frac{\beta}{\omega\epsilon} = \frac{\beta\eta}{k}, \tag{2.72}$$

and it is frequency dependent.

2.2.5.3 TEM waves

TEM waves are characterized by $E_z = 0$ and $H_z = 0$. Evaluating equations (2.51) to (2.54) for TEM waves we see that the transverse fields are non-zero only when the cutoff wavenumber is zero ($k_c = 0$):

$$k_c^2 = k^2 - \beta^2 = 0 \quad \Longrightarrow \quad \beta = k = \omega\sqrt{\mu\epsilon}, \tag{2.73}$$

which means that TEM modes do not have a cutoff frequency and as such any guiding structure supporting TEM modes can be operated for all non-zero frequencies (assuming TEM operation).

For $k_c = 0$, equations (2.51) to (2.54) produce an indeterminate result, therefore, the relationships between the transverse fields of the TEM modes can only be determined

by rewriting equations (2.45) to (2.50) with $E_z = 0$ and $H_z = 0$, yielding:

$$E_x = \frac{\omega\mu}{\beta} H_y, \tag{2.74}$$

$$E_y = \frac{-w\mu}{\beta} H_x, \tag{2.75}$$

$$\frac{\partial E_y}{\partial x} = \frac{\partial E_x}{\partial y}, \tag{2.76}$$

$$H_x = \frac{-\omega\epsilon}{\beta} E_y, \tag{2.77}$$

$$H_y = \frac{\omega\epsilon}{\beta} E_x, \tag{2.78}$$

$$\frac{\partial H_y}{\partial x} = \frac{\partial H_x}{\partial y}. \tag{2.79}$$

Combining equation (2.74) and (2.78) we can eliminate H_x to obtain

$$E_x = \frac{\omega^2\mu\epsilon}{\beta^2} E_x \quad \Longrightarrow \quad \beta = \omega\sqrt{\mu\epsilon} = k, \tag{2.80}$$

which is the same result as in equation (2.73).

In order to calculate the fields, we once again resort to the Helmholtz wave equation and so, for the electric field:

$$\nabla^2 \vec{E} + k^2 \vec{E} = 0. \tag{2.81}$$

Recalling that $\vec{E}(x, y, z) = \hat{\vec{E}}(x, y)e^{-j\beta z}$, the above equation can be reduced to

$$\nabla_t^2 \hat{\vec{E}} - \beta^2 \hat{\vec{E}} + k^2 \hat{\vec{E}} = 0 \quad \Longrightarrow \quad \nabla_t^2 \hat{\vec{E}} + k_c^2 \hat{\vec{E}} = 0, \tag{2.82}$$

where $\nabla_t^2 = \partial^2/\partial x^2 + \partial^2/\partial y^2$ is the Laplacian operator in the transverse dimension. For TEM modes $k_c = 0$ and the longitudinal components of the fields are null, therefore the above equation simplifies to

$$\nabla_t^2 \hat{\vec{E}}_t = 0, \tag{2.83}$$

where $\hat{\vec{E}}_t$ represents the transverse components of the electric field. The same mathematical derivation can be applied to the magnetic field yielding:

$$\nabla_t^2 \hat{\vec{H}}_t = 0, \tag{2.84}$$

where $\hat{\vec{H}}_t$ represents the transverse components of the magnetic field.

According to equations (2.83) and (2.84), the transverse fields of the TEM modes

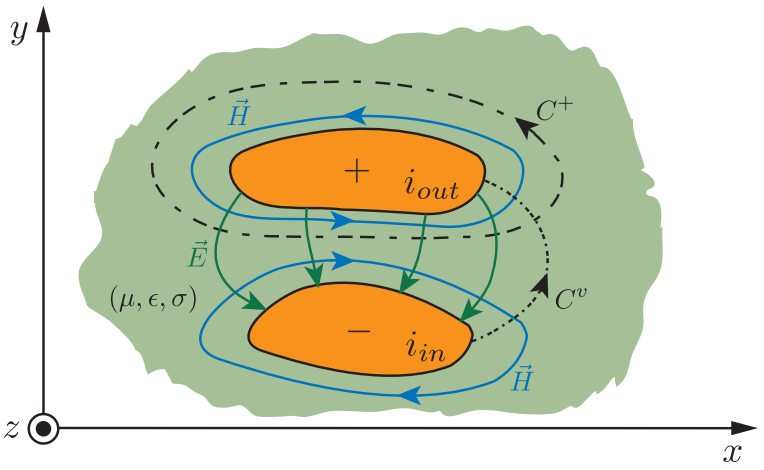

FIGURE 2.2: Transmission line cross-section.

must satisfy Laplace's equation with boundary conditions defined by the geometry of the guiding structure, just like the static fields which would exist on the guiding structure for a null operation frequency:

$$\nabla_t^2 \Phi(x, y) = 0, \tag{2.85}$$

where $\Phi(x, y)$ is the scalar potential.

Thus, for example in a transmission line, the TEM transverse fields $\hat{\vec{E}}_t(x, y)$ and $\hat{\vec{H}}_t(x, y)$ are identical to the static fields for that transmission line [5, 16].

As in the previous cases, the wave impedance for TEM modes is defined from the ratios of the electric and magnetic field components. From equations (2.74) to (2.79) it can be found that:

$$Z_{TEM} = \frac{E_x}{H_y} = \frac{-E_y}{H_x} = \sqrt{\frac{\mu}{\epsilon}} = \eta \tag{2.86}$$

We can see that the wave impedance for TEM modes is the same of that of plane waves in a lossless medium as proved previously. This is because, by nature, plane waves are TEM mode waves.

2.3 Transmission lines

The term "transmission line" in electromagnetics is commonly reserved for those structures which are capable of guiding TEM waves. Transmission lines are a special class of the more general electromagnetic waveguide. As referred before, TEM waves can only be guided by structures that contain two or more separate conductors. Coaxial lines, parallel plates and two-wire lines are some examples of practical transmission-lines.

Figure 2.2 illustrates the electric and magnetic field lines associated with the TEM mode on an arbitrary two-conductor transmission line. According to the definition of the TEM mode, there are no longitudinal fields associated with the wave traveling down the transmission line in the z-direction, and thus $E_z = H_z = 0$.

From the integral form of Maxwell's equations, namely equations (2.7) and (2.8) we get that the line integral of the electric and magnetic fields around the contour C^+ gives

$$\oint_{C^+} \vec{\mathcal{E}} \cdot \vec{dl} = -\mu \frac{\partial}{\partial t} \int_S \cancelto{0}{\vec{\mathcal{H}} \cdot \vec{ds},} \tag{2.87}$$

$$\oint_{C^+} \vec{\mathcal{H}} \cdot \vec{dl} = \epsilon \frac{\partial}{\partial t} \int_S \cancelto{0}{\vec{\mathcal{E}} \cdot \vec{ds}} + \int_S \vec{\mathcal{J}} \cdot \vec{ds} \tag{2.88}$$

where $\vec{ds} = ds\hat{z}$. The surface integrals of $\vec{E}$ and $\vec{H}$ are zero-valued since there is no longitudinal component of the fields on the transmission line. The line integrals of the fields then reduce to

$$\oint_{C^+} \vec{\mathcal{E}} \cdot \vec{dl} = 0, \tag{2.89}$$

$$\oint_{C^+} \vec{\mathcal{H}} \cdot \vec{dl} = I, \tag{2.90}$$

where $I = \int_S \vec{\mathcal{J}} \cdot \vec{ds}$ is the total electric current flowing through the surface S.

These equations show that the transverse field distribution of the TEM mode on a transmission line is identical to the corresponding static distribution of the fields. As an example, the electric field of the TEM mode at any frequency has the same distribution as the electrostatic field of the capacity formed by the two conductors of the transmission line when charged by a DC voltage. The same happens with the magnetic field. For any frequency the TEM mode has the same distribution as the magnetostatic field when the conductors are carrying a DC current.

Considering now the contour C^v in the electric field line integral, we find that

$$\int_{C^v} \vec{E} \cdot \vec{dl} = -\int_-^+ \vec{E}_t \cdot \vec{dl} = V \tag{2.91}$$

where V is the voltage between the two conductors.

Equations (2.90) and (2.91) show that we may define a unique voltage and current at any point on a transmission line operating on TEM mode.

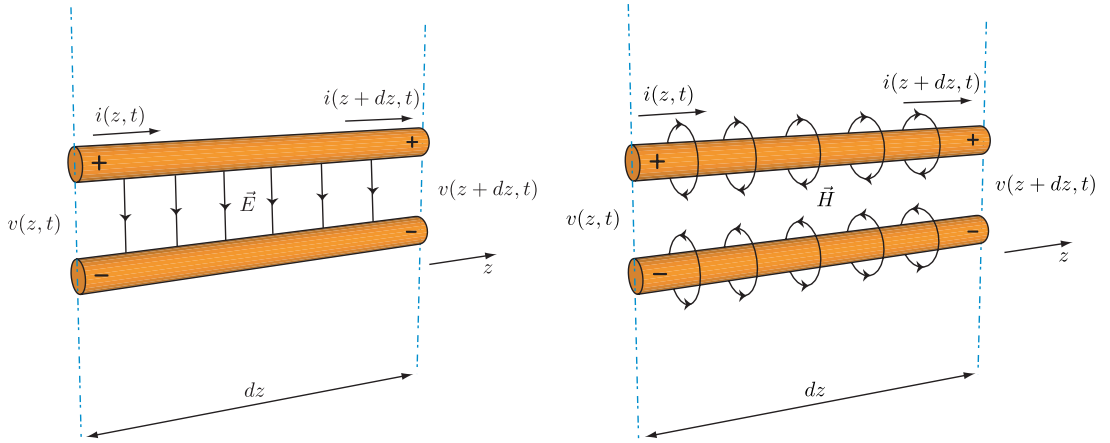

(a) Electric field lines. (b) Magnetic field lines.

FIGURE 2.3: Electromagnetic field lines in a infinitesimal section of transmission line.

Figure 2.3 illustrates the electromagnetic field lines on a infinitesimal short section of a two-wire transmission line with a length dz. If dz is much smaller that the wavelength, we then may consider the fields to be constant along that section length. These fields are perpendicular to each other and to the direction of propagation and thus, in Figure 2.3 TEM mode wave propagation is considered. The structure depicted in Figure 2.3 may also support other propagation modes, but we are only interested on the TEM mode which is the dominant mode.

One of the most important properties of TEM waves propagating on transmission lines is that the electromagnetic fields can be uniquely related to voltages and currents via equations (2.91) and (2.90). For this reason, we can analyze transmission line structures using circuit theory concepts through an equivalent lumped-element circuit, provided that we break the problem into small parts so that the circuit element dimensions will be much smaller than a wavelength.

From Figure 2.3(a) we see that an electric field is established by a potential difference between the two conductors which implies that the equivalent circuit model must contain a capacitor. On the other hand, Figure 2.3(b) illustrates the magnetic field induced by the current flowing on the conductors which points to the presence of an inductor in the circuit model.

Figure 2.4 outlines the equivalent circuit model for a small section of transmission line with length dz. Besides the shunt capacitance C and the series inductance L that originate from the electric and magnetic fields respectively, the equivalent circuit is also constituted by a series resistance R representing the ohmic losses on the conductors and

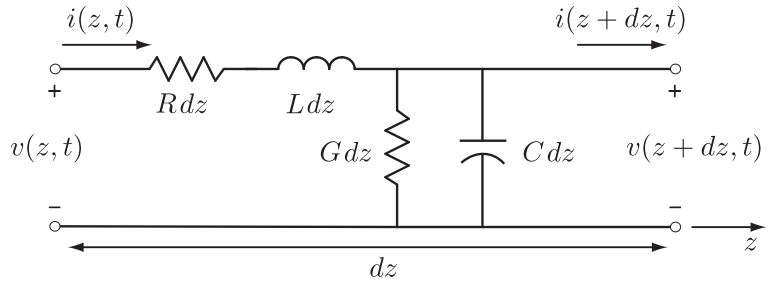

FIGURE 2.4: Transmission line lumped element equivalent circuit.

a shunt conductance G accounting for the losses of the propagation medium.

2.3.1 Waves on a transmission line

The use of an equivalent lumped-element circuit to model the transmission line allows for a deeper insight and better understanding on the operation of transmission lines. A finite length transmission line can be viewed as a cascade of very small sections (of constant field amplitudes) like the one in Figure 2.4. Therefore, the use of an equivalent circuit to model transmission lines facilitates the use of classical circuit theory techniques and concepts on the analysis of these kind of microwave structures.

Applying Kirchhoff's voltage law to the circuit of Figure 2.4 we know that the sum of all potential drops around must be zero and so we have:

$$v(z,t) - Rdzi(z,t) - Ldz\frac{\partial i(z,t)}{\partial t} - v(z+dz,t) = 0. \tag{2.92}$$

From the Kirchhoff's current law we get that the currents flowing into the output node must also be zero and so we can write:

$$i(z,t) - Gdzv(z+dz,t) - Cdz\frac{\partial v(z+dz,t)}{\partial t} - i(z+dz,t) = 0. \tag{2.93}$$

Dividing equation (2.92) and (2.92) by dz and considering the limit case as $dz \to 0$ we obtain:

$$\frac{\partial v(z,t)}{\partial z} = -Ri(z,t) - L\frac{\partial i(z,t)}{\partial t}, \tag{2.94}$$

$$\frac{\partial i(z,t)}{\partial z} = -Gv(z,t) - C\frac{\partial v(z,t)}{\partial t}. \tag{2.95}$$

Equations (2.94) and (2.95) are a set of two coupled equations known as the telegrapher equations. Assuming harmonic time dependence,

$$v(z,t) = V(z)e^{j\omega t}, \tag{2.96}$$

$$i(z,t) = I(z)e^{j\omega t}, \tag{2.97}$$

the telegrapher equations simplify to

$$\frac{dV(z)}{dz} = -(R + j\omega L)I(z), \tag{2.98}$$

$$\frac{dI(z)}{dz} = -(G + j\omega C)V(z). \tag{2.99}$$

Recalling the Maxwell equations (2.17) and (2.18), we note the similarity with the telegrapher equations. Therefore in order to decouple the telegrapher equations for the voltage and current, we can use the same mathematical development as in section 2.2.2 for the electric and magnetic fields, yielding the Helmholtz or wave equation:

$$\frac{d^2V(z)}{dz^2} - \gamma^2 V(z) = 0, \tag{2.100}$$

$$\frac{d^2I(z)}{dz^2} - \gamma^2 I(z) = 0, \tag{2.101}$$

where

$$\gamma = \alpha + j\beta = \sqrt{(R + j\omega L)(G + j\omega C)} \tag{2.102}$$

is the propagation constant which is complex and frequency dependent. The real part α being the attenuation factor (loss) and β the propagation constant. Equation (2.100) is a second-order linear differential equation and the solutions to this equation can be easily obtained in the form:

$$V(z) = V_0^+ e^{-\gamma z} + V_0^- e^{\gamma z}, \tag{2.103}$$

where V_0^+ and V_0^- are constant values and represent the amplitudes of the forward and backward propagating voltage waves respectively. Applying (2.98) to the voltage (2.103) gives the current in the line:

$$I(z) = \frac{\gamma}{R + j\omega L}(V_0^+ e^{-\gamma z} - V_0^- e^{\gamma z}), \tag{2.104}$$

just like with plane waves, the characteristic impedance of the transmission line can be defined as the ratio of voltage to current

$$Z_0 = \frac{R + j\omega L}{\gamma} = \sqrt{\frac{R + j\omega L}{G + j\omega C}} \tag{2.105}$$

and relates the voltage and current on the line as

$$Z_0 = \frac{V_0^+}{I_0^+} = \frac{-V_0^-}{I_0^-}. \tag{2.106}$$

The voltage and current on a transmission line are then given by

$$V(z) = V_0^+ e^{-\gamma z} + V_0^- e^{\gamma z}, \tag{2.107}$$

$$I(z) = \frac{V_0^+}{Z_0} e^{-\gamma z} - \frac{V_0^-}{Z_0} e^{\gamma z}. \tag{2.108}$$

The wave or phase velocity and wavelength are given by

$$v_p = \frac{\omega}{\beta}, \tag{2.109}$$

$$\lambda = \frac{2\pi}{\beta}. \tag{2.110}$$

2.3.2 The lossless line

In most of the practical cases, the transmission line losses are very small and as such can be neglected yielding the ideal transmission line. In this ideal case, the equivalent circuit of Figure 2.4 reduces only to the series inductance and to the shunt capacitance. So, setting $R = G = 0$ in equation (2.102) gives the propagation constant

$$\gamma = \alpha + j\beta = j\omega\sqrt{LC} \tag{2.111}$$

$$\Downarrow$$

$$\beta = \omega\sqrt{LC}. \tag{2.112}$$

From the last set of equations, we see that the attenuation constant α is zero. This is an expected result because the ideal transmission line is considered to be lossless. The characteristic impedance reduces to

$$Z_0 = \sqrt{\frac{L}{C}}. \tag{2.113}$$

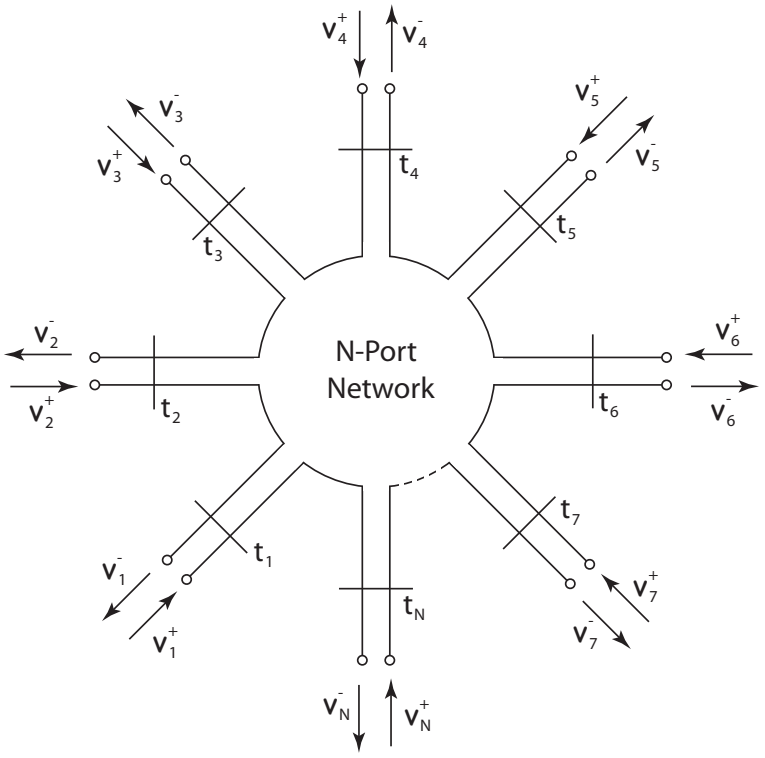

FIGURE 2.5: N-Port Network.

For lossless transmission lines the expressions for voltage and current are the same as before, except that now the propagation constant is given by $j\beta$ and thus

$$V(z) = V_0^+ e^{-j\beta z} + V_0^- e^{j\beta z}, \tag{2.114}$$

$$I(z) = \frac{V_0^+}{Z_0} e^{-j\beta z} - \frac{V_0^-}{Z_0} e^{j\beta z}. \tag{2.115}$$

The phase velocity, and wavelength are given by

$$v_p = \frac{1}{\sqrt{LC}}, \tag{2.116}$$

$$\lambda = \frac{2\pi}{\omega\sqrt{LC}}. \tag{2.117}$$

2.4 The scattering matrix

Like Y- and Z-parameters, the S-parameters completely describe an N-port microwave network as seen at its N ports, and so, are useful to represent a microwave device or circuit as a *black box*, where the "external" behaviour of this *black box* can be predicted without any knowledge about its contents.

From a practical point of view, voltages and currents can not be measured in a direct manner at microwave frequencies. In fact, in some microwave structures voltages may not be well defined, or even defined at all. Only in structures supporting TEM propagating modes is it possible to define voltages and currents as we have shown in Section 2.3. One the other hand, the measurement of incident, reflected and transmitted waves, comes up as a natural technique to represent the behavior of microwave devices. Therefore, and unlike the impedance and admittance parameters that relate the total voltages and currents at the ports, the S-parameters relate the waves incident on the ports with the waves reflected from those ports and also the waves transmitted to the other ports on the network. In order to provide a complete description of microwave systems, these parameters take into account both the magnitude and phase of the wave signals present at each terminal.

In other words, the S-parameters are basically another means for characterizing N-Port networks. They relate the traveling waves that are transmitted or reflected from a junction or terminal relative to the incident wave amplitudes and phase angles. S-parameters are conceptually simple, and capable of providing a detailed insight into a measurement and modeling problem.

In most cases, the scattered and incident waves are linearly related, therefore, the S-parameters are considered linear by default. The matrix describing this linear relationship is called the scattering matrix.

The work described in this thesis is essentially based on transmission lines theory, therefore TEM mode propagation is always implicit. For the rest of this section we shall consider S-parameters as the relation between voltage wave amplitudes at the ports of some N-Port network.

Consider the N-Port junction in Figure 2.5. V_n^+ is the amplitude of the voltage wave incident on terminal plane t_n and V_n^- is the amplitude of the voltage wave reflected from terminal t_n. The scattering matrix $[S]$ describing the relation between the incident and scattered waves for the N-Port or N-terminal network depicted in Figure 2.5 is then given as

$$\begin{bmatrix} V_1^- \\ V_2^- \\ \vdots \\ V_n^- \end{bmatrix} = \begin{bmatrix} S_{11} & S_{12} & \dots & S_{1n} \\ S_{21} & S_{22} & \dots & S_{2n} \\ \vdots & \vdots & \ddots & \vdots \\ S_{n1} & S_{n2} & \dots & S_{nn} \end{bmatrix} \begin{bmatrix} V_1^+ \\ V_2^+ \\ \vdots \\ V_n^+ \end{bmatrix} \tag{2.118}$$

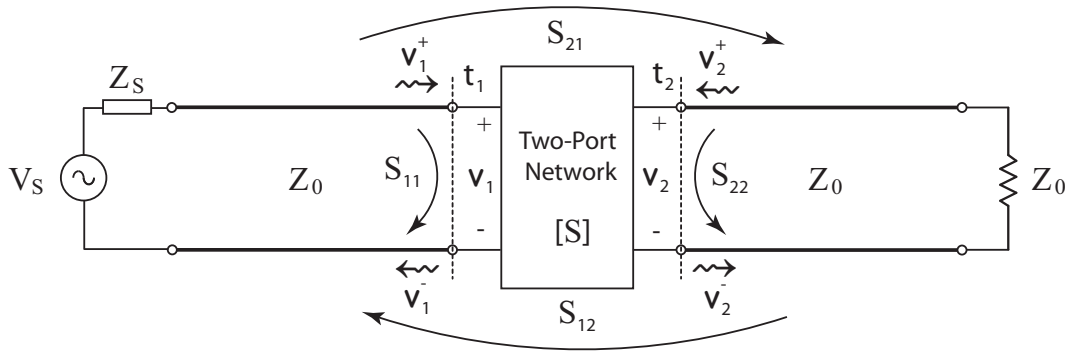

FIGURE 2.6: Two-Port Network.

or

$$[V^-] = [S][V^+], \tag{2.119}$$

where $[V^-]$ are the amplitudes of the reflected waves, $[V^+]$ the amplitudes of the incident waves and $[S]$ is the scattering matrix. The individual elements of the scattering matrix are defined as

$$S_{ij} = \left.\frac{V_i^-}{V_j^+}\right|_{V_k^+=0\ \forall\ k\neq j}. \tag{2.120}$$

Each element S_{ij} of the scattering matrix is calculated by driving terminal (or port) j with an incident wave of voltage amplitude V_j^+, and measuring the scattered voltage wave V_i^- exiting terminal i. This is done considering that there are no incident waves on all the other ports, and also that they should be terminated with matched loads to avoid reflections.

2.4.1 S-parameters and time average power

We have described the relation between voltage waves and the S-parameters. However, the concept of transmitted and reflected power is also of extreme importance. We now derive the relation between the S-parameters and time average power. Figure 2.6 illustrates a generic two-port network connected to a microwave source and with a matched load. From the definition of the S-parameters we calculate the voltage wave amplitudes as

$$V_1^- = S_{11}V_1^+ + S_{12}V_2^+ \tag{2.121}$$

$$V_2^- = S_{21}V_1^+ + S_{22}V_2^+. \tag{2.122}$$

The total voltage at port 1 is the sum of both the forward and backwards traveling waves, so

$$V_1 = V_1^+ + V_1^-, \tag{2.123}$$

and the total time average power P_{av} delivered to port 1 is given by

$$P_{av} = \frac{1}{2} Re\{V_n I_n^*\} = P_{inc} - P_{ref}. \tag{2.124}$$

P_{inc} is the incident power on port 1 and is due to the forward propagating wave,

$$P_{inc} = \frac{|V_1^+|^2}{2Z_0}, \tag{2.125}$$

on the other hand, P_{ref} is the reflected power carried by the backward propagating wave,

$$P_{ref} = \frac{|V_1^-|^2}{2Z_0}. \tag{2.126}$$

Since port 2 is terminated in a matched load no reflections will occur at the load and so, $V_2^+ = 0$. Then,

$$V_2 = V_2^-, \tag{2.127}$$

and consequently, the transmitted power is

$$P_{trans} = \frac{|V_2^-|^2}{2Z_0}. \tag{2.128}$$

which is also the total average power at port 2.

We can now relate the time average power quantities at each port to the S-parameters. Using (2.125) and (2.126) the ratio of reflected and incident power is given by

$$\frac{P_{ref}}{P_{inc}} = \frac{|V_1^-|^2}{|V_1^+|^2} = \left| \frac{V_1^-}{V_1^+} \right|^2. \tag{2.129}$$

Since port 2 is matched, $V_2^+ = 0$. Then, from equation (2.120) and by rearranging equation (2.121) we obtain

$$S_{11} = \left. \frac{V_1^-}{V_1^+} \right|_{V_2^+ = 0}. \tag{2.130}$$

Equation (2.129) then simplifies to

$$\frac{P_{ref}}{P_{inc}} = |S_{11}|^2, \tag{2.131}$$

which teach us that the relative reflected time average power at port 1 equals the squared magnitude of the S_{11} parameter when port 2 is terminated in a matched load.

The same procedure can be applied at second port side. Using equations (2.125) and (2.128), the ratio of transmitted and incident time average power is

$$\frac{P_{trans}}{P_{inc}} = \frac{|V_2^-|^2}{|V_1^+|^2} = \left|\frac{V_2^-}{V_1^+}\right|^2 . \tag{2.132}$$

Moreover, from (2.122) and since $V_2^+ = 0$:

$$\frac{P_{trans}}{P_{inc}} = |S_{21}|^2. \tag{2.133}$$

The last result states that the relative transmitted power to port 2 equals the squared magnitude of the S_{21} parameter when port 2 is terminated in a matched load.

An extremely useful physical understanding of the S-parameters as time average power ratios is provided by equations (2.131) and (2.133). Please note that these equations are still valid regardless of the gain or loss of the network. Nevertheless, if a lossless network is considered, other important relations can be developed using equations (2.131) and (2.133). We know that for a lossless network the $[S]$ matrix must be unitary and so, as a direct result of this

$$S_{11}S_{11}^* + S_{21}S_{21}^* = 1 \quad \Rightarrow \quad |S_{11}|^2 + |S_{21}|^2 = 1 \tag{2.134}$$

$$S_{12}S_{12}^* + S_{22}S_{22}^* = 1 \quad \Rightarrow \quad |S_{12}|^2 + |S_{22}|^2 = 1 \tag{2.135}$$

Considering the network of Figure 2.5 where port two is connected to a matched load and using (2.131) and (2.133) equation (2.134) can be rewritten as

$$P_{inc} = P_{trans} + P_{ref}. \tag{2.136}$$

From the last equation we conclude that (2.134) can be interpreted as a statement of conservation of power for the network. If on the other hand port 2 is set to a different system characteristic impedance than that of port 1, equation (2.134) is still valid but is no longer a conservation of power statement for the network. The next Section shall address this problem.

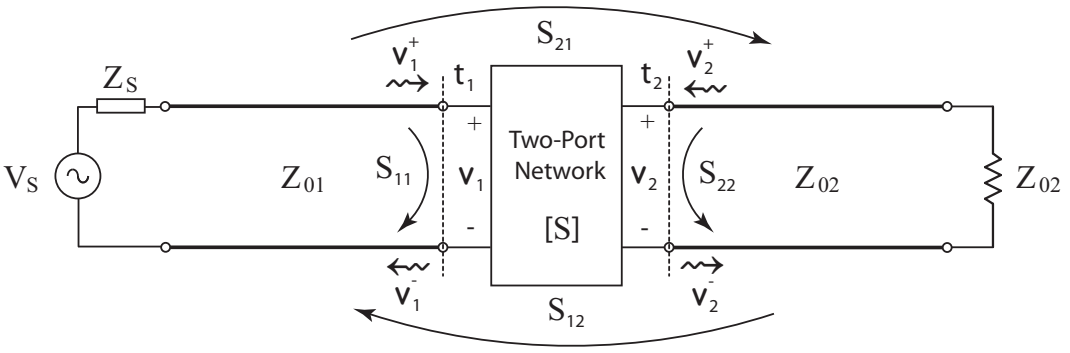

FIGURE 2.7: Two-Port Network.

2.4.2 Generalized scattering parameters

Up to now, the definition of the S-parameters of a N-Port network was done considering that all ports had the same characteristic impedance. However, in the cases that the characteristic impedance of some ports the network is connected to are to be different, it becomes necessary to redefine the S-parameters so that $|S_{ij}|^2$ still relates to the time average power flow.

Figure 2.7 exemplify a two-port network where port 1 and port 2 have characteristic impedances values of Z_{01} and Z_{02} respectively.

From the definition of S-parameters and because port 2 is terminated in a matched load, the incident, reflected and transmitted time average power are respectively,

$$P_{inc} = \frac{|V_1^+|^2}{2Z_{01}}, \tag{2.137}$$

$$P_{ref} = \frac{|V_1^-|^2}{2Z_{01}}, \tag{2.138}$$

$$P_{trans} = \frac{|V_2^-|^2}{2Z_{02}}. \tag{2.139}$$

Following the same derivation as in the previous Section, the ratio of reflected and incident power is

$$\frac{P_{ref}}{P_{inc}} = \frac{|V_1^-|^2/Z_{01}}{|V_1^+|^2/Z_{01}} = \left|\frac{V_1^-}{V_1^+}\right|^2 = |S_{11}|^2, \tag{2.140}$$

which is the same result as for the case of equal characteristic impedances. However, for the ratio of transmitted and incident power we get

$$\frac{P_{trans}}{P_{inc}} = \frac{|V_2^-|^2/Z_{02}}{|V_1^+|^2/Z_{01}} \neq |S_{21}|^2. \tag{2.141}$$

In order to preserve the useful interpretation of $|S_{ij}|^2$ as a relative time average power

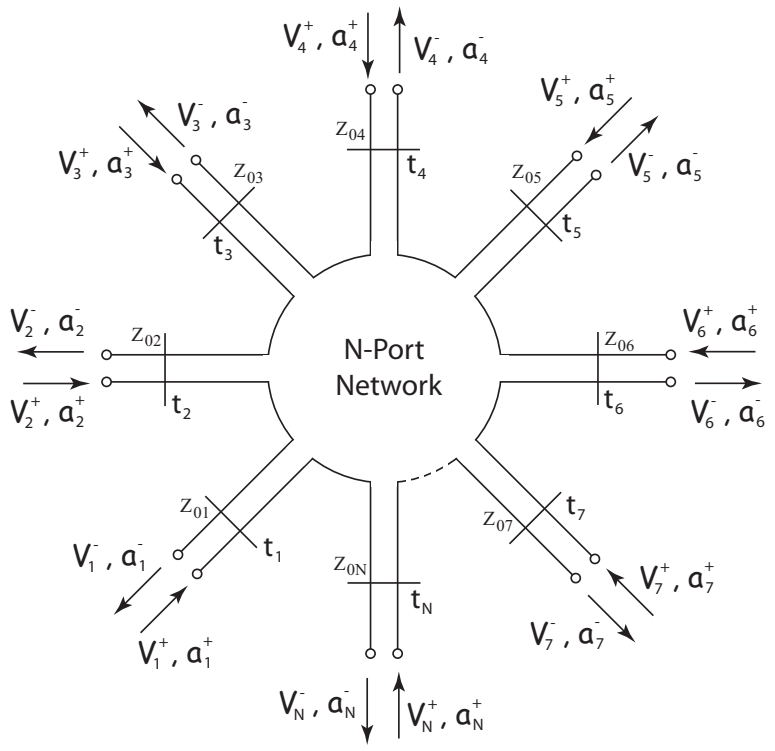

FIGURE 2.8: N-Port Network.

flow, it is necessary to redefine the S-parameters for the cases where the port impedances are different. Defining $|S_{21}|$ as

$$|S_{21}| = \frac{|V_2^-|\sqrt{Z_{01}}}{|V_1^+|\sqrt{Z_{02}}} \tag{2.142}$$

would preserve this interpretation. So, for a N-port network like the one in Figure 2.8, where the characteristic impedances of the ports are different, a new set of wave amplitudes, the normalized wave amplitudes, must be defined as

$$a_n^+ = \frac{V_n^+}{\sqrt{Z_{0n}}}, \tag{2.143}$$

$$a_n^- = \frac{V_n^-}{\sqrt{Z_{0n}}}. \tag{2.144}$$

In the previous equations, a_n^+ represent the incident wave at the nth port, and a_n^- represents the reflected wave from that port. This redefinition leads to the so-called generalized [S] matrix

$$[a^-] = [S][a^+], \tag{2.145}$$

and the individual elements of the scattering matrix are know defined as

$$S_{ij} = \left.\frac{a_i^-}{a_j^+}\right|_{a_k^+=0\ \forall\ k\neq j} = \left.\frac{V_i^-\sqrt{Z_{0j}}}{V_j^+\sqrt{Z_{0i}}}\right|_{V_k^+=0\ \forall\ k\neq j}, \tag{2.146}$$

and are referred to as the generalized S-parameters. Please note that they reduce to the regular S-parameters when all port characteristic impedances are equal.

The total voltage and current at the terminal plane for port n with characteristic impedance Z_{0n} are now

$$V_n = V_n^+ + V_n^- = \sqrt{Z_{0n}}(a_n^+ + a_n^-), \tag{2.147}$$

$$I_n = \frac{1}{Z_{0n}}(V_n^+ - V_n^-) = \frac{1}{\sqrt{Z_{0n}}}(a_n^+ - a_n^-). \tag{2.148}$$

Lastly, the time average power delivered to port n is

$$\begin{aligned} P_{av} &= \frac{1}{2}Re\{V_n I_n^*\} = \frac{1}{2}Re\{|a_n^+|^2 - |a_n^-|^2 + (a_n^-(a_n^+)^* - a_n^+(a_n^-)^*)\} \\ &= \frac{1}{2}|a_n^+|^2 - \frac{1}{2}|a_n^-|^2, \end{aligned} \tag{2.149}$$

where $(a_n^-(a_n^+)^* - a_n^+(a_n^-)^*)$ is imaginary.

From equation (2.149) is easily seen that

$$P_{inc} = \frac{1}{2}|a_n^+|^2, \tag{2.150}$$

$$P_{ref} = \frac{1}{2}|a_n^-|^2, \tag{2.151}$$

where P_{inc} is the power incident on the nth port and P_{ref} is that reflected from the same port.

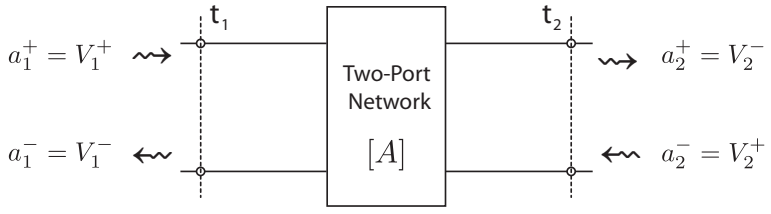

FIGURE 2.9: Microwave network represented as a wave-amplitude transmission matrix.

2.5 The wave-amplitude transmission matrix

Many times, microwave networks consist of a cascade connection of two or more N-port networks. In this situation it is more convenient to represent each individual network by a transmission matrix that relates the incident and reflected wave amplitudes on the input side of the network to those on the output side. In this way, the overall transmission matrix for the cascade connection can be easily calculated by multiplying the individual transmission matrices that compose the complete cascade connection.

In Figure 2.9 is depicted a two-port microwave network represented by its corresponding wave-amplitude transmission matrix $[T]$, which is defined as

$$\begin{bmatrix} a_1^+ \\ a_1^- \end{bmatrix} = \begin{bmatrix} A_{11} & A_{12} \\ A_{21} & A_{22} \end{bmatrix} \begin{bmatrix} a_2^+ \\ a_2^- \end{bmatrix}. \tag{2.152}$$

In the case of a cascade connection of networks as depicted in Figure 2.10 we have

$$\begin{bmatrix} a_1^+ \\ a_1^- \end{bmatrix} = \begin{bmatrix} A_{11}^1 & A_{12}^1 \\ A_{21}^1 & A_{22}^1 \end{bmatrix} \begin{bmatrix} A_{11}^2 & A_{12}^2 \\ A_{21}^2 & A_{22}^2 \end{bmatrix} \begin{bmatrix} A_{11}^3 & A_{12}^3 \\ A_{21}^3 & A_{22}^3 \end{bmatrix} \cdots \begin{bmatrix} A_{11}^n & A_{12}^n \\ A_{21}^n & A_{22}^n \end{bmatrix} \begin{bmatrix} a_n^+ \\ a_n^- \end{bmatrix}. \tag{2.153}$$

Let us consider the network of Figure 2.10. We know from the previous section that the scattering matrix $[S]$ for this network is defined as

$$\begin{bmatrix} a_1^- \\ a_2^+ \end{bmatrix} = \begin{bmatrix} V_1^- \\ V_2^- \end{bmatrix} = \begin{bmatrix} S_{11} & S_{12} \\ S_{21} & S_{22} \end{bmatrix} \begin{bmatrix} V_1^+ \\ V_2^+ \end{bmatrix} = \begin{bmatrix} S_{11} & S_{12} \\ S_{21} & S_{22} \end{bmatrix} \begin{bmatrix} a_1^+ \\ a_2^- \end{bmatrix} \tag{2.154}$$

and can be expanded as

$$a_1^- = S_{11}a_1^+ + S_{12}a_2^-, \tag{2.155}$$

$$a_2^+ = S_{21}a_1^+ + S_{22}a_2^-. \tag{2.156}$$

The relationship between the elements of the $[T]$ matrix and those of the $[S]$ matrix are easily deduced by solving the previous two equations for a_1^+ and a_1^- yielding [16]

$$\begin{bmatrix} a_1^+ \\ a_1^- \end{bmatrix} = \begin{bmatrix} \frac{1}{S_{12}} & \frac{-S_{22}}{S_{12}} \\ \frac{S_{11}}{S_{12}} & \frac{S_{12}^2 - S_{11}S_{22}}{S_{12}} \end{bmatrix} \begin{bmatrix} a_2^+ \\ a_2^- \end{bmatrix} \tag{2.157}$$

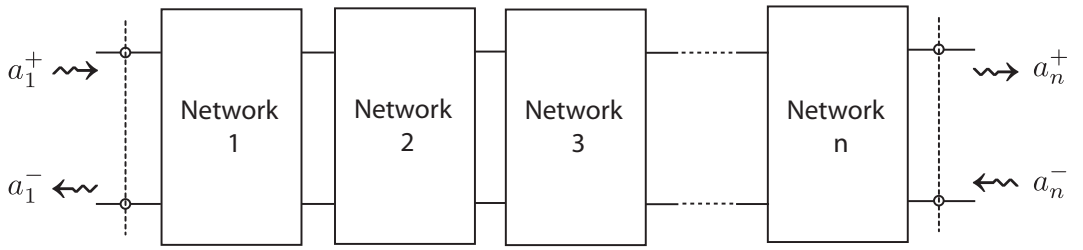

FIGURE 2.10: Cascade connection of n 2-port networks.

hence,

$$\begin{aligned} A_{11} &= \frac{1}{S_{12}}, & A_{12} &= \frac{-S_{22}}{S_{12}}, \\ A_{21} &= \frac{S_{11}}{S_{12}}, & A_{22} &= \frac{S_{12}^2 - S_{11}S_{22}}{S_{12}}. \end{aligned} \tag{2.158}$$

On the other hand and following the same procedure for the wave-amplitude transmission matrix yields the relations

$$\begin{aligned} S_{11} &= \frac{A_{21}}{A_{11}}, & S_{12} &= \frac{A_{22}A_{11} - A_{21}A_{12}}{A_{11}}, \\ S_{21} &= \frac{1}{A_{11}}, & S_{22} &= \frac{-A_{12}}{A_{11}}. \end{aligned} \tag{2.159}$$

The amplitudes a_n^+ and a_n^- are defined in the same way as in section 2.4.2 by equations (2.143) and (2.144). This way, taking the determinant of (2.157) yields

$$\det[T] = A_{11}A_{22} - A_{12}A_{21} = 1, \tag{2.160}$$

which is a relation of great relevance as we shall see further on this thesis.

2.6 Summary

In this chapter we have introduced the concepts of waveguide and transmission line. Furthermore, we have shown using Maxwell equations that energy can be transmitted in the form of unguided waves (plane waves) through space and also that we can transmit energy in the form of guided waves both on waveguides and transmission lines. Also it was demonstrated how transmission lines are capable of supporting TEM waves, hence, may be defined as devices used to guide energy from one point to another.

The S-parameters were introduced as a means for characterizing N-port microwave

networks, and finally the wave-amplitude transmission matrix was introduced as a alternative to the S-parameters for the representation of cascade connections of microwave systems.

Chapter 3

Direct scattering

3.1 Introduction

The direct scattering problem of nonuniform transmission lines, *i.e.*, the analysis problem is considered in this chapter. Here we address several methods that can be used to perform the analysis of nonuniform transmission lines. Essentially we consider two different methods: the coupled mode theory method and the transmission matrix method.

The coupled mode method is a general method which can theoretically be applied to perform the analysis of any nonuniform guided structure. As we saw before, transmission lines are particular cases of wave guiding structures, hence, in this chapter the coupled mode theory method is adapted to perform the analysis of the particular case of NTL structures. Depending on the type of NTL structure under analysis further variations of the more general method are considered.

The transmission matrix method on the other hand is solely suitable for the analysis of transmission line structures and is based on the analysis of cascade connections of very small length transmission lines. Two variations of this method are considered depending on the characteristics of the individual transmission line sections.

3.2 Coupled mode theory

The Coupled Mode Theory (CMT) is a well known and widely used method for the analysis of electromagnetic fields and mode interaction in guided wave and resonant structures. The mode coupling phenomena can occur in two distinct ways: the coupling of modes in time and the coupling of modes in space. For instance, the energy exchange along time between two coupled resonant circuits, or two coupled microwave or optical

resonators are some examples of mode coupling in time. On the other hand, consider a wave filter made by placing a series of obstacles in a waveguide. These obstacles present along the waveguide couple the forward and backward traveling modes in propagation and give rise to pass bands and stop bands. In this case we are faced with the mode coupling in space.

The concept of mode coupling in electromagnetics dates back to the 1950's. It was initially introduced for microwave devices, and then it was applied to optical devices in the early 1970's. The development of CMT started in 1954 with a paper by J. Pierce [17]. Pierce, in his paper uses CMT to perform the analysis of microwave traveling-wave tubes. A lateral development of CMT was performed by S. Miller [18], where he introduced the CMT to the analysis of microwave waveguides and passive devices. The CMT was readily generalized by Louisell [19] to the analysis of tapered waveguides where the coupling coefficients have a dependence with the propagation distance. So far the work developed on the CMT and the formulation of the coupled mode equations was rather heuristic in the sense that the development of the equations was based on power conservation arguments. It was not until 1955 with the work of Schelkunoff [20] that a rigorous derivation of the CMT was carried out using a mode expansion. Schelkunoff used the cross-section method [21] and was able to obtain a set of telegraphist's equations from the Maxwell's equations by expanding the modes of a coupled system from a linear superposition of the known modes of the uncoupled system. The coupling coefficients are then determined through the use of boundary conditions. Later in 1958, Haus [22] took the CMT to a more formal mathematical ground by showing that the CMT was derivable from a variational principle.

Later, in the 1970's, the CMT was applied to nonuniform optical dielectric waveguides by several authors and using several methods. Regarding this, we emphasize the work of Marcuse [23, 24], Snyder [25, 26] and Yariv and Taylor [27]. Also we highlight the work of Yariv [28, 29] that applied the CMT to optical gratings.

A more detailed historical review about CMT can be found in papers by Haus and Huang [30, 31], where also other aspects of CMT are discussed in some detail as is the case of the coupling of modes in time or the mode coupling in coupled systems. In this section we focus only on the coupled mode theory applied to the space mode coupling and how this theory can be used on the analysis of NTL's.

Recently, Lopetegi [32] in order to formulate a general and accurate coupled mode

theory suitable for microwave devices used the cross-section method and rigorously applied the method to the general case of nonuniform open waveguides. As a result, a system of coupled mode equations characterizing the general case of nonuniform waveguides was obtained. This system of coupled mode equations can be applied to the analysis of nonuniform transmission structures such as, microstrip transmission lines, coplanar waveguides, slotlines or striplines, because all these structures are included in the class of open waveguides.

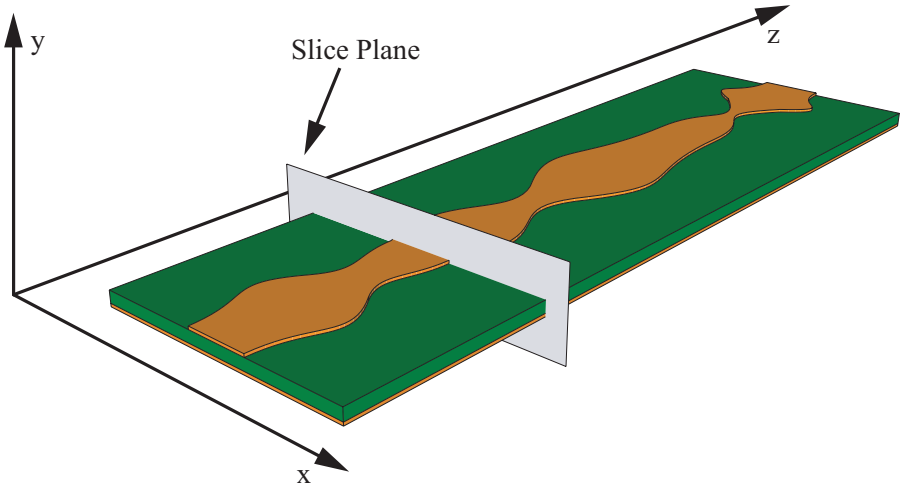

(a) Nonuniform microstrip line.

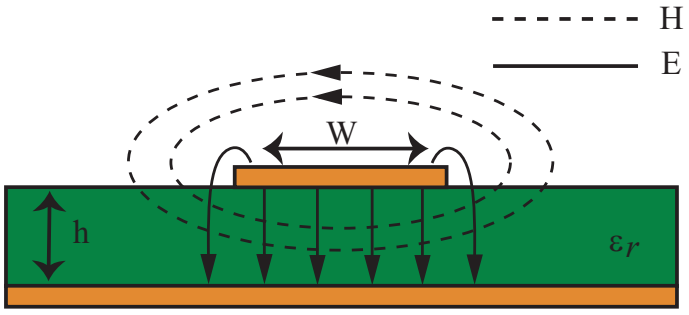

(b) Cross-sectional view - Electric and magnetic filed lines.

FIGURE 3.1: Cross-section method.

3.2.1 The cross-section method

The basic idea of the cross-section method [21] is that the electromagnetic fields at any cross section of a nonuniform waveguide can be represented as a superposition of the forward and backward traveling waves associated to the different modes of an auxiliary uniform waveguide that has the same cross-section. The coefficients of this superposition can be seen as the complex amplitudes of the modes along the nonuniform waveguide

and satisfy a set of first order linear ordinary equations that turn into integro-differential equations for open waveguides, known as the coupled mode equations. The solution of this set of equations yield the nonlinear waveguide frequency response.

In [33] the coupled mode theory formulated by Lopetegi is used to analyze periodic structures, more specifically Electronic Band Gap (EBG) structures implemented in microstrip technology. From his results it becomes obvious that the couple mode equations provide a very good insight into the physical operation of the analyzed structures, constituting therefore an excellent set of tools for the analysis and design of these devices.

The full mathematical development of the couple mode equations for open waveguides is not provided. This development has already been done and can be found in [32], however we are going to present the main results. In the following we adopt the mathematical notation of [32].

3.2.1.1 Uniform waveguides mode expansion

We saw in Chapter 2.2 that the electromagnetic fields solutions for guided waves were given by a set of modes that satisfy the wave equation. Considering a specific uniform waveguide, we may then mathematically identify the different modes by numerating them using an integer superscript index i that can take both positive and negative values. Considering the modes of a waveguide propagating along the z-direction the fields for each mode i are then described by (see section 2.2.5):

$$\hat{\vec{E}}^i(x,y,z) = \vec{E}^i(x,y)e^{-j\beta_i z}, \tag{3.1}$$

$$\hat{\vec{H}}^i(x,y,z) = \vec{H}^i(x,y)e^{-j\beta_i z}. \tag{3.2}$$

We assume a lossless structure, thus, the propagation constant for each mode is given by $\beta_i = \sqrt{k^2 - (k_c^i)^2}$. If conductor or substrate losses are to be considered the propagation constant is replaced by $\gamma_i = \alpha_i + j\beta_i$. From the above equation one might be led to think that the modes are completely independent from each other, but in fact they are not. Note that each mode has both a forward and backward propagating waves and so, the relation between their propagation constant is

$$\beta_{-i} = -\beta_i, \tag{3.3}$$

and so, we can see that the modes with positive i are not totally independent of the negative ones, but that they have in fact the same propagation constant magnitude.

3.2.1.2 Closed Waveguides

For the specific case of closed waveguides, there exist an infinite number of discrete modes which forms an orthogonal system. The modes in a closed waveguide are orthogonal to each other because they all have different propagation constants [21]. The total electromagnetic field inside some specific waveguide is then given by a linear combination of these modes:

$$\hat{\vec{E}}(x,y,z) = \sum_{i=-\infty}^{\infty} A_i \vec{E}^i(x,y) e^{-j\beta_i z} = \sum_{i=-\infty}^{\infty} a_i(z) \vec{E}^i(x,y), \tag{3.4}$$

$$\hat{\vec{H}}(x,y,z) = \sum_{i=-\infty}^{\infty} A_i \vec{H}^i(x,y) e^{-j\beta_i z} = \sum_{i=-\infty}^{\infty} a_i(z) \vec{H}^i(x,y), \tag{3.5}$$

where A_i is an amplitude constant which can take complex values, and a_i is the complex amplitude of the mode i.

3.2.1.3 Open Waveguides

In open waveguides, the mode expansion is somewhat different of that in a closed waveguide. The system of modes in an open waveguide is composed not only by discrete modes (discrete spectrum of modes) but also by radiating modes (continuous spectrum of modes) [34]. Also the set of discrete modes is now formed by a finite number of modes and is no longer infinite like in the close waveguide case. The electromagnetic field configuration in a uniform open waveguide can be expanded as a linear combination of both the modes in the discrete and continuous spectrum including the forward and backward traveling waves. Microstrip transmission lines are an example of open waveguides where the fields are given by

$$\hat{\vec{E}}(x,y,z) = \sum_{i=-M}^{M} a_i(z) \vec{E}^i(x,y) + \sum_{i=-Q}^{Q} \int_0^{\infty} a_i(z,k_t) \vec{E}^i(x,y,k_t) dk_t, \tag{3.6}$$

$$\hat{\vec{H}}(x,y,z) = \sum_{i=-M}^{M} a_i(z) \vec{H}^i(x,y) + \sum_{i=-Q}^{Q} \int_0^{\infty} a_i(z,k_t) \vec{H}^i(x,y,k_t) dk_t. \tag{3.7}$$

For a deeper understanding on the field expansion in open waveguides, please refer to the work of Rozzi and Mongiardo [34–36].

3.2.1.4 Coupled-mode equation for nonuniform waveguides

In an uniform waveguide, both the cross-section geometry and material properties do not vary along its longitudinal axis. This way, the modes propagate or attenuate (modes with complex propagation constant) along the waveguide independently, and thus, without interacting with each other. On the other hand, if the waveguide is not uniform the modes will no longer propagate independently and will transfer power between them. This phenomena is known as "mode-coupling".

According to the cross-section method, to describe the electromagnetic field in a nonuniform waveguide it is necessary to expand the fields at each cross-section in a Fourier-like series of the modal fields of a reference uniform waveguide [21]. In [32] the cross-section method is applied to the general case of open waveguides.

In this section we are going to address the procedure used by Lopetegui [32] to obtain the general coupled mode equations for open waveguides from the cross-section method. We also outline the most important mathematical derivations and results. For the full mathematical development please refer to [32].

Let us consider a straight (along the z-direction) nonuniform open waveguide as is for example the microstrip nonuniform transmission line depicted in Figure 3.1. The cross-section method tell us that the electromagnetic fields at any cross-section of that nonuniform waveguide is given by a linear combination of the transversal field components present in a uniform waveguide (the reference waveguide) with the same cross-section and equal distribution of μ and ϵ as the one for a fixed z in the nonuniform waveguide. So, the transverse field in the nonuniform waveguide can be represented by

$$\hat{E}_x(x,y,z) = \sum_{i=-M}^{M} a_i(z)E_x^i(x,y,z) + \sum_{i=-Q}^{Q}\int_0^\infty a_i(k_t,z)E_x^i(x,y,k_t,z)dk_t, \tag{3.8}$$

$$\hat{E}_y(x,y,z) = \sum_{i=-M}^{M} a_i(z)E_y^i(x,y,z) + \sum_{i=-Q}^{Q}\int_0^\infty a_i(k_t,z)E_y^i(x,y,k_t,z)dk_t, \tag{3.9}$$

$$\hat{H}_x(x,y,z) = \sum_{i=-M}^{M} a_i(z)H_x^i(x,y,z) + \sum_{i=-Q}^{Q}\int_0^\infty a_i(k_t,z)H_x^i(x,y,k_t,z)dk_t, \tag{3.10}$$

$$\hat{H}_y(x,y,z) = \sum_{i=-M}^{M} a_i(z)H_y^i(x,y,z) + \sum_{i=-Q}^{Q}\int_0^\infty a_i(k_t,z)H_y^i(x,y,k_t,z)dk_t. \tag{3.11}$$

Comparing the last set of equations with equations (3.6) and (3.7) we clearly see that both the electromagnetic field distribution (E,H) and the modes complex amplitude

(a_i) now have an explicit z dependency. This comes from the fact that the transverse fields in nonuniform waveguides are arranged as a linear combination of the transverse components of the fields that compose the modes of an uniform auxiliary waveguide. The auxiliary waveguide has the same cross-section and material properties as do the nonuniform structure at a fixed z. At a specific z position the fields in a nonuniform waveguide have to satisfy the same boundary conditions as do the electromagnetic fields in an uniform auxiliary waveguide with the same cross-section characteristics. Therefore, the modal fields in the auxiliary waveguides can be used as a base to expand the fields in the nonuniform waveguides.

Equations (3.8) to (3.11), refer only to the transverse components of the electromagnetic fields in an nonuniform waveguide. For the full description of the fields we use Maxwell's equations to calculate the longitudinal components of the fields. Substituting equations (3.8) and (3.9) into equation (2.47) yields the magnetic field longitudinal component

$$\hat{H}_z(x,y,z) = \sum_{i=-M}^{M} a_i(z) H_z^i(x,y,z) + \sum_{i=-Q}^{Q} \int_0^\infty a_i(k_t,z) H_z^i(x,y,k_t,z) dk_t. \tag{3.12}$$

In the same way, the longitudinal component of the electric field is obtained by substituting equations (3.10) to (3.11) into equation (2.50), leading to

$$\hat{E}_z(x,y,z) = \sum_{i=-M}^{M} a_i(z) E_z^i(x,y,z) + \sum_{i=-Q}^{Q} \int_0^\infty a_i(k_t,z) E_z^i(x,y,k_t,z) dk_t. \tag{3.13}$$

The last two equations shows that the longitudinal fields expansion is analogous to that of the transverse fields. Moreover, they have the same complex amplitude coefficients $a_i(z)$ and $a_i(k_t,z)$, and so, we can assume these coefficients as the complex amplitudes for each mode i in some specific nonuniform waveguide.

Because we are interested in obtaining the expressions for the complex amplitudes of the propagating modes, we now going to introduce the general coupled-mode equations for open nonuniform waveguides. The full mathematical development necessary to obtain the couple-mode equations from the electromagnetic fields in a nonuniform waveguide is detailed in [32]. In the following, we only present the main results.

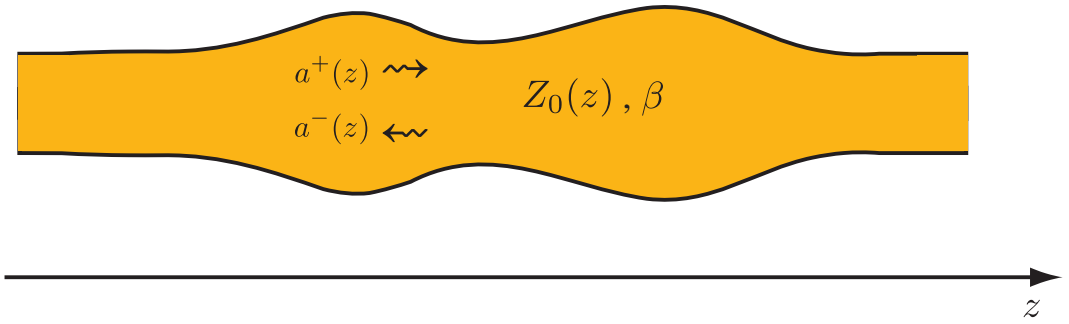

FIGURE 3.2: TEM Nonuniform transmission line.

The couple-mode equations are derived, by substituting equations (3.8) to (3.13) into the expanded form of the Maxwell's equations (2.37)-(2.42), yielding:

$$\frac{da_m}{dz} + j\beta_m a_m = \sum_{i=-M}^{M} a_i C_{mi} + \sum_{i=-Q}^{Q} \int_0^{\infty} a_i(k_t) C_{mi}(k_t) dk_t, \tag{3.14}$$

$$\frac{da_n(\tilde{k_t})}{dz} + j\beta_n(\tilde{k_t}) a_n(\tilde{k_t}) = \sum_{i=-M}^{M} a_i C^c_{ni}(\tilde{k_t}) + \sum_{i=-Q}^{Q} \int_0^{\infty} a_i(k_t) C^c_{ni}(\tilde{k_t}, k_t) dk_t. \tag{3.15}$$

Equation (3.14) describes the coupling of power between modes of the discrete spectrum, and also between modes of the discrete and continuous spectrum. On the other hand, equation (3.15) refers only to the coupling between modes of the continuous spectrum. For the expression of the coupling coefficients ($C_{mi}, C_{mi}(k_t), C^c_{ni}(\tilde{k_t}), C^c_{ni}(\tilde{k_t}, k_t)$) as well as the full mathematical development, please refer to [32].

3.2.1.5 Coupled-mode equations for nonuniform transmission lines

Due to its generalist nature, the coupled-mode equations derived in the previous section are quite cumbersome and complex. For the purpose of the work developed within this thesis, a more simple and elegant set of coupling equations can be derived by considering that the coupling of energy is only occuring between the forward and backward traveling waves of the fundamental mode propagating in a given nonuniform waveguide. Moreover, the majority of the guiding structures contemplated within this work consists on TEM (stripline) or quasi-TEM (microstrip) transmission lines, and as such they can be accurately modeled by the equivalent circuit model presented in Section 2.3. We will also neglect both ohmic and substrate losses as in most practical cases they are very small.

Unlike uniform transmission lines where the characteristic impedance and propagation constant are constant along all of its length, in a nonuniform transmission line

only the propagation constant remais constant. The characteristic impedance depends on the position along the line. Figure 3.2 illustrates a TEM nonuniform transmission line where $Z_0(z)$ is the characteristic impedance which is space-dependent and β is the propagation constant.

From the illustration on Figure 3.2 we clearly see that the cross-section dimensions of an NTL varies along the longitudinal axis. Therefore, the per-unit-length parameters will be a function of the position variable z. Then, for a lossless NTL, the telegrapher equations (2.98) and (2.99) becomes

$$\frac{dV(\omega,z)}{dz} = -j\omega L(z)I(\omega,z), \tag{3.16}$$

$$\frac{dI(\omega,z)}{dz} = -j\omega C(z)V(\omega,z), \tag{3.17}$$

where $L(z)$ is the inductance per unit length and $C(z)$ is the capacitance per unit length of the transmission line. Please note that the solutions to equations (3.16) and (3.17) come in the form

$$V(\omega,z) = V^+(\omega,z) + V^-(\omega,z) \tag{3.18}$$

$$I(\omega,z) = I^+(\omega,z) + I^-(\omega,z) \tag{3.19}$$

The characteristic impedance is given by

$$Z_0(z) = \sqrt{\frac{L(z)}{C(z)}}, \tag{3.20}$$

and the propagation constant is

$$\beta = \omega\sqrt{L(z)C(z)}, \tag{3.21}$$

which has a constant value (along the space variable) as we are considering a TEM mode propagation.

Due to the non-constant nature of the characteristic impedance in an NTL, and in order to obtain physically meaningful power relations in terms of wave amplitudes along the nonuniform transmission line, the generalized S-parameters derived in Section 2.4.2 must be used. So, recalling equations (2.147) and (2.148), we must define the set of

waves amplitudes propagating along the NTL as

$$a^+(\omega, z) = \frac{V^+(\omega, z)}{\sqrt{Z_0(z)}}, \tag{3.22}$$

$$a^-(\omega, z) = \frac{V^-(\omega, z)}{\sqrt{Z_0(z)}}, \tag{3.23}$$

where $V^+(\omega, z)$ and $V^-(\omega, z)$ are the amplitudes of the forward and backward traveling voltage waves associated with the TEM mode propagating in the NTL.

So far we have explicitly pointed out the spectral and spatial dependences of the electrical properties of NTLs. Throughout the remaining of this section and for the sake of mathematical simplicity, both spectral and spacial dependences are omitted.

Regarding equations (3.22) and (3.23), the total voltage and current along the NTL are obtained by summing both the forward and backward traveling waves yielding

$$V = V^+ + V^- = a^+\sqrt{Z_0} + a^-\sqrt{Z_0}, \tag{3.24}$$

$$I = I^+ + I^- = \frac{a^+}{\sqrt{Z_0}} - \frac{a^-}{\sqrt{Z_0}}. \tag{3.25}$$

Substituting the expressions for the voltage and current into equation (3.16) we have

$$\frac{d}{dz}(a^+\sqrt{Z_0} + a^-\sqrt{Z_0}) = -j\omega L\left(\frac{a^+}{\sqrt{Z_0}} - \frac{a^-}{\sqrt{Z_0}}\right). \tag{3.26}$$

Both the wave amplitudes and the characteristic impedance have a z dependence, therefore the derivatives in the last equations are given by

$$\frac{d(a^+\sqrt{Z_0})}{dz} = \frac{da^+}{dz}\sqrt{Z_0} + a^+\frac{1}{2}\frac{1}{\sqrt{Z_0}}\frac{dZ_0}{dz}, \tag{3.27}$$

$$\frac{d(a^-\sqrt{Z_0})}{dz} = \frac{da^-}{dz}\sqrt{Z_0} + a^-\frac{1}{2}\frac{1}{\sqrt{Z_0}}\frac{dZ_0}{dz}. \tag{3.28}$$

Equation (3.26) can then be further developed, yielding

$$\left(\frac{da^+}{dz} + \frac{da^-}{dz}\right)\sqrt{Z_0} + \frac{1}{2}\frac{1}{\sqrt{Z_0}}\frac{dZ_0}{dz}(a^+ + a^-) = -j\frac{\omega L}{\sqrt{Z_0}}(a^+ - a^-). \tag{3.29}$$

Dividing both sides of the equation by $\sqrt{Z_0}$, and taking into consideration from (3.20) and (3.21) that

$$\beta\sqrt{Z_0} = \frac{\omega L}{\sqrt{Z_0}}, \tag{3.30}$$

equation (3.29) can be rewritten as

$$\frac{da^+}{dz} + \frac{da^-}{dz} = -j\beta(a^+ - a^-) - \frac{1}{2}\frac{1}{Z_0}\frac{dZ_0}{dz}(a^+ + a^-). \tag{3.31}$$

In the same way, substituting the current and voltage equations into equation (3.17) we obtain

$$\frac{d}{dz}\left(\frac{a^+}{\sqrt{Z_0}} - \frac{a^-}{\sqrt{Z_0}}\right) = -j\omega C(a^+\sqrt{Z_0} + a^-\sqrt{Z_0}). \tag{3.32}$$

Solving the derivatives in the previous equation we get

$$\frac{d}{dz}\left(\frac{a^+}{\sqrt{Z_0}}\right) = \frac{1}{Z_0}\left(\frac{da^+}{dz}\sqrt{Z_0} - a^+\frac{1}{2}\frac{1}{\sqrt{Z_0}}\frac{dZ_0}{dz}\right), \tag{3.33}$$

$$\frac{d}{dz}\left(\frac{a^-}{\sqrt{Z_0}}\right) = \frac{1}{Z_0}\left(\frac{da^-}{dz}\sqrt{Z_0} - a^-\frac{1}{2}\frac{1}{\sqrt{Z_0}}\frac{dZ_0}{dz}\right). \tag{3.34}$$

Substituting the derivatives into equation (3.32) yields

$$\left(\frac{da^+}{dz} - \frac{da^-}{dz}\right)\sqrt{Z_0} + \frac{1}{2}\frac{1}{\sqrt{Z_0}}\frac{dZ_0}{dz}(a^- - a^+) = -j\omega C Z_0(a^+ + a^-)\sqrt{Z_0}. \tag{3.35}$$

Dividing both sides of the equation by $\sqrt{Z_0}$ and taking into account that

$$\beta = \omega C Z_0, \tag{3.36}$$

equation (3.35) can be rewritten as

$$\frac{da^+}{dz} - \frac{da^-}{dz} = -j\beta(a^+ + a^-) - \frac{1}{2}\frac{1}{Z_0}\frac{dZ_0}{dz}(a^- - a^+). \tag{3.37}$$

In order to obtain the coupled-mode equations for TEM transmission lines, equations (3.31) and (3.37) must be added and subtracted. Therefore, adding both equations we obtain

$$\frac{da^+}{dz} = -j\beta a^+ - \frac{1}{2}\frac{1}{Z_0}\frac{dZ_0}{dz}a^-. \tag{3.38}$$

On the other hand, the subtraction yields

$$\frac{da^-}{dz} = j\beta a^- - \frac{1}{2}\frac{1}{Z_0}\frac{dZ_0}{dz}a^+. \tag{3.39}$$

The last two equations are called the couple-mode equations, and relate the coupling between the forward and backward propagating waves in a NTL structure. By simple

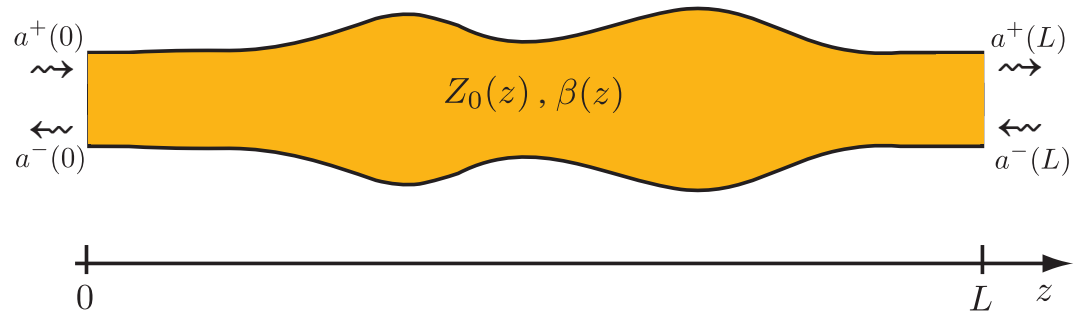

FIGURE 3.3: NTL - Boundary conditions.

inspection of the last equations it is easily seen that the factor responsible for the coupling between the forward and backward propagating waves is

$$K = \frac{1}{2}\frac{1}{Z_0}\frac{dZ_0}{dz}. \tag{3.40}$$

We can now rewrite the coupled-mode equations as

$$\frac{da^+}{dz} = -j\beta a^+ - Ka^-, \tag{3.41}$$

$$\frac{da^-}{dz} = j\beta a^- - Ka^+, \tag{3.42}$$

where K is called the "coupling coefficient".

Please note the resemblance between the couple-mode equations (3.41) and (3.42) and equation (3.14). Taking a closer look at (3.14), we see that by despising the coupling of energy to the modes in the continuous spectrum and considering single mode propagation, equation (3.14) simplifies to (3.41) and also (3.42) if we take into consideration equation (3.3). We then conclude that the set of coupled-mode equations for transmission lines can therefore be obtained from the more general set of equations described by (3.14).

Let us consider the NTL of length L depicted in Figure 3.3. In order to analyze and characterize NTL structures such as this one, we must solve the coupled-mode equations (3.41) and (3.42) for the wave amplitudes at both ports or terminals and then calculate the S-parameters.

The coupled-mode equations form a set of first-order linear ordinary differential equations that have to be solved from $z = 0$ to $z = L$. However, this is not enough because solving the equations only gives us a general solution. For the problem to be completely defined and to obtain the S-parameters of the device, a particular solution

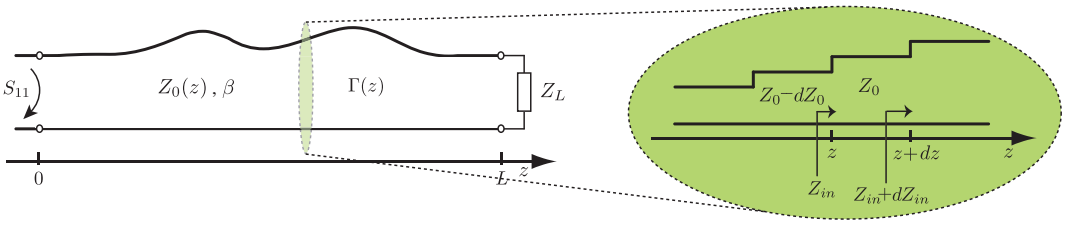

FIGURE 3.4: NTL - Infinitesimal step change in impedance.

must be obtained. This is accomplished by setting the boundary conditions

$$a^+(0) = 1, \tag{3.43}$$

$$a^-(L) = 0. \tag{3.44}$$

The first boundary condition corresponds to the unitary excitation at the input of the device, and the second one has to do with the matching of the structure at the output port.

We now have to solve the coupled-mode equations (3.41) and (3.42) in association with the boundary conditions (3.43) and (3.44). In short, the problem in hands is a system of two first order ordinary differential equations subject to two-point boundary conditions. In order to solve this problem we use a numerical method implemented in Matlab developed for boundary value problems [37]. The name of the Matlab function that implements this method is called *bvp4c*.

Once the solutions for $a^+(z)$ and $a^-(z)$ are found, the S-parameters are easily obtained by using

$$S_{11} = \left.\frac{a^-(0)}{a^+(0)}\right|_{a^-(L)=0}, \tag{3.45}$$

$$S_{21} = \left.\frac{a^+(L)}{a^+(0)}\right|_{a^-(L)=0}. \tag{3.46}$$

3.2.2 Riccati equation for NTLs

Consider the NTL on Figure 3.4 as being constituted by a number of infinitesimal sections of length dz with the impedance step from one section to the adjacent being dZ_0.

As is pointed out in Figure 3.4, let us consider that the input impedance as seen from z is Z_{in} and that $Z_{in} + dZ_{in}$ is the input impedance at $z + dz$. We know that the

relation between both the input impedances is given by

$$\begin{aligned} Z_{in} &= Z_0 \frac{Z_{in} + dZ_{in} + jZ_0 \tan(\beta dz)}{Z_0 + j(Z_{in} + dZ_{in}) \tan(\beta dz)} \\ &\simeq Z_0 \frac{Z_{in} + dZ_{in} + jZ_0 \beta dz}{Z_0 + jZ_{in}\beta dz + dZ_{in}\beta dz}, \end{aligned} \tag{3.47}$$

where due to the small value of βdz we replace the tangent by its argument. Neglecting the product of the differential terms $dZ_{in}\beta dz$, and dividing both the numerator and denominator by Z_0 yields

$$Z_{in} \simeq (Z_{in} + dZ_{in} + jZ_0\beta dz) \left(\frac{1}{1 + j\frac{Z_{in}}{Z_0}\beta dz} \right). \tag{3.48}$$

Multiplying the numerator and denominator of the second term of the product in the previous equation by the complex conjugate of the denominator and neglecting the term with dz^2 gives

$$\begin{aligned} Z_{in} &\simeq (Z_{in} + dZ_{in} + jZ_0\beta dz) \left(1 - j\frac{Z_{in}}{Z_0}\beta dz \right) \\ &\simeq Z_{in} + dZ_{in} + jZ_0\beta dz - j\frac{Z_{in}^2}{Z_0}\beta dz - j\frac{Z_{in}}{Z_0}\beta dz dZ_{in} + Z_{in}\beta^2 dz^2 \\ &\simeq Z_{in} + dZ_{in} + jZ_0\beta dz - j\frac{Z_{in}^2}{Z_0}\beta dz. \end{aligned} \tag{3.49}$$

where the products of differential terms were neglected. The above equation then simplifies to

$$\frac{dZ_{in}}{dz} = j\beta \left(\frac{Z_{in}^2}{Z_0} - Z_0 \right). \tag{3.50}$$

We know that the input impedance as seen from any position z along the NTL structure is

$$Z_{in} = \frac{1 + \Gamma}{1 - \Gamma} Z_0, \tag{3.51}$$

and that, the corresponding derivative is

$$\frac{dZ_{in}}{dz} = \frac{1 + \Gamma}{1 - \Gamma}\frac{dZ_0}{dz} + \frac{2Z_0}{(1 - \Gamma)^2}\frac{d\Gamma}{dz}. \tag{3.52}$$

Substituting (3.51) into equation (3.50) and taking the equality with equation (3.52) yields

$$\begin{aligned} j\beta Z_0\left(\frac{(1+\Gamma)^2}{(1-\Gamma)^2}-1\right) &= \frac{1+\Gamma}{1-\Gamma}\frac{dZ_0}{dz}+\frac{2Z_0}{(1-\Gamma)^2}\frac{d\Gamma}{dz} \\ j\beta Z_0\left(\frac{4\Gamma}{(1-\Gamma)^2}\right) &= \frac{1+\Gamma}{1-\Gamma}\frac{dZ_0}{dz}+\frac{2Z_0}{(1-\Gamma)^2}\frac{d\Gamma}{dz} \\ 4j\beta\Gamma Z_0 &= (1-\Gamma^2)\frac{dZ_0}{dz}+2Z_0\frac{d\Gamma}{dz}. \end{aligned} \tag{3.53}$$

Dividing both sides of the equation by $2Z_0$ and rearranging the equation we finally have

$$\frac{d\Gamma}{dz} = 2j\beta\Gamma-(1-\Gamma^2)\frac{1}{2Z_0}\frac{dZ_0}{dz}. \tag{3.54}$$

This is the exact equation for the reflection coefficient $\Gamma(z)$ along the NTL and is called a Ricatti equation [16]. The S_{11} parameter of the NTL is obtained by calculating $\Gamma(0)$. Equation (3.54) can be rewritten by taking into account equation (3.40) yielding

$$\frac{d\Gamma(z)}{dz} = 2j\beta\Gamma(z)-K(z)(1-\Gamma^2(z)). \tag{3.55}$$

where $K(z)$ is the coupling coefficient and where we have considered spatial dependence.

Unlike the couple-mode equations, the solution of equation (3.54) does not require solving a system of differential equations. Because of the term Γ^2 the Riccati equation is a nonlinear equation and does not have a general solution. In order to numerically solve the equation, we start at the end of the NTL structure and apply the boundary condition

$$\Gamma(L) = 0. \tag{3.56}$$

The Runge-Kutta method can then be used to work the equation backwards to $z = 0$.

We are now going to analyze the relation between the coupled mode equations and the Riccati equation. Let us start by considering the reflection coefficient along the NTL structure as

$$\Gamma(z) = \frac{a^-(z)}{a^+(z)}, \tag{3.57}$$

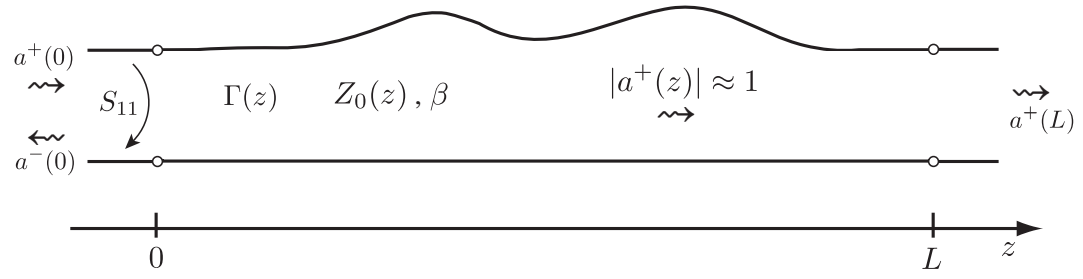

FIGURE 3.5: Low reflectivity NTL.

where $a^+(z)$ and $a^-(z)$ are the forward and backward traveling waves propagating along the NTL. Taking the derivative of the previous equation we get[1]

$$\frac{d\Gamma}{dz} = \frac{d}{dz}\left(\frac{a^-}{a^+}\right) = \frac{\frac{da^+}{dz}a^+ - \frac{da^-}{dz}a^-}{(a^+)^2}. \tag{3.58}$$

From the coupled-mode equations (3.41) and (3.42) we have

$$\frac{da^+}{dz}a^- = (-j\beta a^+ - Ka^-)a^-, \tag{3.59}$$

$$\frac{da^-}{dz}a^+ = (j\beta a^- - Ka^+)a^+. \tag{3.60}$$

Substituting the last two expressions into equation (3.58) we obtain

$$\begin{aligned}\frac{d\Gamma}{dz} &= \frac{(j\beta a^- - Ka^+)a^+ - (-j\beta a^+ - Ka^-)a^-}{(a^+)^2} \\ &= j\beta\frac{a^-}{a^+} - K + j\beta\frac{a^-}{a^+} + K\left(\frac{a^-}{a^+}\right)^2.\end{aligned} \tag{3.61}$$

Recalling (3.57) and rearranging the previous equation yields

$$\frac{d\Gamma}{dz} = 2j\beta\Gamma - K(1-\Gamma^2), \tag{3.62}$$

which is the same result as in equation (3.54).

3.2.3 Weak coupling

Until now we have just looked into the exact solutions of the coupled-mode equations when analyzing NTLs. However, a considerable simplification and also a complexity reduction of the problem can be achieved if we consider the analysis of NTL structures with low reflectivity. By low reflectivity we mean to say that the coupling of energy

[1] For the sake of mathematical simplicity the spacial dependency is omitted.

between the forward and backward propagating waves is very low, hence the name "weak coupling". We show in this subsection that, by assuming the condition of low reflectivity, a simple closed-form solution for the coupled-mode equations can be derived.

Let us consider that $\Gamma(z)$ along the structure is low enough so that the amplitude of the forward propagating wave remains approximately constant throughout the entire NTL. Assuming that $a^+(0) = 1$ and also that the NTL structure is terminated in a matched load, we may then express the forward propagating wave as

$$a^+(z) = e^{-j\beta z}, \tag{3.63}$$

as illustrated in Figure 3.5. The amplitude of the forward wave is therefore unitary, and the exponential term represents the wave propagation in the $+z$ direction.

Recalling the coupled-mode equations, more specifically equation (3.42)

$$\frac{da^-}{dz} = j\beta a^- - Ka^+, \tag{3.64}$$

and using (3.63), we have

$$\frac{da^-}{dz} = j\beta a^- - Ke^{-j\beta z}. \tag{3.65}$$

Multiplying both sides of the previous differential equation by $e^{-j\beta z}$ and rearranging the equation yields

$$\frac{da^-}{dz}e^{-j\beta z} - j\beta a^- e^{-j\beta z} = -Ke^{-2j\beta z}. \tag{3.66}$$

Using the equality

$$\frac{d}{dz}(a^- e^{-j\beta z}) = \frac{da^-}{dz}e^{-j\beta z} - j\beta a^- e^{-j\beta z}, \tag{3.67}$$

we may then rewrite equation (3.65) as

$$\frac{d}{dz}(a^- e^{-j\beta z}) = -Ke^{-2j\beta z}. \tag{3.68}$$

Considering the NTL structure of length L depicted on Figure 3.5, equation (3.68) can now be integrated on both sides between 0 and L as

$$a^- e^{-j\beta z}\Big|_{z=0}^{z=L} = -\int_0^L Ke^{-2j\beta z}dz. \tag{3.69}$$

However, the NTL device is considered to be terminated on a matched load with an unitary input excitation,

$$a^-(L) = 0, \tag{3.70}$$

$$a^-(0) = \Gamma(0). \tag{3.71}$$

Equation (3.69) then reduces to

$$\Gamma(0) = \int_0^L K e^{-2j\beta z} dz, \tag{3.72}$$

and hence[2]

$$S_{11}(\omega) = \int_0^L K(z) e^{-2j\beta z} dz. \tag{3.73}$$

As it can be seen, equation (3.73) expresses the relation between the coupling coefficient for a low reflectivity structure $K(z)$ and its corresponding reflection response $S_{11}(\omega)$.

Regarding the structure in Figure 3.5 we can easily see that the coupling coefficient can only take values within the range $[0, L]$. Therefore, if we assume that the coupling coefficient $K(z) = 0, \forall z \notin [0, L]$ the integration limits can be changed and equation (3.73) becomes

$$S_{11}(\omega) = \int_{-\infty}^{\infty} K(z) e^{-2j\beta z} dz, \tag{3.74}$$

where

$$\beta = \frac{\omega}{c}\sqrt{\epsilon_r}, \tag{3.75}$$

and c is the speed of light in the vacuum.

Let us consider the following definition for the Fourier transform pair:

$$x(t) = \frac{1}{2\pi}\int_{-\infty}^{\infty} X(\omega) e^{j\omega t} d\omega, \tag{3.76}$$

$$X(\omega) = \int_{-\infty}^{\infty} x(t) e^{-j\omega t} dt. \tag{3.77}$$

The similarity between equations (3.74) and (3.77) is evident, therefore we can conclude that the coupling coefficient $K(z)$ and the device reflection response $S_{11}(\omega)$ are related by the Fourier transform in the following way:

$$K(z) \longleftrightarrow S_{11}\left(\frac{2\sqrt{\epsilon_r}}{c}\omega\right). \tag{3.78}$$

[2]With frequency and spatial dependencies.

On the other hand, let us consider the variable change

$$u = \frac{2\sqrt{\epsilon_r}}{c} z \quad \Longrightarrow \quad dz = \frac{c}{2\sqrt{\epsilon_r}} du. \tag{3.79}$$

Equation (3.74) is now rewritten as

$$S_{11}(\omega) = \frac{c}{2\sqrt{\epsilon_r}} \int_{-\infty}^{\infty} K\left(\frac{c}{2\sqrt{\epsilon_r}} u\right) e^{-j\omega u} du. \tag{3.80}$$

From equation (3.76) we have that

$$\frac{c}{2\sqrt{\epsilon_r}} K\left(\frac{c}{2\sqrt{\epsilon_r}} u\right) = \frac{1}{2\pi} \int_{-\infty}^{\infty} S_{11}(\omega) e^{j\omega u} d\omega, \tag{3.81}$$

and therefore $K(z)$ and $S_{11}(\omega)$ are related by the Fourier transform as

$$\frac{c}{2\sqrt{\epsilon_r}} K\left(\frac{c}{2\sqrt{\epsilon_r}} z\right) \overset{\mathcal{F}}{\longleftrightarrow} S_{11}(\omega). \tag{3.82}$$

which is equivalent to (3.78).

Even though it is only valid under the condition of weak coupling, the analysis of low reflectivity NTL is very useful as it stands out the direct relation between coupling coefficient and frequency response with that of the Fourier transform. Further on our work we will see this relation as very handy on interpreting the behavior of NTL structures.

3.2.4 Constant coupling

We now consider the case of NTLs with a constant coupling factor along their length. In this case, the coupled mode equations can be analytically solved even for the case of high reflectivity NTLs. Taking the derivative of the first of the coupled-mode equations (3.41) and considering $K(z) = C^{te}$ we have

$$\frac{d^2 a^+}{dz^2} = -j\beta \frac{da^+}{dz} - K \frac{da^-}{dz}. \tag{3.83}$$

Substituting the coupled-mode equations on the previous equation we have

$$\frac{d^2 a^+}{dz^2} = -j\beta(-j\beta a^+ - K a^-) - K(j\beta a^- - K a^+). \tag{3.84}$$

Finally, simplifying and rearranging the previous equation we get

$$\frac{d^2a^+}{dz^2} = (K^2 - \beta^2)a^+. \tag{3.85}$$

The same procedure can be used for the second of the coupled-mode equations (3.42), yielding

$$\frac{d^2a^-}{dz^2} = (K^2 - \beta^2)a^-. \tag{3.86}$$

We know from subsection 3.2.1.5 that the coupling coefficient for TEM NTLs is obtained from the characteristic impedance $Z_0(z)$ as

$$K = \frac{1}{2}\frac{1}{Z_0}\frac{dZ_0}{dz}. \tag{3.87}$$

The coupling coefficient expression is a first-order linear differential equation. Solving it in order to obtain a closed expression for the characteristic impedance as a function of distance z yields [38]

$$\begin{aligned} Z_0(z) &= C^{te} e^{2\int_0^z K(x)dx} \\ &= Z_0(0) e^{2\int_0^z K(x)dx}. \end{aligned} \tag{3.88}$$

However for the case of constant coupling NTLs we have $K(z) = C^{te}$, which reduces the expression for $Z_0(z)$ to

$$Z_0(z) = Z_0(0)e^{2Kz}. \tag{3.89}$$

hence the exponential impedance profile of the NTL depicted in Figure 3.6.

Let us rewrite the differential equations (3.85) and (3.86) as,

$$\frac{d^2a^+}{dz^2} - \gamma^2 a^+ = 0, \tag{3.90}$$

$$\frac{d^2a^-}{dz^2} - \gamma^2 a^- = 0, \tag{3.91}$$

where $\gamma^2 = K^2 - \beta^2$. Equations (3.90) and (3.91) are second order homogeneous linear differential equations. The general solution to these equations are of the form [38]

$$a^+ = C_1 e^{\gamma z} + C_2 e^{-\gamma z}, \tag{3.92}$$

$$a^- = C_3 e^{\gamma z} + C_4 e^{-\gamma z}, \tag{3.93}$$

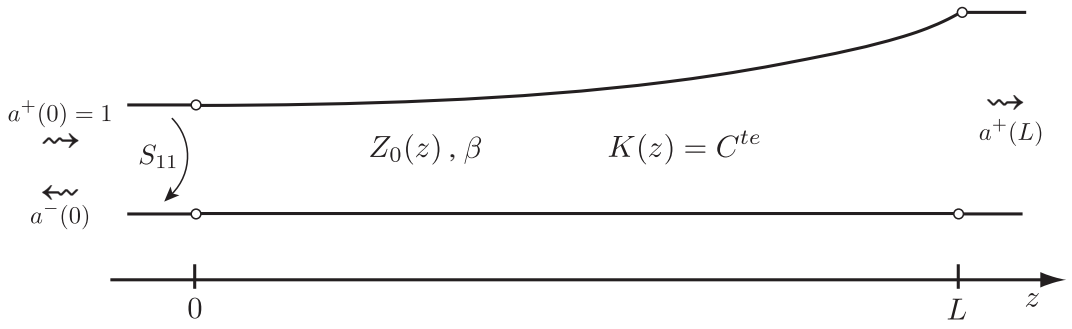

FIGURE 3.6: NTL with positive constant coupling coefficient.

where C_1, C_2, C_3, C_4 are the unknown variables, that are obtained by setting the appropriate boundary conditions and the corresponding derivatives are

$$\frac{da^+}{dz} = \gamma C_1 e^{\gamma z} - \gamma C_2 e^{-\gamma z}, \tag{3.94}$$

$$\frac{da^-}{dz} = \gamma C_3 e^{\gamma z} - \gamma C_4 e^{-\gamma z}. \tag{3.95}$$

Considering an NTL with constant coupling coefficient with length L extending from $z = 0$ to $z = L$ as it is illustrated in Figure 3.6. We consider the output port at $z = L$ to be terminated in a matched load and an unitary excitation of the device, therefore the boundary conditions are given by

$$a^+(0) = 1, \tag{3.96}$$

$$a^-(L) = 0. \tag{3.97}$$

Substituting equations (3.92)-(3.95) into the coupled-mode equations (3.41)-(3.42) and applying the boundary conditions, yields the following system of linear equations

$$\begin{cases} C_1 + C_2 = 1, \\ C_3 e^{\gamma L} + C_4 e^{-\gamma L} = 0, \\ \gamma(C_1 - C_2) = -j\beta - K(C_3 + C_4), \\ \gamma(C_3 e^{\gamma L} - C_4 e^{-\gamma L}) = -K(C_1 e^{\gamma L} + C_2 e^{-\gamma L}). \end{cases} \tag{3.98}$$

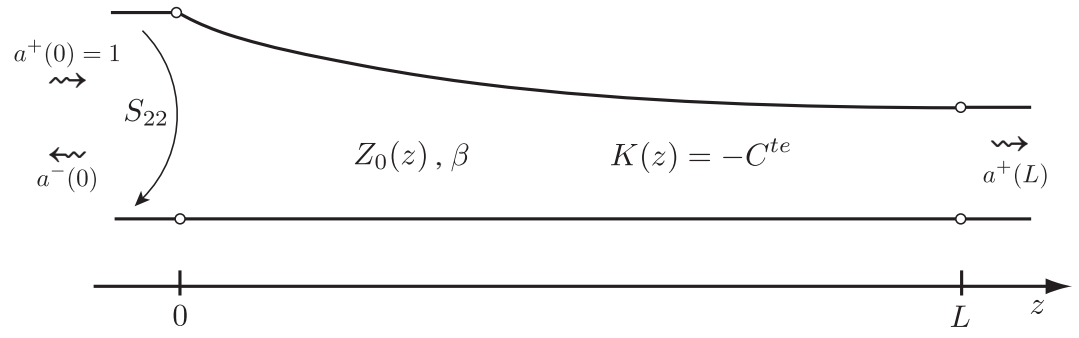

FIGURE 3.7: NTL with negative constant coupling coefficient.

Solving the system in (3.98) and after some mathematical manipulation, the unknown variables in equations (3.92) and (3.93) are given by

$$C_1 = \frac{1}{2} - \frac{\gamma\sinh(\gamma L) + j\beta\cosh(\gamma L)}{2(\gamma\cosh(\gamma L) + j\beta\sinh(\gamma L))}, \tag{3.99}$$

$$C_2 = \frac{1}{2} + \frac{\gamma\sinh(\gamma L) + j\beta\cosh(\gamma L)}{2(\gamma\cosh(\gamma L) + j\beta\sinh(\gamma L))}, \tag{3.100}$$

$$C_3 = \frac{-Ke^{-\gamma L}}{2(\gamma\cosh(\gamma L) + j\beta\sinh(\gamma L))}, \tag{3.101}$$

$$C_4 = \frac{Ke^{\gamma L}}{2(\gamma\cosh(\gamma L) + j\beta\sinh(\gamma L))}. \tag{3.102}$$

Considering the boundary conditions of the device we have that

$$S_{21} = a^+(L) = C_1e^{\gamma L} + C_2e^{-\gamma L}, \tag{3.103}$$

which after substituting C_1 and C_2 yields

$$S_{21} = \frac{\gamma}{\gamma\cosh(\gamma L) + j\beta\sinh(\gamma L)}. \tag{3.104}$$

On the other hand, the reflection coefficient S_{11} is given by

$$S_{11} = a^-(0) = C_3e^{\gamma 0} + C_4e^{-\gamma 0} = C_3 + C_4, \tag{3.105}$$

which after substituting C_3 and C_4 turns into

$$S_{11} = \frac{K\sinh(\gamma L)}{\gamma\cosh(\gamma L) + j\beta\sinh(\gamma L)}. \tag{3.106}$$

In order to fully characterize the NTL device in Figure 3.6 we also need to derive the

expressions for S_{12} and S_{22}. One way to do that is to perform the same analyze as before but from the output end, as illustrated in Figure 3.7. Comparing the two situations, the only thing that differs is that the coupling coefficient as now a negative value although the magnitude is the same. In this case, the unknown variables C_1, C_2, C_3, C_4 are given by

$$C_1 = \frac{1}{2} - \frac{\gamma \sinh(\gamma L) + j\beta \cosh(\gamma L)}{2(\gamma \cosh(\gamma L) + j\beta \sinh(\gamma L))}, \tag{3.107}$$

$$C_2 = \frac{1}{2} + \frac{\gamma \sinh(\gamma L) + j\beta \cosh(\gamma L)}{2(\gamma \cosh(\gamma L) + j\beta \sinh(\gamma L))}, \tag{3.108}$$

$$C_3 = \frac{Ke^{-\gamma L}}{2(\gamma \cosh(\gamma L) + j\beta \sinh(\gamma L))}, \tag{3.109}$$

$$C_4 = \frac{-Ke^{\gamma L}}{2(\gamma \cosh(\gamma L) + j\beta \sinh(\gamma L))}. \tag{3.110}$$

Following the same development as before we have that

$$S_{12} = \frac{\gamma}{\gamma \cosh(\gamma L) + j\beta \sinh(\gamma L)} = S_{21}, \tag{3.111}$$

which is the same as S_{21} because the structure is reciprocal. On the other hand we have that

$$S_{22} = \frac{-K \sinh(\gamma L)}{\gamma \cosh(\gamma L) + j\beta \sinh(\gamma L)} = -S_{11}. \tag{3.112}$$

3.2.5 Periodic coupling

We now are going to consider the case when the coupling coefficient $K(z)$ is periodic. In this case, $K(z)$ can be expanded in a spatial Fourier series, allowing the periodic coupling problem to be reduced to the constant coupling problem for each relevant term of the corresponding Fourier expansion. Basically, each term of the Fourier series of $K(z)$ is associated with one of the several resonant band that the NTL might possess. As we shall see next, an analytical solution can be obtained for each term of the Fourier series of the coupling coefficient. This analytical solution accurately characterizes the behavior of the NTL device within the resonance frequency band associated with the corresponding Fourier series term.

We start from the coupled-mode equations

$$\frac{da^+}{dz} = -j\beta a^+ - Ka^-, \tag{3.113}$$

$$\frac{da^-}{dz} = j\beta a^- - Ka^+. \tag{3.114}$$

Let us consider the following variable change

$$a^+(z) = A^+(z)e^{-j\beta z}, \tag{3.115}$$

$$a^-(z) = A^-(z)e^{j\beta z}. \tag{3.116}$$

Substituting the previous expressions into the coupled-mode equations, yields the following new set of coupled-mode equations

$$\frac{dA^+}{dz} = -K(z)A^-e^{2j\beta z}, \tag{3.117}$$

$$\frac{dA^-}{dz} = -K(z)A^+e^{-2j\beta z}. \tag{3.118}$$

In this section we assume that the coupling coefficient $K(z)$ is periodic, therefore its expansion as a Fourier series is given by [1]

$$K(z) = \sum_{n=-\infty}^{+\infty} K_n e^{jn\frac{2\pi}{\Lambda}z}, \tag{3.119}$$

with

$$K_n = \frac{1}{\Lambda}\int_{\Lambda} K(z)e^{-jn\frac{2\pi}{\Lambda}z} \tag{3.120}$$

and where Λ is the period of the coupling coefficient $K(z)$. The coupling coefficient can therefore be expanded as

$$\begin{aligned} K(z) =& K_1e^{j1\left(\frac{2\pi}{\Lambda}\right)z} + K_{-1}e^{-j1\left(\frac{2\pi}{\Lambda}\right)z} + K_2e^{j2\left(\frac{2\pi}{\Lambda}\right)z} + \\ &+ K_{-2}e^{-j2\left(\frac{2\pi}{\Lambda}\right)z} + K_3e^{j3\left(\frac{2\pi}{\Lambda}\right)z} + K_{-3}e^{-j3\left(\frac{2\pi}{\Lambda}\right)z} + \dots \end{aligned} \tag{3.121}$$

Substituting the previous expansion into the coupled-mode equations (3.117) and (3.118) and rearranging the expression yields

$$\begin{aligned} \frac{dA^+}{dz} = -\Bigg(& K_1e^{j2\left(\beta+\frac{\pi}{\Lambda}\right)z} + K_{-1}e^{j2\left(\beta-\frac{\pi}{\Lambda}\right)z} + K_2e^{j2\left(\beta+\frac{2\pi}{\Lambda}\right)z} + \\ & + K_{-2}e^{j2\left(\beta-\frac{2\pi}{\Lambda}\right)z} + \dots + K_ne^{j2\left(\beta+\frac{n\pi}{\Lambda}\right)z} + K_{-n}e^{j2\left(\beta-\frac{n\pi}{\Lambda}\right)z}\Bigg)A^- \end{aligned} \tag{3.122}$$

and for the counter-propagating mode

$$\frac{dA^-}{dz} = -\Bigg(K_1 e^{-j2\left(\beta-\frac{\pi}{\Lambda}\right)z} + K_{-1} e^{-j2\left(\beta+\frac{\pi}{\Lambda}\right)z} + K_2 e^{-j2\left(\beta-\frac{2\pi}{\Lambda}\right)z} + \\ + K_{-2} e^{-j2\left(\beta+\frac{2\pi}{\Lambda}\right)z} + \ldots + K_n e^{-j2\left(\beta-\frac{n\pi}{\Lambda}\right)z} + K_{-n} e^{-j2\left(\beta+\frac{n\pi}{\Lambda}\right)z}\Bigg) A^+. \tag{3.123}$$

Let us consider a finite length NTL with length that is much more larger than the coupling coefficient period Λ. Since the mode amplitudes $A^+(z)$ and $A^-(z)$ are slowly varying with z [29], we may integrate equation (3.122) over a distance d considerably larger than Λ yet much smaller than the variation scale for the modes amplitudes, yielding a small increment of the mode amplitude ΔA^+ as

$$\Delta A^+ = -\Bigg(K_1 \int_{d\gg\Lambda} e^{j2\left(\beta+\frac{\pi}{\Lambda}\right)z} dz + K_{-1} \int_{d\gg\Lambda} e^{j2\left(\beta-\frac{\pi}{\Lambda}\right)z} dz + \\ + K_2 \int_{d\gg\Lambda} e^{j2\left(\beta+\frac{2\pi}{\Lambda}\right)z} dz + K_{-2} \int_{d\gg\Lambda} e^{j2\left(\beta-\frac{2\pi}{\Lambda}\right)z} dz + \ldots + \\ + K_n \int_{d\gg\Lambda} e^{j2\left(\beta+\frac{n\pi}{\Lambda}\right)z} dz + K_{-n} \int_{d\gg\Lambda} e^{j2\left(\beta-\frac{n\pi}{\Lambda}\right)z} dz\Bigg) A^-. \tag{3.124}$$

From this equation we can see that all of the integrals will have a contribution to ΔA^+ close to zero, except in the case when the exponent in the exponential terms is zero or close to zero. Hence, if we place our frequency band of interest around the n-th resonant frequency band, β will be of the same order of magnitude as $n\pi/\Lambda$ and so all of the integrals in the previous expression except the one associated with the K_{-n} term of the Fourier series will have residual contributions. In this way we may rewrite the coupled-mode equations (3.122) and (3.123) for the n-th resonant frequency band as

$$\frac{dA^+}{dz} = -\Big(K_{-n} e^{j2\Delta\beta z}\Big) A^-, \tag{3.125}$$

$$\frac{dA^-}{dz} = -\Big(K_n e^{-j2\Delta\beta z}\Big) A^+, \tag{3.126}$$

where the variable $\Delta\beta$ is defined as

$$\Delta\beta = \beta - \frac{n\pi}{\Lambda}. \tag{3.127}$$

When considering a frequency band placed around the n-th resonant frequency band, $\Delta\beta$ will have values close to zero. In fact, when $\Delta\beta = 0$ the coupling between forward propagating wave A^+ and the backward propagating wave A^- is maximum and so, we

introduce the condition for resonant coupling as

$$\beta - \frac{n\pi}{\Lambda} = 0 \quad \Longrightarrow \quad \beta = \frac{n\pi}{\Lambda}. \tag{3.128}$$

This resonant coupling condition is a particular case of the more general *longitudinal phase matching* condition introduced by Yariv [28]. Yariv states that the maximum coupling of power between any two modes (k and i) propagating along a waveguide happens when the following condition is satisfied

$$\beta_k - \beta i - n\frac{2\pi}{\Lambda} = 0, \tag{3.129}$$

for some integer n. In our case, the coupling occurs between the forward and backward propagating waves associated with the same mode, therefore

$$\beta^+ - \beta^- - n\frac{2\pi}{\Lambda} = 0 \quad \Longrightarrow \quad (\beta) - (-\beta) = n\frac{2\pi}{\Lambda} \quad \Longrightarrow \quad \beta = \frac{n\pi}{\Lambda}, \tag{3.130}$$

which is the same as (3.128). Furthermore,

$$\beta = \frac{n\pi}{\Lambda} \quad \Longrightarrow \quad \frac{2\pi f\sqrt{\epsilon_r}}{c} = \frac{n\pi}{\Lambda} \quad \Longrightarrow \quad \frac{2\sqrt{\epsilon_r}}{\lambda} = \frac{n}{\Lambda}, \tag{3.131}$$

considering the fundamental resonant frequency band, thus $n = 1$ and rearranging the expression, we have

$$\lambda = 2\sqrt{\epsilon_r}\Lambda. \tag{3.132}$$

Taking into consideration that $n_{eff} = \sqrt{\epsilon_r \mu_r}$ is the effective refractive index, we finally have

$$\lambda = 2n_{eff}\Lambda \tag{3.133}$$

which is the well known Bragg condition widely used on the design of fiber Bragg gratings [39].

Let us consider the coupled-mode equations derived for the n-th resonant frequency band (3.125), (3.126). Defining a new variable change as

$$A^+ = u^+ e^{j\Delta\beta z}, \tag{3.134}$$

$$A^- = u^- e^{-j\Delta\beta z} \tag{3.135}$$

and applying it to the coupled-mode equations (3.125) and (3.126), yields

$$\frac{du^+}{dz} = -j\Delta\beta u^+ - K_{-n}u^-, \tag{3.136}$$

$$\frac{du^-}{dz} = j\Delta\beta u^- - K_n u^+. \tag{3.137}$$

The last two equations form a set of coupled-mode equations of constant coupling value, since both K_{-n} and K_n are constants. We saw in section 3.2.4 that this kind of differential equation system has an analytical solution, however in the case analyzed in section 3.2.4 the same value of coupling coefficient appeared in both differential equations, whereas in the present case the coupling coefficients are different in both equations. In order to find an analytical solution for this problem we must first find the relation between K_{-n} and K_n.

We know from section 3.2.1.5 that the coupling coefficient for NTLs is given by

$$K = \frac{1}{2}\frac{1}{Z_0}\frac{dZ_0}{dz}. \tag{3.138}$$

Since $Z_0(z)$ only takes positive real values, from (3.138) we know that $K(z)$ is a real function. Regarding the properties of the Fourier series [1] we know that the series coefficients for real functions such as $K(z)$ obey to the relation

$$K_{-n} = K_n^*. \tag{3.139}$$

It is important to notice that unlike the case of constant coupling addressed in section 3.2.4, the coupling coefficient K_n considered from the Fourier series terms may usually take constant complex values.

Taking in consideration the previous relation, we can rewrite the coupled-mode equations (3.136) and (3.137) as

$$\frac{du^+}{dz} = -j\Delta\beta u^+ - K_n^* u^-, \tag{3.140}$$

$$\frac{du^-}{dz} = j\Delta\beta u^- - K_n u^+. \tag{3.141}$$

To solve these coupled-mode equations we follow the same procedure as in section 3.2.4. Taking the derivative of equation (3.140) we have

$$\frac{d^2u^+}{dz^2} = -j\Delta\beta\frac{du^+}{dz} - K_n^*\frac{du^-}{dz}. \tag{3.142}$$

Substituting equations (3.140) and (3.141) into the previous expression gives

$$\frac{d^2u^+}{dz^2} = \left(|K_n|^2 - \Delta\beta^2\right)u^+, \tag{3.143}$$

where $|K_n|^2 = K_nK_n^*$. Using the same procedure for equation (3.141) we have

$$\frac{d^2u^-}{dz^2} = \left(|K_n|^2 - \Delta\beta^2\right)u^-. \tag{3.144}$$

Rearranging equations (3.143) and (3.144) yields

$$\frac{d^2u^+}{dz^2} - \gamma^2u^+ = 0, \tag{3.145}$$

$$\frac{d^2u^-}{dz^2} - \gamma^2u^- = 0, \tag{3.146}$$

where $\gamma^2 = |K_n|^2 - \Delta\beta^2$. These second order differential equations are the same type as the ones obtained in section 3.2.4, except for the definition of γ. Therefore, the general solution of these equations is of the form

$$u^+ = C_1e^{\gamma z} + C_2e^{-\gamma z}, \tag{3.147}$$

$$u^- = C_3e^{\gamma z} + C_4e^{-\gamma z}, \tag{3.148}$$

just like in section 3.2.4. The procedure to calculate the unknown variables C_1, C_2, C_3 and C_4 is the same used in section 3.2.4. The derivatives of (3.147) and (3.148) are given by

$$\frac{du^+}{dz} = \gamma C_1e^{\gamma z} - \gamma C_2e^{-\gamma z}, \tag{3.149}$$

$$\frac{du^-}{dz} = \gamma C_3e^{\gamma z} - \gamma C_4e^{-\gamma z}. \tag{3.150}$$

Before we proceed with the solution of (3.145) and (3.146), we must first state the relation between $u^+(z)$ and $u^-(z)$ and the wave amplitudes $a^+(z)$ and $a^-(z)$. From

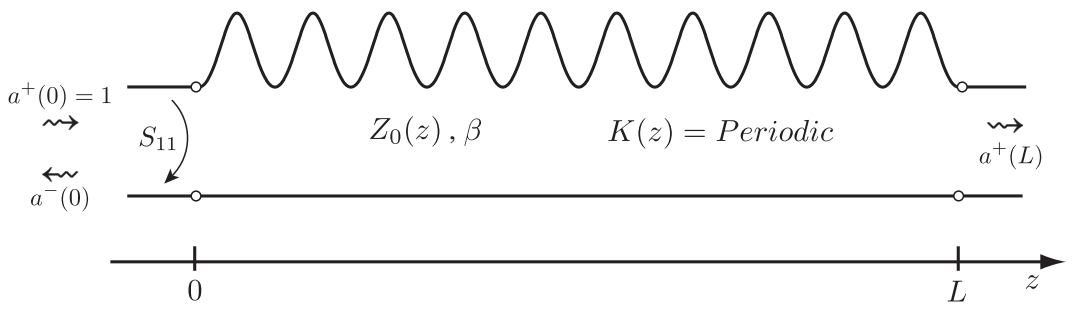

FIGURE 3.8: NTL with periodic coupling coefficient.

(3.115) and (3.116) we know that

$$a^+ = A^+ e^{-j\beta z}, \tag{3.151}$$

$$a^- = A^- e^{j\beta z}. \tag{3.152}$$

Substituting equations (3.134) and (3.135) into the previous expressions we have

$$a^+ = e^{j\Delta\beta z} e^{-j\beta z} u^+ = u^+ e^{-j(\beta-\Delta\beta)z}, \tag{3.153}$$

$$a^- = e^{-j\Delta\beta z} e^{j\beta z} u^- = u^- e^{j(\beta-\Delta\beta)z}. \tag{3.154}$$

Recalling that $\Delta\beta = \beta - \frac{n\pi}{\Lambda}$, the previous equations can be further simplified yielding

$$a^+ = u^+ e^{-j\frac{n\pi}{\Lambda}z}, \tag{3.155}$$

$$a^- = u^- e^{j\frac{n\pi}{\Lambda}z}. \tag{3.156}$$

Let us now consider an NTL device with periodic coupling coefficient with length L extending from $z = 0$ to $z = L$ as illustrated in Figure 3.8. The output port at $z = L$ is assumed to be terminated in a matched load. Further, an unitary excitation of the device is considered, yielding the boundary conditions

$$a^+(0) = 1 \quad \longrightarrow \quad u^+(0) = 1, \tag{3.157}$$

$$a^-(L) = 0 \quad \longrightarrow \quad u^-(L) = 0. \tag{3.158}$$

$$\tag{3.159}$$

Substituting equations (3.147)-(3.150) into the coupled mode equations (3.140)-(3.141) and applying the boundary conditions, yields the following system of linear

equations

$$\begin{cases} C_1 + C_2 = 1, \\ C_3 e^{\gamma L} + C_4 e^{-\gamma L} = 0, \\ \gamma(C_1 - C_2) = -j\Delta\beta - K_n(C_3 + C_4), \\ \gamma(C_3 e^{\gamma L} - C_4 e^{-\gamma L}) = -K_n(C_1 e^{\gamma L} + C_2 e^{-\gamma L}), \end{cases} \tag{3.160}$$

where $\gamma = \sqrt{|K_n|^2 - \Delta\beta^2}$. Solving the equations system in (3.160), the unknown variables in equations (3.147) and (3.148) are given by

$$C_1 = \frac{1}{2} - \frac{\gamma \sinh(\gamma L) + j\Delta\beta \cosh(\gamma L)}{2(\gamma \cosh(\gamma L) + j\Delta\beta \sinh(\gamma L))}, \tag{3.161}$$

$$C_2 = \frac{1}{2} + \frac{\gamma \sinh(\gamma L) + j\Delta\beta \cosh(\gamma L)}{2(\gamma \cosh(\gamma L) + j\Delta\beta \sinh(\gamma L))}, \tag{3.162}$$

$$C_3 = \frac{-K_n e^{-\gamma L}}{2(\gamma \cosh(\gamma L) + j\Delta\beta \sinh(\gamma L))}, \tag{3.163}$$

$$C_4 = \frac{K_n e^{\gamma L}}{2(\gamma \cosh(\gamma L) + j\Delta\beta \sinh(\gamma L))}. \tag{3.164}$$

From (3.147)-(3.148) and considering the boundary conditions of the device, we have that

$$S_{21} = a^+(L) = u^+(L)e^{-j\frac{n\pi}{\Lambda}L} = (C_1 e^{\gamma z} + C_2 e^{-\gamma z})e^{-j\frac{n\pi}{\Lambda}L}, \tag{3.165}$$

which becomes

$$S_{21} = \frac{\gamma e^{-j\frac{n\pi}{\Lambda}L}}{\gamma \cosh(\gamma L) + j\Delta\beta \sinh(\gamma L)}. \tag{3.166}$$

On the other hand, the S_{11} of the device is calculated as

$$S_{11} = \frac{a^-(0)}{a^+(0)} = \frac{u^-(0)}{u^+(0)} = u^-(0) = C_3 + C_4, \tag{3.167}$$

yielding

$$S_{11} = \frac{K_n \sinh(\gamma L)}{\gamma \cosh(\gamma L) + j\Delta\beta \sinh(\gamma L)}. \tag{3.168}$$

The mathematical development performed in this section follows that of [32], [39] and [14].

3.2.6 Iterative solution

So far we have shown that the complete solution for the direct scattering problem (the analysis problem) can be obtained by solving either the coupled mode equations or

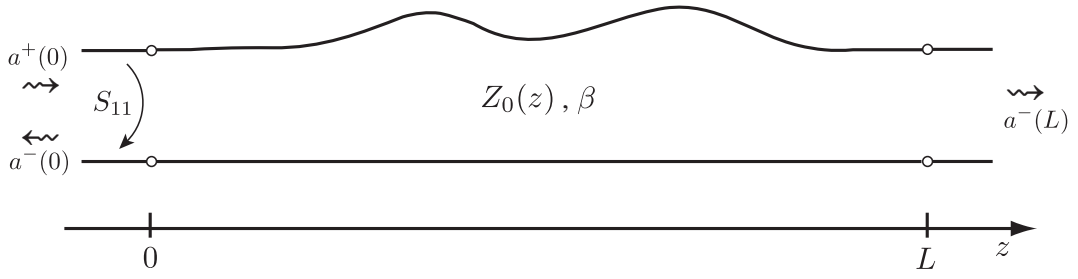

FIGURE 3.9: High reflectivity NTL.

the Riccati equation using numerical methods developed to solve differential equations problems with boundary conditions. One the other hand we have also showed that for some particular cases such as weak coupling, constant or periodic coupling, the solution for the direct scattering problem can be obtained in the form of mathematical expressions. Unlike numerical methods, these expressions give us a better insight on the physical operation of the NTL structures. So, in this subsection we derive the exact solution for the coupled mode equations. As we shall see, they come in the form of a series of integral equations accounting for the infinite number of propagation paths that a wave can take on the NTL. We start from the coupled mode equations

$$\frac{da^+}{dz} = -j\beta a^+ - Ka^-, \tag{3.169}$$

$$\frac{da^-}{dz} = j\beta a^- - Ka^+, \tag{3.170}$$

and let us consider the variable change

$$a^+(z) = A^+(z)e^{-j\beta z}, \tag{3.171}$$

$$a^-(z) = A^-(z)e^{j\beta z}. \tag{3.172}$$

Applying the variable change into the coupled-mode equations yields a new set of coupled-mode equations given by

$$\frac{dA^+}{dz} = -K(z)A^-e^{2j\beta z}, \tag{3.173}$$

$$\frac{dA^-}{dz} = -K(z)A^+e^{-2j\beta z}. \tag{3.174}$$

Considering the case of the NTL structure depicted in Figure 3.9 we set the boundary conditions as

$$A^+(0) = 1, \tag{3.175}$$

$$A^-(L) = 0, \tag{3.176}$$

corresponding to an unitary excitation and a matched load termination at the output of the device respectively.

Taking the integral of equation (3.174) from any point z along the structure up to L yields

$$\begin{aligned} \int_{z_1=z}^{z_1=L} \frac{dA^-}{dz_1} dz_1 &= -\int_{z_1=z}^{z_1=L} K(z_1) A^+(z_1) e^{-2j\beta z_1} dz_1 \\ &\Downarrow \\ A^-(L) - A^-(z) &= -\int_{z_1=z}^{z_1=L} K(z_1) A^+(z_1) e^{-2j\beta z_1} dz_1, \end{aligned} \tag{3.177}$$

however, from the boundary conditions, we know that $A^-(L) = 0$, therefore we have

$$A^-(z) = \int_{z_1=z}^{z_1=L} K(z_1) A^+(z_1) e^{-2j\beta z_1} dz_1. \tag{3.178}$$

Proceeding in the same way with the first coupled-mode equation (3.173) we have

$$\begin{aligned} \int_{z_2=0}^{z_2=z} \frac{dA^+}{dz_2} dz_2 &= -\int_{z_2=0}^{z_2=z} K(z_2) A^-(z_2) e^{2j\beta z_2} dz_2 \\ &\Downarrow \\ A^+(z) - A^+(0) &= -\int_{z_2=0}^{z_2=z} K(z_2) A^-(z_2) e^{2j\beta z_2} dz_2, \end{aligned} \tag{3.179}$$

and taking into consideration that $A^+(0) = 1$ we obtain

$$A^+(z) = 1 - \int_{z_2=0}^{z_2=z} K(z_2) A^-(z_2) e^{2j\beta z_2} dz_2. \tag{3.180}$$

The exact solution for the coupled mode equations and therefore the forward or direct scattering problem is given by first substituting (3.180) into (3.178) and then proceed iteratively. As an example, considering the substitution of equation (3.180) into (3.178)

yields

$$
\begin{aligned}
A^-(z) &= \int_{z_1=z}^{z_1=L} K(z_1)\left(1-\int_{z_2=0}^{z_2=z_1} K(z_2)A^-(z_2)e^{2j\beta z_2}dz_2\right)e^{-2j\beta z_1}dz_1 \\
&\Downarrow \\
A^-(z) &= \int_{z_1=z}^{z_1=L} K(z_1)e^{-2j\beta z_1}dz_1 - \\
&\quad - \int_{z_1=z}^{z_1=L}\int_{z_2=0}^{z_2=z_1} A^-(z_2)K(z_1)e^{-2j\beta z_1}K(z_2)e^{2j\beta z_2}dz_2dz_1.
\end{aligned}
\tag{3.181}
$$

Substituting again equation (3.178) into the previous equation and proceeding iteratively by repeatedly substituting equations (3.178) and (3.180) we obtain the following infinite series

$$
\begin{aligned}
A^-(z) = &\int_{z_1=z}^{z_1=L} K(z_1)e^{-2j\beta z_1}dz_1 - \\
&- \int_{z_1=z}^{z_1=L}\int_{z_2=0}^{z_2=z_1}\int_{z_3=z_2}^{z_3=L} K(z_1)K(z_2)K(z_3)e^{-2j\beta(z_1-z_2+z_3)}dz_3dz_2dz_1 \\
&\qquad + \cdots + \\
&+ (-1)^{n+1}\int_{z_1=z}^{z_1=L}\int_{z_2=0}^{z_2=z_1}\int_{z_3=z_2}^{z_3=L}\cdots\int_{z_{2n-1}=z_{2n-2}}^{z_{2n-1}=L} A^+(z_{2n-1})\cdot \\
&\cdot K(z_1)K(z_2)K(z_3)\cdots K(z_{2n-1})e^{-2j\beta(z_1-z_2+z_3\cdots z_{2n-1})}dz_{2n-1}\cdots dz_3dz_2dz_1,
\end{aligned}
\tag{3.182}
$$

where n is the number of iterations performed. Considering a sufficient large number of iterations n we can say that the last terms of the series only contribute residual values to the overall scattering occurring in the NTL structure and so we can consider that for iteration n the integral term in equation (3.180) is close to zero, therefore $A^+(z_{2n-1}) \approx 1$. Taking this into consideration and also that

$$
S_{11} = \left.\frac{a^-(0)}{a^+(0)}\right|_{a^-(L)=0} = \frac{A^-(0)}{A^+(0)} = A^-(0), \tag{3.183}
$$

the reflection coefficient is given by

$$\begin{aligned} S_{11} = & \int_{z_1=0}^{z_1=L} K(z_1) e^{-2j\beta z_1} dz_1 - \\ & - \int_{z_1=0}^{z_1=L} \int_{z_2=0}^{z_2=z_1} \int_{z_3=z_2}^{z_3=L} K(z_1)K(z_2)K(z_3) e^{-2j\beta(z_1-z_2+z_3)} dz_3 dz_2 dz_1 \\ & \qquad + \cdots + \\ & + (-1)^{n+1} \int_{z_1=0}^{z_1=L} \int_{z_2=0}^{z_2=z_1} \int_{z_3=z_2}^{z_3=L} \cdots \int_{z_{2n-1}=z_{2n-2}}^{z_{2n-1}=L} A^+(z_{2n-1}) \cdot \\ & \cdot K(z_1)K(z_2)K(z_3)\cdots K(z_{2n-1}) e^{-2j\beta(z_1-z_2+z_3\cdots z_{2n-1})} dz_{2n-1}\cdots dz_3 dz_2 dz_1. \end{aligned} \tag{3.184}$$

It is worthwhile referring that each term of (3.184) is an integral that extends to all propagation paths composed by a given number of scattering events. Another interesting conclusion comes by considering only one iteration and therefore $n = 1$. In this particular case, equation (3.184) reduces to

$$S_{11} = \int_{z_1=0}^{z_1=L} K(z_1) e^{-2j\beta z_1} dz_1. \tag{3.185}$$

Recalling the analysis of NTL structures under the condition of weak coupling (subsection 3.2.3), we see that the previous equation is the same as (3.73).

The mathematical development performed in this subsection follows that of [15] and [32].

3.3 Transmission matrix method

As seen in the previous section, the analysis of NTL devices can be accurately performed by solving the coupled-mode equations. However to solve these differential equations the use of complicated and time consuming numerical solvers is necessary. Nevertheless we also proved that for some specific cases, namely constant and periodic coupling, the coupled-mode equations can be solved yielding a analytical solution. In this section we show how by the discretization of either the coupling coefficient or the impedance profile it is possible to use the analytical solutions derived before in order to accurately analyze any NTL device without resorting to differential equations numerical solvers.

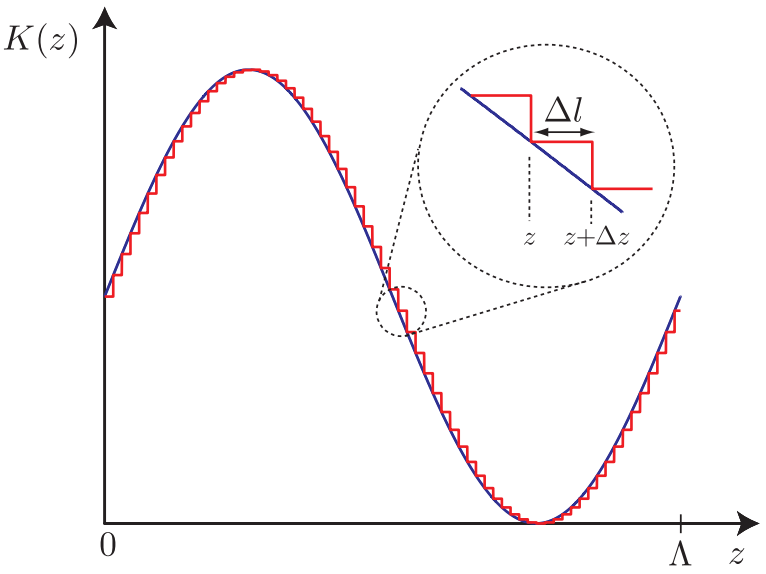

FIGURE 3.10: Constant coupling discretization.

3.3.1 Constant coupling discretization

Let us consider the division of an NTL device into a number N of sufficient small sections of lenght Δl, so that each of the sections can be considered to have a constant coupling. This is illustrated in Figure 3.10 for a sinusoidal coupling coefficient profile. Because each single section i has a constant coupling coefficient we can calculate the individual transmission matrix for each section. Multiplying all of transmission matrices shall yield the overall transmission matrix of the NTL structure from which the S-parameters of the device can then be calculated.

The discretization depicted in Figure 3.10 is only for one period length Λ, but when considering the total length L of the structure, the size of the sections is given by $\Delta l = L/N$.

From section 3.2.4 we know that the S-parameters for each constant coupling section i of the NTL are given by

$$S_{12} = \frac{\gamma}{\gamma \cosh(\gamma \Delta l) + j\beta \sinh(\gamma \Delta l)} = S_{21}, \tag{3.186}$$

$$S_{11} = \frac{K_i \sinh(\gamma \Delta l)}{\gamma \cosh(\gamma \Delta l) + j\beta \sinh(\gamma \Delta l)} = -S_{22}. \tag{3.187}$$

The corresponding transmission matrix is then computed by recalling from section 2.5 that

$$A_{11} = \frac{1}{S_{12}} = \frac{\gamma \cosh(\gamma \Delta l) + j\beta \sinh(\gamma \Delta l)}{\gamma}, \tag{3.188}$$

$$A_{12} = \frac{-S_{22}}{S_{12}} = \frac{K_i \sinh(\gamma \Delta l)}{\gamma}, \tag{3.189}$$

$$A_{21} = \frac{S_{12}^2 - S_{11}S_{22}}{S_{12}} = \frac{K_i \sinh(\gamma \Delta l)}{\gamma}, \tag{3.190}$$

$$A_{22} = \frac{1}{S_{12}} = \frac{\gamma \cosh(\gamma \Delta l) - j\beta \sinh(\gamma \Delta l)}{\gamma}, \tag{3.191}$$

where K_i is the coupling coefficient of i-th section and Δl is the length of each section. In matrix notation we have

$$\begin{bmatrix} a^+(z) \\ a^-(z) \end{bmatrix} = \begin{bmatrix} \cosh(\gamma \Delta l) + \frac{j\beta}{\gamma} \sinh(\gamma \Delta l) & \frac{K_i}{\gamma} \sinh(\gamma \Delta l) \\ \frac{K_i}{\gamma} \sinh(\gamma \Delta l) & \cosh(\gamma \Delta l) - \frac{j\beta}{\gamma} \sinh(\gamma \Delta l) \end{bmatrix} \begin{bmatrix} a^+(z + \Delta z) \\ a^-(z + \Delta z) \end{bmatrix}. \tag{3.192}$$

In order to connect the fields amplitudes at the two ends of the NTL structure the overall transmission matrix is calculated by multiplying all of the individual ones, hence

$$[T] = [T_1][T_2][T_3] \cdots [T_{N-1}][T_N] \tag{3.193}$$

where $[T_i]$ is the transmission matrix in (3.192). We then have for the overall NTL device that

$$\begin{bmatrix} a^+(0) \\ a^-(0) \end{bmatrix} = [T] \begin{bmatrix} a^+(L) \\ a^-(L) \end{bmatrix}. \tag{3.194}$$

The S-parameters of the NTL device are then calculated using (2.159) and so we have

$$S_{11} = \frac{A_{21}}{A_{11}}, \tag{3.195}$$

$$S_{21} = \frac{1}{A_{11}}. \tag{3.196}$$

In comparison with the numerical methods used to solve the coupled-mode equations, this method is stable and more efficient since only a few number of sections are usually necessary to model most of the NTL structures.

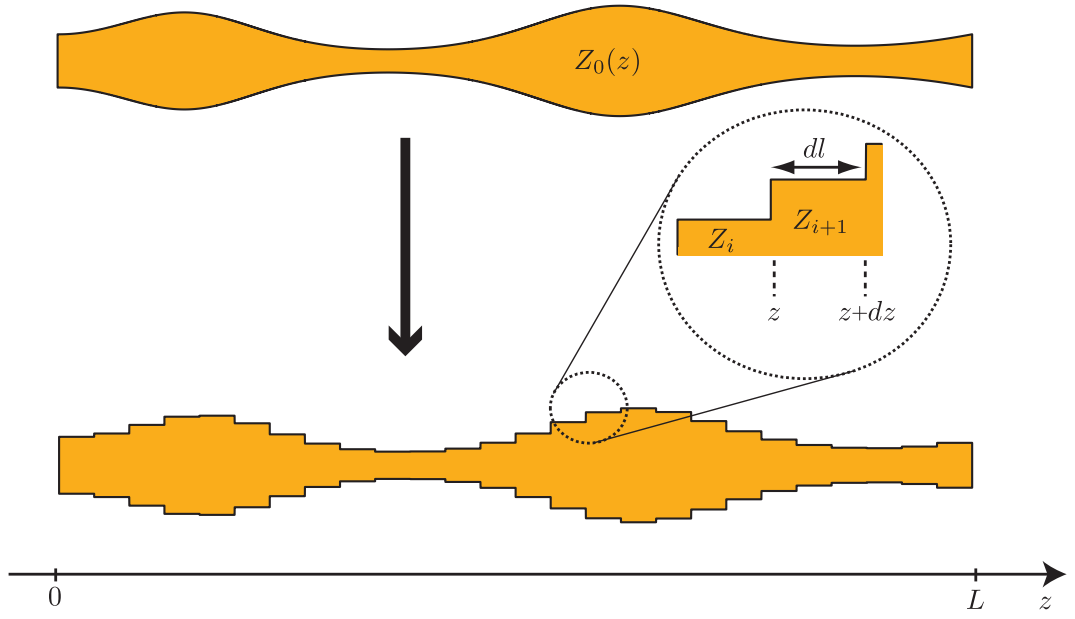

FIGURE 3.11: Constant impedance discretization.

3.3.2 Constant impedance discretization

Instead of considering sections of constant coupling coefficient as before, in this approach we consider the NTL to be constituted by a stack of transmission lines with constant impedance Z_i and infinitesimal length dl. Figure 3.11 illustrates a continuous profile NTL on the top, and the corresponding discretized NTL on the bottom. In fact, due to the discrete nature of its impedance profile, we can consider the discretized NTL to be approximated by a series of discrete reflectors with a distance dl between them. Note that, by reflector we mean the interface between two consecutive constant impedance sections. The transmission matrix $[T]$ of the overall NTL is then obtained by multiplying the individual matrices of each section. Each section is composed by a reflector and a portion of transmission line of length dl as is depicted in Figure 3.12. The transmission matrix for a single section is therefore obtained by multiplying the corresponding transmission matrices of both structures in Figure 3.12.

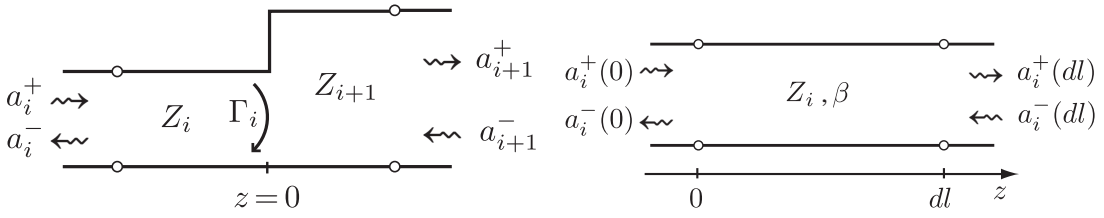

(a) Reflector.

(b) Infinitesimal length transmission line.

FIGURE 3.12: Individual section.

Hence, for the infinitesimal length transmission line in Figure 3.12(b), we have that the transmission matrix is that of a pure propagation structure. Therefore, recalling equation (2.114) we have

$$\begin{cases} a_i^+(0) &= a_i^+(dl)e^{j\beta dl}, \\ a_i^-(0) &= a_i^-(dl)e^{-j\beta dl}. \end{cases} \tag{3.197}$$

Converting the previous equations into matrix notation yields the transmission matrix

$$\begin{bmatrix} a_i^+(0) \\ a_i^-(0) \end{bmatrix} = \begin{bmatrix} e^{j\beta dl} & 0 \\ 0 & e^{-j\beta dl} \end{bmatrix} \begin{bmatrix} a_i^+(dl) \\ a_i^-(dl) \end{bmatrix}. \tag{3.198}$$

Considering the reflector structure in Figure 3.12(a), we are faced by an interface between two transmission lines with different characteristic impedance values. Therefore in order to accurately calculate the the voltage and current values at the interface $z = 0$ we must take into account the relations (2.143) and (2.144). The continuity equation [5] states that the current must be continuous, therefore the voltage and current relations at the interface $z = 0$ are given by

$$\begin{cases} V_i^+ + V_i^- = V_{i+1}^+ + V_{i+1}^-, \\ I_i^+ + I_i^- = I_{i+1}^+ + I_{i+1}^-. \end{cases} \tag{3.199}$$

Recalling the relation between voltage and current on a transmission line (2.106) and considering (2.143)-(2.144) the previous system of equations then becomes

$$\begin{cases} a_i^+\sqrt{Z_i} + a_i^-\sqrt{Z_i} = a_{i+1}^+\sqrt{Z_{i+1}} + a_{i+1}^-\sqrt{Z_{i+1}}, \\ \dfrac{a_i^+}{\sqrt{Z_i}} - \dfrac{a_i^-}{\sqrt{Z_i}} = \dfrac{a_{i+1}^+}{\sqrt{Z_{i+1}}} - \dfrac{a_{i+1}^-}{\sqrt{Z_{i+1}}}, \end{cases} \tag{3.200}$$

where the first equation defines the voltage and the second the current, both at $z = 0$. Solving the linear equation system (3.200) in order to a_i^+ and a_i^- yields

$$\begin{cases} a_i^+ = a_{i+1}^+\left(\dfrac{Z_{i+1}+Z_i}{2\sqrt{Z_iZ_{i+1}}}\right) + a_{i+1}^-\left(\dfrac{Z_{i+1}-Z_i}{2\sqrt{Z_iZ_{i+1}}}\right), \\ a_i^- = a_{i+1}^+\left(\dfrac{Z_{i+1}-Z_i}{2\sqrt{Z_iZ_{i+1}}}\right) + a_{i+1}^-\left(\dfrac{Z_{i+1}+Z_i}{2\sqrt{Z_iZ_{i+1}}}\right). \end{cases} \tag{3.201}$$

Writing the foregoing linear equation system in matrix notation we obtain

$$\begin{bmatrix} a_i^+ \\ a_i^- \end{bmatrix} = \frac{1}{\sqrt{1-\Gamma_i^2}} \begin{bmatrix} 1 & \Gamma_i \\ \Gamma_i & 1 \end{bmatrix} \begin{bmatrix} a_{i+1}^+ \\ a_{i+1}^- \end{bmatrix}, \tag{3.202}$$

where Γ_i is the reflection coefficient at the interface between sections i and $i+1$ and is given by

$$\Gamma_i = \frac{Z_{i+1} - Z_i}{Z_{i+1} + Z_i}. \tag{3.203}$$

The complete transmission matrix for each single section is obtained by multiplying the matrices of both structures in Figure 3.12 yielding

$$[T_i] = \frac{1}{\sqrt{1-\Gamma_i^2}} \begin{bmatrix} e^{j\beta dl} & \Gamma_i e^{-j\beta dl} \\ \Gamma_i e^{j\beta dl} & e^{-j\beta dl} \end{bmatrix}. \tag{3.204}$$

Similarly to the case in section 3.3.1, the overall transmission matrix is calculated by multiplying all of the individual sections matrices $[T_i]$, hence

$$[T] = [T_1][T_2][T_3]\cdots[T_{N-1}][T_N]. \tag{3.205}$$

The transmission matrix $[T]$ connect the fields amplitudes at the two ends of the NTL structure, then for the complete NTL structure we have that

$$\begin{bmatrix} a^+(0) \\ a^-(0) \end{bmatrix} = [T] \begin{bmatrix} a^+(L) \\ a^-(L) \end{bmatrix}. \tag{3.206}$$

The S-parameters of the NTL device are then calculated using (2.159) yielding

$$S_{11} = \frac{A_{21}}{A_{11}}, \tag{3.207}$$

$$S_{21} = \frac{1}{A_{11}}. \tag{3.208}$$

3.4 Summary

In this chapter several nonuniform transmission line analysis method were analyzed. We conclude as far as transmission lines analysis is concerned, all of the methods produce accurate results. However depending on the characteristics of the nonuniform line under analysis, some particular analysis procedures prove to be more simple and efficient.

Considering an overall evaluation however, we elect the the transmission matrix method under constant impedance discretization as the best method given its extreme simplicity and accuracy.

Chapter 4

Inverse scattering

4.1 Introduction

In this chapter we introduce Inverse Scattering (IS) theory. We first give a general overview on the concept of inverse scattering and also on its main applications. After, we establish a parallelism with nonuniform transmission lines and demonstrate how inverse scattering can be applied on the synthesis of nonuniform transmission lines. For the particular case of NTL structures we demonstrate that the IS problem can be solved analytically and we also introduce differential inverse scattering algorithms.

The main objectives of this chapter are to assess the potential of inverse scattering on the synthesis of microwave filters and to adapt the differential inverse scattering algorithms proposed by Skaar *et al.* [54] to the microwave case.

4.2 Inverse scattering

In many areas of physics the interest is in determining the characteristics of a medium from the limited knowledge of the fields propagating through this medium. This is known as an inverse scattering problem and is inherently related to the synthesis problem where the objective is to construct a special medium reproducing some prescribed properties of the fields. In other words, the inverse scattering theory deals with the reconstruction of the geometry and material properties of an object from its scattered field, and evidently the solution to this inverse modeling problem leads directly to the solution of the synthesis problem. Figure 4.1 illustrates the general idea behind inverse scattering.

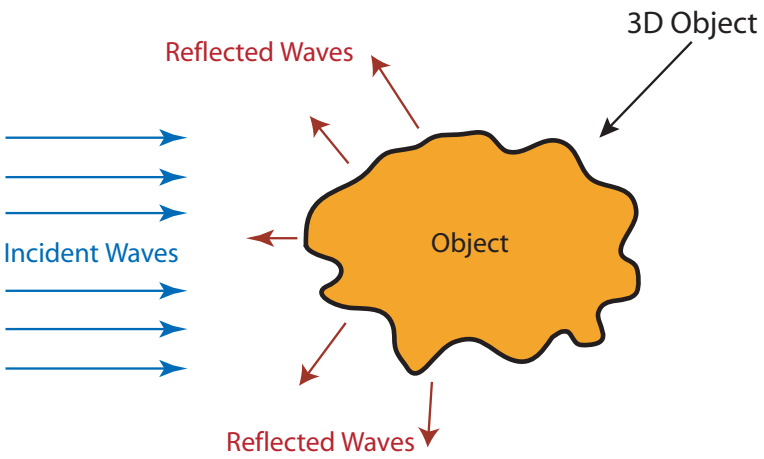

FIGURE 4.1: Inverse Scattering

Inverse scattering theory finds application in several different areas such as in medical imaging, non-destructive evaluation, geophysical prospecting, underwater sound propagation, ionospheric profiling, microwave sensing and quantum physics to name a few.

In the electromagnetic particular case, the inverse scattering problem is concerned with finding electrical parameters of a medium only from the scattering data such as the reflection or transmission coefficients.

Forward modeling of electromagnetic phenomena, where physical properties, namely material properties and geometric properties, are transformed into the electromagnetic realm, has been done for over 100 years, and most equations in electromagnetics serve only to calculate the electric and magnetic fields that result from the physical properties. However, recently the inverse scattering theory has brought some attention to the idea of inverse modeling of the electromagnetic phenomena where the electromagnetic data is translated back into the physical realm.

The difficulty with electromagnetic inverse scattering and therefore inverse modeling lies with the complexity of the electromagnetic laws themselves which when translated into mathematical form give rise to complex differential and integral equations.

In certain cases however waves propagate only in one direction, and so by writing the medium equations in the form of a two-component system describing the interaction of rightward and leftward propagating waves, the electromagnetic inverse problem can be reduced to the one-dimensional inverse scattering problem. Examples of such cases are transmission lines, where the well known telegrapher equations that describe transverse electromagnetic (TEM) wave propagation can be reduced though a Liouville transformation to the one-dimensional Schrödinger equation [40]. During the 1950's, the pioneer

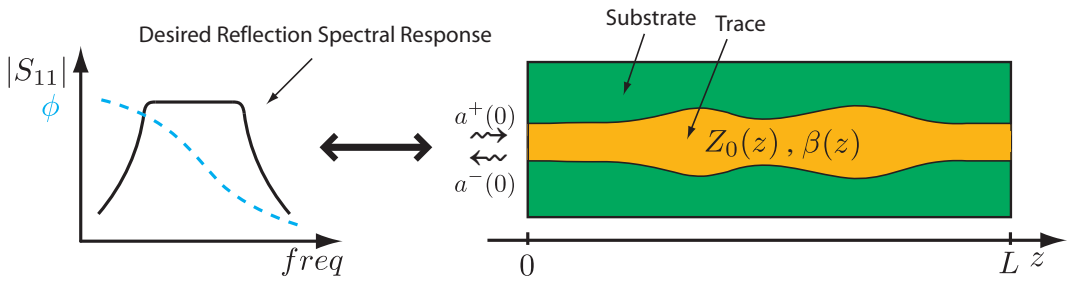

FIGURE 4.2: Inverse Scattering for the particular case of transmission lines.

work of Gel'fand and Levitan led to the first exact inverse solution to this unidimensional Schrödinger equation [41]. Their inverse scattering problem was obtained in the context of reconstructing a second order differential operator from its spectral function, and the solution comes in the form of a linear integral equation. Posterior work developed by Marchenko [42], Krein [43], and others, further sustained the idea that linear integral equations were the solution to the one-dimensional inverse problem. Throughout the literature these integral equations became known as the Gel'fand-Levitan-Marchenko (GLM) equations.

4.2.1 The Schrödinger equation inverse scattering problem

Because the central problem in filter synthesis is to produce a scatterer which realizes a specified frequency response, NTL microwave filters can be synthesized by solving the unidimensional inverse scattering problem provided that the desired reflection coefficient at the filter input as a function of frequency is given to be the starting data and also that a solution for the GLM linear integral equations is achieved. Figure 4.2 illustrates this particular case of inverse scattering.

In section 2.3 we saw that the wave propagation along an uniform transmission line is described by the telegrapher equations 2.98 and 2.99. In the case of NTL structures however the per-unit-lenght parameters such as inductance and capacitance along the transmission line are of variable nature. As discussed in section 3.2.1.5, the telegrapher equations for lossless TEM mode NTLs such as the one illustrated in Figure 4.2 are given by

$$\frac{dV(z)}{dz} = -j\omega L(z)I(z), \tag{4.1}$$

$$\frac{dI(z)}{dz} = -j\omega C(z)V(z), \tag{4.2}$$

where $L(z)$ is the inductance per unit length and $C(z)$ is the capacitance per unit length. The characteristic impedance along the structure is

$$Z_0(z) = \sqrt{\frac{L(z)}{C(z)}}, \tag{4.3}$$

and the propagation constant is

$$\beta = \omega\sqrt{L(z)C(z)} \tag{4.4}$$

and has a constant value along the structure because we are considering a TEM mode propagation. Let us transform the spacial variable z from physical length to travel time x through

$$x(z) = \int_0^z \sqrt{L(u)C(u)}du, \tag{4.5}$$

such that

$$\frac{dx}{dz} = \sqrt{L(z)C(z)}. \tag{4.6}$$

The variable x that we named by *travel time* represents the wave propagation time or travel time for the waves from the origin to position z. Taking into consideration the variable change

$$\begin{aligned} V(z) &\longrightarrow V(x), \\ dz &\longrightarrow \frac{dx}{\sqrt{L(x)C(x)}}, \end{aligned} \tag{4.7}$$

the telegrapher equations (4.1) and (4.2) can be rewritten as

$$\frac{dV(x)}{dx} = -j\omega Z_0(x)I(x), \tag{4.8}$$

$$\frac{dI(x)}{dx} = -j\omega\frac{1}{Z_0(x)}V(x), \tag{4.9}$$

Dividing equation (4.8) by $Z_0(x)$, taking its derivative and then substituting equation (4.9) yields

$$\frac{d}{dx}\left(\frac{1}{Z_0(x)}\frac{dV(x)}{dx}\right) = -\omega^2\frac{1}{Z_0(x)}V(x). \tag{4.10}$$

Due to the variable nature of the characteristic impedance along an NTL structure, it is more convenient to deal with the normalized wave amplitudes (power relations, see section 2.4.2), instead of the voltage wave amplitudes. Therefore, regarding (2.143) and

(2.144) we now consider the following substitution

$$U(x) = \frac{1}{\sqrt{Z_0(x)}} V(x), \tag{4.11}$$

where $U(x)$ is the normalized field amplitude. Equation (4.10) can now be rewritten as

$$\frac{d}{dx}\left(\frac{1}{Z_0(x)}\frac{d}{dx}\left(\sqrt{Z_0(x)}U(x)\right)\right) = -\omega^2 \frac{1}{\sqrt{Z_0(x)}} U(x). \tag{4.12}$$

Expanding the left hand side of the previous equation, rearranging the terms and including the frequency dependence of the fields amplitudes $U(\omega, x)$ yields

$$\frac{d^2U(\omega, x)}{dx^2} + (\omega^2 - q(x))U(\omega, x) = 0, \tag{4.13}$$

where

$$U(\omega, x) = U^+(\omega, x) + U^-(\omega, x) \tag{4.14}$$

is the normalized field amplitude and is composed by the forward- and backward-propagating waves. The function $q(x)$ is known as the potential function and is given by

$$q(x) = \sqrt{Z_0(x)}\frac{d^2}{dx^2}\left(\frac{1}{\sqrt{Z_0(x)}}\right). \tag{4.15}$$

Please note that equation (4.13) is in the form of the well-known one-dimensional Schrödinger equation, hence we consider (4.13) to be the Schrödinger equation for transmission line theory.

The variable changes (4.5) and (4.11) allow us to convert the telegrapher equations into the one dimensional Schrödinger equation. This procedure is referred to as a Liouville transformation.

The solution to the NTL inverse problem is to compute the potential $q(x)$ from equation (4.13) from the knowledge of the fields amplitude $U(\omega, x)$. The impedance profile for the NTL structure can then be retrieved from the potential.

As we above report, the exact solution to the one-dimensional Schrödinger equation inverse scattering problem was first derived by Gel'fand and Levitan and also by Marchenko (see references above). Here we derive the so-called GLM integral equation following the mathematical derivation of Kay [44], [45], [46].

Let us consider the NTL structure illustrated in Figure 4.3 which we consider to

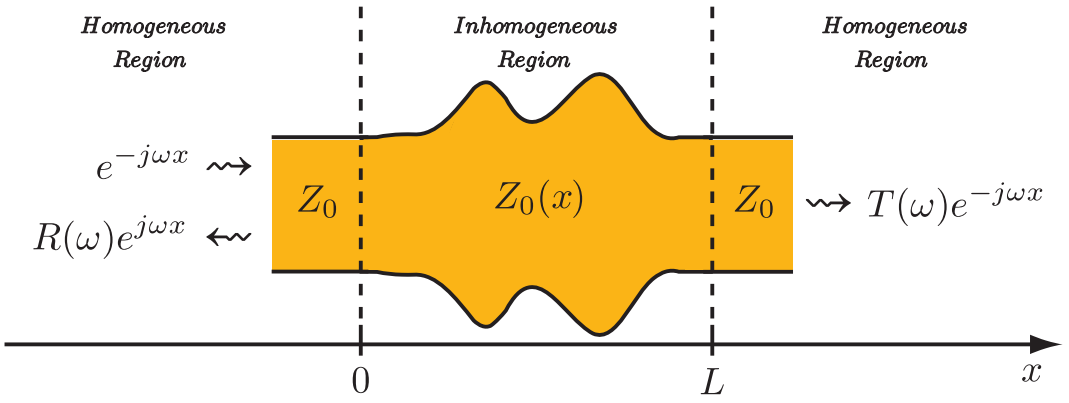

FIGURE 4.3: Scattering by an NTL structure.

be divided into three different regions. The middle region is the inhomogeneous region where the coupling between forward- and backward-propagating waves takes place ($q(x) \neq 0$) and the other two are homogeneous regions where the impedance is constant ($q(z) = 0$) and hence no coupling occurs. So in the homogeneous regions we may write the solutions to the homogeneous Schrödinger equation ($q(z) = 0$) as

$$\begin{cases} U_0(\omega, x) = e^{-j\omega x} + R(\omega)e^{j\omega x}, & x < 0, \\ U_0(\omega, x) = T(\omega)e^{-j\omega x}, & x > L, \end{cases} \tag{4.16}$$

where $e^{-j\omega x}$ is the unitary incident wave, $R(\omega)$ is the reflection response of the NTL at $x = 0$ and $T(\omega)$ is the transmission response at $x = L$.

In order to solve the one-dimensional Schrödinger inverse problem (4.13) in a more simple and intuitive way, we now reformulate the problem into the time domain. Let us define the inverse Fourier transform as

$$u(t) = \frac{1}{2\pi} \int_{-\infty}^{\infty} U(\omega)e^{j\omega t} d\omega, \tag{4.17}$$

in which t is the time variable.

From the definition of inverse Fourier transform and regarding to equation (4.13) we can easily see that $u(t, x)$ satisfies the time-dependent Schrödinger equation

$$\frac{\partial^2 u(t,x)}{\partial x^2} - \frac{\partial^2 u(t,x)}{\partial t^2} - q(x)u(t,x) = 0. \tag{4.18}$$

The transient response on the left side of the NTL structure can be obtained by calculating the inverse Fourier transform of $U_0(\omega, x)$ for when $x < 0$ yielding

$$u_0(t, x) = \delta(t - x) + r(t + x), \qquad x < 0, \tag{4.19}$$

where $r(t)$ is the inverse Fourier transform of the reflection coefficient $R(\omega)$ at the beginning of the inhomogeneous region ($x = 0$). We see from equation (4.19) that the NTL structure is probed from the left by a Dirac delta function, and as a result a reflected transient is produced at $x = 0$ that propagates on the opposite direction, $r(t + x)$.

Due to causality we have that,

$$r(t + x) = 0, \qquad x < -t, \tag{4.20}$$

which means that the reflected transient is not originated until the incident Dirac pulse has reached the inhomogeneous region. From equation (4.13) we know that the fields amplitudes inside the inhomogeneous region are given by $U(\omega, x)$ which is the sum of the forward- and backward-propagating waves. On the other hand, analyzing the problem in the time domain, we see from physical considerations that $u(t, x)$ is a rightward-propagating transient, so that

$$u(t, x) = 0, \qquad x > t, \tag{4.21}$$

which means that the leading edge of the propagating transient only reaches position x when $t = x$. For $x > t$ the medium is still in a "resting" state.

From the work of Jordan [45] we learn that the transient fields amplitudes in the inhomogeneous region $u(t, x)$ can be related to that on the homogeneous region on the left $u_0(t, x)$ (4.19) by a linear transformation. This linear transformation is the solution to equation (4.13) and therefore the inverse scattering problem and is given in the time domain by [44], [45], [46]

$$u(t, x) = \begin{cases} u_0(t, x) + \displaystyle\int_{-x}^{x} k(y, x) u_0(t, y) dy, & 0 \leq x < L, \\ u_0(t, x), & x \leq 0, \quad x > L, \end{cases} \tag{4.22}$$

where $k(t,x)$ is called the kernel function. Substituting equation (4.19) into equation (4.22) results in

$$u(t,x) = \delta(t-x) + r(t+x) + \underbrace{\int_{-x}^{x} k(y,x)\,\delta(t-y)dy}_{k(t,x)} + \int_{-x}^{x} k(y,x)\,r(t+y)dy \qquad (4.23)$$

which by taking into consideration the boundaries (4.20) and (4.21), simplifies to the following integral equation

$$k(t,x) + r(t+x) + \int_{-t}^{x} k(y,x)r(t+y)dy = 0, \qquad x > t. \qquad (4.24)$$

In (4.24) $r(t)$ is the inverse Fourier transform of the reflection response $R(\omega)$ and $k(t,x)$ is the unknown kernel function. Equation (4.24) is the so-called Gel'fand-Levitan-Marchenko integral equation for the one dimensional Schrödinger equation. Kay also demonstrated that if equation (4.22) is to be a solution to equation (4.13) then the kernel function must have the following properties [44]

$$\frac{d}{dx}k(x,-x) = 0, \qquad (4.25)$$

$$\frac{d}{dx}k(x,x) = \frac{q(x)}{2}. \qquad (4.26)$$

The essential results to this inverse scattering process based on the one-dimensional Schrödinger equation are that given the desired frequency reflection response $R(\omega)$ for the NTL as the input data we can use equation (4.24) to compute the kernel function $k(t,x)$. Once the Kernel is obtained, the potential function $q(x)$ is then calculated using (4.26), which leads directly to the NTL impedance profile by taking into consideration equation (4.15).

4.2.1.1 Realizability conditions

So far we have focus our attention on the inverse scattering process itself. However, in order to guaranty that the process is meaningful and that we can in fact synthesize a NTL structure, we first need to make sure that input data namely $R(\omega)$ is physically realizable.

We know for a fact that the characteristic impedance for a lossless transmission line is a real quantity. Recalling equation (4.15) we easily recognize that for $Z_0(x)$ to be real,

$q(x)$ must also be real. The same reasoning leads us to conclude from equations (4.26) and (4.24) that the essential condition for $Z_0(x)$ to be real is that $r(t)$ is a real-valued time function. Therefore, and from the properties of the Fourier transform we have that the reflection response of the NTL, $R(\omega)$, must satisfy the condition

$$R(-\omega) = R^*(\omega). \tag{4.27}$$

Additionally, we know from physical constrains that any NTL structure is a non-anticipative system, therefore its current outputs do not depends on future inputs. This means that NTL devices are causal systems and as such their impulse response must verify

$$r(t) = 0, \qquad t < 0, \tag{4.28}$$

as is already indicated by equation (4.20). Taking into account the causality condition (4.28) and considering equations (4.26) and (4.24), we can rewrite the potential function as

$$q(x) = \begin{cases} 2\frac{d}{dx}k(x,x), & x \geq 0, \\ 0, & x < 0. \end{cases} \tag{4.29}$$

Transmission line filters are passive structures and as such the law of conservation of energy requires that the frequency response to be synthesized obeys to

$$|R(\omega)|^2 \leq 1, \qquad \forall\omega, \tag{4.30}$$

in order for the NTL synthesis to be physically possible.

Also we must take into account that the main objective of this work is the synthesis of NTL structures. And we now for a fact that these kind of structures are made up by a conductive ground plane and strip that extend from the input to the output ports. This physical condition, together with the fact that we most often consider the input and output resistive terminations to be of the same value, implies that for $\omega = 0$ any NTL is just a "short circuit" between the input and output ports and therefore the reflection coefficient is

$$R(0) = 0. \tag{4.31}$$

We shall see in following chapters that this condition is not essential to guaranty the convergence of the inverse scattering procedure. In fact, the not fulfillment of this

condition will allow us to synthesize NTL structures other than filters, namely impedance matching structures.

Another realizability condition is related with the stability of the system to be synthesized. In order to synthesize some given frequency response $R(\omega)$ we must first guaranty that it describes a stable system, otherwise the synthesis procedure will not converge.

Let us consider the Laplace transform of the impulse response $r(t)$ to be $R(s)$. We know from the properties of the Laplace transform that $R(s)$ will only converge for values of s inside the so-called region of convergence (ROC) and also that the ROC does not contain any poles. Furthermore, the corresponding Fourier transform $R(\omega)$ will only converge if the $j\omega$ axis is contained within the ROC [1]. For a right-sided time signal as is $r(t)$ (due to causality) the region of converge (ROC) consists on a strip parallel to the $j\omega$ axis in the s-plane and that extends to the right hand side plane [1]. Because the ROC does not contain any poles and because we must make sure that the $j\omega$ is included in the ROC to guaranty the convergence of $R(\omega)$, we must ensure that $R(s)$ has no poles on the right hand side of the s-plane including the $j\omega$ axis [1].

As a last set of realizability conditions we have that the inverse Fourier transform of $R(\omega) \rightarrow r(t)$ must exist and must be continuous in $-\infty < t < \infty$ and also that $r(t)$ must have continuous first and second derivatives [45], [46].

4.2.1.2 Analytical solutions for the potential function

Explicit and exact analytical solutions to the GLM linear equations have been found by Kay [47], [45], [46] for when the spectral response is described in terms of rational functions.

In this subsection we describe the mathematical steps necessary to obtain the analytical solution for the potential function $q(x)$ from the desired frequency response $R(\omega)$. In order to keep mathematical complexity to a minimum, let us consider the simple case of a second order Butterworth approximation to the ideal lowpass characteristic with an unitary cutoff frequency [46]

$$R(s) = \frac{1}{s^2 + \sqrt{2}s + 1}, \tag{4.32}$$

where from the definition of Laplace transform we know that $s = \sigma + j\omega$. However, we learned from the realizability conditions that for a frequency response to be feasible as

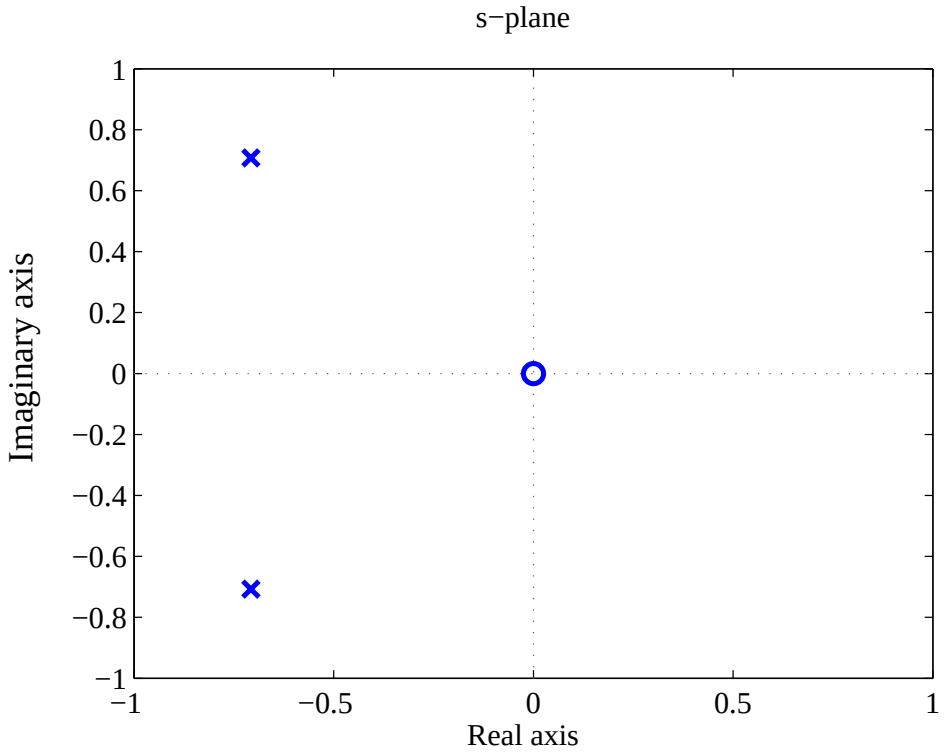

FIGURE 4.4: Pole-Zero map in the s-plane.

an NTL filter we must guaranty $R(0) = 0$. To enforce this condition we must place a zero at the origin of the s-plane. We must also consider a normalization factor k so that $|R(\omega)| = 1$ for $\omega = 1$. Taking into consideration these constrains, equation (4.32) now becomes

$$R(s) = \frac{ks}{s^2 + \sqrt{2}s + 1}, \tag{4.33}$$

where the normalization constant is $k = \sqrt{2}$.

Figure 4.4 shows the position of the zero and poles of the system described by equation (4.33). The poles are located at $s = -\sqrt{2}/2 + j\sqrt{2}/2$ and $s = -\sqrt{2}/2 - j\sqrt{2}/2$ and the zero is located at the origin as discussed before. Recalling the realizability conditions, we know that the impulse response $r(t)$ of the Butterworth system must be causal and thereafter a right-sided time signal. In this way the ROC consists on a strip parallel to the $j\omega$ axis extending from $s = -\sqrt{2}/2$ to infinity. Because the $j\omega$ axis is contained within the ROC the Fourier transform of the system converges and is given by

$$R(\omega) = \frac{j\sqrt{2}\omega}{-\omega^2 + j\sqrt{2}\omega + 1}. \tag{4.34}$$

In short and practically speaking, for the Fourier transform to converge and the stability

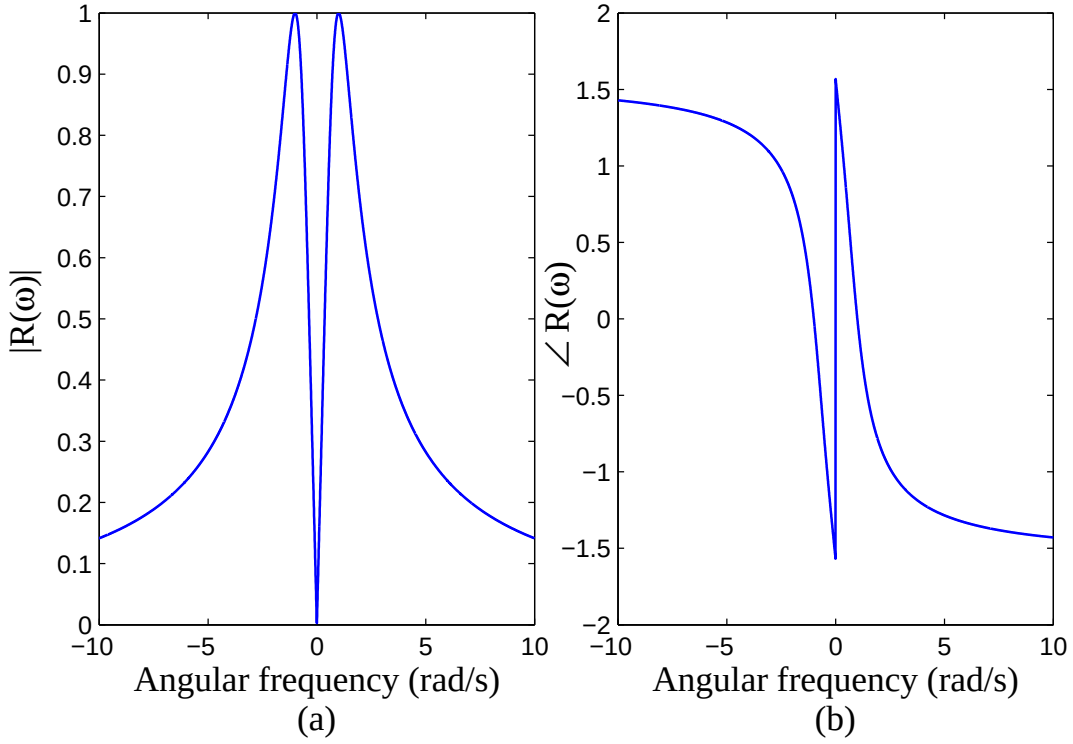

FIGURE 4.5: Second order Butterworth frequency response with zero placed at the origin of the s-plane. (a) Magnitude response and (b) phase response

of the system be guarantied, the essential condition is that all poles of $R(s)$ must be located on the left hand side of the s-plane.

Figure 4.5 depicts the magnitude response of the two pole Butterworth filter when a zero is placed at the origin of the s-plane. We clearly see that $R(0) = 0$ and therefore the filter has a band-pass response with a center frequency of 1 rad/s. Regarding the magnitude response we can see that $|R(\omega)|^2 \leq 1$ for the entire frequency band, thus obeying to the law of conservation of energy. From Figure 4.5 we can also see that the phase response is an odd function of frequency, therefore we meet the condition that $R(-\omega) = R^*(\omega)$. From this analyses to the Butterworth frequency response we have guarantied that it fulfills all of the realizability conditions.

Carrying on with the analytical inverse scattering procedure we can now calculate the impulse response $r(t)$ using the inverse Fourier transform (4.17), yielding

$$\begin{cases} r(t) = \sqrt{2}e^{-\frac{\sqrt{2}}{2}t}\left(\cos\left(\frac{\sqrt{2}}{2}t\right) - \sin\left(\frac{\sqrt{2}}{2}t\right)\right), & x \geq 0, \\ r(t) = 0, & x < 0. \end{cases} \tag{4.35}$$

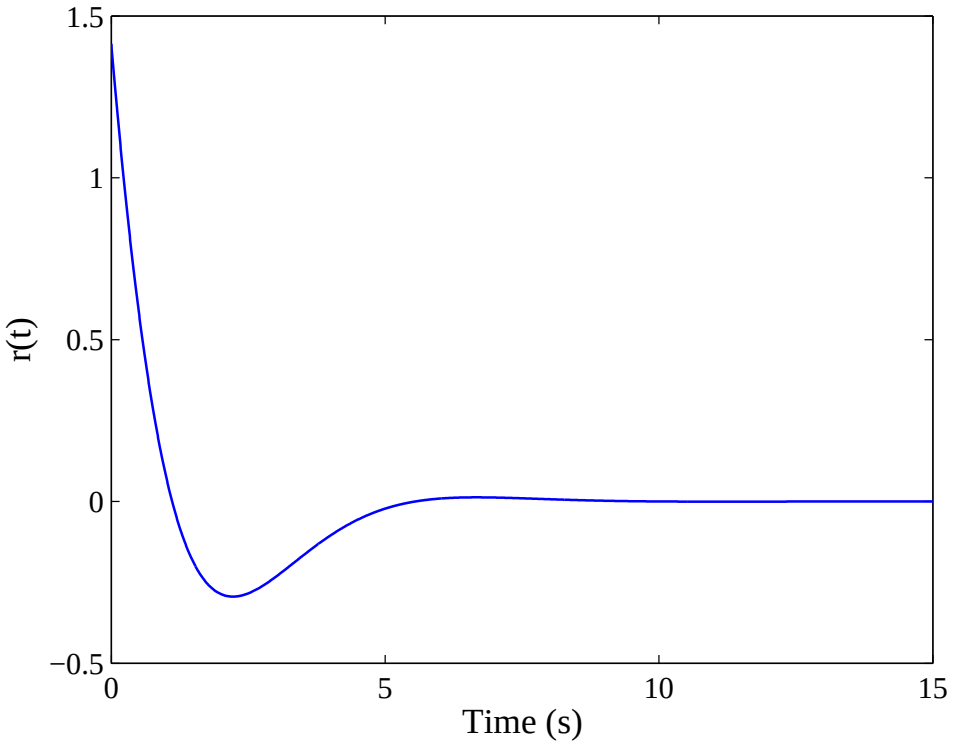

FIGURE 4.6: Second order Butterworth impulse response with zero placed at the origin of the s-plane.

The impulse response is illustrated in Figure 4.6. From the figure we have that $r(t)$ is a real valued function in the entire time domain, it is also a causal or right-sided time signal otherwise the Fourier transform would not converge and is also a bounded signal that actually converges to zero as time increases indicating that this is the impulse response of a stable system. In essence, for a frequency response to be feasible as an NTL device, the three essential and most important realizability conditions can be fulfilled by ensuring that the corresponding impulse response is a real and causal signal, and that it converges to zero as time increases.

Now that the realizability conditions for the band-pass filter ($R(\omega)$) are verified, the next step is to use the impulse response $r(t)$ and solve the Gel'fand-Levitan-Marchenko (GLM) integral equation for the potential function $q(x)$. In order to solve the GLM equation (4.24) a differential operator $f(p)$ is constructed as

$$f(p) = (p - s_{p_1})(p - s_{p_2}), \tag{4.36}$$

where $p = \dfrac{d}{dt}$ and s_{p_1},s_{p_2} are the poles of $R(s)$. In the present case we have that

$$f(p) = p^2 + \sqrt{2}p + 1, \tag{4.37}$$

so that $f(p)r(t) = 0$. Applying $f(p)$ to the GLM equation results in

$$f(p)k(t,x) + f(p)\int_{-t}^{x} k(y,x)r(t+y)dy = 0. \tag{4.38}$$

Using the Leibniz integral rule to solve the second term of the latter equation yields

$$f(p)k(t,x) + \sqrt{2}\frac{k(-t,x)}{dt} = 0, \tag{4.39}$$

or using the differential operator notation

$$f(p)k(t,x) + p\sqrt{2}k(-t,x) = 0. \tag{4.40}$$

A second independent equation can be obtained for $f(-p)$ that results in

$$f(-p)k(-t,x) - p\sqrt{2}k(t,x) = 0. \tag{4.41}$$

The derivative of equation (4.41) gives

$$f(-p)pk(-t,x) - p^2\sqrt{2}k(t,x) = 0. \tag{4.42}$$

Eliminating $k(-t,x)$ between equations (4.40) and (4.42) yields the differential equation for $k(t,x)$

$$\begin{gathered}(p^4 + 2p^2 + 1)k(t,x) = 0 \\ \Downarrow \\ \frac{d^4}{dt^4}k(t,x) + 2\frac{d^2}{dt^2}k(t,x) + k(t,x) = 0,\end{gathered} \tag{4.43}$$

whose general solution is [38]

$$k(t,x) = C_1(x)\sin(t) + C_2(x)\cos(t) + C_3(x)\sin(t)t + C_4(x)\cos(t)t, \tag{4.44}$$

where $C_1(x)$, $C_2(x)$, $C_3(x)$, $C_4(x)$ are the unknown coefficient functions, that are obtained by setting the appropriate boundary conditions.

For the first boundary condition we substitute the general solution for $k(t,x)$ (4.44) into equation (4.40) which results in

$$C_3(x)\cos(t) + \left(\sqrt{2}C_3(x) - C_4(x) - \sqrt{2}C_2(x)\right)\sin(t) + \sqrt{2}C_3(x)\cos(t)t = 0. \tag{4.45}$$

One way to satisfy this mathematical equality for a given instant of time t is to set

$$C_3(x) = 0, \tag{4.46}$$

$$C_4(x) = -\sqrt{2}C_2(x). \tag{4.47}$$

Substituting $C_3(x)$ and $C_4(x)$ into (4.44) the expression for $k(t,x)$ simplifies to

$$k(t,x) = C_1(x)\sin(t) + C_2(x)\cos(t) - \sqrt{2}C_2(x)\cos(t)t, \tag{4.48}$$

where we now only have two unknown coefficient functions. To obtain $C_1(x)$ and $C_2(x)$ we recall the GLM integral equation (4.24) and realize that for $t = -x$ the integral term in the equation is null and so the GLM equation reduces to our second boundary condition

$$k(t,x)\big|_{t=-x} = -r(0). \tag{4.49}$$

As we have two unknown coefficient function we need yet another and third boundary condition. This last boundary condition is obtained by taking the time derivative of the GLM equation using the aforesaid Leibniz rule and evaluating the result at $t = -x$ resulting in

$$\frac{d}{dt}k(t,x)\big|_{t=-x} + r(0)k(x,-t)\big|_{t=-x} = -r'(0), \tag{4.50}$$

where the prime sign represents the first order time derivative which is given by

$$r'(t) = -2e^{-\frac{\sqrt{2}}{2}t}\cos\left(\frac{\sqrt{2}}{2}t\right). \tag{4.51}$$

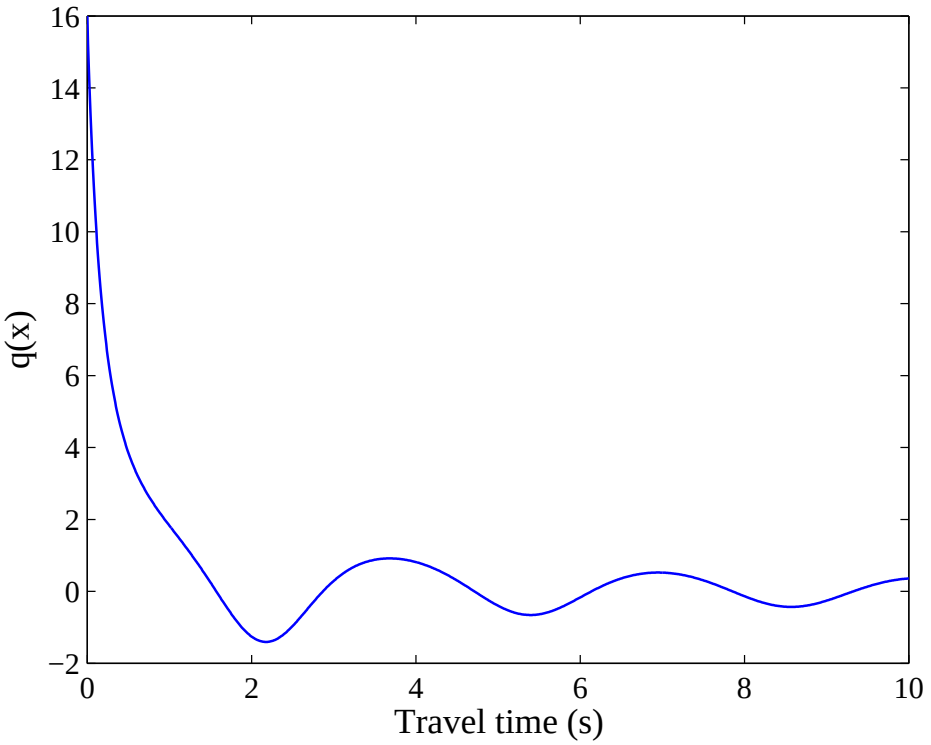

FIGURE 4.7: Reconstructed potential function for the second order Butterworth filter with zero placed at the origin of the s-plane.

Substituting the expression (4.44) for $k(t,x)$ into equations (4.49) and (4.50) we get a system of two linear equations with two unknowns

$$\begin{cases} C_1(x)\sin(x) - C_2(x)\left(\cos(x) + \sqrt{2}\cos(x)x\right) = \sqrt{2}, \\ C_1(x)\left(\cos(x) + \sqrt{2}\sin(x)\right) + C_2(x)\left(\sin(x) + \sqrt{2}\sin(x)x - 2\cos(x)x\right) = 2, \end{cases} \tag{4.52}$$

from which $C_1(x)$ and $C_2(x)$ can be obtained. The kernel function $k(t,x)$ is now completely identified by

$$k(t,x) = C_1(x)\sin(t) + C_2(x)\cos(t) + C_3(x)\sin(t)t + C_4(x)\cos(t)t, \tag{4.53}$$

where the unknown coefficient functions are given by

$$C_1(x) = \frac{2\,\cos(x) + 2\,\sin(x)\,x + \sqrt{2}\sin(x)}{\sqrt{2}\cos(x)\sin(x) + \sqrt{2}x + 1}, \tag{4.54}$$

$$C_2(x) = -\frac{\sqrt{2}\cos(x)}{\sqrt{2}\cos(x)\sin(x) + \sqrt{2}x + 1}, \tag{4.55}$$

$$C_3(x) = 0, \tag{4.56}$$

$$C_4(x) = \frac{2\cos(x)}{\sqrt{2}\cos(x)\sin(x) + \sqrt{2}x + 1}. \tag{4.57}$$

Substituting the coefficient functions into (4.53) and considering $t = x$ yields the kernel function solely as a function of the travel time x (4.5)

$$k(x,x) = -\frac{-2\,\cos(x)\sin(x) + 2\sqrt{2}\,(\cos(x))^2 - 2\,x - \sqrt{2}}{\sqrt{2}\cos(x)\sin(x) + \sqrt{2}x + 1} \tag{4.58}$$

The potential function $q(x)$ can now be determined through (4.29) yielding

$$q(x) = \begin{cases} \dfrac{8\cos(x)\left(2\cos(x) + 2\sin(x)\,x + \sqrt{2}\sin(x)\right)}{2\cos(x)\sin(x)\left(\sqrt{2} + 2\,x\right) + 2\sqrt{2}\,x + 1 - 2\,x^2 - 2\cos(x)^4 + 2\cos(x)^2}, & x \geq 0, \\ 0, & x < 0 \end{cases} \tag{4.59}$$

and is plotted in Figure 4.7. The impedance profile $Z_0(x)$ can now be calculated from the potential function by solving the following second order differential equation (4.15)

$$\frac{d^2W(x)}{dx^2} = W(x)\,q(x), \tag{4.60}$$

where

$$W(x) = \frac{1}{\sqrt{Z_0(x)}}. \tag{4.61}$$

No easily obtainable explicit expression for $W(x)$ and $Z_0(x)$ are immediately apparent, however numerical solutions are easily achievable using computational software tools.

The band-pass filter proposed in this section to demonstrate the inverse scattering analytical procedure was chosen to have a convenient center frequency of $\omega_0 = 1\,rad/s$. We consider this to be the normalized frequency response as the frequency response profile is invariant with ω_0 as we shall see next.

We now show how to obtain the potential function as well as the impedance function for filters with the same frequency response profile but with different ω_0 from the results obtained for the normalized frequency response, without having to repeat the inverse

scattering procedure for each different ω_0. Considering some ω_0 other than unity and recalling equation (4.34) the frequency response now comes in the form

$$R(\omega) = \frac{j\sqrt{2}\left(\frac{\omega}{\omega_0}\right)}{-\left(\frac{\omega}{\omega_0}\right)^2 + j\sqrt{2}\left(\frac{\omega}{\omega_0}\right) + 1}. \tag{4.62}$$

Considering the variable change $\bar{\omega} = \dfrac{\omega}{\omega_0}$ we may rewrite (4.62) as

$$R(\bar{\omega}) = \frac{j\sqrt{2}\bar{\omega}}{-\bar{\omega}^2 + j\sqrt{2}\bar{\omega} + 1}, \tag{4.63}$$

which in $\bar{\omega}$ has the same frequency response as the normalized frequency response (4.34) in ω. The impulse response for (4.62) is obtained from the impulse response of the normalized frequency response $r(t)$ by using the time and frequency scaling property of the Fourier transform [1]

$$R\left(\frac{\omega}{\omega_0}\right) \overset{\mathcal{F}}{\longleftrightarrow} \omega_0\, r(\omega_0 t). \tag{4.64}$$

Lets us recall the NTL structure illustrated in Figure 4.3. The amplitude of the fields on the homogeneous region on the left side of the NTL are now given by

$$U_0(\omega, x) = e^{-j\omega x} + R\left(\frac{\omega}{\omega_0}\right) e^{j\omega x}, \qquad x < 0 \tag{4.65}$$

and the corresponding transient response calculated through the inverse Fourier transform results in

$$u_0(t, x) = \omega_0 \delta\big(\omega_0 t - \omega_0 x\big) + \omega_0 r\left(\omega_0 t + \omega_0 x\right), \qquad x < 0. \tag{4.66}$$

Considering the variable changes

$$\bar{t} = \omega_0\, t, \tag{4.67}$$

$$\bar{x} = \omega_0\, x, \tag{4.68}$$

equation (4.66) can be rewritten as

$$u_0(\bar{t}, \bar{x}) = \omega_0 \delta(\bar{t} - \bar{x}) + \omega_0 r(\bar{t} + \bar{x}), \qquad \bar{x} < 0, \tag{4.69}$$

which is expressed in the same way as (4.19) except for the ω_0 factor. Due to the variable change, the linear transformation given by equation (4.22) must also be redefined, yielding

$$u(\bar{t},\bar{x}) = \begin{cases} u_0(\bar{t},\bar{x}) + \displaystyle\int_{-\bar{x}}^{\bar{x}} k(\bar{y},\bar{x}) u_0(\bar{t},\bar{y}) \frac{d\bar{y}}{\omega_0}, & 0 \le \bar{x} < \omega_0 L, \\ u_0(\bar{t},\bar{x}), & \omega_0 L < \bar{x} \le 0, \end{cases} \tag{4.70}$$

where $\bar{y} = \omega_0\, y$. Using the same mathematical reasoning as before, applying the linear transformation (4.70) to equation (4.69) yields the following GLM integral equation

$$k(\bar{t},\bar{x}) + \omega_0\, r(\bar{t}+\bar{x}) + \int_{-\bar{t}}^{\bar{x}} k(\bar{y},\bar{x})\, r(\bar{t}+\bar{y}) d\bar{y} = 0, \qquad \bar{x} > \bar{t}, \tag{4.71}$$

which can be simplified to

$$\bar{k}(\bar{t},\bar{x}) + r(\bar{t}+\bar{x}) + \int_{-\bar{t}}^{\bar{x}} \bar{k}(\bar{y},\bar{x})\, r(\bar{t}+\bar{y}) d\bar{y} = 0, \qquad \bar{x} > \bar{t}, \tag{4.72}$$

by considering the new kernel variable to be expressed as

$$\bar{k}(\bar{t},\bar{x}) = \frac{1}{\omega_0}\, k(\bar{t},\bar{x}), \tag{4.73}$$

where $\bar{k}(\bar{t},\bar{x})$ is the kernel corresponding to the normalized frequency response and $k(\bar{t},\bar{x})$ is the kernel amplitude for the new frequency response centered at ω_0 but expressed as a function of both normalized time $\bar{t}$ and travel time $\bar{x}$.

We already know from equation (4.26) how to obtain the potential function from the kernel function. Considering the present case we have that

$$q(x) = 2\, \frac{dk(\omega_0\, x, \omega_0\, x)}{dx}, \tag{4.74}$$

which turns into

$$q(\bar{x}) = 2\omega_0\, \frac{dk(\bar{x},\bar{x})}{d\bar{x}} \tag{4.75}$$

when considering the variable change $\bar{x} = \omega_0\, x$. Furthermore, by taking into account the relation (4.73) the potential function reduces to

$$q(\bar{x}) = \omega_0^2\, \bar{q}(\bar{x}), \tag{4.76}$$

where

$$\bar{q}(\bar{x}) = 2\,\frac{d\bar{k}(\bar{x},\bar{x})}{d\bar{x}} \tag{4.77}$$

is the potential function corresponding to the normalized frequency response. Also $q(\bar{x})$ is the amplitude of the potential function corresponding to the new frequency response (centered at ω_0) as a function of normalized travel time $\bar{x}$.

The last step on the procedure is to obtain the impedance profile for the NTL structure. We know from equation (4.15) how the potential function $q(x)$ and the impedance profile function $Z_0(x)$ relate to each other. On the present case however, the frequency response is centered in ω_0 and that relation is now given by

$$\frac{d^2W(\omega_0 x)}{dx^2} = W(\omega_0 x)\, q(\omega_0 x), \tag{4.78}$$

where

$$W(\omega_0 x) = \frac{1}{Z_0(\omega_0 x)}. \tag{4.79}$$

Making the variable change $\bar{x} = \omega_0\, x$, equation (4.78) turns into

$$\frac{d^2W(\bar{x})}{d\bar{x}^2}\,\omega_0^2 = W(\bar{x})\, q(\bar{x}). \tag{4.80}$$

Furthermore, if we take into consideration equation (4.76) the previous relation (4.80) reduces to

$$\frac{d^2W(\bar{x})}{d\bar{x}^2} = W(\bar{x})\,\bar{q}(\bar{x}), \tag{4.81}$$

where $\bar{W}(\bar{x}) = \dfrac{1}{\sqrt{Z_0(\bar{x})}}$ and $\bar{q}(\bar{x})$ is the potential function of the normalized frequency response.

We conclude that the variable change $\bar{\omega} = \dfrac{\omega}{\omega_0}$ in the frequency response will affect the potential function by an amplitude factor of ω_0^2 as shown by equation (4.76). It will also introduce a linear scaling by a factor of ω_0 on the independent variable (travel time x). However, from equation (4.81) we see that the impedance profile function only comes affected by the linear scaling factor ω_0 on the independent variable. This means that the entire NTL design procedure can be carried out considering the normalized frequency response ($\omega_0 = 1$) and that the final result for a particular center frequency ω_0 is easily attainable by simply scaling the length of this solution in the inverse proportion to the center frequency, i.e. $x = \dfrac{\bar{x}}{\omega_0}$.

The last step on this inverse procedure has to do with transforming the spatial variable from travel time x back to physical length z. For that, let us recall equation (4.5), and rearrange it so that

$$z(x) = \int_0^x \frac{1}{\sqrt{L(u)C(u)}} du. \tag{4.82}$$

However, when considering a pure TEM NTL, as is the case, we have a constant propagation velocity along the NTL structure

$$v_p = \frac{1}{\sqrt{L(x)\,C(x)}} = C^{te}, \tag{4.83}$$

which simplifies equation (4.82) to

$$z(x) = \frac{1}{\sqrt{L(x)\,C(x)}}\, x. \tag{4.84}$$

On the other hand we know that for a transmission line supporting a pure TEM propagating wave the propagation velocity can also be given by [5]

$$v_p = \frac{1}{\sqrt{\mu_0\,\epsilon_0}\sqrt{\epsilon_r}}, \tag{4.85}$$

therefore the relation given by equation (4.84) reduces to

$$z = \frac{c}{\sqrt{\epsilon_r}}\, x, \tag{4.86}$$

where c is the speed of light in vacuum and ϵ_r is the relative permitivity of the medium surrounding the transmission line.

4.2.2 The Zakharov-Shabat inverse scattering problem

In section 4.2.1.2 it has been shown that through the telegrapher equations for transmission lines, we could easily derive the one dimensional Schrödinger equation (4.13). From that, we demonstrated that the inverse scattering problem could be reduced to that of solving an integral equation which throughout the literature is commonly referred to as the GLM integral equation. The solution to the GLM integral equation is the potential function $q(x)$. We demonstrated that for rational reflection coefficient functions, analytical solutions are achievable. However, in order to obtain an analytical expression

for the transmission line impedance profile $Z_0(x)$ from the potential function requires solving a second order differential equation with non-constant coefficients (4.60). This proves to be somewhat difficult and the simplest way to deal with this problem is to resort to numerical resolution techniques.

In this section we consider a different approach based on the coupled mode equations derived in section 3.2. In the mathematical derivations that will follow, we demonstrate that the coupled-mode equations for NTL structures and therefore the coupled-wave interactions can be described by the Zakharov-Shabat (ZS) system of quantum mechanics and also that the solution to the inverse problem reduces to a set of coupled GLM type integral equations [48], [49], [50].

Let us remember the telegrapher equations for transmission lines from section 3.2

$$\frac{dV(z)}{dz} = -j\omega L(z)I(z), \tag{4.87}$$

$$\frac{dI(z)}{dz} = -j\omega C(z)V(z), \tag{4.88}$$

where $L(z)$ is the inductance per unit length and $C(z)$ is the capacitance per unit length of the transmission line and z is the spatial variable. As in the case of the Schrödinger equation inverse problem, in order to solve the ZS inverse problem in a more simple and intuitive way we start by considering an unitary propagation velocity along the NTL structures so that $\beta = \omega$. To do so, and similarly to the approach taken in the Schrödinger equation inverse problem case, we adopt the following variable change

$$x(z) = \int_0^z \sqrt{L(u)C(u)}du, \tag{4.89}$$

such that

$$\frac{dx}{dz} = \sqrt{L(z)C(z)}. \tag{4.90}$$

The variable x is the *travel time*. Taking into consideration the variable change

$$\begin{aligned} V(z) &\longrightarrow V(x), \\ dz &\longrightarrow \frac{dx}{\sqrt{L(x)C(x)}}, \end{aligned} \tag{4.91}$$

the telegrapher equations (4.1) and (4.2) can be rewritten as

$$\frac{dV(x)}{dx} = -j\omega Z_0(x) I(x), \tag{4.92}$$

$$\frac{dI(x)}{dx} = -j\omega \frac{1}{Z_0(x)} V(x). \tag{4.93}$$

From equations (4.92) and (4.93) the coupled mode equations for transmission lines can be easily obtained by following the same mathematical derivation as in section 3.2.1.5, yielding

$$\frac{da^+(\omega,x)}{dx} = -j\omega\, a^+(\omega,x) - K(x)\, a^-(\omega,x), \tag{4.94}$$

$$\frac{da^-(\omega,x)}{dx} = j\omega\, a^-(\omega,x) - K(x)\, a^+(\omega,x), \tag{4.95}$$

where $K(x)$ is the coupling coefficient. For the remaining of this section and for the sake of mathematical simplicity, the spectral an spatial dependence of the fields amplitudes as well as the spatial dependence of the coupling coefficient shall be omitted.

Reorganizing the coupled-mode equations in order to express them in the form of the ZS system and expressing them in matrix format, we have

$$j \begin{bmatrix} \frac{d}{dx} & K \\ -K^* & -\frac{d}{dx} \end{bmatrix} \begin{bmatrix} a^+ \\ a^- \end{bmatrix} = \omega \begin{bmatrix} a+ \\ a- \end{bmatrix}, \tag{4.96}$$

where $K^* = K$ is the coupling coefficient given by

$$K = \frac{1}{2} \frac{1}{Z_0} \frac{dZ_0}{dx}, \tag{4.97}$$

and is a real valued function for the NTL devices under consideration. For any type of realizable or usable NTL device no matter how long it is, it must have an homogeneous TL section at the beginning as well as another one at the end. So, even if we consider an infinitely long NTL structure we have that the coupling coefficient $K(x)$ must vanish for $|x| \to \infty$. In this case we may consider that the coupling of waves that occur in the non-uniform or inhomogeneous region extends from $-\infty < x < +\infty$. Nevertheless, the coupling coefficient will always tend to zero on either side of the NTL device, as it can be depicted in Figure 4.8. It is important to note that when the coupling coefficient is zero the coupled-mode equations simplify to a system of two independent first order

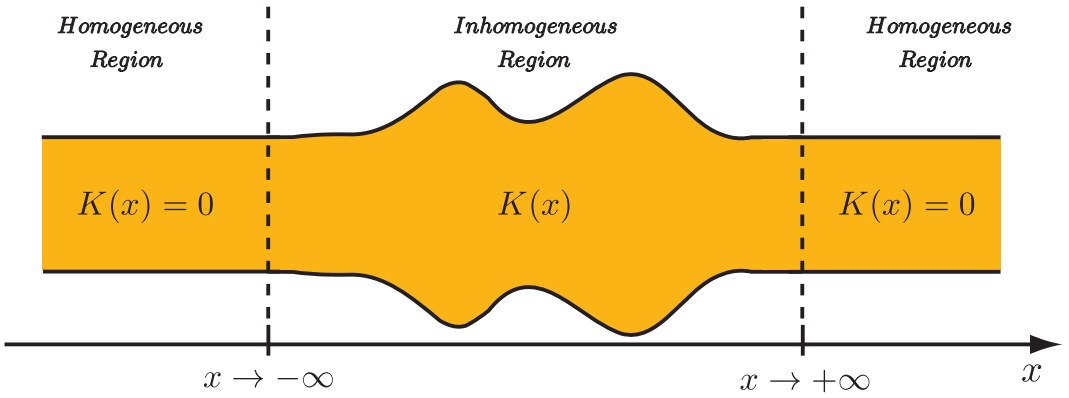

FIGURE 4.8: Infinitely long NTL structure.

homogeneous differential equations with trivial solutions given by

$$a^{+}(\omega, x) = e^{-j\omega x}, \tag{4.98}$$

$$a^{-}(\omega, x) = e^{j\omega x}. \tag{4.99}$$

We now introduce a two component function $\phi(\omega, x)$ known as a Jost function that is a particular solution to the ZS system. The behavior of $\phi(\omega, x)$ in the limit $x \to -\infty$ is [48], [49], [32]

$$\lim_{x\to-\infty} \phi(\omega, x) = \begin{bmatrix} \phi_1(\omega, x) \\ \phi_2(\omega, x) \end{bmatrix} = \begin{bmatrix} 1 \\ 0 \end{bmatrix} e^{-j\omega x}. \tag{4.100}$$

Another particular solution to the ZS system which is linearly independent of the previous one can be obtained by applying the complex conjugate operator to the ZS system. This yields another Jost solution that is given by [48], [49]

$$\bar{\phi}(\omega, x) = \begin{bmatrix} \bar{\phi}_1(\omega, x) \\ \bar{\phi}_2(\omega, x) \end{bmatrix} = \begin{bmatrix} \phi_2^*(\omega, x) \\ \phi_1^*(\omega, x) \end{bmatrix} \tag{4.101}$$

whose limit for $x \to -\infty$ is

$$\lim_{x\to-\infty} \bar{\phi}(\omega, x) = \begin{bmatrix} 0 \\ 1 \end{bmatrix} e^{j\omega x}. \tag{4.102}$$

Figure 4.9 illustrate the solutions $\phi(\omega, x)$ and $\bar{\phi}(\omega, x)$ for the ZS system. It is important to note that these two solutions represent different *physical events*. While Figure 4.9(b) refers to the coupling of energy from the backward propagating wave (wave incident from the right) $\phi_1^*(\omega, x) = a^{-}(\omega, x)$ to the forward propagating wave

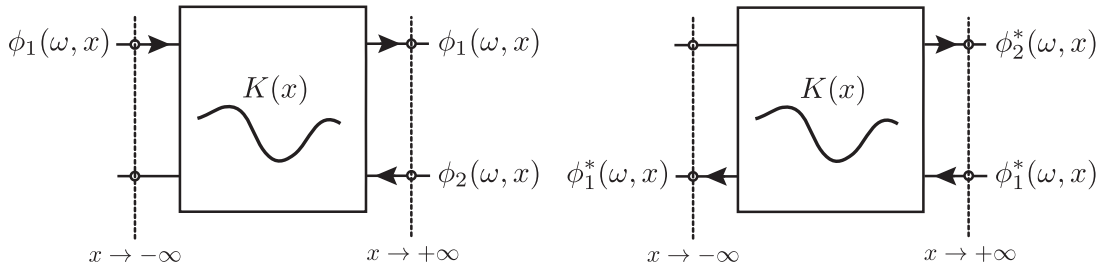

(a) Solution $\phi(\omega, x)$. (b) Solution $\bar{\phi}(\omega, x)$.

FIGURE 4.9: Schematic representation of the linear independent solutions to the ZS system.

$\phi_2^*(\omega, x) = a^+(\omega, x)$, the physical event depicted in Figure 4.9(a) represents the time-reversed process [48]. Because these two linear independent solutions of the ZS system represent different physical events, we can say that they fully describe the ZS system, as any other solution to the system can be obtained by a linear combination of $\phi(\omega, x)$ and $\bar{\phi}(\omega, x)$.

So far, the Jost solutions considered for the ZS system (4.96) are defined by considering their tendency or asymptotic behavior in the limit $x \to -\infty$. However, considering the asymptotic behavior for when $x \to +\infty$ we have that

$$\lim_{x\to\infty} \psi(\omega, x) = \begin{bmatrix} \psi_1(\omega, x) \\ \psi_2(\omega, x) \end{bmatrix} = \begin{bmatrix} a^+(\omega, x) \\ a^-(\omega, x) \end{bmatrix} = \begin{bmatrix} 1 \\ 0 \end{bmatrix} e^{-j\omega x} \tag{4.103}$$

is yet another solution to the ZS system. Please note that this new solution is not linear independent from $\phi(\omega, x)$ nor $\bar{\phi}(\omega, x)$. Furthermore, from the properties of the Jost functions [48], [49], [32] and as stated before, we know that each Jost function can be represented as a linear combination of two other linear independent functions as long as they are solutions to the ZS system. Therefore, we may consider a linear combination of solutions $\phi(\omega, x)$ and $\bar{\phi}(\omega, x)$, and make use of this linear combination to represent $\psi(\omega, x)$ as

$$\psi(\omega, x) = a(\omega)\phi(\omega, x) + b(\omega)\bar{\phi}(\omega, x). \tag{4.104}$$

Considering the limit $x \to -\infty$, the solution $\phi(\omega, x)$ describes the incident wave to the left of the structure whereas the solution $\bar{\phi}(\omega, x)$ stands for the reflected wave.

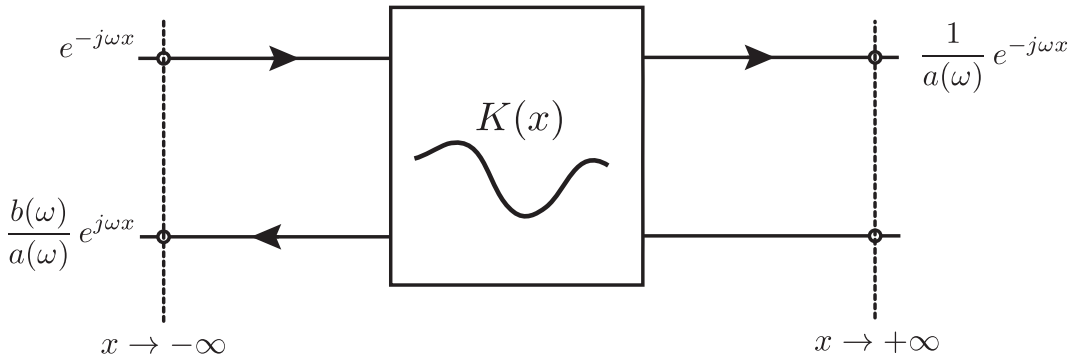

FIGURE 4.10: ZS system solution corresponding to equation (4.105).

Let us now consider the solution $\psi(\omega, x)$ given by equation (4.104) and divide it by $a(\omega)$. We now have yet another solution to the ZS system in the form

$$G(\omega, x) = \frac{1}{a(\omega)}\psi(\omega, x) = \phi(\omega, x) + \frac{b(\omega)}{a(\omega)}\bar{\phi}(\omega, x). \tag{4.105}$$

When evaluated at $|x| \to \infty$ the previous solution clearly indicates an unitary incident wave $\phi_1(\omega, x) = e^{-j\omega x}$ to the left of the NTL structure as well as a reflected wave given by

$$\lim_{x\to-\infty} U(\omega, x) = \frac{b(\omega)}{a(\omega)}\,\bar{\phi}_2(\omega, x) = \frac{b(\omega)}{a(\omega)}\, e^{j\omega x} = R(\omega)e^{j\omega x}. \tag{4.106}$$

where $R(\omega)$ stands for the reflection coefficient at the beginning of the coupling or inhomogeneous region. Equation (4.105) also features the transmitted wave which is given by

$$\lim_{x\to+\infty} G(\omega, x) = \frac{1}{a(\omega)}\psi_1(\omega, x) = \frac{1}{a(\omega)}\, e^{-j\omega x}. \tag{4.107}$$

A schematic illustration of the ZS system solution given by equation (4.105) for an infinitely long NTL is depicted by Figure 4.10.

Let us assume that the complete solution for $\phi(\omega, x)$ can be given by [48],[49],[32]

$$\phi(\omega, x) = \begin{bmatrix} 1 \\ 0 \end{bmatrix} e^{-j\omega x} + \int_{-\infty}^{+\infty} A(y, x)\, e^{-j\omega y} dy, \tag{4.108}$$

where

$$A(\omega, y) = \begin{bmatrix} A_1(y, x) \\ A_2(y, x) \end{bmatrix} \tag{4.109}$$

is known as the *kernel* of the Jost function. On the other hand, from equation (4.101) we have

$$\bar{\phi}(\omega,x)=\begin{bmatrix}0\\1\end{bmatrix}e^{j\omega x}+\int_{-\infty}^{+\infty}\begin{bmatrix}A_2^*(y,x)\\A_1^*(y,x)\end{bmatrix}e^{j\omega y}dy. \tag{4.110}$$

As in section 4.2.1 for the solution of the Schrödinger equation inverse problem, we are now going to reformulate the ZS inverse problem in to the time domain. This reformulation allows for a more intuitive understanding and resolution of the problem by applying causality conditions. For that we consider the inverse Fourier transform to be defined as

$$u(t,x)=\frac{1}{2\pi}\int_{-\infty}^{+\infty}U(\omega,x)e^{j\omega t}d\omega. \tag{4.111}$$

In the time domain and considering the previous inverse Fourier transform the coupled mode equations described in equations (4.94) and (4.95) turn in to

$$\frac{\partial u(t,x)}{\partial x}=-\frac{\partial u(t,x)}{\partial t}-K(x)\,v(t,x), \tag{4.112}$$

$$\frac{\partial v(t,x)}{\partial x}=\frac{\partial v(t,x)}{\partial t}-K(x)\,u(t,x), \tag{4.113}$$

where

$$\begin{aligned}u(t,x)&=\mathcal{F}^{-1}\left\{a^+(\omega,x)\right\},\\ v(t,x)&=\mathcal{F}^{-1}\left\{a^-(\omega,x)\right\}.\end{aligned} \tag{4.114}$$

Applying the inverse Fourier transform to equations (4.108) and (4.110) results in

$$\Phi(t,x)=\begin{bmatrix}1\\0\end{bmatrix}\delta(t-x)+\begin{bmatrix}A_1(t,x)\\A_2(t,x)\end{bmatrix}, \tag{4.115}$$

which is the time domain version of solution $\phi(\omega,x)$ and

$$\bar{\Phi}(t,x)=\begin{bmatrix}0\\1\end{bmatrix}\delta(t+x)+\begin{bmatrix}A_2^*(-t,x)\\A_1^*(-t,x)\end{bmatrix} \tag{4.116}$$

the time domain version of $\bar{\phi}(\omega,x)$. Both are solutions to the time domain ZS system.

Figure 4.11 illustrates the coupling process in space (for some instant of time t) as expressed by $\bar{\phi}(\omega,x)$ and whose schematic representation is depicted in Figure 4.9(b). A wave is incident from the right upon the coupling region (ϕ_1^*), partly is transmitted and

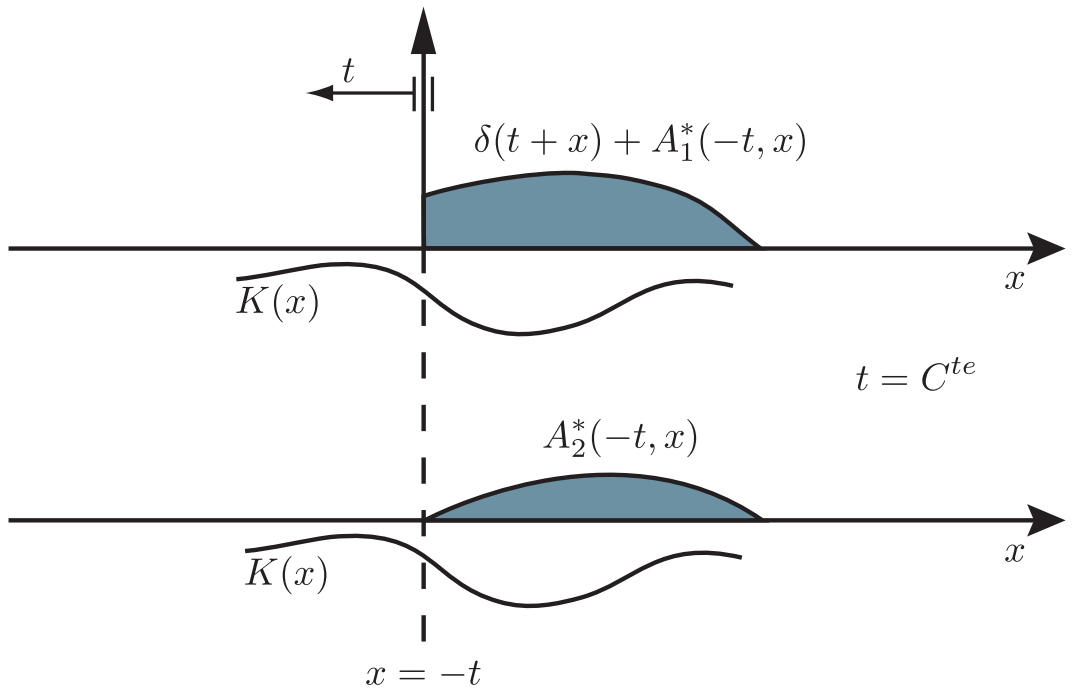

FIGURE 4.11: Spatial representations of the coupling via $K(x)$ expressed by $\bar{\Phi}(t,x)$.

partly is coupled to the counter-propagating wave(ϕ_2^*). Furthermore, we clearly see from equation (4.116) that the time domain analysis shows an incident unit impulse coming from the right that when interacting with the coupling region will originate scattering events. The scattering will spread inside the coupling region as far to the left as the unit impulse has penetrated the region. The scattering and spreading phenomena are illustrated by the colored areas in Figure 4.11. In equation (4.116) the kernels $A_1^*(t,x)$ and $A_2^*(t,x)$ contain the information regarding the spreading and scattering inside the coupling region [48]. A careful observation of of Figure 4.11 and equation (4.116) tell us that the overall transient (colored area plus unit impulse) is moving to the left and that the leading edge is at position $x = -t$. This means that for $x < -t$ or $t + x < 0$ and because the transient is moving from right to left, the time has not advanced enough for the unit impulse to have passed. Therefore we have that

$$\begin{bmatrix} A_1^*(-t,x) \\ A_2^*(-t,x) \end{bmatrix} = 0, \qquad x < -t, \tag{4.117}$$

which is a restriction due to causality. On the other hand, Figure 4.12 illustrates the coupling process in space for some fixed time t as expressed by $\phi(\omega,x)$ and whose schematic representation is depicted in Figure 4.9(a). Please note that we have previously referred

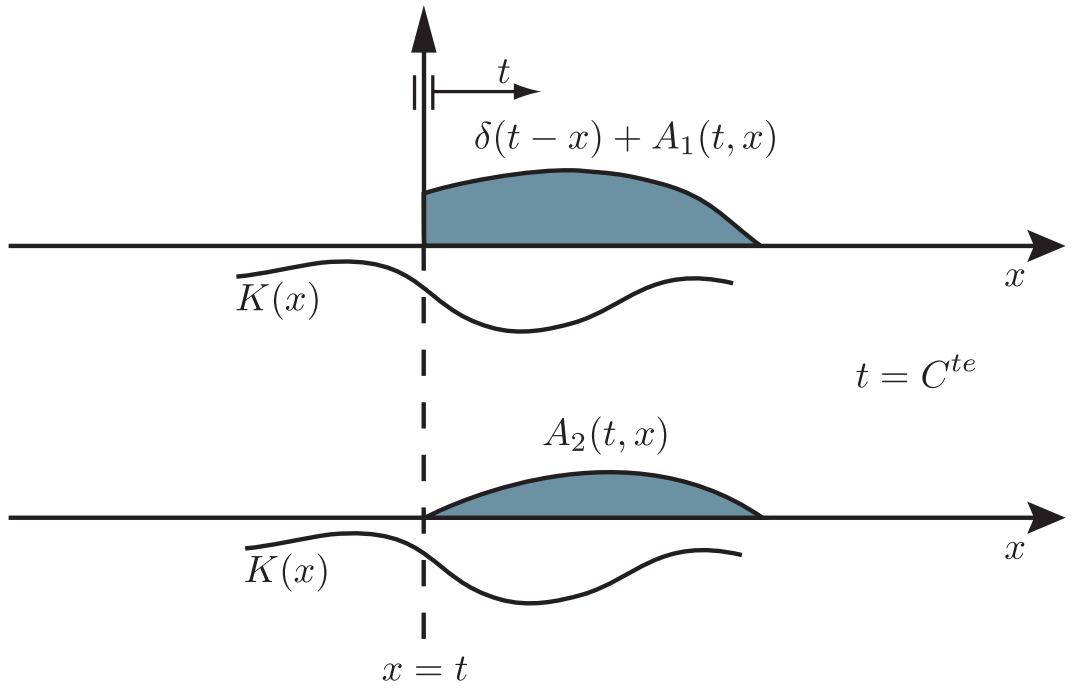

FIGURE 4.12: Spatial representations of the coupling via $K(x)$ expressed by $\Phi(t,x)$.

that solution $\phi(\omega,x)$ is represents the time reversed process of solution $\bar{\phi}(\omega,x)$ and vice-versa. We then see from the illustration in Figure 4.12 and from equation (4.115) that the transient (colored area) is moving to the right, clearing the coupling region to the left of the unit impulse of scattering events. This means that for $t-x>0$ or $x<t$ enough time as passed by for the transient to clear the portion of coupling region contained in $-\infty<x<t$. Therefore, the kernels $A_1(t,x)$ and $A_2(t,x)$ which contain the information regarding the spreading and scattering inside the coupling region are restricted to

$$\begin{bmatrix} A_1(t,x) \\ A_2(t,x) \end{bmatrix} = 0, \qquad x<t, \tag{4.118}$$

which similarly to the previous case is a restriction due to causality. Furthermore, the boundary conditions (4.117) and (4.118) can be combined, yielding

$$\begin{bmatrix} A_1(t,x) \\ A_2(t,x) \end{bmatrix} = 0, \qquad x<|t|. \tag{4.119}$$

Next we show that the Jost functions obeys to the GLM equations type. Let us consider the time domain version of the composed solution $G(\omega,x)$. So, applying the

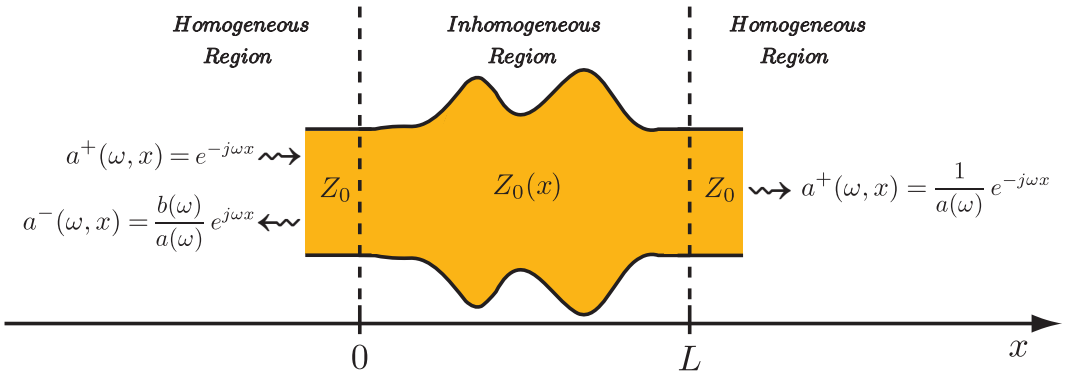

FIGURE 4.13: Finite length NTL.

inverse Fourier transform to equation equation (4.105) results in

$$g(t,x)=\begin{bmatrix}1\\0\end{bmatrix}\delta(t-x)+\begin{bmatrix}A_1(t,x)\\A_2(t,x)\end{bmatrix}+\begin{bmatrix}0\\1\end{bmatrix}r(t+x)+\int_{-\infty}^{+\infty}\begin{bmatrix}A_2^*(y,x)\\A_1^*(y,x)\end{bmatrix}r(t+y)dy, \quad (4.120)$$

where $r(t)$ is the inverse Fourier transform of the reflection at the beginning of the coupling region $R(\omega)$ (see equation (4.106)).

Due to the mathematics involved on the solution process for the ZS system we have considered so far NTL structures of infinite length. However, in reality we are interested on finite length structures as the one depicted in Figure 4.13. From here on, we consider the solutions for NTL structures whose coupling region begins at $x = 0$ and have a length of L, so that

$$K(x)=0, \qquad x<0\cup x>L, \quad (4.121)$$

as it can be seen from Figure 4.13. Furthermore we have seen in section 4.2.1.1 that due to physical constrains any NTL structure is a non-anticipative system. Therefore they are classified as causal systems so that their impulse response must always verify

$$r(t)=\mathcal{F}^{-1}\left\{\frac{b(\omega)}{a(\omega)}\right\}=0, \qquad t<0. \quad (4.122)$$

Moreover, from the realizability conditions (see section 4.2.1.1) we have that $r(t)$ must be a real-valued time function.

Taking into consideration the conditions (4.119) and (4.122) we can now rewrite the time domain version of the composed solution $G(\omega, x)$ as

$$g(t,x)=\begin{bmatrix}1\\0\end{bmatrix}\delta(t-x)+\begin{bmatrix}A_1(t,x)\\A_2(t,x)\end{bmatrix}+\begin{bmatrix}0\\1\end{bmatrix}r(t+x)+\int_{-t}^{x}\begin{bmatrix}A_2^*(y,x)\\A_1^*(y,x)\end{bmatrix}r(t+y)dy, \quad (4.123)$$

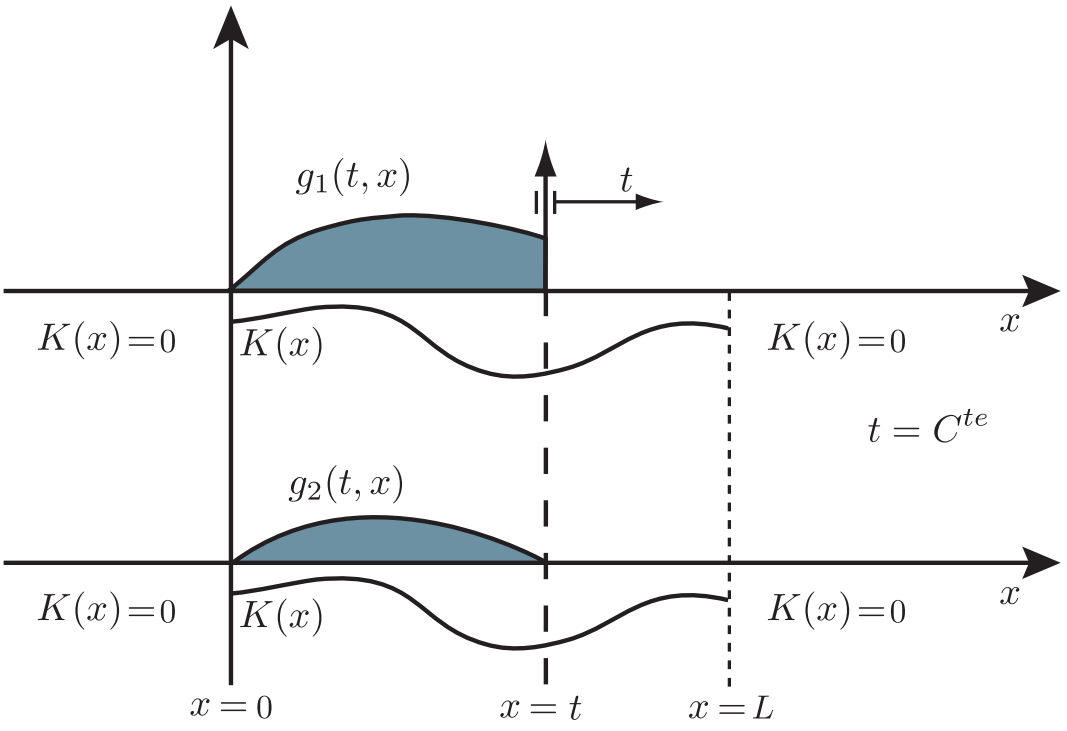

FIGURE 4.14: Spatial representation of the coupling via $K(x)$ expressed by $G(\omega, x)$ for an NTL of length L.

with the integration range now limited from $-t$ to x.

A spatial representation for some fixed instant of time is illustrated in Figure 4.14 for an NTL structure of length L characterized by a coupling coefficient $K(x)$. From the illustration we see that $g(t,x)$ is a rightward-propagating transient, so that

$$g(t,x) = 0, \qquad x > t, \tag{4.124}$$

which means that due to causality the leading edge of the propagating transient only reaches position x when $t = x$. From equation (4.123) we clearly identify the term $\delta(t-x)$ as the incident unit impulse responsible for producing the response of the NTL structure. Obviously there can not be any response until the impulse has arrived, thus the condition expressed in equation (4.124) leads to the following expression

$$\begin{bmatrix} A_1(t,x) \\ A_2(t,x) \end{bmatrix} + \begin{bmatrix} 0 \\ 1 \end{bmatrix} r(t+x) + \int_{-t}^{x} \begin{bmatrix} A_2^*(y,x) \\ A_1^*(y,x) \end{bmatrix} r(t+y)dy = 0, \qquad x > t, \tag{4.125}$$

meaning that for $x > t$ the medium is still in a resting state and thus no scattering events have yet occurred.

Analyzing equation (4.125) we clearly see that the functions which constitute the

expression are the kernel functions $A_1(t,x)$ and $A_2(t,x)$, the kernel functions complex conjugates and the impulse response of the NTL device. From the realizability conditions (section 4.2.1.1) we know that the impulse response $r(t)$ must be a real-valued function, therefore, for equation (4.125) to be verified we have that the kernel functions must also be real-valued function, thus

$$\begin{aligned} A_1^*(t,x) &= A_1(t,x), \\ A_2^*(t,x) &= A_2(t,x). \end{aligned} \tag{4.126}$$

Please note that as the kernel functions are solely a function of time t and space x, it would make no sense for them to be complex valued when describing the scattering and spreading phenomena in a real life NTL structure. We may then consider the fact that the kernel functions must be real valued as yet another realizability condition. Considering the condition (4.126), equation (4.125) can be rewritten in the form of the following system of equations

$$\begin{cases} A_1(t,x) + \displaystyle\int_{-t}^{x} A_2(y,x)\, r(t+y)dy = 0, & x > t, \\ A_2(t,x) + r(t+x) + \displaystyle\int_{-t}^{x} A_1(y,x)\, r(t+y)dy = 0, & x > t, \end{cases} \tag{4.127}$$

which are called the GLM coupled integral equations.

Now that we have derived the GLM coupled equations, we need to find the relation between the kernel functions $A_1(t,x)$ and $A_2(t,x)$ and the coupling coefficient $K(x)$ so that we can retrieve the physical characteristics of the coupling regions which in the case of NTL devices is the impedance profile $Z_0(x)$. To do that, let us consider the Jost function $\Phi(t,x)$ given by equation (4.115)and consider that

$$\begin{aligned} u(t,x) &= \Phi_1(t,x) = \delta(t-x) + A_1(t,x), \\ v(t,x) &= \Phi_2(t,x) = A_2(t,x). \end{aligned} \tag{4.128}$$

From Figure 4.13 we see that the coupling region is only defined for $x \geq 0$, thus due to causality and without loss of generality the previous equations can be rewritten as

$$u(t,x) = \delta(t-x) + h(-t+x)\, A_1(t,x), \tag{4.129}$$

$$v(t,x) = h(-t+x)\, A_2(t,x), \tag{4.130}$$

where $h(t)$ is the unit step function. Substituting equations (4.129) and (4.130) into equation (4.113) results in

$$\begin{aligned} &h(-t+x)\,\frac{\partial A_2(t,x)}{\partial x} + \delta(-t+x)\,A_2(t,x) = \\ &= h(-t+x)\,\frac{\partial A_2(t,x)}{\partial t} - \delta(-t+x)\,A_2(t,x) - K(x)\,\delta(t-x) - K(x)\,h(-t+x)\,A_1(t,x). \end{aligned} \tag{4.131}$$

Equating the Dirac delta terms in (4.131) and because the Dirac functions only evaluate different from zero at $t = x$, yields the relation

$$K(x) = -2\,A_2(x,x), \tag{4.132}$$

which by considering (4.126) is also a real valued function.

In the next section we shall demonstrate how from the coupled GLM integral equations we can obtain the analytical expressions for the kernel functions. Unlike the Schrödinger equation inverse problem we shall see that an analytical expression for the impedance profile is easily obtainable.

4.2.2.1 Analytical solutions for the impedance profile

Similarly to the Schrödinger equation inverse problem, in this section we describe the necessary steps to obtain the coupling coefficient $K(x)$ from the desired reflection response $R(\omega)$ as long as it can be represented as a rational function [51].

The mathematical procedure is similar to the one used before on the Schrödinger inverse problem. The difference is that instead of solving one GLM integral equation, we now calculate the solution for two coupled GLM integral equations. As in section 4.2.1.2, in order to keep the mathematical complexity to a minimum we consider the simple case of a Butterworth filter with a zero placed at the origin of the s-plane. Please note that in this section no reference is made to the realizability conditions as these are already addressed in section 4.2.1.1 and are the same independently of the inverse scattering method to be used.

Recalling equation (4.34) we have that the frequency response to be synthesized is given by

$$R(\omega) = \frac{j\sqrt{2}\omega}{-\omega^2 + j\sqrt{2}\omega + 1}, \tag{4.133}$$

with the impulse response being

$$\begin{cases} r(t) = \sqrt{2}e^{-\frac{\sqrt{2}}{2}t}\left(\cos\left(\frac{\sqrt{2}}{2}t\right) - \sin\left(\frac{\sqrt{2}}{2}t\right)\right), & x \geq 0, \\ r(t) = 0, & x < 0 \end{cases} \tag{4.134}$$

and the corresponding first derivative of the impulse response

$$r'(t) = -2e^{-\frac{\sqrt{2}}{2}t}\cos\left(\frac{\sqrt{2}}{2}t\right), \qquad t > 0. \tag{4.135}$$

In order to solve the coupled GLM equations a differential operator is constructed (4.36)

$$f(p) = p^2 + \sqrt{2}p + 1, \tag{4.136}$$

so that $f(p)r(t) = 0$ and where $p = \dfrac{d}{dt}$. Applying (4.136) to the coupled GLM equations and using the Leibnitz integral rule yields

$$f(p)A_1(t,x) + p\sqrt{2}A_2(-t,x) = 0 \tag{4.137}$$

$$f(p)A_2(t,x) + p\sqrt{2}A_1(-t,x) = 0. \tag{4.138}$$

Similarly, another two equations which are independent of the previous ones can be obtained for $f(-p)$ whose respective time derivative results in

$$f(-p)\,p\,A_1(-t,x) - p^2\sqrt{2}A_2(t,x) = 0 \tag{4.139}$$

$$f(-p)\,p\,A_2(-t,x) - p^2\sqrt{2}A_1(t,x) = 0. \tag{4.140}$$

Eliminating $A_2(-t,x)$ between equations (4.137) and (4.140) yields

$$\begin{gathered} (p^4 + 2p^2 + 1)A_1(t,x) = 0 \\ \Downarrow \\ \frac{d^4}{dt^4}A_1(t,x) + 2\frac{d^2}{dt^2}A_1(t,x) + A_1(t,x) = 0. \end{gathered} \tag{4.141}$$

In the same way, eliminating $A_1(-t,x)$ between equations (4.138) and (4.139) yields

$$\begin{gathered}(p^4+2p^2+1)A_2(t,x)=0\\ \Downarrow\\ \frac{d^4}{dt^4}A_2(t,x)+2\frac{d^2}{dt^2}A_2(t,x)+A_2(t,x)=0.\end{gathered}\tag{4.142}$$

The general solutions to $A_1(t,x)$ and $A_2(t,x)$ are given by [38]

$$A_1(t,x)=C_1(x)\sin(t)+C_2(x)\cos(t)+C_3(x)\sin(t)t+C_4(x)\cos(t)t,\tag{4.143}$$

$$A_2(t,x)=C_5(x)\sin(t)+C_6(x)\cos(t)+C_7(x)\sin(t)t+C_8(x)\cos(t)t,\tag{4.144}$$

where the functions $C_1(x)$ to $C_8(x)$ are the unknown coefficient functions which are obtained next by setting the appropriate boundary conditions.

As a first boundary condition we substitute equations (4.143) and (4.144) into equations (4.137) and (4.138), which results in

$$\begin{aligned}&\cos(t)\left(2C_3(x)+\sqrt{2}C_1(x)+\sqrt{2}C_4(x)-\sqrt{2}C_5(x)-\sqrt{2}C_8(x)\right)+\\&+\sin(t)\left(-2C_4(x)-\sqrt{2}C_2(x)+\sqrt{2}C_3(x)-\sqrt{2}C_6(x)+\sqrt{2}C_7(x)\right)+\\&+\cos(t)t\left(\sqrt{2}C_3(x)+\sqrt{2}C_7(x)\right)+\sin(t)t\left(\sqrt{2}C_8(x)-\sqrt{2}C_4(x)\right)=0\end{aligned}\tag{4.145}$$

for the first equation, and in

$$\begin{aligned}&\cos(t)\left(2C_7(x)+\sqrt{2}C_5(x)+\sqrt{2}C_8(x)-\sqrt{2}C_1(x)-\sqrt{2}C_4(x)\right)+\\&+\sin(t)\left(-2C_8(x)-\sqrt{2}C_6(x)+\sqrt{2}C_7(x)-\sqrt{2}C_2(x)+\sqrt{2}C_3(x)\right)+\\&+\cos(t)t\left(\sqrt{2}C_t(x)+\sqrt{2}C_3(x)\right)+\sin(t)t\left(\sqrt{2}C_4(x)-\sqrt{2}C_8(x)\right)=0\end{aligned}\tag{4.146}$$

for the second equation. By simple inspection of the previous equations, we easily see that one possible solution is obtained by setting

$$\begin{cases}C_3(x)=\dfrac{C_5(x)-C_1(x)}{\sqrt{2}},\\ C_4(x)=-\dfrac{C_6(x)+C_2(x)}{\sqrt{2}},\\ C_7(x)=-C_3(x),\\ C_8(x)=C_4(x).\end{cases}\tag{4.147}$$

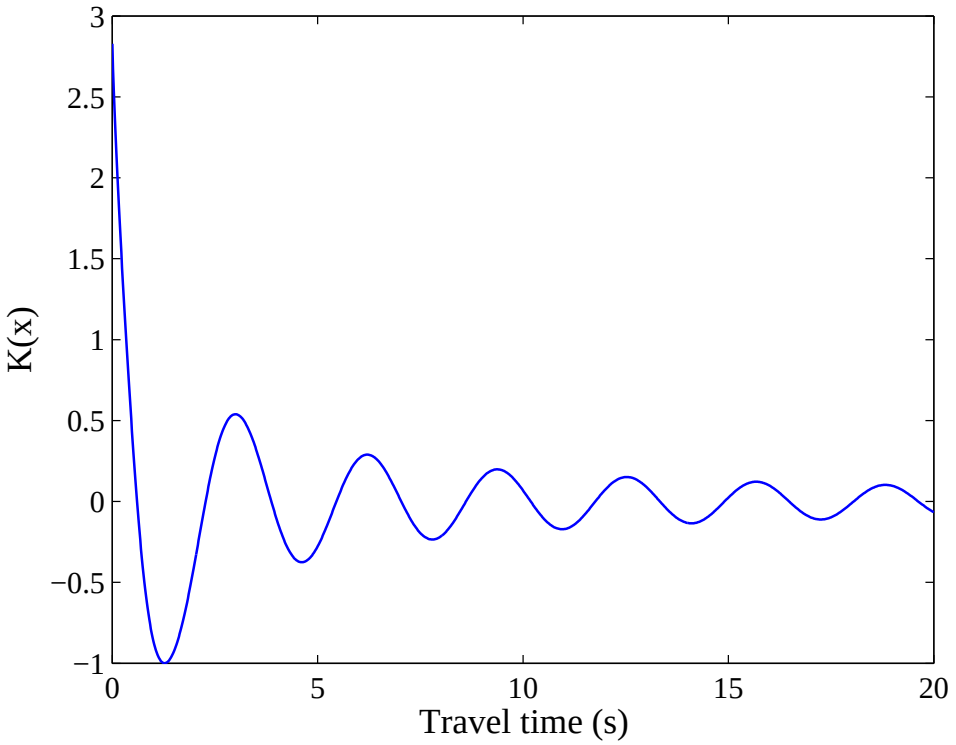

FIGURE 4.15: Reconstructed coupling coefficient for the second order Butterworth filter with zero placed at the origin of s-plane.

The four remaining independent coefficient functions can be obtained through the GLM coupled equations 4.127. Evaluating the GLM equations at $t = -x$ results in

$$A_1(-x, x) = 0, \tag{4.148}$$

$$A_2(-x, x) = -r(0). \tag{4.149}$$

Because we have four unknowns two more equations are needed, therefore, taking the time derivative derivative of the GLM equations and evaluating the result at $t = -x$ gives

$$\frac{\partial}{\partial t} A_1(t, x)|_{t=-x} + r(0) A_2(t, x)|_{t=-x} = 0, \tag{4.150}$$

$$\frac{\partial}{\partial t} A_2(t, x)|_{t=-x} + r(0) A_1(t, x)|_{t=-x} = -r'(0) \tag{4.151}$$

where $r'(0) = -2$ and $r(0) = \sqrt{2}$.

Substituting the coefficient relations expressed by (4.147) in the kernel functions given by (4.143) and (4.144) and then applying the kernel functions to equations (4.148)

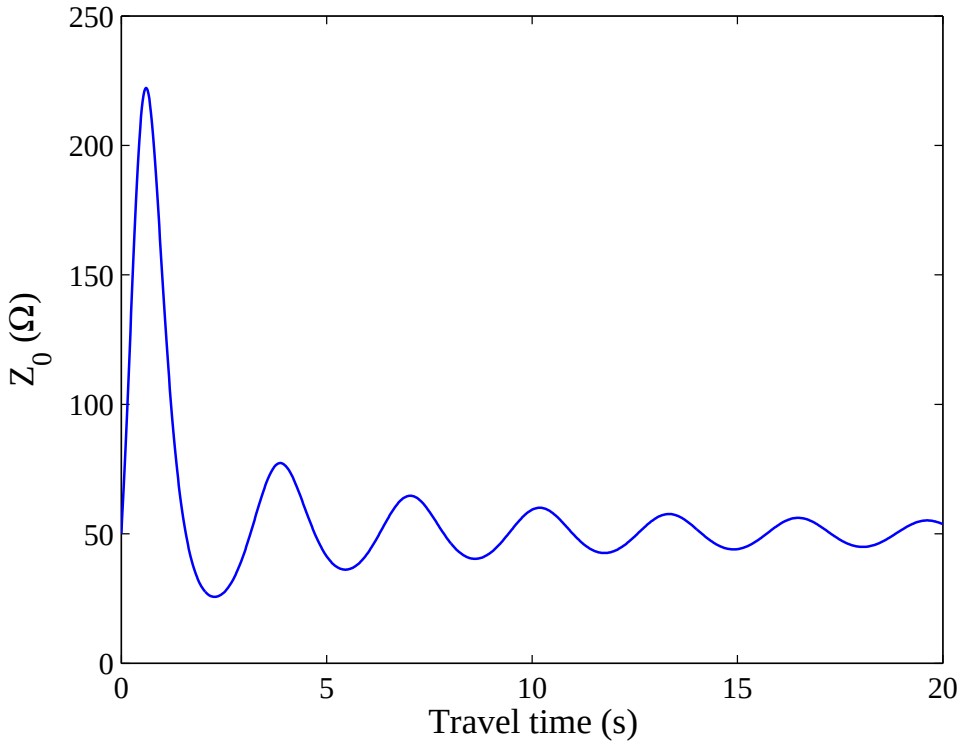

FIGURE 4.16: Reconstructed impedance profile for the second order Butterworth filter with a zero placed at the origin of s-plane.

to (4.149) yields a system of four equations with four unknown coefficient functions. Solving the system and considering the relations (4.147) enable us to calculate the unknown coefficient functions and therefore the analytical expressions for the kernels $A_1(t,x)$ and $A_2(t,x)$. Moreover, our main goal is to find the analytical expression for the coupling coefficient, therefore, considering (4.132) we have that

$$K(x) = 2\,\frac{-2\cos(x)\sin(x) + 4\cos(x)^2\,x - 2x + 2\cos(x)^2\sqrt{2} - \sqrt{2}}{2\cos(x)^4 + 2\sqrt{2}x + 2\,x^2 - 2\cos(x)^2 + 1}, \tag{4.152}$$

which is depicted in Figure 4.15.

Unlike the case of the potential function $q(x)$ that was related to the impedance function $Z_0(x)$ by means of a second order homogeneous differential equation with non-constant coefficients as seen in section 4.2.1.2, the coupling coefficient $K(x)$ on the other hand is related to $Z_0(x)$ by an homogeneous first order differential equation given by

$$\frac{Z_0(x)}{dx} - 2K(x)\,Z_0(x) = 0. \tag{4.153}$$

The solution to this equation was already derived in section 3.2.4 for the analysis of constant coupling NTL devices and is given by

$$Z_0(x) = C^{te} e^{2\int_0^x K(u)du} \tag{4.154}$$

where at $x = 0$ we have that $Z_0 = C^{te}$. This initial value boundary condition can be set to $C^{te} = 50\,\Omega$ yielding

$$Z_0(x) = 50\, e^{2\int_0^x K(u)du}. \tag{4.155}$$

Substituting equation (4.152) into equation (4.155) and solving the integral equation, we have that the solution to the inverse problem for the second order Butterworth filter is the impedance profile given by

$$Z_0(x) = 50\, \frac{\left(2\,x + \sqrt{2} + 2\,\cos(x)\sin(x)\right)^2}{\left(-2x - \sqrt{2} + 2\cos(x)\sin(x)\right)^2}, \tag{4.156}$$

which is plotted in Figure 4.16.

The impedance profile depicted in Figure 4.16 corresponds to a band-stop filter with a center frequency of 1 rad/s. In section 4.2.1.2 we refer to this response as the normalized frequency response. It was also seen in section 4.2.1.2 that in order to obtain the impedance function for the same frequency response profile but with a different center frequency ω_0 it is only necessary to scale the length of the solution for the normalized frequency response in the inverse proportion to the center frequency such that

$$x = \frac{\bar{x}}{\omega_0}, \tag{4.157}$$

where x is the new traveling time variable and $\bar{x}$ the traveling time corresponding to the normalized frequency response. Furthermore and to finish the inverse procedure, the spatial variable has to be transformed from travel time x to physical length z. In section 4.2.1.2 we saw that this transformation is given by

$$z = \frac{c}{\sqrt{\epsilon_r}} x, \tag{4.158}$$

where c is the speed of light in vacuum and ϵ_r is the permitivity of the medium surrounding the transmission line.

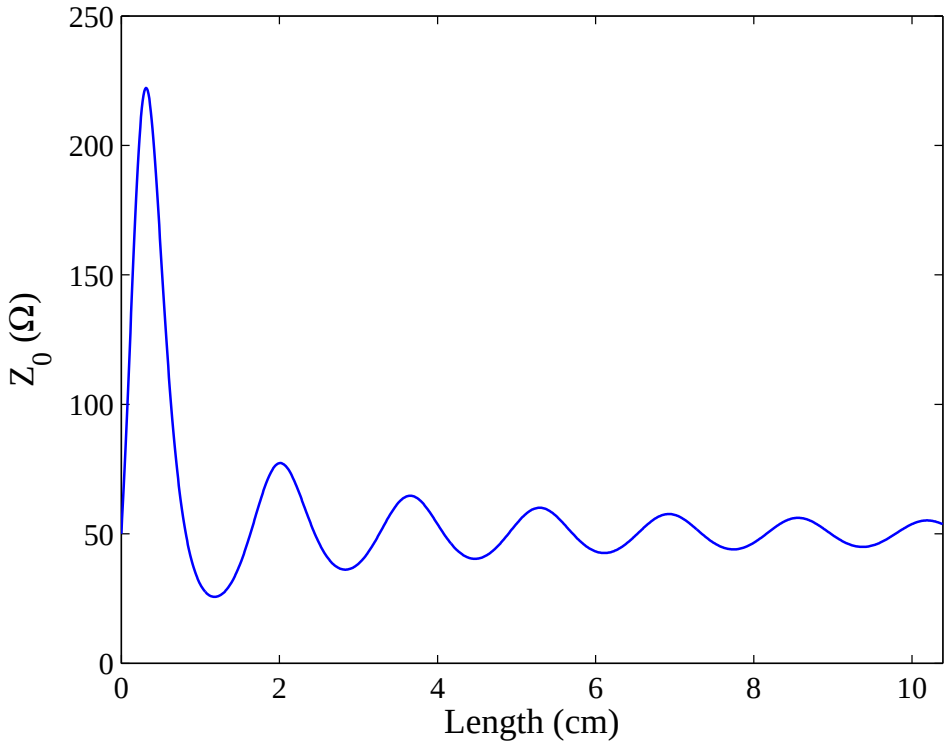

FIGURE 4.17: Reconstructed impedance profile as a function of physical length for a central frequency of $f_0 = 5\,\text{GHz}$ and a dielectric permitivity of $\epsilon_r = 3.38$.

Let us now consider as an example that we want to calculate the impedance profile for a center frequency of $f_0 = 5\,\text{GHz}$ and a permitivity of $\epsilon_r = 3.38$. In this case and combining equations (4.157) and (4.158) we have that the physical length of the filter is given by

$$z = \frac{c}{\sqrt{\epsilon_r}} \frac{\bar{x}}{\omega_0} \tag{4.159}$$

and the corresponding impedance profile is depicted in Figure 4.17.

4.2.2.2 Series solution - iterative algorithm

Let us now consider the second part of equation (4.127). Considering the limit case where $t = x$ yields

$$A_2(x,x) + r(2x) + \int_{-x}^{x} A_1(y,x)\, r(x+y) dy = 0. \tag{4.160}$$

Substituting equation (4.132) into the previous expression gives us the coupling coefficient as a function of the kernel function $K_1(t,x)$ and the impulse response $r(t)$

$$K(x) = 2\,r(2x) + 2\int_{-x}^{x} A_1(y,x)\,r(x+y)dy. \tag{4.161}$$

It is important to note that if we neglect the the contribution of the integral term, the calculation of the coupling coefficient is reduced to

$$K(x) = 2\,r(2x), \tag{4.162}$$

which is the zeroth order approximation, commonly referred to as the first order Born approximation. This is in fact the case previously analyzed in section 3.2.3.

The series solution, which can be solved using an iterative method, is obtained by starting from the first order born approximation, i.e., solving equation (4.127) in order to $A_2(t,x)$ and neglecting the integral term, thus,

$$A_2(t,x) = -r(t+x).$$

The kernel $A_2(t,x)$ is then substituted in the remaining GLM equation in (4.127) yielding

$$A_1(t,x) = \int_{-t}^{x} r(t+x)r(t+y)dy,$$

which is the first order approximation for $A_1(t,x)$. Substituting $A_1(t,x)$ into equation (4.161) yields the first order approximate solution for the coupling coefficient. The second order approximation for $A_2(t,x)$ is computed by substituting the first order $A_1(t,x)$ into the second equation of (4.127). The second order $A_1(t,x)$ is obtained by substituting the second order $A_2(t,x)$ into the first equation of (4.127). The series solution is thus obtained by proceeding in an iterative manner, i.e., by obtaining the second order approximation from the first order and so forth up to to the ith order approximation. The ith order approximation for the coupling coefficient is obtained from the ith order approximation of $A_1(t,x)$ though equation (4.161).

4.3 The layer-peeling algorithm

The inverse scattering procedures mentioned in section 4.2 are formulated in terms of integral equations, thereafter, one may think that the only way to solve inverse problems require the solution of such equations. However, independently of the work of mathematicians and physicists, other approaches to perform exact inverse scattering were developed by geophysicists like Robinson and Goupillaud [52], [53]. Their methods to perform inverse scattering are called differential or direct methods, and fully exploit the physical properties of the layered media where waves propagate. These differential methods heavily rely on causality principles, and upon the medium discretization in layers. The inverse scattering is then performed by reconstructing the medium layer by layer in a recursive manner, and for this reason they are sometimes referred to as layer-peeling algorithms.

When compared to the iterative solutions proposed by Kitrikos, Frangos and Jaggard to solve the GLM integral equations, these differential inverse scattering methods stand out due to their simplicity, simple numerical implementation as a computer routine, numerical stability, higher algorithm efficiency and most importantly, provide exact solutions.

In the electromagnetic realm, some important work was performed on the optical domain using differential inverse scattering. Notably the work of Feced *et al.* [15], and later Skaar *et al.* [54] on the synthesis of fiber Bragg gratings using layer-peeling algorithms. Adopting the nomenclature of Skaar one can divide the layer-peeling algorithms into two types: the discrete layer-peeling (DLP) algorithm and the continuous layer-peeling (CLP) algorithm. In his work, Skaar compares these two algorithms, both mathematically and numerically, and shows that they are based on the same principle, and that the CLP is equivalent to the DLP when considering infinitesimally thin layers.

We now describe and analyze in detail both these layer-peeling algorithms and show that they can easily be adapted to the synthesis of microwave filters. Furthermore, we shall demonstrate the advantages of these direct methods when compared to the classical inverse scattering methods analyzed in section 4.2.

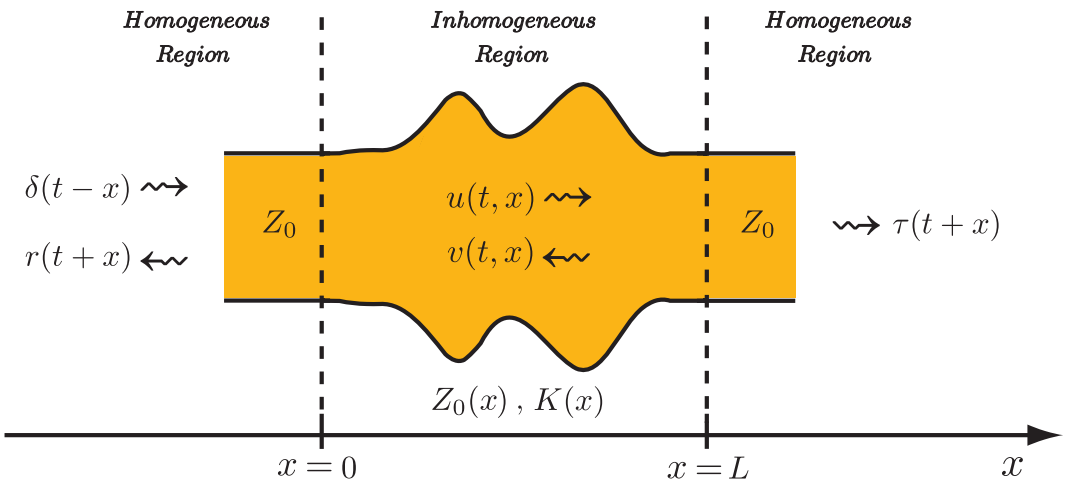

FIGURE 4.18: Finite length NTL structure. The NTL is considered to be probed from the left by a rightward propagating impulse $\delta(t)$. The reflection and transmission impulse responses are given by $r(t)$ and $\tau(t)$ respectively.

4.3.1 Continuous layer-peeling

The differential inverse scattering methods developed by geophysicists directly exploit the physical properties of layered media. In fact, by considering a layered media approach, the inverse scattering problem can be dealt with as simply as the direct scattering problem, i.e. we can find the impedance profile for the NTL structure from the reflection frequency response by simply propagating the fields along the NTL structure, while simultaneously evaluating the coupling coefficient using simple causality arguments.

The nomenclature *continuous layer peeling* was adopted by Skaar *et al.* when referring to the differential methods used by him on the synthesis of fiber Bragg gratings [55]. However the development of these methods was done earlier by Bruckstein et al. in the context of his study on scattering models in signal processing. The recursive procedure developed by Bruckstein and later adopted by Skaar as the *continuous layer peeling* constitutes a continuous version of an algorithm derived by Schur for testing the boundedness of analytic functions inside the unit circle [53]. Bruckstein refers to this method as the *continuous parameter Schur recursions*.

We know from section 4.2 that the propagation and coupling of waves in an NTL structure as the one illustrated in Figure 4.18 is described by the coupled mode equations (4.94) and (4.95). Similarly to the development undertaken in section 4.2 both for the one-dimensional Schrödinger equation and the Zakharov-Shabat inverse scattering problems, we now reformulate the scattering and coupling process occurring on an NTL in the time domain. This allows for a more intuitive understanding and formulation of

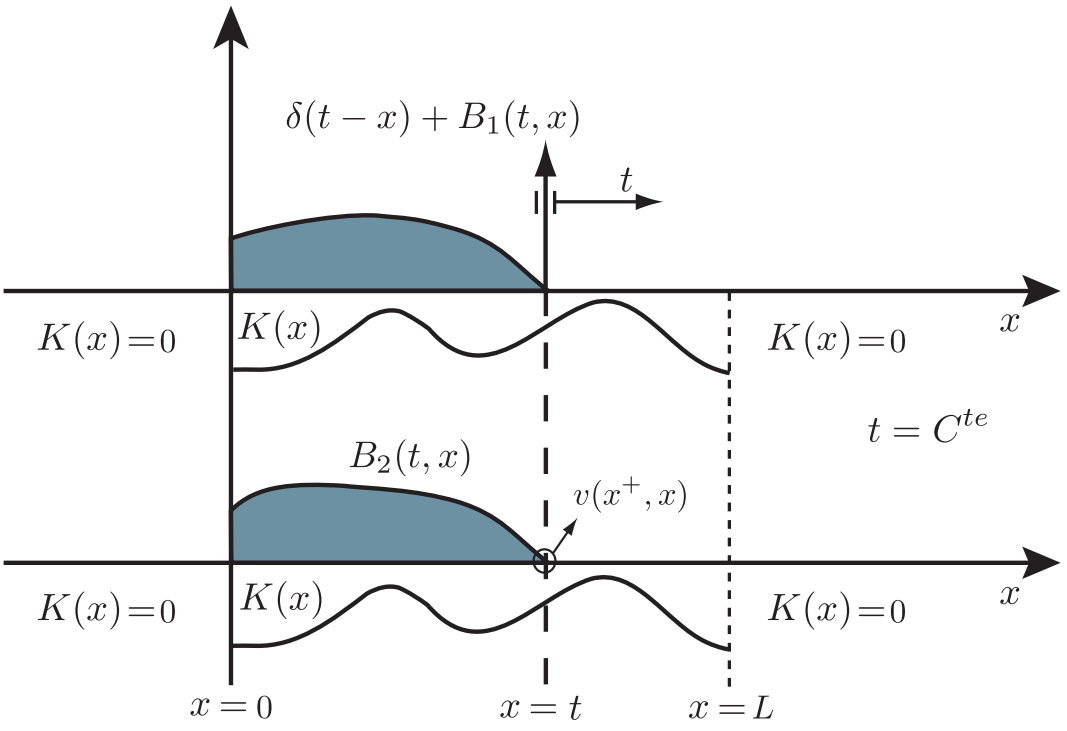

FIGURE 4.19: Spatial representation of the coupling process taking place on the NTL structure illustrated in Figure 4.18. The propagation velocity v_p is considered to be unitary.

the inverse scattering problem as it heavily relies on causality arguments. Therefore, we now consider the time domain version of the coupled-mode equations which are given by

$$\frac{\partial u(t,x)}{\partial x} = -\frac{\partial u(t,x)}{\partial t} - K(x)\, v(t,x), \tag{4.163}$$

$$\frac{\partial v(t,x)}{\partial x} = \frac{\partial v(t,x)}{\partial t} - K(x)\, u(t,x), \tag{4.164}$$

where $u(t,x) = \mathcal{F}^{-1}\{a^+(\omega,x)\}$ and $v(t,x) = \mathcal{F}^{-1}\{a^-(\omega,x)\}$ are time domain representation of the rightward and leftward propagating waves propagating in the inhomogeneous region as illustrated by Figure 4.18.

Figure 4.19 depicts a representation of the scattering events occurring in the NTL illustrated in Figure 4.18 for some time instant t. Please note that the illustration in Figure 4.19 is essentially the same as the ones presented in section 4.2 for the Jost solutions to the ZS system. In the present case scenario, the one depicted in Figure 4.19, the NTL is assumed to be in a quiescent state at $t = 0$. Therefore causality states that there are no scattering or coupling events for $t \leq 0$. At $t = 0^+$ the structure is probed from the left by a rightward propagating impulse (see Figure 4.18) which triggers the

scattering events inside the coupling region that are represented by the colored areas in Figure 4.19. Therefore from Figure 4.19 we can describe the transient corresponding to the forward propagating waves inside the NTL as an impulse followed by a continuous function $B_1(t,x)$, which due to causality must verify $B_1(t,x) = 0$ for $x > t$. The lower colored area in Figure 4.19 describes the leftward propagating waves and is described by $B_2(t,x)$ which verifies the same causality restriction. Thus, from the previous analysis of Figure 4.19 and enforcing the causality constrains, the transient fields in the NTL structure can be described by [53], [55]

$$u(t,x) = \delta(t-x) + h(t-x)\ B_1(t,x), \tag{4.165}$$

$$v(t,x) = h(t-x)\ B_2(t,x), \tag{4.166}$$

where $h(t)$ is the unit step function, $\delta(t)$ the Dirac delta function and where $h(t-x)$ evaluates to zero for $t < x$ and to one for $t \geq x$. Please note that equations (4.165) and (4.166) are essentially the same as the Jost solution $\bar{\Phi}(t,x)$ given by (4.116) for the ZS system in section 4.2, the only difference being that in the case of the Jost solution $\bar{\Phi}(t,x)$ the impulse is considered to be incident upon the right side of the NTL whereas in the present case we consider the NTL structure to be probed from the left.

Substituting equations (4.165) and (4.166) into equation (4.164) and equating the coefficients of the Dirac functions, we have that

$$K(x) = 2\ B_2(t,x)|_{t=x^+}. \tag{4.167}$$

Equation (4.167) for the coupling coefficient is the same as equation (4.132) obtained in the context of the ZS system Jost solution except for the minus signal. The reason for this difference has to do with the fact that equation (4.132) is obtained from a Jost solution of the ZS system which is time reversed when compared to the present case.

Please note that due to causality, the leading impulse requires an amount of time equal to x to reach the position x within the NTL structure. However, at $t = x$ the medium in the NTL extending from x to L is still at rest. It is not until $t = x^+$ that the first scattering event and therefore coupling occurs at the position x, hence the notation used in the previous equation. Furthermore, we easily see from equation (4.166) that

when $t = x^+$ the step function $h(t-x)$ evaluates to unity yielding the relation

$$v(t = x^+, x) = B_2(t = x^+, x). \tag{4.168}$$

The coupling coefficient can then be rewritten as [53], [55]

$$K(x) = 2\ v(x^+, x). \tag{4.169}$$

Equation (4.169) tell us that the coupling coefficient for any depth x along the NTL coupling region ($0 \leq x \leq L$) can be directly calculated from the the reflected transient waves $v(t, x)$ by considering the instant of time $t = x^+$ which is when the leading impulse $\delta(t-x)$ reaches and interacts with the medium at position x. Therefore, it is only when $t = x^+$ that the first scattering event occurs at depth x, thus, $v(x^+, x)$ corresponds to the value of the leading edge of the transient representing the leftward propagating waves as indicated in Figure 4.19. We may then conclude from the previous analysis and by simple inspection of Figure 4.19 that the coupling coefficient function $K(x)$ can be directly reconstructed by simply calculating the first value of the impulse response of the NTL for all depths x as we shall prove next.

We have seen in section 4.2 that due to physical constrains, NTL structures are classified as causal systems. As such, we can use some special properties of the unilateral Laplace transform on their analysis. Let us consider the initial value theorem for the unilateral Laplace transform [1]

$$x(0^+) = \lim_{s\to\infty} sX(s). \tag{4.170}$$

Considering the theorem in the Fourier transform domain and applying it to the leftward propagating waves transient yields

$$v(0^+, x) = \lim_{\omega\to\infty} j\omega a^-(\omega, x). \tag{4.171}$$

Using the time shifting property of the Fourier transform on the previous equation we can evaluate the leading edge of the transient corresponding to the leftward propagating waves $v(x^+, x)$ (see Figure 4.19) as

$$v(x^+, x) = \lim_{\omega\to\infty} j\omega a^-(\omega, x)e^{j\omega x} = \lim_{\omega\to\infty} j\omega \frac{a^-(\omega, x)}{e^{-j\omega x}}, \tag{4.172}$$

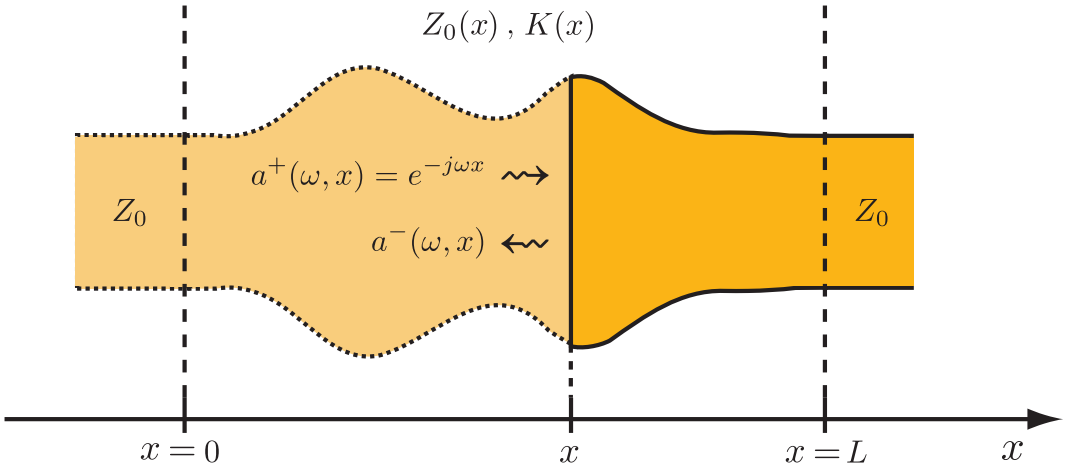

FIGURE 4.20: Evaluation of the coupling coefficient $K(x)$ at depth x as expressed by equations (4.172) and (4.173). The reflection coefficient at depth x is given by $R(\omega, x) = a^-(\omega, x)/a^+(\omega, x)$.

where we clearly identify that $\lim_{\omega\to\infty} a^+(\omega, x) = e^{-j\omega x}$ is the leading impulse of $u(t, x)$ (equation (4.165)) that probes the NTL structure at depth x, as it is illustrated in Figure 4.20. Therefore, by substituting equation (4.172) into equation (4.169) we have that the coupling coefficient function is now given by

$$K(x) = \lim_{\omega\to\infty} 2j\omega R(\omega, x), \tag{4.173}$$

where $R(\omega, x) = a^-(\omega, x)/a^+(\omega, x)$ is the partial reflection frequency response at some depth x along the length of the NTL. Please note that we define the term *partial reflection frequency response* as the reflection frequency response measured at some specified depth along the NTL [56], whereas the total reflection frequency response $R(\omega, 0) = R(\omega)$ is measured at the left end side of the NTL ($x = 0$).

Applying once again the initial value theorem to equation (4.173) we have that the coupling coefficient along the NLT is simply given by [53]

$$K(x) = 2r(0^+, x), \tag{4.174}$$

where $r(0^+, x)$ correspond to the first value i.e., the leading edge of the impulse response when evaluated at depth x. A further development by using the inverse Fourier transform definition given by equation (4.111) yields [55]

$$K(x) = \frac{1}{\pi}\int_{-\infty}^{+\infty} R(\omega, x)e^{j\omega 0^+}\, d\omega. \tag{4.175}$$

We must stress out that the evaluation of $K(x)$ at $t = 0^+$ as given by (4.175) is exact. It would be incorrect to evaluate $K(x)$ considering $t = 0$, therefore eliminating the exponential term in (4.175) as it is done in [56]. In [55] Skaar has addressed this issue and provided a solution for this as we shall see next.

It is of most importance to notice that due to causality the impulse response is discontinuous at $t = 0$, hence the evaluation of the inverse Fourier transform at $t = 0$ must be given by the average of the impulse response at $t = 0^-$ and $t = 0^+$, as pointed out by Skaar [55]. This is known as the *half-maximum convention*. Hence, considering the inverse Fourier transform given by (4.111) we have that the impulse response for $t = 0$ reduces to

$$r(0, x) = \frac{1}{2\pi} \int_{-\infty}^{+\infty} R(\omega, x) d\omega. \tag{4.176}$$

On the other hand, considering the half-maximum convention we obtain

$$r(0, x) = \frac{r(0^-, x) + r(0^+, x)}{2}, \tag{4.177}$$

where $r(0^-, x) = 0$ and $r(0^+, x)$ is the leading edge of the impulse response which is used to calculate $K(x)$. Therefore, substituting equation (4.177) into equation (4.176), and taking into consideration the relation (4.174) we obtain the correct expression for the coupling coefficient $K(x)$, yielding

$$K(x) = \frac{2}{\pi} \int_{-\infty}^{+\infty} R(\omega, x) d\omega. \tag{4.178}$$

Please keep in mind that equations (4.175) and (4.178) are equivalent. However equation (4.178) is in a more convenient format if we are to consider posterior numerical calculations.

Let us now take a closer look at equation (4.174). We now point out that the result expressed by equation (4.174) is not new to this thesis. In fact, from the coupled mode analysis of NTL structures in section 3.2, we saw that under the assumption of weak coupling operation, $K(x)$ is given by equation (3.82) as

$$\frac{1}{2} K\left(2x\right) \overset{\mathcal{F}}{\longleftrightarrow} S_{11}(\omega), \tag{4.179}$$

where $S_{11}(\omega)$ corresponds to reflection frequency response as seen from the left-hand side of the NTL device. Please note that equation (4.179) is the same as (3.82) except

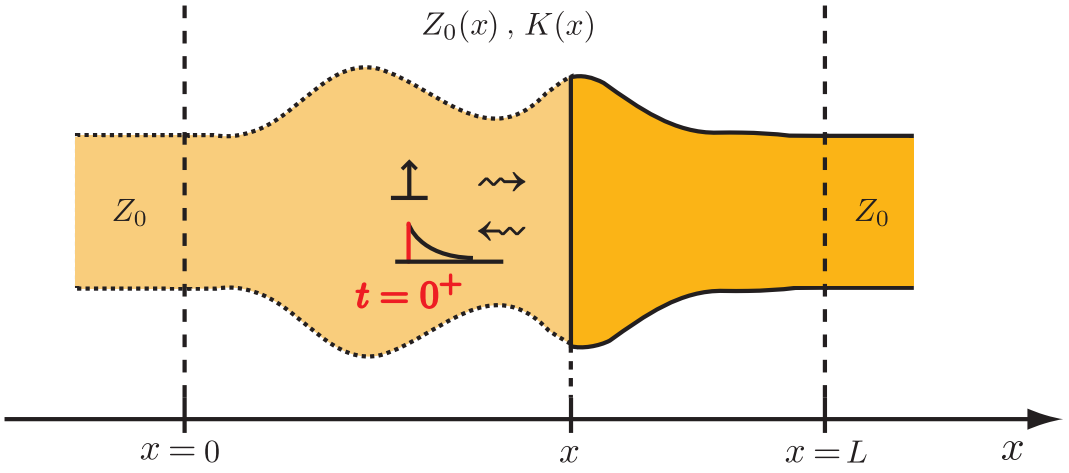

FIGURE 4.21: Evaluation of the coupling coefficient $K(x)$ at depth x as expressed by equations (4.174) and (4.181). The leading edge of the reflection impulse response at depth x is illustrated in red color.

we now assume an unitary propagation velocity, $v_p = c/\sqrt{\epsilon_r} = 1$. Rewriting (4.179) to consider the inverse Fourier transform we have that the coupling coefficient when considering weak coupling is given by

$$K(2x) = 2r(t), \tag{4.180}$$

where $r(t)$ is the NTL impulse response. The similarity between equations (4.180) and (4.174) is evident.

The weak coupling assumption states that the forward propagating wave $a^+(\omega, x)$ remains constant (unaltered) throughout its propagation along the NTL. This approximation is also known as the theory of small reflections [5]. Although it proves to be very useful on the understanding of some properties of NTL structures as it was discussed in section 3.2, the weak coupling method breaks down for the synthesis of high reflectivity NTL devices. However, if we consider the initial instant of time $t = 0^+$ when the NTL is probed from the left at $x = 0$ by a rightward propagating impulse, equation (4.180) becomes

$$K(0) = 2r(0^+). \tag{4.181}$$

In fact, equation (4.181) evaluates as the exact value of the coupling coefficient at $x = 0$, even in the case of strong coupling or high reflectivity NTL structures. This is because at $t = 0^+$ the probing impulse has not yet penetrated the NTL (where the weak coupling approximation is considered) but only interacted with the left boundary edge of the NTL. Comparing equations (4.181) and (4.174) we clearly see that these two equations

are very similar. The only difference being that equation (4.181) evaluates the coupling coefficient at $x = 0$ from the value of the leading edge of the complete NTL impulse response, whereas equation (4.174) evaluates the coupling coefficient at some depth x from the knowledge of the leading edge of the impulse response when evaluated at that same depth.

From what we have seen so far, we can conclude that the continuous layer-peeling method works by independently evaluating the coupling coefficient along the NTL structure at any depth x. This process is carried out by considering that a rightward propagating impulse probes the NTL at the depth x of interest. Then from the resulting reflection response the coupling coefficient $K(x)$ is calculated using equation (4.174). Also, we have shown that equation (4.174) agrees to a certain extent with the theory of small reflections (weak coupling).We know that when using the theory of small reflections the first value for the coupling coefficient $K(0)$ is always exact. Therefore the calculation of $K(x)$ through equation (4.174) can be understood as an discrete procedure, in which for every depth x of the NTL structure, the exact coupling coefficient value for that depth is obtained by using the theory of small reflections as expressed by equation (4.181), where $r(0^+)$ is the leading edge of the impulse reflection response evaluated at x. This is illustrated in Figure 4.21.

Until now, we have seen that an exact calculation of the coupling coefficient function $K(x)$ can be carried out by individually evaluating the local coupling coefficient at every depth x. Also we know that this individual evaluation can be performed either by using equations (4.174) or (4.178), which are equivalent for that matter. However, both these equations require the knowledge of the reflection response at the corresponding depth x. For that, we resort to the coupled mode equations

$$\frac{da^+(\omega,x)}{dx} = -j\omega\, a^+(\omega,x) - K(x)\, a^-(\omega,x), \tag{4.182}$$

$$\frac{da^-(\omega,x)}{dx} = j\omega\, a^-(\omega,x) - K(x)\, a^+(\omega,x). \tag{4.183}$$

Due to the discrete nature of the coupling coefficient evaluation process, we can not analytically calculate an expression for $K(x)$, therefore, the NTL structure must be divided into a stack of layers where the coupling coefficient is assumed to be constant.

From section 3.3.1, within the context of the analysis of NTL structures, we know that the amplitude of the fields along the NTL can be calculated by considering the division of the NTL into sufficient small sections of length Δl. In this way, each of

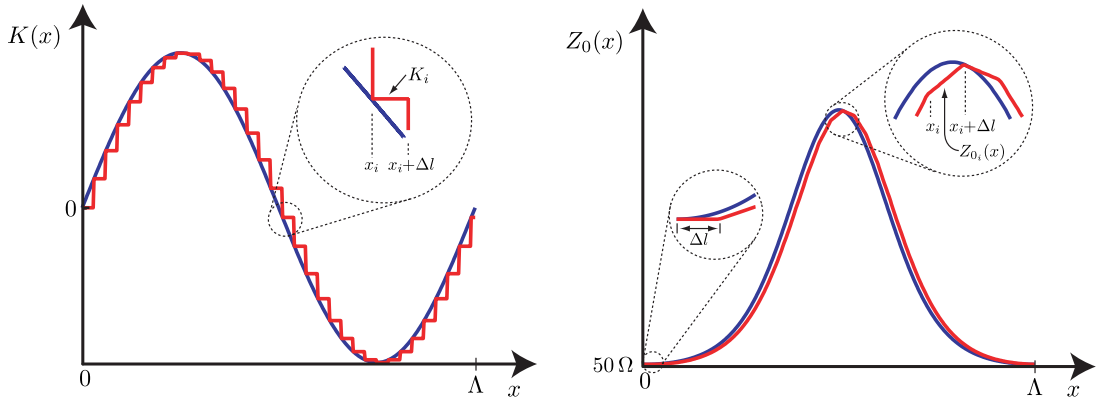

(a) Coupling coefficient.

(b) Impedance profile.

FIGURE 4.22: Coupling coefficient discretization and corresponding impedance profile over one period length Λ . The blue and red line represent the continuous and discrete cases, whereas K_i and $Z_{0_i}(x)$ are the coupling coefficient and corresponding impedance profile of section i respectively.

the sections can be considered to have a constant coupling. We call this the constant coupling discrete model. Therefore, the fields amplitudes at some depth x along the NTL can be calculated simply by multiplying the transmission matrices of each layer up to that depth. The transmission matrices for each layer are given by equation (3.192) as

$$\begin{bmatrix} a^+(\omega,x) \\ a^-(\omega,x) \end{bmatrix} = \begin{bmatrix} \cosh(\gamma\Delta l) + \frac{j\omega}{\gamma}\sinh(\gamma\Delta l) & \frac{K_i}{\gamma}\sinh(\gamma\Delta l) \\ \frac{K_i}{\gamma}\sinh(\gamma\Delta l) & \cosh(\gamma\Delta l) - \frac{j\omega}{\gamma}\sinh(\gamma\Delta l) \end{bmatrix} \begin{bmatrix} a^+(\omega,x+\Delta l) \\ a^-(\omega,x+\Delta l) \end{bmatrix}, \tag{4.184}$$

where $\gamma^2 = K_i^2 - \omega^2$.

The constant coupling discretization model is illustrated in Figure 4.22(a). A sinusoidal coupling coefficient is considered and the corresponding impedance profile in Figure 4.22(b) is obtained through

$$Z_0(x) = Z_0(0)\, e^{2\int_0^x K(u)du}, \tag{4.185}$$

where $Z_0(0) = 50\Omega$. Please note that in the discretized case (red line) the impedance profile can also be calculated independently for each section. In this case the impedance profile for each section along its length Δl is given by

$$Z_{0_i}(x) = Z_{0_{i-1}}(\Delta l)\; e^{2K_i x}. \tag{4.186}$$

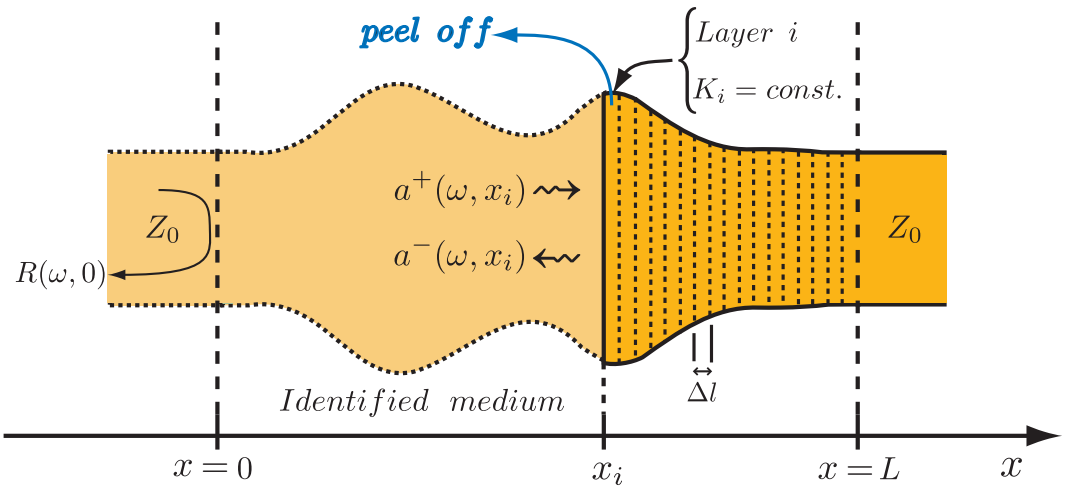

FIGURE 4.23: Continuous layer-peeling algorithm. The medium is approximated as a stack of layers of length Δl with constant coupling coefficient. The amplitude of the forward- and backward-propagating waves at the beginning of layer i are given by $a^+(\omega, x_i)$ and $a^-(\omega, x_i)$ respectively.

where K_i is the coupling of section i. From Figure 4.22(b) we see that the reconstructed impedance profile for the discretized case is slightly shifted to the right when compared to the exact case (blue line). This has directly to do with the length of the sections Δl. In the case illustrated in Figure 4.22 we have considered a large value of Δl for a demonstration purpose.

Figure 4.23 illustrates the continuous layer peeling algorithm. The procedure consists on identifying the medium layer-by-layer from left to right. Each layer is considered to have a constant coupling coefficient K_i. As an example, let us consider the identification process for layer i which is located at depth x_i as illustrated by Figure 4.23. The identification of layer i consists on the determination of its coupling coefficient K_i through equation (4.178) where $R(\omega, x_i) = a^-(\omega, x_i)/a^+(\omega, x_i)$. The impedance profile for the layer is calculated using (4.186). Upon identification, layer i is peeled off and the fields amplitudes at the beginning of the next layer ($a^-(\omega, x_{i+1})$, $a^+(\omega, x_{i+1})$) are calculated using the relation (4.184).

In the more general case, the continuous layer peeling algorithm is performed by taking the following steps:

1. Specify the desired reflection response $R(\omega, 0)$ for the NTL as indicated in Figure 4.23. However, $R(\omega, 0)$ must be physically realizable, thus, it must verify the realizability conditions previously discussed in section 4.2.1.1. Please note that at

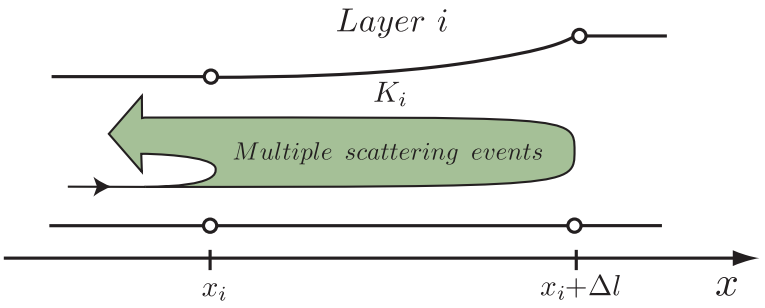

FIGURE 4.24: Constant coupling layer. The coupling of energy between the forward- and backward-propagating modes takes place continuously along the length of the layer.

$x = 0$ the fields amplitudes are given by

$$a^+(\omega, 0) = 1, \tag{4.187}$$

$$a^-(\omega, 0) = R(\omega, 0). \tag{4.188}$$

2. Calculate the coupling coefficient $K(x_i)$ at the current position x_i from equation (4.178). However, the medium is approximated by a stack layers with length Δl and constant coupling coefficient K_i, hence

$$K_i = \frac{2}{\pi} \int_{-\infty}^{+\infty} R_i(\omega) d\omega, \tag{4.189}$$

where $R_i(\omega) = R(\omega, x_i)$ is the frequency reflection response at the beginning of layer i.

3. Compute the amplitude of the fields at the beginning of the next layer (layer $i+1$) using the inverse of the transfer matrix relation (4.184), i.e.

$$\begin{bmatrix} a^+(\omega, x_{i+1}) \\ a^-(\omega, x_{i+1}) \end{bmatrix} = \begin{bmatrix} \cosh(\gamma\Delta l) - \frac{j\omega}{\gamma}\sinh(\gamma\Delta l) & -\frac{K_i}{\gamma}\sinh(\gamma\Delta l) \\ -\frac{K_i}{\gamma}\sinh(\gamma\Delta l) & \cosh(\gamma\Delta l) + \frac{j\omega}{\gamma}\sinh(\gamma\Delta l) \end{bmatrix} \begin{bmatrix} a^+(\omega, x_i) \\ a^-(\omega, x_i) \end{bmatrix}, \tag{4.190}$$

where $x_{i+1} = x_i + \Delta l$. Peel off layer i.

4. Repeat step 2. and 3. until the the entire NTL structure is identified. As we will show later, a stopping condition must be devised as the impulse response of any NTL is infinite in nature.

The principle behind the continuous layer peeling algorithm is based on the discretization of the coupling coefficient and the correspondent propagation of the fields

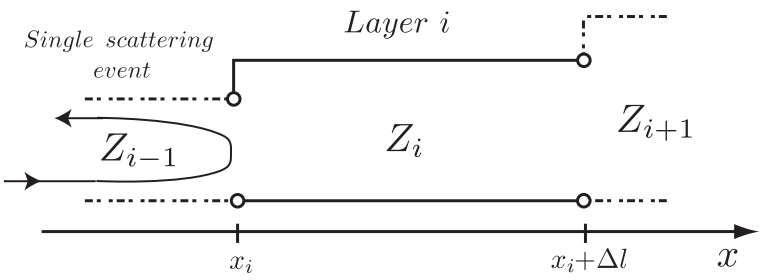

FIGURE 4.25: Constant impedance layer. The coupling of energy between the forward- and backward-propagating modes is an instantaneous and localized event that takes place at depth x_i. Z_i is the impedance of layer i and is a constant value along that layer.

amplitudes from one layer to the next. However, the actual coupling process is continuous as all the layers have some constant coupling coefficient along their length as it is illustrated in Figure 4.24. Hence the name *continuous layer peeling*. On the other hand, instead of making this piecewise uniform approximation of the coupling coefficient we can discretize the NTL structure as a series of discrete reflectors, *i.e.*, a layered medium approximation. We call this, the constant impedance discrete model (see section 3.3.2). In this model each layer is characterized by a constant impedance as illustrated in Figure 4.25. Furthermore and considering the constant impedance discrete model in conjunction with the inverse scattering process described above, we have yet another differential inverse scattering procedure known as the *discrete layer peeling* algorithm.

4.3.2 Discrete layer-peeling

Let us consider the NTL infinitesimal layer of constant coupling depicted in Figure 4.24. If we account for the total coupling occurring along that layer we have that

$$K_{tot_i} = \int_{x_i}^{x_i+\Delta l} K_i(x)\, dx = K_i\, \Delta l, \tag{4.191}$$

where $K_i(x) = K_i = C^{te}$ is the coupling function.

Now, let us consider that the total coupling K_{tot_i} occurring along such a layer of constant coupling is concentrated in a single location and that no coupling phenomena takes place at any other location along that same layer. Hence, if we assume that the coupling occurs at the beginning of the layer, we can approximate each layer as a constant impedance TL of length Δl preceded by a reflector, as it is illustrated in Figure 4.25. Thereafter, considering the layer model depicted in Figure 4.25, the continuous

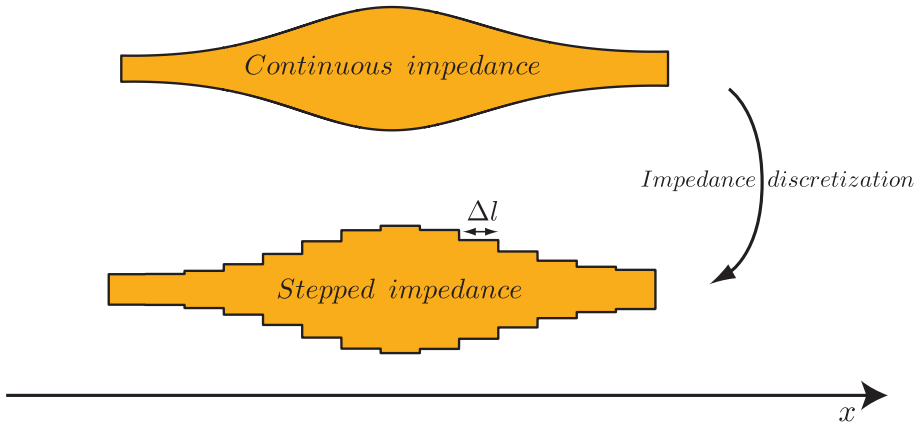

FIGURE 4.26: Constant impedance discrete model conversion.

NTL structure is discretized as a series of discrete reflectors separated by sections of constant impedance TL with length Δl. This is illustrated in Figure 4.26.

Assuming that the total coupling occurring along a layer of constant coupling now takes place for instance at $x = 0$ we have that the new coupling coefficient function now takes the form

$$K_d(x) = K_{tot}\,\delta(x), \tag{4.192}$$

where K_{tot} is the total coupling as calculated in (4.191). However, by considering that the coupling occurs at the beginning of the layer as illustrated in Figure 4.25 the coupling coefficient function at some layer i is in fact given by

$$K_{d_i}(x) = K_{tot_i}\delta(x - x_i). \tag{4.193}$$

Taking a closer look at equation (4.193) we see that the evaluation of the coupling function at $x = x_i$ translates in an infinite value $|K_{d_i}| = \infty$ due to the Dirac function, however as we saw before the actual overall coupling taking place at layer i is actually evaluated as

$$K_{tot_i} = \int_{x_i}^{x_i+\Delta l} K_{d_i}\,dx = \int_{x_i}^{x_i+\Delta l} K_{tot_i}\delta(x - x_i)\,dx = K_i\,\Delta l, \tag{4.194}$$

which is a finite value.

Let us now reconsider the transmission matrix given by equation (4.184) for a single layer which stands as the base for the CLP inverse scattering method and that as discussed in the previous section describes the propagation of the fields within layers of

constant coupling coefficient as the one illustrated by Figure 4.24:

$$\begin{bmatrix} a^+(\omega,x) \\ a^-(\omega,x) \end{bmatrix} = \begin{bmatrix} \cosh(\gamma\Delta l) + \frac{j\omega}{\gamma}\sinh(\gamma\Delta l) & \frac{K_i}{\gamma}\sinh(\gamma\Delta l) \\ \frac{K_i}{\gamma}\sinh(\gamma\Delta l) & \cosh(\gamma\Delta l) - \frac{j\omega}{\gamma}\sinh(\gamma\Delta l) \end{bmatrix} \begin{bmatrix} a^+(\omega,x+\Delta l) \\ a^-(\omega,x+\Delta l) \end{bmatrix}. \tag{4.195}$$

Please remember that $\gamma^2 = K_i^2 - \omega^2$ and K_i is the constant coupling along the layer.

Following the same approach as in [55], we now derive the equivalent transmission matrix for the DLP case by starting from 4.195. As we have demonstrated, the transmission matrix in (4.195) was obtained in section 3.3 under the assumption of a constant coupling constrain. However on the present case, for the DLP inverse scattering method, the coupling coefficient function is no longer a constant function. Instead, the coupling is now the one given by equation (4.193) which evaluates as $|K_{d_i}| = 0$ for the entire length of layer i except for the beginning of the layer where $|K_{d_i}| = \infty$. Therefore we now consider two different cases: one for $|K_{d_i}| = 0$ and another for $|K_{d_i}| = \infty$. So, considering the simpler situation where there is no coupling.*i.e.*, $|K_{d_i}| = 0$, we have that $\gamma = j\,\omega$ and the transmission matrix in equation (4.195) simplifies into

$$\begin{bmatrix} a^+(\omega,x) \\ a^-(\omega,x) \end{bmatrix} = \begin{bmatrix} \cosh(j\,\omega\Delta l) + \sinh(j\,\omega\Delta l) & 0 \\ 0 & \cosh(j\,\omega\Delta l) - \sinh(j\,\omega\Delta l) \end{bmatrix} \begin{bmatrix} a^+(\omega,x+\Delta l) \\ a^-(\omega,x+\Delta l) \end{bmatrix}. \tag{4.196}$$

The final form of the transmission matrix for when $|K_{d_i}| = 0$ is obtained by realizing that

$$\cosh(j\,\omega\Delta l) = \cos(\omega\Delta l), \tag{4.197}$$

$$\sinh(j\,\omega\Delta l) = j\,\sin(\omega\Delta l), \tag{4.198}$$

yielding

$$\begin{bmatrix} a^+(\omega,x) \\ a^-(\omega,x) \end{bmatrix} = \begin{bmatrix} e^{j\,\omega\Delta l} & 0 \\ 0 & e^{-j\,\omega\Delta l} \end{bmatrix} \begin{bmatrix} a^+(\omega,x+\Delta l) \\ a^-(\omega,x+\Delta l) \end{bmatrix}. \tag{4.199}$$

In the case concerning the first single point on layer i where all the coupling occurs we have that $|K_{d_i}| \to \infty$. In this case the substitution in (4.195) is not direct as in the previous case. We now have that

$$\gamma\big|_{K_{d_i}\to\infty} = \quad K_{d_i}, \tag{4.200}$$

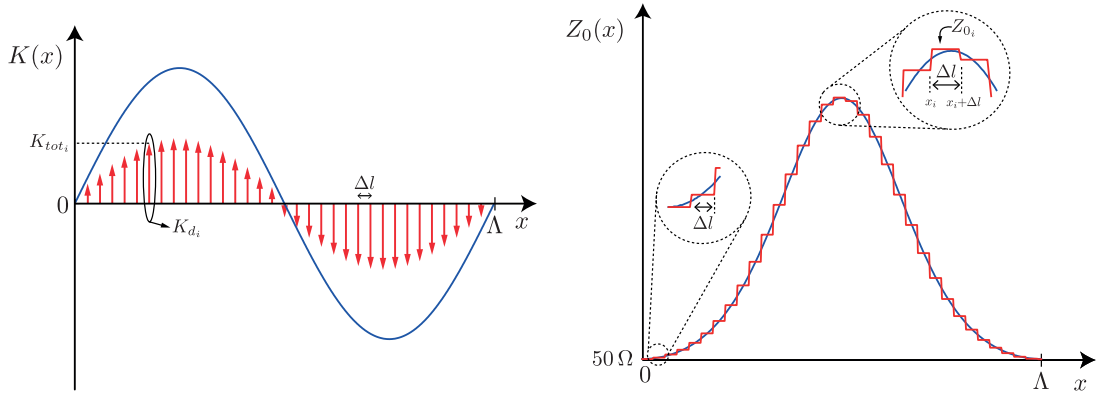

(a) Coupling coefficient.

(b) Impedance profile.

FIGURE 4.27: Sinusoidal coupling coefficient and corresponding impedance profile over one period length Λ. The blue and red lines represent the continuous (analytical) and discrete cases (DLP method) respectively.

however, and accordingly to [55] the product

$$\gamma\,\Delta l = K_{tot_i} \tag{4.201}$$

has a finite value as it corresponds to the total amount of coupling occurring on layer i. Substituting equations (4.200) and (4.201) into the transmission matrix (4.195) we now have that

$$\begin{bmatrix} a^+(\omega,x) \\ a^-(\omega,x) \end{bmatrix} = \cosh(K_{tot_i}) \begin{bmatrix} 1 & \tanh(K_{tot_i}) \\ \tanh(K_{tot_i}) & 1 \end{bmatrix} \begin{bmatrix} a^+(\omega,x+\Delta l) \\ a^-(\omega,x+\Delta l) \end{bmatrix}. \tag{4.202}$$

The final form of the transmission matrix for when $|K_{d_i}| = \infty$ is obtained by performing the variable change

$$\Gamma_i = \tanh(K_{tot_i}) \tag{4.203}$$

and realizing that

$$\cosh(K_{tot_i}) = \frac{1}{\sqrt{1-\tanh^2(K_{tot_i})}}, \tag{4.204}$$

which yields

$$\begin{bmatrix} a^+(\omega,x) \\ a^-(\omega,x) \end{bmatrix} = \frac{1}{\sqrt{1-\Gamma_i^2}} \begin{bmatrix} 1 & \Gamma_i \\ \Gamma_i & 1 \end{bmatrix} \begin{bmatrix} a^+(\omega,x+\Delta l) \\ a^-(\omega,x+\Delta l) \end{bmatrix}. \tag{4.205}$$

The complete transmission matrix that stands as the basis for the DLP inverse scattering

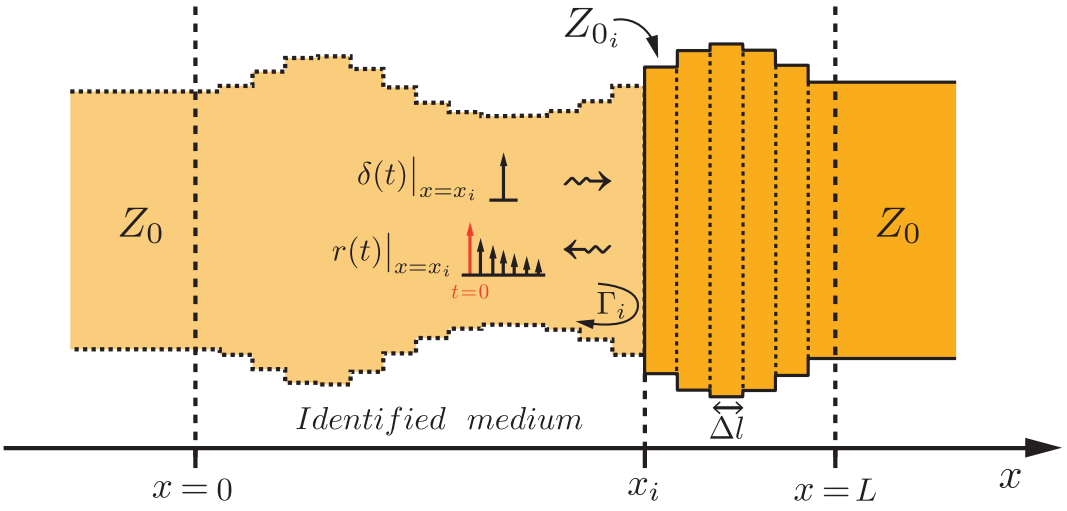

FIGURE 4.28: Evaluation of the local reflection coefficient Γ_i at depth x_i. The first impulse of the reflection impulse response is illustrated in red color

method is obtained from the product of the matrices in (4.205) and (4.199), yielding

$$\begin{bmatrix} a^+(\omega,x) \\ a^-(\omega,x) \end{bmatrix} = \frac{1}{\sqrt{1-\Gamma_i^2}} \begin{bmatrix} e^{j\,\omega\Delta l} & \Gamma_i\, e^{-j\,\omega\Delta l} \\ \Gamma_i\, e^{j\,\omega\Delta l} & e^{-j\,\omega\Delta l} \end{bmatrix} \begin{bmatrix} a^+(\omega,x+\Delta l) \\ a^-(\omega,x+\Delta l) \end{bmatrix}. \tag{4.206}$$

With no surprise we easily verify that the transmission matrix (4.206) is the same as the transmission matrix (3.204) that was obtained in section 3.3 in the context of the analysis of NTL structures with constant impedance discretization. The only difference being that in this section our spatial variable is the travel time whereas in section 3.3 we consider the actual physical length. Please note that by considering the space variable to be the travel time, we have that the propagation constant β in equation (3.204) simplifies to the angular frequency ω in equation (4.206) and also that the sections length dl in (3.204) are measured in meters while Δl in (4.206) comes in seconds.

Figure 4.27 compares the coupling coefficient and corresponding impedance profiles between the analytical (exact solution) case and the constant impedance discretization model for the case of a sinusoidal coupling coefficient. From figure we see that the coupling function for the constant impedance discrete model (in which the DLP method is based) is composed by a series of Dirac deltas K_{d_i} each representing the coupling K_{tot_i} occurring at the interface between layer $i-1$ and i. Please note that the the coupling function for the discrete model consider in this section $K_{d_i}(x)$ is simply a sampled version of the analytical coupling function $K(x)$ with sampling period Δl.

Figure 4.27(b) depicts the impedance profiles where Z_{0_i} is the impedance of section

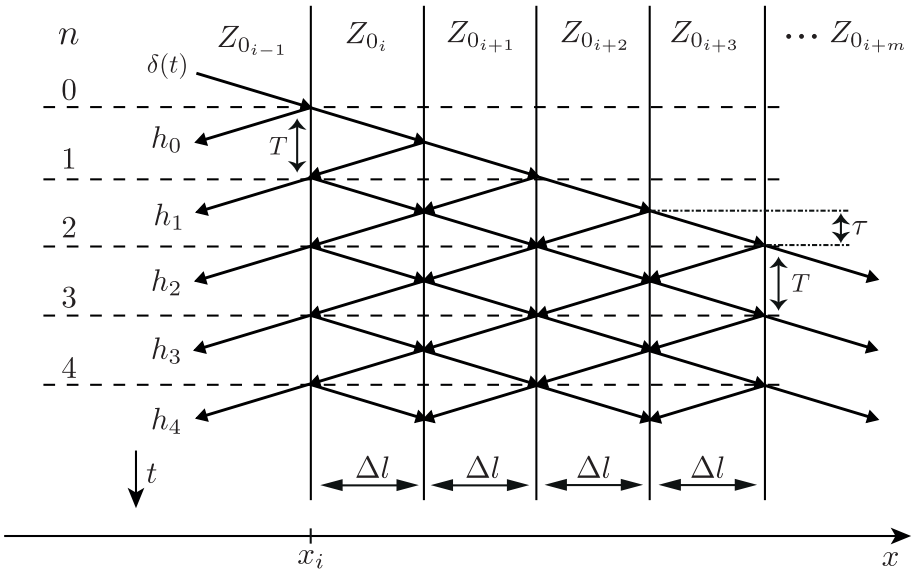

FIGURE 4.29: Space-time diagram of incident and reflected pulses. Where T is the time spacing between reflected or transmitted pulses and τ is the propagation time corresponding to one section. Please note that the space variable x is actually the travel time as defined in section 4.2.1.

i that is constant. Please note that through equation (4.203) the impedance profile is easily obtained from the coupling coefficient by realizing that

$$Z_{0_i} = \frac{1 + \tanh(K_{tot_i})}{1 - \tanh(K_{tot_i})} Z_{0_{i-1}}, \tag{4.207}$$

where the initial condition is defined as $Z_{0_i} = 50\Omega$ for $i = 0$.

So far we have seen that both the CLP and DLP methods are formulated under the consideration of some sort of discretization or division of the NTL structure into a stack of sections or layers. We have shown that at a structural level the modifications required to obtain the NTL model for the DLP method from the CLP model consists in assuming that the coupling of the forward and backward propagating waves occurs only at a single location in each layer, whereas the NTL model considered for the CLP method presumes a continuous and constant coupling throughout each section. In terms of the inverse scattering procedure itself, we shall now see that the DLP inverse scattering method is very similar to the one used with CLP except for some small differences that arise from the different model considered for the approximation to the NTL. Essentially, these differences lay with the procedure used in the calculation of the coupling coefficients and also in the propagation of the fields between layers.

Let us now consider an n-section cascade connection of transmission line junctions as the one illustrated in Figure 4.28, where each junction is separated by a transmission

line of infinitesimal length Δl. Furthermore, let us assume that the first $(i-1)th$ layers (up to depth x_i) are already identified and thus can be removed leaving a structure composed by the layers yet to be identified as illustrated by Figure 4.28. Assuming that the remaining unidentified structure is probed from the left by a rightward propagating impulse $\delta(t)$ at $t = 0$, then, the scattering events triggered by $\delta(t)$ along the first four sections of the structure can be visualized in the space-time diagram depicted in Figure 4.29. Due to causality and assuming the subsisting unidentified structure to be at a quiescent state for $t < 0$, we clearly see by analyzing Figure 4.29 that the impulse reflection response for $t = 0$ is constituted by a single reflected pulse *i.e.*, $r(0) = h_0$. This is the case, because not enough time has passed so that the incident impulse could propagate its effect to the adjacent layers. In other words, the impulse response of the remaining unidentified structure for $t = 0$ is the same response as if only the first reflector were present. From this analysis, it becomes evident that the reflection coefficient Γ_i at the first junction (depth x_i) can be directly computed as the first value of the reflection impulse response $r(t)$ as evaluated at depth x_i, thus

$$\Gamma_i = r_i(0) = h_0. \tag{4.208}$$

So far, we have seen that the analysis of the space-time diagram proves to be very important in the sense that is provides a clear picture regarding the scattering events within the structure and clearly proves that due to the discrete nature of the impedance profile of the considered model we can always calculate the reflection coefficient at the first impedance interface for some depth x_i provided that the reflection coefficient at that depth is previously known. Once the reflection coefficient Γ_i is obtained, the characteristic impedance of layer i can be computed from equation (4.207). Please note that at this point all the previous layers are already identified. Hereupon, we are left with the problem of obtaining the reflection response $r(t)$ at depth x_i. However, this problem can be easily overcome by realizing that the reflection frequency response at the beginning of any layer is related by means of the transmission matrix (4.206) to the reflection frequency response of the adjacent layer to the right. Thus in order to compute the frequency reflection response at the beginning of layer i using the frequency data at the

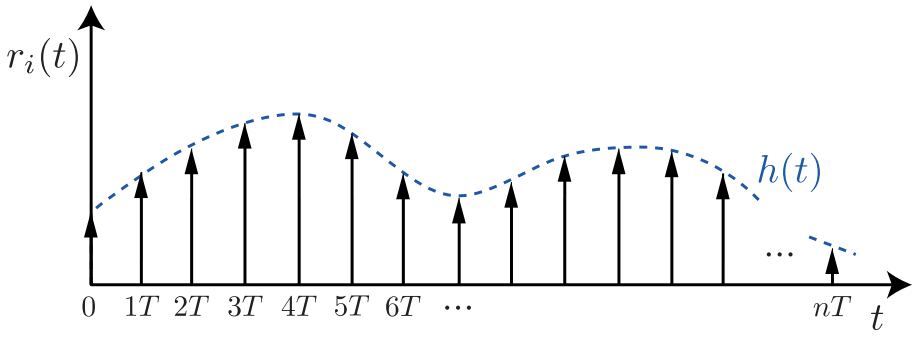

FIGURE 4.30: Impulse reflection response evaluated at depth x_i as it is illustrated in Figure 4.28. The envelope function is given by $h(t)$.

beginning of layer $i-1$ we consider the inverse of (4.206) yielding

$$\begin{bmatrix} a^+(\omega, x_i) \\ a^-(\omega, x_i) \end{bmatrix} = \frac{1}{\sqrt{1-\Gamma_i^2}} \begin{bmatrix} e^{-j\,\omega\Delta l} & -\Gamma_i\, e^{-j\,\omega\Delta l} \\ -\Gamma_i\, e^{j\,\omega\Delta l} & e^{j\,\omega\Delta l} \end{bmatrix} \begin{bmatrix} a^+(\omega, x_{i-1}) \\ a^-(\omega, x_{i-1}) \end{bmatrix}. \tag{4.209}$$

Assuming that the reflection frequency response at x_{i-1} is known, the corresponding fields amplitudes can be given by

$$\begin{bmatrix} a^+(\omega, x_{i-1}) \\ a^-(\omega, x_{i-1}) \end{bmatrix} = \begin{bmatrix} 1 \\ R_{i-1}(\omega) \end{bmatrix}, \tag{4.210}$$

which corresponds to the Fourier transform of the incident impulse and the reflection transient as illustrated in Figure 4.28. Substituting (4.210) into (4.209) enables us to calculate the fields at x_i and the corresponding reflection response as

$$R_i(\omega) = \frac{a^-(\omega, x_i)}{a^+(\omega, x_i)} = \frac{R_{i-1}(\omega) - \Gamma_{i-1}}{1 - \Gamma_{i-1}\, R_{i-1}(\omega)}\, e^{j2\omega\Delta l}. \tag{4.211}$$

From the scattering diagram in Figure 4.29 we can easily see that the reflection impulse response at depth x_i is given by the sum of the reflected pulses yielding

$$r_i(t) = \sum_{n=0}^{\infty} h_n\, \delta(t - nT), \tag{4.212}$$

where T is the time spacing between reflected pulses, and h_n is the respective area value. Taking a closer look to the space-time diagram we see that $T = 2\tau$, where τ is

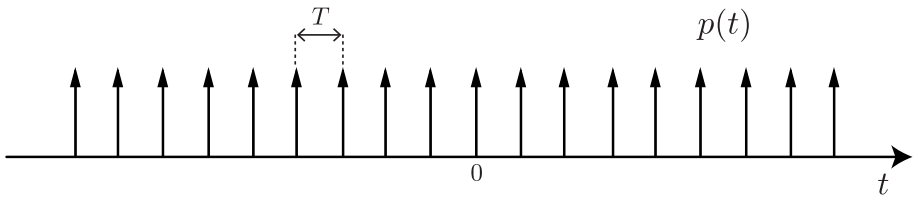

FIGURE 4.31: Sampling function $p(t)$.

the propagation time per layer which is given by

$$\tau = \frac{\Delta l}{v_p}. \tag{4.213}$$

Please note that v_p is the propagation velocity along the transmission line medium. However, and because we consider the spatial variable to be x, the traveling time, we assume that $v_p = 1\text{m/s}$ and thus

$$\Delta l = \tau. \tag{4.214}$$

In order to gain a better understanding on the operation of these structures, we now re-illustrate the impulse response $r_i(t)$ in Figure 4.30. From the illustration we conclude that the reflection response $r_i(t)$ can be interpreted as being the sampled version of some continuous envelope function $h(t)$. Thus, we can now rewrite equation (4.212) as

$$r_i(t) = \sum_{n=0}^{\infty} h(nT)\,\delta(t - nT), \tag{4.215}$$

where $T = 2\,\tau$ is in fact the sampling period and τ is the propagation time corresponding to a single layer (see Figure (4.29)). On the other hand, and considering sampling theory, we can rewrite equation (4.215) as the product of two functions. The continuous envelope function $h(t)$ and a sampling function which in this case is an infinite impulse train $p(t)$ yielding

$$r_i(t) = h(t)\,p(t), \tag{4.216}$$

where $p(t) = \sum_{n=-\infty}^{\infty} \delta(t - nT)$ is depicted in Figure 4.31. Please note that causality constrains imply that $h(t) = 0$ for $t < 0$.

From the modulation property of the Fourier transform [1], we can compute the Fourier transform of (4.216) as

$$R_i(\omega) = \frac{1}{2\pi}\,\left[H(\omega) * P(\omega)\right]. \tag{4.217}$$

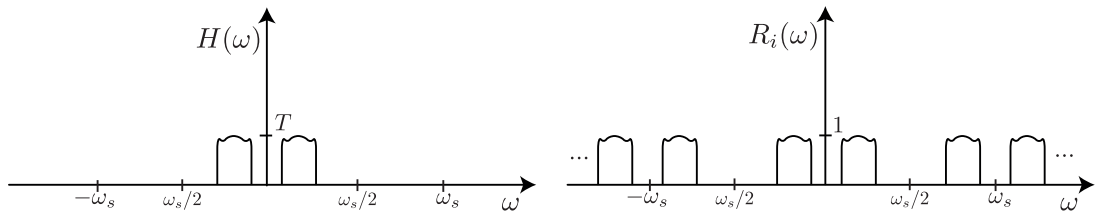

(a) Continuous envelope frequency response..

(b) Discrete NTL structure frequency response.

FIGURE 4.32: Fourier transform for both the continuous envelope function $h(t)$ and the actual frequency response of the discrete NTL structure.

Furthermore, we see from Figure 4.31 that $p(t)$ is a periodic function with period (the sampling period) T. From the Fourier transform of periodic signals theory [1] we have that

$$P(\omega) = \sum_{k=-\infty}^{\infty} 2\pi\, a_k\, \delta(\omega - k\omega_s), \tag{4.218}$$

where a_k represent the Fourier series coefficients which for $p(t)$ are given by

$$a_k = \frac{1}{T}\int_{-T/2}^{T/2} \delta(t)\, e^{-jk\omega_s t}\, dt = \frac{1}{T}. \tag{4.219}$$

Substituting equation (4.219) into (4.218) we have that

$$P(\omega) = \frac{2\pi}{T} \sum_{k=-\infty}^{\infty} \delta(\omega - k\omega_s) \tag{4.220}$$

where

$$\omega_s = \frac{2\pi}{T} \tag{4.221}$$

is the angular sampling frequency.

The Fourier transform of $r_i(t)$ and thus, the reflective frequency response of the discrete NTL structure at depth x_i can be obtained by substituting equation (4.220) into (4.217) yielding

$$R_i(\omega) = \frac{1}{T} \sum_{k=-\infty}^{\infty} H(\omega - k\omega_s). \tag{4.222}$$

From equation (4.222) and from the corresponding illustration in Figure 4.32 we see that the frequency response of a constant impedance discrete NTL structure is a frequency-scaled repetition of the Fourier transform of the envelope function $H(\omega)$. Please note that the repetition is periodic with period ω_s.

Taking a closer look at Figure 4.30 we easily see that the impulse response for a

discrete NTL structure resembles that of an discrete-time system. That is, the reflected signal only takes values different from zero for when $t = T$ and any of the integer multiples of T. Therefore and without loss of generality, we can represent the impulse response of discrete NTL structures as discrete-time signals. Thus, the reflection impulse response in equation (4.215) can be written as [1]

$$R_i(\omega) = \sum_{n=0}^{\infty} h(nT)\, e^{-j\omega nT}, \tag{4.223}$$

which is in fact the definition of discrete Fourier transform and where $h(nT) = h_n$. Please note that the spectrum periodicity stated by equation (4.222) is also a characteristic of any discrete-time system [1]. Further on this thesis, we shall explore in more detail the relation between discrete NTL structures and discrete-time systems.

So far we have been identifying the main properties of the constant impedance discretization model for NTL structures. We saw that the coupling phenomena is not continuous but rather a discrete and localized process. Also we saw that the reflection impulse response for these structures is discrete and given by the sum of a train of pulses spaced in time by T. As a consequence, the frequency response (both reflection and transmission) is periodic with period $\omega_s = 2\pi/T$. From this, we have realized the frequency response at any depth along the structures can be written as a discrete-time Fourier transform (see equation (4.223)). However, one of the most useful characteristics of this model is the ability to identify the characteristic impedance of the individual layers from the reflection frequency response at the beginning of the layers. Furthermore, we have from equation (4.208) that only the first reflection pulse from $R_i(t)$ is necessary to identify layer i. So, if we consider the reflection frequency response to be written in the form of equation (4.223) we can compute the first pulse of the reflection impulse response as

$$\Gamma_i = r_i(0) = h_0 = \frac{1}{\omega_s} \int_{-\omega_s/2}^{\omega_s/2} R_i(\omega)\, d\omega. \tag{4.224}$$

Thus far, all the mathematical development has been made based on the constant impedance discrete NTL model, therefore based on inherently discrete functions, except in the frequency domain where we have a continuous spectral dependence. However, for numerical implementation as a computer routine, the spectral dependence must also be discrete. This way, the calculation of the local reflection coefficient between adjacent

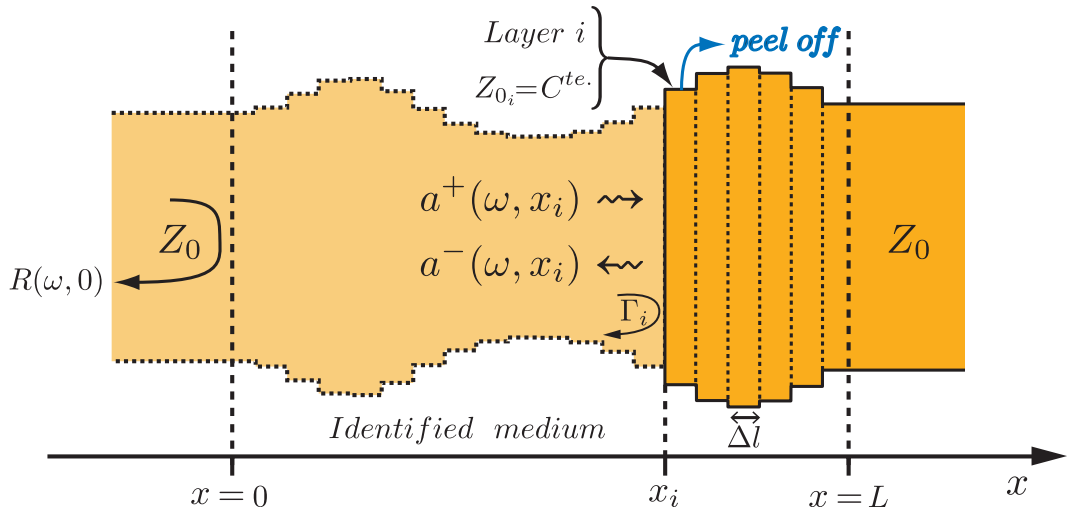

FIGURE 4.33: Discrete layer-peeling algorithm. The medium is approximated as a stack of layers of length Δl with constant characteristic impedance The amplitude of the forward- and backward-propagating waves at the beginning of layer i are given by $a^+(\omega, x_i)$ and $a^-(\omega, x_i)$ respectively.

layers reduces to (discrete-time Fourier series)

$$\Gamma_i = \frac{1}{M} \sum_{m=1}^{M} R_i[m], \tag{4.225}$$

where M is the number of points considered within a spectral period, that is, in the range $-\omega_s/2 \leq \omega \leq \omega_s/2$. As we shall see in the next section, the number of points M should be as high as possible in order to approximate the ideal case (continuous spectral dependence) and should always be greater than or equal to the number of layers considered for the structure.

Figure 4.33 illustrates the discrete layer peeling algorithm. The procedure consists on identifying the medium layer-by-layer from left to right. Each layer is considered to have a constant characteristic impedance Z_{0_i}. As an example, let us consider the identification process for layer i which is located at depth x_i as illustrated by Figure 4.33. The identification of layer i consists on the determination of the reflection coefficient Γ_i at x_i, the interface between layers $i-1$ and i respectively through equation (4.224) where $R_i(\omega) = a^-(\omega, x_i)/a^+(\omega, x_i)$. However, when considering a numerical implementation, equation (4.225) should be used instead. From the computed value of Γ_i the characteristic impedance Z_{0_i} is then obtained using equations (4.203) and (4.207). Upon identification, layer i is peeled off and the reflection frequency response at the beginning of the next layer ($R_{i+1}(\omega)$) is calculated using the relation (4.211).

In the more general case, the discrete layer-peeling algorithm is performed by taking the following steps:

1. Specify the desired reflection response $R_0(\omega) = R(\omega, 0)$ for the NTL as illustrated in Figure 4.33.The desired frequency response R_0 must be physically realizable, thus, it must verify the realizability conditions previously discussed in section 4.2.1.1. The R_0 specification comes in the range $-\omega_s/2 \leq \omega \leq \omega_s/2$.

2. Considering a numerical implementation, calculate the local reflection coefficient Γ_0 at the current position x_0 from equation (4.225)

$$\Gamma_0 = \frac{1}{M} \sum_{m=1}^{M} R_0[m]. \tag{4.226}$$

3. Compute the reflection coefficient $R_1(\omega)$ at the beginning of the next layer using the transmission matrix (4.209) or directly through equation (4.211)

$$R_1(\omega) = \frac{R_0(\omega) - \Gamma_0}{1 - \Gamma_0 R_0(\omega)} e^{j2\omega\Delta l}. \tag{4.227}$$

4. Peel off layer i.

5. Repeat steps 2. to 3. until the entire structure is identified. As we will show in the next chapter, a stopping condition must be devised as the impulse response of any NTL structure is infinite in nature.

The length of each layer is given by equation (4.214), which when combined with (4.221) yields

$$\Delta l = \frac{\pi}{\omega_s}. \tag{4.228}$$

The DLP algorithm result, comes as a reconstructed discrete impedance NTL structure with a given length given in seconds (travel time). In order to obtain the length dimensions in terms of the space variable (meters) we use the same procedure as in section 4.2 through equation (4.86).

As a last note regarding the discussion of the DLP algorithm, we call attention upon the task described in step 1 of the DLP procedure in respect of the target spectrum $R_0(\omega)$. Most of the times the target spectrum $R_0(\omega)$ used as the starting data for the DLP procedure is obtained from an analog prototype. A simple example of this fact is the synthesis of classical filters such as Butterworth or Tchebishev filters. As we

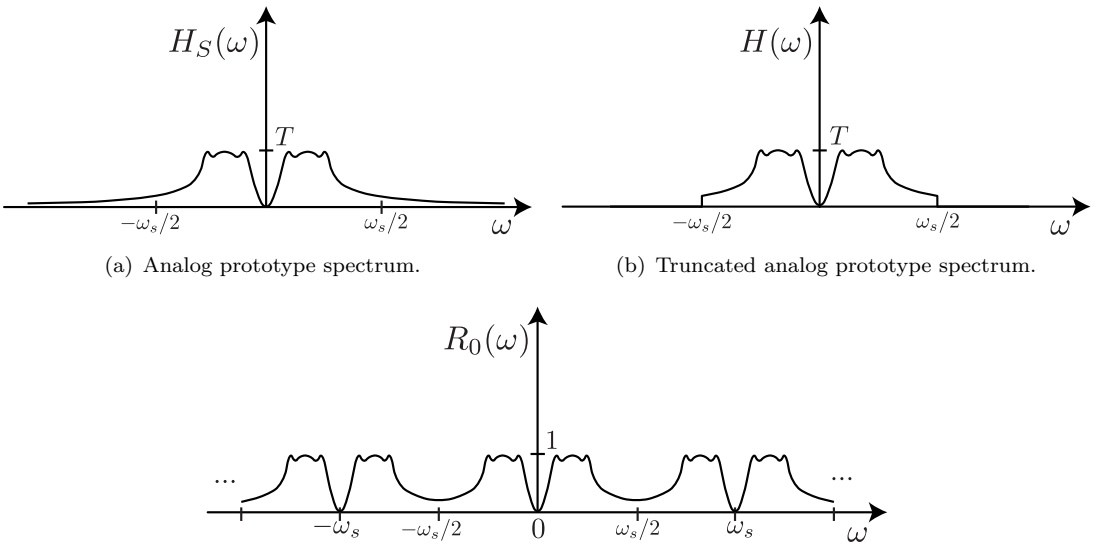

(a) Analog prototype spectrum.

(b) Truncated analog prototype spectrum.

(c) Target frequency response.

FIGURE 4.34: Target spectrum $R_0(\omega)$ as obtained from an analog prototype. Given by (a) we have the analog prototype frequency response, which when forced to zero outside the interval $-\omega_s/2 \leq \omega \leq \omega_s/2$ yields $H(\omega)$ in (b). Please note that the time-domain counterpart of $H(\omega)$ is $h(t)$, as illustrated in Figure 4.30. The sampling of $h(t)$ with sampling period T results in the target response in (c).

can see from Figure 4.34(a), the frequency response for these type of prototype filers extends (takes values different from zero) to the whole frequency spectrum. In order to perform inverse scattering using the DLP method, the analog prototype response must be truncated do the frequency region of interest $-\omega_s/2 \leq \omega \leq \omega_s/2$ as illustrated by Figure 4.34(b). This in turn, sets the sampling frequency ω_s and the corresponding sampling period T. Furthermore, by establishing the frequency region of interest and accordingly to equation (4.228) the length of each section for the resulting DNTL structure is also defined.

Please note that, as we have previously discussed, the larger the interval $-\omega_s/2 \leq \omega \leq \omega_s/2$, the larger the sampling frequency ω_s becomes and the smaller the length of each section Δl gets. Thus, in the limiting case of $\omega_s = \infty$, therefore the whole frequency range is consider, the result of the DLP procedure comes as a CNTL.

4.4 Summary

All the inverse scattering methods considered so far on this thesis can be divided into two major groups. The first group consists on the integral equation based IS methods, which are based on the solution of an integral equation (GLM) or a system of integral

equations (ZS system). The solution to these integral equations can be obtained through mathematical manipulation as a closed form analytical expression, or through numerical or iterative procedures. The outcome of these procedures inherently translates into CNTL structures. On the other hand, the second group comprises the so-called differential inverse scattering methods. These methods are based on discrete NTL models and rely on recursive identification procedures. Two differential inverse scattering methods were addressed in section 4.3, namely the CLP and DLP procedures.

Chapter 5

Microwave applications of inverse scattering theory

5.1 Introduction

In Chapter 4 we have made a detailed survey over the inverse scattering theory. More specifically, we have analyzed the one dimensional inverse scattering case and how it can be applied to the synthesis of non-linear transmission line structures. Moreover, we have discussed several methods that allow us to perform the synthesis of non-uniform transmission line structures through inverse scattering as well as their advantages, limitations and complexity. From that analysis, the layer-peeling algorithm stood out as the best method due to its simplicity, accuracy and reliability. Consequently, the discrete layer-peeling algorithm is elected as the method of choice to perform inverse scattering throughout this Chapter.

The analysis made in Chapter 4 is purely theoretical and focus solely on the complexity and performance of the methods used to perform inverse scattering, thus, only simple examples such as the synthesis of low complexity band-stop filters are considered.

In this Chapter, however, we shall demonstrate the potential and versatility of the inverse scattering theory by performing the synthesis of more complex microwave devices, such as, band-stop filters, chirped delay lines and directional couplers. Moreover, we shall address the physical implementation procedures for these devices as well as the inherently associated impairments and how they influence the electrical performance of the devices when compared to the theoretical goals.

5.2 Band-stop filters

As seen in Chapter 4, inverse scattering theory is inherently suited for the synthesis of band-stop filters. This is mainly because the structures resulting from the direct use of inverse scattering come as non-uniform transmission lines, which by itself excludes the direct synthesis of high-pass and band-pass filters. On the other hand and as we shall prove in this chapter, the direct synthesis of pure low-pass filters result in impedance profiles with prohibiting high impedance values which practically speaking invalidate the direct synthesis of low pass filters. A *quasi*-low-pass filter can however be obtained from a band-stop filter by considering a large enough bandwidth. Similarly, a *quasi*-band-pass filter can be obtained from a dual-band band-stop filter.

It is important to understand at this point that, by stop-band frequency response we refer to the transmission frequency response, however, and because the inverse scattering methods work by identifying the medium (transmission line) from its reflection response, in order to synthesize a transmission stop-band filter we must ultimately obtain a reflection response band-pass filter which is then fed to the inverse scattering procedure. The relation between the transmission and reflection magnitude responses is given by

$$|T(\omega)|^2 + |R(\omega)|^2 = 1, \tag{5.1}$$

where $T(\omega)$ and $R(\omega)$ are the transmission and reflection frequency responses, respectively. Furthermore, $T(\omega)$ is minimum phase, thus, the associated phase response can be easily obtained from the magnitude through the Hilbert transform. The reflection phase response on the other hand does not obey to the minimum phase criteria and can be arbitrarily specific so long as it complies with the realizability conditions discussed in section 4.2.1.1.

In Chapter 4 and so as to demonstrate different inverse scattering synthesis methods we have only considered the synthesis of very simple two poles band-stop filters with a well established rational transfer function. In this section we shall demonstrate the synthesis of considerably more complex band-stop filters. We start by the synthesis of classical band-stop filters, *i.e.*, Chebyshev, Butterworth and elliptic filters. Afterwords, we shall demonstrate the synthesis of stop-band filters with arbitrary magnitude and phase frequency responses.

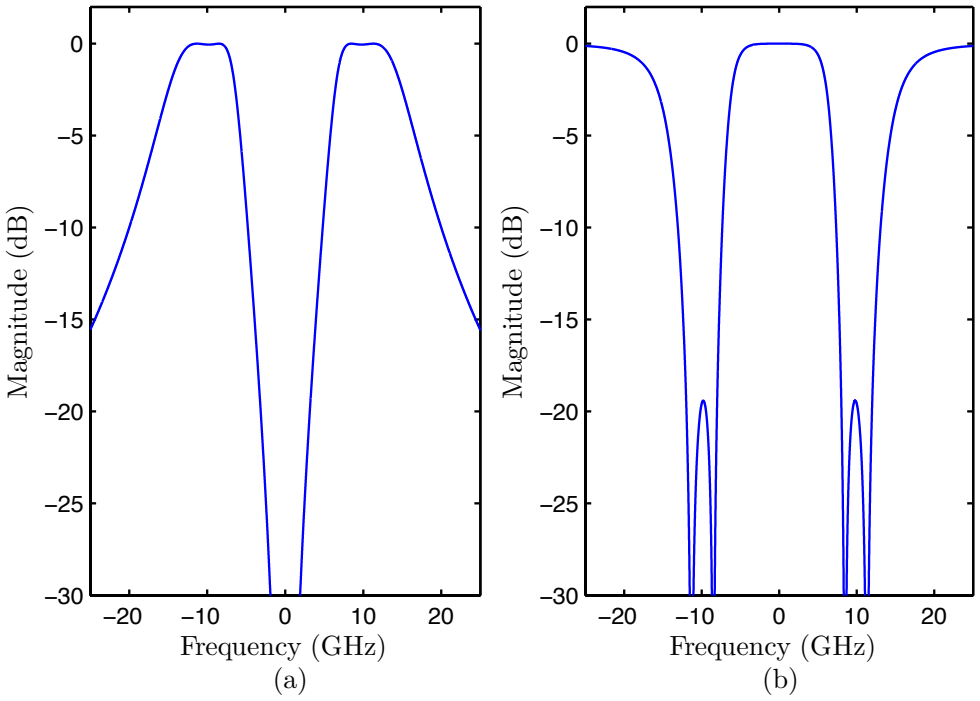

FIGURE 5.1: Second order Chebyshev type I frequency response. Figure (a) depicts the reflection frequency response $|R(\omega)|$, whereas in (b) is the transmission frequency response $|T(\omega)|$, which is obtained from that in (a) through equation 5.1.

5.2.1 Classical Band-stop filter synthesis

Similarly to the first order band-stop filter example considered throughout Chapter 4, the filters considered throughout this section are also characterized by a rational and well defined transfer function, thus, are suitable to be synthesized through an analytical inverse scattering procedure. However, because the level of complexity is relatively higher, an analytical inverse scattering approach to the synthesis of this filters proves to be a cumbersome and very time consuming task. Alternatively, we use a numerical method, more specifically, the discrete layer-peeling algorithm which as we know from Chapter 4, is a fast, simple and accurate inverse scattering method.

In order to demonstrate the synthesis of classical band-stop filters using inverse scattering theory, let us consider a second order band-pass Chebyshev type I filter with 0.05 dB in-band ripple, 40% bandwidth and a center frequency of 10 GHz. This filter is referred to as the reflection target filter and its transfer function is given by

$$R(\omega) = \frac{0.0117\omega^2}{\omega^4 + j0.1452\omega^3 + j0.0421\omega^2 - j0.0022\omega - 0.0002}, \tag{5.2}$$

whose coefficients are readily obtainable from Matlab through the command *cheby1*.

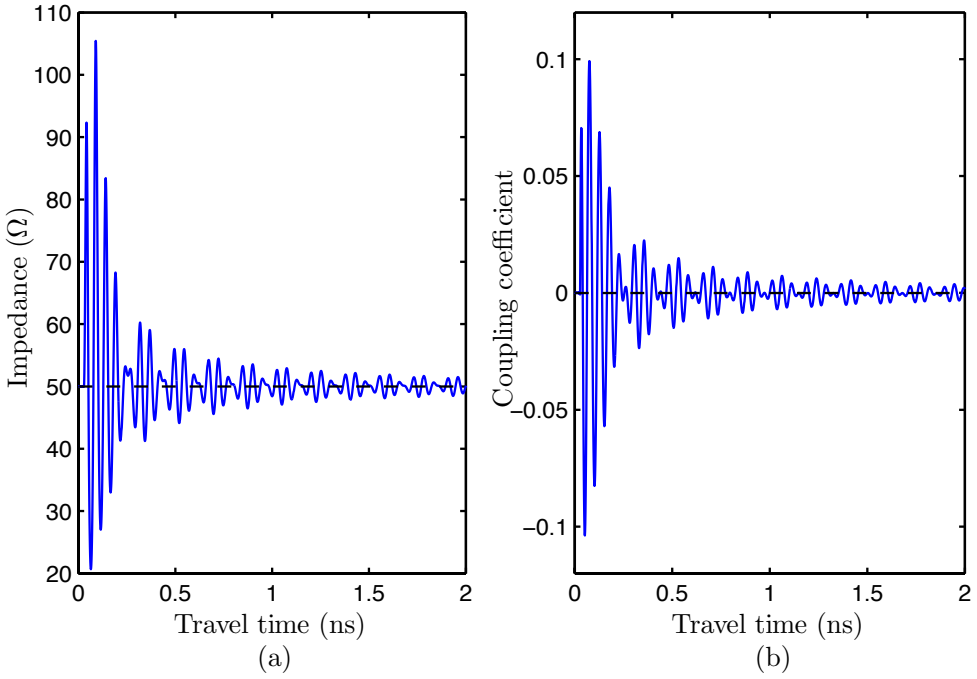

FIGURE 5.2: Impedance profile $Z_0(x)$ returned by the layer-peeling algorithm after 2000 iterations in (a) and the associated coupling coefficient $K(x)$ in (b). These results are given independently of the medium propagation speed, hence, as a function of travel time, and considering a sampling frequency $\omega_s = 500$ Grad/s.

The corresponding magnitude frequency response is depicted in Figure 5.1 (a). Notice that, the inverse scattering methods work by identifying the transmission line profile from its reflection response, hence, in order to obtain a transmission band-stop filter, we must specify a reflection band-pass frequency response. The corresponding band-stop transmission frequency response is that given in Figure 5.1 (b) and its magnitude is related to that of the reflection response through equation (5.1).

It is known for a fact that, Chebyshev filters are inherently represented by stable systems, thus, the poles of $R(s)$ are contained within the LHP of the s-plane, furthermore, it can be shown that the impulse response associated to $R(\omega)$ is real valued and causal and also that the condition $|R(\omega)|^2 < 1$ is verified for the entire frequency spectrum. From this, we conclude that the target reflection frequency response $R(\omega)$ given by equation (5.2), fulfills the realizability conditions described in section 4.2.1.1 and is therefore suitable to be synthesized as a nonuniform transmission line. Notice that the same reasoning can be applied at the other classical filters, *i.e.*, Butterworth and elliptical filters. Hence, all classical filters are suitable to physical realization through IS as nonuniform transmission lines when considered as the target reflection response.

Once the realizability conditions are verified, the target reflection frequency response $R(\omega)$, *i.e.*, the band-pass response given in Figure 5.1(a), is fed to the layer-peeling algorithm, which in turn returns the impedance profile $Z_0(x)$ depicted in Figure 5.2 (a), *i.e.*, the impedance profile of a continuous nonuniform transmission line (CNTL).

At this point, we find relevant to present not only the impedance profile of the CNTL but also its associated coupling coefficient *i.e.*, $K(x)$, which is depicted in Figure 5.2(b). As we shall see next, the coupling coefficient plays an important role on determining the optimum length for the final impedance profile. The layer-peeling algorithm however and unlike other inverse scattering methods, does not directly provide the coupling coefficient. Alternatively, the coupling coefficient can be obtained directly from the impedance profile through (3.40) or from the reflection coefficients along the CNTL structure through equation (4.203).

The impedance profile depicted in Figure 5.2 is obtained after 2000 iterations of the layer-peeling algorithm and is by no means the complete impedance profile. The total impedance profile has in fact an infinite length, consequently, it is not suitable for physical implementation. In this way, a method must be devised in order to truncate the size of the filter to a manageable length, while at the same time keeping the spectral prejudice to a minimum.

In the same way as the impedance profile has infinite length, so does the coupling coefficient. However, it becomes clear by a simple visual inspection of Figure 5.2 (b) that the most significant part of $K(x)$ is located near the origin and that the higher the length considered the lower the values of $K(x)$ are, thus, the less influence they shall have over the frequency response. This effect, can in fact be conveniently quantified by analyzing the signal energy of $K(x)$ as a function of length, where the majority of the energy of the coupling coefficient energy is located at the beginning of the CNTL structure. In this way, we now define the quantity *coupling energy* as

$$E_K(x) = \int_0^x |K(x)|^2 dx, \tag{5.3}$$

where x is the length variable, *i.e.*, travel time.

In order to get a better understanding from the energy evaluation of $K(x)$, thus, a meaningful energy evaluation, we must consider a normalized evaluation of $E_K(x)$.

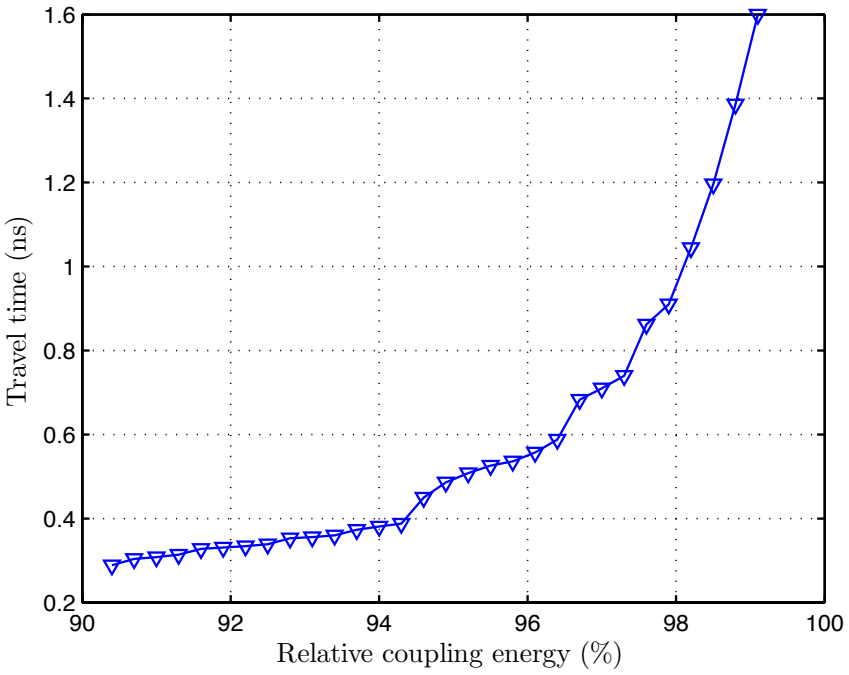

FIGURE 5.3: Impedance profile length versus the relative coupling coefficient energy $E_{K_r}(x)$. Notice that, the relation depicted in this figure is particular to the Chebyshev filter specified in equation (5.2).

Hence we define the *relative coupling energy* which is given by

$$E_{K_r}(x) = \frac{E_K(x)}{E_{K_{max}}} \tag{5.4}$$

where $E_{K_{max}}$ is the total coupling energy.

In fact, because the impedance profile returned by the layer-peeling algorithm has an infinite length and accordingly to equation (5.3), it is not possible to exactly calculate the total coupling energy *i.e.*, $E_{K_{max}}$. However, a good estimate can be made by setting the layer-peeling algorithm to return a long enough (large number of iterations) impedance profile, so that we can fairly say that all the energy is contained within such impedance profile. The total coupling energy is then set to the total energy of the coupling coefficient associated to this long impedance profile. In the present case it was found that 50000 iterations provide a good estimate of the total coupling energy.

Figure 5.3 depicts the relation between the impedance profile length and the associated relative coupling energy. Clearly we see that the filter length varies exponentially with the relative coupling energy. Notice that, up to 94% of coupling energy, the length of the filter is kept relatively small, however approximately from 94% to 97.5%, *i.e.*,

within just a 3.5% relative coupling energy variation, the length of the filter doubles its value. Moreover, for larger coupling energy values the the rate of growth for the length variable is even higher.

From the analysis of Figure 5.3, we conclude that the majority of the energy of the coupling coefficient energy is located at the beginning of the CNTL structure, *i.e.*, the filter. Thus, the process of reducing the length of the filter from infinite to a manageable length translates into a simple truncation procedure. That is, the impedance profile is truncated at a given length corresponding to some specified relative coupling energy (provided it is high enough). In this way, the last few percent of coupling energy are neglected as they are considered to have a small influence over the frequency response. Clearly, the higher the the truncation relative coupling energy is, the better the filter response will approximate the target frequency response.

In order to access the effect of the truncation process on the spectral performance of the truncated filter we now define the magnitude *error function* as

$$\mathrm{EF} = \int_{\Delta\omega} (|R(\omega)| - |S_{11}(\omega)|)^2 \, d\omega, \tag{5.5}$$

where $R(\omega)$ is the target reflection response, $S_{11}(\omega)$ is the frequency reflection response of the truncated filter, and $\Delta\omega$ is the frequency region over which the approximation error is evaluated.

Equation (5.5) measures the squared value of the total area associated with the difference between the magnitude response of the target response and that of the truncated filter, within the considered frequency region. So as to obtain a more general and meaningful error evaluation, we must consider a normalized error function, *i.e.*, a *relative error function*, which is given by

$$\mathrm{EF_r} = \frac{\mathrm{EF}}{\mathrm{EF_{max}}}, \tag{5.6}$$

where $\mathrm{EF_{max}}$ corresponds to the maximum evaluation possible for EF and is computed by

$$\mathrm{EF_{max}} = \int_{\Delta\omega} 1 \, d\omega = \Delta\omega. \tag{5.7}$$

Figure 5.4 depicts a parametric analysis of the relative error function $\mathrm{EF_r}$ as a function of the relative coupling energy truncation value, for the Chebyshev filter given in (5.2). The error evaluation is performed over a 15 GHz frequency band ranging from

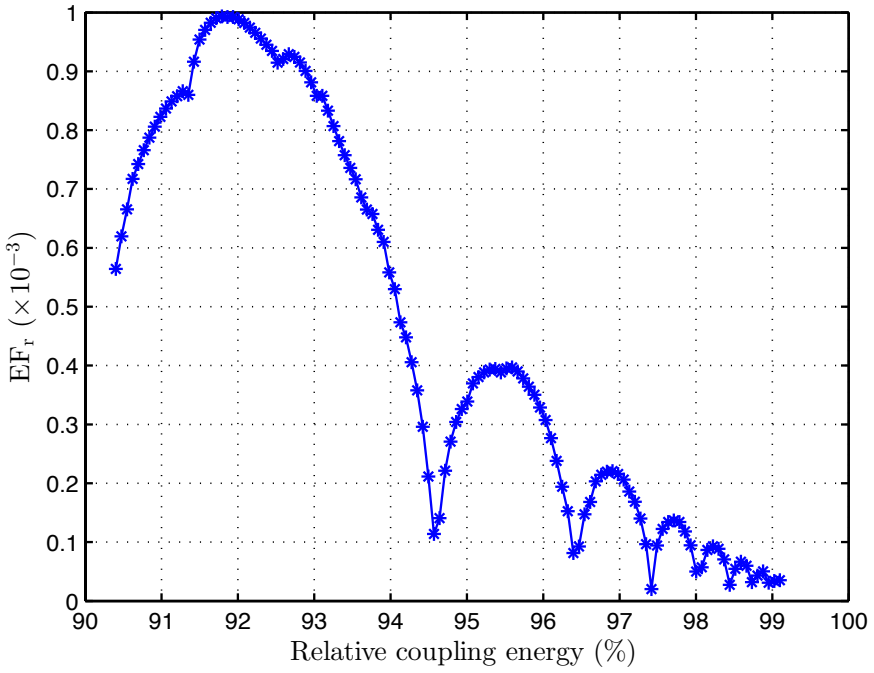

FIGURE 5.4: Error function values as a function of the relative coupling energy considered. Notice that, the error evaluation depicted in this figure is particular to the Chebyshev filter specified in equation (5.2).

5 GHz to 20 GHz. The selection for the frequency band was made based on the filter center frequency and bandwidth. Moreover, the filter is always adapted at both input and output ports. That is, depending on the relative coupling energy truncation value, *i.e.*, the truncation length, the last value of the impedance profile does not necessarily evaluate to $50\,\Omega$ as does the input port. Thus, in our analysis, the output port characteristic impedance always match the last value of the impedance profile so as to avoid errors due to port mismatch.

An analysis of Figure 5.4 immediately reveals that the error function evaluation does not monotonically decreases with the increasing of coupling energy as it should be expected. Instead it is characterized by minimums and maximums. The reason for the minimums and maximums observed in Figure 5.4 has to do with the shape of the impedance profile and/or the coupling coefficient (see Figure 5.2). These are characterized by regions of high amplitude impedance variation interleaved with regions of low amplitude impedance variation. When the truncation occurs at one of those regions of low amplitude impedance variation we get a minimum in Figure 5.4. This is because this low amplitude truncation acts like a smooth termination for the impedance profile. On the other hand when the truncation occurs at a high amplitude variation

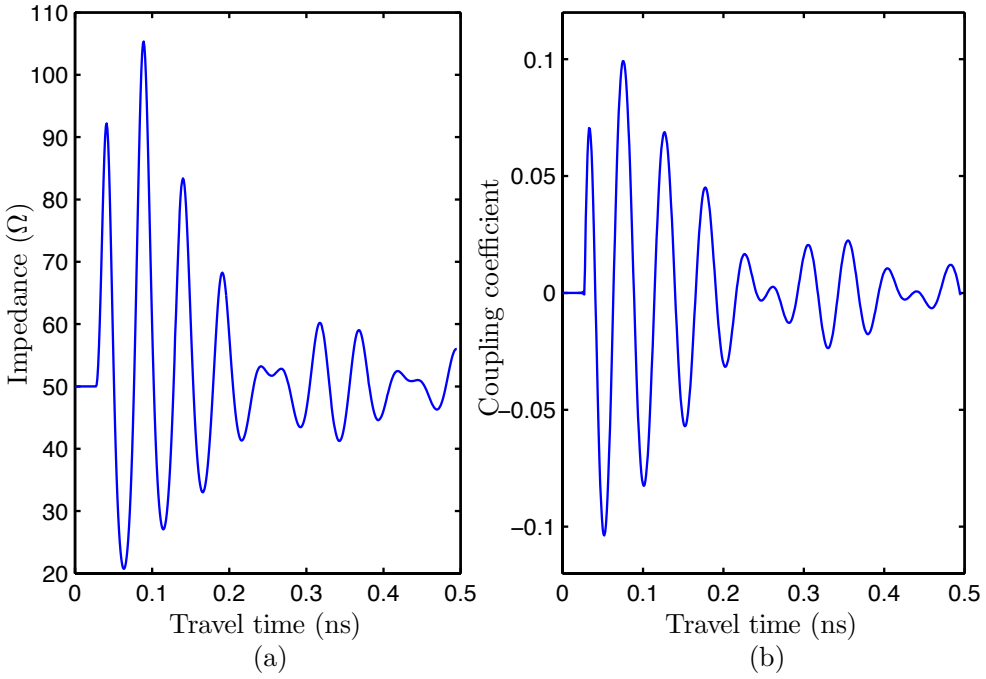

FIGURE 5.5: Impedance profile $Z_0(x)$ truncated at a relative coupling energy of 95 % in (a) and the associated coupling coefficient $K(x)$ in (b). These results are given independently of the medium propagation speed, hence, as a function of travel time.

region we get an error maximum, because the impedance profile is abruptly terminated.

Essentially and apart from the local minimums and maximums observed, we conclude from the analysis of Figure 5.4 that, the amplitude or envelope of the error function evaluation is monotonically decreasing with increasing relative coupling energy, thus, the higher the coupling energy (the longer the filter) considered the better the lower the error, as expected. As a rule of thumb, we consider that a relative coupling energy of 95 % constitutes a good compromise given the trade-off between filter length and accuracy. The error evaluation for a 95 % of relative coupling energy is $\mathrm{EF_r} = 0.330 \times 10^{-3}$, for this particular case.

Figure 5.5(a) shows the impedance profile after a truncation at 95 % of relative coupling energy. The corresponding coupling coefficient is depicted in Figure 5.5(b). Moreover, the total length of the truncated filter is of 0.5 ns.

Notice from Figure 5.5(a) that, the first impedance value for the impedance profile is 50 Ω, however, the last value is 56 Ω, hence, a correct analysis for this specific filter must be carried on by considering a termination port with characteristic impedance of 56 Ω, so as to avoid higher error function evaluation due to port mismatch.

Figure 5.6 depicts the comparison between the ideal frequency response and that of

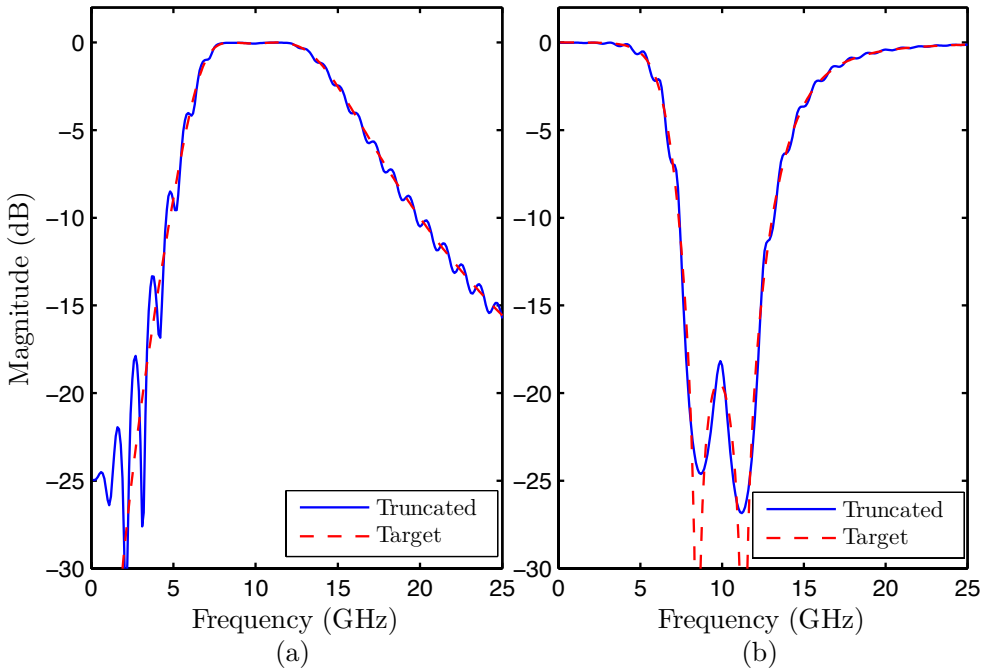

FIGURE 5.6: Comparison between the ideal frequency response and that of the truncated filter. In (a) is the reflection frequency response whereas in (b) is the associated transmission frequency response. The analysis of the truncated filter is performed using the transmission matrix method presented in section 3.3.2.

the truncated impedance profile, where the theoretical spectral analysis for the truncated filter is made through the transmission matrix method discussed in section 3.3.2.

As we can see from the Figure, the truncated filter response closely follows that of the target filter, both in reflection and transmission. However, the truncation procedure introduces a considerable amount of ripple in the filter response, which is undesirable. This ripple factor, is the dominant source of the error shown in Figure 5.4. The amount of ripple is dependent on the truncation length and there are optimum truncation lengths for which the ripple effect is minimized. These optimum lengths correspond to the error minimums observed in Figure 5.4. Most often however, performing the truncation at these minimums translates into the necessity of different input and output characteristic impedances as observed in Figure 5.5(a). This is an undesirable feature given that most microwave systems are set to a specified characteristic impedance, usually $50\,\Omega$. Broadly speaking however, and considering the tendency of the error curve depicted in Figure 5.4, longer filters exhibit less ripple, moreover, for longer filters the output characteristic impedance tends to be closer to that of the input characteristic impedance, as it can be seen in Figure 5.2(a).

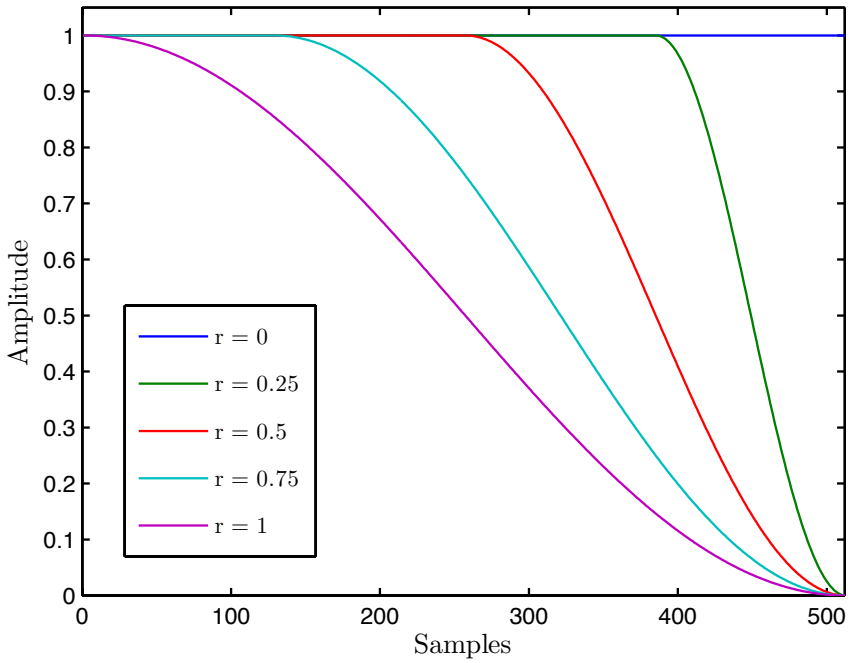

FIGURE 5.7: Tukey windows with five different values of "window ratio" r.

In order to eliminate the ripple factor and guaranty a matched output characteristic impedance with the same value as that of the input without increasing the length of the filter, we can deliberately manipulate the truncated coupling coefficient so as the resulting impedance profile has a smoother convergence towards the output characteristic impedance. This can be easily accomplished by indirectly tapering the coupling coefficient along the filter by means of a windowing process as we shall demonstrate next.

In fact, by directly tapering the coupling coefficient along the filter, one would eliminate the ripple in the filter frequency response, however, we would not guaranty an equal impedance termination at both the input and output ports of the filter. We know from section 3.2.4 that the impedance profile of any CNTL can be computed from the associated coupling coefficient as

$$Z_0(x) = Z_0(0)e^{2K_I(x)}, \tag{5.8}$$

where $Z_0(0)$ is the input port characteristic impedance and $K_I(x)$ is the integral of the coupling coefficient, $K(x)$, *i.e.*

$$K_I(x) = \int_0^x K(u)\,du. \tag{5.9}$$

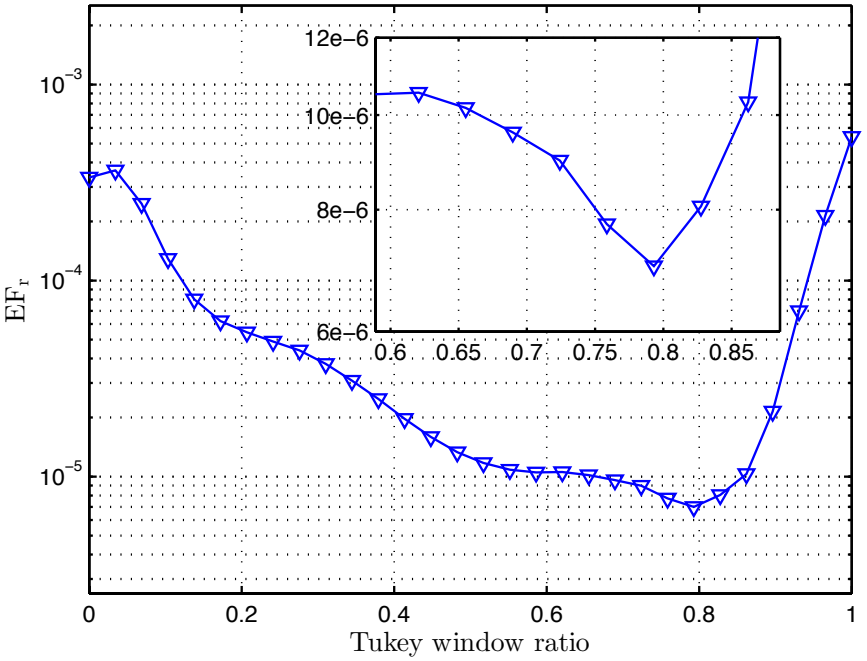

FIGURE 5.8: Relative error function as a function of the ratio value for the Tukey window. Notice that, the error evaluation depicted in this figure only applies for a truncation relative coupling energy of 95 %.

It becomes clear from equation (5.8) that, in order for the impedance profile to equally valued at both terminals, the integral of the coupling coefficient, *i.e.*, $K_I(x)$ must evaluate as zero both at the beginning and at the end of the filter. Thus, in order to eliminate the ripple factor and at the same time guaranty equal impedance terminations for the filter, we must perform the tapering/windowing process on $K_I(x)$ and not on the coupling coefficient.

The windowing procedure is very simple and consists on multiplying a window function by $K_I(x)$. There is a wide variety of windows that can be used for the windowing process of $K_I(x)$, however, from an universe of seventeen windows that were evaluated, only six are terminated with amplitude zero (a necessary condition to enforce equal impedance termination for the filter). From the evaluation of these six eligible windows it was found that, except for the *Tukey* window, all other windows introduce a relatively high amount of distortion, which in fact worsens the spectral performance of the resulting filter. That is, the relative error evaluation of the filters resulting from using these windows is higher than that obtained without performing the windowing procedure.

A Tukey window is in fact a rectangular window whose last $r/2$ (r=ratio) percent of samples are given as a cosine-tapered section. Figure 5.7 depicts the shape of the

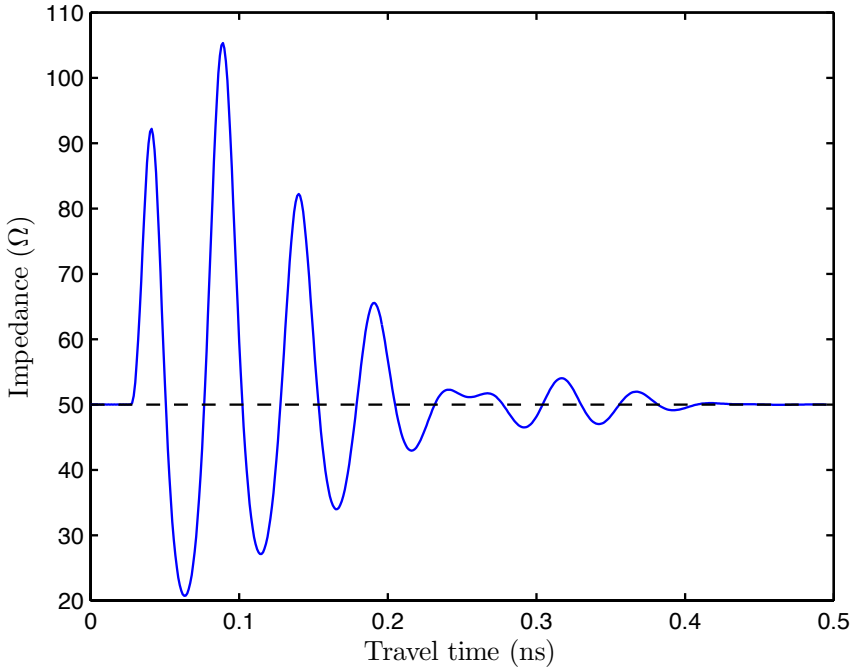

FIGURE 5.9: Impedance profile $Z_0(x)$ truncated at a relative coupling energy of 95 % and obtained from a tapering process through a Tukey window with $r = 0.7931$.

Tukey window for five different window ratios. Notice that for $r = 1$ the turkey window is equivalent to the *Hann* window and for $r = 0$ it reduces to the rectangular window.

Figure 5.8 depicts a parametric analysis of the relative error $\mathrm{EF_r}$ as a function of the window ratio. Clearly, we see that the higher error evaluations areas are located at the lower and higher window ratio values. Notice that, the relative error evaluation at $r = 0$ (rectangular window) is equivalent to the error evaluation without windowing (error due to truncation). Furthermore, the highest error is obtained for $r = 1$, *i.e.*, for the Hann window which has been previously ruled out as a suitable window. On the other hand, we find that the optimum window ratio is $r = 0.7931$ with an associated relative error of 7×10^{-6}, which is significantly lower than that obtained without windowing, *i.e.*, the error resulting from a simple truncation at 95 % coupling energy. It is important to refer at this point that the analysis depicted in Figure 5.8 only applies for the Chebyshev filter under consideration, and only for a truncation coupling energy of 95 %. The same analysis for a different truncation length would most certainly result in a different optimum window ratio value. Empirically however, we found that this different optimum window ratio is most likely to be located within the range $0.5 \leq r \leq 0.95$.

Figure 5.9 depicts the impedance profile resulting from a relative coupling energy truncation of 95 % as well as from a tapering process through a Tukey window with

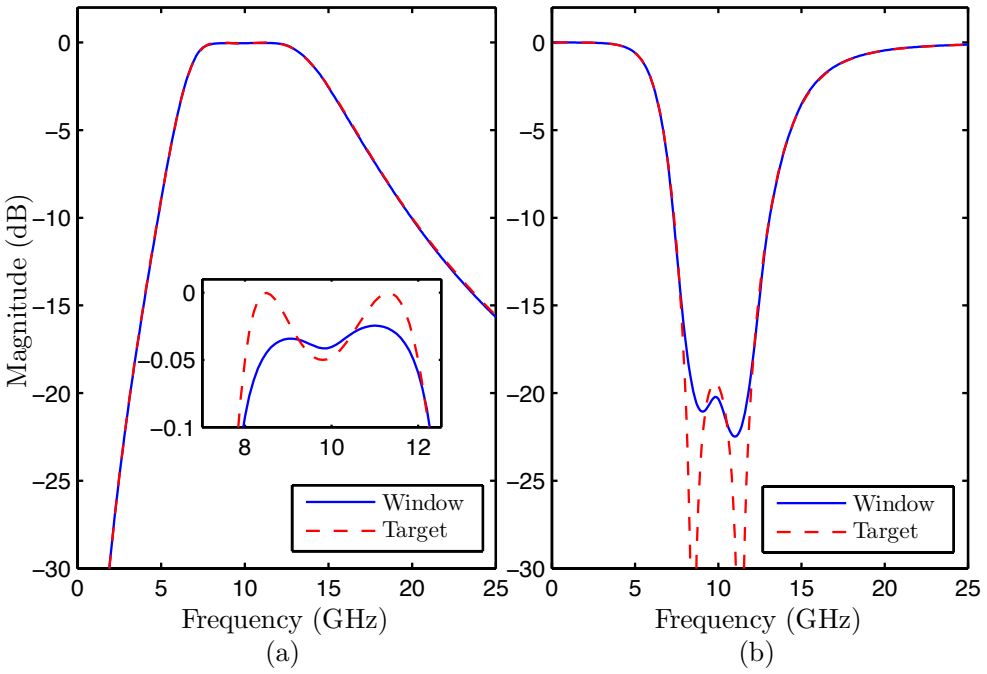

FIGURE 5.10: Comparison between the ideal frequency response and that resulting from the windowing procedure, *i.e.*, the analysis of the impedance profile depicted in Figure 5.9. In (a) is the reflection frequency response whereas in (b) is the associated transmission frequency response. The analysis of the filter is performed using the transmission matrix method presented in section 3.3.2.

$r = 0.7931$, *i.e.* the optimum ratio. Comparing the impedance profile in Figure 5.9 with that obtained without tapering (see Figure 5.5 (a)) we see that, as a result of the windowing process, the former impedance profile has a smoother convergence towards the end characteristic impedance. Furthermore, the end characteristic impedance is the same as the input characteristic impedance, whereas in the case without tapering these values have different evaluations.

The frequency response associated to the tapered impedance profile is illustrated in Figure 5.10. Apart from some minor differences in the reflection pass-band, we see that the truncation ripple was in fact successfully eliminated and that the resulting frequency response accurately follows the target response.

The results shown in Figure 5.10 prove to be excellent given the trade-off between length and accuracy. However, if for some given application the approximation to the target response obtained so far is not accurate enough, or if the size constrains allow for a longer filter, a further improvement on accuracy can be easily achieved by increasing the length of the filter.

Figure 5.11 depicts the error evaluation as a function of the length of the filter

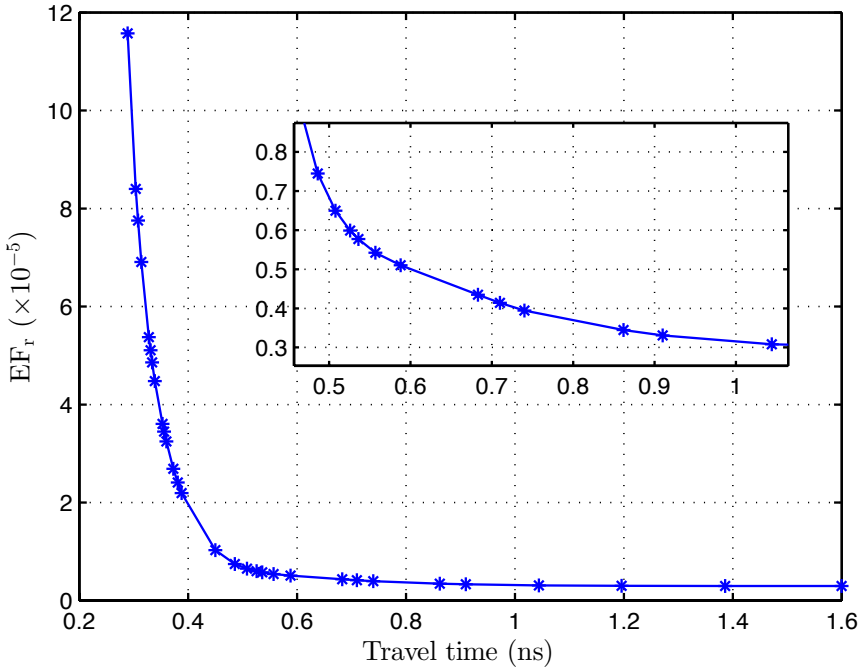

FIGURE 5.11: Relative error evaluation as a function of the length of the filter. Notice that, the error evaluation depicted in this figure takes into consideration tapering by a Tukey window with $r = 0.7931$.

when considering the same tapering window used previously, *i.e.*, a Tukey window with a window ration of $r = 0.7931$. On this analysis, we chose error evaluation versus travel time instead of error evaluation versus relative coupling energy, they are however equivalent. As expected, the larger the filter, the better is the corresponding frequency response approximation to the target response. It is interesting to see that, unlike the error analysis performed without tapering (see Figure 5.4), on this analysis the relative error evaluation monotonically decreases with increasing length. This is because the windowing/tapering process provides for a smooth convergence towards the output port characteristic impedance, hence, eliminating the minima observed in Figure 5.4.

For demonstrative purposes, let us now consider the same filter with its length extended to 0.84 ns (corresponding to a relative coupling energy of 97.5 %). Notice that, for a length of 0.84 ns and accordingly to Figure 5.11 the error is approximately half of that obtained previously for a length of 0.5 ns.

It is important to emphasize at this point that, despite the electrical performance improvement obtained by extending the length of the filter, the resulting impedance profile does not necessarily comes as the optimum impedance profile for the given specifications. Notice that, the length of the filter was increased while the window ratio

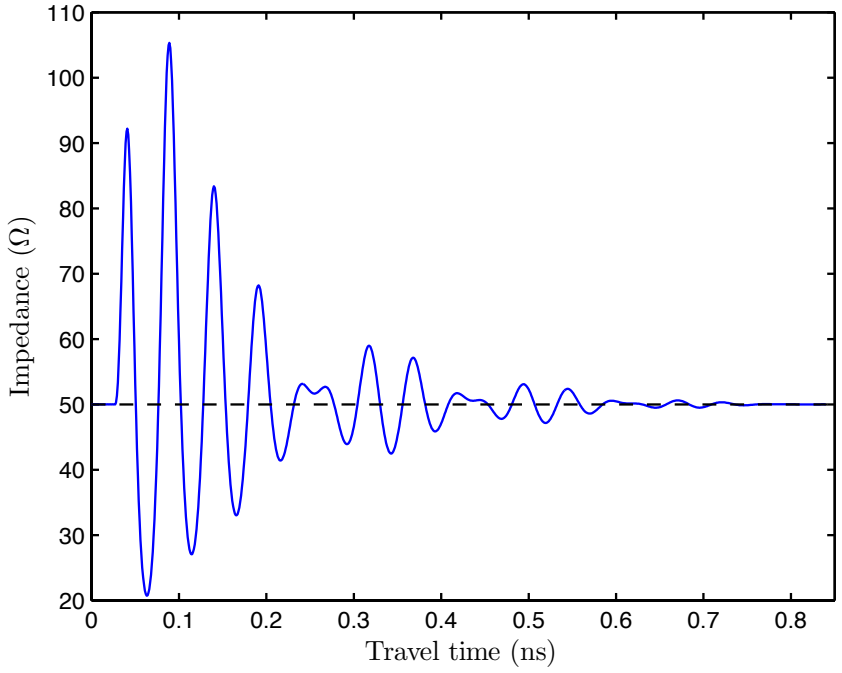

FIGURE 5.12: Impedance profile $Z_0(x)$ obtained by considering an extended length of 0.84 ns and considering a tapering process through a Tukey window with $r = 0.7931$.

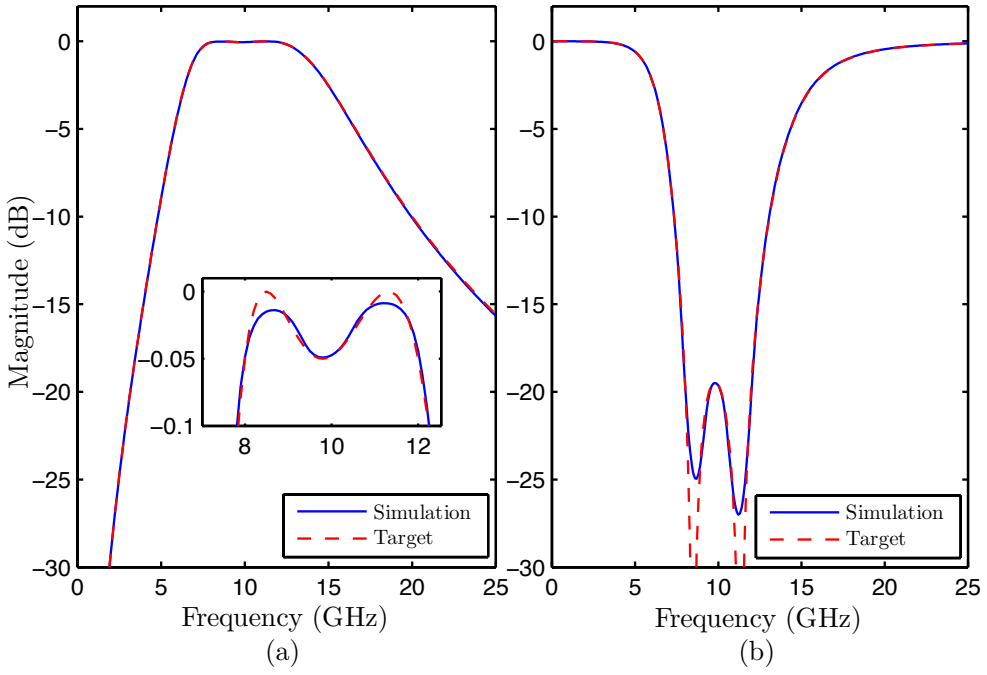

FIGURE 5.13: Comparison between the ideal frequency response and that resulting from extending the filters length, *i.e.*, the analysis of the impedance profile depicted in Figure 5.12. In (a) is the reflection frequency response whereas in (b) is the associated transmission frequency response. The analysis of the filter is performed using the transmission matrix method presented in section 3.3.2.

was kept the same and as it was previously referred, the optimum Tukey window ratio is dependent on the length of the filter. Obtaining the optimum impedance profile for the new length would however imply starting the synthesis procedure almost from the beginning which might not justify the difference in performance.

The impedance profile resulting from extending the length of the filter is plotted in Figure 5.12. Apart from the length increase, a comparison with the impedance profile for the shorter version (Figure 5.9) shows that, although the new impedance profile has the same type of convergence towards $50\,\Omega$ (uses the same window), it does so at a latter length stage, hence, it contemplates a larger number of impedance nuances, which inevitably translates into a lower error evaluation. The corresponding frequency response is given in Figure 5.13 which, by comparison with that in Figure 5.10, clearly shows an electrical performance improvement over the reflective pass-band region and consequently over the transmissive stop-band region.

So as to evaluate the use of inverse scattering theory in the synthesis of classical band-stop filters as well as to validate the theoretical analysis made so far, we now focus on the experimental analysis of the Chebyshev band-stop filter whose impedance profile is given in Figure 5.12. The experimental analysis shall be divided into four stages so as to gradually and independently identify the problems/issues and procedures associated with the physical implementation of the impedance profile into planar technology (microstrip, stripline). In all stages, the electromagnetic analysis of the structures is made using commercial electromagnetic simulators, more specifically, Agilent ADS or Ansys HFSS.

In the first stage, the filter is implemented in lossless stripline technology, *i.e.*, considering a lossless substrate as well as perfect conducting metallic layers with no thickness. Because stripline transmission lines support a pure TEM propagation mode, the electromagnetic analysis of the CNTL filter under these conditions should in principle be equivalent to the theoretical analysis considered so far, *i.e.*, should provide similar results. In the second stage we change to lossless microstrip technology (lossless substrate and perfect conducting metallic layers with no thickness) so as to account for the influence of a non-homogeneous medium on the frequency response. The third stage contemplates the electromagnetic analysis over a realistic microstrip implementation (substrate losses, finite metal conductivity and thickness). The final stage consists on the physical implementation of the filter in microstrip technology and experimental evaluation.

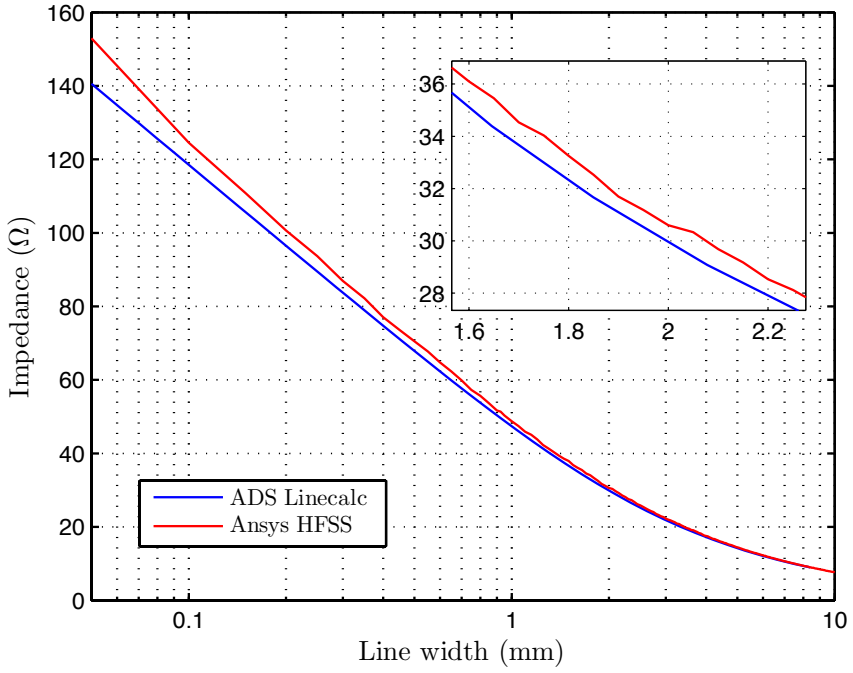

FIGURE 5.14: Transmission line characteristic impedance as a function of line width for a lossless stripline implementation with zero thickness perfect conducting metal layers. The substrate properties are: $\epsilon_r = 3.55$, $b = 1.626\,\text{mm}$ and $\tan\delta = 0$. Two independent impedance evaluation tools are considered: Agilent Linecalc and Ansys HFSS.

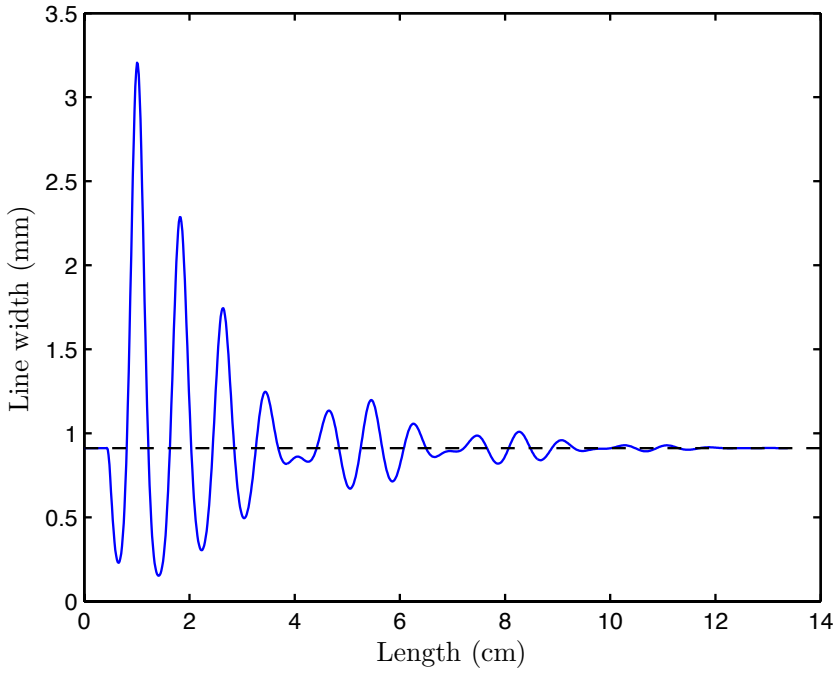

FIGURE 5.15: Physical dimensions for the impedance profile depicted in Figure 5.12 when considering a stripline implementation. The line width dimensions are obtained through interpolation from the simulation data provided by Figure 5.14. The physical length dimensions are obtained from the travel time information through equation (5.10) for a relative permittivity of $\epsilon_r = 3.55$.

The first steps towards the physical implementation of the impedance profile plotted in Figure 5.12 are to set the substrate specifications and to obtain the physical dimensions of the non-uniform transmission line for that substrate setup. For the stripline implementation we consider a substrate with relative permittivity $\epsilon_r = 3.55$, height (between ground planes) of $b = 1.626\,\text{mm}$, zero dissipation factor tangent and perfect conducting metal layers with zero thickness.

Figure 5.14 shows the characteristic impedance evaluation as a function of line width on a lossless stripline substrate. Moreover, two independent impedance evaluation tools are considered, namely Agilent Linecalc and Ansys HFSS. The evaluation performed by Linecalc is based on an analytical approach whereas the results given by HFSS result from an electromagnetic evaluation. Furthermore, unlike the Linecalc results, the HFSS results curve has some impedance fluctuations (ripple). Clearly, we see that both curves have the same shape and tendency and that for higher line widths both methods evaluate practically the same. However, for smaller line widths the impedance values discrepancies between both curves becomes quite high. In light of these results, we choose to use the Linecalc impedance evaluation to perform the conversion from impedance to line width as it lacks the fluctuation observed in the HFSS results.

The physical dimensions for the impedance profile depicted in Figure 5.12 are obtained through interpolation from the Linecalc data provided by Figure 5.14. On the other hand and for a stripline implementation, the spatial length dimensions, z, of the filter are only dependent on the relative permittivity, thus, are readily obtained from the travel time dimensions through equation (4.86), *i.e.*

$$z = \frac{c}{\sqrt{\epsilon_r}}\, x, \tag{5.10}$$

where c is the speed of light and x is travel time.

The complete set of dimensions for the stripline filter is given in Figure 5.15 and results in a filter with a length of 13.37 cm. The corresponding frequency response obtained through electromagnetic simulation on ADS is depicted in Figure 5.16 where it is compared to that resulting from the theoretical analysis using the TMM method.

From Figure 5.16 we see that, apart from a minimum frequency shift both frequency responses are in excellent agreement with each other. For higher frequencies however, more specifically in the reflection frequency response, we observe some degradation on the EM simulation result. We have however identified impedance mismatch as being the

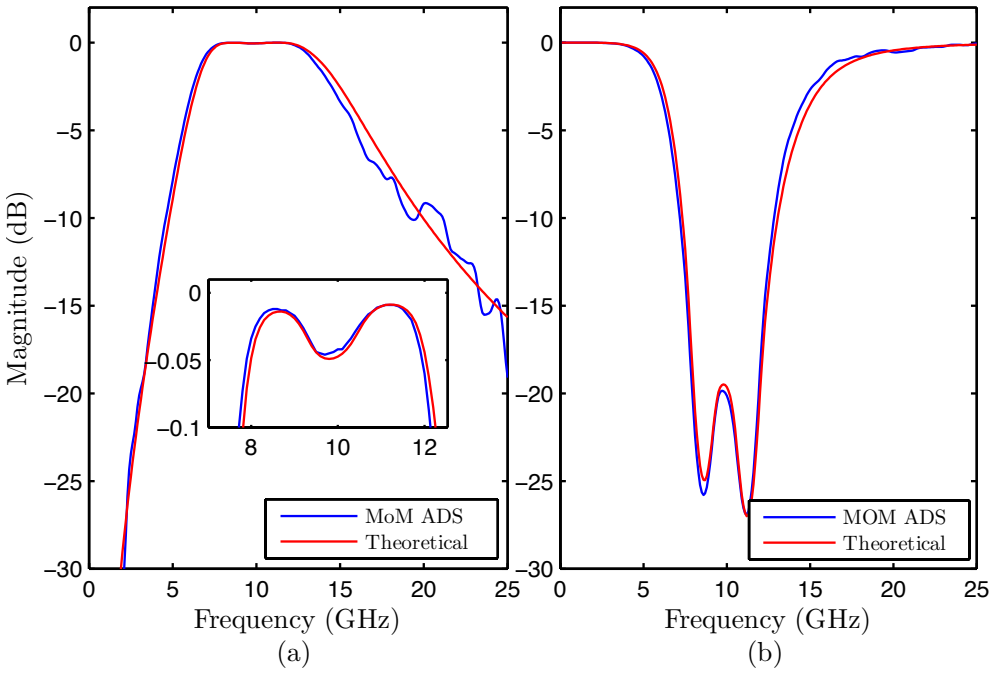

FIGURE 5.16: Comparison between the theoretical frequency response resulting from the analysis of the filter using the transmission matrix method and that resulting from MoM electromagnetic simulation on Agilent ADS. In (a) is the reflection frequency response whereas in (b) is the associated transmission frequency response.

main reason for this deviation from the theoretical response at higher frequencies. From Figure 5.14 we clearly see that the accuracy of the impedance to line width mapping procedure is clearly dependent on the tool used to compute the mapping data. On the other hand, the mesh/spatial resolution of the EM simulator strongly influences the impedance evaluation along the non-uniform transmission line. Moreover, the curve divergency in Figure 5.16(a) is more pronounced due to the low reflectivity values. For the same frequency values, the transmission frequency response in Figure 5.16(b) evaluates at higher values which visually denotes a better fitting between both curves.

From the results obtained through the EM simulation of the lossless stripline and from the previous discussion, we conclude that inverse scattering theory can in fact be successfully applied to the synthesis of nonuniform transmission line filters, provided that an accurate impedance to line width mapping process is used and that the filter is physically implemented on stripline technology. Most often however and due to its fabrication process simplicity, the planar technology of choice for implementing microwave devices is usually microstrip technology. Accordingly, we shall next assess the challenges associated with the implementation of CNTL structures in microstrip technology.

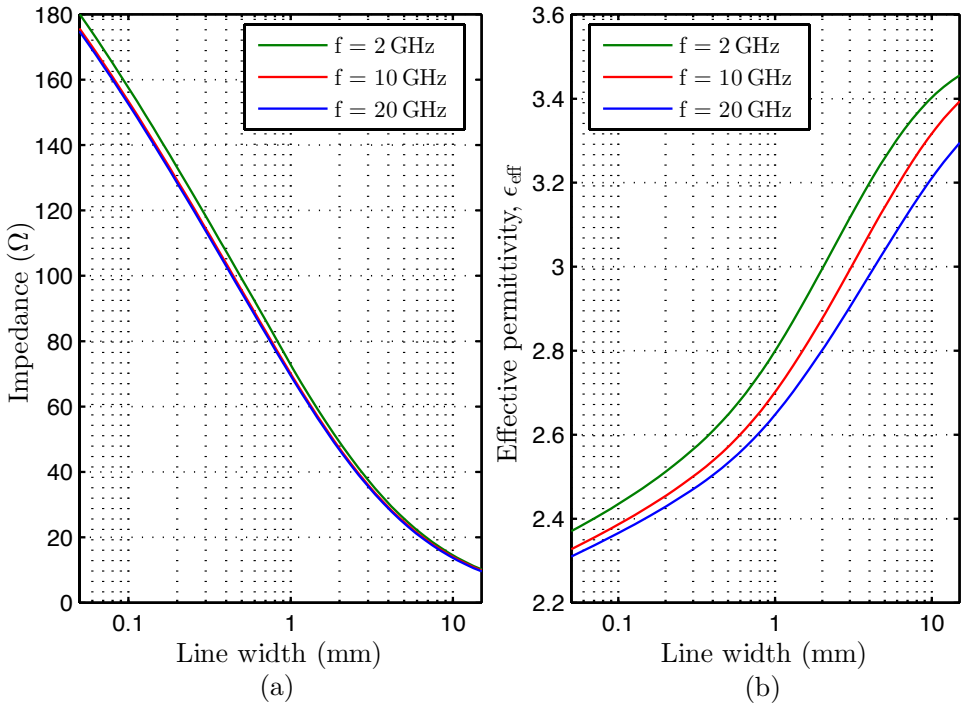

FIGURE 5.17: Transmission line characteristic impedance as a function of line width for a lossless microstrip implementation with zero thickness perfect conducting metal layers. The substrate properties are: $\epsilon_r = 3.55$ and $h = 0.813\,\text{mm}$. Both impedance and effective permittivity curves were obtained from ADS Linecalc.

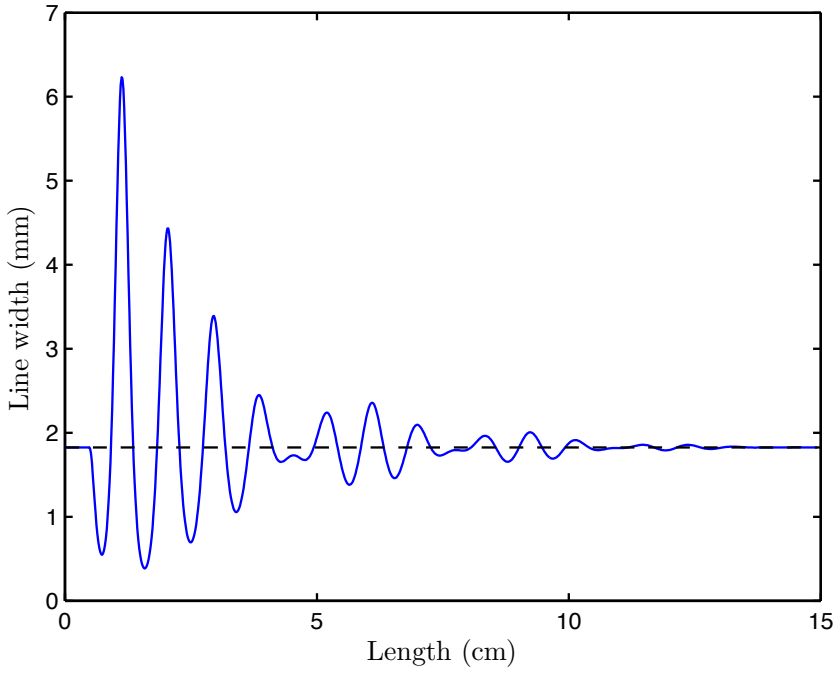

FIGURE 5.18: Physical dimensions for the impedance profile depicted in Figure 5.12 when considering a microstrip implementation. The line width dimensions are obtained through interpolation from the simulation data provided by Figure 5.17. The length dimensions are obtained from the travel time information through equation (5.11).

Similarly to the procedure undertaken before for the stripline case, the fist step consists on converting the impedance profile given in Figure 5.12 into the corresponding physical dimensions of microstrip technology. Unlike the stripline case however, microstrip technology is inherently dispersive due to its inhomogeneous nature, which poses some problems relatively to the characteristic impedance to line width mapping as it is frequency depend as is the effective permittivity. Aside from the dispersion issue however, and more importantly, is the fact that unlike with the stripline case, in microstrip, the effective permittivity is highly dependent on the line width dimension, also a result of the inhomogeneous nature of microstrip technology.

Figure 5.17 depicts the microstrip electrical properties, *i.e.*, characteristic impedance and effective permittivity, as a function of line width and evaluated for three different frequencies. The curves were obtained through the ADS Linecalc tool. From Figure 5.17(a) wee see that the characteristic impedance curve as a function of line width is similar to that on the stripline case. For the same impedance values however, microstrip lines are considerably larger than that of stripline which from a fabrication viewpoint comes as an advantage. Due to the microstrip inhomogeneous nature however, the impedance evaluation as a function of line width is different for different frequencies. Moreover, Figure 5.17(a) shows that, the impedance difference is higher for thinner lines whereas for thicker lines the impedance values (for the frequency range considered) are practically the same. In light of these results and because, even for thinner lines the relative impedance difference is quite small we choose to neglect the dispersion effect.

Figure 5.17(b) shows the evaluation of the effective permittivity as a function of line width. In the same way as with the impedance, the evaluation of the effective permittivity is also affected by dispersion. However, dealing with the dispersion effect would imply complex modifications to the inverse scattering procedures which is out of the scope of this work. Hence, we neglect the dispersion effect and select from Figure 5.17(b) the effective permittivity curve that best suites the application at hands.

Aside from the dispersion effect, we see from Figure 5.17(b) that the effective permittivity values strongly depend on the width of the microstrip line. Clearly, this is a far greater problem than that of dispersion as the permittivity values variation with line width if far greater. The simplest way to cope with this problem is to consider an average value for the relative permittivity and use equation (5.10) to obtain the spatial length dimensions of the filter from the travel time variable. Although this is a simple and elegant solution it proves to be useless as it is possible to completely account for

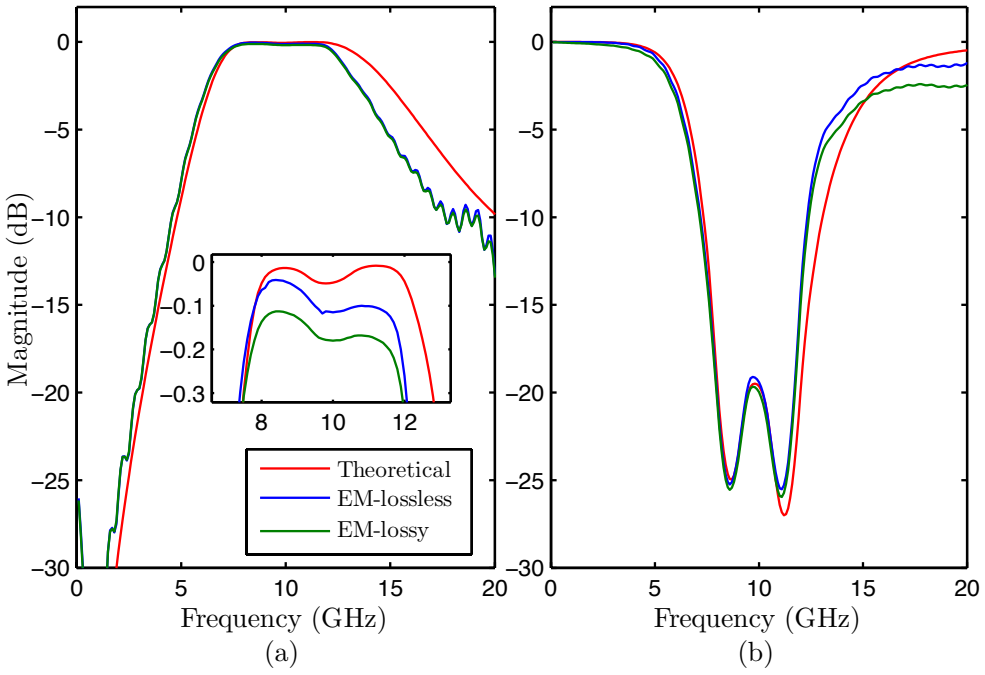

FIGURE 5.19: Comparison between the theoretical frequency response resulting from the analysis of the filter using the transmission matrix method and those resulting from MoM electromagnetic simulation on Agilent ADS for the lossless and lossy ($\tan\delta = 0.0027$) cases. In (a) is the reflection frequency response whereas in (b) is the associated transmission frequency response.

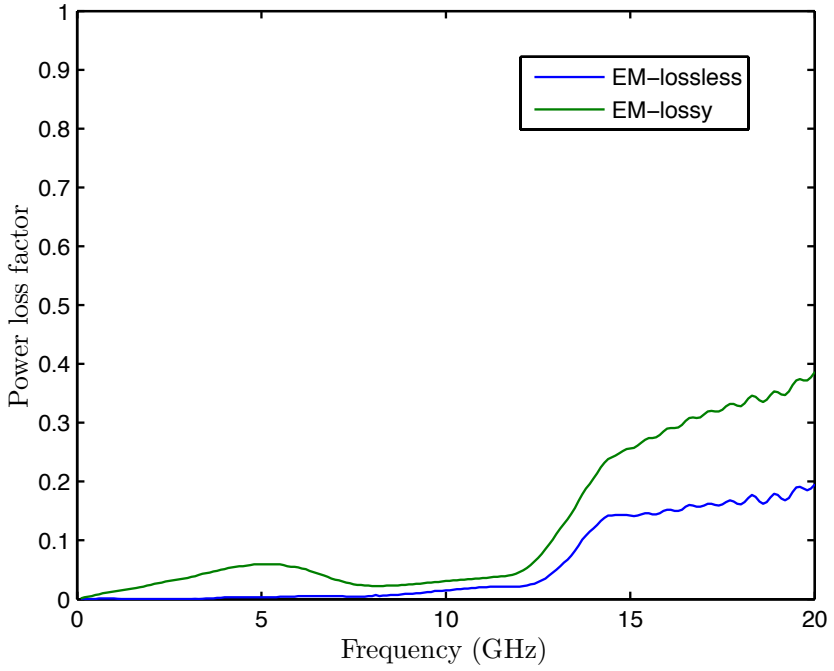

FIGURE 5.20: Power loss factor as a function of frequency resulting from MoM electromagnetic simulation on Agilent ADS for the lossless and lossy ($\tan\delta = 0.0027$) cases, respectively.

this permittivity dependence during the synthesis procedure. We know from Chapter 4 that the effective permittivity dependence on line width only influences the length of the resulting filter and does not directly interfere with the inverse scattering procedures. Hence, the spatial length dimensions of the filter, z, can be exactly computed from the travel time dimensions through equation (4.82), *i.e.*,

$$z = c \int_0^x \frac{1}{\sqrt{\epsilon_{\text{eff}}(u)}}\, du, \tag{5.11}$$

where c is the speed of light and x is travel time.

The complete set of dimensions for the microstrip filter is obtained by mapping the impedance profile given in Figure 5.12 and is depicted in Figure 5.18. The resulting microstrip filter has a length of 15 cm. Because the band-stop filter is centered at 10 GHz and to minimize the dispersion effects, the impedance and permittivity mapping curves considered are those in Figure 5.17 obtained for 10 GHz. The corresponding frequency analysis of the resulting microstrip filter is given in Figure 5.19, where the theoretical analysis using the TMM method is compared to the lossless and lossy (considering substrate losses and metallic layers thickness and finite conductivity) electromagnetic simulations performed on ADS.

Given that we are currently analyzing a microstrip implementation of the Chebyshev filter several factors/effects particular to microstrip must be considered. Notice that a microstrip transmission line is an inhomogeneous structure (does not support a pure TEM mode) as well as an open wave guiding system, thus, it is susceptible to radiation effects as well surface waves among other propagation modes. Furthermore we are now considering the effect of substrate losses on the EM simulations, hence, the *quasi*-TEM mode power dissipation as well the power transfer to higher modes must be taken into consideration when analyzing the EM simulations. In order to account for the power dissipation due to substrate losses as well as power transfer to higher propagating modes (including radiation modes) we now define the *power loss factor* (PLF) as

$$\text{PLF} = 1 - |S_{11}|^2 - |S_{21}|^2. \tag{5.12}$$

Notice that the latter expression is simply the application of the power conservation theorem, which states that for a given mode in propagation the condition $|S_{11}|^2 - |S_{21}|^2 = 1$ must hold. If this condition is not satisfied, then power from that mode is being

dissipated of transferred to other propagating modes.

Figure 5.20 shows the power loss factor evaluation resulting from EM simulation on both lossless and lossy substrates. Clearly for the lossless case we see that PLF evaluates different from zeros after 13 GHz (notice that for stripline PLF = 0 is verified within the entire band). Because on this case the substrate is lossless this can only mean that power from the *quasi*-TEM mode (the excited mode) is being coupled to higher modes such as surface waves and radiation modes. As expected and given the power loss due to modal power transfer, the PLF for the lossy case is significantly higher due to the substrates losses, *i.e.*, due to the power dissipation through heating within the substrate.

Figure 5.19 depicts the frequency response for both lossless and lossy EM simulations. We see that, up to 13 GHz both EM responses are in good agreement with the theoretical prediction (single mode simulation). However, the effects of power transfer to other modes becomes evident for frequencies above 13 GHz as both lossy and lossless frequency responses no longer accurately follow the theoretical frequency response. In Figure 5.19(a) the effects of the substrate losses are not visible as both EM simulations differ by only some tenths of dB. On the other hand, from the transmission frequency response in Figure 5.19(a) the effects of substrate losses become clear for higher frequencies.

Associated with the power loss factor, other factors contributing for the differences observed between EM and theoretical results have to do with microstrip dispersion, impedance to line width mapping accuracy, port impedance mismatch, EM solver mesh issues and spatial resolution, transverse resonance for regions with considerably low impedance (large line width) and mild fringing fields occurring at the low to high impedance transitions regions.

As a last step on the analysis of the stop-band Chebyshev filter, the 15 cm length prototype given in Figure 5.18 was implemented in a Rogers Duroid 4003 substrate, with a dielectric constant of 3.55 and a thickness 0.813 mm and measured using a vectorial network analyzer (VNA). The corresponding microstrip conductor layout is displayed in Figure 5.23.

Figure 5.21 shows the comparison between the measured results of the implemented filter and those obtained through theoretical and EM simulations. From the figure it can be seen that all three responses are very similar up to about 13 GHz and, as it was expected, however the measured response denotes a slight frequency shift to the left which can be explained by the dispersion effect on the effective permittivity. Moreover, for higher frequencies and although the frequency response has the same tendency as

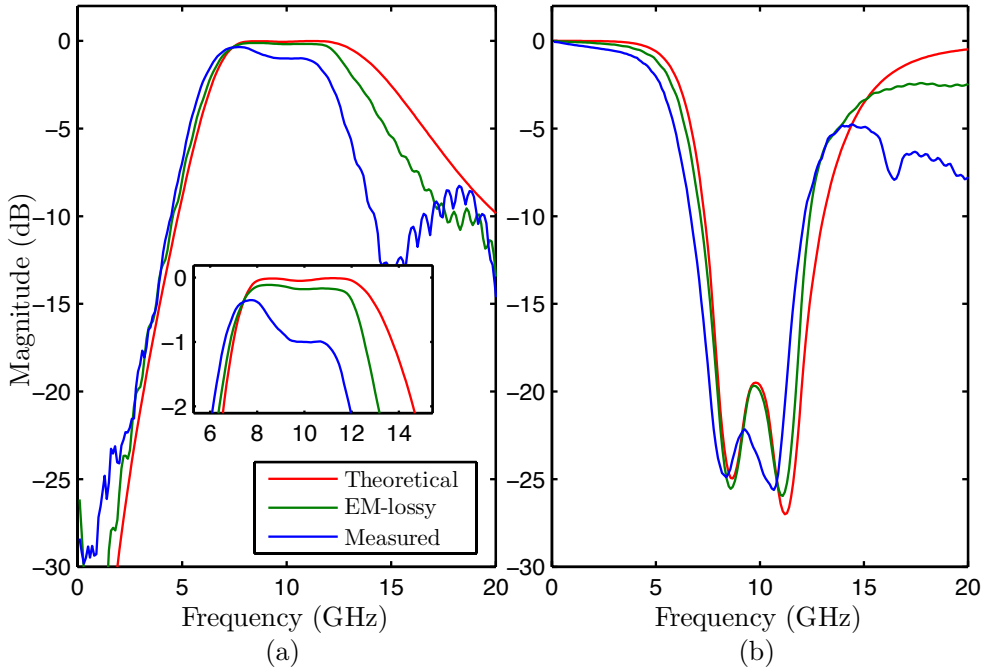

FIGURE 5.21: Comparison between the theoretical frequency response resulting from the analysis of the filter using the transmission matrix method, from lossy MoM electromagnetic simulation on Agilent ADS and from experimental results. In (a) is the reflection frequency response whereas in (b) is the associated transmission frequency response.

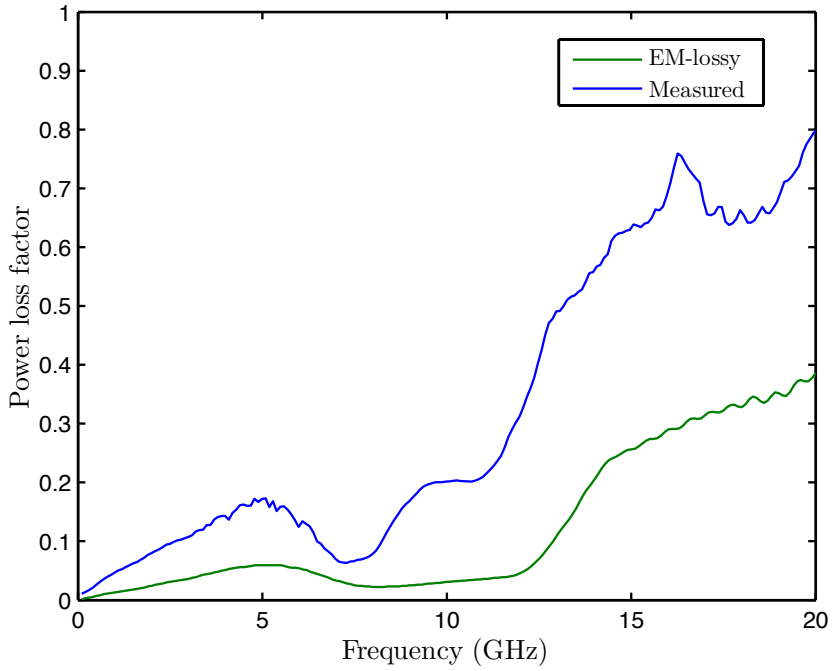

FIGURE 5.22: Power loss factor as a function of frequency resulting from lossy MoM electromagnetic simulation on Agilent ADS from experimental results, respectively.

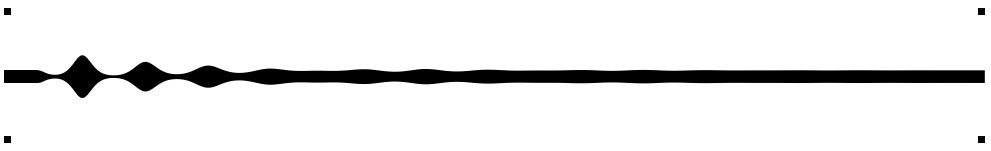

FIGURE 5.23: Filter layout

those from simulation, we clearly see that the experimental response starts to deviate from the simulation frequency responses which clearly cripples the performance of the filter for high frequencies. Notice however that this deviation is in accordance with the PLF results given in Figure 5.22, where we see that the experimental evaluation of the PLF is considerably higher throughout the entire frequency band. This is not unexpected however, as the physical implementation of the filter introduces a whole new set of unknown factors. Among these factors we must highlight the fotolitic process accuracy, which due to the handmade process used in manufacturing is a source inaccuracies, soldering problems, connector reflections at the coaxial to microstrip transitions.

From the previous analysis we conclude that, it is in fact feasible to synthesize a classical band-stop filter recurring to the inverse scattering theory. Furthermore, from the simulations results we clearly acknowledged both the synthesis algorithm, *i.e.*, the layer-peeling algorithm, as well as the theoretical analysis method, *i.e.* the transmission matrix method as being accurate, theoreticaly exact and numerically efficient methods. On the other hand, regarding the experimental results, we recognize that a high quality industrial-class fabrication process would naturally improve the experimental results.

So far on this section we have only consider the analises of a particular type-I Chebyshev filter. Nonetheless and so as to provide some theoretical insight over the synthesis of other types of classical band-stop filters, as well as to provide some useful synthesis data, we now provide some very useful information obtained from a series of theoretical parametric simulations and regarding the filter length and maximum impedance values (most important features) as a function of the multiple parameters which configure a classical filter, *i.e.*, bandwidth, central frequency, maximum reflectivity, filter order, pass-band and stop-ban ripple. Moreover, this information is in fact relevant as different type of filters have different behavior as a function of the filter parameters.

Figure 5.24 depicts the influence of the many filter parameters on the final filter length. Notice that the length information is obtained considering the filter truncation for a coupling energy of 95 % without windowing. Furthermore, the length evaluation as a function of a specific parameter is performed considering that the remaining parameters

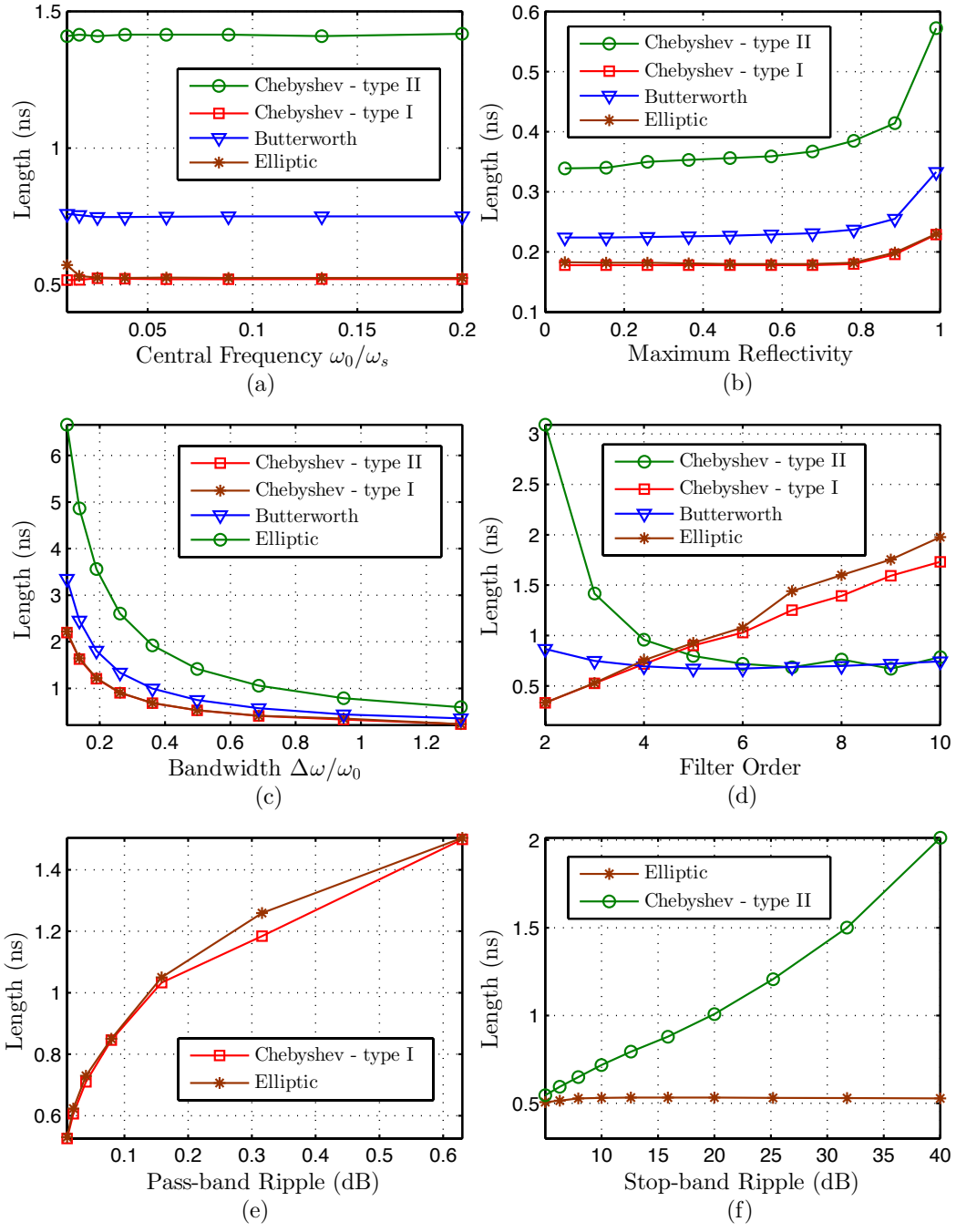

FIGURE 5.24: Physical length values associated with the impedance profiles resulting from the synthesis of classical band-pass filters. The length evaluation is performed independently for each filter parameter and for a coupling energy of 95%. Figures (a),(b),(c) and (d) depict the length evaluation as a function of central frequency, maximum reflectivity, bandwidth and filter order, respectively. Moreover, these evaluations are performed for Chebyshev type I and type II filters as well as for Butterworth and elliptic filters. Figures (e) and (f) depict the length evaluation as a function of the pass-band ripple for elliptic and type I Chebyshev filters and stop-band ripple for elliptic and type II Chebyshev filters respectively. When evaluating the impedance profile length as a function of a specific parameter, the remaining parameters are set to fixed default values. The considered default filter parameters are: central frequency of $\omega_0/\omega_s = 0.02$, a maximum reflectivity of 1, bandwidth of $\Delta\omega/\omega_0 = 0.5$, filter order 3, pass-band ripple of 0.01 dB and a stop-band ripple of 30 dB. The impedance profiles are obtained by computing the corresponding impedance profiles through the discrete layer-peeling algorithm as described in section 4.3.2.

are set to fixed default values, that is, central frequency of $\omega_0/\omega_s = 0.02$, a maximum reflectivity of 1, bandwidth of $\Delta\omega/\omega_s = 0.5$, filter order 3, pass-band ripple of 0.01 dB and a stop-band ripple of 30 dB.

It is interesting to notice that a quick inspection of the figure suffices to get some sensibility regarding the length of a filter for some specific configuration. For instance from Figures 5.24(a) and (c) we easily see that regarding the filter frequency parameters, the filter central frequency does not influences the length of the filter. The length is solely dependent on the selected bandwidth. Figure 5.24(b) indicates that the length of the filter is fairly constant up to 0.8 of maximum reflectivity (reflective pass-band amplitude). For higher reflectivity the length starts to grow exponentially. Figure 5.24(b) shows that the length for Chebyshev type-II filters decrease with increasing filter order and is fairly constant for Butterworth filters. On the other hand for elliptic and Chebyshev type-I filters, the length increases with increasing order. Finally the length of Chebyshev type-I and elliptic filters increases with increasing pass-band ripple amplitude, whereas the length of Chebyshev type-II filters increases with increasing stop-band ripple amplitude.

Figure 5.25 depicts the influence of the several filter parameters on the maximum impedance profile characteristic impedance value. Is is important to refer at this point that, the maximum impedance value evaluation is of most importance due to construction limitations. That is, the higher the impedance the thinner the transmission line, thus, very high characteristic impedances are not feasible due to manufacturing limitations. Within the scope of this work we consider the maximum feasible impedance to be located around $160\,\Omega$ (depending on substrate properties).

From Figure 5.25 we see that all filter parameters directly influence the maximum impedance value. The most critical however seem to be related to the frequency specifications. From Figure 5.25 (a) we see that lower central frequency filters have higher maximum impedance values. On the other hand and from Figure 5.25 (c) we conclude that filters with larger bandwidths have higher maximum impedance values. The same behavior is depicted in Figure 5.25 (b) for increasing maximum reflectivity. Figure 5.25 (d) shows that the maximum impedance for Chebyshev type-I and elliptic filters decreases with increasing order whereas the opposite behavior is observed for Chebyshev type-II filters. For Butterworth filters however, the maximum impedance seems to be independent from the filter order. Finally, Figure 5.25 (e) shows that the maximum impedance for Chebyshev type-I and elliptic filters decreases with increasing pass-band ripple amplitude.

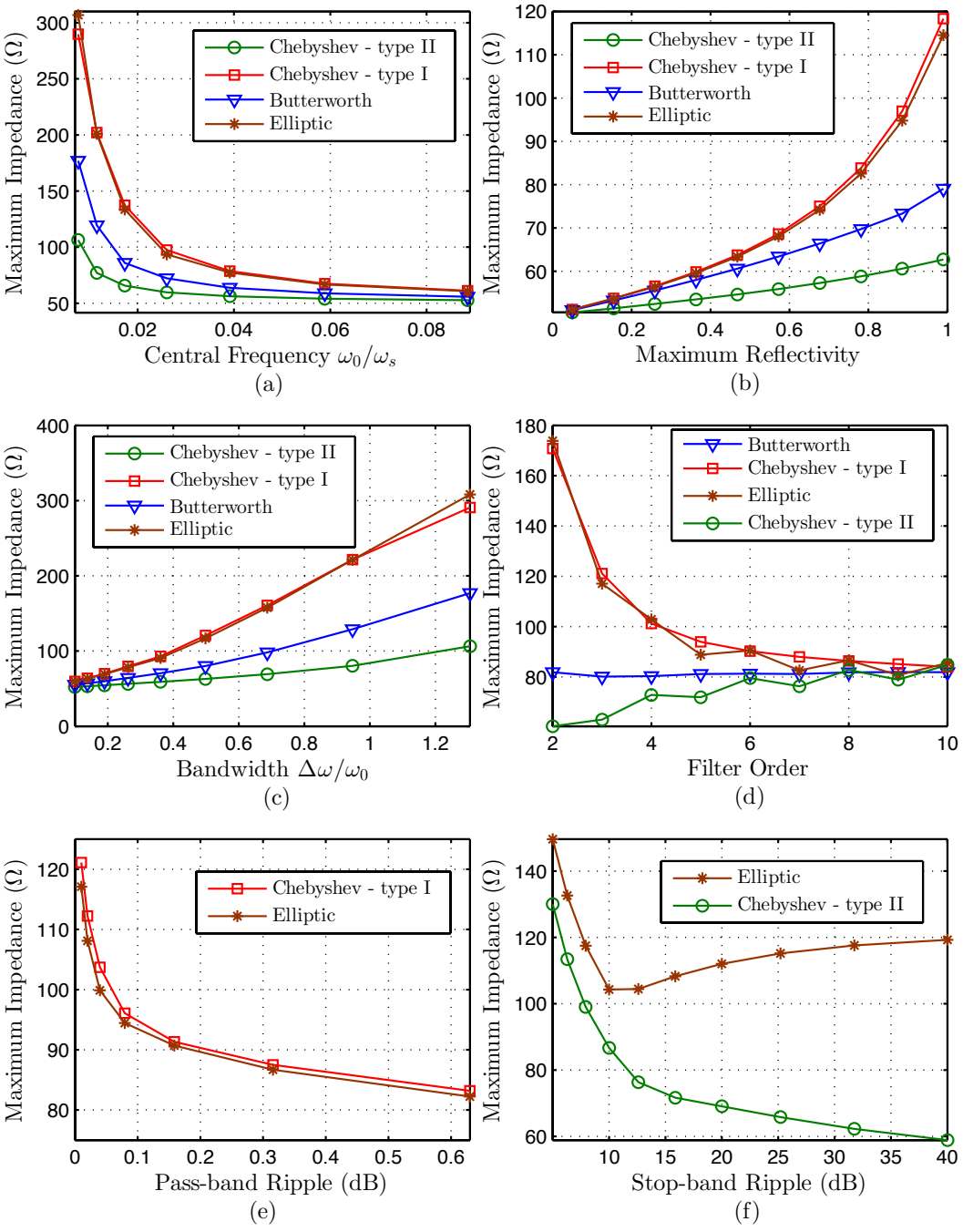

FIGURE 5.25: Maximum impedance values associated with the impedance profiles resulting from the synthesis of classical band-pass filters. The maximum impedance values are evaluated independently for each filter parameter. Figures (a),(b),(c) and (d) depict the evaluation of the maximum impedance as a function of central frequency, maximum reflectivity, bandwidth and filter order, respectively. Moreover, these evaluations are performed for Chebyshev type I and type II filters as well as for Butterworth and elliptic filters. Figures (e) and (f) depict the evaluation of the maximum impedance as a function of the pass-band ripple for elliptic and type I Chebyshev filters and stop-band ripple for elliptic and type II Chebyshev filters respectively. When evaluating the maximum impedance as a function of a specific parameter, the remaining parameters are set to fixed default values. The considered default filter parameters are: central frequency of $\omega_0/\omega_s = 0.02$, a maximum reflectivity of 1, bandwidth of $\Delta\omega/\omega_0 = 0.5$, filter order 3, pass-band ripple of 0.01 dB and a stop-band ripple of 30 dB. The impedance profiles are obtained by computing the corresponding impedance profiles through the discrete layer-peeling algorithm as described in section 4.3.2.

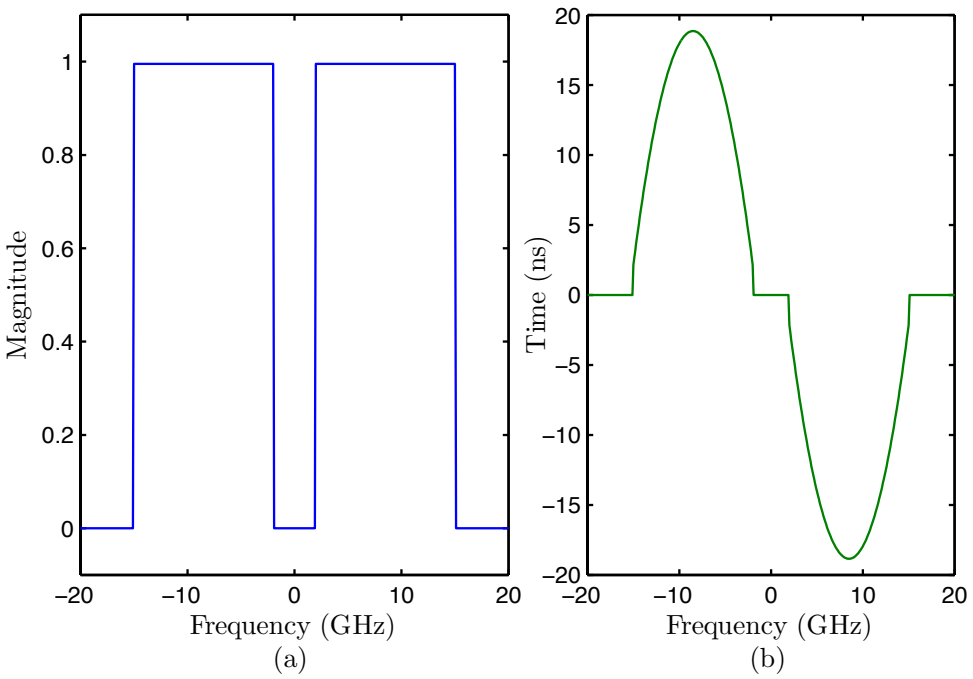

FIGURE 5.26: Ideal target frequency response. In (a) is the magnitude response of the ideal rectangular filter, whereas in (b) is the quadratic phase response characteristic of chirped delay lines.

5.2.2 Arbitrary reflection group delay band-stop filters

Inverse scattering methods prove to be very useful tools for the synthesis of classical microwave microstrip filters, as demonstrated in the previous chapter. In fact, inverse scattering theory methods prove to be very versatile since they are not only limited to the synthesis of classical filters such as Chebyshev, Butterworth and Bessel filters. In fact, with inverse scattering, any frequency response can be synthesized as long as that frequency response is physically realizable, *i.e.*, as long as it fulfills the realizability conditions discussed in section 4.2.1.1.

When performing filter synthesis using the layer-peeling algorithm, it is possible to synthesize microwave microstrip filters with both an arbitrary specified reflection magnitude response as well as an independently specified reflection phase response. Consequently, once control over the phase response is achieved, control over the reflection group delay is also obtained.

The ability to synthesize filters with arbitrary group delay response is in fact a very interesting capability as some applications for this type of synthesis are the design of dispersionless square filters with high reflectivities, the design of chirped delay lines [57],

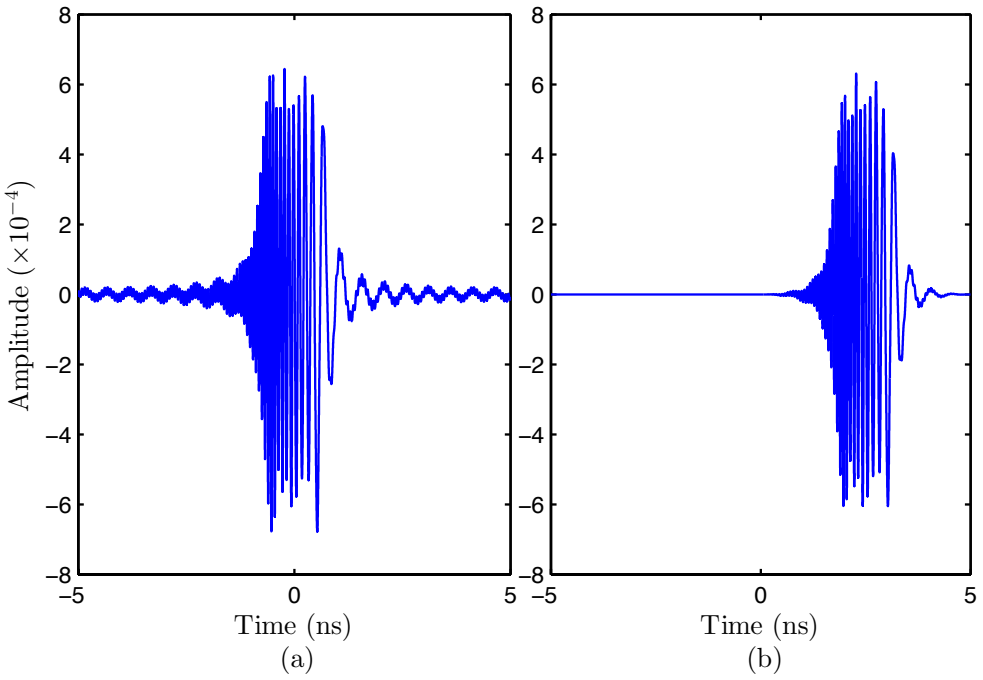

FIGURE 5.27: Impulse response modification accordingly to the realizability conditions. In (a) is the impulse response associate to the ideal filer given in Figure 5.26, whereas in (b) is the truncated and causal impulse response.

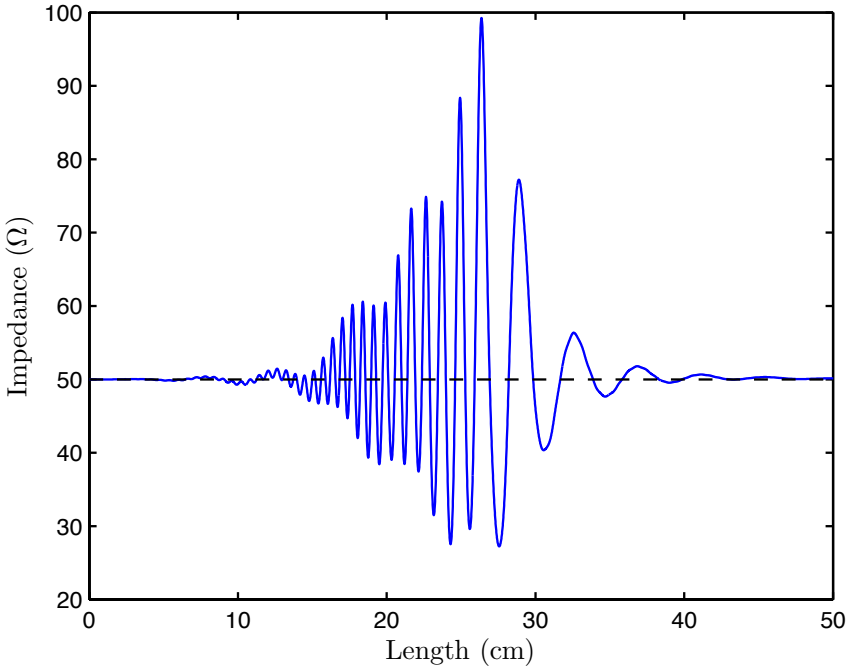

FIGURE 5.28: Chirped delay line impedance profile.

which in turn can be used in real time spectrum analysis [58] and also on the synthesis of dispersion compensating filters.

So as to demonstrate the necessary procedure for the synthesis of arbitrarily defined group delay response structures, we focus on the design of chirped delay lines.

Reflection chirped delay lines are filters characterized by uniform reflection losses, quadratic reflection phase response and thus linear reflection group delay.

The starting point for this synthesis procedure is to define the ideal and desired filter reflection response, both in magnitude and phase, *i.e.*,

$$H(\omega) = A(\omega) \cdot e^{j \cdot \phi(\omega)} \quad . \tag{5.13}$$

For the particular case of reflection chirped delay lines, the desired response is as shown in Figure 5.26, where the return loss $A(\omega)$ is uniform and equal to unity, and the phase $\phi(\omega)$ has quadratic shape, yielding a linear group delay. The corresponding group delay is defined as,

$$\tau(\omega) \quad = \quad -\frac{d\phi(\omega)}{d\omega} \quad . \tag{5.14}$$

Once the desired response is defined, the next step is to make this ideal response physically realizable. This is accomplished by modifying the impulse response of this ideal filter accordingly to the realizability conditions.

We now set our target frequency response to be similar similar to that in Figure 5.26, thus a standard chirped delay transmission line. Moreover we target a linear group delay with a slope of $2e^{-20}s^2/rad$ and an operation frequency band characterized by a center frequency of 8.5 GHz and a bandwidth of 13 GHz.

Figure 5.27 shows the impulse response of the specified target frequency response. In order to become physically realizable, we must modify the target frequency response so as to comply with the realizability conditions. Hence, the ideal target frequency response

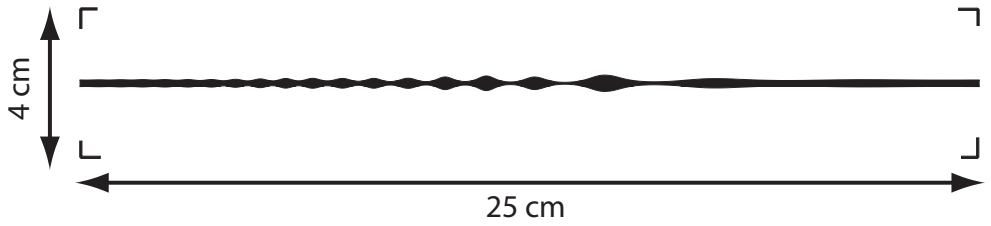

FIGURE 5.29: Chirped delay line layout.

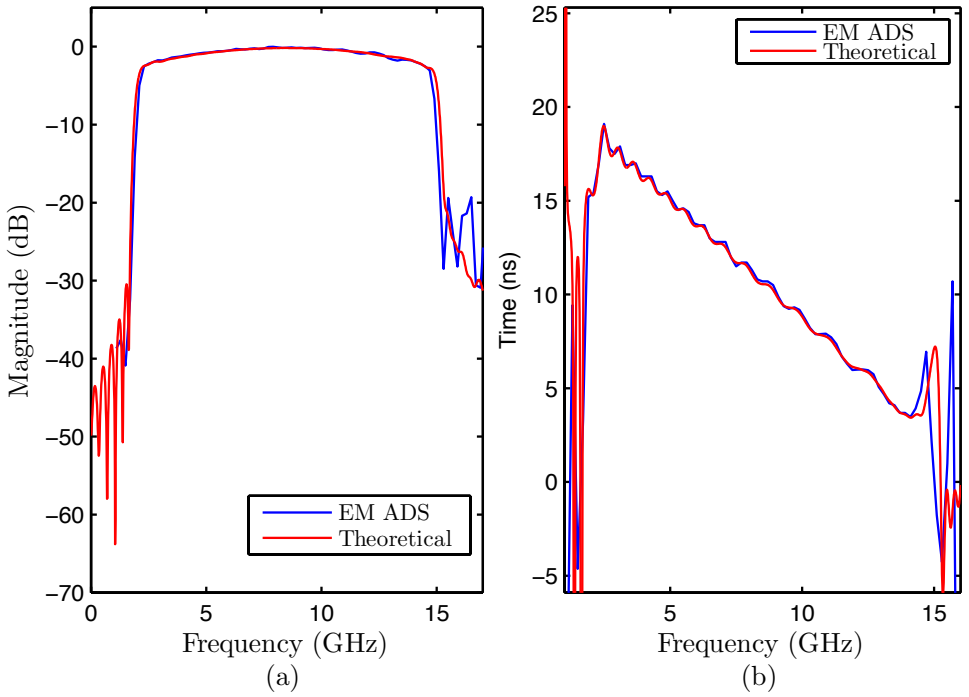

FIGURE 5.30: Reflection frequency response comparison between theoretical and electromagnetic simulations results. In (a) is the magnitude response, whereas in (b) is the phase response. The theoretical results were obtained using the TMM method whereas the EM simulation was performed on Agilent ADS.

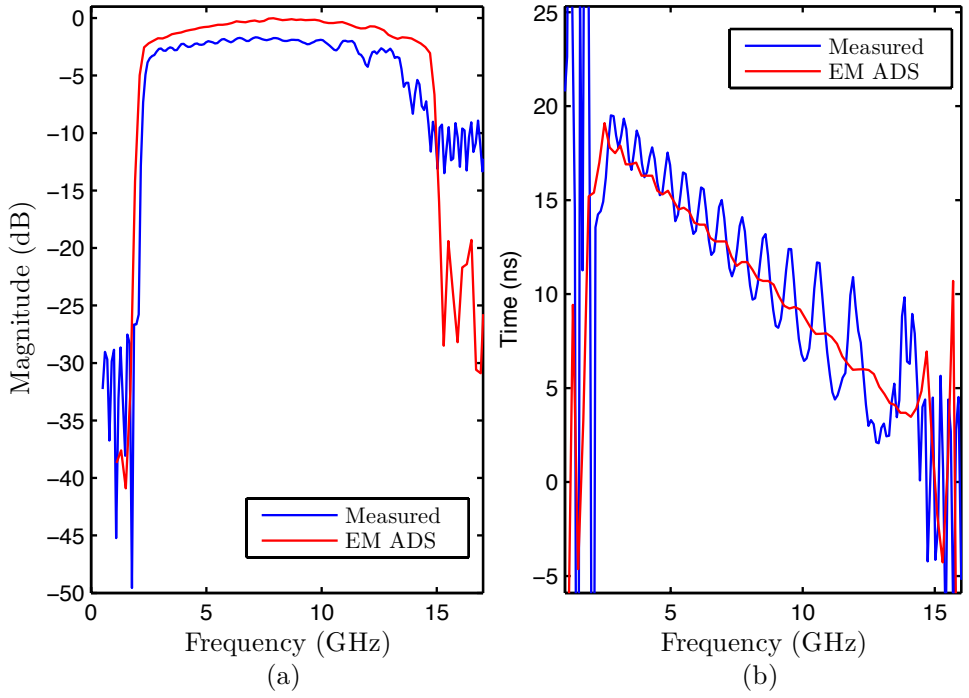

FIGURE 5.31: Reflection frequency response comparison between electromagnetic simulation and measurements results. In (a) is the magnitude response, whereas in (b) is the phase response. The EM simulation was performed on Agilent ADS.

has to be truncated, windowed and ultimately shifted to the right be made causal [54]. The end result of this process comes as the impulse response shown in Figure 5.27 (b). This new impulse response is referred to as the "target realizable impulse response". The corresponding inverse Fourier transform is the input data for the layer peeling algorithm.

The design method, *i.e.*, the layer-peeling algorithm is implemented in the Matlab environment and the data resulting from the inverse scattering procedure is the impedance profile of the filter, which is given in Figure 5.28.

In order to verify the design method, the reflective chirped delay line filter is implemented in microstrip technology.

The layout for the microstrip filter is depicted in Figure 5.29 and was implemented in a Rogers Duroid RO4003 substrate, with a dielectric constant of 3.38 and a thickness of 0.813 mm.

The filter was first simulated in Matlab using the transfer matrix method, *i.e.*, the theoretical simulation. The validity of the theoretical results are then verified with an electromagnetic simulation performed using the ADS "momentum" simulator. The corresponding result comparison is given in Figure 5.30. From the Figure it can be seen that both theoretical and electromagnetic simulation are in excellent agreement.

Figure 5.31 depicts the measurement results and corresponding comparison with the electromagnetic simulation results. From Figure 5.31 one can see that the measured response follows the electromagnetic simulation as expected, but exhibits ripple in the group delay response. Also the response for high frequencies becomes worst both in magnitude and group delay. One of the causes for these differences between the measurements and the simulation has to do with the SMA connectors and the transition from coaxial to microstrip, thus with the power transfer from the Quasi-TEM mode, which is the fundamental mode, to higher propagating modes such as surface waves and radiation modes.

In summary, a chirped delay line *i.e.* a linear group delay filter was successfully synthesized and construted, with the electromagnetic simulation results being in good agreement with those from theoretical simulation. This points out that the difference observed to the measured results has mostly to do with construction issues namely with the transition from coaxial to microstrip which is critical at high frequencies and originate higher propagation modes such as radiation modes.

5.3 Directional couplers

The wave propagation along sets of parallel conductors is a subject that has been investigated since the early ninety's. The first full mathematical analysis of transmission line directional couplers was performed in 1954 by Oliver [59]. Until then, and related with the problem of crosstalk, energy coupling between parallel conductors was regarded as an undesired phenomena. Therefore, all the research was focus on eliminating the coupling problem, rather then using it in all of its potential.

In his work, Oliver made a full mathematical analysis of the natural coupling between parallel transmission lines and was able to foresee the potential applications of such devices such as directional couplers, filters and transformers.

Later, in 1963, Young [60] has shown that every cascaded transmission line directional coupler has a cascaded stepped impedance transformer prototype, and that the reflection coefficient of this prototype is identical to the coupling coefficient of the cascaded directional coupler. Similarly, the transmission coefficient of the stepped impedance prototype is also identical to the transmission coefficient of the directional coupler.

As the work of Young strongly suggests, the design of directional TEM-mode coupling devices reduces to that of the so-called impedance transformer prototype which is nothing more than a nonuniform transmission line (NTL).

As we have shown before, inverse scattering is a very useful tool for the synthesis and design of nonuniform transmission line microwave filters . In fact, we have shown that inverse scattering allows for the synthesis of any physically realizable frequency response. Also the possibility of arbitrary reflection group delay response is addressed in the previous section, where the synthesis of chirped delay lines is described.

The analogy between stepped impedance transformers (or NTL filters) and cascaded directional couplers described by Young is the key idea to the work presented in this section as it allows us to extend the use of inverse scattering and all of its advantages to the synthesis of nonuniform TEM-mode directional couplers. In this section we describe the procedure for the synthesis of nonuniform directional couplers using inverse scattering, based on the microwave filter synthesis method described in the previous section. We also address the limitations of the procedure, namely synthesis level limitations, such as the feasibility of the prototype NTL filter as a nonuniform directional coupler, and also implementation constraints concerned with the fabrication of couplers in inhomogeneous media such as microstrip.

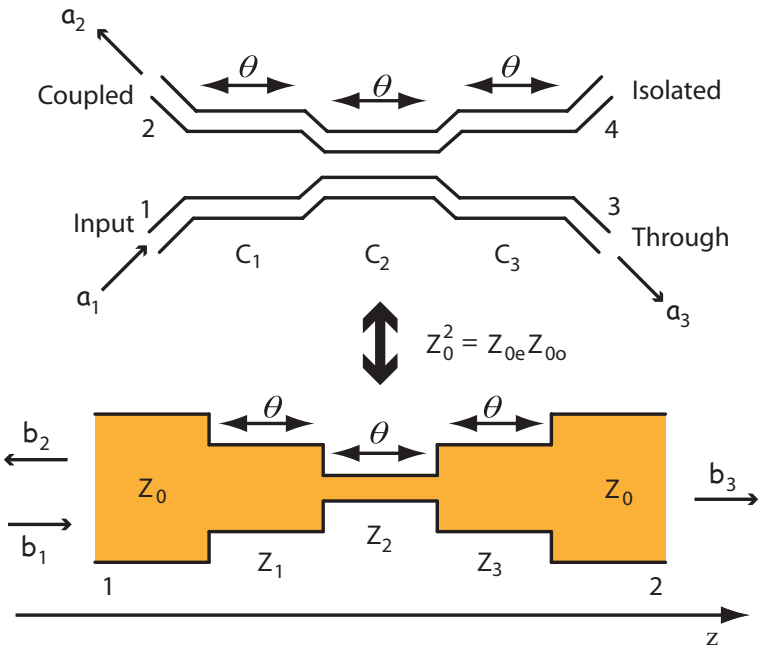

FIGURE 5.32: Equivalence principle of TEM-mode directional couplers and nonuniform transmission lines.

5.3.1 Equivalence principle

The configuration of directional couplers consists on two transmission lines parallel to each other and in close proximity. Since the lines are very close to one another, the electromagnetic fields of the wave traveling on one line induces a current on the other. This is how the coupling phenomena takes place. Hence, the overall electromagnetic field configuration along coupled lines is made by a linear combination of two different propagation modes. These modes are both TEM-modes and are usually referred to as the even-mode and the odd-mode respectively [5].

Figure 5.32 illustrates the equivalence principle reported by Young that relates TEM-mode directional couplers and nonuniform transmission lines. The top structure in Figure 5.32 is a 3-section nonuniform coupler and the bottom one is the corresponding NTL prototype. Provided that all four ports of the coupler are terminated with lines of characteristic impedance Z_0 and that both the even-mode impedance Z_{0e} and the odd-mode impedance Z_{0o} satisfy the condition

$$Z_0^2 = Z_{0e} Z_{0o}, \tag{5.15}$$

the equivalence principle states that the characteristic impedance profile $Z(z)$ of the prototype NTL is equal to the even-mode impedance profile $Z_{0e}(z)$ of the corresponding

nonuniform coupler. Under these conditions, the return loss of the NTL prototype is equal both in magnitude and phase to the coupled-arm response of the coupler

$$S_{11_{NTL}} = \frac{b_2}{b_1} = S_{21_{Coup}} = \frac{a_2}{a_1}, \tag{5.16}$$

also the insertion loss of the NTL is equal to the through-arm response of the coupler

$$S_{21_{NTL}} = \frac{b_3}{b_1} = S_{31_{Coup}} = \frac{a_3}{a_1}. \tag{5.17}$$

The equalities in equations (5.16) and (5.17) show that any method suitable for the synthesis and design of NTL filters is also applicable to the design and synthesis of nonuniform couplers, provided that TEM-mode operation is considered in both prototype NTL and coupler.

Regarding to Figure 5.32, the relation between the coupling coefficients along the coupler structure and the even- and odd-mode impedances is given by [5]

$$C_i = \frac{Z_{0e}^i - Z_{0o}^i}{Z_{0e}^i + Z_{0o}^i}, \tag{5.18}$$

where C_i, Z_{0e}^i and Z_{0o}^i are the coupling coefficient and the even- and odd-mode impedances for each section of the coupler (3 sections in the case of Figure 5.32). Rearranging equation (5.15) and substituting it into equation (5.18) we get

$$C_i = \frac{(Z_{0e}^i)^2 - Z_0^2}{(Z_{0e}^i)^2 + Z_0^2}. \tag{5.19}$$

Applying the equivalence principle to (5.19) we obtain

$$C_i = \frac{Z_i^2 - Z_0^2}{Z_i^2 + Z_0^2}, \tag{5.20}$$

where Z_i represents the impedance of each section of the prototype NTL. Equation (5.20) gives us the relation between the coupling coefficients along the coupler and the impedances along the prototype NTL filter.

5.3.2 Arbitrary coupling

In order to demonstrate the potential and versatility of the synthesis method, we next describe the procedure to synthesize a 13 dB coupler with a 5 GHz center frequency a

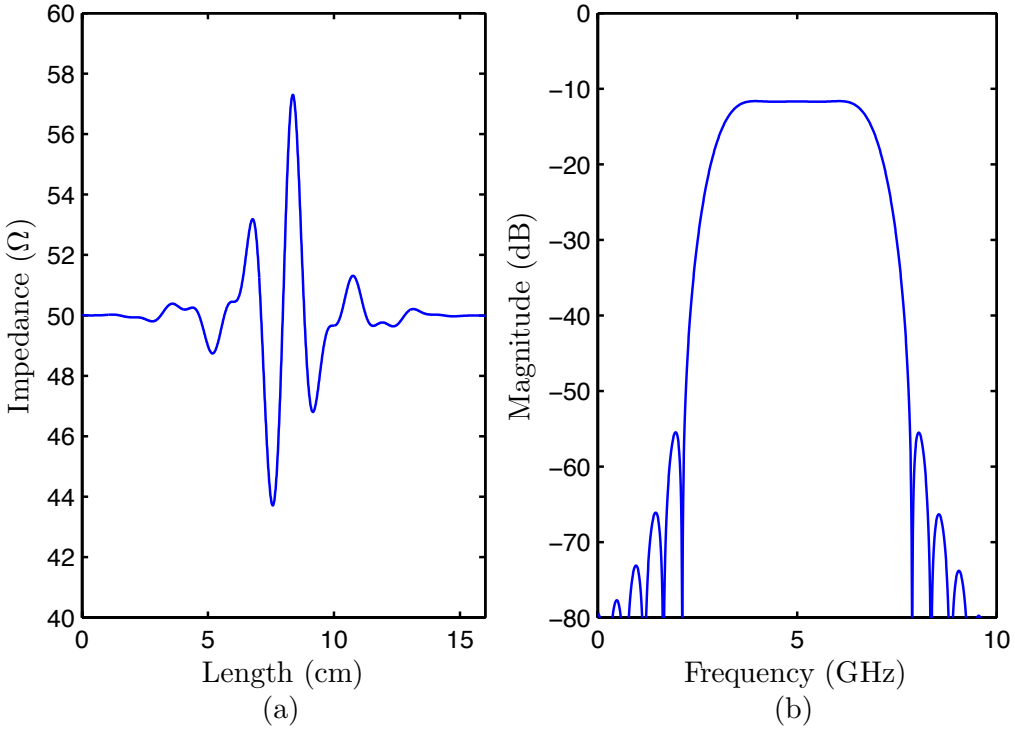

FIGURE 5.33: Nonuniform transmission line prototype filter. In (a) is the 16 cm long impedance profile whereas in (b) is the corresponding reflection frequency response.

3 dB bandwidth of approximately 3.5 GHz and a constant group delay (dispersionless coupler) within the coupling band.

The first step in the synthesis procedure is to design the prototype NTL filter. For that, we use inverse scattering theory. The synthesis procedure for the NTL fprototype is based on the discrete layer-peeling algorithm, which is described in detail in section 4.3.

Figure 5.33(a) shows the impedance profile of the prototype filter returned by the layer peeling algorithm whereas Figure 5.33(b) depicts the corresponding reflective frequency response. Note that unlike Figure 5.32 where the NTL prototype filter is composed by discrete impedance steps, we now have a continuous impedance profile prototype filter. The equivalence principle is still valid in this case, the only difference is that the corresponding coupler will not have a finite number of sections with constant coupling like the one in Figure 5.32 but will have a continuous coupling profile instead:

$$C(z) = \frac{Z^2(z) - Z_0^2}{Z^2(z) + Z_0^2}, \tag{5.21}$$

where $Z_0 = 50\,\Omega$ and $Z(z)$ is the impedance profile of the prototype filter. From equation

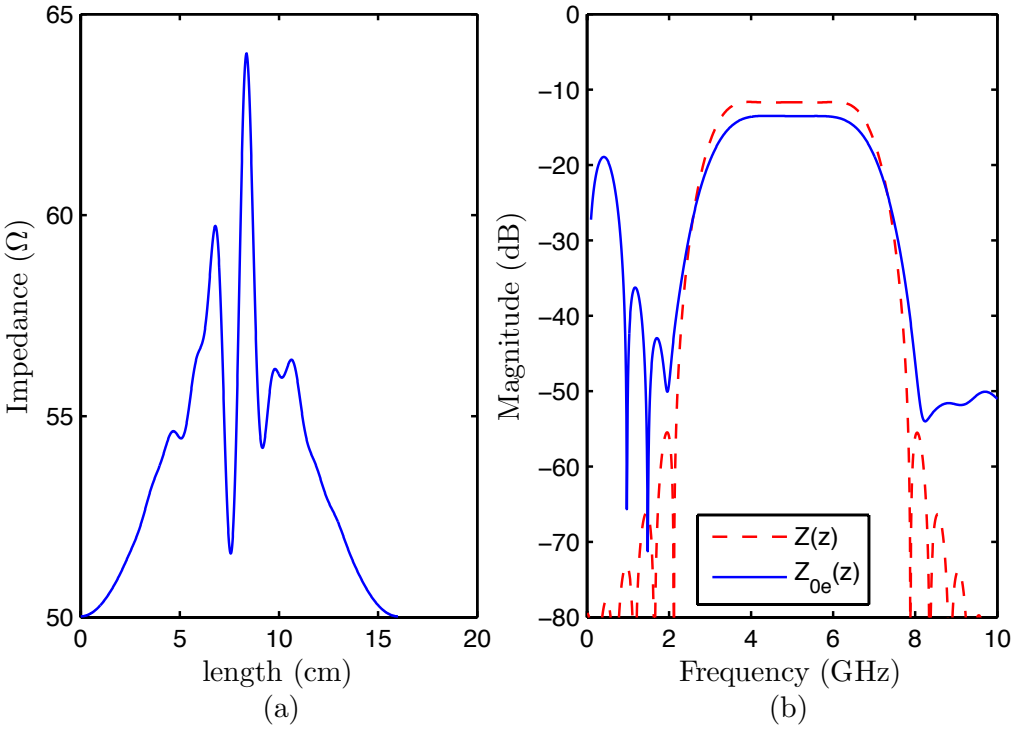

FIGURE 5.34: Nonuniform coupler prototype filter. In (a) the modified impedance profile, whereas in (b) is the corresponding frequency response.

(5.21) we can see that if $Z(z)$ is lower than Z_0 we will get negative coupling values which are not physically feasible. In order to obtain a positive set of coupling values along the length of the coupler, the values of $Z(z)$ must be made higher than or equal to Z_0. One way of achieving this, with minimum impact on the desired frequency response, is to add a *window* type function to the impedance profile of the prototype filter $Z(z)$. The new impedance profile, that we may now refer to as the even-mode impedance profile, is given by

$$Z_{0e}(z) = Z(z) + W(z), \tag{5.22}$$

where $W(z)$ is the windowing function. If the window function were to be a constant value, it would suffice to guarantee the feasibility of the coupler provided it was large enough. However, both at the beginning as well as at the end of the coupler, the even-mode impedance would be higher than Z_0 and so the coupler would not be matched, therefore the desired frequency response would be severely compromised. Because the minimum value of $Z(z)$ occurs approximately at the middle of the coupler, a Hamming window was used as the window function, resulting in the impedance profile of Figure 5.34(a).

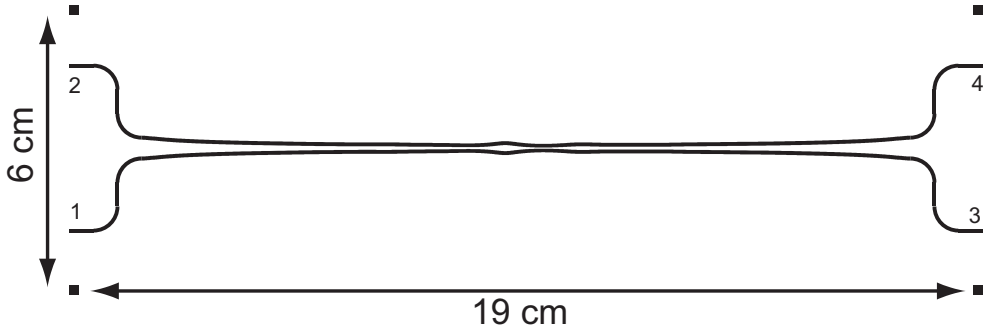

FIGURE 5.35: Coupler layout

Figure 5.34(b) compares the frequency response of the designed even-mode impedance profile with that of the NTL prototype. It is easily seen that a high coupling value band of roughly -20dB appears at around 0.5 GHz. Also the windowing process reduced the in-band coupling by around 2.5 dB and the roll-off rate has also been slightly reduced.

The most logical and easy way to implement the coupler would be in microstrip due to the cheap and rather simple construction procedure. However, due to the fact that microstrip lines are inhomogeneous, the propagation velocities of the even- and odd-mode are different, resulting in a significant distortion of the frequency response. Therefore, we chose to implement the coupler in stripline technology. The prototype coupler was implemented in a Rogers Duroid RO4003, with a dielectric constant of 3.55 and a thickness of $h = 0.813$mm. The physical dimensions of the coupler stripline (line width and spacing) were obtained by inserting the values of Z_{0e} calculated in the previous section and assuming a characteristic impedance of $Z_0 = 50\,\Omega$ in the ADS Linecalc application. The stripline conductor layout is displayed in Figure 5.35.

The fabrication process followed that of microstrip technology, but to achieve a

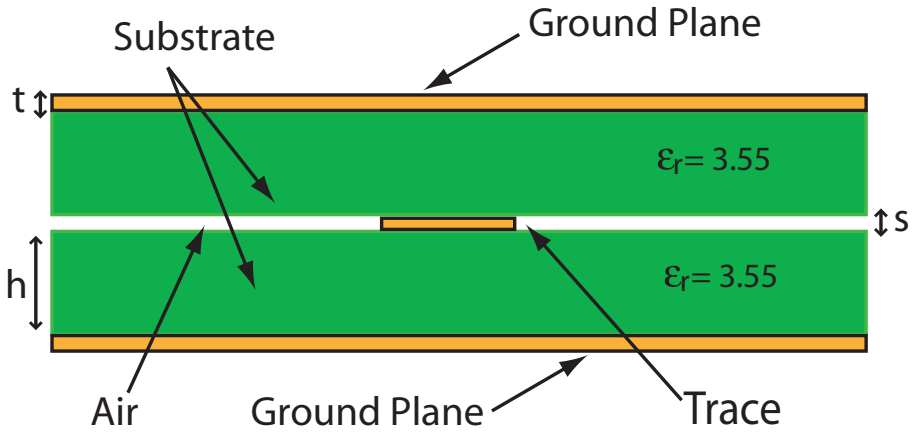

FIGURE 5.36: *Quasi*-stripline Configuration.

stripline configuration another slab of substrate with the corresponding ground plane was added on top of the microstrip strucute, just like it is illustrated in figure 5.36. Furthermore, via-holes are placed along the contour of the coupler structure in order to provide a proper connection between the two stripline ground planes and to minimize the air gap between the two slabs.

Up to now only theoretical simulations have been shown. These simulation were performed in Matlab environment. The method used to perform these simulations is the transmission matrix method presented in section 3.3. Notice that all the theoretical analysis performed in the previous sections was done considering TEM-mode propagation in a medium with effective dielectric permittivity of 3.55. We now present electromagnetic (EM) simulation results as well as measurement results. The electromagnetic simulations were carried out in Agilent ADS using the method of moments. In Figure 5.37 both theoretical and EM simulation results are presented for the magnitude of the coupled arm response $|S_{21}|$ and compared with the measurements. The theoretical and EM simulation results match very well, except for a small difference in amplitude in the coupling band. We hold the substrate losses accountable for this difference since no losses were considered in the theoretical simulations. Concerning the measured response, we clearly see an excellent agreement with the theoretical and EM simulation results. Figure 5.38 compares the results for the group delay of the coupled-arm response. In the coupling band, both experimental measurement and EM simulation results are in good agreement. The theoretical value of the group delay, however, is slightly lower than the measured one because the extra length of stripline on all ports necessary to accommodate the SMA connectors was not taken into account in this simulation.

In conclusion, we have successfully synthesized a wide-band dispersionless coupler using inverse scattering theory and managed to fabricate it in a quasi-stripline configuration. Moreover, the use of the inverse scattering method assures that any frequency response can be achieved, as long as the prototype NTL filter is feasible. As last, and although the measurement results are in good agreement with both theoretical and EM simulations, a stripline high quality industrial-class fabrication process would naturally improve the experimental results.

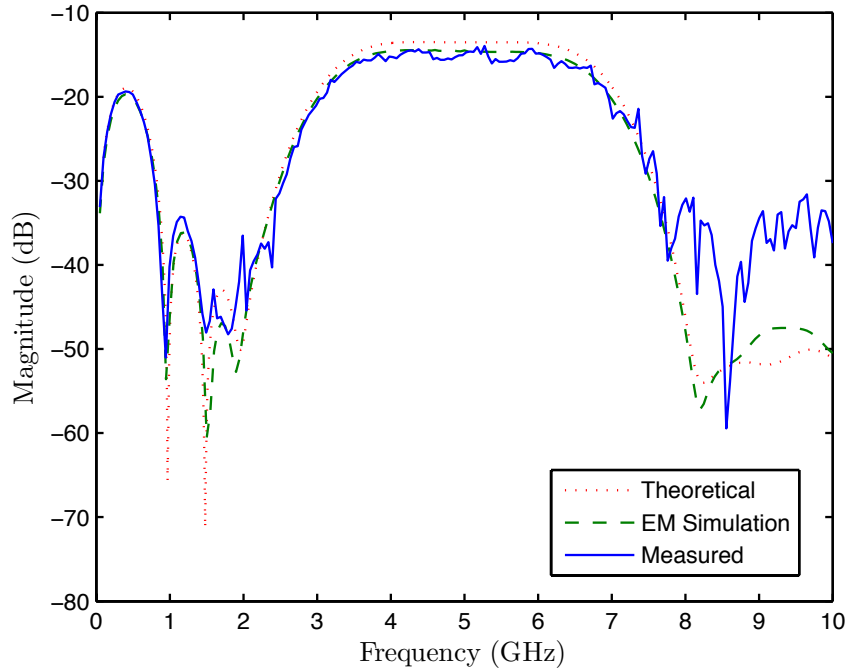

FIGURE 5.37: Coupled-Arm Frequency Response. Comparison between theoretical, electromagnetic simulation and measurements results. The theoretical results were obtained using the TMM method whereas the EM simulation was performed on Agilent ADS.

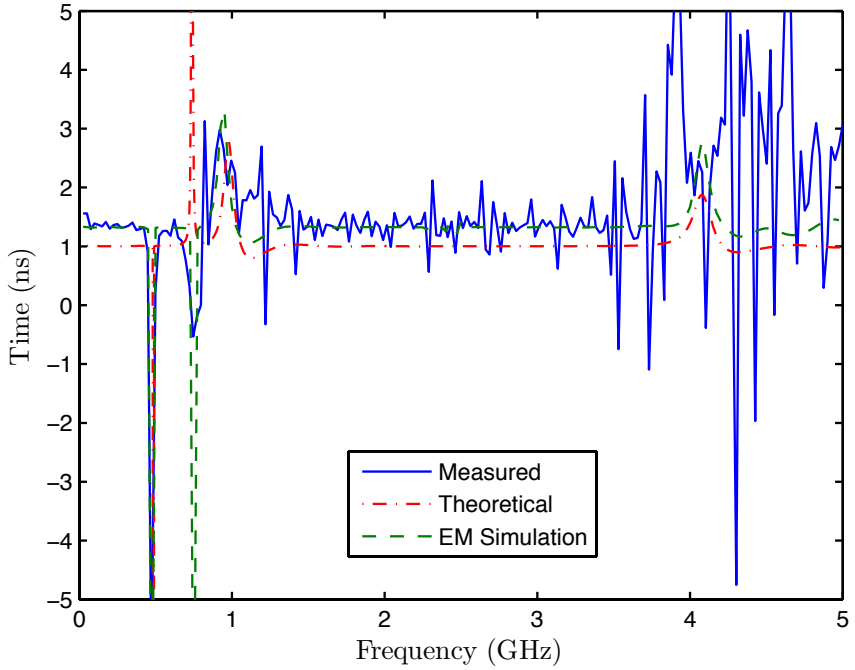

FIGURE 5.38: Coupled-Arm Group Delay Response. Comparison between theoretical, electromagnetic simulation and measurements results. The theoretical results were obtained using the TMM method whereas the EM simulation was performed on Agilent ADS.

5.4 Summary

The potential and versatility of the inverse scattering theory on the synthesis of nonuniform transmission line based structures is demonstrated in this chapter. Here, we address the synthesis of several passive microwave devices, namely: bandstop filters, filters with arbitrary reflective group delay response and TEM directional couplers with arbitrary coupling response. Additionally, we assess the impact of the truncation and windowing procedures on the synthesis of classical band-stop filters and identify the optimum windowing configurations which reduce the truncation error on the approximation to the ideal frequency response. The influence of the different classical filter parameters on the length and maximum characteristic impedance values of the synthesized filters is evaluated and finally the synthesis procedures is evaluated through a comparative study between numerical, analytical and EM simulations as well experimental measurements.

Chapter 6

Discrete nonuniform transmission line structures

6.1 Introduction

In this chapter we introduce the concept of *Discrete Nonuniform Transmission Lines* (DNTL) which we may consider to be a particular kind of NTL structure. Unlike in the previous chapters where the term *Nonuniform Transmission line* is associated to structures consisting of a transmission lines with a continuous and smooth varying impedance profile, as it is illustrated in Figure 6.1(a), we now consider the case of discrete transmission lines where the impedance profile no longer has a smooth variation. We define a DNTL as an NTL that is constituted by a cascade of commensurate sections of transmission line with constant impedance and physical length l as illustrated in Figure 6.1(b).

So far, all the NTL structures that have been synthesized in the previous chapters are all based on nonuniform transmission line structures with a smooth impedance profile.

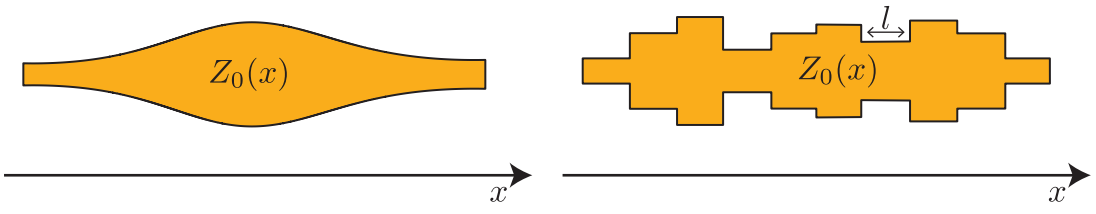

(a) Continuous NTL structure. (b) Discrete NTL structure.

FIGURE 6.1: Continuous impedance profile versus discrete impedance profile nonuniform transmission lines.

We have also seen that any arbitrary reflection frequency response (both in phase and magnitude) can be achieved provided that the realizability conditions are fulfilled (see section 4.2.1.1). However, and despite the good results obtained from a functional point of view, thus proving the usefulness and versatility of this technique, the outcome of these inverse scattering techniques usually results in very long structures which poses some problems as the size is usually a constrain for the designer. To some extent, this size property is due to the fact that the starting data (desired frequency response) given to the inverse scattering procedure is not the adequated one to provide a minimum length filter or structure for the application at hands. For instance, in the case of filter design, most of the times the designer is only interested on the magnitude response. On other applications only the passband magnitude shape and cutoff frequency are of importance and the stop-band characteristic is of no importance or can be relaxed. Furthermore, when designing a filter, most of the times the designer is only focusing on a certain band of operation and this band of operation is usually very small. With this we mean to say that because the inverse scattering methods as we have been using them up until now take into consideration the hole frequency spectrum, there is an infinite number of different "starting data" (frequency response) that can be fed to the algorithm (while maintaining the band of operation with the same desired response) that will always provide the desired performance in the operational band. However, because outside of this band the frequency response is of no interest, i.e. it can have any shape (both magnitude and phase but fulfilling the realizability conditions), the inverse scattering procedures will produce different results in terms of both length and maximum and minimum characteristic impedances. Therefore, in order to achieve the optimum NTL filter or structure in terms of both performance and size we must first realize what is the optimum "starting data" for the inverse scattering procedures. One way of accomplish that is to realize the direct relation existing between DNTL structures and digital filters.

6.2 Discrete NTL structures properties

The DNTL concept proposed in this chapter is actually not new to this thesis. In fact, in section 3.3.2 we have considered the DNTL approximation model in the analysis of CNTL structures under the alias of "constant impedance discretization". Also, in section 4.3, more specifically during the study of the DLP inverse scattering method we have considered the DNTL model (which we then refer to as the "constant impedance

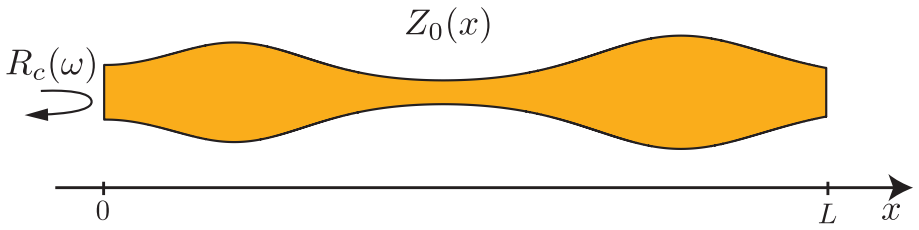

(a) Continuous NTL structure as obtained from the analytical IS method.

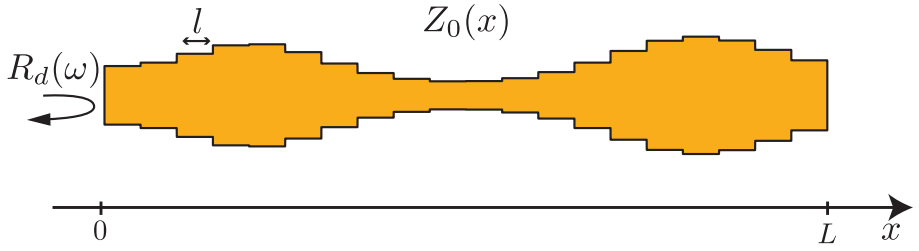

(b) Discrete NTL structure as obtained from the DLP IS algorithm.

FIGURE 6.2: Continuous impedance profile versus discrete impedance profile nonuniform transmission lines. Both NTL lines are the result of different inverse scattering procedures but considering the same inverse scattering problem.

discrete NTL model") to be the basis of the DLP IS algorithm. Regarding the later, we actually saw that the outcome of the DLP IS procedure inherently translates into pure DNTL structures and thus, we consider the DLP IS method to be an exact inverse scattering procedure with regards to the synthesis of DNTL structures.

In sections 3.3.2 and 4.3, the DNTL model was used as an approximation model which due to its properties (a stack of constant impedance layers) simplified the analysis and synthesis procedures of CNTL structures as is allows the use of simple recursive relations. In this chapter however, we turn our attention to the synthesis of actual DNTL structures. Thus, the DNTL model is no longer consider to be an approximation, since DNTL structures are the physical type of structures that we aim to synthesize. This in turn makes the DLP IS algorithm the method of choice as it is an exact inverse scattering procedure regarding the synthesis of DNTL structures. That being said, we can now use the knowledge acquired in section 4.3 regarding the DLP method and further use it in the synthesis of DNTL structures.

First and foremost, let us derive some properties of the DNTL structures, some of them already addressed in section 4.3. Consider the CNTL depicted in Figure 6.2(a). Let us suppose that this CNTL structure was obtained as the result of an analytical inverse scattering procedure when considering the reflection frequency response depicted in Figure 6.3(a) as the target spectrum response. This is therefore the ideal case in which no NTL approximation model is used and a closed and exact analytical expression for

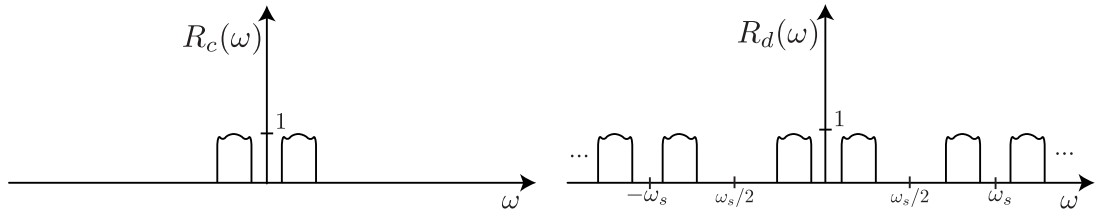

(a) Continuous NTL reflection frequency response. (b) Discrete NTL reflection frequency response.

FIGURE 6.3: Possible spectral response for the CNTL and DNTL structures depicted in Figure 6.2.

the impedance profile $Z_0(x)$ is obtained as a result from the IS procedure as in the example considered in section 4.2.2. Now let us assume that instead of an analytical IS procedure we use the DLP algorithm to solve the same inverse scattering problem. In this case, and because we are using a differential inverse scattering method our solution is going to have a numerical nature. The outcome of the DLP IS method is the DNTL structure illustrated in Figure 6.2(b). Basically, the resulting DNTL is a stair-shaped version of the CNTL. However the reflection frequency response for this structure is no longer the target spectrum but instead, a frequency repetition of the target response with period ω_s as it is depicted in Figure 6.3(b). Please recall from section 4.3 that the length of each section of the DNTL returned by the DLP algorithm is given in seconds (travel time) by equation (4.228) as

$$l = \frac{\pi}{\omega_s}, \tag{6.1}$$

thus establishing the relation between the length of each section and the spectral repetition period. Moreover, equation (6.1), demonstrates how in spite of the results returned by the DLP algorithm are given as DNTL structures, the DLP algorithm can still be used for synthesizing CNTL structures. In equation (6.1) we see that the relation between the sampling frequency ω_s and the sections length is inversely proportional. Let us take a closer look to Figure 6.2 which depicts the results of two different inverse scattering procedures for the same IS problem. It is evident that the smaller the length consider for the sections of the DNTL structure the closest is the result of the DLP procedure to that of the analytical procedure. Thus, in the limit case, where the layers become infinitesimal small *i.e.*, $l \to 0$ the DLP solution actually comes as a CNTL structure which matches the one obtained through the analytical IS procedure. In this case we have that $R_d(\omega) = R_c(\omega)$. Please note that the equivalence between both spectral

responses when considering the limiting case can also be obtained by considering the inverse proportionality between l and ω_s expressed by equation (6.1) . Therefore, in the limit case where $l \to 0$ we have that $\omega \to \infty$, hence the frequency response depicted by Figure 6.3(b) becomes the same as $R_c(\omega)$.

From the analysis of the NTL structures depicted in Figure 6.2(b), we have seen that under the restriction of very small sections length the solution provided by the DLP algorithm approximates that of the integral IS methods. Please note that the same principle applies to the CLP IS algorithm. In fact, all the prototype NTL structures synthesized in the previous chapters are CNTL structures and were obtained though the DLP procedure under the restriction of very small sections length. In summary, all the inverse scattering methods analyzed in Chapter 4 are suitable to perform the synthesis of CNTL structures. With more or less accuracy, all of them, whether they are differential IS methods (CLP and DLP) or integral equation based IS methods (exact analytical solution, numerical solution, iterative solution), produce the same result, regarding the synthesis of CNTL structures.

Unlike integral IS methods, the results provided by the DLP inverse scattering method do not necessarily have to come as CNTL structures. In fact, and particularly in the case of the DLP algorithm we have already seen that the solutions produced by this inverse scattering procedure are given in the form of discrete NTL structures. This in turn makes the DLP algorithm an inherently exact method regarding the synthesis of DNTL structures.

This being said, we can now use the knowledge acquired in section 4.3 regarding the DLP method and apply it in the synthesis of pure DNTL structures. We start by exploiting the properties associated with the discrete nature of the DNTL structures.

From section 4.3 we have seen that the reflection frequency response associated to DNL structures is given as a sum of weighted complex exponentials (4.223) yielding

$$R_d(\omega) = \sum_{n=0}^{\infty} h_n \, e^{j\omega nT}. \tag{6.2}$$

Please regard the periodicity of $e^{j\omega nT}$ as a function of ω. Due to this periodicity property we have that for $\omega = 0$ and $\omega = \omega_s$ the evaluation of the complex exponential yields the same value *i.e.*, they correspond to the same discrete-time signal, moreover, the frequencies near these values or any other even multiple of $\omega_s/2$ correspond to low frequencies. Similarly, the high frequencies correspond to the values near the odd multiples of $\omega_s/2$.

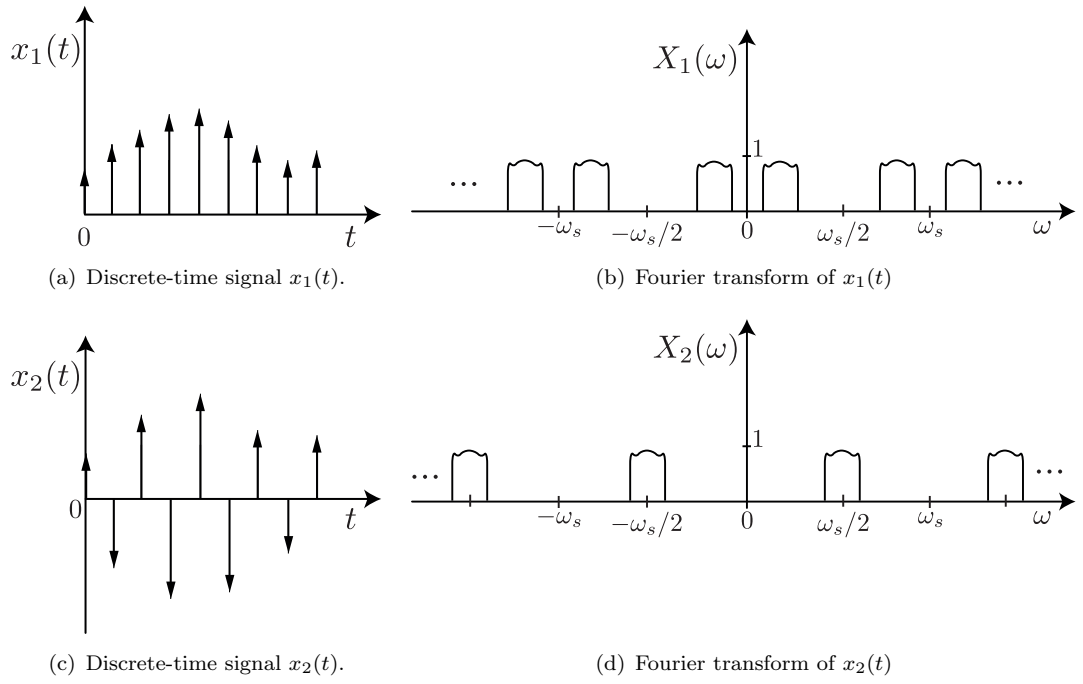

(a) Discrete-time signal $x_1(t)$.

(b) Fourier transform of $x_1(t)$

(c) Discrete-time signal $x_2(t)$.

(d) Fourier transform of $x_2(t)$

FIGURE 6.4: Comparison between the spectrum of slowly varying discrete-time signals and that of rapidly varying signals. In (a) and (c) are depicted the slowly and rapidly varying signals respectively, whereas in (b) and (d) are illustrated the corresponding frequency spectrums.

This periodicity of the complex exponential function justifyes the spectrum periodicity observed for DNTL structures as it is illustrated in Figure 6.3(b). Furthermore, as seen from Figure 6.3, the spectral response of the DNTL structure $R_d(\omega)$ consists on the frequency repetition of the entire spectral response of the continuous counterpart $R_c(\omega)$. Let us consider the following discrete-time complex exponential with frequency $(\omega_0+\omega_s)$

$$e^{j(\omega_0+\omega_s)Tn}. \tag{6.3}$$

We know that $\omega_s = 2\pi/T$, thus, equation (6.3) simplifies to

$$e^{j(\omega_0 T+2\pi)n} = e^{j\omega_0 Tn}\, e^{j2\pi n} = e^{\omega_0 Tn}. \tag{6.4}$$

From equations (6.3) and (6.4) we clearly see that the discrete-time signals with frequencies ω_0 and $(\omega_0+\omega_s)$ actually correspond to the same discrete-time signal. In fact, signals with frequencies $(\omega_0 \pm 2\omega_s)$, $(\omega_0 \pm 4\omega_s)$ and so on, are also equal to that with frequency ω_0. Therefore, when considering discrete-time signals, we need only to consider a frequency interval of length ω_s in which to identify all the frequencies that compose the signals. Along this thesis we shall consider that interval to be $-\omega_s/2 \leq \omega \leq \omega_s/2$.

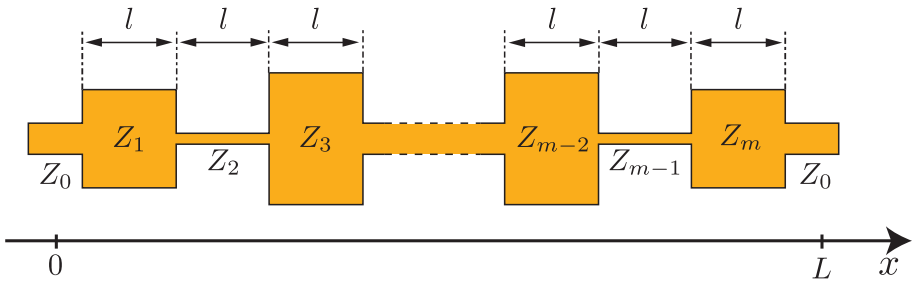

FIGURE 6.5: DNTL structure with m layers. This DNTL is the result of the DLP IS method when considering a target response of the type of that considered in Figure 6.4(d). The structure is constituted by a cascade of alternating low- and high-impedance sections of uniform TL.

Also, and due to the periodicity inferred by equation (6.4), discrete-time signals do not have a continually increasing rate of oscillation as their frequency ω_0 is increased in magnitude. Rather, as we increase ω_0 from 0 to $\omega_s/2$ there is a correspondent rise in the rate of oscillation, however, as we proceed to increasing the value of ω_0 we decrease the rate of oscillation down to zero which is when we reach $\omega_0 = \omega_s$. Therefore, we conclude that the slowly varying (low frequency) discrete-time signals have their frequency spectra near 0, $\pm\omega_s$, $\pm 2\omega_s$, or any other even multiple of ω_s whilst the rapidly varying (high frequency) discrete-time signals have their frequency spectra concentrated around $\pm\omega_s/2$ or any other odd multiples of $\omega_s/2$. This property of discrete-time signals is illustrated in Figure 6.4. In the figure we can clearly see that the slowly varying signal $x_1(t)$ is constituted by a spectrum of frequencies that cluster near even multiples of $\omega_s/2$, whereas for the rapidly varying signal $x_2(t)$ the frequency cluster comes around the odd multiples of $\omega_s/2$.

Let us now consider that the bidirectional transformation $q(x) \leftrightarrow R(\omega)$ is in some sense analogous to the Fourier transform. Indeed, as it is shown in section 3.2.3 this is actually a valid approximation under the assumption of weak coupling. Hence, we can use the Fourier transform approximation to infer some basic properties. Namely, we realize that applying the DLP inverse scattering method to a frequency spectrum in which all the frequencies cluster around even multiples of $\omega_s/2$ but at the same time are relatively far from $\omega_s/2$, such as the one in Figure 6.4(b), will translate in a slow varying coupling coefficient similarly to $x_1(t)$, which in turn results in an DNTL structure that approximates a CNTL structure. An example would be the DNTL structure depicted in Figure 6.2(b). On the other hand, applying the DLP inverse scattering method to a frequency spectrum in which all the frequencies cluster around odd multiples of $\omega_s/2$, such as the one in Figure 6.4(d), translates in rapidly varying coupling coefficient similar

to $x_2(t)$, which in turn results in a DNTL structure such as the one illustrated in Figure 6.5. Taking a closer look at Figure 6.4(c) we see that a coupling coefficient with the same time-domain behavior as that of $x_2(t)$, thus a rapid varying coupling coefficient, will be constituted by a train of pulses which are alternating positive and negative. On the other hand, the evaluation of the pulses is given by the local reflection coefficient (reflection coefficient between adjacent layers) which in turn explains the alternating low- and high-impedance nature of the DNTL depicted in Figure 6.5.

We know that the length for the sections of any DNTL structure is given by equation (6.1) in seconds (travel time). Considering the transformation from travel time x (seconds) to physical length z (meters) accordingly to (4.158)

$$z = v_p\, x \tag{6.5}$$

and considering the propagation velocity to be the speed of light ($v_p = c$), we have that the length in meters of each section in a DNTL structure such as the one in Figure 6.5 evaluates as

$$l = c\,\frac{\pi}{\omega_s} = \frac{c\,\pi}{2\pi\, f_s} = \frac{\lambda_s}{2}, \tag{6.6}$$

where c is the speed of light and λ_s is the sampling frequency wavelength.

One important property regarding the type of DNTL structures as the one depicted in Figure 6.5 lies in the fact that the length l of the DNTL sections are of same order of magnitude of that of the wavelength of the sampling frequency. This is easily verified by comparing the spectrum of Figure 6.4(b) with that of Figure 6.4(d) in the frequency range $-\omega_s/2 \leq \omega \leq \omega_s/2$. Notice that in order for $x_1(t)$ to be a slowly varying discrete-time signal, the frequency values of $X_1(\omega)$ must be clustered around $\omega_s = 0$. Furthermore, the sampling frequency must be several orders of magnitude higher than the maximum frequency value in $X_1(\omega)$. On the other hand we clearly see that the frequency values of $X_2(\omega)$ (rapidly varying signal) are in the same order of magnitude of that of the sampling frequency. Hence we have that for the structure in Figure 6.5 the length for each section is half of the wavelength of the sampling frequency which in turn is comparable to the wavelength of the frequencies in $X_2(\omega)$. As a result, the physical length for the sections of a DNTL structure with a rapidly varying discrete-time impulse response are considerably larger than that of a DNTL structure with a slowly varying discrete-time impulse response.

It is important to realize that, for a kind of spectrum as is $X_1(\omega)$, the DNTL resulting from the DLP inverse process can approximate the results provided by integral IS methods provided that ω_s is set to a sufficiently high value. Therefore, in some sense the differential IS methods and the integral IS method are equivalent. On the other hand the type of structures obtained through DLP IS based on frequency responses such as $X_2(\omega)$ can only be obtained by using the DLP inverse scattering method. This is thus, a clear advantage of the DLP inverse scattering procedure over the other procedures, as it proves to be a more versatile IS method when compared to the integral based IS methods.

Now that we have cleared some of the most relevant properties of DNTL structures, we shall demonstrate the direct relation between DNTL structures and digital filters and how we can take advantage of the the vast set of tools developed along the years on the field of digital signal processing in order to analyze and design NTL structures.

6.3 Discrete NTL structures and digital filters

The relationship between DNTL structures and digital filters has already been briefly referred in section 4.3 (by means of the equations (4.223) and (4.225)) when analyzing the DLP IS procedure, yet the link with digital filters was not fully exploited. In order to do so, we start by recalling the differences between *analog domain* and *digital domain*.

The term *analog* indicates something that is mathematically represented as a function of a set of continuous values. As an example of analog signals we have the impulse responses $h(t)$ and $r(t)$ which can be depicted in Figure 6.6(a) and Figure 6.6(c), respectively. Please note that, unlike $h(t)$ that has a continuous amplitude variation, $r(t)$ has a discrete amplitude variation (array of Dirac deltas), however, both are analog signals as the independent variable t is continuum ($\mathbb{R}$-domain). That is, $r(t)$ can be interpreted as the result of the sampling process of a continuous-time signal $g(t)$ with sampling period T which is evaluated for any value of t as zero except for multiples of T. On the other hand, we have the digital-domain (discrete-time), in which the signals are represented as sequences, as it is illustrated in Figure 6.6(e). Unlike in the analog-domain where the signals are represented as a function of a continuous independent variable, in the digital domain the independent variable is discrete. In the conversion from the sampled impulse response (impulse train $r(t)$) to discrete-time sequence we obtain $r[n]$ which corresponds to the same sequence of samples of $r(t)$ but with unitary spacing regarding

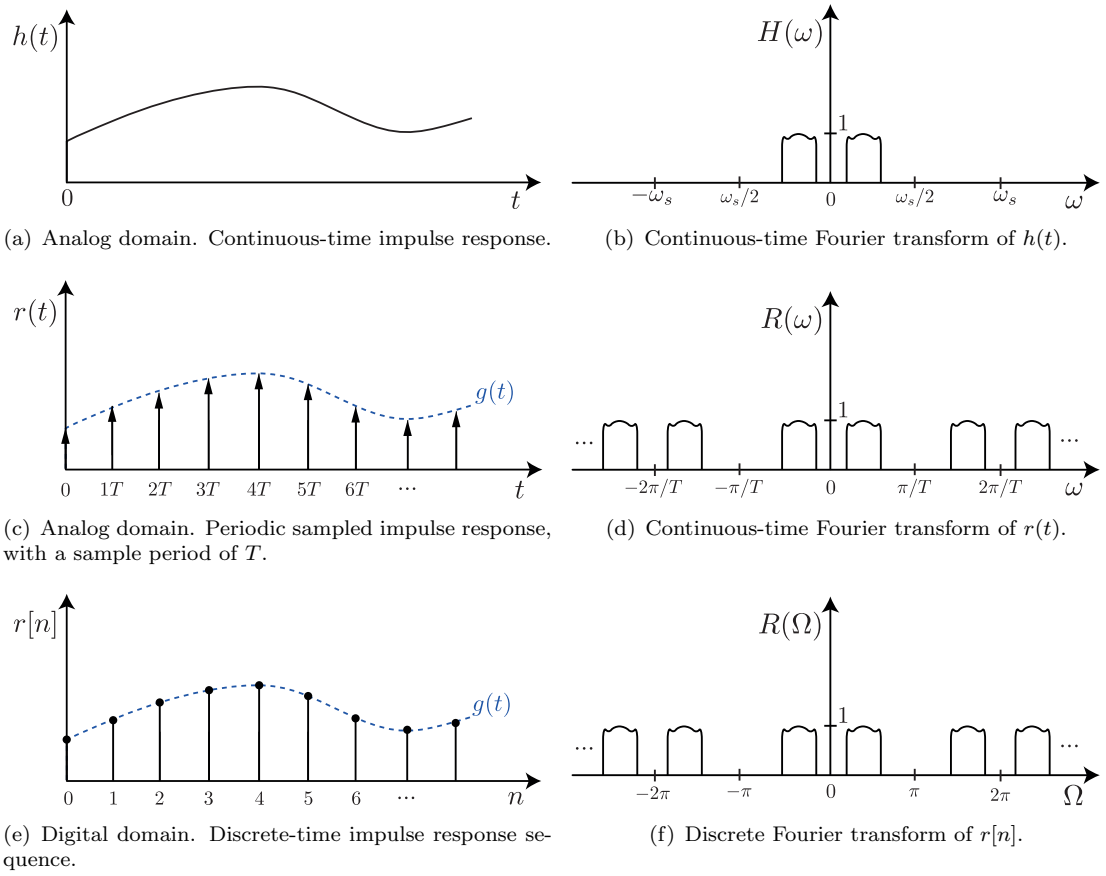

(a) Analog domain. Continuous-time impulse response.

(b) Continuous-time Fourier transform of $h(t)$.

(c) Analog domain. Periodic sampled impulse response, with a sample period of T.

(d) Continuous-time Fourier transform of $r(t)$.

(e) Digital domain. Discrete-time impulse response sequence.

(f) Discrete Fourier transform of $r[n]$.

FIGURE 6.6: Relationship between analog domain and digital domain.

the new independent variable n. Figure 6.6(e) depicts the impulse response sequence $r[n]$ corresponding to the analog counterpart $r(t)$. The Dirac deltas are substituted by Kronecker deltas which are the respective digital counterparts. Please note that unlike $r(t)$, the digital sequence $r[n]$ is only evaluated for integer numbers ($\mathbb{Z}$-domain). The discrete sequence $r[n]$ is then related to the analog counterpart $r(t)$ through

$$r[n] = g(nT), \tag{6.7}$$

where $g(t) = T\,h(t)$.

In short, a continuous-time signal (analog-domain) unlike a discrete-time signal (digital-domain) is a function of a continuous argument, however, it can be converted to the digital-domain by sampling from a continuous-time signal $g(t)$ as depicted in Figure 6.6(c). Thus each value in the digital sequence $r[n]$ is called a sample. Also, when a discrete-time signal is obtained by sampling a sequence in uniformly spaced times, it has an associated sampling rate T which is not apparent in the digital data sequence, and

so needs to be associated as a separate data item.

In many applications, there is a significant advantage in processing an analog domain signal by first converting it into the digital domain. Clearly the inverse scattering method using the DLP method is one of those applications. Two reasons make the DLP method suitable for discrete-time processing. First, because the DLP inverse scattering method is a numerical and recursive procedure, its implementation must carried out in a computer or microprocessor as a routine which in itself implies digital signal processing. Secondly, and most importantly, we have that (as seen in section 4.3), the discrete nature of the DNTL model considered as the basis of the DLP method, intrinsically leads to discrete-time responses as it is illustrated in Figure 6.6(c) which makes it suitable for digital processing.

Please note that, in fact, all of the IS methods considered so far are subjected at some point to a numerical manipulation. Even the analytical methods studied in Chapter 4.2 are subject to some sort of numerical discretization whether we are considering the numerical solution for the GLM integral equations, or even in the case where an actual analytical expression can be derived for the impedance profile some kind of discretization must be introduced when considering the computational handling and preparation to physical implementation.

The relationship between analog-domain and digital-domain as considered in the particular case of DNTL structures is illustrated in Figure 6.6. Regarding Figure 6.6(c) we easily see that the sampled impulse response $r(t)$ is given by

$$r(t) = \sum_{n=0}^{\infty} g(nT)\,\delta(t - nT). \tag{6.8}$$

The corresponding frequency response is then computed through the Fourier transform of (6.8) yielding

$$R(\omega) = \sum_{n=0}^{\infty} g(nT)\,e^{-j\omega nT}. \tag{6.9}$$

Now for the digital counterpart $r[n]$, let us consider the discrete-time Fourier transform

$$R(\Omega) = \sum_{n=0}^{\infty} r[n]\,e^{-j\Omega n}, \tag{6.10}$$

where we consider Ω to be the digital frequency variable.

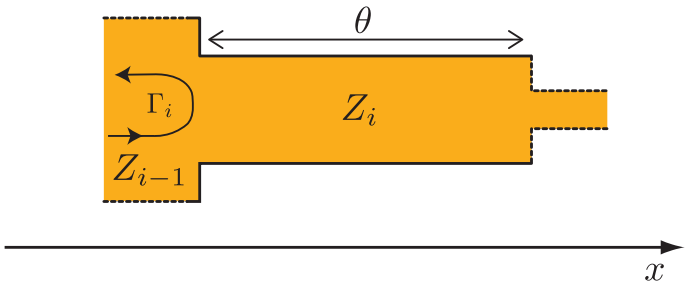

FIGURE 6.7: Single section of a DNTL structure. It is constituted by a reflector (impedance junction) characterized by a reflection coefficient of Γ_i followed by a section of uniform TL (pure propagation section) with electrical length θ.

The relationship between analog- and digital-domain becomes apparent by comparing equations (6.9) and (6.10), thus

$$r[n] = g(nT), \tag{6.11}$$

$$\Omega = \omega\, T. \tag{6.12}$$

The similarity between $R(\omega)$ and $R(\Omega)$ becomes evident from Figures 6.6(d) and 6.6(f). Both are periodic, however, the digital spectrum $R(\Omega)$ is periodic in Ω always with period 2π. This periodicity is a characteristic of any discrete-time Fourier transform and consequently a characteristic of any discrete-time system.

Now that we have seen some of the most important properties of DNTL structures and how they can be related to the digital domain we shall now proceed to reformulate the *discrete NTL model* (section 3.3.2) using Z-transform techniques. In order to do so, let us consider an n-section cascade connection of transmission line junctions as the one illustrated in Figure 6.5, where each junction is separated by a transmission line of length l. We know from section 3.3.2 that the frequency response of these kind of structures can be calculated by multiplying the transmission matrices of each section or layer as

$$[M] = [T_0][T_1][T_2]\cdots[T_{m-1}][T_m], \tag{6.13}$$

where the transmission matrix for each section is given by an impedance junction characterized by a reflection coefficient Γ_i followed by a pure propagation section, as illustrated in Figure 6.7, yielding

$$[T_i] = \frac{1}{\sqrt{1-\Gamma_i^2}} \begin{bmatrix} e^{j\theta} & \Gamma_i e^{-j\theta} \\ \Gamma_i e^{j\theta} & e^{-j\theta} \end{bmatrix} \tag{6.14}$$

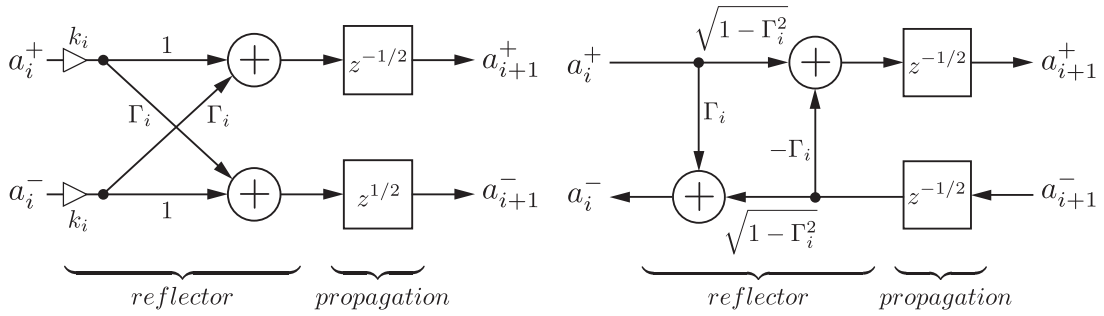

(a) Transmission diagram, where $k_i = (1-\Gamma_i^2)^{-1/2}$. (b) Causal scattering.

FIGURE 6.8: Wave propagation for the discrete nonuniform transmission line model in the digital domain.

where θ is the electrical length of each section and is given by

$$\theta = \beta l. \tag{6.15}$$

Please note that we consider the spatial variable x in Figure 6.7 to be the traveling time (see section 4.2 equation (4.86)), thus the electrical length reduces to

$$\theta = \omega\tau, \tag{6.16}$$

which in turn can be specified in the digital-domain as

$$\theta = \frac{\Omega}{2}, \tag{6.17}$$

where Ω is the digital frequency variable.

Since the NTL model is inherently discrete we can conveniently convert the transmission matrix model from the frequency domain to the Z-domain simply by defining the unit delay z^{-1} as

$$z^{-1} = e^{-j2\theta} = e^{-j2\omega\tau} = e^{-j\Omega}, \tag{6.18}$$

where $\tau = T/2$ is the propagation time for a single layer, whereas T is the round-trip propagation time.

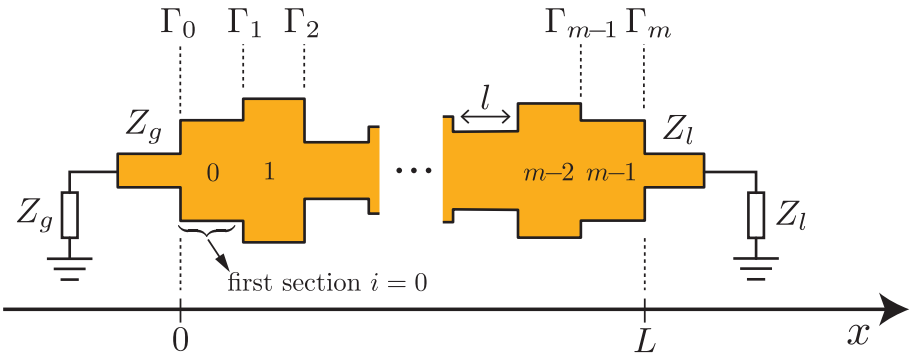

FIGURE 6.9: Typical application for DNTL structures. Both input and output ports are terminated with matched loads.

Considering the variable change in equation (6.18) the transmission matrix for a single DNTL section (Figure 6.7) now comes as

$$[T_i] = \underbrace{\frac{1}{\sqrt{1-\Gamma_i^2}}\begin{bmatrix} 1 & \Gamma_i \\ \Gamma_i & 1 \end{bmatrix}}_{reflector} \underbrace{\begin{bmatrix} z^{1/2} & 0 \\ 0 & z^{-1/2} \end{bmatrix}}_{propagation\ \ delay} = \frac{1}{\sqrt{1-\Gamma_i^2}}\begin{bmatrix} z^{1/2} & \Gamma_i z^{-1/2} \\ \Gamma_i z^{1/2} & z^{-1/2} \end{bmatrix}. \tag{6.19}$$

Figure 6.8(a) depicts the signal flow-graph representation of the wave propagation along the DNTL section illustrated in Figure 6.7 as defined by equation (6.19). Analyzing the diagram, we note the presence of an time-advance operator $z^{1/2}$ which does not correspond to a causal signal flow as it would be expected from a DNTL structure. However, a physically meaningful representation can be obtained through standard flow-graph manipulation techniques [5]. Particularly, we can reverse the direction of signal flow for the backward propagating wave a^- which will convert the time-advance operator into a causal time-delay operator. The resulting causal signal flow-graph representation is illustrated in Figure 6.8(b). Please note that the causal diagram can be mathematically described as

$$[S] = \begin{bmatrix} \Gamma_i & \sqrt{1-\Gamma_i^2}\, z^{-1/2} \\ \sqrt{1-\Gamma_i^2}\, z^{-1/2} & -\Gamma_i z^{-1} \end{bmatrix} \tag{6.20}$$

which translates into the scattering matrix for a single DNTL section. The same result can be obtained mathematically through algebraic rearrangement (see section 2.5, equation (2.159)).

Let us now consider the DNTL structure illustrated in Figure 6.9. This is a typical application for NTL structures, where both ports are terminated with matched loads thus avoiding reflections. In fact, in Figure 6.9, the DNTL structure itself is completely

defined between $x = 0$ starting with the first reflector Γ_0 and $x = L$ ending with the last reflector Γ_m, regardless of the length of the uniform transmission lines that connect the structure both to the source and to the load. Please note that the uniform transmission line sections at both ends contribute only with a linear phase factor to the overall frequency response. Now, from equation 6.13 we have that the mathematical characterization of the DNTL structure in Figure 6.9 is computed through the multiplication of the transmission matrices of the individual sections, where each section is comprised of a reflector followed by an uniform TL of length l. Although this would actually characterize the DNTL structure, it is not in agreement with the interpretation made from Figure 6.9 as it would also account for the extra uniform TL of length l connecting the DNTL to the load Z_l. This would in turn add a linear phase factor to the overall frequency response. Taking a closer look at the DNTL in Figure 6.9 we easily see that between $x = 0$ and $x = L$ the structure is comprised of m propagation sections (uniform TL) and $m + 1$ reflectors. Thus the overall transmission matrix $[M]$ for the DNTL structure now becomes

$$[M] = \begin{bmatrix} A_{11} & A_{12} \\ A_{21} & A_{22} \end{bmatrix} = \underbrace{\left[\prod_{i=0}^{m-1} \begin{bmatrix} A_{11_i} & A_{12_i} \\ A_{21_i} & A_{22_i} \end{bmatrix}\right]}_{m \text{ sections}} \underbrace{k_m \begin{bmatrix} 1 & \Gamma_m \\ \Gamma_m & 1 \end{bmatrix}}_{\text{last reflector}}, \tag{6.21}$$

where $k_m = (1 - \Gamma_m^2)^{-1/2}$.

Furthermore, by considering the individual transmission matrices in the Z-domain (6.19) we have that the elements of $[M]$ can be expressed as polynomials in the variable z^{-1}. Thereafter, both the transmission and reflection frequency responses

$$\begin{aligned} S_{11}(z) &= \frac{A_{21}(z)}{A_{11}(z)}, \\ S_{21}(z) &= \frac{1}{A_{11}(z)}, \end{aligned} \tag{6.22}$$

are given as rational functions of polynomials in z as we shall prove next. Please note that the frequency reflection and transmission responses relate to $S_{11}(z)$ and $S_{21}(z)$ as

$$S_{11}(\Omega) = S_{11}(z)\big|_{z=e^{j\Omega}}, \tag{6.23}$$

$$S_{21}(\Omega) = S_{21}(z)\big|_{z=e^{j\Omega}}. \tag{6.24}$$

We now are going to compute the transmission matrices accordingly to (6.21) for

three different DNTL structures. Namely, we consider the cases for $m = 0$, $m = 1$ and $m = 2$. For the first case, $m = 0$, [M] is simply given by

$$[M] = k_0 \begin{bmatrix} 1 & \Gamma_0 \\ \Gamma_0 & 1 \end{bmatrix}, \tag{6.25}$$

in the second case $m = 1$ the overall transmission matrix is given by

$$[M] = k_0 k_1 \begin{bmatrix} z^{1/2} + \Gamma_0\Gamma_1 z^{-1/2} & \Gamma_1 z^{1/2} + \Gamma_0 z^{-1/2} \\ \Gamma_0 z^{1/2} + \Gamma_1 z^{-1/2} & \Gamma_0\Gamma_1 z^{1/2} + z^{-1/2} \end{bmatrix}, \tag{6.26}$$

whereas for $m = 2$ the transmission matrix translates into

$$[M] = k_0 k_1 k_2 \begin{bmatrix} z^1 + (\Gamma_0 + \Gamma_2)\Gamma_1 + \Gamma_0\Gamma_2 z^{-1} & \Gamma_2 z^1 + (1 + \Gamma_0\Gamma_2)\Gamma_1 + \Gamma_0 z^{-1} \\ z^1\Gamma_0 + (1 + \Gamma_0\Gamma_2)\Gamma_1 + \Gamma_2 z^{-1} & \Gamma_0\Gamma_2 z^1 + (\Gamma_0 + \Gamma_2)\Gamma_1 + z^{-1} \end{bmatrix}, \tag{6.27}$$

where $k_i = (1 - \Gamma_i^2)^{-1/2}$.

From equations (6.25) to (6.27) we see that the mathematical expression for the elements of $[M]$ starts to become cumbersome after $m = 2$. However, by comparing equation (6.26) to equation (6.27) we can easily see that the elements in $[M]$ for any m can be expressed as

$$A_{11}(z) = z^{m/2} \sum_{i=0}^{m} \alpha_i \, z^{-i}, \tag{6.28}$$

$$A_{21}(z) = z^{m/2} \sum_{i=0}^{m} \beta_i \, z^{-i}, \tag{6.29}$$

$$A_{22}(z) = z^{m/2} \sum_{i=0}^{m} \alpha_{m-i} \, z^{-i}, \tag{6.30}$$

$$A_{12}(z) = z^{m/2} \sum_{i=0}^{m} \beta_{m-i} \, z^{-i}, \tag{6.31}$$

where α_i and β_i are real coefficients computed from the reflection coefficients Γ_i. Furthermore, from the analysis of (6.26) and (6.27) it can be shown that

$$A_{22}(z) = A_{11*}(z), \tag{6.32}$$

$$A_{12}(z) = A_{21*}(z), \tag{6.33}$$

where the subscript asterisk stands for the para-Hermitian conjugate operation. The para-Hermitian conjugate of any function of z such as $A_{11}(z)$ is defined by

$$A_{11*}(z) = A_{11}^{*}(1/z^{*}), \tag{6.34}$$

where the superscript asterisk stands for the complex conjugate operation. When operated over polynomial functions the para-Hermitian conjugate has the effect of reversing and complex conjugating the polynomial coefficients, *i.e.*,

$$A_{11*}(z) = z^{m/2} \sum_{i=0}^{m} \alpha_{m-i}^{*} \, z^{-i}, \tag{6.35}$$

however in the case of DNTL structures the polynomial coefficients are real valued, thus equation (6.35) simplifies to the relation (6.33). Notice that the the para-Hermitian conjugate is equal to the complex conjugate[1] only on the unit circle.

From equations (6.32) and (6.33) we have that the overall transmission matrix for any DNTL structure can be expressed in the form

$$[M] = \begin{bmatrix} A_{11}(z) & A_{21*}(z) \\ A_{21}(z) & A_{11*}(z) \end{bmatrix} \tag{6.36}$$

which satisfy

$$\det([M]) = A_{11}(z)A_{11*}(z) - A_{21}(z)A_{21*}(z) = 1 \tag{6.37}$$

accordingly to the properties of reciprocal and lossless transmission line structures as previously discussed in section 2.5. Please note that the determinant of M can alternatively be written as

$$\det([M]) = |A_{11}(z)|^2 - |A_{21}(z)|^2 = 1, \tag{6.38}$$

where $|.|$ represent the modulus.

[1] The Hermitian conjugate.

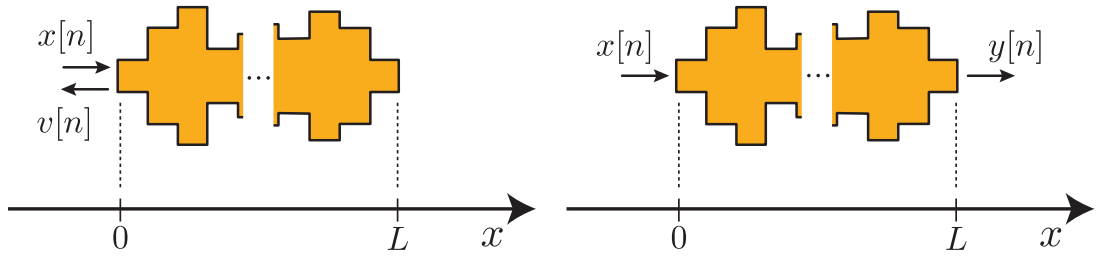

(a) Reflection system, where $S_{11}(z) = V(z)/X(z)$. (b) Transmission system, where $S_{21}(z) = Y(z)/X(z)$.

FIGURE 6.10: Transmission and reflection systems as implemented by DNTL structures. In both cases $x[n]$ is the input time sequence whereas $v[n]$ and $y[n]$ are the output sequences. In the z-domain we have $X(z)$ for the input spectra and $V(z)$ and $Y(z)$ for the output. In both situations the input and output ports are considered to be terminated in matched loads.

Both the transmission and reflection frequency responses in the z-domain can now be expressed accordingly to (6.22) as

$$S_{11}(z) = \frac{\sum_{i=0}^{m} \beta_i \, z^{-i}}{\sum_{i=0}^{m} \alpha_i \, z^{-i}}, \tag{6.39}$$

$$S_{21}(z) = \frac{z^{-m/2}}{\sum_{i=0}^{m} \alpha_i \, z^{-i}}. \tag{6.40}$$

Furthermore, dividing both the numerator and denominator of the previous equations by α_0 we obtain the general form of the reflection and transmission coefficients in the z-domain as

$$S_{11}(z) = \frac{\sum_{i=0}^{m} b_i \, z^{-i}}{1 + \sum_{i=1}^{m} a_i \, z^{-i}} = \frac{V(z)}{X(z)}, \tag{6.41}$$

$$S_{21}(z) = \frac{bz^{-m/2}}{1 + \sum_{i=1}^{m} a_i \, z^{-i}} = \frac{Y(z)}{X(z)}, \tag{6.42}$$

where a_i, b_i and b are real coefficients. Also, $V(z)$ and $Y(z)$ are the numerator polynomials and $X(z)$ is the common denominator polynomial.

It is important to realize that equations (6.41) and (6.42) (apart from the $z^{-m/2}$ factor) are in the general form of discrete-time system functions [61]. From the viewpoint

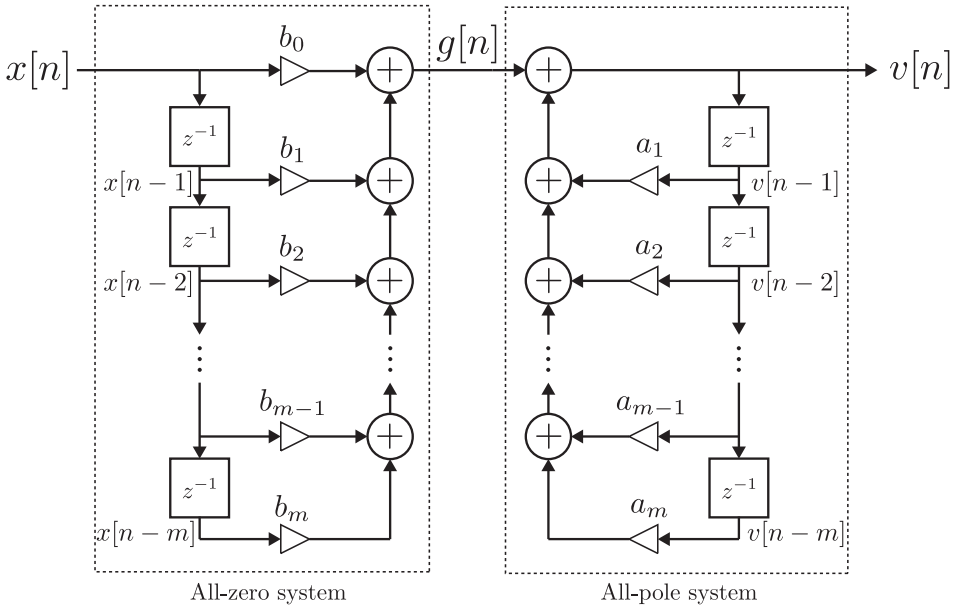

FIGURE 6.11: Direct Form I realization associated to the reflection system ($S_{11}(z)$).

of digital signal processing (digital filters), this means that DNTL structures can also be treated as linear time-invariant (LTI) discrete-time systems. More importantly, it means that many of the tools already developed in the field of digital signal processing (DSP) theory are readily applicable into the synthesis and analysis of DNTL structures, as we shall see further on this thesis.

Figure 6.10 illustrates the two digital systems that characterize any DNTL structure, namely the reflection system and the transmission system which in the z-domain are defined by the system functions (6.41) and (6.42) respectively. So, through the inverse z-transform of the system function in (6.41) we have that the difference equation characterizing the reflection system in Figure 6.10(a) is given by

$$v[n] = -\sum_{i=1}^{m} a_i\, v[n-i] + \sum_{i=0}^{m} b_i\, x[n-i]. \tag{6.43}$$

For the transmission system however, the computation of the difference equation is not so straightforward due to the $z^{-m/2}$ factor in the numerator of equation (6.42). The reason for this factor to appear in the system function for the transmission case and be absent in the reflection system becomes clear as we analyze Figure 6.10. In fact, for the reflection system in Figure 6.10(a), both input and output sequences are evaluated at the same physical point $x = 0$, however in the transmission case in Figure 6.10(b) the input sequence is evaluated at $x = 0$ whereas the output sequence is evaluated at $x = L$. Thus, due to causality, the transmission system has to account for the propagation time

from input $x = 0$ to output $x = L$, which translates into a delay in the form of $z^{-m/2}$ in the system function (6.42). Please note that in the cases where m is not even, the number of delay samples will not be an integer (which does not makes sense from a DSP point of view). This is because the delay unit z^{-1} as we have defined it in equation (6.18) accounts for the round-trip propagation time of each section, that is, it is suited for the modeling of reflection sequences. In the transmission system however, in addition to scattering events (reflection), we have also to account for the pure propagation time from input to output as input and output ports are located in different spatial positions, thus for an DNTL structure with m sections we have that

$$\left(z^{-1/2}\right)^m = \left(e^{-j\omega\tau}\right)^m \tag{6.44}$$

where τ is the propagation time (not round-trip propagation time) for each section, and ω is the analog-domain frequency variable defined by equation (6.12).

As seen from equation (6.44) , this delay factor translates into a linear phase factor in the analog domain transmission response, which from a DSP point of view can be omitted during both the analysis and synthesis procedures, provided that at some convenient stage along the procedures this linear phase factor is included so that to comply with the causality conditions required by DNTL structures. Furthermore, from the point of view of the synthesis procedure (the discrete layer-peeling method), this transmission response delay factor is usually not an issue as we are mostly interested in the reflection response (see section 4.3). In this way, we can rewrite the system function for the transmission case as

$$S'_{21}(z) = \frac{Y(z)}{U(z)} = \frac{b}{1 + \sum_{i=1}^{m} a_i\, z^{-i}}, \tag{6.45}$$

where $U(z) = z^{-m/2}\, X(z)$, thus omitting the delay factor present in $S_{21}(z)$.

Using the linearity and time-shifting properties of the z-transform [1], namely

$$w[n] \overset{\mathcal{Z}}{\longleftrightarrow} W(z), \tag{6.46}$$

$$a\, w_1[n] + b\, w_2[n] \overset{\mathcal{Z}}{\longleftrightarrow} a\, W_1(z) + b\, W_2(z), \tag{6.47}$$

$$w[n - n_0] \overset{\mathcal{Z}}{\longleftrightarrow} z^{-n_0}\, W(z), \tag{6.48}$$

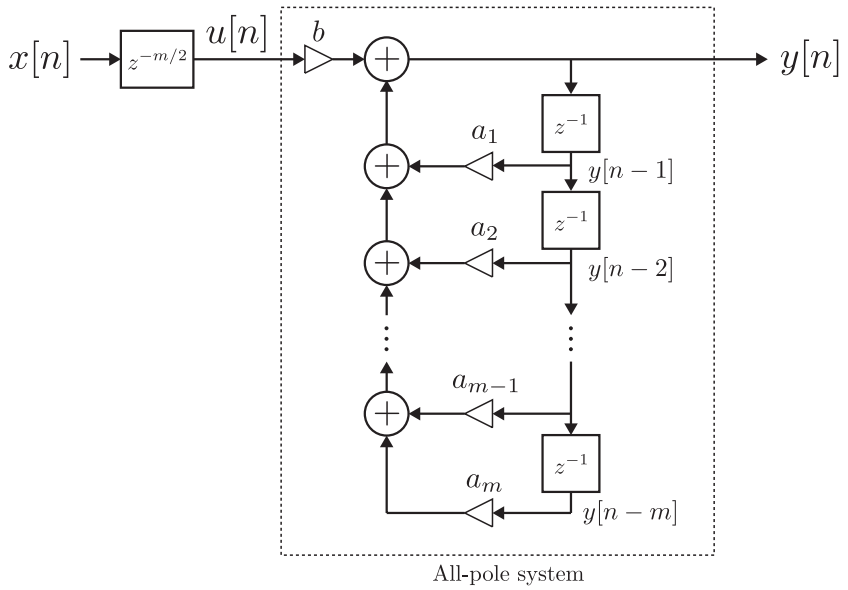

FIGURE 6.12: Direct Form I realization associated to the transmission system ($S_{21}(z)$).

we can now obtain the difference equation for the transmission system from the inverse z-transform of (6.45) as

$$y[n] = -\sum_{i=1}^{m} a_i\, y[n-i] + b\, u[n], \tag{6.49}$$

where the sequence $u[n]$ is a delayed version of the input sequence $x[n]$.

In both difference equations (6.43) and (6.49) $x[n]$ correspond to the input sequence. In the case of equation (6.49) however, $u[n]$ is the actually input sequence considered in the difference equation. On the other hand, the output sequences are given by $v[n]$ and $y[n]$ as illustrated in Figure 6.10, whilst a_i, b_i and b are the systems coefficients.

In DSP theory is common to represent the difference equations in terms of a block diagram representation. In the case of LTI discrete-time systems such as the ones with the DNTL structures these block diagrams are simply constituted by adders, multipliers and memory for storing delayed sequence values. One of the most common and simple block diagram representation is called the "Direct Form I realization". This kind of structure is easily constructed from the knowledge of the difference equations. Thus, from equation (6.43) we easily obtain the general Direct Form I realization for the reflection system associated with DNTL structures. This is illustrated by Figure 6.11. On the other hand, equation (6.49) enable us to obtain the general Direct Form I realization for the transmission system which is depicted in Figure 6.12.

The block diagram in Figure 6.11 is an explicit pictorial representation of the difference equation (6.43) which characterize the reflection system. In fact, equation (6.43) can be represented as a pair of difference equations, namely

$$g[n] = \sum_{i=0}^{m} b_i \, x[n-i], \tag{6.50}$$

$$v[n] = -\sum_{i=1}^{m} a_i \, v[n-i] + g[n]. \tag{6.51}$$

In the same way, the block diagram of Figure 6.11 can be viewed as a cascade of two sub-systems, the first representing the computation of $g[n]$ from $x[n]$ accordingly to equation (6.50) and the second representing the computation of $v[n]$ from $g[n]$ as in equation (6.51). Please note that the corresponding system function in equation (6.41) is given by the coefficient of two polynomials (in z), which can alternatively be represented by their roots. The roots of the numerator correspond to the zeros of the system function whereas the roots of the denominator account for the poles of the system function. This is illustrated in Figure 6.11, where the left sub-system account for all the zeros whereas the sub-system on the right (which is of a recursive nature) represents the poles.

Analysing Figure 6.11 and considering the block diagram as a cascade of two sub-systems it is not difficult to realize that the impulse response corresponding to the sub-system on the left translates into a finite number of samples and the sub-system is a so-called finite impulse response (FIR) system or non-recursive system, whereas for the recursive sub-system on the right, the impulse response is infinite and the sub-system is a so-called infinite impulse response (IIR) system.

As a curiosity we refer that in the context of filtered stochastic processes [62], FIR systems are usually referred to as moving average (MA) systems whilst IIR systems are referred to as auto-regressive (AR) or auto-regressive moving average (ARMA) systems, depending on whether they are purely recursive (all-pole system) or have a non-recursive part (all-zero system), respectively. Therefore and regarding the case of DNTL structures, we can easily see from Figure 6.11 that the reflection system $S_{11}(z)$ is an IIR system due the all-pole sub-system however it is not purely recursive as it also contains a FIR component due to the all-zeros sub-system on the left. Thus, the reflection system of a DNTL structure implements an ARMA system. The transmission system $S_{21}(z)$ on the other hand, is a purely recursive IIR system as shown by Figure 6.12 , thus it is classified as an AR system.

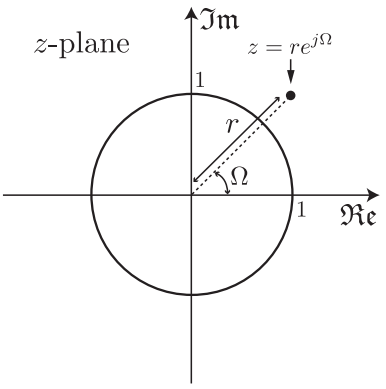

FIGURE 6.13: Complex z-plane. The evaluation of some $R(z)$ in the unit circle ($r = 1$) corresponds to the frequency domain response, that is $R(e^{j\Omega}) = R(\Omega)$ [1].

6.4 Realizable spectra for DNTL structures

Now that we have established the relationship between DNTL structures and digital filters, we proceed to evaluate the necessary feasibility conditions arising from causality and stability constrains. In this section and similarly to subsection 4.2.1.1 for the case of CNTL structures, we address the realizability conditions that the reflection spectrum (input data for the discrete layer-peeling procedure) must satisfy in order to be realizable as a DNTL structure with a prescribed number of sections.

We start by redefining the complex variable in the z-domain accordingly to Figure 6.13 as

$$z = r\, e^{j\Omega}, \tag{6.52}$$

where r is the magnitude of z and Ω which represents the digital domain frequency variable, is the angle of z. Please note that in the previous section we have considered $z = e^{j\Omega}$ as we were only concerned with the frequency response. In this section however, the more general definition of z in equation (6.52) must be consider if we are to analyze among other parameters the stability and causality conditions for digital filters [1] and thus DNTL structures.

Let us consider for the purposes of this section and for the sake of mathematical simplicity that the reflection and transmission scattering parameters are defined as

$$R(\Omega) = S_{11}(\Omega), \tag{6.53}$$

$$T(\Omega) = S_{21}(\Omega). \tag{6.54}$$

Similarly to the conditions in subsection 4.2.1.1 for CNTL structures, it can be proven

from the properties of the discrete Fourier transform [1] that in order for the DLP synthesis procedure to return a real valued impedance profile, $R(\Omega)$ must satisfy

$$R(-\Omega) = R^*(\Omega). \tag{6.55}$$

Additionally, we know from physical constrains that any NTL structure is a non-anticipative system, that is, its current outputs depend exclusively on the past inputs. So, due to causality, and similarly to CNTL structures the impulse response sequence $r[n]$ for DNTL structures must verify

$$r[n] = 0, \qquad n < 0, \tag{6.56}$$

where $r[n]$ is the inverse discrete Fourier transform of $R(\Omega)$ or equivalently the inverse z-transform of $R(z)$.

Most often, DNTL structures are synthesized so that the input port characteristic impedance is the same as in the output port. The synthesis of filters is one of the most common applications where this condition must be verified as both input and output ports usually have the same characteristic impedance. Therefore, in order to guaranty equal impedance termination, the target spectrum must verify

$$R(\Omega = 0) = 0. \tag{6.57}$$

In the z-domain this means that $R(z)$ must have a zero at $z = e^{j0} = 1$. Please note that condition (6.57) is not strictly speaking a realizability condition as it is not essential to guaranty the convergency of the IS procedure, however it must be enforced in order to synthesize structures with equal impedance terminations.

We know for a fact that DNTL structures are passive structures. As such, and for the lossless case, another realizability condition for the target spectrum arises from the law of conservation of energy, namely

$$0 \leq |R(\Omega)|^2 \leq 1, \qquad \forall\Omega. \tag{6.58}$$

Condition (6.58) is directly obtained from the evaluation of equation (6.38) at the unit circle, $|z| = 1$, thus

$$|A_{11}(\Omega)|^2 - |A_{21}(\Omega)|^2 = 1. \tag{6.59}$$

By considering equations (6.22) the previous equation can be further developed so that to relate the reflection power $|S_{11}|^2$ and the transmission power $|S_{21}|^2$ as

$$\left|\frac{1}{S_{21}}\right|^2 - \left|\frac{S_{11}}{S_{21}}\right|^2 = 1 \quad \Longleftrightarrow \quad |S_{11}(\Omega)|^2 + |S_{21}(\Omega)|^2 = 1, \tag{6.60}$$

where the target spectrum $R(\Omega)$ is represented by the reflection coefficient $S_{11}(\Omega)$. This condition is in fact not new. Please note that the same result is given by equation (2.134) as a property of passive and lossless networks in section 2.4.

Another realizability condition comes as a stability condition. That is, the target spectrum $R(\Omega)$ must correspond to the frequency response of a stable system, otherwise the synthesis procedure will not converge. The stability conditions are set through the analysis of the z-transform of the target spectrum $R(z)$. Similarly to the to the analog-domain analysis in subsection 4.2.1.1 for the case of CNTL structures using the Laplace transform properties, we now consider $R(z)$ to be the z-transform of the impulse response sequence $r[n]$. Similarly to the analog-domain with the Laplace analysis, there is associated with the z-transform a range of values of z for which $R(z)$ converges. This range of values is in the same way referred to as the *region of convergence* (ROC), however, in the digital-domain the discrete Fourier transform shall only converge if the unit circle is included within the ROC region [1]. Furthermore, in the z-domain, the ROC of $R(z)$ always consists of a ring in the z-plane centered about the origin and it is defined by the position of the poles as it can never contain any poles [1]. We have previously referred that due to causality, the impulse response sequence associated to any DNTL structure is always a right-sided sequence. Therefore and accordingly to the properties of the z-transform the ROC shall consist of a ring centered about the origin and extending from $|z| = r_0$ (position of the outermost pole) to infinity. So, because the ROC can not contain any poles and in order for the correspondent discrete Fourier transform $R(\Omega)$ to converge (the unit circle must be contained within the ROC), we must ensure that $R(z)$ has all its poles inside the unit circle [1] so that $r_0 < 1$.

In the previous section we have derived the general form for the expressions of the elements of the transmission matrix $[M]$ for DNTL structures. These expressions are given by equations (6.28) to (6.31). A quick look at the expressions and we easily see that all of them are affected by the delay factor $z^{m/2}$. As already discussed, this delay factor is inherent to the physical aspects of the DNTL structures and can be ignored from the point of view of DSP. In this way we now redefine the transmission matrix

parameters as

$$A'_{11}(z) = \sum_{i=0}^{m} \alpha_i \, z^{-i}, \tag{6.61}$$

$$A'_{21}(z) = \sum_{i=0}^{m} \beta_i \, z^{-i}, \tag{6.62}$$

keeping in mind that $A_{12}(z) = A^*_{21}$ and $A_{22}(z) = A^*_{11}$.

Analyzing equations (6.25) to (6.27) and comparing them to the expansion of $A'_{11}(z)$, a restriction arises for the possible values of α_0 as we clearly see that

$$\alpha_0 = \prod_{i=0}^{m} k_i, \tag{6.63}$$

where $k_i = (1 - \Gamma_i^2)^{-1/2} > 0$. Thus, another realizability condition arises in the form

$$\alpha_0 > 0, \tag{6.64}$$

that is, the first coefficient of the A_{11} parameter in the transmission matrix of any DNTL structure must always be positive.

From equations (6.61) and (6.62) we see that all realizable reflection spectra $R(z)$ can be expressed by rational functions, in the form

$$R(z) = \frac{A'_{21}(z)}{A'_{11}(z)} = \frac{\beta_0 + \beta_1 z^{-1} + ... + \beta_{m-1} z^{-(m-1)} \beta_m z^{-m}}{\alpha_0 + \alpha_1 z^{-1} + ... + \alpha_{m-1} z^{-(m-1)} \alpha_m z^{-m}}, \tag{6.65}$$

where α_i and β_i are real coefficients. In the same way, the transmission coefficient is given by

$$T(z) = \frac{1}{A'_{11}(z)} = \frac{1}{\alpha_0 + \alpha_1 z^{-1} + ... + \alpha_{m-1} z^{-(m-1)} \alpha_m z^{-m}}, \tag{6.66}$$

where the coefficients α_i are the same as in $R(z)$.

It is often convenient to factor the polynomials in the numerator and denominator of equation (6.65) and to write the reflection transfer function in terms of those factors as

$$R(z) = \frac{A'_{21}(z)}{A'_{11}(z)} = K \frac{\prod_{i=1}^{m} (1 - c_i z^{-1})}{\prod_{i=1}^{m} (1 - p_i z^{-1})}, \tag{6.67}$$

where $K = \beta_0/\alpha_0$ is a real number and c_i and p_i are the zeros and the poles of $R(z)$

respectively. On the other hand, from equation (6.66) we have that the transmission coefficient for DNTL structures is always represented (apart from the delay factor $z^{m/2}$) as

$$T(z) = \frac{1}{A'_{11}(z)} = \frac{b}{\prod_{i=1}^{m}(1 - p_i z^{-1})}, \tag{6.68}$$

where $b = 1/\alpha_0$ is a real number and p_i are the poles of $T(z)$ (which are the same as for $R(z)$).

The stability and causality conditions addressed above regarding the location of the poles in the z-plane can now be stated as

$$|p_i| < 1, \tag{6.69}$$

that is, all the roots of $A'_{11}(z)$ must be located inside the unit circle. Furthermore, it is easily verified that the transmission coefficient $T(z)$ must always be minimum phase. From equation (6.68) we find that in addition to having m poles, $T(z)$ also have m zeros, all of them at $z = 0$. Therefore, if the stability condition (6.69) is verified, $T(z)$ has all its poles and zeros inside the unit circle, thus fulfilling the minimum phase conditions [61]. Please note that the minimum phase condition can also be fulfilled by assuring that at the unit circle $\angle A'_{11}(\Omega)$ and $\ln(|A'_{11}(\Omega)|)$ form a discrete Hilbert transform pair.

In summary and from the discussion above, we conclude that all rational functions in the form of equation (6.65), that is, the ratio of two polynomials, are realizable as DNTL structures with $m + 1$ coupling points (impedance reflectors) if the following conditions are fulfilled:

1. Both numerator and denominator polynomials must have real coefficients, thus

$$\alpha_i, \beta_i \quad \in \mathbb{R}. \tag{6.70}$$

   As a result, all the complex poles and zeros in (6.67) occur in complex conjugate pairs which in turn verifies condition (6.55).

2. From the law of conservation of energy we must ensure that at the unit circle ($|z| = 1$)

$$|A'_{11}(\Omega)|^2 - |A'_{21}(\Omega)|^2 = 1, \tag{6.71}$$

   as DNTL structures are passive structures.

3. The first coefficient of the denominator must always verify

$$\alpha_0 > 0. \tag{6.72}$$

4. Stability and causality conditions are fulfilled by ensuring that

$$|p_i| < 1, \tag{6.73}$$

where p_i are the roots of the denominator polynomial. Equivalently we have that

$$\angle A'_{11}(\Omega) = \mathcal{H}\{\ln|A'_{11}(\Omega)|\}, \tag{6.74}$$

where $\mathcal{H}$ stands for the discrete Hilbert transform.

Please note that, equivalent realizability conditions can be found in [63] for the synthesis of fiber Bragg gratings.

6.5 The Discrete layer peeling procedure and the Schur recursions

So far we have seen that there exists a close relationship between DNTL structures and digital signal processing theory. In a certain way, this relationship was already implicit when we first derived the DLP inverse scattering algorithm in section 4.3. However, within the context of this chapter, *i.e.* the context of DSP, we can further understand the direct relationship that exists between the physical inverse scattering problem and the assessment of stability, causality and boundedness properties of digital systems.

In the previous chapters, the DLP inverse scattering procedure is performed in the frequency domain. That is, the starting point for the DLP procedure is given by the specification of the target reflection response $R_0(\omega)$, which is a function of the frequency variable and also that all the subsequent processing occurring through the procedure is performed in the ω domain.

However and similarly to what has been done in the previous sections, we can take advantage of some DSP tools and techniques, namely the z-transform in order to simplify the DLP procedure and in some way improve the computational efficiency of the DLP algorithm.

In this way, the DLP inverse scattering procedure is performed by taking the following steps:

1. Specify the target reflection spectra in the z-domain as the ratio of two polynomials of order m, thus for $i = 0$

$$R_0(z) = \frac{B(z)}{A(z)} = \frac{\sum_{i=0}^{m} b_i z^{-i}}{\sum_{i=0}^{m} a_i z^{-i}}, \tag{6.75}$$

   provided that $R(z)$ fulfills the realizability conditions set in section 6.4.

2. Calculate the local reflection coefficient Γ_i on the interface between sections $i-1$ and i through

$$\Gamma_i = \frac{b_0}{a_0}, \tag{6.76}$$

   that is, the ratio of the first coefficients of the numerator and denominator coefficients respectively.

3. Compute the reflection response at the beginning of the next layer as a ratio of two polynomials using

$$R_{i+1}(z) = \frac{R_i(z) - \Gamma_i}{1 - \Gamma_i R_i(z)}\, z \tag{6.77}$$

   and clearly identifying the coefficients for the numerator and denominator polynomials.

4. Peel off layer i.

5. Repeat steps 2. to 3. until the number of iterations reaches m. Please note that for a DNTL structure to be feasible as an m-section structure the transmission response $T_0(z)$ associated to $R_0(z)$ must have an all-pole transfer function.

The calculation of the characteristic impedance of each layer or section is then computed from the reflection coefficients using

$$Z_{0_i} = Z_{0_{i-1}} \frac{1 + \Gamma_i}{1 - \Gamma_i}, \tag{6.78}$$

where Z_0 for $i = 0$, that is, the characteristic impedance for the first section is to be specified by the designer[2] and is usually 50Ω.

[2]Boundary condition at the left side of the DNTL structure.

Making the parallelism with the DLP algorithm first derived in section 4.3 we see that the present procedure is conceptually the same and shall theoretically produce the same output. However, when comparing the individual steps of both algorithms three major differences arise in steps 1., 2. and 5. respectively. First, in step 1., the specification of $R_0(z)$ and the subsequently representation of $R_i(z)$ is made as quotient of two polynomials. Second, in step 2. the first value of the impulse response sequence is calculated through the initial value theorem. And third, in step 5., the number of iterations performed is equal to the order of $R_0(z)$ and thus it is not dependent on a stopping condition. The first and third differences are in fact related, that is, given a target reflection response $R_0(z)$ represented by the quotient of two m-order polynomials the number of iterations necessary to reconstruct the DNTL impedance profile is m provided that the transmission response $T_0(z)$ associated with $R_0(z)$ has an all-pole transfer function. As for step 2., instead of using the discrete Fourier transform to calculate the first value of the impulse response sequence, we now use the initial value theorem [1]. The initial value theorem in the z-domain states that for any causal sequence the first value of the sequence, *i.e.* for $n = 0$, is given by

$$r_i[0] = \lim_{z\to\infty} R_i(z). \tag{6.79}$$

Consequently and because $R_i(z)$ is always given as the quotient of two polynomials as a function of z, the values $r_i[0]$ given by equation (6.79) can be easily computed from the first coefficients of the numerator and denominator coefficients as

$$\Gamma_i = r_i[0] = \frac{b_0}{a_0}. \tag{6.80}$$

We now point out the intimate connection that exists between the DLP inverse scattering procedure and an algorithm devised by Schur in 1917 for testing the boundedness of a function $S(z)$ analytic outside the unit circle. We start by rewriting equations (6.77) and (6.79) as

$$S_{i+1}(z) = \frac{S_i(z) - k_i}{1 - k_i\, S_i(z)}\, z, \tag{6.81}$$

$$k_i = \lim_{z\to\infty} S_i(z), \tag{6.82}$$

where

$$S(z) = S_0(z) = \frac{B_0(z)}{A_0(z)} \tag{6.83}$$

is some scattering system function. Equations (6.81) and (6.82) are known in the the DSP domain as the Schur recursions. These recursions come as the result of the work developed by Schur regarding the stability and boundedness of discrete-time systems [64],[65]. Let us assume that the system function $S(z) = S_0(z)$ is analytic outside the unit circle, that is, has all its poles contained within the unit circle fulfilling this way the stability criteria. Schur proved that under this condition we have that $|S(z)| \leq 1$ for $|z| \geq 1$ if and only if the sequence of coefficients k_i (usually referred to as the reflection coefficients) generated by the recursions (6.81) and (6.82) are such that $|k_i| \leq 1$. In other words, if $S(z)$ is analytic in the strict outer unit disk[3] and if the coefficients k_i produced by the recursions verify the condition $|k_i| < 1$, then the magnitude of $S(z)$ will be bounded by one in the outer disk. Under these conditions, $S(z)$ is usually referred to as a Schur function. Furthermore, $S(z)$ will only be stable if and only if all reflection coefficients have magnitude less than one. Please note that if the boundedness by one of $|S(z)|$ inside the unit circle is verified, then the evaluation of the scattering system function at the unit circle translates into a passive scattering function, that is, $|S(\Omega)| \leq 1$.

Another property of the Schur algorithm is that by starting with $S(z)$ such that $|S(z)| \leq 1$ for $|z| \geq 1$, that is, with a passive scattering function, then the algorithm will generate a sequence of such functions and thus we have that $|S_i(z)| \leq 1$ for $|z| \geq 1$. Therefore, if $S(z)$ is a Schur function, so are $S_i(z)$. This is in fact the essence of the DLP inverse scattering procedure. When applied to a Schur function $S(z)$, that is to the scattering response of a passive medium, the algorithm leaves after each step a medium with the same properties, which makes it possible to apply the same steps again and again. Please note that the recursion (6.81) corresponds to the process of layer removal (peeling) in the DLP procedure.

Essentially, the Schur recursions can be understand as a procedure for testing the feasibility of a DNTL structures having $S(z)$ as the reflection response, which on physical grounds must be stable, causal, and bounded (representing a passive system) $|S(z)| \leq 1$ for all z in the region of convergence that includes, at least, the unit circle and all the

[3]The strict outer disk is defined as the region $|z| > 1$ in the complex plane.

points outside it. Furthermore, the coefficients k_i given by (6.82) represent the reflection coefficients at the layer interfaces.

From a functional point of view and considering the system reflection response (6.83) as the starting point, the Schur recursions start with $B_0(z)$ and $A_0(z)$ which are the numerator and denominator polynomials of order m and at each step of the algorithm the recursion (6.81) reduces the order of the polynomials by one until it reaches the 0th order polynomials $B_m(z)$ and $A_m(z)$.

As a curiosity, we refer that a continuous version of the Schur recursions can also be devised in the form

$$\frac{dR(x,\omega)}{dx} = 2j\omega R(x,\omega) - k(x)(1 - R(x,\omega)^2), \tag{6.84}$$

$$k(x) = \lim_{\omega\to\infty} 2j\omega R(x,\omega). \tag{6.85}$$

It is interesting to note that these recursions have the same role in the synthesis of CNTL structures as have the discrete version recursions (6.81) and (6.82) in the synthesis of DNTL structures. In fact and during the study of the CLP inverse scattering procedure in section 4.3 we have already come across these recursions. Let us recall the steps of the CLP algorithm described in section (4.3). We clearly see that in step 2. the computation of K_i through equation (4.189) is mathematically equivalent to the recursion (6.85) where $k(x)$ is obtained by using the initial value theorem. Please note that K_i corresponds to $k(x)$ when evaluated as depth $x = x_i$. Furthermore, the relation between the reflection response at adjacent layers given by the transmission matrix (4.190) in step 3., can equivalently be expressed by the Riccati equation (6.84) whose numerical computation can be performed by using a backward difference scheme, thus a backward difference discretization.

As a last remark regarding the importance of the Schur recursions and consequently the testing for stability, causality and boundedness of digital systems on the synthesis of DNTL structures, we now make a comparison with the classical network synthesis [66]. One of the most important theorems in network synthesis states that the driving point impedance $Z_{in}(s)$ of any passive network containing only passive elements is a positive real function in the s-plane [67] [68] [66] [69] [70],[71]. Let us now rewrite the reflection frequency response at the input of some DNTL structure as

$$S_0(z) = \pm\frac{Z_{in}(z) - Z_0}{Z_{in}(z) + Z_0}, \tag{6.86}$$

where $Z_{in}(z)$ is the input impedance an Z_0 is the port characteristic impedance. Also, $S_0(z)$ may be negative corresponding to the reversal impedance profile. It follows from the properties of positive real functions for discrete linear systems, *i.e.*, in the z-plane, that $S_0(z)$ is a Schur function if and only if $Z_{in}(z)$ is a positive real function in the z-plane [72].

It is interesting to point out that the role of Schur functions in the synthesis of DNTL structures is in fact equivalent to that of positive real functions in the classical network synthesis, that is, both require the driving point impedance to be a positive real function. However, while in the field of classical network synthesis we start the synthesis procedure with a polynomial representation for the driving point impedance, *i.e.* the input impedance, which must be positive-real in the s-plane, in the synthesis of DNTL structures we start the synthesis with the frequency reflection response $S_0(z)$ which must be a Schur function, *i.e.*, a passive bounded real function in the z-plane.

6.6 Optimum synthesis of NTL structures

In section 6.4 we have established the necessary and sufficient conditions which a target reflection frequency response $S_{11}(z)$ must fulfill in order to be realizable as an DNTL structure. These conditions are enough from a functional viewpoint as they assure the physical feasibility of an NTL structure that has a reflection frequency response which is the same as the target spectra. However, no conditions were established regarding size constrains. Despite the good results obtained from a functional point of view, the outcome of the DLP inverse scattering procedure usually results in very long structures which by itself poses as a problem as the physical size of the structure is often a constrain for the designer. Therefore and accordingly to the discussion in section 6.1 a compromise between the desired frequency response and the size of the structure must be obtained. In this section we address the conditions which the target spectra must fulfill as well as the necessary procedure steps to be taken in order to obtain such a target spectra which when fed to the DLP inverse scattering procedure returns a minimum length structure.

As we have seen in the previous sections, the reflection spectra $S_{11}(z)$ given by DNTL structures is always expressed as the ratio of two polynomials, in the form

$$S_{11}(z) = \frac{\beta_0 + \beta_1 z^{-1} + ... + \beta_{m-1} z^{-(m-1)} \beta_m z^{-m}}{\alpha_0 + \alpha_1 z^{-1} + ... + \alpha_{m-1} z^{-(m-1)} \alpha_m z^{-m}}, \tag{6.87}$$

where α_i and β_i are real coefficients. On the other hand, for the transmission coefficient (leaving out the delay factor $z^{m/2}$) we have that

$$S_{21}(z) = \frac{1}{\alpha_0 + \alpha_1 z^{-1} + ... + \alpha_{m-1} z^{-(m-1)} \alpha_m z^{-m}}, \tag{6.88}$$

where the coefficients α_i are the same as in the denominator of $S_{11}(z)$.

Furthermore, we know from the realizability conditions that the relation between the transmission and reflection spectra must be given by

$$|S_{11}(z)|^2 + |S_{21}(z)|^2 = 1. \tag{6.89}$$

When associated with stochastic processes theory, we observe that the reflection spectra is well represented by an ARMA process, whereas the transmission spectra implements an AR process, that is, an all-pole transfer function. Please note that both processes share the same denominator polynomial.

It is clear from equation (6.88) and from the analysis made in section (6.3) that the transmission frequency response of an m-section DNTL structure is always given by an all-pole transfer function[4] with m-poles, that is, the denominator polynomial is of order m. The converse is also true, that is, if we are to synthesize any DNTL structure from an all-pole transmission transfer function of order m then the synthesized structure shall be composed by m sections, provided that the target spectra $S_{11}(z)$ which is feed to the DLP inverse scattering procedure is obtained from the all-pole transmission spectra through the relation given by equation (6.89) as

$$|S_{11}(z)|^2 = 1 - |S_{21}(z)|^2 . \tag{6.90}$$

Analyzing the realizability conditions described in section 6.4 we find that these conditions are in fact addressed not only to the reflection target spectra but they also indirectly contemplate the transmission frequency response. This is easily verified by realizing that except for condition (6.71) all the realizability conditions are directly related to the denominator polynomial which accordingly to (6.87) and (6.88) is the same for both transmission and reflection spectra. Most importantly, there are no realizability conditions restricting the transmission transfer function to an all-pole system, *i.e.*, an AR process. However, as discussed above and from the analysis made in section (6.3)

[4] $S_{21}(z)$ also has m zeros at $z = 0$.

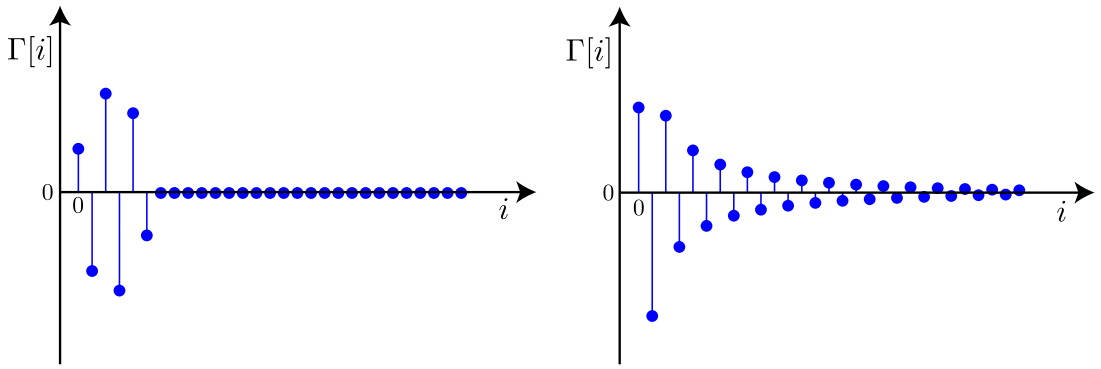

(a) Fifth order transmission AR process. (b) First order transmission ARMA process.

FIGURE 6.14: Reflection coefficients along the DNTL structure as returned from the DLP algorithm. In (a) the target transmission spectra is given by a fifth order all-pole system, whilst in (b) the target transmission spectra is given by a first order system with one pole and one zero.

we know that the transmission transfer function must always be given as an AR process. Therefore, it is important to understand what is the outcome of the DLP inverse scattering procedure when the transmission frequency response is specified in the form of an ARMA process.

Let us then suppose that the target transmission spectra is given in the form of an m-th order ARMA process such that

$$S_{21}(z) = \frac{\sum_{i=0}^{m} \upsilon_i \, z^{-i}}{\sum_{i=0}^{m} \alpha_i \, z^{-i}}. \tag{6.91}$$

Clearly the transmission transfer function in equation (6.91) is not in the form of an all-pole system as it also composed by a numerator polynomial of order m. However, if we consider that the inverse of (6.91) can be represented as

$$\frac{1}{S_{21}(z)} = \frac{\sum_{i=0}^{m} \alpha_i z^{-i}}{\sum_{i=0}^{m} \upsilon_i z^{-i}} = \sum_{n=0}^{\infty} h[n] \, z^{-n}, \tag{6.92}$$

then we can rewrite the transmission spectra in (6.91) as

$$S_{21}(z) = \frac{1}{\sum_{n=0}^{\infty} h[n] \, z^{-n}}, \tag{6.93}$$

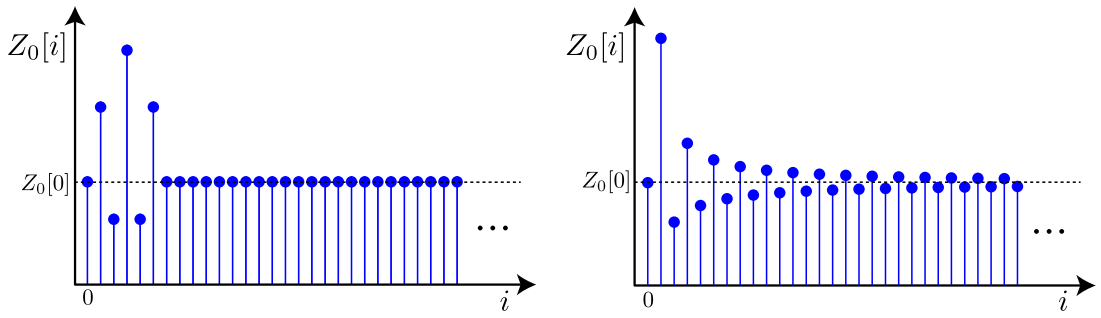

(a) Fifth order AR process.

(b) First order ARMA process.

FIGURE 6.15: Impedance profile correspondent to the refraction coefficients given in Figure 6.14. The impedance values are computed using equation (6.78) and $Z_0[0]$ is specified by the designer. In (a) we clearly see that the DNTL is constituted by five sections, whilst in (b) the DNTL is infinite in length.

which is now in the form of an all-pole transfer function. In equation (6.93) $h[n]$ is given by

$$h[n] = \mathcal{Z}^{-1}\left\{\frac{1}{S_{21}(z)}\right\}, \tag{6.94}$$

that is, $h[n]$ is the inverse z-transform, *i.e.*, the impulse response sequence of the inverse of the transmission transfer function $(S_{21}(z))^{-1}$.

From the analysis above we conclude that in fact the transmission frequency response is always represented by an all-pole system even when specified in the form of an ARMA process. However, when the target transmission response is represented by an ARMA process, the corresponding all-pole representation comes in the form of equation (6.93) which has an infinite number os poles. Consequently and accordingly to the analysis made in section (6.3), the corresponding DNTL structure will have an infinite number of sections. This is illustrated in Figure 6.14 where the DLP synthesis results for the case of a fifth order AR transmission process is compared to that of a first order ARMA process. The AR process is characterized by an all-pole transfer function with five poles whereas the ARMA process transfer function is constituted by a a singe pole and a single zero[5]. From both target transmission specters the correspondent reflection responses are computed through (6.90) and fed to the DLP algorithm which then returns the reflection coefficients between sections, as it is depicted in Figure 6.14. The corresponding DNTL impedance profiles are depicted in Figure 6.15. These are easily obtained from the reflection coefficients through equation (6.78) and by setting the microwave system characteristic impedance $Z_0[0]$. Usually a 50Ω system is considered.

[5]This zero is not at the origin.

From Figure 6.14(a) it becomes readily apparent that the reflection frequency response obtained from a fifth order AR process is realizable as a series of six reflectors[6] which in turn translates into a five section DNTL structure as illustrated in Figure 6.15(a). On the hand, we see from Figure 6.14(b) that the first other ARMA process is not realizable in a finite number of reflectors as the reflection coefficients returned by the DLP procedure only converge to zero at infinity. However we also realize from the figure that the first reflectors are the most influent in the frequency response. Thus, similarly to the procedure used in Chapter 5 we can use a apodizing/windowing procedure in order to force the reflection coefficients to be zero outside of a certain window. Please note that even though the order of the ARMA process is five times lower than that of the AR process the number of sections necessary to implement a DNTL using apodizing/windowing techniques will still be far greater than five if we are to accurately approximate the target response.

So, in order to achieve the minimum length when synthesizing DNTL structures, we must first approximate the desired transmission frequency response by an all-pole transfer function of order m. This all-pole transfer function now becomes the transmission target spectra from which the target reflection response is obtained and then fed to the DLP inverse scattering algorithm. As a result, a DNTL structure with m sections is obtained.

As we have just seen, for a DNTL structure to be synthesized with minimum length regarding the order of the target frequency response, the reflection frequency response which is to be fed to the DLP algorithm must be first obtained from an all-pole transmission frequency response though the relation (6.90). For that we follow a procedure described in [73]. In order to demonstrate this procedure let us consider that the target transmission frequency response given by equation (6.88) is rewritten in a factored form as

$$S_{21}(z) = \frac{b}{\prod_{i=1}^{m}(1 - p_i z^{-1})}, \tag{6.95}$$

where $b = 1/\alpha_0$ is a real number and p_i are the poles of the transmission transfer function witch are usually complex values.

[6] For $i \geq 6$ we have that $\Gamma[i] = 0$.

We start by computing the square of the absolute value of the transmission spectra as

$$|S_{21}(z)|^2 = S_{21}(z)\, S_{21*}(z), \tag{6.96}$$

where $S_{21*}(z)$ is the para-Hermitian conjugate of the transmission spectra which is computed accordingly to (6.34). Substituting equation (6.95) into (6.96) yields

$$|S_{21}(z)|^2 = \frac{b^2}{\prod_{i=1}^{m}(1-p_i z^{-1})(1-p_i^* z)} = \frac{b^2\, z^{-m}}{\prod_{i=1}^{m}\left(1-p_i z^{-1}\right)\left(1-\frac{1}{p_i^*}z^{-1}\right)}, \tag{6.97}$$

where p_i and $1/p_i^*$ are the poles of the squared magnitude of the transmission spectra. The computation of the squared magnitude of the reflection spectra $|S_{11}(z)|^2$ follows directly by substituting equation (6.97) into (6.90) yielding

$$|S_{11}(z)|^2 = \frac{\prod_{i=1}^{m}\left(1-p_i z^{-1}\right)\left(1-\frac{1}{p_i^*}z^{-1}\right) - b^2\, z^{-m}}{\prod_{i=1}^{m}\left(1-p_i z^{-1}\right)\left(1-\frac{1}{p_i^*}z^{-1}\right)}. \tag{6.98}$$

From the equation we verify that the zeros of $|S_{11}(z)|^2$ are directly related to the poles of $|S_{21}(z)|^2$. Furthermore the number of zeros is the same as the number of poles. Ergo, the square magnitude of the reflection coefficient can be written as

$$|S_{11}(z)|^2 = K^2 \frac{\prod_{i=1}^{m}\left(1-c_i z^{-1}\right)\left(1-\frac{1}{c_i^*}z^{-1}\right)}{\prod_{i=1}^{m}\left(1-p_i z^{-1}\right)\left(1-\frac{1}{p_i^*}z^{-1}\right)}, \tag{6.99}$$

where c_i and $1/c_i^*$ are the roots of the numerator, *i.e.*, the zeros of the square magnitude of the reflection coefficient and K is a real number. We emphasize that the computation of the zeros of $|S_{11}(z)|^2$ is dependent on the poles of $|S_{21}(z)|^2$. Hence, the values of c_i are obtained from those of p_i by expanding the numerator of (6.98) and computing the roots of the resulting polynomial.

Let us consider that the reflection frequency response given by equation (6.87) is rewritten in a factored form as

$$S_{11}(z) = K \frac{\prod_{i=1}^{m}(1 - d_i z^{-1})}{\prod_{i=1}^{m}(1 - p_i z^{-1})}, \tag{6.100}$$

where d_i are the zeros of the reflection frequency response. As we have seen before, the reflection and transmission frequency responses share a common denominator polynomial. Therefore, the poles pi in (6.100) are the same as those of the transmission frequency response in (6.95). Notice that accordingly to the realizability conditions the poles of $|S_{11}(z)|$ must be inside the unit circle, however no condition is set regarding the zeros d_i. Comparing equations (6.99) and (6.100), we find that the number of zeros in $|S_{11}(z)|^2$ is twice that of $S_{11}(z)$. Furthermore we see that the same situation holds regarding the poles. However, we already know in advance that the poles given by $1/pi^*$ are not suitable to be selected as the poles of $S_{11}(z)$ as they are located outside the unit circle. Regarding the zeros, we find that for each zero d_i in $S_{11}(z)$ there are two zeros c_i and $1/c_i^*$ in $|S_{11}(z)|^2$. Therefore, in order to obtain $S_{11}(z)$ from $|S_{11}(z)|^2$ we must select one zero from each pair of zeros (c_i and $1/c_i^*$) in $|S_{11}(z)|^2$. This shows that we have a maximum of 2^m choices for the selection of the zeros of $S_{11}(z)$, which in turn translates in 2^m distinct reflection frequency responses. Notice that the different zeros choices do not influence the magnitude response of the reflection frequency response. However the phase response for the reflection frequency response will differ for different combinations of zeros. This in turn translates into different impedance profiles after the synthesis process. That is, each different selection os zeros for $S_{11}(z)$ will lead to different physical configurations, which depending on the maximum and minimum values of the impedance profile may or may not be practically feasible due to technology limitations.

Let us consider again the transmission transfer function for an ARMA process given by equation (6.93), which when rewritten in a factored form becomes

$$S_{21}(z) = \frac{b}{\prod_{i=1}^{\infty}(1 - p_i z^{-1})}. \tag{6.101}$$

Following the procedure described above to obtain $S_{11}(z)$ from $S_{21}(z)$ we find that the reflection frequency response is given by

$$S_{11}(z) = K \frac{\prod_{i=1}^{\infty}(1 - d_i z^{-1})}{\prod_{i=1}^{\infty}(1 - p_i z^{-1})}, \tag{6.102}$$

where the number of poles and zeros is infinite, which means that $S_{11}(z)$ is given by the quotient of two infinite order polynomials. We saw in section 6.5 that the DLP inverse scattering procedure or equivalently the Schur recursions start with the numerator and denominator polynomials of $S_{11}(z)$ and at each step reduce the order of both numerator and denominator polynomials by one. The procedure stops when the order of the polynomials becomes zero. Thus, when the reflection frequency response given by (6.102) is fed to the Schur recursions we find that due to the infinite order of the numerator and denominator polynomials the inverse scattering procedure will return an infinite DNTL structure, as the Schur recursions extend to infinity. This is illustrated in Figure (6.15).

6.7 Synthesis of discrete NTL filters using DSP techniques

In the previous section we have demonstrated that in order to synthesize any given target transmission transfer function in the optimum sense, *i.e.*, in the form of a minimum length DNTL structure with m sections, we must first be able to approximate the target transmission response by an all-pole transfer function with m poles, or equivalently, an all-pole transfer function where the denominator polynomial has order m. At this point, we can usefully take advantage of DSP *system identification* techniques in order to achieve such an approximation. Thus, in order to approximate the target transmission frequency response by an all-pole system such as

$$S_{21}(z) = \frac{1}{\sum_{i=0}^{m} \alpha_i z^{-i}}, \tag{6.103}$$

we may use *parametric modeling* tools. These parametric modeling tools are readily available in DSP commercial software such as Matlab and can be used to find the coefficients α_i of the linear all-pole system (6.103) that best approximates the target response.

Most often, the process of filter synthesis is carried out focusing almost exclusively on the magnitude response of the frequency response. Actually, in most cases only targeting the transmission magnitude response as the reflection magnitude readily follows from this one. In this scenario, the phase response both in transmission and reflection can be relaxed so that we can use the techniques derived in the previous section to perform the synthesis of DNTL filters with arbitrary magnitude transmission frequency response.

Next, we describe a procedure for synthesizing DNTL structures with arbitrary magnitude transmission frequency response. The procedure is carried out in the Matlab environment and follows from that reported in [73], [74].

We start the procedure by defining $T(\Omega)$ as the target magnitude for the transmission frequency response. We consider $T(\Omega)$ to be an ideal target response. As such, it shall be specified as an ideal filter with sharp or linear transitions between flat pass-bands and stop-bands. As an example of an ideal target response we may consider the magnitude response of the ideal rectangular low-pass filter which is simply defined by a constant magnitude of one in all the pass-band region immediately followed by a magnitude of zero in the stop-band region.

The objective of this procedure is to approximate the target response (magnitude response) by an all-pole system as the one given by equation (6.103). However, from the realizability conditions we know that in order for the system in (6.103) to be realizable as an DNTL structure it must be stable and causal, thus a minimum phase system. However, because $T(\Omega)$ is specified only in terms of magnitude response, it is not suitable to represent the frequency response of a minimum phase system. So, before we proceed to the all-pole system approximation, we must first compute a new target response $T'(\Omega)$. This new target frequency response must be characterized by the same magnitude response as that of $T(\Omega)$ but also by a phase response $\Phi(\Omega)$. The phase response $\Phi(\Omega)$ must be computed so that $T'(\Omega)$ represents a minimum phase system. Therefore, after specifying the target magnitude $T(\Omega)$ we proceed to obtain the transmission phase response through the Hilbert transform as

$$\Phi(\Omega) = \mathcal{H}\{\ln\left(T(\Omega)\right)\}. \tag{6.104}$$

The new target response $T'(\Omega)$ can now be specified as

$$T'(\Omega) = T(\Omega)e^{\Phi(\Omega)}. \tag{6.105}$$

Notice that because the new target frequency response $T'(\Omega)$ is minimum phase, it is suitable to represent a stable and causal all-pole system.

The final step in the procedure is the approximation of $T'(\Omega)$ by the all-pole system (6.103). For that, we resort to the parametric modeling toolbox provided by Matlab [75]. Very simply put, parametric modeling techniques compute the parameters of some mathematical model that describes a system or process. In order to do so, appropriate information about the system to be modeled such as impulse and frequency responses or input and output sequences must be given to the parametric modeling functions. For the case of DNTL structures system the output from the parametric modeling functions are the coefficients α_i of the all-pole mathematical model given by equation (6.103).

Parametric modeling functions can be divided in two groups: time-domain based modeling and frequency-domain based modeling. The time-domain modeling is carried out from the knowledge of the impulse response or input and output sequences of the unknown system, *i.e.*, the system to be approximated, whereas the frequency-domain modeling is performed from the knowledge of the frequency response of the unknown system. Some of the time-domain based Matlab parametric modeling functions are *arburg*, *lpc*, *arcov*, *aryule*, *prony* and *stmcb*. On the other hand, the frequency-domain parametric modeling can be performed by the function *invfreqz*. For a deeper understanding regarding the parametric modeling toolbox please refer to [75].

In order to get a better interpretation from a practical viewpoint of the procedure outlined above for the synthesizing DNTL structures with arbitrary magnitude transmission frequency response, we summarise the procedure in the following steps:

1. Specify the ideal target transmission magnitude response $T(\Omega)$.

2. Compute the minimum phase target transmission response $T'(\Omega)$ as

$$T'(\Omega) = T(\Omega)e^{\Phi(\Omega)}, \tag{6.106}$$

   where

$$\Phi(\Omega) = \mathcal{H}\{\ln(T(\Omega))\} \tag{6.107}$$

   and $\mathcal{H}$ represents the Hilbert transform.

3. Compute the coefficients of the all-pole system that best approximates $T'(\Omega)$ using the parametric modeling functions referred above and construct the all-pole

transfer function as

$$S_{21}(z) = \frac{b}{1 + \sum_{i=1}^{m} a_i \, z^{-i}}, \tag{6.108}$$

where b and a_i are the coefficients returned by the parametric modeling functions. Notice that equation (6.108) is equivalent to (6.103), however it is expressed in the general form of (6.42).

4. Obtain the transfer function for the reflection frequency response $S_{11}(z)$ associated to $S_{21}(z)$ through the relation

$$|S_{11}(z)|^2 = 1 - |S_{21}(z)|^2 \tag{6.109}$$

using the procedure described in section 6.6.

5. Compute the DNTL filter impedance profile using the discrete layer-peeling inverse scattering procedure described in section 6.5 on the reflection frequency response $S_{11}(z)$.

To demonstrate the synthesis of DNTL filters using parametric modeling tools, we now provide two examples. For the first example we synthesize a filter in which the target magnitude transmission frequency response has a linear variation with frequency when considering a logarithmic scale for the magnitude.

So, for the first step in the procedure, we set the ideal target magnitude response in dB as $m = [-15, 0, 0, 0, -15]$ at the frequencies $\Omega = [-\pi, -0.05\pi, 0, 0.05\pi, \pi]$ respectively. Figure 6.16(a) depicts the target magnitude response $T(\Omega)$ as function of normalized frequencies for the first example. In the second step, we calculate the minimum phase target response $T'(\Omega)$ using the discrete-time Hilbert transform[7] to compute the phase response of $T'(\Omega)$ from $T(\Omega)$ accordingly to (6.107). Figure 6.16 depicts the minimum phase target frequency response $T'(\Omega)$. In Figure 6.17 are depicted the impulse responses corresponding to $T(\Omega)$ and $T'(\Omega)$ respectively. Through visual inspection of Figure 6.17(a) we easily see that the impulse response of $T(\Omega)$ is not causal, *i.e.*, not suitable to be approximated by an all-pole system. On the other hand, from Figure 6.17(b) we have that the impulse response of $T'(\Omega)$ is causal. Furthermore, the energy of the impulse response is maximally concentrated toward the beginning of the impulse response which

[7]This can be done in Matlab using the command *hilbert*.

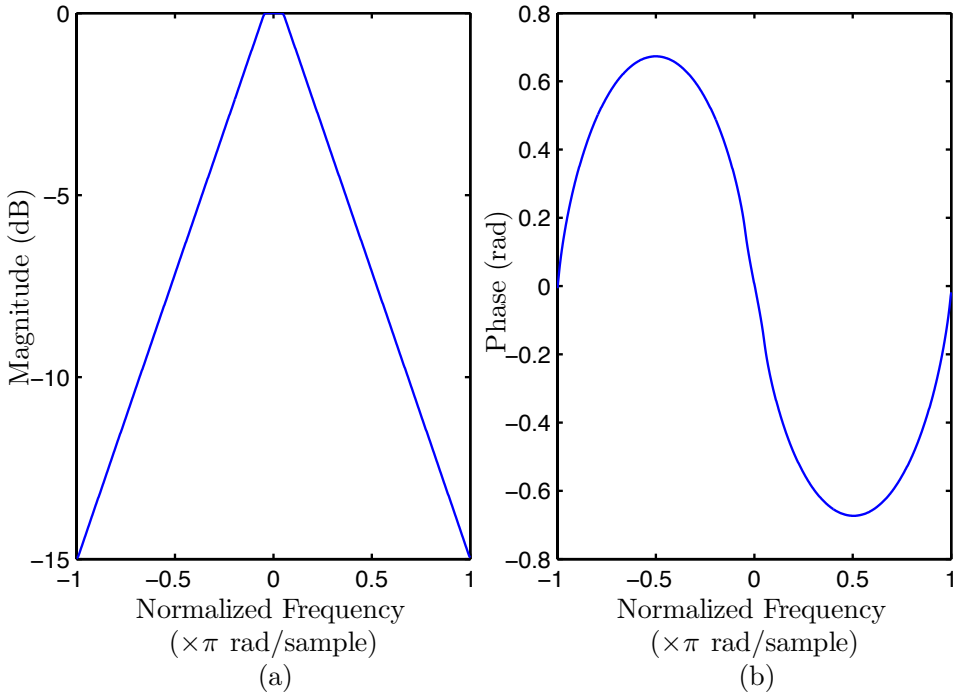

FIGURE 6.16: Minimum phase target frequency response $T'(\Omega)$. In (a) is depicted the magnitude response whereas in (b) we have the phase response which when associated with the magnitude response represents the response of a minimum phase system. Notice that (a) also represents the response of $T(\Omega)$.

denote the minimum phase nature of $T'(\Omega)$. These properties make $T'(\Omega)$ suitable to be approximated by an all-pole system.

In the third step we apply the parametric modeling functions to $T'(\Omega)$ and calculate the coefficients for the all-pole transfer function that better approximates the minimum phase target response. In order to do so, all the functions in the parametric modeling toolbox are considered for the approximation and we select the one that minimizes the magnitude *error function* (EF) defined by

$$\mathrm{EF} = \int_{-\pi}^{\pi} \left(|\mathrm{T}'(\Omega)| - |\mathrm{S}_{21}(\Omega)|\right)^2 \mathrm{d}\Omega, \tag{6.110}$$

where $S_{21}(\Omega)$ is the all-pole transfer function obtained from the approximation (6.108) when evaluated at $z = e^{-j\Omega}$, *i.e.*, at the unit circle.

Equation (6.110) measures the discrepancy between the magnitude of the target function and the magnitude of the approximation all-pole system, that is, it works as a fitness function. Analyzing equation (6.110) we easily realize that the EF value corresponds to the squared value of the total area associated with the difference between

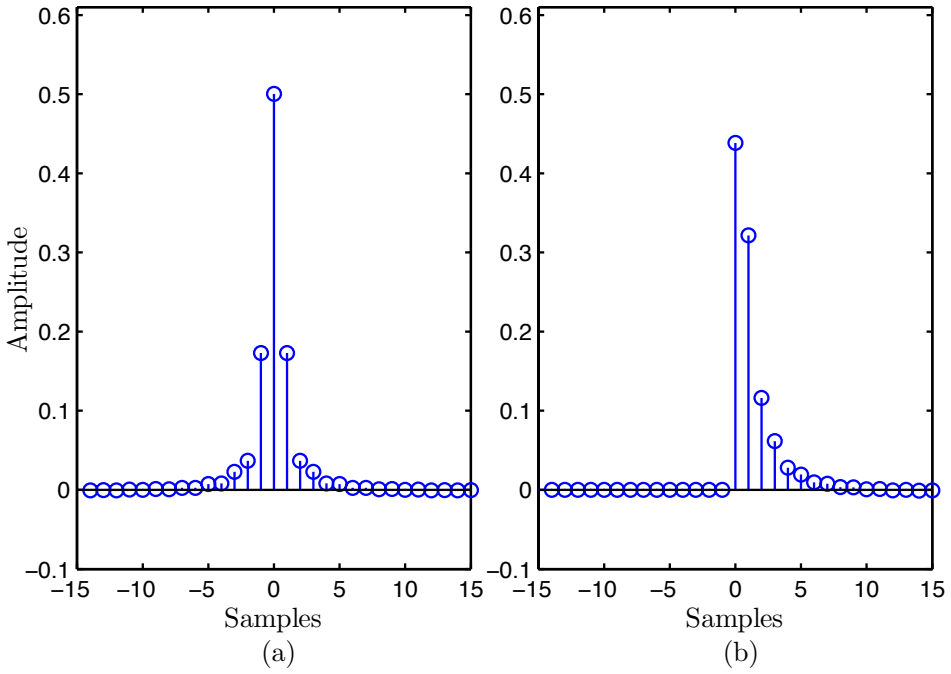

FIGURE 6.17: Impulse response associated with (a) the target magnitude response $T(\Omega)$ and (b) The minimum phase target frequency response $T'(\Omega)$. Notice that the impulse response in (a) is stable but not causal, whereas in (b) the impulse response is both stable and causal.

the magnitude curves of the target and all-pole system frequency responses.

In order to obtain a more general and meaningful error evaluation regarding the approximation of the target response by the all-pole system, we consider a normalized version of error function (6.110) defined as the *relative error function* and given by

$$\mathrm{EF_r} = \frac{\mathrm{EF}}{\mathrm{EF_{max}}}, \tag{6.111}$$

where $\mathrm{EF_{max}}$ corresponds to the maximum evaluation possible for the EF function. Notice that due to physical constrains, the magnitude values of the target function and for the all-pole system must be within the ranges $0 \leq |T'(\Omega)| \leq 1$ and $0 \leq |S_{21}(\Omega)| \leq 1$. Thus, the maximum EF value is obtained when $|T'(\Omega)| = 0$ and $|S_{12}(\Omega)| = 1$ or vice-versa. Thus the maximum EF value is given by

$$\mathrm{EF_{max}} = \int_{-\pi}^{\pi} 1 \; \mathrm{d}\Omega = 2\pi. \tag{6.112}$$

In this way, we have that a very small value of $\mathrm{EF_r}$ indicates a tight fit of the all-pole transfer function $S_{21}(\Omega)$ to the target function $T'(\Omega)$, whereas a large value of $\mathrm{EF_r}$

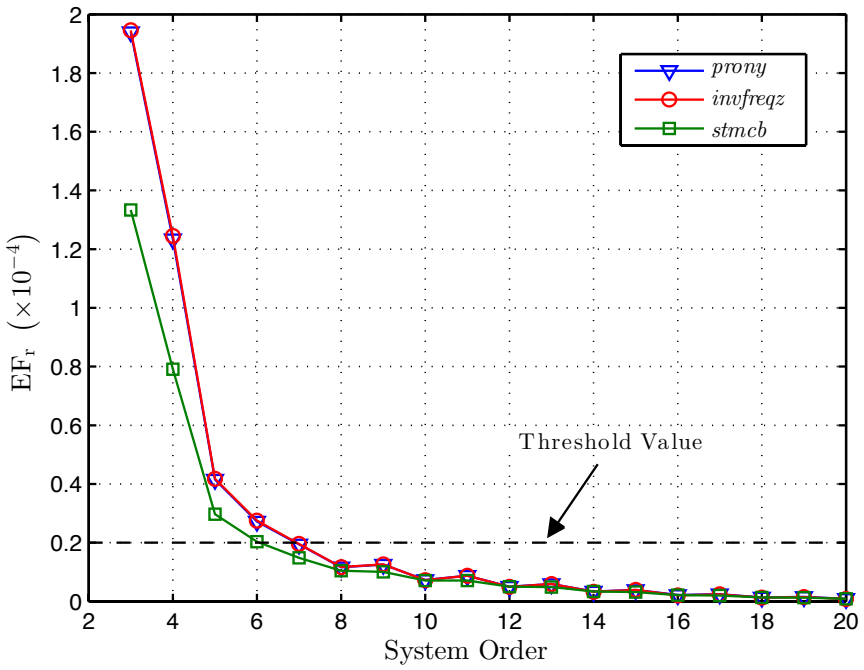

FIGURE 6.18: Error function values as a function of the order of the all-pole function used to approximate the target function. The parametric modeling functions consider in this analysis are *prony*, *invfreqz* and *stmcb*.

indicates a very bad fit.

A preliminary analysis of the parametric modeling functions provided by the Matlab toolbox indicates that the more effective functions for the time-domain modeling are the functions *prony* and *stmcb*. As for the frequency-domain based modeling the only available function is *invfreqz*. In this sense, the analysis that follows regarding the performance of the modeling functions will focus only on these three functions.

Figure 6.18 depicts the evaluation of the $\mathrm{EF_r}$ value as a function of the order of the all-pole system that approximates the minimum phase target response. The curves shown in Figure 6.18 are associated with the modeling of the minimum phase target function $T'(\Omega)$ depicted in Figure 6.16. The first conclusion that we can draw from Figure 6.18 is that the functions *prony* and *invfreqz* have the same performance. Secondly and as expected, we see that the higher the order of the system that approximates $T'(\Omega)$ the lower the value of $\mathrm{EF_r}$. However and because the order of the all-pole system that approximates $T'(\Omega)$ will translate directly into the number of sections of the DNTL structure to be synthesized, a compromise between performance and size (i.e., system order) must be achieved. In this sense, it was considered that a suitable approximation of the target magnitude response is obtained for values of $\mathrm{EF_r}$ bellow $\mathrm{EF_r} = 0.2 \times 10^{-4}$,

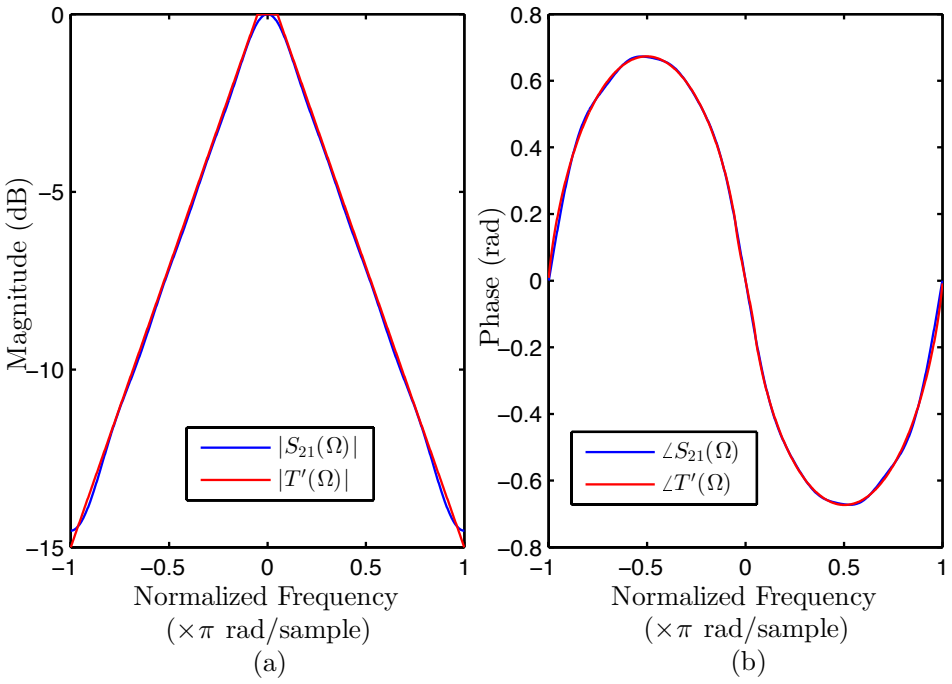

FIGURE 6.19: Target frequency response $T'(\Omega)$ versus the $8th$ order transmission all-pole frequency response $S_{21}(z)$. In (a) is depicted the magnitude response whereas in (b) is depicted the phase response.

when the $\mathrm{EF_r}$ value is calculated using (6.111). Thus, we identify $\mathrm{EF_r} = 0.2 \times 10^{-4}$ as the *threshold* value.

Analyzing Figure 6.18, we conclude that for lower system orders, the $\mathrm{EF_r}$ value regarding the modeling with the *stmcb* function seems to provide better approximations to the target function than that of *prony* and *invfreqz*. However, for system orders higher than eight, the three parametric modeling functions seem to be equivalent from an $\mathrm{EF_r}$ analysis viewpoint. Our goal is to obtain the best possible compromise between performance and size for the DNTL structure to be synthesized. Thus, considering

Coefficients	*stmcb*
b	0.4355
a_1	−0.7327
a_2	0.2723
a_3	−0.1450
a_4	0.0723
a_5	−0.0484
a_6	0.0275
a_7	−0.0171
a_8	0.0066

TABLE 6.1: Coefficients of the $8th$ order all-pole system $S_{21}(z)$ computed by the *stmcb* parametric modeling function.

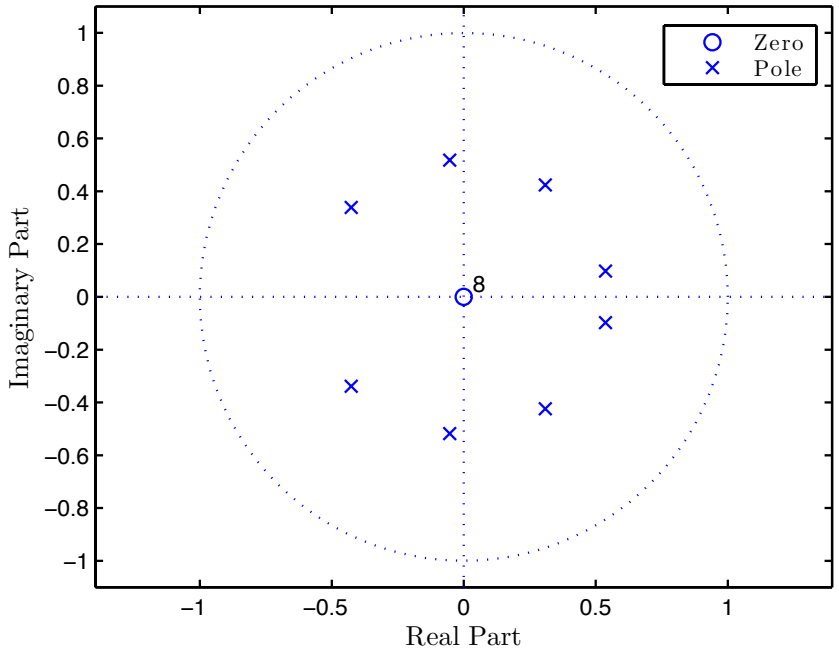

FIGURE 6.20: Pole-Zero plot associated to the $8th$ transmission all-pole system $S_{21}(z)$.

the conclusions drawn from the analysis of Figure 6.18 regarding the performance of the parametric modeling functions, we find that a seventh order all-pole system is the minimum order all-pole system suitable to approximate $T'(\Omega)$, provided that we use the *stmcb* function to perform the parametric modeling. It is easily seen from the figure that the minimum system order for which the $\mathrm{EF_r}$ evaluation is bellow the threshold value is seven, but only for the *stmcb* function. However, it is also clear that there is a significant improvement on the $\mathrm{EF_r}$ value from a seventh to an eight order system. So, in order to obtain a better compromise between size and performance, we choose to decide for an eight order all-pole system to approximate the target function.

From Figure 6.18 we see that for an eight order all-pole system the value of $\mathrm{EF_r}$ for the three modeling functions is practically the same, so, any of the three modeling functions would be suitable. However, we choose the *stmcb* function as this is the one from all the three modeling functions considered, that has best overall performance.

Now that we have established the best performing parametric modeling function as well as the order for the all-pole system that will approximate the target response, we carry on with step 3 of the synthesis procedure. Then, from the knowledge of the minimum phase target function $T'(\Omega)$, the parametric modeling function *stmcb* is used to calculate the coefficients a_i for an $8th$ order all-pole system $S_{21}(z)$ which is defined

by equation (6.108). The coefficient values computed by the *stmcb* function are given in Table 6.1.

Figure 6.19 depicts the overlapping for the frequency responses of the all-pole system $S_{21}(\Omega)$ and the minimum phase target response $T'(\Omega)$. From the figure we clearly see a tight fit between the magnitude of $S_{21}(\Omega)$ and the target function $T(\Omega)$. In addition and though the procedure for finding the minimum suitable order for the approximating all-pole system was based on the magnitude fitting error (6.110), we have that a very tight fit for the phase response is also achieved. This should be an expected result as both $T'(\Omega)$ and all-pole systems are minimum phase. Thus the magnitude and phase frequency responses are uniquely related through the Hilbert transform. So, by assuring a tight fit in the magnitude response, automatically the same shall be verified regarding the phase response.

Figure 6.20 shows the location of the eight poles representing the eighth order transmission frequency response $S_{21}(\Omega)$ shown in Figure 6.19 . Notice that all eight poles and zeros are located inside the unit circle, which by itself fulfills the minimum phase property for the transmission frequency response of any DNTL structure. Furthermore, it verifies realizability condition number four (see section 6.4) regarding the stability of the system accordingly to (6.73).

Now that the all-pole transmission system $S_{21}(z)$ approximating the target function $T(\Omega)$ is defined, we carry on to the fourth step in the procedure for synthesizing DNTL structures with arbitrary magnitude frequency response. This step consists on finding the reflection system $S_{11}(z)$ associated to $S_{21}(z)$ through the relation (6.109). In order to do so, we follow the approach described in section 6.6.

We start by obtaining the square magnitude of the transmission system $|S_{21}(z)|^2$ through equation (6.96). Then, the computation of $|S_{11}(z)|^2$ directly follows by substituting $|S_{21}(z)|^2$ into equation (6.109). In the particular case of this example, the square magnitude of the reflection system when written in a factored form comes as

$$|S_{11}(z)|^2 = K^2 \frac{\prod_{i=1}^{8} \left(1 - c_i z^{-1}\right) \left(1 - \frac{1}{c_i^*} z^{-1}\right)}{\prod_{i=1}^{8} \left(1 - p_i z^{-1}\right) \left(1 - \frac{1}{p_i^*} z^{-1}\right)}, \tag{6.113}$$

where the values p_i, $1/p_i^*$ and c_i, $1/c_i^*$ are the respective poles and zeros and K is defined as the normalizing gain factor. The locations for the zeros and poles of $|S_{11}(z)|^2$ in the

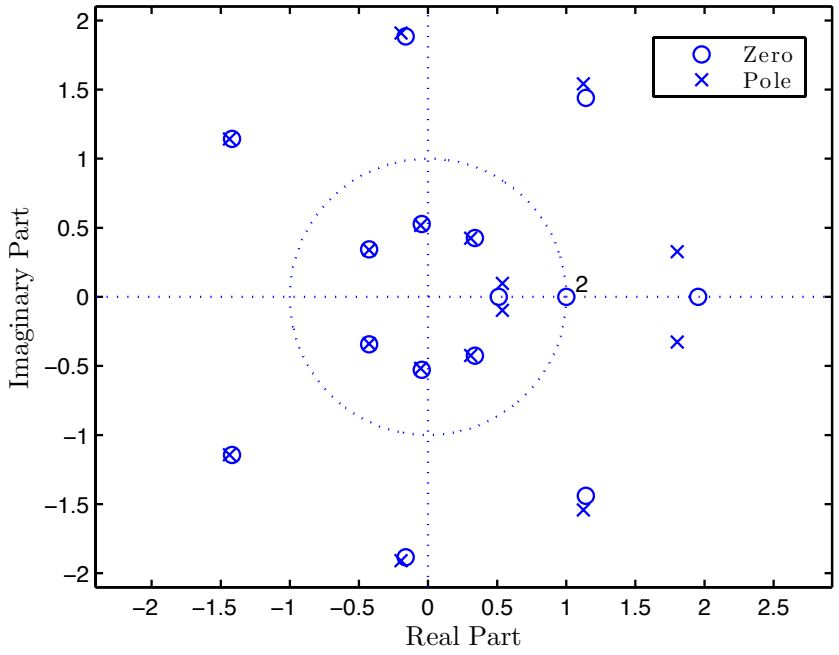

FIGURE 6.21: Pole-Zero plot of the square magnitude of the $8th$ order reflection system $|S_{11}(z)|^2$ associated to $S_{21}(z)$ through the relation (6.109).

z-plane are depicted in Figure 6.21. Notice that the poles of $|S_{11}(z)|^2$ which are inside the unit circle are given by p_i and correspond to the poles of $S_{21}(z)$ that are depicted in Figure 6.20.

The main objective however, is to compute the reflection frequency response. Thus and following the process described in section 6.6, we must select one zero and one pole from each pair of poles and zeros of $|S_{11}(z)|^2$. The selection of the poles is straightforward. Accordingly to the realizability conditions all the poles of $S_{11}(z)$ must be inside the unit circle. So the poles of $S_{11}(z)$ are the ones given by p_i which are the same of $S_{21}(z)$. Therefore, $S_{11}(z)$ is cast in the form

$$S_{11}(z) = K \frac{\prod_{i=1}^{8}(1 - d_i z^{-1})}{\prod_{i=1}^{8}(1 - p_i z^{-1})}, \tag{6.114}$$

where d_i are the eight zeros of $S_{11}(z)$ selected from the zeros of $|S_{21}(z)|^2$ and K is the normalizing gain factor. The selection of the zeros of $S_{11}(z)$ however, are not subjected to stability constrains as are the poles. So, the selection of the zeros is not restricted to the ones inside the unit circle. Nonetheless, some conditions owing to symmetry

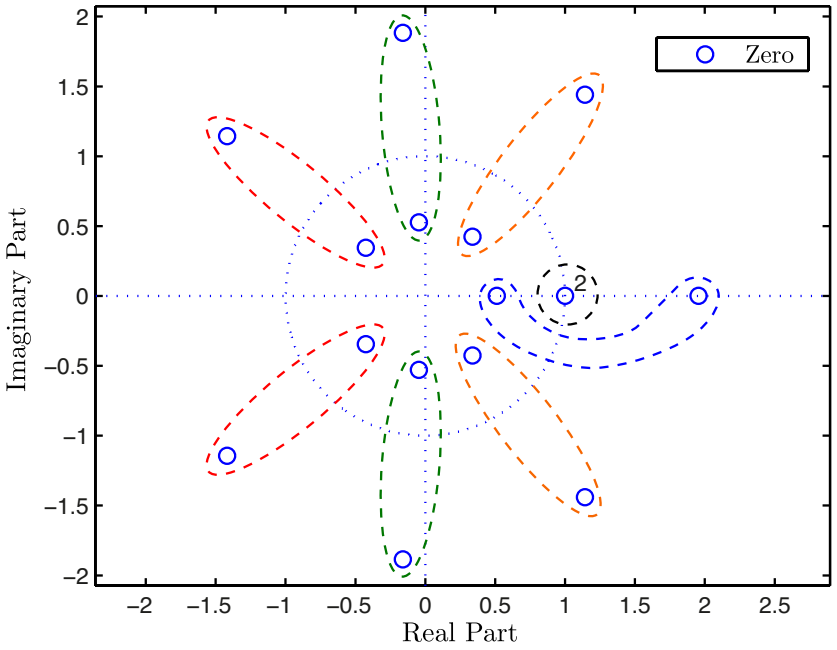

FIGURE 6.22: Zero plot of the square magnitude of the $8th$ order reflection system $|S_{11}(z)|^2$. The zeros are grouped in pairs and to each group is assigned a color. The zero at $z = 1$ is of multiplicity two.

properties of the reflection frequency response $S_{11}(\Omega)$ must be verified. Namely, the selection for the zeros of $S_{11}(z)$ must be such that the selected zeros come as complex conjugate pairs.

Figure 6.22 depict the zeros of $|S_{11}(z)|^2$. In the figure the zeros are arranged in groups of two and to each group is assigned a color. Notice that the zeros in the same group have the same angular frequency whereas zeros belonging to different groups but with the same color have opposite angular frequencies. Therefore, in order to fulfill the symmetry conditions only one zero within each of the groups depicted in Figure 6.22 can be selected. Furthermore, the selection of the zeros within different groups of the same color must be such that the magnitude of the zeros selected from each group have the same magnitude. As an example let us consider the red groups in the figure. Furthermore, let us name the one in the second quadrant as the upper group and the one in the third quadrant as the lower group. Assuming that we chose from the upper group the zero that is inside the unit circle, then, from the symmetry conditions, we have that the zero to be chosen from the lower group is automatically selected and must also be the one inside the unit circle. For the present example and considering Figure 6.22 we have that the total number of different selections for the configuration of the zeros should be

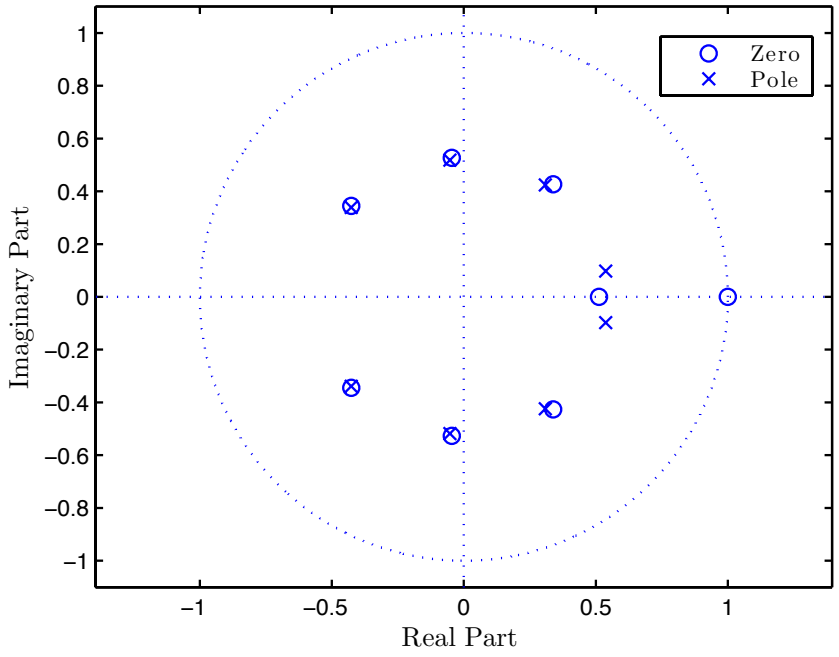

FIGURE 6.23: Pole-Zero plot of the $8th$ order reflection system $S_{11}(z)$. The zeros selected from those of $|S_{11}(z)|^2$ are the zeros within the unit circle.

2^5 because we have five different color groups each with two zeros. However, the two zeros inside the black group are equal, thus, independently of which one is chosen the overall configuration for the zeros is the same. So, the number of different possible zeros configuration is $2^4 = 16$.

Evidently, not all sixteen different zero configurations will be addressed here. However, in order to understand the importance of the different zero selections, two different configurations shall be addressed. First we consider choosing all the zeros of $|S_{21}(z)|^2$ that are inside the unit circle. Figure 6.23 depicts the pole-zero plot for this case.

Numerator		Denominator	
b_1	-1.2434	a_1	-0.7327
b_2	0.4211	a_2	0.2723
b_3	-0.2382	a_3	-0.1450
b_4	0.1079	a_4	0.0723
b_5	-0.0762	a_5	-0.0484
b_6	0.0425	a_6	0.0275
b_7	-0.0265	a_7	-0.0171
b_8	0.0127	a_8	0.0066

TABLE 6.2: Coefficients of the $8th$ order reflection frequency response $S_{11}(z)$ computed from the transmission frequency response $S_{21}(z)$. The gain factor is $K = 0.7198$.

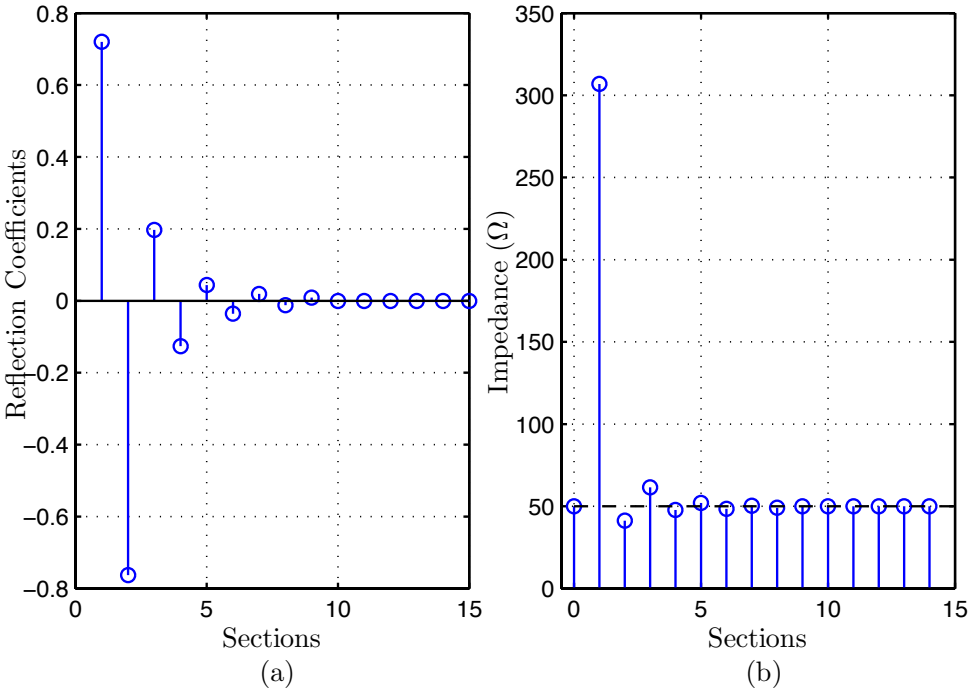

FIGURE 6.24: Inverse scattering results corresponding to 15 iterations of the DLP algorithm. In (a) the reflection coefficient values along the DNTL structure as returned by the DLP algorithm. In (b) the impedance profile of the DNTL structure obtained from the reflection coefficients. The impedance values are computed using (6.78) considering 50Ω as the microwave system characteristic impedance.

Let us rewrite equation (6.114) as the quotient of two polynomials, thus

$$S_{11}(z) = K \frac{1 + \sum_{i=1}^{8} b_i \, z^{-i}}{1 + \sum_{i=1}^{8} a_i \, z^{-i}}. \tag{6.115}$$

From the values of the poles and zeros of $S_{11}(z)$ the coefficients b_i and a_i associated with the numerator and denominator, are easily obtainable through Matlab. The coefficient values for the numerator and denominator of $S_{11}(z)$ are given in Table 6.2. The normalizing gain factor is evaluated as $K = 0.7198$. Notice that the denominator coefficients are the same as those of the transmission system $S_{21}(z)$.

The fifth and final step in the procedure for synthesizing DNTL structures using DSP techniques consist on obtaining the impedance profile for the DNTL structure that implements $S_{11}(\Omega)$ (given by the evaluation of (6.115) in the unit circle) as its reflection frequency response. For that we feed $S_{11}(\Omega)$ to the DLP inverse scattering procedure. Notice that the transmission frequency response associated with $S_{11}(\Omega)$ is given by the

Section	Impedance (Ω)
0	50
1	306.93
2	41.26
3	61.52
4	47.72
5	52.07
6	48.43
7	50.32
8	49.09
9	50

TABLE 6.3: Impedance values for each section of the DNTL synthesized for the first example. The impedance value for section 0, *i.e.*, the first section, is set to that of the microwave system characteristic impedance, 50Ω.

eight order all-pole system $S_{21}(\Omega)$ in (6.108) which approximates the target response $T(\Omega)$. Thus, the synthesis of an DNTL structure by inverse scattering from $S_{11}(z)$ automatically assures that (in ideal conditions) the transmission frequency response for the synthesized DNTL structure will match that of the target response $T'(\Omega)$.

We start by rewriting $S_{11}(z)$ given in (6.115) as the quotient of two polynomials, thus

$$S_{11}(z) = \frac{B(z)}{A(z)}. \tag{6.116}$$

By feeding the numerator and denominator polynomials $B(z)$ and $A(z)$ to the Schur recursions, *i.e.*, to the DLP inverse scattering procedure (see section 6.5), we obtain the reflection coefficients at the interfaces between adjacent sections of the DNTL structure. The inverse scattering procedure results are given in Figure 6.24(a) where the computed values for the reflection coefficients along the DNTL structure are plotted.

In order to obtain the impedance profile from the reflection coefficients, we start by setting the microwave system characteristic impedance to be 50 Ω. Then, the impedance for each section of the DNTL structure is computed from the reflection coefficients through the recursion given by equation (6.78). The resulting impedance profile for the present example is depicted in Figure 6.24(b).

In order to correctly interpret the results presented in Figure 6.24 we must understand that the reflection coefficients values occur at the junction of adjacent sections so, in the graph they are represented by stems located at the interface of each section. On the other hand, the impedance values are also represented by stems, however in this case each stem represents the beginning of a section that extends to the next stem

which in turn is the beginning of another section. As an example lets us consider the first value for the reflection coefficient which is represented by a stem located at section 1. This reflection coefficient characterizes the interface between section 0 and section 1. Thus, the stems for the reflection coefficients represent a single location in space whereas the stems for the impedance values represent the beginning of a transmission line with constant impedance and a given spatial length. The impedance value for the section is given by the amplitude of the stem. Analyzing Figure 6.24(a), we see that the reflection coefficient values along the DNTL structure become zero after the interface between sections eight and nine. This is an expected result as the reflection system $S_{11}(z)$ used as the starting data for the DLP IS algorithm (or Schur recursions) was obtained from an eight order all-pole transmission system $S_{21}(z)$. That is, the target response $T(\Omega)$ was synthesized in the form of a minimum length DNTL structure as discussed in section 6.6. So, for an eight order system, the optimum inverse scattering synthesis procedure results in an DNTL structure with ten distinct impedance sections and nine corresponding reflection coefficients. Evidently, the same situation is verified regarding the impedance profile depicted in Figure 6.24(b) where all sections after section eight have the same impedance value, 50Ω. The impedance values for each section are given in Table 6.3. Notice that the impedance values for sections higher than nine are irrelevant as they all evaluate as 50Ω, thus the structure is comprised only by eight sections. Notice that the first and last sections in Table 6.3 correspond to the microwave system characteristic impedance, thus are not accounted for in the total number of sections of the DNTL structure.

Regarding the impedance values given in Table 6.3 one problem arises. Due to manufacturing limitations, the physical feasibility of the synthesized DNTL may not be possible due to the impedance value for section 1 which is very high. Usually, when considering for instance a microstrip implementation, the largest impedance value achievable is around $160\,\Omega$.

However, it was previously discussed that by considering a different zero configuration for the zeros of $S_{11}(\Omega)$ we should obtain different impedance profiles. Furthermore, each different impedance profile will have the same transmission frequency response as well as the same reflection magnitude response. Only the reflection phase response is affected by the zero configuration.

In an attempt to overcome this physical feasibility problem and still synthesize a DNTL structure with the same transmission frequency characteristics (approximating

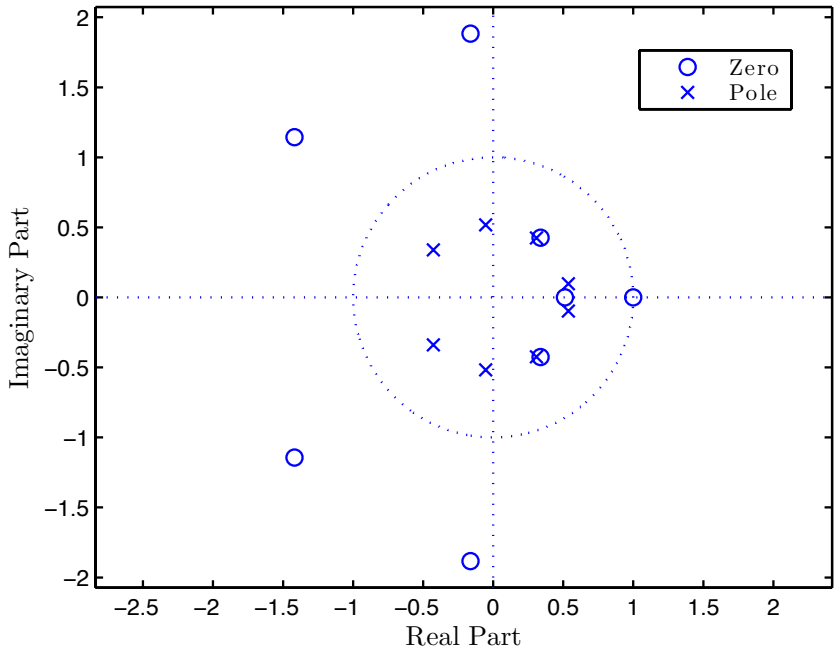

FIGURE 6.25: Pole-Zero plot of the new $8th$ order reflection system $S_{11}(z)$. The set of zeros selected from those of $|S_{11}(z)|^2$ is the optimum set from a physical feasibility viewpoint.

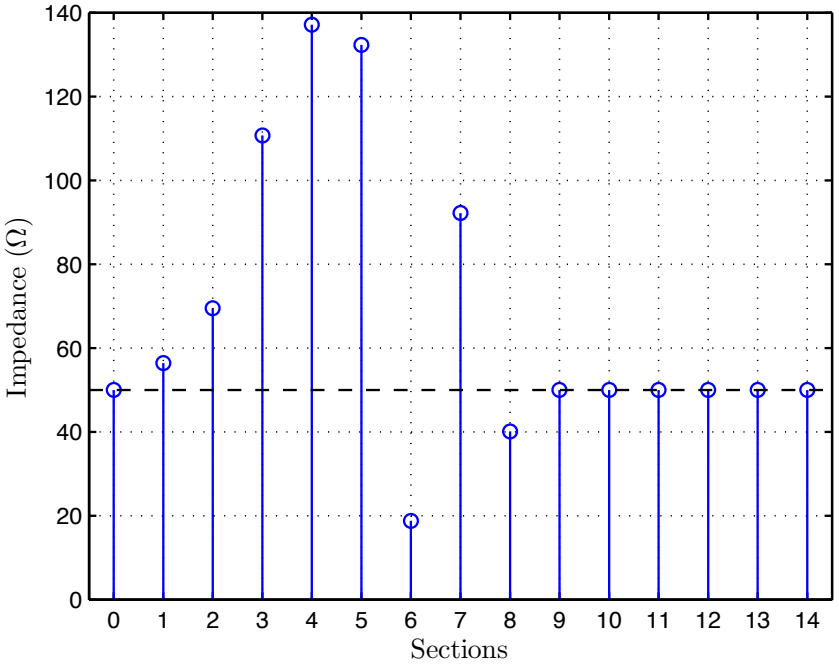

FIGURE 6.26: Impedance profile associated to the new $S_{11}(z)$, which is characterized by the pole-zero configuration depicted in Figure 6.25. The depicted impedance profile was obtained from 15 iterations of the DLP inverse scattering algorithm.

Numerator		Denominator	
b_1	0.9748	a_1	-0.7327
b_2	2.7309	a_2	0.2723
b_3	-0.8882	a_3	-0.1450
b_4	-0.7295	a_4	0.0723
b_5	-11.1845	a_5	-0.0484
b_6	14.0293	a_6	0.0275
b_7	-7.7341	a_7	-0.0171
b_8	1.8013	a_8	0.0066

TABLE 6.4: Coefficients of the $8th$ order reflection frequency response $S_{11}(z)$ for the new pole-zero configuration depicted in Figure 6.25. The gain factor is $K = 0.0606$.

$T(\Omega)$) we have chosen within the sixteen possible configurations the one that minimizes the impedance values problem. The pole-zero plot for the new reflection system $S_{11}(z)$ is depicted in Figure 6.25. From the location of the zeros and the poles, the transfer function $S_{11}(z)$ associated with the new reflection system is then represented as the quotient of two polynomials, prior to be fed to the DLP algorithm. The coefficients for the numerator and denominator polynomials accordingly to (6.115) are given in table 6.4. The corresponding impedance profile is obtained from fifteen iterations of the DLP algorithm and is shown in Figure 6.26.

The impedance values for each section of the new DNTL structure are given in Table 6.5. Again, notice that the impedance values for sections higher than nine are irrelevant as they all evaluate as 50Ω. Thus, the structure is comprised only by eight sections. The first and last sections in Table 6.5 correspond to the microwave system characteristic impedance, thus are not accounted for in the total number of sections of the DNTL structure.

Section	Impedance (Ω)
0	50
1	56.45
2	69.52
3	110.71
4	137.14
5	132.33
6	18.84
7	92.20
8	40.17
9	50

TABLE 6.5: Impedance values for each section of the DNTL synthesized for the first example considering the new zero configuration depicted in Figure 6.25. The impedance value for section 0, *i.e.*, the first section, is set to that of the microwave system characteristic impedance, 50Ω.

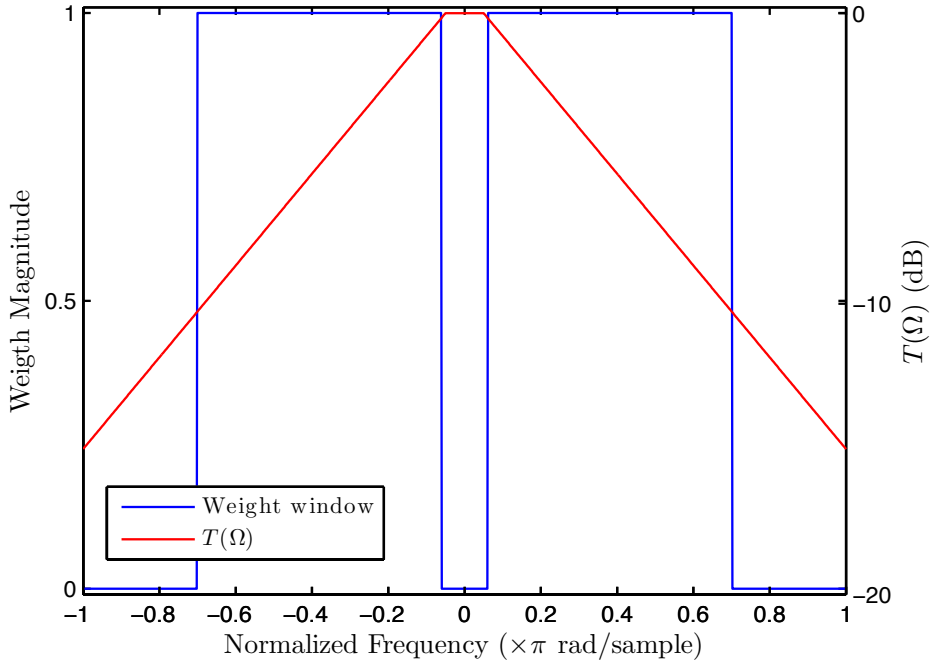

FIGURE 6.27: Target response $T(\Omega)$ versus the weighting function $W(\Omega)$. The weighting is chosen so that the fitting error evaluation is restricted only to the linear sections of $T(\Omega)$.

It becomes clear from Figure 6.26 and from Table 6.5 that, with the new pole-zero configuration, the synthesis of $S_{11}(z)$ leads to an impedance profile in which the maximum impedance value is of 137.14 Ω. Therefore, the new DNTL structure is suitable to physical implementation. Notice that the denominator polynomial coefficients of $S_{11}(z)$ for both zero-pole configurations is the same, which in turn is the same for $S_{21}(z)$. So, although we get different impedance profile for both zero-pole configurations, the transmission frequency response $S_{21}(\Omega)$ remains the same.

In the previous example, the order for the all-pole approximating system, $S_{21}(z)$, was obtained from the evaluation of the error function given by (6.110). This error evaluation was performed considering the approximation error in the entire frequency spectrum, *i.e.*, $-\pi \leq \Omega \leq \pi$. In many practical situations however, the designer is interested in obtaining a good fitting/approximation but only for a specific frequency band. In such cases, the fitting error calculation through equation (6.110) is no longer adequate. However, a meaningful error function can be obtained by including a weighting factor $W(\Omega)$ in to equation (6.110). In this way, we define a new weighted error function as

$$\mathrm{EFW} = \int_{-\pi}^{\pi} \mathrm{W}(\Omega) \left(|\mathrm{T}'(\Omega)| - |\mathrm{S}_{21}(\Omega)|\right)^2 \mathrm{d}\Omega, \tag{6.117}$$

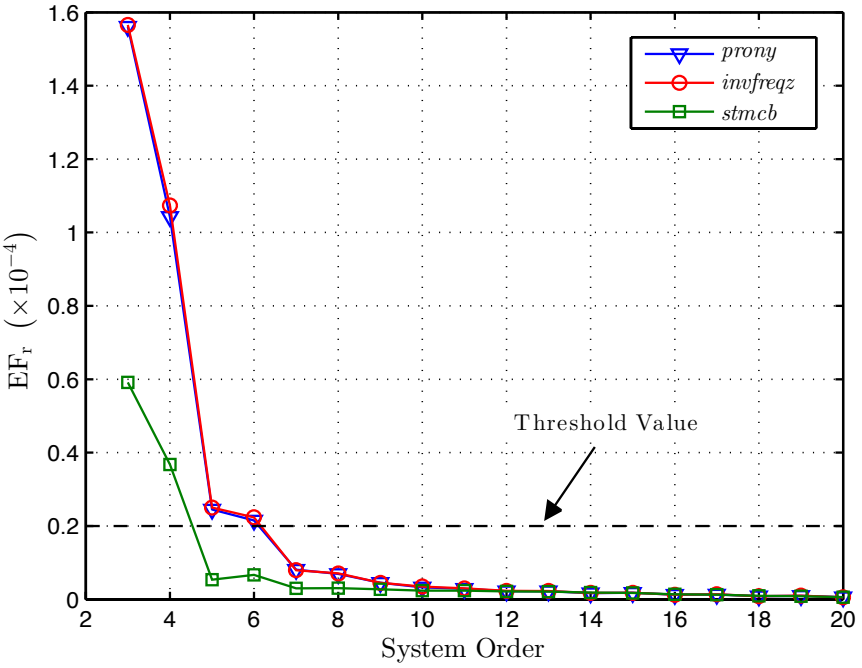

FIGURE 6.28: Weighted error function values as a function of the order of the all-pole function used to approximate the target function. The parametric modeling functions consider in this analysis are *prony*, *invfreqz* and *stmcb*.

with $W(\Omega)$ representing the weighting function. The *relative error function* is then given by

$$\mathrm{EF_r} = \frac{\mathrm{EFW}}{\mathrm{EFW_{max}}}, \tag{6.118}$$

where the associated weighted maximum error $\mathrm{EFW_{max}}$ evaluates as

$$\mathrm{EFW_{max}} = \int_{-\pi}^{\pi} \mathrm{W}(\Omega)\ \mathrm{d}\Omega. \tag{6.119}$$

Now, we address the case in which the goal is to synthesize a DNTL structure whose magnitude transmission frequency response approximates the target response $T(\Omega)$ as before, however, in this case we are only concerned with obtaining a good fitting in a specific band. This is unlike the previous case where the fitting is evaluated on the entire frequency domain.

Figure 6.27 depicts both the target magnitude response $T(\Omega)$ and the weighting function. Notice that the weighting function evaluates as one for the spectrum regions that we are most interested in get a good fitting and is otherwise zero for the remaining regions. In this particular case we are most interested in assure a good fitting in the

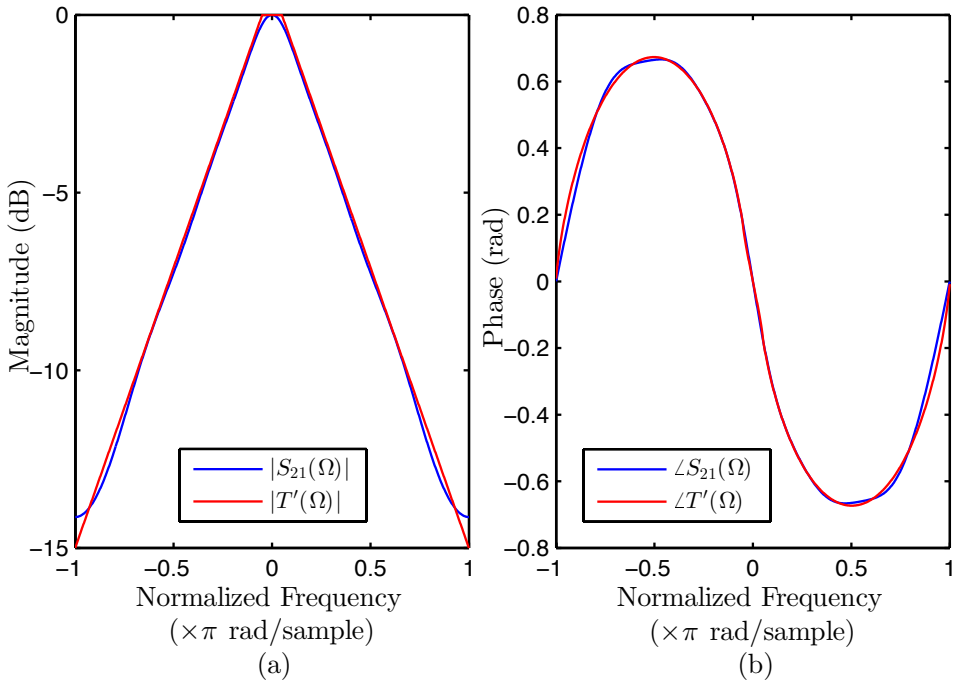

FIGURE 6.29: Target frequency response $T'(\Omega)$ versus the $6th$ order transmission all-pole frequency response $S_{21}(z)$. In (a) is depicted the magnitude response whereas in (b) is depicted the phase response.

frequency regions where the target magnitude response has a linear behavior and not so much for the the regions containing magnitude discontinuities, thus alleviating the fitting effort. In this sense, we have specified the weighting window as shown in Figure 6.27. From the figure we see that the weighting function clearly avoids the discontinuity regions of $T(\Omega)$. Therefore and because the fitting effort is relatively reduced when compared to the previous example, it should be expected that an order lower than eight for the approximating all-pole function $S_{21}(z)$ suffices as to guaranty an $\mathrm{EF_r}$ value below the threshold.

Figure 6.28 depicts the evaluation of the $\mathrm{EF_r}$ value as a function of the order for the all-pole system approximating the minimum phase target response. The values for the error function $\mathrm{EF_r}$ were computed considering the weighted error function given by equation (6.118). The analysis of Figure 6.28 shows that similarly to the previous example, the parametric modeling function *stmcb* provides the best approximation for the lowest system order. On the order hand and unlike the previous case, our fitting assessment is based on a weighted error evaluation. As a result and considering the chosen weighting function, $W(\Omega)$, the lowest system order for which the $\mathrm{EF_r}$ evaluation drops bellow the threshold value is significantly lower than that of the previous example.

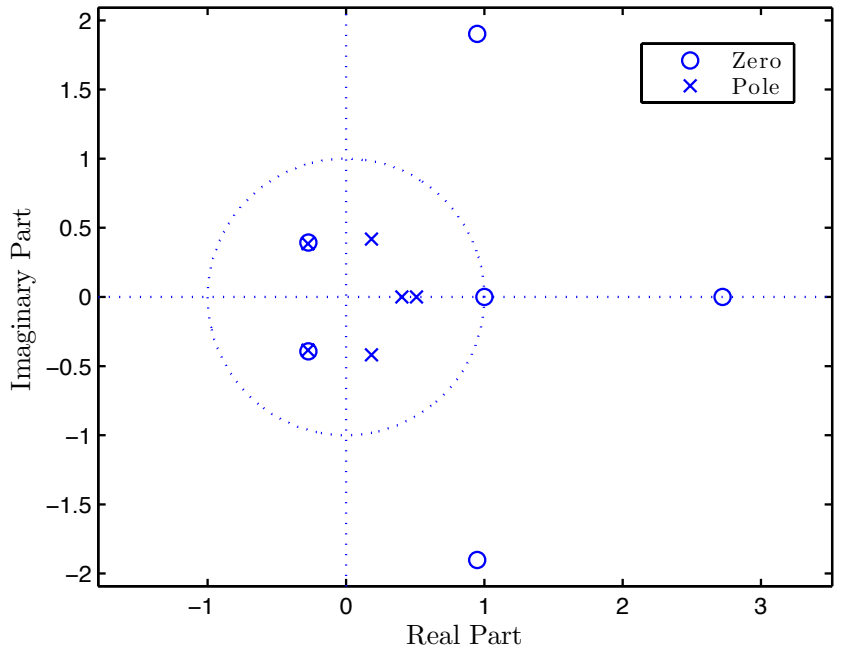

FIGURE 6.30: Pole-Zero plot of the new $6th$ order reflection system $S_{11}(z)$. The set of zeros selected from those of $|S_{11}(z)|^2$ is the optimum set from a physical feasibility viewpoint.

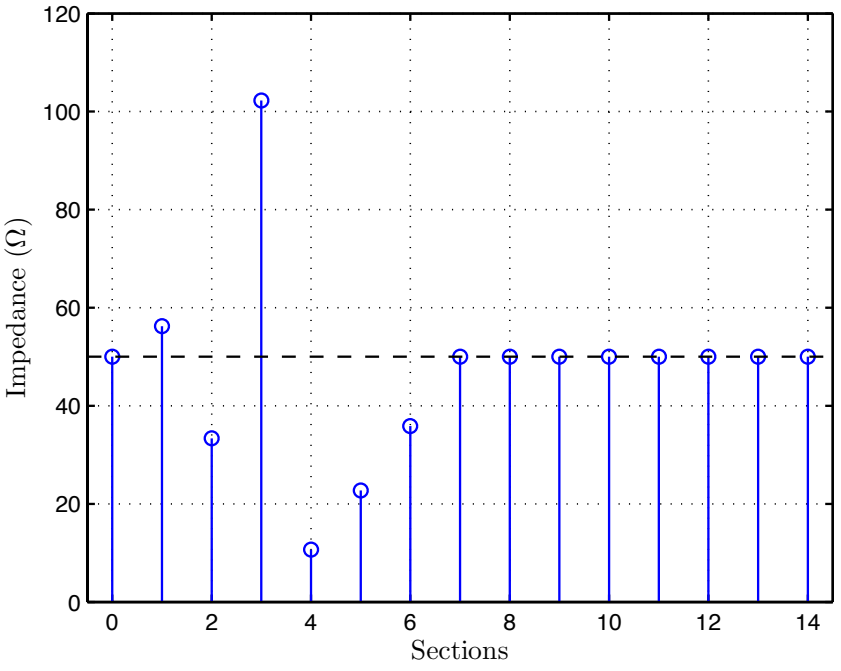

FIGURE 6.31: Impedance profile associated to the $S_{11}(z)$ system, which is characterized by the pole-zero configuration depicted in Figure 6.30. The depicted impedance profile was obtained from 15 iterations of the DLP inverse scattering algorithm.

Numerator		Denominator	
b_1	-5.0756	a_1	-0.7317
b_2	11.4716	a_2	0.2699
b_3	-15.4803	a_3	-0.1407
b_4	3.6024	a_4	0.0648
b_5	1.6680	a_5	-0.0361
b_6	2.8139	a_6	0.0096

TABLE 6.6: Coefficients of the $6th$ order reflection frequency response $S_{11}(z)$ for the pole-zero configuration depicted in Figure 6.30. The gain factor is $K = 0.0585$.

While in the previous case an eight order system was necessary to fulfill the fitting criteria, the error evaluation shown in Figure 6.28 indicates that in the current case a fifth order system will suffice.

Although the values from the error function evaluation regarding the *stmcb* modeling function suggests that a fifth order system should suffice to fulfill the established approximation criteria, it was found that for a fifth order system, none of the impedance profiles resulting from the inverse scattering procedure met the physical feasibility conditions. That is, each one of the possible five section impedance profiles returned by the DLP algorithm features at least one section with an associated characteristic impedance greater than $160\,\Omega$. To overcome this problem while still fulfilling the fitting restrictions, we increase the order of the all-pole approximation system by one.

Figure 6.29 depicts the overlapping for the frequency responses of the all-pole system $S_{21}(\Omega)$ and the minimum phase target response $T'(\Omega)$. From the figure we clearly see a tight fit between the magnitude of $S_{21}(\Omega)$ and the target function $T(\Omega)$ within the frequency region where the weighting function evaluates as one.

From the location of the zeros and the poles, the transfer function $S_{11}(z)$ is then

Section	Impedance (Ω)
0	50
1	56.22
2	33.37
3	102.25
4	10.66
5	22.73
6	36.86
7	50

TABLE 6.7: Impedance values for each section of the DNTL synthesized for the first example considering the pole-zero configuration depicted in Figure 6.30. The impedance value for section 0, *i.e.*, the first section, is set to that of the microwave system characteristic impedance, 50Ω.

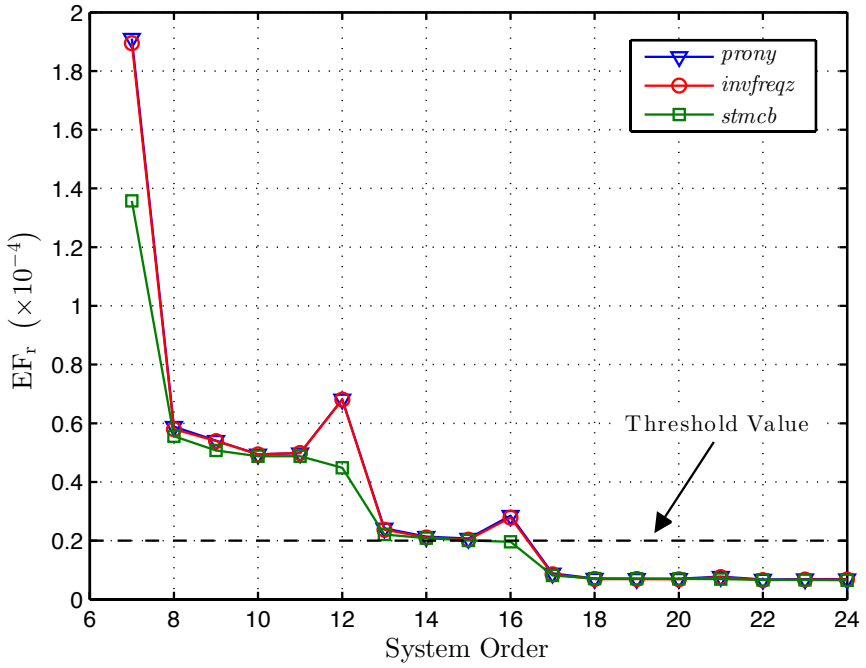

FIGURE 6.32: Error function values as a function of the order of the all-pole function used to approximate the target function. The parametric modeling functions consider in this analysis are *prony*, *invfreqz* and *stmcb*.

represented as the quotient of two polynomials, prior to be fed to the DLP algorithm. The coefficients for the numerator and denominator polynomials accordingly to (6.115) are given in table 6.6. The corresponding impedance profile is obtained from fifteen iterations of the DLP algorithm and is shown in Figure 6.31. The impedance values for each section of the new DNTL structure are given in Table 6.7 and are well within manufacturing constrains as the maximum impedance value is bellow 160 Ω.

The conclusion to be drawn from this last synthesis is that, by considering a weighted fitness error assessment and in this way averting the approximation error in frequency regions where $T(\Omega)$ has discontinuities, we were able to reduce the length of the synthesized DNTL structure. However, in some cases, the approximation of highly discontinue target response magnitudes is necessary in the entire digital frequency spectrum, resulting on the synthesis of large DNTL structures.

Hereupon and for the next example, we chose to synthesize a stair shaped target magnitude response with five constant magnitude levels and linear transitions between levels. Thus, we set the values for the target magnitude response $T(\Omega)$ in decibels as $m = [-15, -15, -7.5, -7.5, -7.5, 0, 0, 0, -7.5, -7.5, -7.5, -15, -15]$ at the frequencies $\Omega = [-\pi, -0.8\pi, -0.6\pi, -0.48\pi, -0.32\pi, -0.135\pi, 0, 0.135\pi, 0.32\pi, 0.48\pi, 0.6\pi, 0.8\pi, \pi]$.

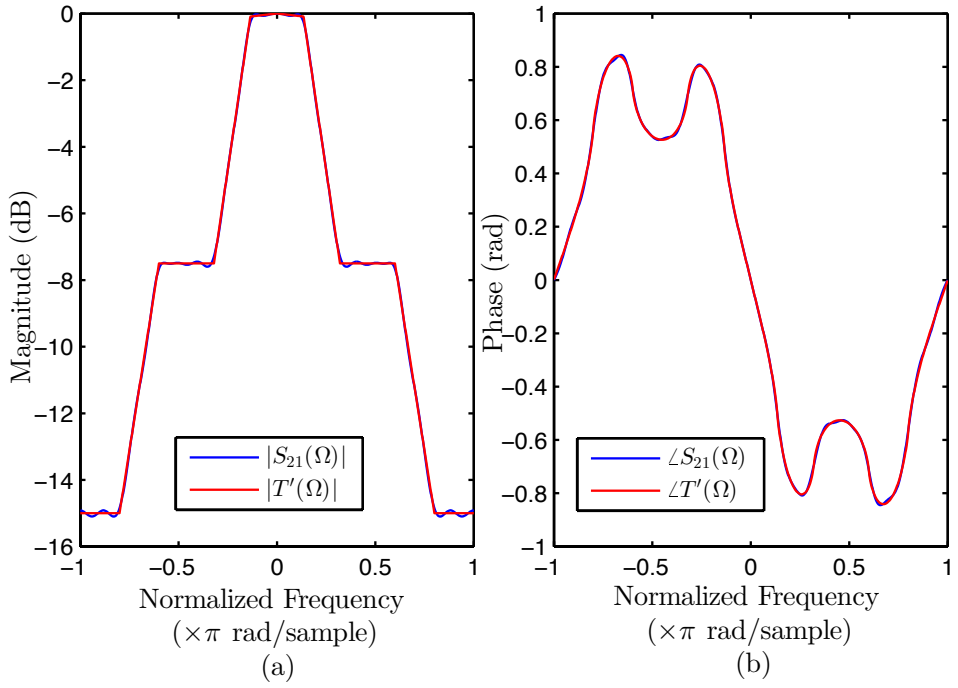

FIGURE 6.33: Target frequency response $T'(\Omega)$ versus the $17th$ order transmission all-pole frequency response $S_{21}(z)$. In (a) is depicted the magnitude response whereas in (b) is depicted the phase response.

It becomes apparent from the target magnitude response specification that the new $T(\Omega)$ is composed by a relatively large amount of discontinuities when compared with the previous example. As a result and considering that we aim for a good fitting in the entire frequency spectrum, it is to be expected the DNTL structure whose magnitude frequency response approximates the new $T(\Omega)$ to be considerably larger then the ones synthesized for the previous example.

Figure 6.32 depicts the evaluation of the $\mathrm{EF_r}$ value as a function of the order for the all-pole system approximating the new minimum phase target response. The values for the error function $\mathrm{EF_r}$ were computed considering the weighted error function given by equation (6.111). The analysis of Figure 6.32 shows that similarly to the previous example, the parametric modeling function *stmcb* provides the best approximation for the lowest system order. Furthermore, we verify that for this example the minimum order for the approximating all-pole system that clears the $\mathrm{EF_r}$ threshold value is seventeen. This in turn, translates in to a DNTL structure with seventeen sections.

Figure 6.33 depicts the minimum phase target response $T'(\Omega)$ associated to the specified target response, as well as the frequency response for the approximating all-pole transmission system $S_{21}(\Omega)$. Notice that the magnitude of $T'(\Omega)$ correspond to the

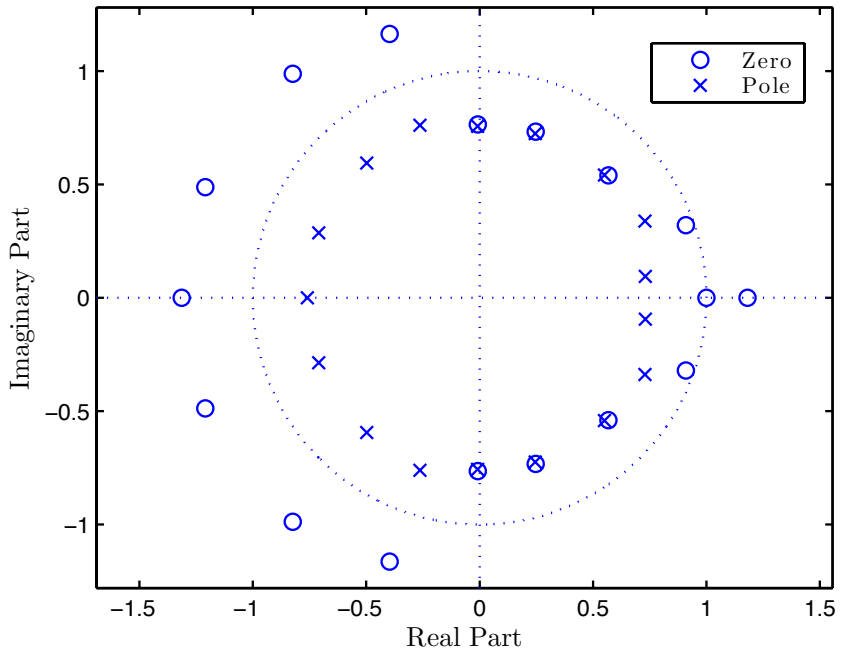

FIGURE 6.34: Pole-Zero plot of the new $17th$ order reflection system $S_{11}(z)$. The set of zeros selected from those of $|S_{11}(z)|^2$ is the optimum set from a physical feasibility viewpoint.

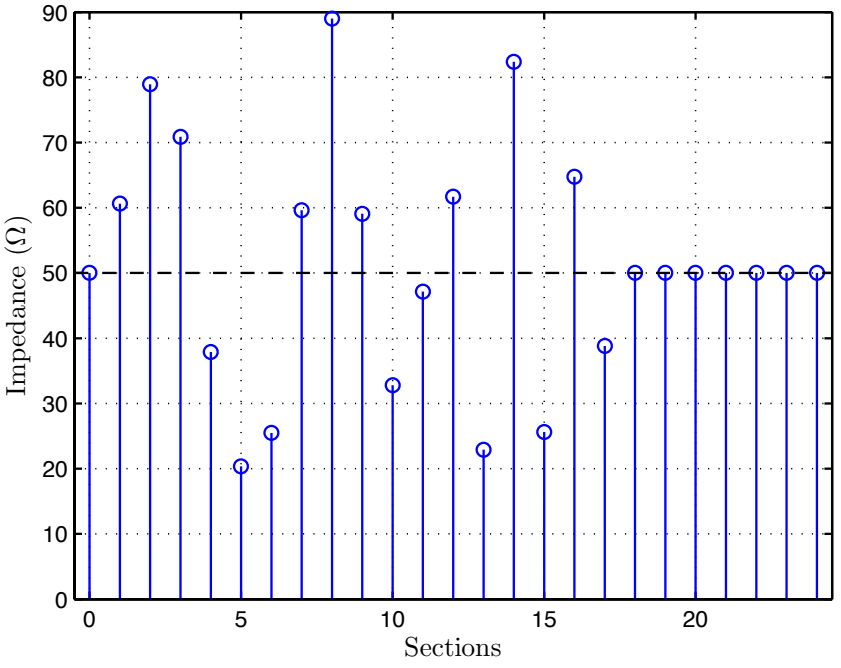

FIGURE 6.35: Impedance profile associated to the $S_{11}(z)$ system, which is characterized by the pole-zero configuration depicted in Figure 6.34. The depicted impedance profile was obtained from 25 iterations of the DLP inverse scattering algorithm.

Numerator		Denominator	
b_1	-0.5629	a_1	-0.7904
b_2	-1.3291	a_2	0.3014
b_3	-2.4605	a_3	-0.2562
b_4	-0.7201	a_4	0.0640
b_5	2.6998	a_5	0.1170
b_6	1.9286	a_6	-0.0579
b_7	-0.8969	a_7	0.0462
b_8	-1.1861	a_8	-0.0163
b_9	-0.1640	a_9	-0.0204
b_{10}	1.5805	a_{10}	0.0122
b_{11}	-1.9256	a_{11}	-0.0097
b_{12}	-1.2080	a_{12}	0.0190
b_{13}	5.6315	a_{13}	-0.0090
b_{14}	-7.7257	a_{14}	-0.0084
b_{15}	6.5058	a_{15}	0.0082
b_{16}	-3.6066	a_{16}	-0.0169
b_{17}	1.3137	a_{17}	0.0121

TABLE 6.8: Coefficients of the $17th$ order reflection frequency response $S_{11}(z)$ associated to the pole-zero configuration depicted in Figure 6.34. The gain factor is $K = 0.096$.

magnitude target response $T(\Omega)$. From the figure we verify that despite the demanding target magnitude response that was established, a seventeenth order all-pole system suffices to accurately model $T'(\Omega)$, within our fitting error evaluation.

After the process for obtaining the approximating all-pole system, the procedure to synthesize the corresponding DNTL structure follows from the same used in the the previous example. That is, we start by obtaining the square magnitude of the transmission system $|S_{21}(z)|^2$ through equation (6.96). Then, the computation of $|S_{11}(z)|^2$ directly

Section	Impedance (Ω)	Section	Impedance (Ω)
0	50	9	59.10
1	60.62	10	32.78
2	78.92	11	47.16
3	70.89	12	61.67
4	37.91	13	22.93
5	20.37	14	82.38
6	25.50	15	25.61
7	59.63	16	64.75
8	89.01	17	38.80
$\cdots$	$\cdots$	18	50

TABLE 6.9: Impedance values for each section of the DNTL synthesized for current example considering the pole-zero configuration depicted in Figure 6.34. The impedance value for section 0, *i.e.*, the first section, is set to that of the microwave system characteristic impedance, 50Ω.

follows by substituting $|S_{21}(z)|^2$ into equation (6.109). The transfer function for the reflection system $S_{11}(z)$ is obtained by choosing a set of seventeen zeros and seventeen poles from those of $|S_{11}(z)|^2$. The selection of the poles is straightforward, that is, to ensure the stability of the system, only the seventeen poles of $|S_{11}(z)|^2$ inside the unit circle can be selected. On the other hand, for the selection of the zeros we have $2^9 = 512$ different possibilities. As we saw in the previous example, not all the zeros configurations result in physical feasible filters due to manufacturing constrains. Hence, a particular set of seventeen zeros must be chosen so that the maximum characteristic impedance value returned by the inverse scattering procedure is less than $160\,\Omega$. The selected pole-zero configuration describing $S_{11}(z)$ is depicted in Figure 6.34. Prior to be fed to the DLP algorithm, $S_{11}(z)$ is represented in the form of (6.115), and the corresponding values for the coefficients for the numerator and denominator polynomials are given in Table 6.8. The corresponding impedance profile is obtained from fifteen iterations of the DLP algorithm and is shown in Figure 6.35. The impedance values for each section of the new DNTL structure are given in Table 6.9 and are well within manufacturing constrains.

6.7.1 DNTL physical implementation

Before presenting the experimental results regarding the DNTL synthesis made in the previous examples, we shall address once again the relationship between the analog domain and the digital domain. Notice that the transition from one domain to the other is of the most importance as it allows for the correct physical implementation of digital filters as DNTL structures. The results obtained so far in this chapter come in the form of the impedance profiles of the DNTL structures that implement some given frequency responses in the digital domain. However, in the digital domain, each DNTL section is identified in the spatial domain by an associated section number and no reference is explicitly made regarding its length. In order to convert the DNTL structures from the digital domain into the analog domain we must first compute a meaningful physical length for the sections of the DNTL structure.

Figure 6.36(a) illustrates a portion of from a DNTL structure. This piece of DNTL is composed by two reflectors and a uniform transmission line connecting both reflectors. The corresponding space-time diagram of incident and reflected pulses is depicted in Figure 6.36(b). This diagram is obtained by considering that the DNTL section on Figure 6.36(a) is probed from the left by a Dirac delta $\delta(t)$ at $t = 0$. It becomes evident

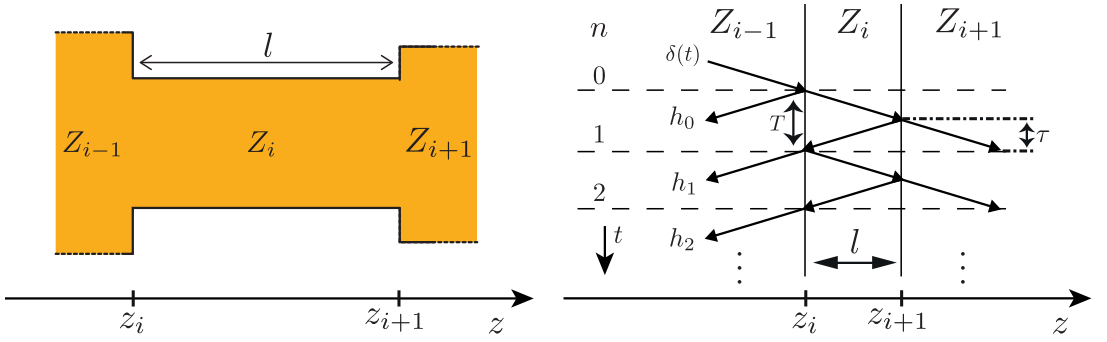

(a) Single section of a DNTL structure.

(b) Space-time diagram of incident and reflected pulses.

FIGURE 6.36: Single section of a DNTL transmission line and the corresponding space-time diagram for a DNTL single section. Notice that the time spacing between reflected pulses is given by the roundtrip propagation time T which is twice of that corresponding to the single layer propagation time τ.

from the analysis of the space-time diagram that time spacing between reflected pulses is given by T whereas the amount of time that the pulses take to propagate along the section of length l is

$$\tau = \frac{T}{2}. \tag{6.120}$$

Therefore, considering the ideal case where the propagation velocity along the DNTL is constant (independent of the physical dimensions of the TL) and given by v_p we have that the physical length for the DNTL sections is given by

$$l = v_p\,\tau. \tag{6.121}$$

From the space-time diagram it is rather simple to verify that the reflection impulse response for a simple DNTL structure as the one illustrated in Figure 6.36(a) is given by

$$r_i(t) = \sum_{n=0}^{\infty} h(nT)\,\delta(t - nT), \tag{6.122}$$

where T is the time spacing between reflected pulses, which is the same of the roundtrip propagation time and $h(t)$ is a continuous function of time. That is, $r_i(t)$ is a sampled version of the continuous function $h(t)$. We know from sampling theory (see section 4.3) that the spectral counterpart of $r_i(t)$ is a scaled frequency repetition of the Fourier transform of the envelope function $H(\omega)$. Furthermore the spectral repetition is periodic and with period ω_s given by

$$\omega_s = \frac{2\pi}{T}. \tag{6.123}$$

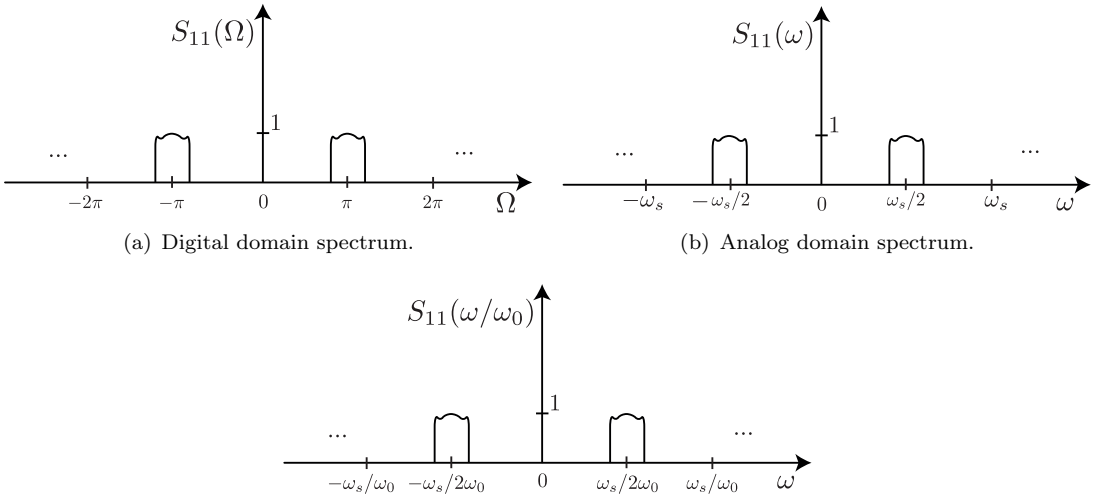

(a) Digital domain spectrum.

(b) Analog domain spectrum.

(c) Normalized analog domain spectrum.

FIGURE 6.37: Equivalence between digital domain to analog domain frequency responses.

Notice that ω_s is usually called the sampling frequency.

Rearranging equation (6.121) and making the corresponding substitution into equation (6.120) yields

$$\tau = \frac{\pi}{\omega_s}, \tag{6.124}$$

which in turn when applied to (6.121) results

$$l = v_p \frac{\pi}{\omega_s}, \tag{6.125}$$

which is the physical length for the sections of the DNTL structure and is measured in meters.

Equation (6.125) tells us that the effective length for the individual sections of any DNTL structure as defined in section 6.1 is determined by the spectral repetition period ω_s, *i.e.*, the sampling frequency and by the the propagation velocity. Notice however that, the propagation velocity along the sections of any DNTL structure when considering the case of ideal transmission line sections, *i.e.*, pure TEM propagation, is a constant value expressed by

$$v_p = \frac{c}{\sqrt{\epsilon_r}} \tag{6.126}$$

where c is the speed of light and ϵ_r is the relative permittivity. Taking this into consideration, we conclude that the length l for the individual sections of any DNTL structure is uniquely defined by its sampling frequency ω_s and vice-versa.

In the digital domain however, the spectrum periodicity is always with a period of 2π as it shown in section 6.3, as a result the length for the sections of any DNTL structure are always given by

$$l = \frac{v_p}{2}. \tag{6.127}$$

The equivalence between the digital domain and analog domain frequency responses is that shown by Figure 6.37. The relation between the frequency variable in both domains was obtained in section 6.3 is given by equation 6.12. Thus the conversion from digital domain to analog domain can be carried out using

$$\omega = \frac{\Omega}{T}. \tag{6.128}$$

The most important conclusion to draw from this analysis is that the synthesis of DNTL structures can be conveniently taken in the digital domain, afterwards, the conversion from the digital domain to the analog domain can be performed by a simple frequency scaling. In other words, due to the inherent discrete nature of DNTL structures, the frequency specifications and the consequent inverse scattering procedure can be carried out by taking advantage of DSP tools such as parametric modeling functions and the Schur recursions respectively. As a result however, all the processing must be carried out under the digital frequency variable Ω domain which is inherently periodic with period 2π. On the other hand, we aim for a physical implementation of the DNTL structures, which means that some equivalence must be established between the digital and analog domains. This equivalence is given by equation (6.128) as a simple linear frequency scaling.

From equation (6.128) we clearly see that $\Omega = 2\pi$ in the digital domain corresponds to $\omega = \omega_s$ in the analog domain. This relationship between the frequency response in the digital and analog domains is illustrated by Figure 6.37(a) and Figure 6.37(b). In summary, from Figure 6.37 we conclude that the relation between the digital and analog spectrums is confined to a simple linear frequency scaling represented by equation (6.128). Thus, trough equation (6.128) we can conveniently choose an analog sampling frequency (other than 2π) by setting the appropriate sampling period T. Notice that the physical length for the sections of the DNTL structure can be specified as a function

of the sampling wavelength, yielding

$$l = v_p \frac{\pi}{\omega_s} = \frac{v_p \pi}{2\pi f_s} = \frac{\lambda_s}{2}, \tag{6.129}$$

where f_s is the sampling frequency and λ_s is the corresponding wavelength.

Most often however, the frequency response is represented in the analog domain in the form of a frequency normalized spectrum as illustrated in Figure 6.37(c). Let us consider the frequency normalization given by

$$\bar{\omega} = \frac{\omega}{\omega_0}, \tag{6.130}$$

where ω_0 is the normalization frequency and is usually chosen to be whether the cutoff frequency in low/high-pass filters or the center frequency in bandpass/bandstop filters. In these cases the physical length for the sections of the DNTL structure is given as the normalized length by

$$\bar{l} = v_p \frac{\pi}{\bar{\omega}_s}, \tag{6.131}$$

where $\bar{\omega}_s = \omega_s/\omega_0$. The DNTL structure can then be scaled to unnormalized length through

$$l = \frac{\bar{l}}{\omega_0}. \tag{6.132}$$

As an example let us consider that $\omega_0 = \omega_s/2$, in this case we have that the normalized sampling frequency is $\bar{\omega}_s = 2$. The normalized physical length for each section of the DNTL structure is given by

$$\bar{l} = v_p \frac{\pi}{2}, \tag{6.133}$$

and the real length is given by

$$l = \frac{\bar{l}}{\omega_0} = \frac{v_p \pi}{2\,\omega_0} = \frac{\lambda_0}{4}. \tag{6.134}$$

The electric length at ω_0 for each section is given by (l is given by (6.125))

$$\theta_0 = \beta\, l = \frac{\omega_0}{v_p} \frac{v_p \pi}{\omega_s} = \pi \frac{\omega_0}{\omega_s} = \pi \frac{f_0}{f_s} = \pi \frac{\lambda_s}{\lambda_0}, \tag{6.135}$$

which under the condition $\omega_0 = \omega_s/2$ reduces to

$$\theta_0 = \frac{\pi}{2}. \tag{6.136}$$

6.8 Synthesis of discrete DNTL filters using analog prototype filters

In section 6.7 we have described a procedure to perform the synthesis of DNTL structures with arbitrary magnitude frequency response. The procedure consists on defining an ideal magnitude target response after which parametric modeling tools are used in order to find the coefficients for an all-pole system which frequency response approximates the target magnitude response within a certain error margin. The order of the all-pole system and consequently the length for the synthesized DNTL structure strongly depends on the maximum error allowed for the fitting between target and all-pole frequency responses. From the approximating all-pole system, the DNTL structure impedance profile is then computed by inverse scattering through the DLP algorithm.

Most of the times however, the application for DNTL structures is that of frequency selective filters. Thus, in such cases, the objective is to perform the synthesis of DNTL structures whose frequency response approximate that of an ideal rectangular filter. The design of selective frequency filters is one example among others where analog systems can be successfully used as prototypes on the synthesis of DNTL structures. This works by using readily available analog/continuous system designs and converting them into discrete-time systems with similar specifications. However, in order to do so we must be able to transform the analog IIR systems (continuous-time) into discrete IIR systems (discrete-time).

The motivation for considering the use of analog prototypes stems from the fact that the art of continuous-time IIR systems design is highly advanced. As such, system designs available for continuous-time systems can be transformed to designs for discrete-time system with related specifications through the the use of transformations from the continuous to the discrete domains. Furthermore, many continuous-time IIR systems design methods have relatively simple closed-form design formulas (*e.g.*, Butterworth, Chebyshev polynomials) which makes the conversion to discrete-time a rather simple process to carry out. We emphasize however that, although the procedure described in section 6.7 for synthesizing DNTL structures can be successful used in every situation, we find that the use of analog prototypes greatly simplifies the synthesis procedure as it avoids the parametric modeling step.

6.8.1 Transformation between continuous- and discrete-time systems

As we have discussed above, in many situations it is of interest to transform a continuous-time system into a discrete-time system. However such transformation must be established under some pre established conditions.

Let us consider that $H_c(s)$ represents the analog prototype system whereas $H_d(z)$ represents its digital counterpart. The basic idea behind the conversion of $H_c(s)$ into $H_d(z)$ is to apply a mapping from the s-domain to the z-domain, so that, the essential properties of the analog frequency response are preserved in the digital domain. In this way, the mapping process must be carried out so that the imaginary axis $j\omega$ in the s-plane is mapped onto the unit circle in the z-plane, furthermore, a stable analog system must be mapped into a stable digital system.

In this section we discuss three transformations for mapping continuous-time IIR systems to discrete-time IIR system. The transformations are the *impulse invariance thechnique*, *bilinear transform* and *approximation of derivatives method*, [1] [61] [76]. Notice that, these methods were long ago developed in DSP theory, however and as we shall demonstrate next, not all of them are applicable in the optimum sense to the synthesis of DNTL structures The goal of this section is to analyze the transformation methods and understand and how well are they suited to the synthesis of minimum length DNTL structures. Furthermore and considering the optimum synthesis of DNTL structures addressed in section 6.6, the objective with these transformations is to obtain optimum discrete transmission systems from the analog prototypes. Thus, besides the stability and causality conditions, the discrete-time system obtained from the transformations must also be all-poles systems. In that sense, in this section we shall consider the synthesis of frequency selective filters, whose analog prototype counterparts are Butterworth and Chebyshev filters, which in turn are all-pole systems in the analog domain (Laplace domain).

We emphasize that, although the primary focus in this section is on the design of frequency selective filters, the techniques here discussed are more broadly applicable. Furthermore, the following derivations regarding the transformation methods closely follow those found in [1] [61] [76], taking however special attention to synthesis of DNTL structures.

6.8.1.1 Impulse invariance technique

The basic idea behind the impulse invariance method is to take the impulse response $h_c(t)$ from a given continuous-time (analog) prototype system and to obtain the impulse response $h_d[n]$ for the corresponding discrete time system through sampling. That is, in the context of filter design, we can understand this technique as a method to obtain a discrete-time system whose frequency response is determined by the analog prototype system. The impulse response for the digital counterpart of the analog prototype system consists of equally spaced samples of $h_c(t)$ so that

$$h_d[n] = h_c(nT), \tag{6.137}$$

where T is the sampling time interval or sampling period. Furthermore, from the sampling process know that the sampled impulse response can be expressed as the product of the analog prototype system impulse response with an infinite impulse train $p(t)$, yielding

$$\begin{aligned} h_p(t) &= h_c(t) \sum_{n=-\infty}^{+\infty} \delta(t - nT) \\ &= \sum_{n=-\infty}^{+\infty} h_c(nT)\, \delta(t - nT). \end{aligned} \tag{6.138}$$

Notice the resemblance between (6.138) and (4.215) which was obtained in the context of the layer peeling procedure in section 4.3. Furthermore, notice that (6.138) reduces to (4.215) when considering the analog prototype system to be a causal system. Following the same reasoning as in section 4.3 regarding the discrete layer-peeling algorithm, we easily see that the spectrum of an impulse response constituted by the sum of delta functions with an uniform spacing T, as is $h_p(t)$, is given by the periodic repetition of the scaled frequency response of the analog prototype $H_c(\omega)$. The repetition period is given by $\omega_s = 2\pi/T$. The spectrum for the sampled impulse response $h_p(t)$ is given accordingly to equation (4.222) as[8]

$$H_p(\omega) = \frac{1}{T} \sum_{k=-\infty}^{\infty} H(j\omega - jk\omega_s). \tag{6.139}$$

[8]Here we consider the Fourier transform expressed as a function of $j\omega$ rather than w as in section 4.3.

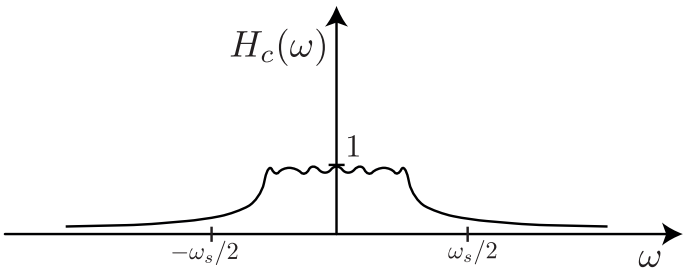

(a) Analog prototype frequency response.

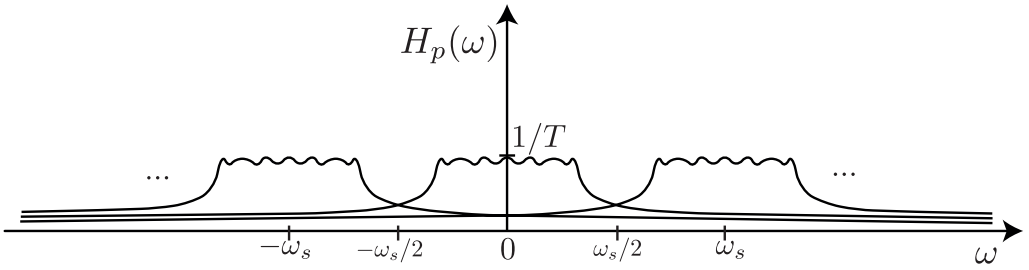

(b) Aliasing as given by equation (6.139) which results from the sampling process.

FIGURE 6.38: Comparison between the frequency responses for the analog prototype system (a) and for the system obtained by sampling the impulse response $h_c(t)$ in (b), where the aliasing effect resulting from the sampling process is clearly visible.

Figure 6.38 illustrates the frequency response for the analog prototype system as well as the frequency response accordingly to (6.139) for the system obtained from the sampling process. It is clear from Figure (6.38(b)) that $H_p(\omega)$ has the frequency characteristics of the analog prototype if the sampling period T is chosen small enough to avoid or minimize the aliasing effects. For high values of T however, the frequency response replicas overlap each other, significantly distorting the passband response. In the figure we show the first three aliasing parts, which when summed up with all the other aliasing parts yield the total frequency response $H_p(\omega)$.

Let us now consider the more general case where we replace the $j\omega$ variable by the Laplace transform variable s. In this way we have the system response given by

$$H_p(s) = \frac{1}{T} \sum_{k=-\infty}^{\infty} H(s - jk\omega_s), \tag{6.140}$$

where $\omega_s = 2\pi/T$. Following the same reasoning as in section 4.3, we can rewrite equation (6.140) by directly calculating the Laplace transform of (6.138), thus

$$H_p(s) = \mathcal{L}\{h_p(t)\} = \sum_{n=-\infty}^{+\infty} h_c(nT)\, e^{-snT}. \tag{6.141}$$

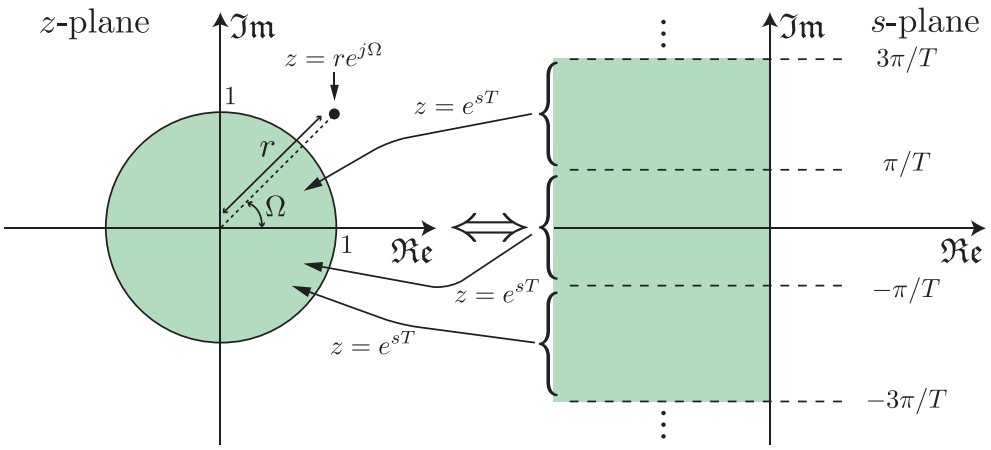

FIGURE 6.39: Mapping produced by the impulse invariance method, accordingly to the transformation $z = e^{sT}$.

On the other hand and considering the relation (6.137), the z-transform of $h_d[n]$ is from the definition given by

$$H_d(z) = \mathcal{Z}\{h_d[n]\} = \sum_{n=-\infty}^{+\infty} h_d[n]\, z^{-n}. \tag{6.142}$$

From the comparison between equations (6.141) and (6.142), we easily realize that accordingly to the impulse invariance method the transformation between the analog prototype system $H_c(s)$ and its digital counterpart is represented by the relation

$$z = e^{sT}. \tag{6.143}$$

Substituting the analog domain complex variable $s = \sigma + j\omega$ into the mapping equation and expressing the digital domain complex variable according to (6.52) we get

$$z = r\, e^{j\Omega} = e^{\sigma T}\, e^{j\omega T}. \tag{6.144}$$

From the previous relation we easily realize that

$$r = e^{\sigma T}, \tag{6.145}$$

$$\Omega = \omega T. \tag{6.146}$$

From the relation (6.145) we have that $\sigma < 0$ implies $0 < r < 1$ and $\sigma > 0$ implies that $r > 1$. Furthermore when $\sigma = 0$, we have $r = 1$. Thus, the left-hand plane (LHP) of the s-plane is mapped inside the unit circe in the z-plane and the right-hand plane

(RHP) of the s-plane is mapped to the outside of the unit circe in the z-plane. Also, the $j\omega$-axis in the s-plane is mapped onto the unit circle on the z-plane. However, due to the periodicity of $e^{j\omega T}$ in equation (6.144), the mapping of $j\omega$ into the unit circle is not one-to-one, *e.g.*, the values for $-\pi/T \leq \omega \leq \pi/T$ in the analog domain correspond to $-\pi \leq \Omega \leq \pi$ in the digital domain, but the values for $\pi/T \leq \omega \leq 3\pi/T$ are also mapped into $-\pi \leq \Omega \leq \pi$, and so on. This fact is illustrated in Figure 6.39 which illustrates the mapping from s-plane to z-plane and vice-versa, accordingly to the relation 6.143. We see that the mapping of the imaginary axis $j\omega$ into the z-plane is such that each segment of length $\omega = 2\pi/T$ is mapped once around the unit circle. Actually, entire strips of width $\omega = 2\pi/T$ in the s-plane map onto the entire z-plane. Furthermore we clearly see that the LHP of the s-plane is mapped inside the unit circle in the z-plane, thus, it should be expected for stable poles from the analog prototype to be transformed into stable poles in the digital system. In fact, this is the case for the mapping of the poles, however, the mapping of the zeros is not ruled by the transformation $z = e^{sT}$ as we shall demonstrate further on.

Let us consider the *Nth* order transfer function $H_c(s)$ for an analog prototype system, which is conveniently expressed in a partial-fraction form. For convenience, let us also assume $H_c(s)$ to be constituted by distinct poles, thus

$$H_c(s) = \sum_{k=1}^{N} \frac{A_k}{s - p_k}, \tag{6.147}$$

where p_k are the poles for the analog system and A_k are the residues of the partial faction expansion. From the Laplace transform tabulated pairs [1] we have that

$$\frac{1}{s + \alpha} \overset{\mathcal{L}}{\longleftrightarrow} e^{-\alpha t}\, u(t). \tag{6.148}$$

Therefore, the impulse response corresponding to $H_c(s)$ is given by

$$h_c(t) = \sum_{k=1}^{N} A_k\, e^{p_k t}\, u(t). \tag{6.149}$$

Through the sampling of $h_c(t)$ periodically at $t = nT$, we obtain the unit sample response for the corresponding discrete-time system, thus

$$h_d[n] = h_c(nT) = \sum_{k=1}^{N} A_k\, e^{p_k nT}\, u[n] = \sum_{k=1}^{N} A_k\, (e^{p_k T})^n\, u[n]. \tag{6.150}$$

The corresponding transfer function is easily obtained from the tabulated z-transform pair

$$\alpha^n\, u[n] \overset{\mathcal{Z}}{\longleftrightarrow} \frac{1}{1-\alpha\, z^{-1}}. \tag{6.151}$$

In this way we have that the discrete system obtained through the impulse invariance method from the analog prototype $H_c(s)$ is given by

$$H_d(z) = \sum_{k=1}^{N} \frac{A_k}{1 - e^{p_k T}\, z^{-1}}. \tag{6.152}$$

From a simple inspection of (6.152), we easily see that the N poles of $H_d(z)$ are located at

$$z = e^{p_k T}, \qquad k = 1, 2, 3, ..., N. \tag{6.153}$$

Comparing the digital system transfer function (6.152) with that of the analog prototype (6.147) we see that the partial fraction residues A_k are preserved, but more importantly the poles in the analog domain are mapped into the digital domain through the relation (6.143). As a consequence of this pole mapping we conclude that any digital system obtained from an stable analog prototype system using the impulse invariance technique will always be a stable system. That is, if the poles for the analog system are such that $\mathfrak{Re}\{p_k\} < 0$, then $|e^{p_k T}| < 1$. Unlike the poles, the mapping for the zeros of $H_d(z)$ do not follows from a direct mapping. Instead, the zeros for $H_d(z)$ are a function of the poles and the residues A_k. The following example demonstrates this fact.

Let us consider a second order analog prototype given by the transfer function

$$\begin{aligned} H_c(s) &= \frac{s+a}{(s+a)^2 + b^2} \\ &= \frac{1/2}{s+a+jb} + \frac{1/2}{s+a-jb}, \end{aligned} \tag{6.154}$$

which has one zero at $s = -a$, the second zero at infinity, and a complex conjugate pair of poles at $s = -a \pm jb$.

The digital domain transfer function $H_d(z)$ resulting from the impulse invariance method is obtained directly from $H_c(s)$ accordingly to (6.152). Thus we have

$$\begin{aligned} H_d(z) &= \frac{1/2}{1 - e^{-aT} e^{-jbT}\, z^{-1}} + \frac{1/2}{1 - e^{-aT} e^{jbT}\, z^{-1}} \\ &= \frac{z(z - e^{-aT}\, \cos(bT))}{z^2 - 2e^{-aT}\, \cos(bT)\, z + e^{-2aT}}. \end{aligned} \tag{6.155}$$

The resulting digital system in (6.155) has one zero at $z = 0$ and another one at $z = e^{-aT\cos(bT)}$. Therefore, we see that although the poles are mapped by $z = e^{p_k T}$, the zeros are not mapped accordingly to this relation. Notice that the aliasing effect depicted in Figure 6.38(b) actually results in a distortion of the passband centered around $\omega = 0$. When considering the same effect associated with the previous example, we may conclude that the spectrum distortion resulting from the aliasing phenomena, is mathematically described by a different mapping for the zeros of the system.

It is important to emphasize that the mapping from the s-plane to the z-plane as induced by the impulse invariance method is not a simple algebraic mapping, as are the mapping procedures based on the numerical solution of differential equations, *e.g.*, the *bilinear transform* or the *approximation of derivatives method* that shall be addressed in the upcoming subsections. This is because unlike these methods, the mapping entailed by the impulse invariance method is actually a many-to-one mapping. That is, each one of the infinite number of strips with width $2\pi/T$ in the s-plane, as illustrated in Figure 6.39, is mapped to the entire z-plane through the relation (6.143). Thus, the impulse invariance method does not actually correspond to the simple mapping of points between the s-plane and the z-plane as given by the relation (6.143). Instead, the points mapped in to the z-plane, from the s-plane, are the result of the overlap of the infinite number of individual mappings of strips of width $2\pi/T$. The mapping from the s-plane into the z-plane for each individual strip however, is done through the relation (6.143). Notice that the many-to-one mapping process is in fact a manifestation of the aliasing effect illustrated in Figure 6.38(b), which in turn is due to the sampling process.

At this point, it is important to recall that our goal is that of the optimum synthesis of DNTL structures. That is, the synthesis of minimum length DNTL structures whose transmission frequency responses approximate within a given region of interest those specified by the prototype analog systems. Also, we know from section 6.6 that the synthesis of minimum length DNTL structures must always start by the specification of the transmission discrete-time system and that it must be given by an all-pole transfer function. Under such conditions, the number of sections composing the synthesized DNTL structures is always the same as the order of the all-pole transmission discrete-time system. Thus, our objective with the impulse invariance method is to be able to compute all-pole discrete-time systems from suitable analog prototype systems. The all-pole discrete-time systems shall then be used to perform the synthesis of the minimum length DNTL structures by inverse scattering.

From the example in (6.154), we have verified that the mapping for zeros is different from that for the poles which is given by the relation (6.143). We have also concluded that this is verified so as to account for the distortion introduced in the frequency response due to aliasing. As referred above, our goal is that of the optimum synthesis of DNTL structures, therefore, we must assess the impulse invariance method as a means for the computation of digital all-pole systems.

Unlike all-pole analog systems which have all the zeros placed at infinity $s = \infty$, the zeros for all-pole digital systems can either be located at $z = 0$ or $z = \infty$. Furthermore, it is not hard to realize that in order to obtain an all-pole digital system, the analog prototype system itself must be an all-pole system. Due to its inherent aliasing effect however, we could as of now conclude that the impulse invariance method, when applied to an analog all-pole prototype, will not in general result in to an all-pole discrete-time system. That is, due to the more complex mapping for the zeros it should be expected that the mapping for the infinite zeros of the analog all-pole prototype to be different from $z = 0$ and $z = \infty$ in the z-plane. However, as we shall see next, there are a couple of exceptions.

The first exception is that of first order all-pole systems and it becomes obvious from the comparison of equations (6.147) and (6.152). From the equations we clearly see that any first order analog all-pole system will always translate into a first order digital system. Notice that by considering $N = 1$ in equation (6.152), $H_d(z)$ reduces to a first order system characterized by one pole at $z = e^{p_k T}$ and one zero at $z = \infty$, hence, a first order all-pole system. The second exception is that of second order all-pole systems and can be easily verified by considering a generic second order all-pole system given by the transfer function

$$\begin{aligned} H_c(s) &= \frac{K}{(s+a+jb)(s+a-jb)} \\ &= \frac{jK/(2b)}{s+a+jb} - \frac{jK/(2b)}{s+a-jb}, \end{aligned} \tag{6.156}$$

which has both zeros at $s = \infty$ and a complex conjugate pair of poles at $s = -a \pm jb$. Notice that in order to comply with the physical realizability conditions (see section 4.2.1.1) the complex poles must always come in conjugate pairs. The digital domain transfer function $H_d(z)$ resulting from the impulse invariance method is obtained directly

from $H_c(s)$ accordingly to 6.152. Thus we have

$$\begin{aligned} H_d(z) &= \frac{jK/(2b)}{1-e^{(-a-jb)T}\,z^{-1}} - \frac{jK/(2b)}{1-e^{(-a+jb)T}\,z^{-1}} \\ &= \frac{(K/b)\,e^{-aT}\,\sin(bT)\,z^{-1}}{(1-e^{(-a-jb)T}\,z^{-1})(1-e^{(-a+jb)T}\,z^{-1})}. \end{aligned} \tag{6.157}$$

Analyzing the transfer function (6.157), we clearly see that the resulting digital system has two poles at $z = e^{-a-jb}$ and $z = e^{-a+jb}$, along with two zeros. One zero at $z = 0$ and the other at $z = \infty$. The location of the zeros identifies the system in (6.157) as an all-pole digital system, thus, making this a suitable system for the optimum synthesis of DNTL structures. Notice that, although the impulse invariance method only results in digital all-pole systems for first and second order systems, it still proves to be a very useful tool for the synthesis of DNTL structures for higher order systems as we shall demonstrate.

The method to perform the synthesis of DNTL structures using the impulse invariance method is quite similar to that used in section 6.7 regarding the use of parametric meddling tools. In the present case however, the parametric modeling step is substituted by the continuous-time to discrete-time transformation. Thus, the procedure is carried by undertaking the following steps:

1. Determine the target analog prototype (continuous-time) transfer function $H_c(s)$. Many design methods for continuous-time systems have relatively simple closed-form design formulas (e.g., Butterworth, Chebyshev polynomials). Furthermore, extensive tables are available for analog filter design. Express $H_c(s)$ in a partial fraction form as

$$H_c(s) = \sum_{k=1}^{N} \frac{A_k}{s - p_k}, \tag{6.158}$$

   where p_k are the analog system poles, and A_k are the partial fraction residues.

2. Set the sampling period T. Notice that the value of T strongly influences the resulting digital system spectrum as it controls the amount of aliasing effect.

3. Transform the analog prototype into its digital counterpart $H_d(z)$ by mapping of the poles accordingly to the relation (6.143)

$$z = e^{p_k T}. \tag{6.159}$$

The digital system transfer function is then given by

$$H_d(z) = \sum_{k=1}^{N} \frac{A_k}{1 - e^{p_k T}\, z^{-1}}. \tag{6.160}$$

4. Calculate the numerator and denominator polynomial coefficients, and express the transfer function (6.160) as

$$H_d(z) = \frac{\sum_{i=0}^{m} b_i\, z^{-1}}{1 + \sum_{i=1}^{m} a_i\, z^{-1}}, \tag{6.161}$$

where m is the order of the filter and the coefficients a_i and b_i must be real so as to comply with the realizability conditions.

5. Normalize the digital transfer function so that the maximum magnitude for the frequency response becomes equal to one, hence

$$T(z) = K_T \frac{\sum_{i=0}^{m} b_i\, z^{-1}}{1 + \sum_{i=1}^{m} a_i\, z^{-1}}, \tag{6.162}$$

where K_T is the constant and real valued normalizing gain factor. This step is due to the aliasing phenomena which distorts the frequency response. Notice that we have conveniently changed our nomenclature from $H_d(z)$ to $T(z)$ so that we can from now on differentiate from transmission $T(z)$ and reflection $R(z)$ systems respectively.

6. Obtain the transfer function for the reflection frequency response $R(z)$ associated to $T(z)$ through the relation

$$|R(z)|^2 = 1 - |T(z)|^2 \tag{6.163}$$

using a similar procedure to that described in section 6.6. The transfer function for the reflection system is given as

$$R(z) = K_R \frac{1 + \sum_{i=1}^{m} e_i \, z^{-i}}{1 + \sum_{i=1}^{m} a_i \, z^{-i}}, \tag{6.164}$$

where e_i and a_i are the coefficients for the numerator and denominator polynomials, and K_R is the normalizing gain factor.

7. Compute the DNTL filter impedance profile by applying the discrete layer-peeling inverse scattering procedure described in section 6.5 on the reflection frequency response $R(z)$.

In order to demonstrate the synthesis of DNTL structures using the impulse invariance method we now consider two practical examples. Both examples refer to Chebyshev low-pass filters. The first example is a second order filter whereas the second one is that of a fifth order filter. Hence, for both cases, the procedure starts by setting type-I low-pass Chebyshev analog prototypes with in-band ripple $R_p = 0.5\,\text{dB}$ and normalized cutoff frequency $\omega_c = 0.4\pi\,\text{rad/s}$. The coefficients for the analog prototypes can be readily obtained from tables available in the literature or through the Matlab function *cheby1*.

For the second order example and following the procedure outlined above, we start by setting the analog prototype as

$$\begin{aligned} H_c(s) &= \frac{2.2604}{s^2 + 1.7915s + 2.3943} \\ &= \frac{j0.896}{s + 0.896 + j1.262} - \frac{j0.896}{s + 0.896 - j1.262}. \end{aligned} \tag{6.165}$$

Next, the sampling period must be conveniently chosen, keeping in mind however that, the lower the sampling period value is, the less significative is the aliasing effect, hence

Numerator		Denominator	
b_0	0	a_1	-1.032
b_1	0.3376	a_2	0.4083
b_2	0		

TABLE 6.10: Coefficients obtained from the Matlab function *impinvar* for the $2nd$ order transmission system $T(z)$ when considering $T = 0.5$. The gain factor is $K_T = 1.0338$ and $T(z)$ is in the form of (6.162).

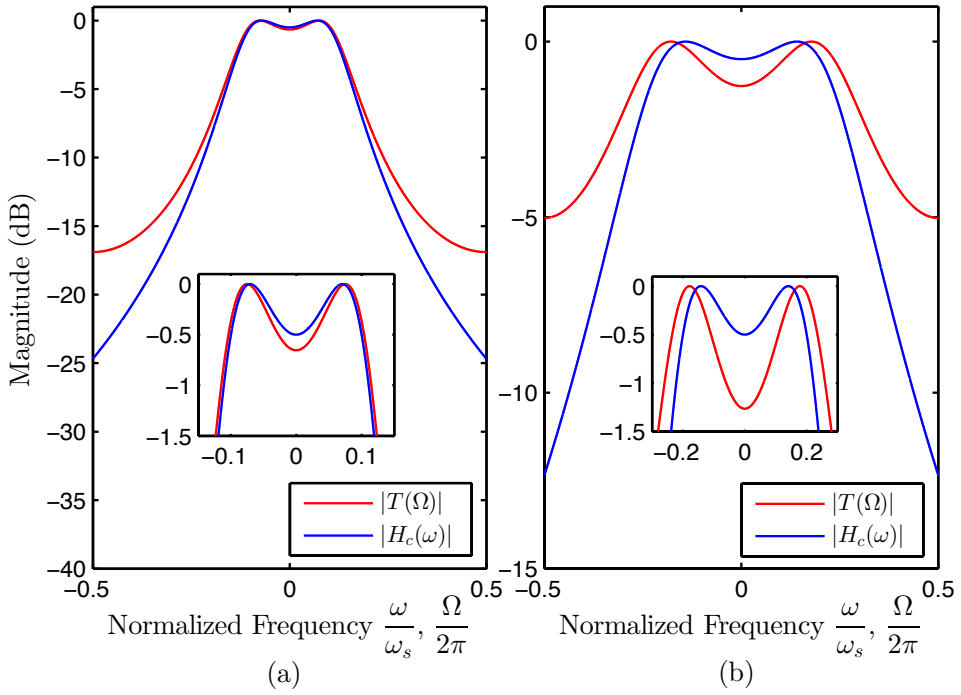

FIGURE 6.40: Magnitude response for the $2nd$ order target analog prototype $H_c(\omega)$ versus the magnitude response of the $2nd$ order digital counterpart $T(\Omega)$ obtained through the impulse invariance method with $T = 0.5$ in (a) and $T = 1$ in (b). Notice that the frequency normalizations ω/ω_s ($\omega_s = 2\pi/T$) for the analog domain and $\Omega/2\pi$ for the digital domain enables the comparison of both responses under a common domain.

better approximations to the analog frequency response are obtained. So as to demonstrate this fact, we shall consider two sampling period values, namely $T = 0.5$ and $T = 1$.

Steps 3. and 4. in the procedure can be conveniently carried out using Matlab function *impinvar*, which when provided with both the sampling period and the analog prototype filter coefficients, automatically returns the coefficients a_i and b_i for the digital system transfer function as given by (6.161). The transmission system for the DNTL structure is ultimately set in step 5. in the form of (6.162) by including the normalizing gain factor K. The values for the coefficients as well as for the gain factors are given in Table 6.10 for $T = 0.5$ and Table 6.11 for $T = 1$.

Numerator		Denominator	
b_0	0	a_1	-0.2484
b_1	0.6968	a_2	0.1667
b_2	0		

TABLE 6.11: Coefficients obtained from the Matlab function *impinvar* for the $2nd$ order transmission system $T(z)$ when considering $T = 1$. The gain factor is $K_T = 1.1392$ and $T(z)$ is in the form of (6.162).

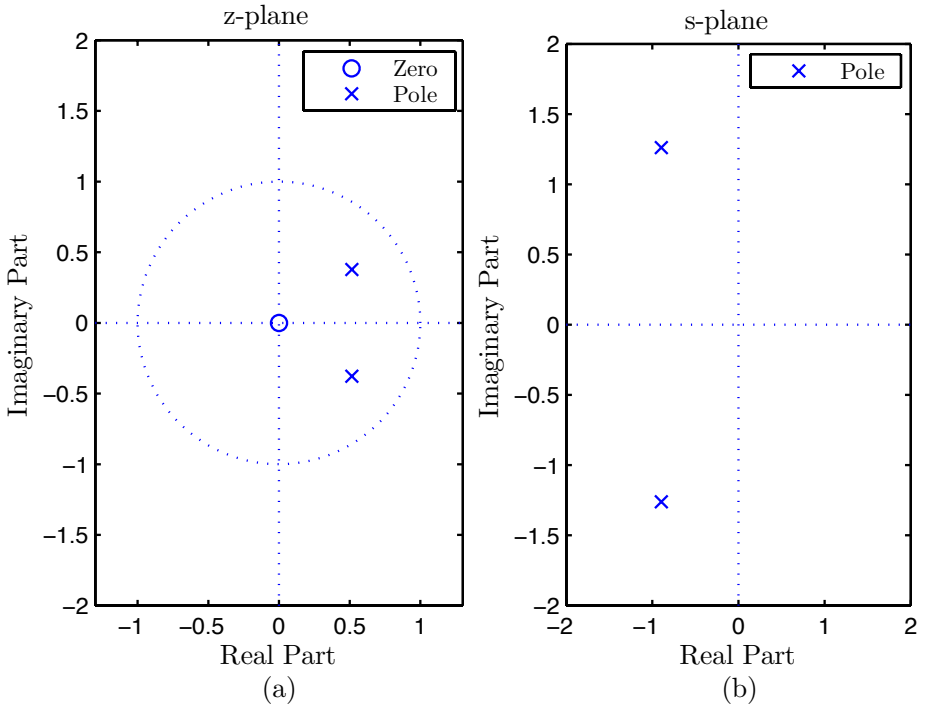

FIGURE 6.41: Pole-Zero plot associated to the $2th$ order digital transmission system $T(z)$ in (a) and Pole-Zero plot associated to the corresponding analog prototype $H_c(s)$ in (b).

The magnitude of the frequency response for the digital transmission system $T(\Omega)$ is plotted in Figure 6.40 (a) for a sampling period of $T = 0.5$ and in Figure 6.40 (b) for $T = 1$. For comparison purposes, we have also plotted the magnitude of the frequency response of the analog prototype $H_c(\omega)$. We clearly see from the figure that the aliasing effect is significantly stronger for $T = 1$ than for $T = 0.5$, that is, we get a better fitting between the analog and digital responses for lower values of T, or equivalently, for higher values for the sampling frequency $\omega_s = 2\pi/T$. Thus, it is important to select a small value for T to minimize the aliasing effect. Also, the cutoff frequency for the digital system directly depends on the selected value of T.

Figure 6.41 (a) depicts the locations of the zeros and poles on the z-plane for the transmission system, $T(z)$, when considering a period sampling of $T = 0.5$. Figure 6.41 (b) shows the locations for the poles of the analog prototype $H_c(s)$ on the s-plane. Clearly we see that the poles for the stable analog system, which are located on the LHP of the s-plane, are mapped inside of the unit circle on the z-plane. Thus, the digital system $T(z)$, obtained through the impulse invariance method, is also a stable system. Furthermore, $H_\omega(s)$ has two zeros located at $s = \infty$. These zeros are mapped into the z-plane at $z = 0$ and $z = \infty$, which in turn, characterizes $T(z)$ as an all-pole system,

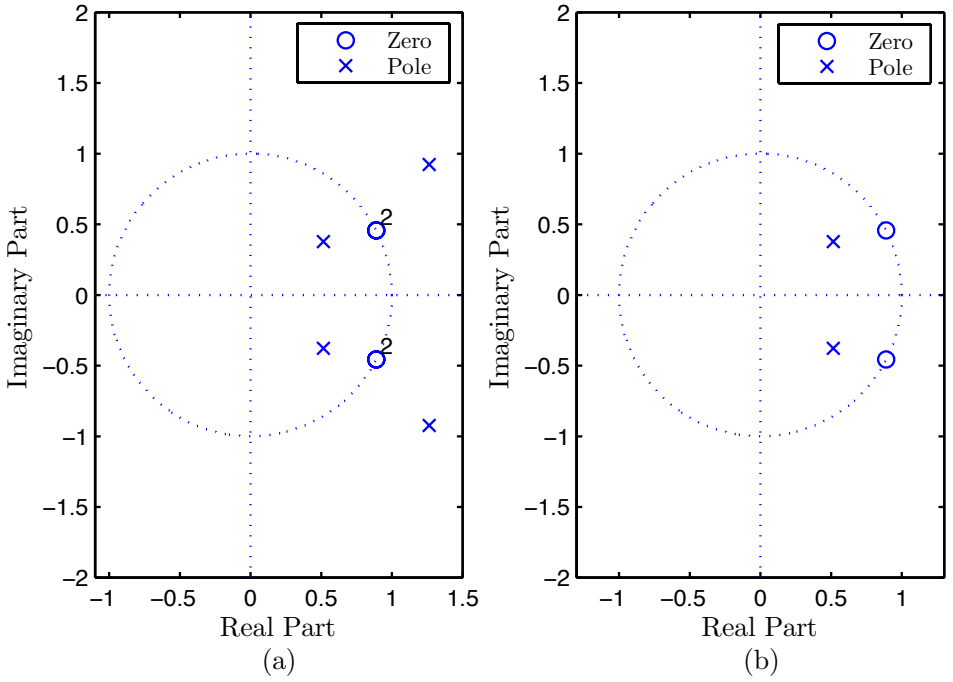

FIGURE 6.42: Pole-Zero plots associated to the $2nd$ order reflection system $R(z)$ for $T = 0.5$. In (a) are depicted the zeros and poles for $|R(z)|^2$, whereas in (b) we have the zeros and poles of $R(z)$ which in turn are selected from those of $|R(z)|^2$.

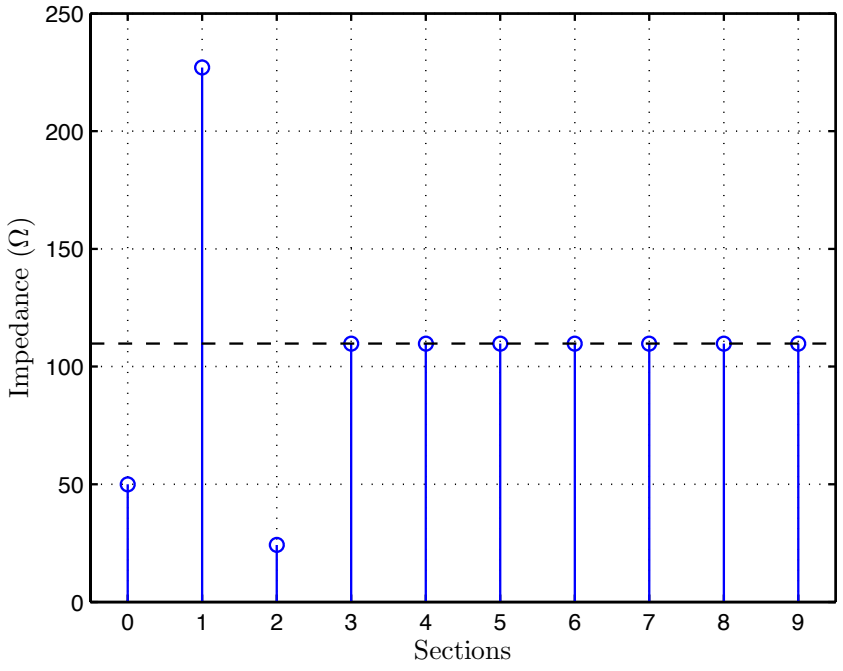

FIGURE 6.43: Impedance profile associated to $R(z)$, which is characterized by the pole-zero configuration depicted in Figure 6.42(b). The depicted impedance profile was obtained from 10 iterations of the DLP inverse scattering algorithm.

Numerator		Denominator	
e_1	-1.7797	a_1	-1.032
e_2	1	a_2	0.4083

TABLE 6.12: Coefficients for the $2nd$ order reflection system $R(z)$ computed from the transmission system $T(z)$ when considering $T = 0.5$. The gain factor is $K_R = 0.639$ and $R(z)$ is in the form of (6.164).

and consequently a minimum phase system.

We now carry on to step 6. of the procedure, where the reflection system transfer function, $R(z)$, is computed from its associated transmission system, $T(z)$, through the relation (6.163). The process for computing $R(z)$ is the same as the one used in the previous section. We start by computing the poles and zeros for $|R(z)|^2$ through (6.163). The reflection system $R(z)$ is then obtained from $|R(z)|^2$ by selecting one pole and one zero from each pair of poles and zeros of $|R(z)|^2$. Figure 6.42(a) depicts the poles and zeros for $|R(z)|^2$. The selection for the poles of $R(z)$ is obvious since due to stability constrains we must choose the poles inside the unit circle. Hence, the poles for $R(z)$ are the same as those for $T(z)$. The selection for the zeros on the other hand, is not affected by this constrain. However, because all the zeros are second order zeros, only one configuration is possible. The zeros and poles of $R(z)$ is given in Figure 6.42(b). The corresponding transfer function is given in the form of (6.164) and the respective coefficients for the numerator and denominator polynomials are given in Table 6.12.

Finally, in step 7 and to finalize the synthesis procedure, we feed the computed reflection system transfer function, $R(z)$, to the DLP inverse scattering procedure. The resulting DNTL impedance profile is plotted in Figure 6.43. The relevant impedance values for the DNTL structure are given in Table 6.13. Notice that, because the transmission system $T(z)$ is a second order all-pole system, the resulting DNTL structure is simply constituted by two sections. However, we see from Table 6.13 that the impedance

Section	Impedance (Ω)
0	50
1	227.0
2	24.17
3	109.74

TABLE 6.13: Impedance values for each section of the DNTL synthesized for the first example considering the pole-zero configuration depicted in Figure 6.42(b). The impedance value for section 0, *i.e.*, the first section, is set to that of the microwave system characteristic impedance, 50Ω.

value for section 0 and section 3 are different. In the case of a two section DNTL structure, it would be expected for the impedance value for section 3 to be equal to that of section 0, that is, the microwave system characteristic impedance 50Ω. The reason for this difference becomes clear from the transmission magnitude response given in Figure 6.40(a), where we easily verify that for $\Omega = 0$ the value of $T(\Omega)$ is less than one. The only way for passive structures, such are DNTL structures, to have gain at $\Omega = 0$ is by setting different impedance levels at the input and output ports. In the present case the input port impedance is set to 50Ω. The resulting impedance for the output port is given as a result from the DNTL algorithm, however it can be obtained alternatively as

$$Z_{0_{end}} = Z_{0_{init}} \frac{1 + |R(\Omega)|}{1 - |R(\Omega)|}\bigg|_{\Omega=0}, \tag{6.166}$$

where $Z_{0_{init}}$ is the microwave system characteristic impedance, 50Ω. Notice that, the DNTL structure obtained in this example is in fact a second order impedance matching structure as it performs the matching from 50Ω to 109.74Ω, within the pass-band given in Figure 6.40(a).

As a final remark regarding this example, we refer that the impedance value given for section 1 may not be practically feasible as it is very high. This problem, can be overcome by reducing the sampling period. However, as we clearly see from Figure 6.40(b), reducing the sampling period might not be an option due to increasing of the aliasing effect. Another solution may come by considering a higher order for the filter as we shall next demonstrate through the synthesis of a fifth order Chebyshev filter.

For the fifth order Chebyshev filter example and following the same procedure as for the previous example, we start by setting the analog prototype transfer function as

$$H_c(s) = \frac{0.5607}{s^5 + 1.4734s^4 + 3.0594s^3 + 2.5987s^2 + 1.8765s + 0.5607}, \tag{6.167}$$

whose coefficients were obtained from Matlab.

Next, the sampling period must be conveniently chosen, keeping in mind however that, the lower the sampling period value is, the less significative is the aliasing effect, hence better approximations to the analog frequency response are obtained. For the present case we select $T = 1.25s$.

Using the function *impinvar* from Matlab, along with the coefficients of the analog prototype filter and for a sampling period of $T = 1.25s$, we obtain the coefficients a_i

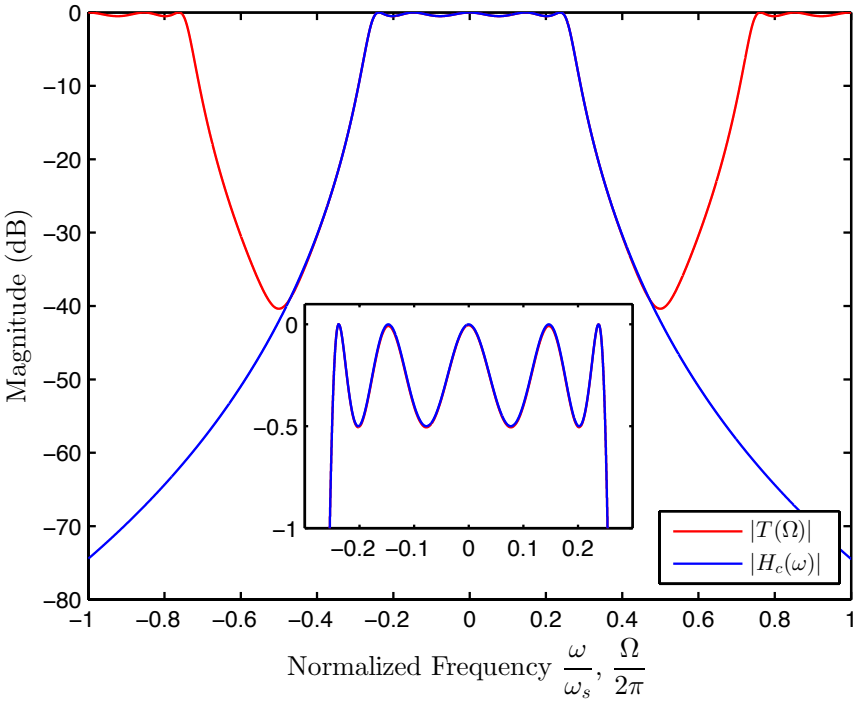

FIGURE 6.44: Magnitude response for the $5th$ order target analog prototype $H_c(\omega)$ versus the magnitude response of the $5th$ order digital counterpart $T(\Omega)$ obtained through the impulse invariance method with $T = 1.25$. Notice that the frequency normalizations ω/ω_s ($\omega_s = 2\pi/T$) for the analog domain and $\Omega/2\pi$ for the digital domain enables the comparison of both responses under a common domain.

and b_i for the digital system transfer function as given by (6.161). The transmission system for the DNTL structure is ultimately set in the form of (6.162) by including the normalizing gain factor K_T. The values for the coefficients as well as for the normalizing gain factor are given in Table 6.14.

The magnitude of the frequency response for the digital transmission system $T(\Omega)$ is plotted in Figure 6.44. For comparison purposes the magnitude of the frequency response for the analog system $H_c(\omega)$ is also plotted. From the figure it becomes evident the perfect match between the magnitude responses on both domains. Furthermore,

Numerator		Denominator	
b_0	0	a_1	-1.2364
b_1	0.0438	a_2	1.4597
b_2	0.2741	a_3	-1.0924
b_3	0.1922	a_4	0.5523
b_4	0.0146	a_5	-0.1585
b_5	0		

TABLE 6.14: Coefficients obtained from the Matlab function *impinvar* for the $5th$ order transmission system $T(z)$ when considering $T = 1.25s$. The gain factor is $K_T = 0.9994$ and $T(z)$ is considered in the form of (6.162).

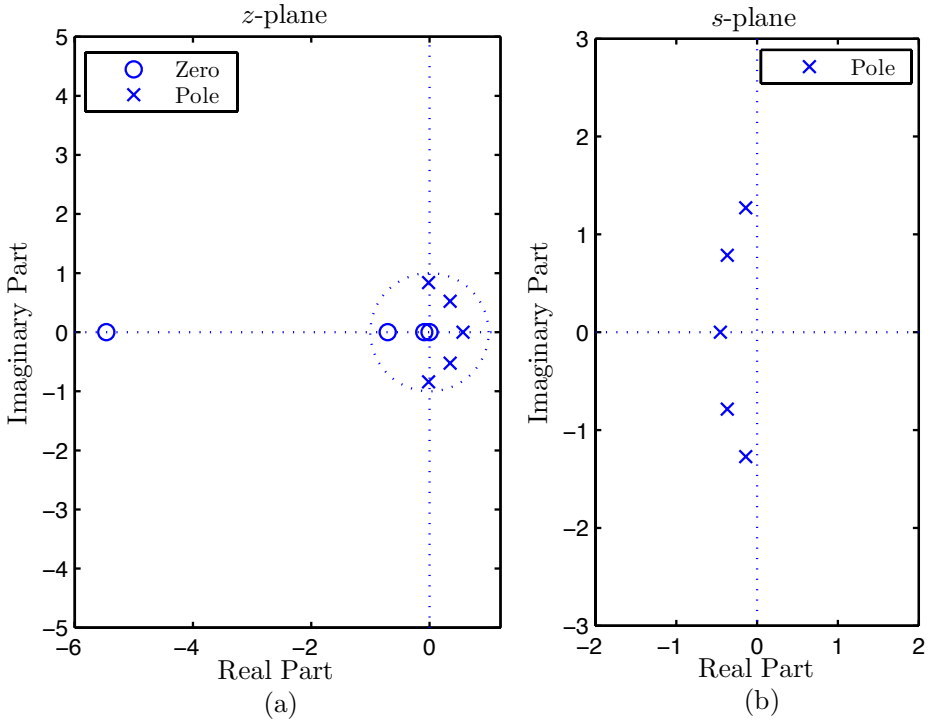

FIGURE 6.45: Pole-Zero plot associated to the $5th$ order digital transmission system $T(z)$ in (a) and Pole-Zero plot associated to the corresponding analog prototype $H_c(s)$ in (b).

we conclude that for a sampling period of $T = 1.25s$ the aliasing effect is very small. Actually, from the figure the aliasing effect is not perceptible as in the previous examples, however, we shall see next that even though it is very small, the aliasing effect is in fact present.

Figure 6.45 (a) depicts the locations of the zeros and poles on the z-plane for the transmission system, $T(z)$, when considering a period sampling of $T = 1.25\,s$. Figure 6.45 (b) shows the locations for the poles of the analog prototype $H_c(s)$ on the s-plane.

Clearly we see that the analog system is stable because all the poles are located on the LHP of the s-plane. On the other hand we see that, as a result from the analog to digital transformation, the the analog system poles are mapped inside of the unit circle

Numerator		Denominator	
e_1	-2.4241	a_1	-1.2364
e_2	3.6890	a_2	1.4597
e_3	-3.7221	a_3	-1.0924
e_4	2.5086	a_4	0.5523
e_5	-1.0926	a_5	-0.1585

TABLE 6.15: Coefficients for the $5th$ order reflection system $R(z)$ computed from the transmission system $T(z)$. The gain factor is $K_R = 0.3809$ and $R(z)$ is in the form of (6.164).

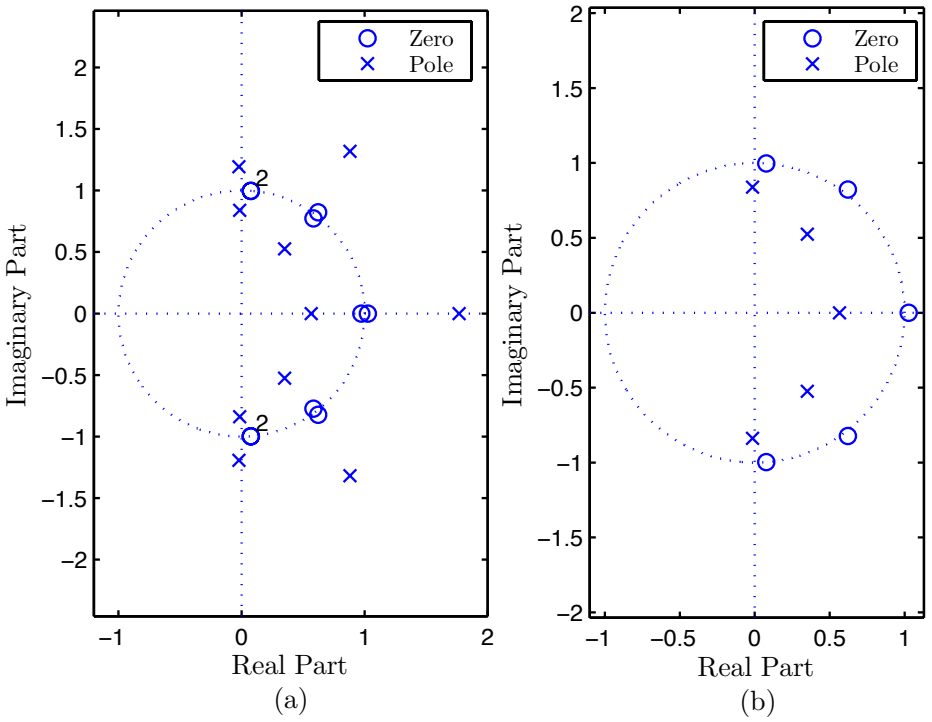

FIGURE 6.46: Pole-Zero plots associated to the $5th$ order reflection system $R(z)$ for $T = 1.25$. In (a) are depicted the zeros and poles for $|R(z)|^2$, whereas in (b) we have the zeros and poles of $R(z)$ which in turn are selected from those of $|R(z)|^2$.

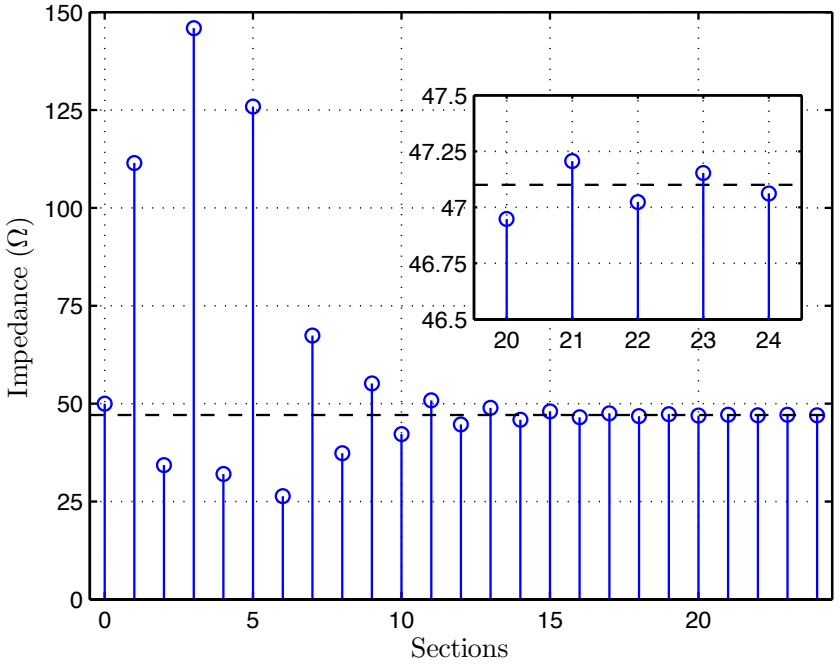

FIGURE 6.47: Impedance profile associated to $R(z)$, which is characterized by the pole-zero configuration depicted in Figure 6.46(b). The depicted impedance profile was obtained from 25 iterations of the DLP inverse scattering algorithm. Notice that the impedance profile is constituted by an infinite number of sections and the impedance values converges to 47.1Ω as the number of sections goes to infinity.

Section	Impedance (Ω)	Section	Impedance (Ω)
0	50	13	48.89
1	111.53	14	45.88
2	34.34	15	47.98
3	145.92	16	46.49
4	32.02	17	47.53
5	125.91	18	46.79
6	26.38	19	47.31
7	67.37	20	46.95
8	37.29	21	47.21
9	55.15	22	47.02
10	42.25	23	47.15
11	50.81	24	47.06
12	44.66	...	...

TABLE 6.16: Impedance values for each section of the DNTL synthesized for the fifth order filter example considering the pole-zero configuration depicted in Figure 6.42(b). The impedance value for section 0, *i.e.*, the first section, is set to that of the microwave system characteristic impedance, 50Ω. Notice that the impedance profile converges to 47.1Ω as the number of sections goes to infinity.

on the z-plane. Thus, the digital system $T(z)$, obtained through the impulse invariance method, is also a stable system. Regarding the zeros, we see that $H_c(s)$ has five zeros located at $s = \infty$. Two of these zeros are mapped into the z-plane at $z = 0$ and $z = \infty$, similarly to the previous example, however the mapping for the other zeros results in the zeros distribution plotted in Figure 6.45 (a). Thus and unlike the previous example, the transmission system, $T(z)$, is not an all-pole system. Next we shall see that, because $T(z)$ is not an fifth order all-pole system, the corresponding DNTL structure will be constituted by an infinite number of sections.

From the transmission system $T(z)$ and using the relation (6.163), the square of the reflection system transfer function, $|R(z)|^2$ is easily computed. The corresponding pole-zero plot is given in Figure 6.46(a). The pole-zero plot for $R(z)$ is depicted in Figure 6.46(b) and is obtained from that of $|R(z)|^2$ by selecting the stable poles and one zero from each pair of zeros. From this pole-zero selection the transfer function for $R(z)$ is easily computed in the form of equation (6.164). The coefficients for the numerator and denominator polynomials of $R(z)$ are given in Table 6.15. The synthesis of the DNTL structure which implements as its transmission frequency response the fifth order Chebishev filter, thus $T(\Omega)$, is now a straightforward process. For that and similarly to the previous example we run the DLP inverse scattering algorithm on the reflection response system $R(z)$. The resulting DNTL structure impedance profile is depicted in Figure 6.47. The most relevant values for the impedance profile are given in

Table 6.16.

It important to understand at this point that although we are synthesizing a fifth order system, the impedance profile given in Figure 6.47 is constituted by twenty-three sections. This is because unlike the previous examples the fifth order transmission system $T(z)$ is not an all-pole function. This is discussed in section 6.6, under the context of the optimum synthesis of DNTL structures. In fact and from the analysis made in section 6.6 the complete impedance profile is actually constituted by an infinite number of sections. Nonetheless, it becomes clear from the analysis of Figure 6.47 that, as the index number for the sections becomes higher, the corresponding impedance values start converging for the constant value $Z_{0_{end}}$, where $Z_{0_{end}}$ is given by (6.166). Furthermore and even though the impedance values only reach that of $Z_{0_{end}}$ at infinity, we see that after only a couple tens of sections the impedance values have converged enough towards $Z_{0_{end}}$ so that we can truncate and thus, disregard the rest of the impedance profile. For the current example, we consider that a suitable truncation section index is obtained when the impedance difference between adjacent sections is in module bellow 0.1Ω, hence the twenty-three section DNTL given in Figure 6.47.

Notice that for a microwave system with characteristic impedance $Z_{0_{init}} = 50\Omega$ and from the evaluation of the reflection frequency response at $\Omega = 0$ as $|R(0)| = 0.03$ we have from (6.166) that $Z_{0_{end}} = 47.1\Omega$. Thus and even though we are synthesizing an odd order system, we have different values for the input and output ports. Please note that, although this impedance difference is small, it can not be overlooked and comes as a disadvantage when considering the synthesis of filters, which usually require equal impedance values on both input and output ports. Notice that this problem arises due to the aliasing effect. Otherwise, we would have $|R(0)| = 0$ and consequently $Z_{0_{init}} = Z_{0_{end}} = 50\,\Omega$.

In order to tackle with this problem, we need to perform some kind of "impedance profile correction" so as to achieve the same impedance value for the input and output ports. In that sense, we now propose four different solutions.

The first solution consists on taking the impedance profile obtained from the synthesis process (see Figure 6.47), and increase the impedance value for all sections, except the first one, by the amount $|50\Omega - Z_{0_{last}}|$, where $Z_{0_{last}}$ is the impedance value for the last section of the truncated impedance profile (the $25th$ section on this example). In this way, we guaranty that the input and output impedances are 50Ω. The impedance profile resulting from this correction is depicted in Figure 6.48(b) in blue color and

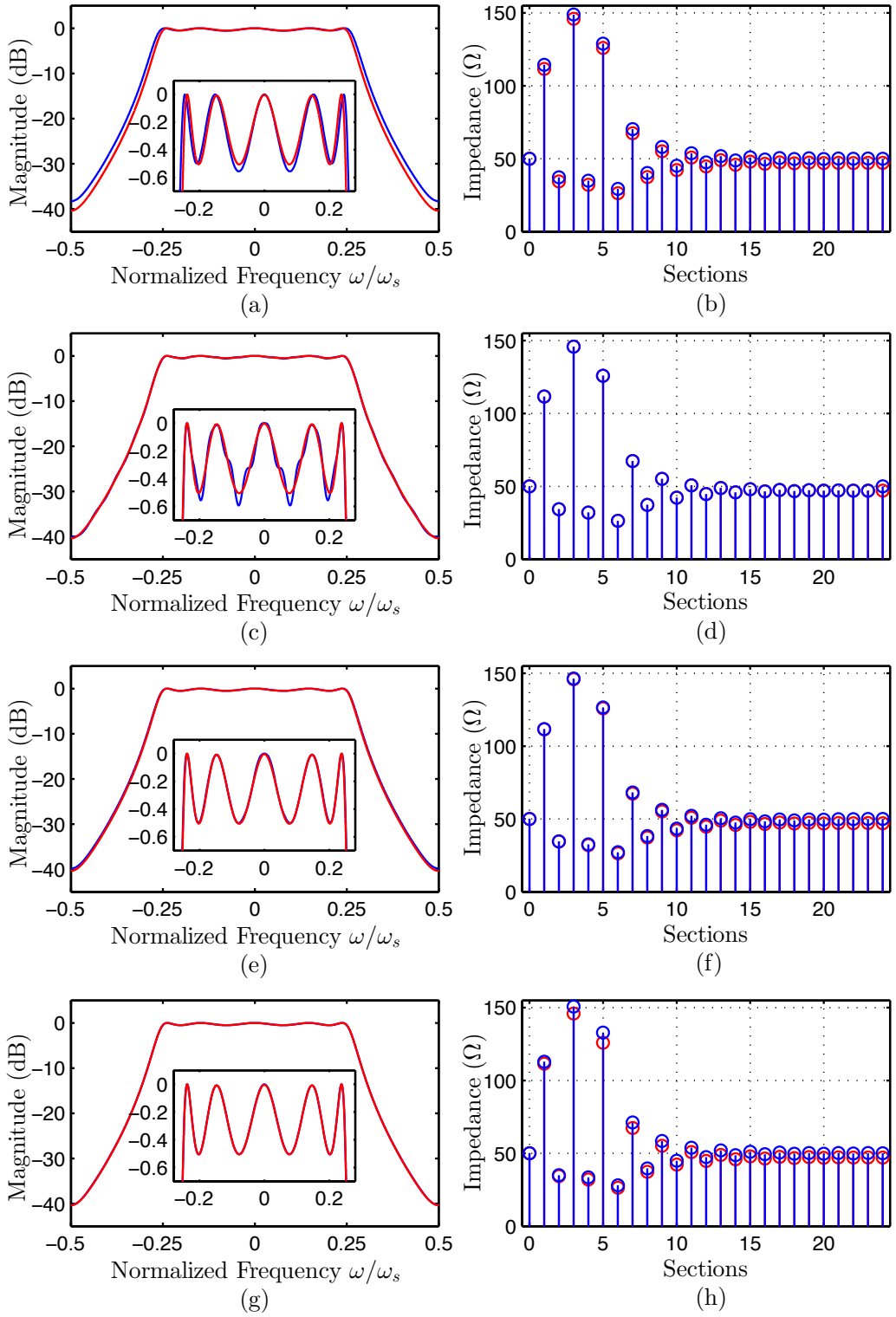

FIGURE 6.48: Results associated with the four solutions proposed to solve the problem regarding the different input and output characteristic impedances for the fifth order filter example. In (a), (c), (e) and (g) we have the comparison between the magnitude response for the DNTL given in Figure 6.47 (red color) and those obtained after impedance profile correction (blue color). In (b), (d), (f) and (h) we have the comparison between the original impedance profile (red color) as given in Figure 6.47 and those obtained after impedance correction (blue color). All the frequency responses are computed from the respective impedance profiles using the TMM method.

the corresponding magnitude frequency response as obtained from the TMM method is given in Figure 6.48(a) also in blue color.

The second impedance profile correction method is the most simple one as it only consists in forcing the impedance for the last section in the impedance profile to 50Ω. The resulting impedance profile is given in 6.48(d) in blue color and the corresponding magnitude frequency response as obtained from the TMM method is given in Figure 6.48(c) also in blue color.

The third method consists on gradually increase (from zero to $|50\Omega - Z_{0_{last}}|$) the amount of extra impedance added to each section of the impedance profile. Hence, for the first section the we add zero whereas for the last section the impedance amount added is $|50\Omega - Z_{0_{end}}|$. The resulting impedance profile is given in 6.48(f) in blue color and the corresponding magnitude frequency response as obtained from the TMM method is given in Figure 6.48(e) also in blue color.

The last proposed solution is a more intricate one as it involves an explicit manipulation of the zeros of the reflection system $R(z)$. Let us remember that the problem at hands arises due to the aliasing effect and that, otherwise, we would have $|R(0)| = 0$ and consequently $Z_{0_{init}} = Z_{0_{end}} = 50$. Therefore and prior to the inverse scattering step, we can force $R(\Omega) = 0$ for $\Omega = 0$ just by manipulating the zeros of $R(z)$. In order for $R(\Omega) = 0$ for $\Omega = 0$ the reflection system $R(z)$ must have at least a real zero on the unit circle, that is, at $z = re^{j\Omega} = 1e^{j0} = 1$. From Figure 6.46(b) we clearly see that the reflection frequency response is not zero at $\Omega = 0$ because the zero occurring at $\Omega = 0$ has a magnitude of $r = 1.0272$. Hence, we substitute this zero by one with $r = 1$. In this way we guaranty that $Z_{0_{end}} = 50$. However, although $Z_{0_{end}} = 50$ the structure obtained from the inverse scattering process will be infinite. Thus and to finalize the impedance profile is truncated and the impedance for the last section is set to $Z_{0_{last}} = 50$. The resulting impedance profile is given in 6.48(h) in blue color and the corresponding magnitude frequency response as obtained from the TMM method is given in Figure 6.48(g) also in blue color.

Analyzing the results given in Figure 6.48 we conclude that, provided that the aliasing effect is kept to a minimum, all four approaches produce very good and acceptable results, however we must stand out the superior performance for the last two methods.

From our analysis on the impulse invariance method as a technique to be used in the synthesis of DNTL structures, we conclude that it successfully enables the synthesis of DNTL structures whose magnitude frequency response accurately follows that from the

analog prototype in the range $-f_s/2 \leq \omega \leq f_s/2$. However, such is only possible provided that a suitable sampling period is chosen, where by suitable we mean the smallest possible sampling period. Otherwise, severe aliasing effect will occur and as a result we shall have severe distortion on the frequency response resulting from the transformation from analog to digital. Also, we saw that in the analog to digital conversion promoted by the impulse invariance method, the mapping for the poles and zeros is inherently different. Thus, except for first and second order analog all-poles prototypes, the impulse invariance method is not suitable to the synthesis of optimum DNTL structures (se section 6.6). As a last remark regarding the impulse invariance method we refer that due to the always present aliasing effect and also the infinite length for the synthesized DNTL structures (which must be truncated), the characteristic impedance for the input and output ports is usually different. However this problem can be alleviated by the use of the impedance profile correction techniques described above.

6.8.1.2 Bilinear transformation

In this subsection we evaluate the bilinear transform as a tool in the synthesis of DNTL structures. As we shall see next, the bilinear transform, unlike the impulse invariance method, avoids the aliasing phenomena. This in fact, is our major motivation to consider the bilinear transform in the synthesis of DNTL structures. Next, we shall demonstrate that, with the bilinear transformation, the transformation between the analog and digital domains, *i.e.*, between the variables s and z, is such that the entire $j\omega$ axis in the s-plane maps to a single revolution of the unit circle in the z-plane, hence avoiding the aliasing effect. Furthermore, with the bilinear transform, all the points in the LHP of the s-plane are mapped inside the unit circle, thus all stable analog prototype filters are converted into stable digital filters. On the other hand, the bilinear transform is highly non-linear which translates in a frequency warping phenomena between the ω and Ω frequency domains.

The following mathematical derivations, which directly follows from those on [76], shows how the bilinear transform arises from applying the trapezoidal rule, as a numerical integration method, to the solution of differential equations. They demonstrate how the difference equation associated with some digital system transfer function $H_d(z)$ can be obtained by using the trapezoidal rule on the differential equation associated with the the analog system transfer function $H_c(s)$. Let us consider a first order all-pole system

given by

$$H_c(s) = \frac{b}{s+a}, \tag{6.168}$$

whose corresponding differential equation is obtained through the inverse Laplace transform as

$$\frac{d\,y(t)}{dt} + ay(t) = bx(t). \tag{6.169}$$

In the differential equation (6.169), $x(t)$ corresponds to input time-domain signal whereas $y(t)$ is the corresponding time-domain output. Now, $y(t)$ can be related to its derivative by

$$y(t) = \int_{t_0}^{t} y'(\tau)d\tau + y(t_0), \tag{6.170}$$

where $y'(t)$ represents the first order derivative of $y(t)$. The approximation of the integral given by equation (6.170) implies the discretization of the time variable, with a sampling period T. Thus, the evaluation of (6.170) through the trapezoidal formula at the instant $t = nT$, and knowing that the previous sampling time instant is $t_0 = nT - T$, yields

$$y(nT) = T\left(\frac{y'(nT) + y'(nT-T)}{2}\right) + y(nT-T), \tag{6.171}$$

where n is an integer. Taking into consideration the time variable discretization, the evaluation of the differential equation that characterizes the analog system at $t = nT$ yields

$$y'(nT) = -a\,y(nT) + b\,x(nT). \tag{6.172}$$

Substituting equation (6.172) into equation (6.171) and expressing the result in the form of discrete time sequences, that is, considering

$$\begin{cases} y[n] & = y(nT), \\ x[n] & = x(nT), \end{cases} \tag{6.173}$$

we obtain the difference equation

$$\left(1 + \frac{aT}{2}\right) y[n] - \left(1 - \frac{aT}{2}\right) y[n-1] = \frac{bT}{2}\left(x[n] + x[n-1]\right). \tag{6.174}$$

Taking the z-transform of the previous difference equation and after some mathematical rearrangement we obtain the digital system transfer function in the form of

$$H_d(z) = \frac{Y(z)}{X(z)} = \frac{b}{\frac{2}{T}\left(\frac{1-z^{-1}}{1+z^{-1}}\right) + a}. \tag{6.175}$$

From the comparison between the analog system transfer function (6.168) and that of the associated digital system (6.175), it becomes clear that the mapping from the s-plane to the z-plane is given by

$$s = \frac{2}{T}\left(\frac{1-z^{-1}}{1+z^{-1}}\right). \tag{6.176}$$

The transformation given by equation (6.176) is called the *bilinear transformation.*

We refer at this point that, even though the previous mathematical development is performed on a first order system, the same result with regard to obtaining the bilinear transform, still holds for higher order systems. Thus, generally speaking, the bilinear transformation corresponds to replacing the analog variable s accordingly to (6.176), that is

$$H_d(z) = H_c\left(\frac{2}{T}\left(\frac{1-z^{-1}}{1+z^{-1}}\right)\right). \tag{6.177}$$

Notice that unlike the impulse invariance technique and as we shall see next, the bilinear transform avoids the aliasing effect, as it represents a conformal mapping.

In order to investigate the properties of the bilinear transform, we solve equation (6.176) for z, which results in

$$z = \frac{1+(T/2)s}{1-(T/2)s}. \tag{6.178}$$

Substituting $s = \sigma + j\omega$ into the previous equation yields

$$z = \frac{(1+(T/2)\sigma) + j\omega\, T/2}{(1-(T/2)\sigma) - j\omega\, T/2}. \tag{6.179}$$

It is not difficult to realize from equation (6.179) that for $\sigma < 0$, we have $|z| < 1$ for any value of ω. In a similar way, for $\sigma > 0$, we have $|z| > 1$ for any value of ω. From this simple analysis, we easily conclude that the LHP of the s-plane maps to the inside of the unit circle on the z-plane, whereas the RHP of the s-plane maps to the outside of the unit circle. Furthermore, when $\sigma = 0$ we have $|z| = 1$, thus, the imaginary axis $j\omega$ on the s-plane maps to the unit circle ($r = 1$) on the z-plane. The mapping produced by the bilinear transformation is illustrated in Figure 6.49. From the figure we easily see

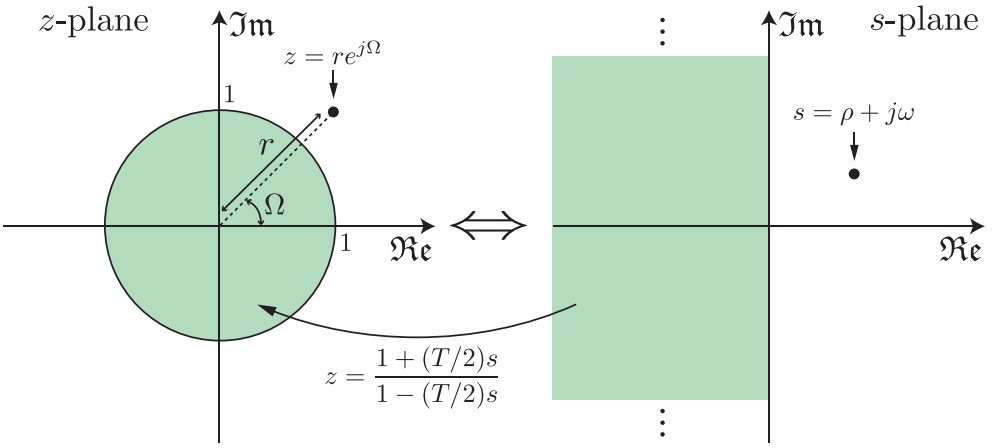

FIGURE 6.49: Mapping produced by the bilinear transformation, accordingly to equation (6.178).

that through the bilinear transform any causal stable analog system will always result in a causal stable digital system.

Let us now consider the substitution of $z = r\,e^{j\Omega}$ into equation (6.176), yielding

$$s = \frac{2}{T}\left(\frac{re^{j\Omega} - 1}{re^{j\Omega} + 1}\right). \tag{6.180}$$

In order to derive the relation between the analog and digital frequency variables we set $r = 1$ (thus $\sigma = 0$), hence, equation (6.180) simplifies to

$$j\omega = \frac{2}{T}\left(\frac{e^{j\Omega} - 1}{e^{j\Omega} + 1}\right) = \frac{2}{T}\left(\frac{j\sin(\Omega/2)}{\cos(\Omega/2)}\right) = j\,\frac{2}{T}\tan\left(\frac{\Omega}{2}\right). \tag{6.181}$$

Hence, the relationship between both analog and digital frequency variables is given by

$$\omega = \frac{2}{T}\tan\left(\frac{\Omega}{2}\right), \tag{6.182}$$

$$\Omega = 2\arctan\left(\frac{\omega T}{2}\right). \tag{6.183}$$

Notice that, accordingly to the previous two equations, the entire analog frequency domain ($-\infty \leq \omega \leq \infty$), that is, the $j\omega$ axis, is mapped only once onto the unit circle ($-\pi \leq \Omega \leq \pi$). This is unlike the impulse invariance method where there were an infinite number of mappings. Thus, with the bilinear transformation the conversion from analog to digital domain is carried on without aliasing.

Figure 6.50 illustrates the mapping between the digital and analog frequency domains. From the figure is becomes clear that the entire range for the analog frequency is

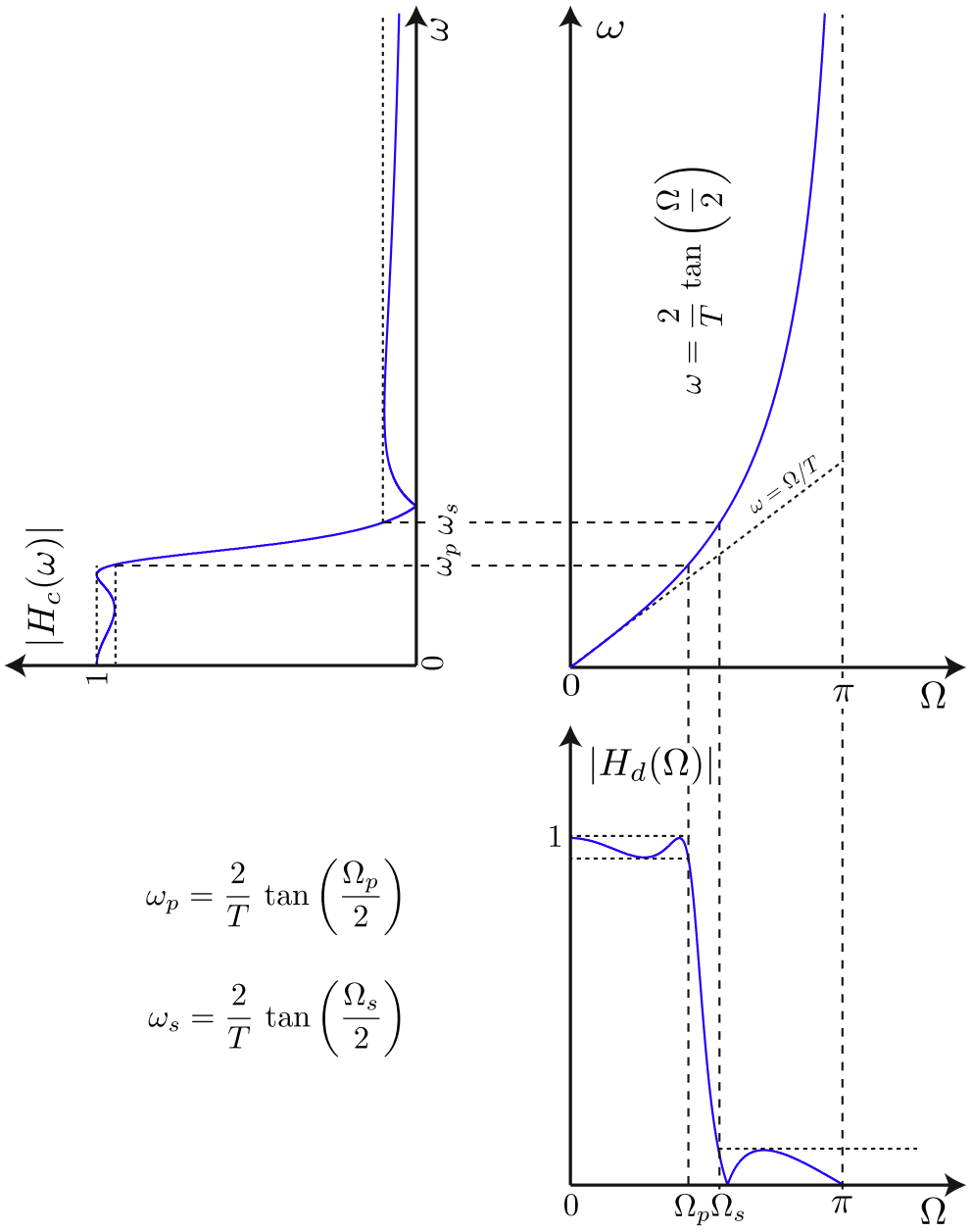

FIGURE 6.50: Mapping of the continuous-time frequency axis onto the discrete-time frequency axis and vice-versa. The illustration clearly shows the warping effect inherent to the bilinear transformation. Thus, to achieve the desired digital domain cutoff frequencies, the corresponding analog domain frequencies must be pre-warped as shown. The presented illustration is based on a third order low-pass elliptic filter.

mapped only once in the digital domain into the range $-\pi \leq \Omega \leq \pi$. Furthermore we see that the mapping is highly nonlinear. From the analysis of Figure 6.50 it becomes evident the frequency compression for ω into the digital domain. This frequency compression is usually referred to as frequency *wraping*, and is due tho the nonlinearity of the tangent function in (6.182). Notice however, that the frequency response of the analog system is exactly replicated on the digital domain. That is, from the example given in Figure

6.50 we see that through the bilinear transformation, the analog equiripple filter results in a digital equiripple filter with the same passband and stopband equiripple characteristics. However, the frequency locations for the ripples as well as for the passband and stopband edges are evidently affected. Hence we easily conclude that the bilinear transformation only affects the independent variable, *i.e.* the frequency variable. In this way, in order to design a digital filter using an analog prototype in conjunction with the bilinear transformation, the digital frequency specifications must be set in advance and then pre-warped into specifications in the analog domain though (6.182) so that the frequency warping caused by the bilinear transformation is taken into consideration. A last and very important characteristic regarding the bilinear transformation has to do with the pole-zero mapping from the s-plane to the z-plane. Unlike with the impulse invariance method, the bilinear transformation is in fact an algebraic transformation, which means that both poles and zeros of the analog system are mapped to the z-plane accordingly to (6.178). It is however interesting to note that the poles and zeros located at $s = \infty$ in the s-plane are mapped to the point $z = -1$ in the z-plane. Hence, an all-pole analog system will never result in an all-pole digital system.

The method to perform the synthesis of DNTL structures using the bilinear transform is quite similar to that previously described regarding the use of the impulse invariance method. In the present case however, the procedure is carried out by undertaking the following steps:

1. The procedure begins by specifying the digital system frequency properties, *i.e.* ripple level, cutoff frequency, etc. These specifications are afterwards converted or pre-warp into analog frequency specifications (*e.g.* cutoff frequency) through the frequency mapping function

$$\omega = \frac{2}{T} \tan\left(\frac{\Omega}{2}\right). \tag{6.184}$$

   The desired frequency specifications for the analog system are obtained from (6.184) by a convenient selection of the sampling period T. Notice that the value of T strongly influences how the warping effect distorts the resulting digital system spectrum when compared to the analog one. High values of T imply a strong warping effect at low frequencies, whereas small values of T push the warping effect to higher frequencies. Thus, for small values of T, the digital spectrum shape at the

lower frequency bands is kept basically the same as that of the analog prototype system. (See Figure 6.50).

2. From the analog system specifications, the target analog prototype (continuous-time) transfer function $H_c(s)$ is determined. Many design methods for continuous-time systems have relatively simple closed-form design formulas (e.g., Butterworth, Chebyshev polynomials). Furthermore, extensive tables are available for analog filter design.

3. Transform the analog prototype transfer function $H_c(s)$ into its digital counterpart $H_d(z)$ by performing the following variable change

$$s = \frac{2}{T}\left(\frac{1-z^{-1}}{1+z^{-1}}\right). \tag{6.185}$$

Equivalently we can also compute the zeros and poles for the analog system and use the mapping function (6.178) to map them from the s-plane to the z-plane. In both cases, the transfer function for the digital system is ultimately expressed by

$$T(z) = H_d(z) = \frac{\sum_{i=0}^{m} b_i\, z^{-1}}{1 + \sum_{i=1}^{m} a_i\, z^{-1}}, \tag{6.186}$$

where m is the order of the filter and the coefficients a_i and b_i must be real so as to comply with the realizability conditions. At this point we refer that, unlike with the impulse invariance method, with the bilinear transformation there is no need for a normalizing gain factor as there are no aliasing phenomena. Notice that we have conveniently changed our nomenclature from $H_d(z)$ to $T(z)$ so that we can from now on differentiate from transmission $T(z)$ and reflection $R(z)$ systems respectively.

4. Obtain the transfer function for the reflection frequency response $R(z)$ associated to $T(z)$ through the relation

$$|R(z)|^2 = 1 - |T(z)|^2 \tag{6.187}$$

using a similar procedure to that described in section 6.6. The transfer function for the reflection system is given as

$$R(z) = K_R \frac{1 + \sum_{i=1}^{m} e_i \, z^{-i}}{1 + \sum_{i=1}^{m} a_i \, z^{-i}}, \tag{6.188}$$

where e_i and a_i are the coefficients for the numerator and denominator polynomials, and K_R is the normalizing gain factor.

5. Compute the DNTL filter impedance profile by applying the discrete layer-peeling inverse scattering procedure described in section 6.5 on the reflection frequency response $R(z)$.

In order to demonstrate the synthesis of DNTL structures using the bilinear transformation we now consider one practical example. For comparison purposes we chose a similar analog prototype to that in the last example regarding the impulse invariance method. Thus, the analog system is a fifth order type-I Chebyshev low-pass filter with in-band ripple $R_p = 0.1\,\text{dB}$ and normalized cutoff frequency $\omega_c = 0.4\pi\,\text{rad/s}$. Notice that the coefficients for the analog prototype can be readily obtained from tables available in the literature or through the Matlab function *cheby1*.

We start by setting the analog prototype transfer function as

$$H_c(s) = \frac{1.2833}{s^5 + 2.1915s^4 + 4.37534s^3 + 4.7565s^2 + 3.5798s + 1.2833}, \tag{6.189}$$

whose coefficients were obtained from Matlab. As we refer above and for comparison purposes, we set the sampling period to $T = 1.25s$, as it is the same used in the fifth order filter synthesis example regarding the impulse invariance method.

Step 3. in the procedure can be conveniently carried out using Matlab function *bilinear*, which when provided with both the sampling period and the analog prototype transfer function coefficients (6.189), automatically returns the coefficients a_i and b_i for the digital system transfer function as given by (6.186). The values for the coefficients as well as for the normalizing gain factor are given in Table 6.17.

The magnitude of the frequency response for the digital transmission system $T(\Omega)$ is plotted in Figure 6.51. For comparison purposes, we have also plotted the magnitude of the frequency response of the analog prototype $H_c(\omega)$. Unlike with the impulse

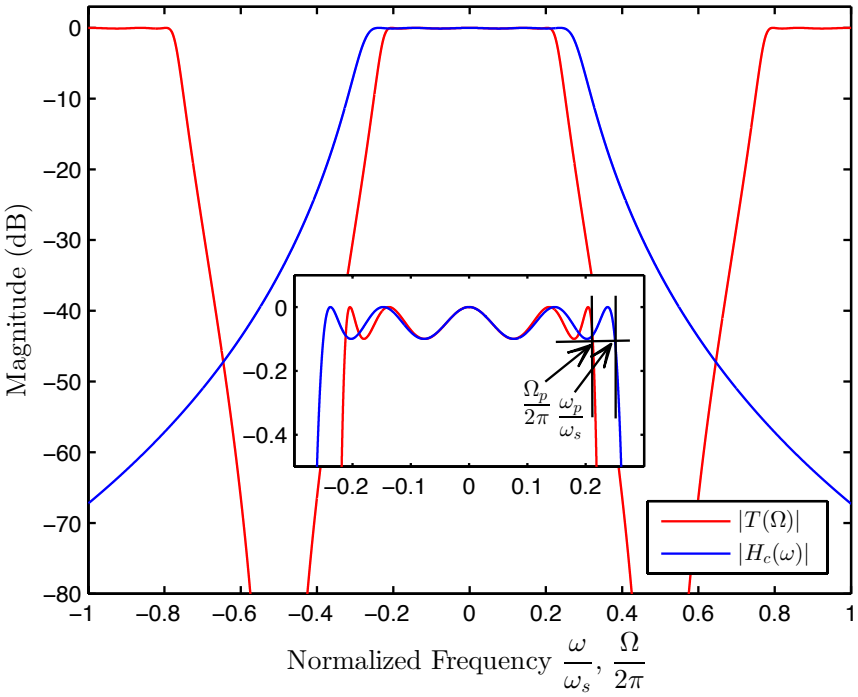

FIGURE 6.51: Magnitude response for the $5th$ order target analog prototype $H_c(\omega)$ versus the magnitude response of the $5th$ order digital counterpart $T(\Omega)$ obtained through the bilinear transformation with $T = 1.25$. Notice that the frequency normalizations ω/ω_s ($\omega_s = 2\pi/T$) for the analog domain and $\Omega/2\pi$ for the digital domain enables the comparison of both responses under a common domain.

invariance method and due to the wrapping effect, we clearly do not have a good match between both magnitude responses, except for the low frequency values around zero. However, we also see that the main frequency response features of the analog system, such as ripple, ripple amplitude as well as the pass-band and stop-band regions are also present on the digital system frequency response. The warping effect only affects the frequency locations for these features. For instance, we see from Figure 6.51 that due to the warping effect the normalized cutoff frequency for the digital system $\Omega_p/2\pi$ is different from that of the analog system ω_p/ω_s. Nevertheless, they are closely related

Numerator		Denominator	
b_0	0.0207	a_1	-1.2535
b_1	0.1036	a_2	1.5765
b_2	0.2071	a_3	-1.0211
b_3	0.2071	a_4	0.4628
b_4	0.1036	a_5	-0.1019
b_5	0.0207		

TABLE 6.17: Coefficients obtained from the Matlab function *bilinear* for the $5th$ order transmission system $T(z)$ when considering $T = 1.25s$. $T(z)$ is considered in the form of (6.186).

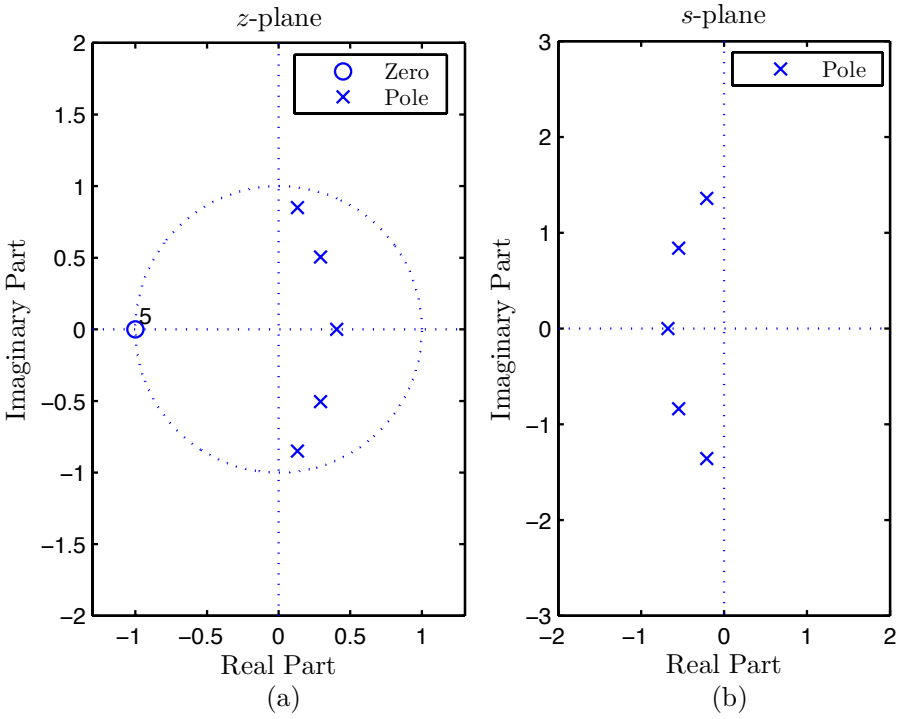

FIGURE 6.52: Pole-Zero plot associated to the $5th$ order digital transmission system $T(z)$ in (a) and Pole-Zero plot associated to the corresponding analog prototype $H_c(s)$ in (b).

through the frequency warping relation given by equation (6.184).

In this example, the sampling period T was selected, for comparison purposes, so as to match that of the example of the fifth order system regarding the impulse invariance procedure. However, for a proper synthesis of DNTL structures using the bilinear transformation, the procedure usually begins with the specifications (ripple level, cutoff frequency,...) for the frequency response in the digital domain. These specifications, are then converted to the analog domain via the frequency warping relation (6.184). From these values, the analog system is designed and then converted into its digital counterpart through the bilinear transformation (6.185).

Figure 6.52(a) depicts the locations of the zeros and poles on the z-plane for the transmission system, $T(z)$, when considering a period sampling of $T = 1.25s$. On the other hand, Figure 6.52(b) shows the locations for the poles of the analog prototype $H_c(s)$ on the s-plane. Clearly we see that the poles for the stable analog system, which are located on the LHP of the s-plane, are mapped to the inside of the unit circle on the z-plane. Thus, the digital system $T(z)$, as obtained through the bilinear transformation, is also a stable system. Furthermore, $H_c(s)$ has five zeros located at $s = \infty$. These zeros are mapped into the z-plane as a zero at $z = -1$ of multiplicity five, as depicted in

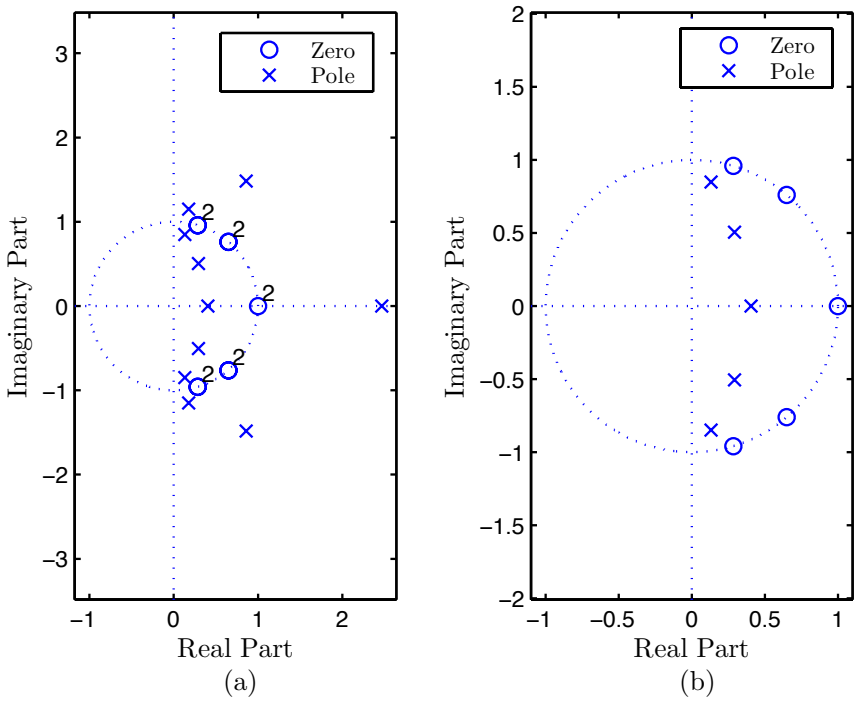

FIGURE 6.53: Pole-Zero plots associated to the $5th$ order reflection system $R(z)$ for $T = 1.25$. In (a) are depicted the zeros and poles for $|R(z)|^2$, whereas in (b) we have the zeros and poles of $R(z)$ which in turn are selected from those of $|R(z)|^2$.

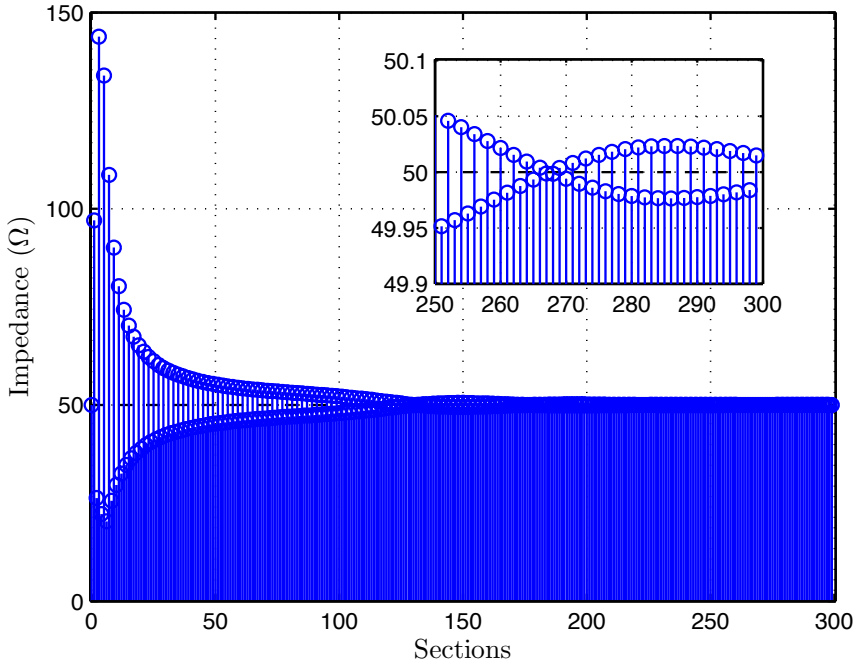

FIGURE 6.54: Impedance profile associated to $R(z)$, which is characterized by the pole-zero configuration depicted in Figure 6.53(b). The depicted impedance profile was obtained from 300 iterations of the DLP inverse scattering algorithm. Notice that the impedance profile is constituted by an infinite number of sections and the impedance values converges to 50Ω as the number of sections goes to infinity.

Numerator		Denominator	
e_1	-2.8662	a_1	-1.2550
e_2	4.6038	a_2	1.5779
e_3	-4.6038	a_3	-1.0224
e_4	2.8662	a_4	0.4632
e_5	-1.0000	a_5	-0.1020

TABLE 6.18: Coefficients for the $5th$ order reflection system $R(z)$ computed from the transmission system $T(z)$. The gain factor is $K_R = 0.32$ and $R(z)$ is in the form of (6.188).

Figure 6.52(a).

In step 4. of the procedure, the reflection system transfer function $R(z)$ is computed from its associated transmission system, $T(z)$, through the relation (6.187). We start by computing the poles and zeros for the squared magnitude of the reflection system transfer function, $|R(z)|^2$. The corresponding pole-zero plot is given in Figure 6.53(a). The pole-zero plot for $R(z)$ is depicted in Figure 6.52(b) and is obtained from that of $|R(z)|^2$ by selecting the stable poles and one zero from each pair of zeros. From this pole-zero selection the transfer function for $R(z)$ is easily computed in the form of equation (6.188). The coefficients for the numerator and denominator polynomials of $R(z)$ are given in Table 6.18.

The computation of the impedance profile for the DNTL structure which implements as its transmission frequency response the fifth order Chebyshev filter, thus $T(\Omega)$, is done in the fifth and final step of the procedure. For that and similarly to the previous examples, we run the DLP inverse scattering algorithm on the reflection response system $R(z)$. The resulting DNTL structure impedance profile, as computed by the inverse scattering procedure, is depicted in Figure 6.54, and is constituted by 300 sections.

Similarly to the example for the impulse invariance method, we realize that although we are synthesizing a fifth order filter, the resulting impedance profile is constituted by a far larger number of sections. This is because the transmission system $T(z)$ is not an all-pole or AR system. In fact and because $T(z)$ is represented by an ARMA process, the complete DNTL structure is actually constituted by an infinite number of sections. Nonetheless, analyzing Figure 6.54 it becomes clear that, the impedance value for the individual sections tend to converge for a constant impedance value $Z_{0_{end}}$, as the corresponding index number increases to infinity. The limit value $Z_{0_{end}}$ is given by (6.166). Furthermore, although the impedance value $Z_{0_{end}}$ is only obtained at infinity, we clearly see that after a couple hundreds of sections the impedance values have converged

enough towards $Z_{0_{end}}$ so that we can truncate the impedance profile , thus disregard the rest of the impedance profile. For the current example, and similarly to the criteria used in the example for the impulse invariance method, we consider that a suitable truncation section index is obtained when the amplitude of the impedance profile variation is within 0.1Ω. In the present case and as it can be observed from Figure 6.54, after index 250 the amplitude variation meets this criteria, thus a suitable DNTL structure would have a 250 section length. The truncation process is completed by assigning the last section with an impedance value of $Z_{0_{end}}$. Notice that, with the bilinear transformation, the aliasing problem inherent to the impulse invariance method, is not present, thus, for a microwave system with characteristic impedance of $Z_{0_{init}} = 50\Omega$ and from the evaluation of the reflection frequency response at $\Omega = 0$ as $|R(0)| = 0$ we have from (6.166) that $Z_{0_{end}} = 50\Omega$.

A comparison between the impedance profile results for the impulse invariance method and bilinear transformation examples reveals that, the later technique results in abnormally larger structures than the former when considering similar synthesis conditions. This fact is due to the distortion produced by the warping effect. Although it will be the object of study further on, we refer at this point that two factors contribute to the considerably larger length of the DNTL structure obtained through the bilinear transformation when compared to that obtained through the impulse invariance method. They are, the higher roll-off rate due to the frequency warping and foremost the transmission zeros located at $z = -1$ for the transmission system. Regarding the last one, notice that this location for the zeros translates into the frequency domain as an infinite attenuation for the transmission frequency response, that is, $|T(\Omega)| = 0$ for the frequency values $\Omega = \pm\pi$. It is not difficult to comprehend that such a value for the magnitude of the transmission frequency response is only achievable when considering an infinitely long DNTL structure and most importantly that the convergency of the impedance profile values of such structure towards $Z_{0_{end}}$ is more gradual when compared to cases where the attenuation on the stoptband is finite. Notice that, the more gradually the convergency is, the greater the length of the DNTL structure will be in order to meet the truncation criteria. Thus, the maximum attenuation value for $T(\Omega)$ directly influences the size of the synthesized DNTL structures.

From the previous discussion, we conclude that in order to reduce the length of the DNTL structure to an acceptable length, it should suffice to reduce the attenuation value in the stop band. That can be indirectly accomplish in step 4. of the synthesis procedure

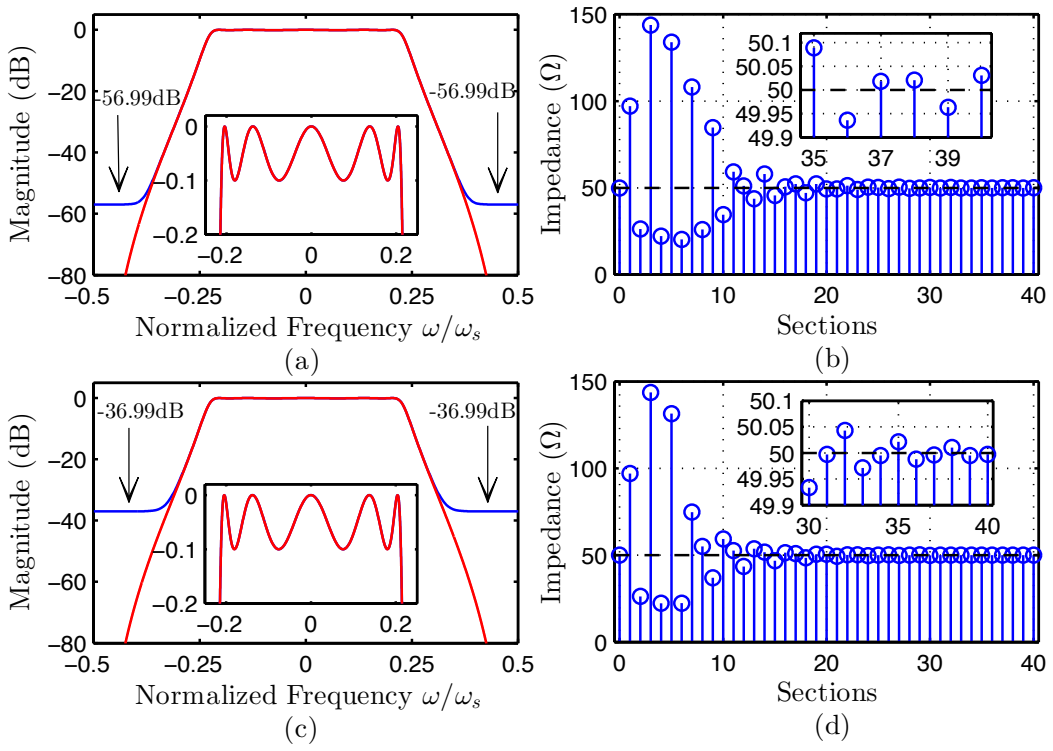

FIGURE 6.55: Results associated with the solution proposed to reduce the length of the DNTL given in Figure 6.54 for the fifth order filter example. In (a) and (c) we have the comparison between the magnitude response for the DNTL given in Figure 6.54 (red color) and those obtained after impedance profile length reduction (blue color). In (b) and (d) we have the corresponding impedance profiles obtained after impedance correction. The results in (a) and (b) correspond to the scaling factor K_{atten_1}, whereas, (c) and (d) are associated to K_{atten_2}. All the frequency responses are computed from the respective impedance profiles using the TMM method.

by properly scaling the reflection system transfer function $R(z)$, before proceeding to the inverse scattering step. As a result, we should expected a considerably length reduction for the DNTL structure. Furthermore, by reducing the attenuation value of $T(\Omega)$ at $\Omega = \pm\pi$ to values similar to that of the transmission frequency response from the impulse invariance method example, we should obtain a DNTL structure with a comparable length.

In order to evaluate how influent the scaling of the reflection response system is, let us consider the following two scaling factors

$$K_{atten_1} = 1 - 10^{-6} = 0.999999, \tag{6.190}$$

$$K_{atten_2} = 1 - 10^{-4} = 0.9999. \tag{6.191}$$

With these scaling factors and accordingly to (6.187), the attenuation for $T(\Omega)$ at $\Omega = \pm\pi$ comes as

$$|T(\pm\pi)| = \sqrt{1 - K_{atten_1}^2} \quad \Longrightarrow \quad -56.99\,\text{dB}, \tag{6.192}$$

$$|T(\pm\pi)| = \sqrt{1 - K_{atten_2}^2} \quad \Longrightarrow \quad -36.99\,\text{dB}. \tag{6.193}$$

Figure 6.55 shows the results for both scaling factors. It becomes clear from Figure 6.55(b) and Figure 6.55(d) that the length of the DNTL structure is drastically reduced for both scaling factors, whereas from Figure 6.55(a) and Figure 6.55(c) we confirm that the essential characteristics for the magnitude frequency response are maintained, and only the stopband region response is changed, more specifically the maximum attenuation values, which are given by (6.192) and (6.193).

Accordingly to the truncation criteria and from the analysis of Figures 6.55(b) and 6.55(d) we easily verify that the scaling factor K_{atten_1} results in an DNTL structure composed by thirty-five sections, whereas K_{atten_2} results in a twenty-nine length section DNTL structure.

It is interesting to note that, as predicted and for the scaling factor K_{atten_2}, the value for $T(\Omega)$ at $\Omega = \pm\pi$ is similar to that of the impedance invariance method example and as a result the impedance profile length is reduced to twenty-nine sections, which is almost the same length as with the impulse invariance method example. This further confirms that the maximum attenuation value for $T(\Omega)$ is the most influent factor in the length of the DNTL structures.

We refer at this point that, although the selection for the analog prototype used in this example was made to be the same as the one used in a similar example for the impulse invariance method, there is one important difference. The ripple level is different for both examples to keep the synthesized impedance values within feasible values. Keeping the same ripple level for the present example, *i.e.* $R_p = 0.5\,\text{dB}$ would result in impedance profiles with values up to 180Ω, which are outside the feasible range, as we have defined it. We further refer that this ripple value difference does not seems to interfere with the DNTL structure length.

As a last topic concerning the synthesis of DNTL structures using the bilinear transformation and regarding a practical/functional point of view, we refer that the synthesis of DNTL structures for the implementation of Chebyshev filters using the bilinear transformation can be radically simplified by understanding the relationship between type-I

and type-II Chebyshev frequency responses, and taking advantage from the tools provided by Matlab. Let us consider the magnitude of the analog transmission frequency response for a generic type-I Chebyshev filter, which is given by [76]

$$|T_c(\omega)| = \frac{1}{\sqrt{1+\epsilon^2 T_N^2(\omega/\omega_p)}}, \tag{6.194}$$

where $T_N(x)$ is the N-*th* order Chebyshev polynomial, ϵ is the ripple factor and ω_p is the cutoff frequency. Now, let us compute the corresponding magnitude of the reflection response as

$$\begin{aligned} |R_c(\omega)| &= \sqrt{1-|T_c(\omega)|^2} \\ &= \frac{1}{\sqrt{1+\dfrac{1}{\epsilon^2 T_N^2(\omega/\omega_p)}}}. \end{aligned} \tag{6.195}$$

It can be seen from [76] that, equation (6.195) is in the form of a highpass type-II Chebyshev filter. Furthermore, the Matlab function *cheby2* can be used to directly compute the coefficients for the analog system $R_c(s)$. In fact, it turns out that the function *cheby2* can also, if properly configured, automatically convert the analog filter to the digital domain through the bilinear transformation [75]. Thus, in the case of Chebyshev filters, the synthesis of DNTL structures through the bilinear transformation can be simplified as the steps 2., 3. and 4. on the synthesis procedure can be replaced by a single step where the digital reflection system is readily obtained from the digital system specifications given in the first step.

6.8.1.3 Approximation of derivatives method

Two methods have been analyzed so far regarding the conversion of analog systems into digital systems. They are, the the impulse invariance method and the bilinear transformation. Although we demonstrate that both these methods can be successfully applied to the synthesis of DNTL structures, we also see that the end result always comes in the form of an infinite length DNTL structure, which must ultimately undergo a truncation procedure. Furthermore, the total length (in terms of number of sections) for the final DNTL structure strongly depends on the truncation procedure and usually results in a far greater number of sections than that of the order of the system to be synthesized.

In this subsection we address the length issues inherent to the previous two analog-to-digital conversion methods and work towards the derivation of a new analog-to-digital transformation, suitable to the optimum synthesis of DNTL structures, as discussed in section 6.6.

We know from section 6.6 that, in order to perform the synthesis of DNTL structures in the optimum sense, *i.e.*, in the form of minimum length structures, we must first derive a suitable target transmission digital system, $T(z)$, whose transfer function is given in the form of an AR process, that is, an all-pole transfer function. This is in fact the reason why both, the impulse invariance method and the bilinear transformation, fail in the synthesis of minimum length structures. It is clearly seen from the examples previously given for both methods that, although the starting point is given as an all-pole analog prototype, both analog-to-digital conversion methods result in target transmission digital systems, $T(z)$, constituted by both zeros and poles (except for first and second order systems with the impulse invariance method).

The goal in this subsection, is to derive an analog-to-digital conversion method, which converts an analog all-pole system in to a digital all-pole system, and thus fulfill the minimum length synthesis conditions

In the previous subsection, we saw that the bilinear transformation is obtained by considering the trapezoidal rule as a numerical integration method for the solution of differential equations. As a result, the bilinear transformation (6.176) comes in the form of a quotient of two polynomials. It is important to realize at this point that, the denominator polynomial in (6.176) is responsible for the zeros at $z = -1$ which characterize the digital systems obtained through the bilinear transformation of all-pole analog prototype systems. This is because the roots of the denominator polynomial of the transformation (6.176) are automatically converted in to the zeros of the resulting digital system. Thus, in order to obtain all-pole digital systems from all-pole analog prototype systems, we must select a transformation whose denominator polynomial roots are placed either at $z = \infty$ or $z = 0$.

In order to derive an alternative transformation, we now consider the backward-difference approximation as a numerical differentiation method for the solution of differential equations. Basically, the backward-difference approximation replaces the derivative expressions in differential equations with finite difference approximations, *e.g.*, for

the derivative $dy(t)/dt$ at the instant $t = nT$ we have that

$$\frac{d\,y(t)}{dt} \triangleq \lim_{\delta\to\infty} \frac{y(t) - y(t-\delta)}{\delta} \approx \frac{y(nT) - y(nT-T)}{T}, \tag{6.196}$$

where T represents the sampling period.

The following mathematical derivations closely follows those from [1] and demonstrate how the difference equation associated with some digital transfer function $H_d(z)$ can be readily obtained from the differential equation associated with the analog system transfer function $H_c(s)$ by using the backward-difference approximation. To illustrate the procedure, let us consider a first order analog all-pole system given by

$$H_c(s) = \frac{b}{s+a}, \tag{6.197}$$

whose corresponding differential equation is obtained through the inverse Laplace transform as

$$\frac{d\,y(t)}{dt} + ay(t) = bx(t). \tag{6.198}$$

In the differential equation (6.198), $x(t)$ corresponds to input time-domain signal whereas $y(t)$ is the corresponding time-domain output. Substituting the derivative in the differential equation (6.198) by its backward-difference approximation (6.196) and expressing the result in the form of discrete time sequences, *i.e.*, considering

$$\begin{cases} y[n] &= y(nT), \\ x[n] &= x(nT), \end{cases} \tag{6.199}$$

we obtain the difference equation

$$\frac{y[n] - y[n-1]}{T} + ay[n] = bx[n]. \tag{6.200}$$

Taking the z-transform of the previous difference equation and after some mathematical rearrangement, we obtain the digital system transfer function in the form

$$H_d(z) = \frac{Y(z)}{X(z)} = \frac{b}{\left(\dfrac{1-z^{-1}}{T}\right) + a}. \tag{6.201}$$

A simple comparison between the analog system transfer function (6.197) and that of the

corresponding digital system (6.201), enable us to conclude that the mapping between both the s-plane and z-plane is performed accordingly to the transformation:

$$s = \frac{1 - z^{-1}}{T}. \tag{6.202}$$

Furthermore, for second order derivatives, the approximation is given by the second order difference, that is

$$\begin{aligned} \frac{d^2y(t)}{dt^2} &= \frac{d}{dt}\left[\frac{dy(t)}{dt}\right] \\ &\approx \frac{[y(nT) - y(nT - T)]/T - [y(nT - T) - y(nT - 2T)]/T}{T} \\ &\equiv \frac{y[n] - 2y[n-1] + y[n-2]}{T^2}. \end{aligned} \tag{6.203}$$

Transforming both sides of the previous equation in to the respective domains, that is, taking the Laplace transform of the second order derivative and the z-transform of the difference equation yields

$$s^2 = \frac{1 - 2z^{-1} + z^{-2}}{T^2} = \left(\frac{1 - z^{-1}}{T}\right)^2. \tag{6.204}$$

It follows from (6.204) that higher derivatives are approximated similarly, therefore, for the *k-th* derivative we have that

$$s^k = \left(\frac{1 - z^{-1}}{T}\right)^k. \tag{6.205}$$

From equation (6.205), we easily conclude that through the method of approximation of derivatives, the digital system transfer function is easily obtained by a simple variable change, *i.e.*,

$$H_d(z) = H_c\left(\frac{1 - z^{-1}}{T}\right), \tag{6.206}$$

where $H_c(s)$ is the analog prototype system.

It is important to realize at this point that, unlike with the bilinear transformation, the denominator polynomial of the transformation given by equation (6.202) has it roots at $z = \infty$, hence, the resulting digital system obtained through (6.202) from an analog prototype all-pole system is also an all-pole system, thus fulfilling the optimum synthesis conditions given in section 6.6.

Now, let us investigate in more detail the properties of the transformation given

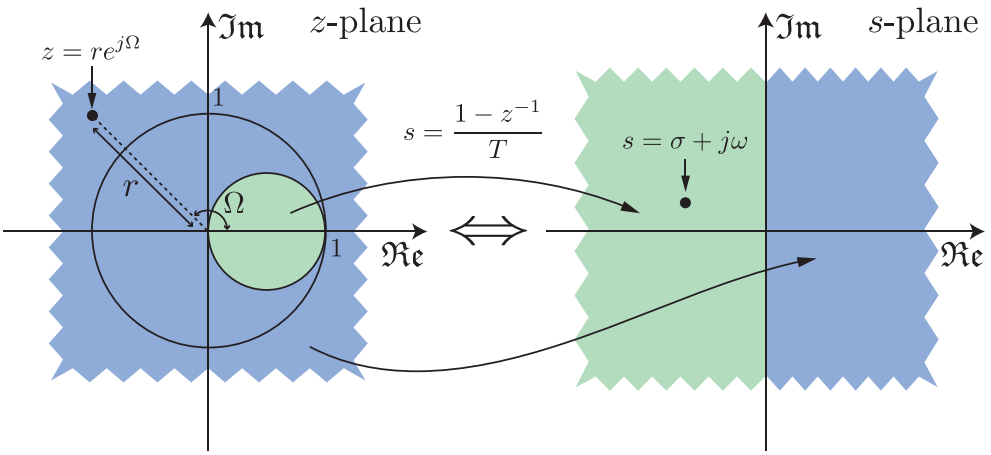

FIGURE 6.56: Mapping produced by the approximation of derivatives method, accordingly to equation (6.202).

by (6.202) and assess its feasibility as an analog-to-digital conversion method in the synthesis of minimum length DNTL structures. We start by inverting the transformation equation (6.202), so as to express z as a function of s, thus

$$z = \frac{1}{1 - sT}. \tag{6.207}$$

Substituting $s = \sigma + j\omega$ into the previous equation and calculating the corresponding magnitude, yields

$$|z| = \frac{1}{\sqrt{(1 - \sigma T)^2 + (\omega T)^2}}. \tag{6.208}$$

From equation (6.208) we see that, independently of the value of ω, $|z|$ will always evaluate as $|z| < 1$ provided that $\sigma < 0$. This means that stable analog systems are always converted in to stable digital systems through (6.202), *i.e.*, poles on the LHP of the s-plane are mapped to poles inside the unit circle in the z-plane.

If we now substitute $s = j\omega$ in (6.207), we have that

$$z = \frac{1}{1 - j\omega T} = \frac{1}{1 + (\omega T)^2} + j\frac{\omega T}{1 + (\omega T)^2}. \tag{6.209}$$

From (6.209), we easily verify that, as ω varies from $\omega = -\infty$ to $\omega = \infty$ the associated locus of points in the z-plane corresponds to a circle of radius $1/2$ and center at $z = 1/2$, as illustrated in Figure 6.56. Furthermore, it can be shown that points in the LHP of the s-plane are mapped inside this circle whereas points in the RHP are mapped outside. This is illustrated in Figure 6.56, where by simple inspection we realize that the possible pole locations for stable digital systems are confined to a relatively small

area when compared to the entire unit circle. This by itself limits the the use of this transformation to the synthesis of lowpass filters with very small bandwidths. In other words, only when the frequencies of interest ω, in the frequency response of the analog system, are much smaller than the sampling frequency, $1/T$, is that the transformation (6.202) is a feasible transformation for the synthesis of DNTL structures.

At this point we conclude that the transformation given by (6.202) has in fact desirable qualities. Namely, it avoids the aliasing problem encountered in the impulse invariance method and unlike the bilinear transformation it allows the transformation of all-pole analog systems in to all-pole digital systems. However, it is limited by frequency range considerations and thus, not suitable for the synthesis of DNTL structures.

In an attempt to overcome these frequency range limitations while still maintaining the same advantages over the other analog-to-digital conversion methods, we now introduce a new transformation, given by

$$s = \frac{1 - z^{-1}}{T\, z^{-1/2}} = \frac{z^{1/2} - z^{-1/2}}{T}. \tag{6.210}$$

Notice that, the new transformation is obtained from the transformation given in (6.202) by introducing the factor $z^{-1/2}$ in the denominator.

Substituting $z = re^{j\Omega}$ in to the new transformation yields

$$s = \frac{\sqrt{r}\, e^{j\Omega/2} - (1/\sqrt{r})e^{-j\Omega/2}}{T}. \tag{6.211}$$

Solving the above equation, so as to obtain the corresponding real and imaginary parts and considering $s = \sigma + j\omega$, we get

$$\sigma = \frac{\cos\left(\dfrac{\Omega}{2}\right)(r-1)}{T\sqrt{r}}, \tag{6.212}$$

$$\omega = \frac{\sin\left(\dfrac{\Omega}{2}\right)(r+1)}{T\sqrt{r}}. \tag{6.213}$$

Analyzing equation (6.212) we easily verify that when $r = 1$ and considering the entire digital-domain frequency space, *i.e.*, $-\pi \leq \Omega \leq \pi$, then $\sigma = 0$. Thus, points on the imaginary axis in the s-plane are mapped onto the unit circle in the z-plane. Furthermore, keeping in mind that $-\pi \leq \Omega \leq \pi$, it not difficult to verify from (6.212) that if $r < 1$ then $\sigma < 0$. On the other hand, when $r > 1$ we have $\sigma > 0$. Thus, through

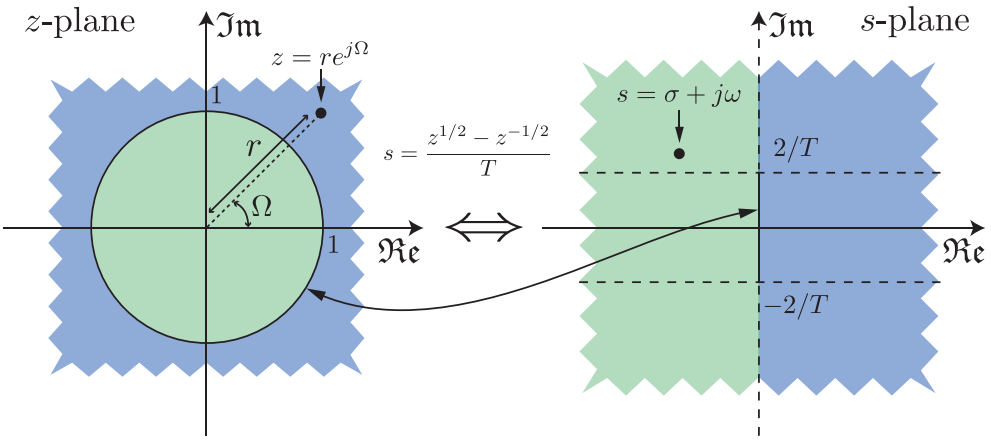

FIGURE 6.57: Mapping produced by the approximation of derivatives method, accordingly to equation (6.210).

the transformation given by (6.210) any causal stable analog system will always result in a causal stable digital system. Furthermore, analyzing equation (6.213) we easily verify that when $r = 1$, we obtain the relation between the analog and digital frequency variables as

$$\omega = \frac{2}{T} \sin\left(\frac{\Omega}{2}\right). \tag{6.214}$$

From equation (6.214), as we cover the entire digital frequency domain, *i.e.*, as Ω varies from $\Omega = -\pi$ to $\Omega = \pi$, the corresponding locus of points in the s-plane is given by the segment of the $j\omega$ axis extending from $\omega = -2/T$ to $\omega = 2/T$.

The mapping produced by the transformation given in (6.210) is illustrated in Figure 6.57. From the figure we clearly see that the LHP of the s-plane is mapped inside of the unit circle in the z-plane, whereas the RHP of the s-plane maps to the outside of the unit circle. Furthermore, the points located on the imaginary axis of the s-plane ranging from $\omega = -2/T$ to $\omega = 2/T$ are mapped to the entire unit circle on the z-plane, whereas the points located on the imaginary axis of the s-plane for $\omega > 2/T$ are mapped outside the unit circle and the points located on the imaginary axis for $\omega < -2/T$ are mapped inside of the unit circle.

The inverse frequency relation, *i.e.*, the mapping of the unit circle onto the $j\omega$ axis of the s-plane is given by

$$\Omega = 2 \arcsin\left(\frac{\omega T}{2}\right) \quad \text{for} \quad \frac{-2}{T} \leq \omega \leq \frac{2}{T}. \tag{6.215}$$

Notice that, by definition and accordingly to (6.215), the function arcsine is only defined as the inverse of the sine function in the domain $-1 \leq \omega T/2 \leq 1$. In other words, for

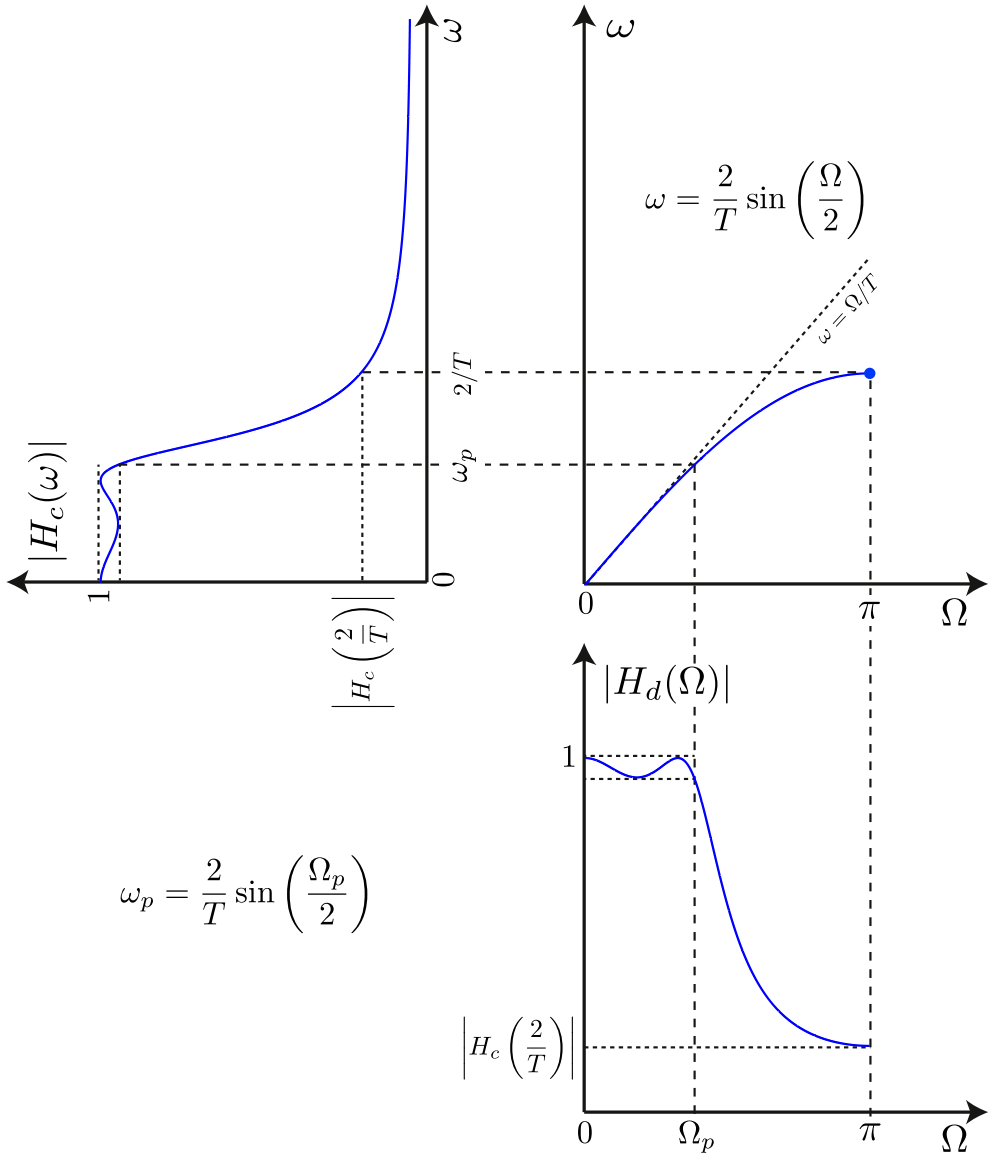

FIGURE 6.58: Mapping of the continuous-time frequency axis onto the discrete-time frequency axis and vice-versa. The illustration clearly shows that similarly to the bilinear transformation there is also a warping effect inherent to the transformation in (6.210). Thus, to achieve the desired digital domain cutoff frequencies, the corresponding analog domain frequencies must be pre-warped as shown. The presented illustration is based on a third order low-pass all-pole filter.

the digital frequency variable Ω to take real values, the domain for the analog frequency value must be limited to the range $-2/T \leq \omega \leq 2/T$.

Figure 6.58 illustrates the mapping between the digital and analog frequency domains. Unlike with the bilinear transformation, where the entire analog frequency domain is compressed into the digital frequency domain *i.e.*, $-\pi \leq \Omega \leq \pi$, it becomes clear from Figure 6.58 that with the transformation given in (6.210) only the analog frequency values in the range $-2/T \leq \omega \leq 2/T$ are mapped to the digital domain $-\pi \leq \Omega \leq \pi$.

We refer to this phenomena as *frequency clipping*, given that the analog frequency values outside this range are clipped off and do not translate into digital frequency values. That is, the remaining frequency values of the analog domain are mapped off the unit circle, *i.e.*, are mapped either inside or outside the unit circle depending on whether they are negatively or positively valued, but never on the unit circle.

From Figure 6.58 it becomes evident that besides the frequency clipping effect and similarly to the bilinear transformation, the transformation given by (6.210) also introduces a considerable amount frequency warping. Notice however that, the frequency response of the analog system $H_c(\omega)$ considered in the domain $-2/T \leq \omega \leq 2/T$ is exactly replicated on the digital domain, only the cutoff frequency an the frequency locations for the ripples are affected by the warping effect, *i.e.* only the independent variable, the frequency variable, is affected by the transformation. This means that on the synthesis procedure and to compensate for the warping effect, the digital frequency specifications must be set in advance and then pre-warped into specifications for the analog system $H_c(\omega)$ through (6.214).

In the same way as with the bilinear transformation and unlike with the impulse invariance method, the transformation resulting from the approximation of derivatives method is an algebraic transformation, thus, we should expect the process of converting the analog system into its digital counterpart to be as simple as substituting (6.210) into the analog system function, very much like in the bilinear transformation case. However, the process of obtaining the transfer function for the digital system $H_d(z)$ is not as straight forward as in the bilinear case, *i.e.*, it is not a simple matter of performing a variable change on the analog transfer function $H_c(s)$ by substituting the variable s by (6.210).

In order to demonstrate the process of obtaining $H_d(z)$ from $H_c(s)$, let us now consider as an example a first order analog Chebyshev system (all-pole) whose transfer function is given by

$$H_c(s) = \frac{a}{s+a}. \tag{6.216}$$

Following the same analog-to-digital conversion process as for the bilinear transformation, thus, substituting (6.210) into (6.216), we obtain

$$H'_d(z) = \frac{a}{\left(\dfrac{1-z^{-1}}{T\,z^{-1/2}}\right)+a} = \frac{aTz^{-1/2}}{1+aTz^{-1/2}-z^{-1}}. \tag{6.217}$$

It becomes evident from (6.217) that the direct substitution of (6.210) into the analog transfer function $H_c(s)$ is not a suitable method to obtained the correct digital system transfer function $H_d(z)$ associated to $H_c(s)$. First of, we clearly see that due to the presence of the $z^{-1/2}$ factor, both the numerator and denominator of $H'_d(z)$ are not in the polynomial form, consequently, the transfer function given by (6.217) can not represent a digital system transfer function. Secondly, we have demonstrated in section 6.3 that, the correct transfer function for a system that models the transmission system of a DNTL structure is given in the form of (6.45). Clearly the system in (6.217) is not in the form of (6.45), thus, it is not suitable to model the transmission response of a DNTL structure.

From the previous analysis, we may be led to think that, the transformation given by (6.210) is not suitable for the synthesis of DNTL structures. However, as we shall demonstrate next, we may in fact successfully use the transformation (6.210), by performing the variable change not directly on the analog system transfer function as before, but instead, on the system function associated to the magnitude-squared of the frequency response, $|H_c(\omega)|^2$.

The magnitude-squared of the frequency response of the first order analog system $H_c(s)$, is obtained by substituting $s = j\omega$ in equation (6.216), and then, computing its squared magnitude as

$$|H_c(\omega)|^2 = H_c(\omega)H_c^*(\omega) = \frac{a^2}{\omega^2 + a^2}, \tag{6.218}$$

where the superscript asterisk stands for the complex conjugate operation. From equation (6.218) we must obtain a new system function (or transfer function), which we identify as $H_{cs}(s)$ and that gives rise to $|H_c(\omega)|^2$. In order to do so, we start by realizing that accordingly to the realizability conditions (see section 4.2.1.1, condition (4.27)) the numerator and denominator of $H_c(s)$ must be polynomials with real coefficients. Consequently and accordingly to the properties of the Fourier transform we have that

$$H_c^*(\omega) = H_c(-\omega), \tag{6.219}$$

thus, the magnitude-squared function can alternatively be computed as

$$|H_c(\omega)|^2 = H_c(\omega)H_c(-\omega) = \frac{a^2}{\omega^2 + a^2}. \tag{6.220}$$

By taking into consideration the relation $s = j\omega$ in equation (6.220) we easily obtain the system function associated with the magnitude-squared of the frequency response as

$$H_{cs}(s) = H_c(s)H_c(-s) = \left(\frac{a}{s+a}\right)\left(\frac{-a}{s-a}\right) = \frac{-a^2}{s^2-a^2}. \tag{6.221}$$

The relation between $H_{cs}(s)$ and the magnitude-squared of the frequency response is given by

$$H_{cs}(s)\big|_{s=j\omega} = |H_c(\omega)|^2. \tag{6.222}$$

From (6.221) we see that $H_{cs}(s)$ is a second order system with poles located at $s_1 = -a$ and $s_2 = a$, which are respectively the poles of $H_c(s)$ and $H_c(-s)$. Furthermore, we clearly see that the location for the pole of $H_c(-s)$ on the s-plane is mirrored from that of the pole of $H_c(s)$ about the $j\omega$ axis . As a result, the polynomial denominator for $H_{cs}(s)$ comes in the form of a second order even polynomial.

Now that we have computed the system function associated to the squared magnitude frequency response of $H_c(s)$ we can proceed to obtain the digital system associated to $H_{cs}(s)$ by substituting equation (6.210) into (6.221), *i.e.*,

$$H_{ds}(z) = H_{cs}(s)\Big|_{s=\dfrac{1-z^{-1}}{T\,z^{-1/2}}}. \tag{6.223}$$

As a result we obtain the digital system function $H_{ds}(z)$ as given by

$$H_{ds}(z) = \frac{-a^2}{\dfrac{1-2z^{-1}+z^{-2}}{T^2z^{-1}} - a^2} = \frac{-a^2T^2z^{-1}}{1-(2+a^2T^2)z^{-1}+z^{-2}}. \tag{6.224}$$

The advantage of computing $H_{cs}(s)$ first and only then perform the variable change starts to be clear now. Because the denominator of $H_{cs}(s)$ is an even polynomial, the term $z^{-1/2}$ is eliminated, consequently the numerator and denominator of equation (6.224) are polynomials in z, thus, $H_{ds}(z)$ represents a digital system. This is in contrast with the result obtained in (6.217) which follows from a direct substitution of (6.210) in $H_c(s)$. Notice that, in the same way as with $H_{cs}(s)$, the digital system function $H_{ds}(z)$ is associated to the squared magnitude frequency response of $H_d(z)$ by

$$H_{ds}(z)\big|_{z=e^{j\Omega}} = |H_d(\Omega)|^2. \tag{6.225}$$

From (6.224) and similarly to $H_{cs}(s)$, we verify that $H_{ds}(z)$ is also a second order

system whose poles are given by the roots of the denominator polynomial. Additionally, $H_{ds}(z)$ also has two zeros, one located at $z = 0$ and the other at $z = \infty$, hence, $H_{ds}(z)$ is an all-pole digital system.

As with the bilinear transformation and unlike with the impulse invariance method, the transformation resulting from the approximation of derivatives method is an algebraic transformation, which means that both poles and zeros on the analog domain are directly mapped to the z-plane through the corresponding inverse transformation, *i.e.*, the inverse function of (6.210).

In order to obtain the inverse function of (6.210), we start by computing the squared of equation (6.210), which is given as

$$s^2 = \frac{1 - 2z^{-1} + z^{-2}}{T^2 z^{-1}}. \tag{6.226}$$

The inverse transformation, *i.e.*, the equation that maps points on the s-plane into points on the z-plane, can then be obtained by conveniently solving equation (6.226) in order to z, yielding

$$z = \frac{(sT)^2}{2} + 1 \pm sT\sqrt{\left(\frac{sT}{2}\right)^2 + 1}. \tag{6.227}$$

However and as we can see from equation (6.227), the result of solving (6.226) in order to z yields two distinct solutions, namely, one associated with the "plus" sign and the other with the "minus" sign. The identification of the correct choice of sign for the inverse transformation can be done by resorting to the poles of (6.221), *i.e.*, the system function associated with the magnitude-squared frequency response of the first order system example. Considering the first pole, $s_1 = -a$ which is located on the LHP of the s-plane and substituting it in (6.227) we obtain two solutions accordingly to the selected sign, namely z_+ and z_-, which relate as $|z_-| > |z_+|$. From equation (6.212) we know that the correct transformation must map points on the LHP of the s-plane inside the unit circle of the z-plane. Thus, because the solution z_+ has the lower magnitude, the "plus" sign must necessarily be the correct choice. The correct inverse transformation is then set by choosing the "plus" sign, hence,

$$z = \frac{(sT)^2}{2} + 1 + sT\sqrt{\left(\frac{sT}{2}\right)^2 + 1}. \tag{6.228}$$

In fact, it can be shown that the transformation obtained by selecting the "plus" sign

maps the points on the LHP of the s-plane inside the unit circle on the z-plane and points on the RHP outside the unite circle, whereas the selection of the "minus" sign works the other way around, *i.e.*, maps the points on the LHP of the s-plane outside the unit circle on the z-plane and points on the RHP inside the unite circle. Hence, the selection of the "plus" sign for the correct transformation.

Equation (6.228) can be further simplified and conveniently expressed as a quotient, thusly, after some mathematical steps we get

$$z = \frac{\sqrt{(sT)^2 + 4} + sT}{\sqrt{(sT)^2 + 4} - sT}. \tag{6.229}$$

Now that we have properly defined the inverse transformation, we can directly compute the poles of $H_{dc}(z)$ from those of $H_{cs}(s)$ in (6.221) through (6.229), *i.e.*,

$$s_1 = -a \quad \leftrightarrow \quad z_1 = \frac{\sqrt{(aT)^2 + 4} - aT}{\sqrt{(aT)^2 + 4} + aT}, \tag{6.230}$$

$$s_2 = a \quad \leftrightarrow \quad z_2 = \frac{\sqrt{(aT)^2 + 4} + aT}{\sqrt{(aT)^2 + 4} - aT}. \tag{6.231}$$

Notice that the same values for z_1 and z_2 can be obtained by computing the roots of the denominator polynomial of $H_{ds}(z)$ *i.e.* (6.224).

We clearly see form (6.230) and (6.231) that the poles of $H_{ds}(z)$ are related as $z_1 = 1/z_2$. Moreover and assuming that $|a| > 0$, the pole z_1 is located inside the unit circle, whereas z_2 is located outside the circle.

We are now in a position to finally obtain the digital system transfer function $H_d(z)$ associated to the first order analog system $H_c(s)$ in (6.216). In order to do so, we select the pole of $H_{ds}(z)$ that is located inside the unit circle *i.e.*, the stable pole z_1. From the pole z_1 we assemble the transfer function of $H_d(z)$ in the form of (6.68) , thus,

$$H_d(z) = \frac{b}{1 - z_1 z^{-1}} = \frac{2aT}{\sqrt{(aT)^2 + 4} + aT - (\sqrt{(aT)^2 + 4} - aT)z^{-1}}, \tag{6.232}$$

where b is the normalizing scale factor, which is calculated as $b = 1 - z_1$, so that the frequency response at dc ($z = 1$) is equal to unity.

Equation (6.232) is the resulting digital system function obtained from the first order analog prototype system $H_c(s)$ (see (6.216)) by using the approximation of derivatives method. Notice that, by approximation of derivatives method we mean the transformation given by (6.210).

Clearly, the transfer function of $H_d(z)$ is very different from that obtained by performing a direct substitution, *i.e.*, $H'_d(z)$ (see (6.217)). Recall that $H'_d(z)$, is the transfer function resulting from directly substituting equation (6.210) in the first order analog prototype system transfer function (6.216), *i.e.*, $H_c(s)$. Moreover, notice that unlike $H'_d(z)$, the transfer function of $H_d(z)$ is only constituted by integer powers of z, hence, it is a legitimate digital system.

Early on, we have seen that $H'_d(z)$ can not represent a digital system because its transfer function includes a term of $z^{1/2}$. Anyway and by substituting $z = e^{j\Omega}$ in (6.217), we can still obtain a frequency response associated to $H'_d(z)$. Comparing the frequency responses corresponding to $H'_d(\Omega)$ and $H_d(\Omega)$ we have that

$$|H'_d(\Omega)| = |H_d(\Omega)|, \tag{6.233}$$

$$\angle H'_d(\Omega) \neq \angle H_d(\Omega). \tag{6.234}$$

As expected both have the same magnitude response, however, they differ on their phase response. This is because the conversion from analog-to-digital is performed in $H_{cs}(s)$ which only carries the magnitude information of $H_c(\Omega)$. Furthermore, it can be shown that contrary to $H_d(\Omega)$, the frequency response $H'_d(\Omega)$ is not minimum phase, thus, it is not suitable to represent the transmission system associated to a DNTL structure (see section 6.4).

In the light of the above results and similarly to $H_{cs}(s)$ it can be shown that the digital system function $H_{ds}(z)$ associated to the magnitude-squared frequency response of $H_d(z)$ is also given by the product of two digital systems, *i.e.*,

$$H_{ds}(z) = H_d(z)H_d(1/z) = H_d(z)H_{d*}(z), \tag{6.235}$$

where the subscript asterisk stands for the para-Hermitian conjugate operation. In addition, comparing (6.235) with (6.221) we see that $H_d(z)$ and $H_d(1/z)$ are the digital counterparts of $H_c(s)$ and $H_c(-s)$, respectively. Thus, and accordingly to (6.229), in the same way that the poles of $H_c(-s)$ are the opposite (additive inverse) of those of $H_c(s)$, the poles of $H_d(1/z)$ are the reciprocal (multiplicative inverse) of those of $H_d(z)$. This is in fact true for any system order.

To get a better understanding of how the poles of higher order systems are distributed

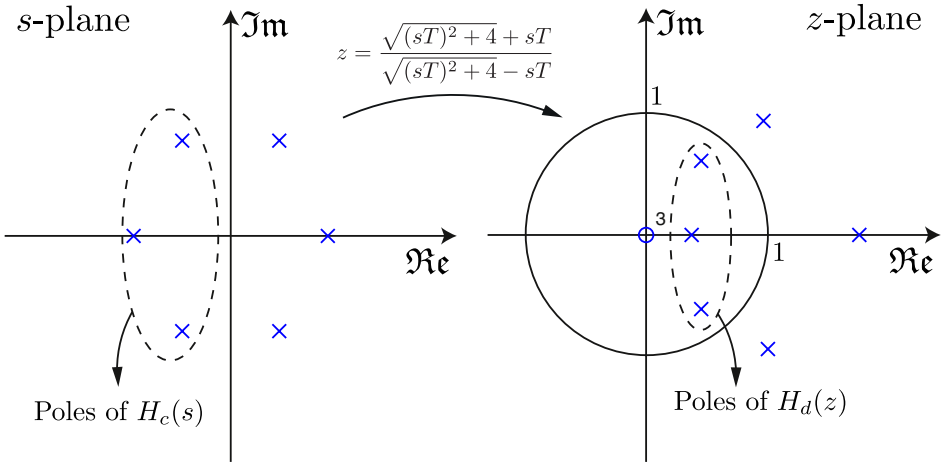

(a) Pole-zero plot for $H_{cs}(s)$. (b) Pole-zero plot for $H_{ds}(z)$.

FIGURE 6.59: Example of third order Butterworth (all-pole) analog system $H_c(s)$. Pole-zero diagrams for the analog and digital systems associated with the magnitude-squared frequency responses.

both in the analog an digital domains and because the first order system example previously analyzed is somewhat limited in this regard, we show in Figure 6.59 the pole-zero plot for a third order system. Figure 6.59(a) depicts the poles for the analog system $H_{cs}(s)$ associated with the magnitude-square frequency response of a third order Butterworth filter, whereas Figure 6.59(b) depicts the pole-zero plot for the digital counterpart system $H_{ds}(z)$ obtained from $H_{cs}(s)$ via the approximation of derivatives method.

We know from section 4.2.1.1, more specifically from condition (4.27), that, in order for an analog system to be physically realizable, the numerator and denominator polynomials of the corresponding system function must be constituted by real valued coefficients. In this way, and from the complex conjugate root theorem, we have that, if $P(s)$ is a polynomial in s with real coefficients and $a + jb$ (a and b real numbers) is a root of $P(s)$, then its complex conjugate $a - jb$ is also a root of $P(s)$. Thus, the poles for the third order Butterwort system $H_c(s)$ (whose denominator is given by a polynomial with real valued coefficients) are given in complex conjugate pairs, hence are symmetrically placed around the real axis on LHP of the s-plane, as shown in Figure 6.59(a). The poles on the RHP are those of $H_c(-s)$ and are a mirrored version about the imaginary axis of those of $H_c(s)$.

As a consequence of the complex conjugate root theorem, that is, because the numerator and denominator polynomials of the analog system $H_c(s)$ are solely constituted by real coefficients, it can be shown that the numerator and denominator polynomials of the system function associated to the magnitude-squared of the frequency response

of any analog system are even polynomials, *i.e.*, polynomials only constituted by even powers of s. This is in fact the key to successfully use equation (6.210) as an analog-to-digital transformation. In other words, because both the numerator and denominator polynomials of $H_{cs}(s)$ are always even polynomials, the resulting digital system $H_{ds}(z)$ obtained by substituting (6.210) onto $H_{cs}(s)$ will be always constituted by numerator and denominator polynomials with integer powers of z, thus eliminating the fractional powers of z obtained when performing a direct substitution of (6.210) onto $H_c(s)$.

We must emphasize, however, that, even though the analog-to-digital transformation can be successfully performed by substituting (6.210) onto $H_{cs}(s)$, only the magnitude response of $H_c(s)$ is in fact mapped to the digital domain. Notice that the phase response information of $H_c(s)$ is lost in the analog-to-digital conversion process because the phase frequency response associated to $H_{cs}(s)$ is zero. The phase response associated to the resulting digital system, *i.e.*, $H_d(z)$, results from a realizability constrain, that is, the transmission frequency response associated to any DNTL structure must always be a minimum phase frequency response. Thus, the phase response of $H_d(\Omega)$ is automatically defined from its magnitude response (see section 6.4, condition (6.73)).

Figure 6.59(b) depicts the poles for the digital system $H_{ds}(z)$ which are readily obtainable from those in Figure 6.59(a) through (6.229). The poles inside the unit circle result from the mapping of the poles of $H_c(s)$, *i.e.*, those on the LHP of the s-plane. In the same way, the poles outside the unit circle result from the mapping of the poles of $H_c(-s)$, *i.e.*, those on the RHP of the s-plane. As for the analog system zeros, they are located at $s = \pm\infty$, and accordingly to (6.229) half of them are mapped at $z = 0$ and the other half at $z = \infty$, which makes $H_{ds}(z)$ an all-pole system. It is important to recall that because the resulting digital system is always an all-pole system, the transformation given by (6.210) is ideal for the optimum synthesis of DNTL structures. The digital system $H_d(z)$ is finally obtained by selecting only the poles inside the unit circle and the corresponding digital system function is assembled in the form of (6.68).

From the previous analysis, it becomes clear that the process of obtaining $H_d(z)$ from $H_c(s)$ is in fact a very simple procedure. It simply consists on computing the poles of $H_d(z)$ by mapping those of $H_c(s)$ through equation (6.229) and from the poles of $H_d(z)$ assembling the corresponding transfer function accordingly to (6.68).

Let us now recall the frequency mapping illustrated in Figure 6.58 which results from using the approximation of derivatives method in the analog-to-digital conversion of some analog system $H_c(s)$. Moreover, let us assume that $H_c(s)$ is a generic type-I

Chebyshev system whose corresponding magnitude-squared frequency response is given by

$$|H_c(\omega)|^2 = \frac{1}{1+\epsilon^2 T_N^2(\omega/\omega_p)}, \tag{6.236}$$

where ω_p is the analog cutoff frequency, similarly to the example given in Figure 6.58 for a third order filter. In the same way that we obtain $H_{ds}(z)$ by substituting equation (6.210) into $H_{cs}(s)$, we can also directly work in the frequency domain and readily obtain the digital system magnitude-squared frequency response, *i.e.*, $|H_d(\Omega)|^2$, by substituting equation (6.214) into the analog magnitude-squared Chebyshev filter response (6.236). By doing so, the digital domain magnitude-squared frequency response is given by

$$|H_d(\Omega)|^2 = \frac{1}{1+\epsilon^2 T_N^2\left(\dfrac{\sin(\Omega/2)}{\sin(\Omega_p/2)}\right)}, \tag{6.237}$$

where ω_p is the digital cutoff frequency.

In light of the direct relation between DNTL structures and digital filters discussed in section 6.3, equation (6.237) can alternatively be represented as a function of the electrical length variable, since we know from section 6.3 that $\Omega = 2\theta$, thus

$$|H_d(\theta)|^2 = \frac{1}{1+\epsilon^2 T_N^2\left(\dfrac{\sin(\theta)}{\sin(\theta_p)}\right)}, \tag{6.238}$$

where θ_p is the cutoff electrical length.

The magnitude-squared frequency response in (6.238) is the same used by Young [77] and Levy [78] for the synthesis of commensurate stepped-impedance filters (DNTL filters under our nomenclature). In fact, the works of Levy and Young in the synthesis of stepped-impedance filters derives from that of Collin [79] and later Riblet [80] on the design and synthesis of wide-band multi-section quarter-wave impedance transformers. In his work, Collin states that the insertion loss function for an n-section impedance transformer can always be expressed as an even and real polynomial in $\cos(\theta)$. Hence, Collin's theorem can be stated as

$$P_L = 1 + Q_n^2(\cos(\theta)), \tag{6.239}$$

where P_L stands for insertion loss and Q_n is either an even or odd polynomial.

From Collin's theorem, Young and Levy readily realize that in a similar way, the insertion loss function for an n-section stepped impedance filter must be given by

$$P_L = 1 + Q_n^2(\sin(\theta)), \tag{6.240}$$

Notice from (6.238) that, the insertion loss function associated to $|H_d(\theta)|^2$ is given by its denominator, which clearly is in the form of (6.240).

Although their statement regarding the form of the insertion loss function for both impedance transformers and stepped impedance filters is completely correct, it lacks the mathematical evidence that we provide in this section, by making the connection between digital systems and DNTL structures.

In order to summarize, from a practical viewpoint, the synthesis procedure of DNTL structures using the approximation of derivatives method, we now highlight the essential steps of the procedure. The procedure is similar to that previously described regarding the bilinear transformation, in the present case however it is carried out by undertaking the following steps:

1. The procedure begins by specifying the digital system frequency properties, *i.e.* ripple level, cutoff frequency, etc. These specifications are afterwards converted or pre-warp into analog frequency specifications (*e.g.* cutoff frequency) through the frequency mapping function

$$\omega = \frac{2}{T}\sin\left(\frac{\Omega}{2}\right). \tag{6.241}$$

   The desired frequency specifications for the analog system are obtained from (6.241) by a convenient selection of the sampling period T. Notice that similarly to the bilinear transformation, the value of T strongly influences how the warping effect distorts the resulting digital system spectrum when compared to the analog one. Furthermore and most importantly, the sampling period T directly influences the frequency clipping phenomena, *i.e.*, the amount of the analog frequency response that is in fact mapped to the digital frequency domain. Hence, high values of T imply a strong clipping effect, *i.e.*, only a small analog frequency band is mapped to the digital frequency domain, whereas for small values of T a wider range of the analog frequency domain is mapped to the digital frequency domain (See Figure 6.58).

2. From the analog system specifications, the target all-pole analog prototype transfer function $H_c(s)$ is determined. Many design methods for continuous-time systems have relatively simple closed-form design formulas (e.g., Butterworth, Chebyshev polynomials). Furthermore, extensive tables are available for analog filter design.

3. Transform the analog prototype transfer function $H_c(s)$ into its digital counterpart $H_d(z)$. In order to do so, first compute the poles of the analog system $H_c(s)$ (all-pole system), then map them from the s-plane to the z-plane accordingly to

$$z = \frac{\sqrt{(sT)^2 + 4} + sT}{\sqrt{(sT)^2 + 4} - sT}. \tag{6.242}$$

From the poles, the transfer function for the digital system is then assembled in the form of (6.68) and ultimately expressed by

$$T(z) = H_d(z) = \frac{b}{1 + \sum_{i=1}^{m} a_i \, z^{-1}}, \tag{6.243}$$

where m is the order of the filter and the denominator polynomial coefficients a_i must be real so as to comply with the realizability conditions. The numerator constant, or normalizing scaling factor, is given by

$$b = 1 + \sum_{i=1}^{m} a_i. \tag{6.244}$$

Notice that, in (6.243) we have conveniently changed our nomenclature from $H_d(z)$ to $T(z)$ so that we can from now on differentiate from transmission $T(z)$ and reflection $R(z)$ systems respectively.

4. Obtain the transfer function for the reflection frequency response $R(z)$ associated to $T(z)$ through the relation

$$|R(z)|^2 = 1 - |T(z)|^2 \tag{6.245}$$

using the procedure described in section 6.6. The transfer function for the reflection system is given as

$$R(z) = K_R \frac{1 + \sum_{i=1}^{m} e_i \, z^{-i}}{1 + \sum_{i=1}^{m} a_i \, z^{-i}}, \tag{6.246}$$

where e_i and a_i are the coefficients for the numerator and denominator polynomials, and K_R is the normalizing gain factor.

5. Compute the DNTL filter impedance profile by applying the discrete layer-peeling inverse scattering procedure described in section 6.5 on the reflection frequency response $R(z)$.

So as to demonstrate the synthesis of DNTL structures using the approximation of derivatives method we now consider one practical example. For comparison purposes we chose an analog prototype similar to that of the last example regarding the bilinear transformation. Thus, the analog system is a fifth order type-I Chebyshev low-pass filter with in-band ripple $R_p = 0.1\,\text{dB}$ and normalized cutoff frequency $\omega_c = 0.4\pi\,\text{rad/s}$. Notice that the coefficients for the analog prototype can be readily obtained from tables available in the literature or through the Matlab function *cheby1*.

We start by setting the analog prototype transfer function as

$$H_c(s) = \frac{1.2833}{s^5 + 2.1915s^4 + 4.37534s^3 + 4.7565s^2 + 3.5798s + 1.2833}, \tag{6.247}$$

whose coefficients were obtained from Matlab. Furthermore, for this example, we set the sampling period to $T = 1s$.

Now that the analog prototype system is defined, step 3. in the procedure can be carried out starting from the computation of the poles of $H_c(s)$. The poles of the

Poles		Coefficients	
p_1	$0.0728 + j0.7510$	b	0.3850
p_2	$0.0728 - j0.7510$	a_1	-1.4105
p_3	0.5143	a_2	1.4469
p_4	$0.3753 + j0.4081$	a_3	-0.9792
p_5	$0.3753 - j0.4081$	a_4	0.4178
		a_5	-0.0900

TABLE 6.19: Poles and numerator and denominator coefficients coefficients for the $5th$ order transmission system function $T(z)$ when considering $T = 1s$. $T(z)$ is considered in the form of (6.243).

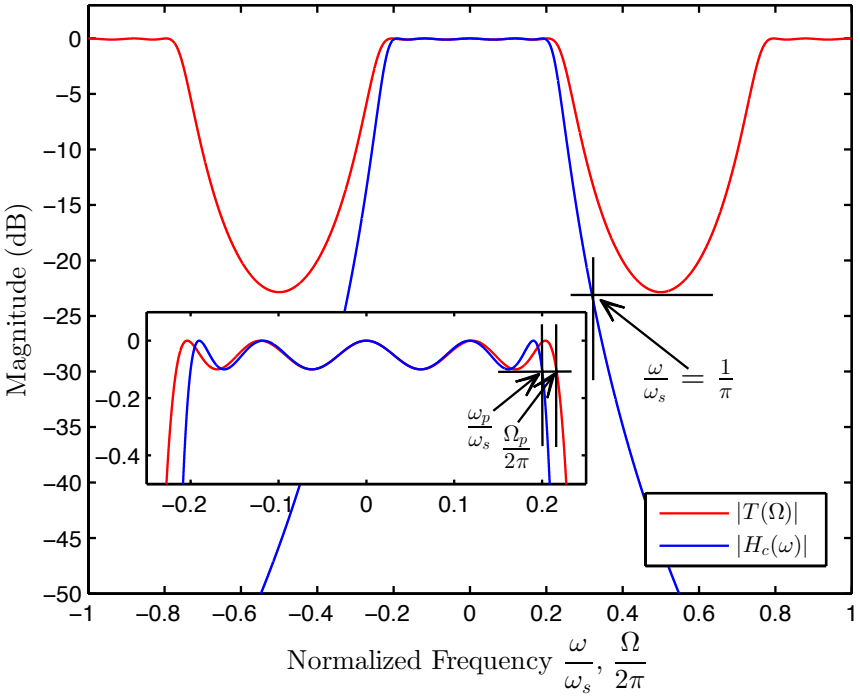

FIGURE 6.60: Magnitude response for the $5th$ order target analog prototype $H_c(\omega)$ versus the magnitude response of the $5th$ order digital counterpart $T(\Omega)$ obtained through the approximation of derivatives method with $T = 1s$. Notice that the frequency normalizations ω/ω_s ($\omega_s = 2\pi/T$) for the analog domain and $\Omega/2\pi$ for the digital domain enables the comparison of both responses under a common domain.

digital system $T(z)$ are then obtained through equation (6.242) from the analog system poles and for the specified sampling period T. The coefficients a_i and b_i for the digital transmission system transfer function are readily obtainable from the poles and $T(z)$ is set in the form of (6.243). The pole evaluation of $T(z)$ as well as the numerator and denominator polynomials coefficients are given in Table 6.19.

The magnitude of the frequency response for the digital transmission system $T(\Omega)$ is plotted in Figure 6.60. For comparison purposes, we have also plotted the magnitude of the frequency response of the analog prototype $H_c(\omega)$. Like with the bilinear transformation and due to the wrapping effect, we clearly do not have a good match between both magnitude responses, except for the low frequency values around zero. However, the main frequency response features of the analog system, such as ripple, ripple amplitude as well as the pass-band and stop-band regions are also present on the digital system frequency response. The warping effect only affects the frequency locations for these features. For instance, we see from Figure 6.60 that due to the warping effect the normalized cutoff frequency for the digital system, *i.e.*, $\Omega_p/2\pi$, is different from that of the analog system, *i.e.*, ω_p/ω_s. Nevertheless, they are closely related through the

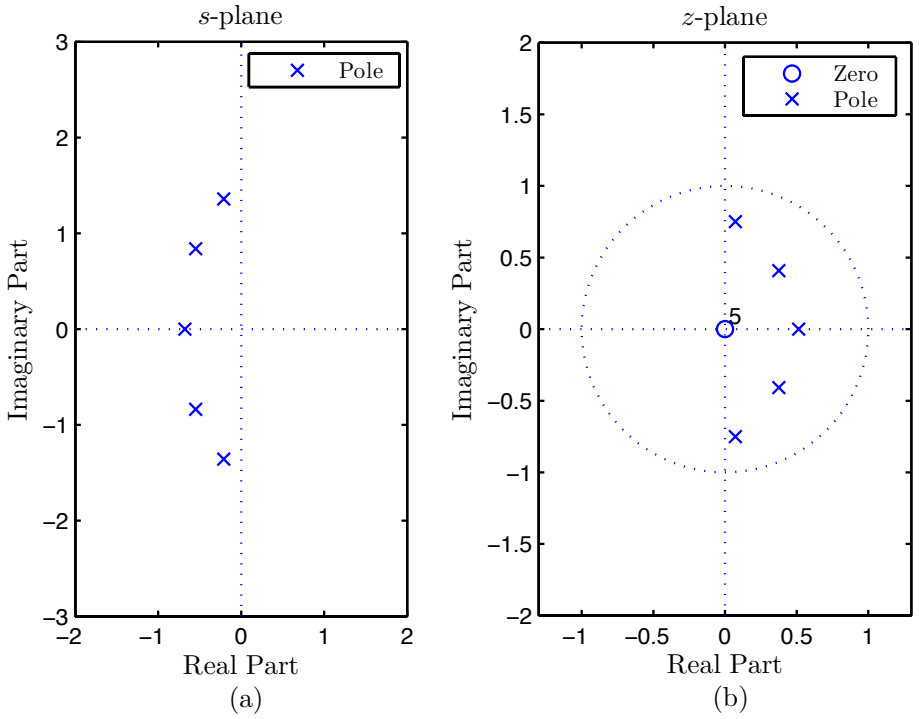

FIGURE 6.61: Pole-Zero plot associated to the $5th$ analog prototype $H_c(s)$ in (a) and Pole-Zero plot associated to the corresponding digital transmission system $T(z)$ in (b).

frequency warping relation given by equation (6.241). Moreover, we clearly see from Figure 6.60 that the maximum attenuation value for the stop band of $T(z)$ equals the evaluation of $H_c(\omega)$ at $|\omega/\omega_s| = 1/\pi$. This is the result of the frequency clipping effect. In other words, we see from Figure 6.60 that only the magnitude values of $H_c(\omega)$ in the range $-1/\pi \leq \omega/\omega_s \leq 1/\pi$ are mapped to the entire digital frequency domain, *i.e.*, $-1/2 \leq \Omega/2\pi \leq 1/2$.

In this example and for demonstration purposes, the sampling period was deliberately set to $T = 1s$ so as to obtain a reasonable stop-band attenuation. As for the analog system parameters and for comparison purposes, they were kept the same as for the examples regarding the impulse invariance method and the bilinear transformation. However, for a proper synthesis of DNTL structures using the bilinear transformation, the procedure usually begins with the specifications (ripple level, cutoff frequency, maximum stop-band attenuation,...) for the frequency response in the digital domain. These specifications, are then converted to the analog domain via the frequency warping relation (6.241). From these values, the analog system is designed and then converted into its digital counterpart through the approximation of derivatives method (6.210).

Figure 6.61(a) shows the locations for the poles of the analog prototype system $H_c(s)$ on the s-plane. On the other hand, Figure 6.61(b) depicts the locations of the zeros and

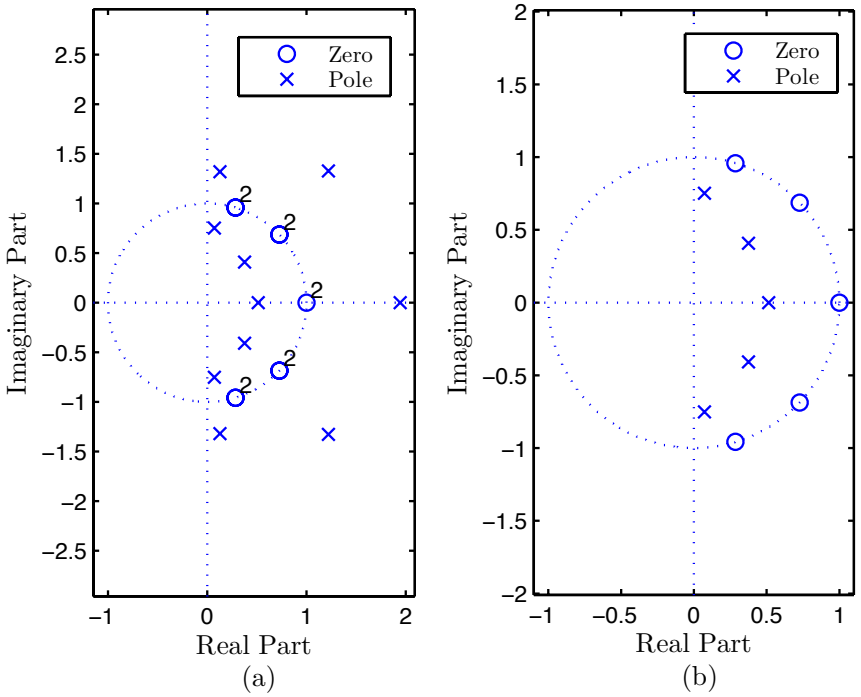

FIGURE 6.62: Pole-Zero plots associated to the $5th$ order reflection system $R(z)$ for $T = 1s$. In (a) are depicted the zeros and poles for $|R(z)|^2$, whereas in (b) we have the zeros and poles of $R(z)$ which in turn are selected from those of $|R(z)|^2$.

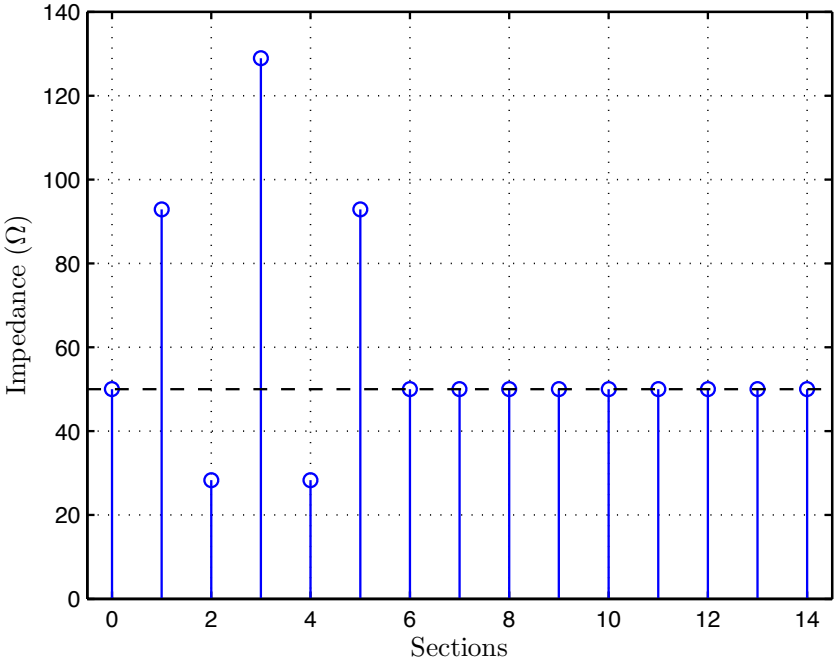

FIGURE 6.63: Impedance profile associated to $R(z)$, which is characterized by the pole-zero configuration depicted in Figure 6.62(b). The depicted impedance profile was obtained from 15 iterations of the DLP inverse scattering algorithm. Notice that the impedance profile is in fact solely constituted by five sections as the impedance values only evaluate differently from 50Ω on five sections.

Numerator		Denominator	
e_1	-3.0261	a_1	-1.4105
e_2	4.8575	a_2	1.4469
e_3	-4.8575	a_3	-0.9792
e_4	3.0261	a_4	0.4178
e_5	-1.0000	a_5	-0.0900

TABLE 6.20: Coefficients for the $5th$ order reflection system $R(z)$ computed from the transmission system $T(z)$. The gain factor is $K_R = 0.3$ and $R(z)$ is in the form of (6.246).

poles on the z-plane for the transmission system, $T(z)$. As previously referred, the poles of $T(z)$ are obtained through the approximation of derivatives method by considering a period sampling of $T = 1s$. Clearly, we see that the poles for the stable analog system, which are located on the LHP of the s-plane, are mapped to the inside of the unit circle on the z-plane. Thus, the digital system $T(z)$, as obtained through the approximation of derivatives method, is also a stable system. Furthermore, $H_c(s)$ has five zeros located at $s = \infty$. When mapped into the z-plane through the approximation of derivatives method, these infinite zeros of $H_c(s)$ originate a zero at $z = 0$ of multiplicity five, as depicted in Figure 6.61(b). Thus the resulting digital system $T(z)$ is classified as an all-pole digital system.

In step 4. of the procedure, the reflection system transfer function $R(z)$ is computed from its associated transmission system, $T(z)$, through the relation (6.245). We start by computing the poles and zeros for the squared magnitude of the reflection system transfer function, $|R(z)|^2$. The corresponding pole-zero plot is given in Figure 6.62(a). The pole-zero plot for $R(z)$ is depicted in Figure 6.62(b) and is obtained from that of $|R(z)|^2$ by selecting the stable poles and one zero from each pair of zeros. From this pole-zero selection the transfer function for $R(z)$ is easily computed in the form of equation

Section	Impedance (Ω)
0	50
1	92.86
2	28.32
3	128.91
4	28.32
5	92.86
6	50

TABLE 6.21: Impedance values for each section of the DNTL synthesized for the fifth order filter example considering the pole-zero configuration depicted in Figure 6.62(b). The impedance value for section 0, *i.e.*, the first section, is set to that of the microwave system characteristic impedance, 50Ω.

(6.246). The coefficients for the numerator and denominator polynomials of $R(z)$ are given in Table 6.20.

The computation of the impedance profile for the DNTL structure which implements as its transmission frequency response the fifth order Chebyshev filter, thus $T(\Omega)$, is done in the fifth and final step of the procedure. For that and similarly to the previous examples, we run the DLP inverse scattering algorithm on the reflection response system $R(z)$. The resulting DNTL structure impedance profile, as computed by the inverse scattering procedure, is depicted in Figure 6.63, and is given as a five section length DNTL structure. The corresponding impedance profile values are given in Table 6.21.

In summary, we conclude that the approximation of derivatives method, when used through the transformation given in (6.210), proves to be very useful in the synthesis of DNTL structures. This is mainly due to size constrains, *i.e.*, when compared with both the impulse invariance method and the bilinear transformation, the approximation of derivatives method allow for the synthesis of finite length DNTL structures. This is unlike with the other two methods where the resulting DNTL structure is usually of infinite length and further depends on truncation procedures. Moreover, we have seen that using the approximation of derivatives method on a *n-th* order analog all-pole systems always results in an *n-th* all-pole digital systems. Consequently and accordingly to the discussion undertaken in section 6.3, using the approximation of derivatives method on the synthesis of a *n-th* order all-pole analog system always results in an n section DNTL structure.

6.9 Summary

In this chapter we have introduced the concept of discrete nonuniform transmission line (DNTL), that is NTL structures with a discrete impedance profile, which is unlike the continuous impedance profile observed on the NTL structures observed on the previous chapters. The properties of DNTL structures were investigated and the realizability conditions assessed.

The parallelism between DNTL structures and digital filters was established and a modified version of the discrete layer-peeling inverse scattering algorithm was derived from digital filter theory.

The specific conditions for the optimum synthesis (minimum length) of DNTL structures were investigated and a new method to perform the synthesis of DNTL structures

using DSP techniques was derived.

Finally the synthesis of DNTL filters using analog filters prototypes was considered, and a new analog-to-digital conversion technique was developed.

Chapter 7

Conclusions

The primary goal of this research work is to set a solid working base and propose innovative methods/procedures and tools for the synthesis of high performance structures employing inverse scattering theory.

An overview on transmission line theory and network analysis was presented in Chapter 2, where it is shown through the Maxwell equations that energy can be transmitted in the form of guided waves. Moreover, the concepts of waveguide and transmission line were introduced. A special attention was given to the mathematical analysis of transmission lines, from which it was demonstrated their capability of guiding TEM propagating waves. Additionally, the scattering parameters were introduced as a means for characterizing N-port microwave systems and the wave-amplitude transmission matrix as a tool for the analysis of cascade connection systems.

The analysis of nonuniform transmission lines is addressed in Chapter 3 where several direct scattering tools are presented. Two main direct scattering approaches are considered: the coupled mode theory and the transmission matrix method. The former is a more generic method (both waveguides and transmission lines) and is based on the spatial coupling of modes within guiding wave structures whereas the later method is particular to the analysis of nonuniform transmission line structures. In this chapter, the generic coupled mode theory method is adapted to the analysis of nonuniform transmission lines structures assuming single mode TEM propagation. Furthermore, for three specific cases the simplification of the coupled mode theory led to analytical solutions, namely for weak, constant and periodic coupling nonuniform transmission lines. For the later method, *i.e.* the transmission matrix method, two different strands were presented: the constant coupling discretization strand and the constant impedance discretization

strand.

The theory of inverse scattering is introduced in Chapter 4, where an in-depth analysis of analytical and numerical inverse scattering methods is presented. The inverse scattering methods presented are divided into two major groups. The first group consists on integral equation based inverse scattering methods and are based on the solution of the GLM integral equation or alternatively the solution of a system of integral equations (ZS system). The solution to these integral equations can be obtained through mathematical manipulation in the form of a closed form analytical expression, or through numerical and iterative procedures. On the other hand, the second group comprises the so-called differential inverse scattering methods. These methods are based on discrete nonuniform transmission line models and rely on recursive identification procedures. Two differential inverse scattering methods were addressed, namely the CLP and DLP procedures. The outcome of these procedures inherently translates into the synthesis of continuously varying impedance profile transmission lines.

The potential and versatility of the inverse scattering theory on the synthesis of nonuniform transmission line based structures is demonstrated in Chapter 5, where we address the synthesis of several passive microwave devices, namely: bandstop filters, filters with arbitrary reflective group delay response and TEM directional couplers with arbitrary coupling response. Additionally, we assess the impact of the truncation and windowing procedures on the synthesis of classical band-stop filters and identify the optimum windowing configurations which reduce the truncation error on the approximation to the ideal frequency response. The influence of the different classical filter parameters on the length and maximum characteristic impedance values of the synthesized filters is evaluated and finally the synthesis procedures is evaluated through a comparative study between numerical, analytical and electromagnetic simulations as well as experimental measurements.

Finally, the concept of discrete nonuniform transmission line (DNTL) is introduced in Chapter 6. Discrete nonuniform transmission lines are nonuniform transmission lines with a discrete impedance profile, which is unlike the nonuniform transmission lines considered in the previous chapters. Due to their discrete nature, DNTL structures possess peculiar characteristic which denote some similarity with digital systems. In this sense, in this chapter, the parallelism between DNTL structures and digital filters was established and a modified version of the discrete layer-peeling inverse scattering algorithm

was accordingly derived with the corresponding digital filter theory parallelism. Moreover, a new theoretical framework regarding the parallelism between discrete nonuniform transmission lines and digital filters is established. Within this framework, specific conditions for the optimum synthesis (minimum length) of DNTL structures were investigated and a novel analog-to-digital conversion technique was developed.

In summary, this work has provided a deep insight into the theory and methods/procedures used both for the analysis, *i.e.*, direct scattering and synthesis , *i.e.*, inverse scattering of nonuniform transmission line based structures. Moreover, from the work basis established on the first chapters (direct and inverse scattering) novel broad-band devices have been synthesized as well innovative procedures have been developed. We higgling however the work developed in Chapter 6 regarding DNTL structures and the corresponding parallelism with digital filter theory. The work presented on this chapter provides a new set of tools that might potentially assist in future developments on the subject of synthesis of enhanced performance microwave devices using inverse scattering theory.

7.1 Recommendations for future work

Based on the work presented on this thesis, several research directions for future work can be taken. Among this directions, we now highlight the ones that we consider to be the most relevant:

- Apply inverse scattering theory to the synthesis of other microwave structures so as to enhance their performances. For instance power dividers, slot antennas, impedance transformers, bandpass filters and phase shifters.

- Investigate the use of inverse scattering on the synthesis microwave resonators so as to synthesize multi-band resonators with arbitrarily defined resonant frequencies.

- Apply digital filters design tools and techniques on the synthesis of DNTL based directional couplers as well as high-pass and all-pass filters.

- Further study regarding the physical implementation of DNTL structures, more specifically, the evaluation of the influence of sampling rate, bandwidth, system order, and curt-off frequencies on the length and maximum characteristic impedance values of the synthesized DNTL structures.

- Synthesis of reduced size UWB filters based on DNTL impedance transformers structures composed by quarter-wave length resonators and impedance inverters.
- Synthesis of *quasi*-elliptical filters using recurring to input port and output port located stubs which are liable to be synthesized as all-pass DNTL filters.
- Synthesis of DNTL based slot antennas.

Bibliography

[1] A.V. Oppenheim, A.S. Willsky, and S.H. Nawab. *Signals and systems*, volume 2. Prentice-Hall Englewood Cliffs, NJ, 1983.

[2] George L Matthaei, Leo Young, and EMT Jones. *Microwave filters, impedance-matching networks, and coupling structures*, volume 5. McGraw-Hill New York, 1964.

[3] PAUL I Richards. Resistor-transmission-line circuits. *Proceedings of the IRE*, 36 (2):217–220, 1948.

[4] K Kuroda. General properties and synthesis of transmission-line networks in microwave filters and circuits. *Matsumoto, Ed, Tech*, 22, 1970.

[5] D.M. Pozar. Microwave engineering, 2nd, 1998.

[6] A. T. Starr. The nonuniform transmission line. *Radio Engineers, Proceedings of the Institute of*, 20(6):1052–1063, June 1932. ISSN 0731-5996. doi: 10.1109/JRPROC.1932.227748.

[7] Khair Shamaileh, Mohammad Almalkawi, Vijay Devabhaktuni, Nihad Dib, Bassem Henin, and Amin Abbosh. Non-uniform transmission line ultra-wideband wilkinson power divider. *Progress In Electromagnetics Research C*, 44, 2013.

[8] P.M. Narayanan, P. Rulikowski, and J. Barrett. Miniaturization of nonuniform transmission lines for ultra-wideband pulse shaping. In *Microwaves, Communications, Antennas and Electronics Systems (COMCAS), 2011 IEEE International Conference on*, pages 1–6, Nov 2011. doi: 10.1109/COMCAS.2011.6105892.

[9] P. Rulikowski and J. Barrett. Application of nonuniform transmission lines to ultra wideband pulse shaping. *Microwave and Wireless Components Letters, IEEE*, 19 (12):795–797, Dec 2009. ISSN 1531-1309. doi: 10.1109/LMWC.2009.2033509.

[10] Khair Ayman Al Shamaileh, Abdullah Mazen Qaroot, and Nihad I Dib. Non-uniform transmission line transformers and their application in the design of compact multi-band bagley power dividers with harmonics suppression. *Progress In Electromagnetics Research*, 113:269–284, 2011.

[11] C. Caloz, S. Gupta, Qingfeng Zhang, and B. Nikfal. Analog signal processing: A possible alternative or complement to dominantly digital radio schemes. *Microwave Magazine, IEEE*, 14(6):87–103, Sept 2013. ISSN 1527-3342. doi: 10.1109/MMM.2013.2269862.

[12] Israel Arnedo, Iván Arregui, Magdalena Chudzik, Fernando Teberio, Aintzane Lujambio, David Benito, Txema Lopetegi, and Miguel AG Laso. Passive microwave component design using inverse scattering: Theory and applications. *International Journal of Antennas and Propagation*, 2013, 2013.

[13] PP Roberts and GE Town. Design of microwave filters by inverse scattering. *IEEE Transactions on Microwave Theory and Techniques*, 43(4 Part 1):739–743, 1995.

[14] J. Skaar. *Synthesis and characterization of fiber bragg gratings.* PhD thesis, Department of Electronics and Telecommunications, Norwegian University of Science and Technology, 2000.

[15] R. Feced, M.N. Zervas, and M.A. Muriel. An efficient inverse scattering algorithm for the design of nonuniform fiber bragg gratings. *Quantum Electronics, IEEE Journal of*, 35(8):1105–1115, 1999.

[16] R.E. Collin. *Foundations for microwave engineering.* Wiley India Pvt. Ltd., 2007.

[17] J. R. Pierce. Coupling of modes of propagation. *Journal of Applied Physics*, 25(2): 179 –183, feb 1954. ISSN 0021-8979. doi: 10.1063/1.1721599.

[18] SE Miller. Coupled wave theory and waveguide applications. *Bell Syst. Tech. J*, 33 (661):5–7, 1954.

[19] WH Louisell. Analysis of the single tapered mode coupler. *Bell Syst. Tech. J*, 34 (4):853–870, 1955.

[20] SA Schelkunoff. Conversion of maxwell's equations into generalized telegraphist's equations. *Bell Syst. Tech. J*, 34(5):995–1043, 1955.

[21] BZ Katsenelenbaum, L.M. Del Rio, M. Pereyaslavets, M. Thumm, and M.S. Ayza. *Theory of nonuniform waveguides: the cross-section method*. Iet, 1998.

[22] H.A. Haus. *Electron beam waves in microwave tubes*. Massachusetts Institute of Technology, Research Laboratory of Electronics, 1958.

[23] D. Marcuse. Tl1e coupling of degenerate modes in two parallel dielectric waveguides. *Bell System Technical Journal*, 1971.

[24] D. Marcuse. Coupled mode theory of round optical fibers. *Bell Syst. Tech. J*, 52 (6):817–842, 1973.

[25] A.W. Snyder. Coupled-mode theory for optical fibers. *JOSA*, 62(11):1267–1277, 1972.

[26] A.W. Snyder. Coupling of modes on a tapered dielectric cylinder. *Microwave Theory and Techniques, IEEE Transactions on*, 18(7):383–392, 1970.

[27] H.F. Taylor and A. Yariv. Guided wave optics. *Proceedings of the IEEE*, 62(8): 1044–1060, 1974.

[28] A. Yariv. Coupled-mode theory for guided-wave optics. *Quantum Electronics, IEEE Journal of*, 9(9):919–933, 1973.

[29] A. Yariv and P. Yeh. *Optical waves in crystals*, volume 5. Wiley New York, 1984.

[30] H.A. Haus and W. Huang. Coupled-mode theory. *Proceedings of the IEEE*, 79(10): 1505–1518, 1991.

[31] BE Little and WP Huang. Coupled-modetheory for optical waveguides. *Progress In Electromagnetics Research*, 10:217–270, 1995.

[32] J. M. L. Beregana. *Photonic bandgap structures in microstrip technology: study using the couple mode formalism and aplications*. PhD thesis, Departamento de Inginiería Eléctrica y Electrónica de la Universidad Pública de navarra, 2002.

[33] T. Lopetegi, MAG Laso, MJ Erro, M. Sorolla, and M. Thumm. Analysis and design of periodic structures for microstrip lines by using the coupled mode theory. *IEEE microwave and wireless components letters*, 12(11):441–443, 2002.

[34] T. Rozzi and M. Mongiardo. *Open electromagnetic waveguides*, volume 43. Inspec/Iee, 1997.

[35] T. Rozzi and PD Sewell. The continuous spectrum of open waveguides of nonseparable cross section. *Antennas and Propagation, IEEE Transactions on*, 40(11): 1283–1291, 1992.

[36] M. Mongiardo and T. Rozzi. Continuous spectrum, characteristic modes, and leaky waves of open waveguides. *Microwave Theory and Techniques, IEEE Transactions on*, 41(8):1329–1335, 1993.

[37] J. Kierzenka and L.F. Shampine. A bvp solver based on residual control and the maltab pse. *ACM Transactions on Mathematical Software (TOMS)*, 27(3):299–316, 2001.

[38] D.G. Zill and M.R. Cullen. *Differential equations with boundary-value problems*. Brooks/Cole Pub Co, 2008.

[39] T. Erdogan. Fiber grating spectra. *Lightwave Technology, Journal of*, 15(8):1277–1294, 1997.

[40] M. Jaulent. The inverse scattering problem for lcrg transmission lines. *Journal of Mathematical Physics*, 23:2286, 1982.

[41] I.M. Gelfand and B.M. Levitan. On the determination of a differential equation from its spectral function. *Izvestiya Rossiiskoi Akademii Nauk. Seriya Matematicheskaya*, 15(4):309–360, 1951.

[42] VA Marchenko. On reconstruction of the potential energy from phases of the scattered waves. In *Dokl. Akad. Nauk SSSR*, volume 104 of *5*, pages 695–698, 1955.

[43] M.G. Krein. Solution of the inverse sturm-liouville problem. In *Dokl. Akad. Nauk SSSR*, volume 76 of *1*, pages 21–24, 1951.

[44] Irvin Kay. The inverse scattering theory. Technical report, New York University, Institute of Mathematical Sciences, Division of Electromagnetic Research, 1955.

[45] AK Jordan and S. Lakshmanasamy. Inverse scattering theory applied to the design of single-mode planar optical waveguides. *JOSA A*, 6(8):1206–1212, 1989.

[46] A. Jordan and H. Kritikos. An application of one-dimensional inverse-scattering theory for inhomogeneous regions. *Antennas and Propagation, IEEE Transactions on*, 21(6):909–911, 1973.

[47] I. Kay. The inverse scattering problem when the reflection coefficient is a rational function. *Communications on pure and applied mathematics*, 13(3):371–393, 1960.

[48] HA Haus. Physical interpretation of inverse scattering formalism applied to self-induced transparency. *Reviews of Modern Physics*, 51:331–340, 1979.

[49] G.H. Song and S.Y. Shin. Design of corrugated waveguide filters by the gelfandle-vitanmarchenko inverse-scattering method. *JOSA A*, 2(11):1905–1915, 1985.

[50] I. Arnedo, M.A.G. Laso, F. Falcone, D. Benito, and T. Lopetegi. A series solution for the single-mode synthesis problem based on the coupled-mode theory. *Microwave Theory and Techniques, IEEE Transactions on*, 56(2):457 –466, feb. 2008. ISSN 0018-9480. doi: 10.1109/TMTT.2007.914628.

[51] P.V. Frangos and D.L. Jaggard. Analytical and numerical solution to the two-potential zakharov-shabat inverse scattering problem. *Antennas and Propagation, IEEE Transactions on*, 40(4):399–404, 1992.

[52] A.M. Bruckstein and T. Kailath. Inverse scattering for discrete transmission line models. *SIAM review*, pages 359–389, 1987.

[53] A.M. Bruckstein, B.C. Levy, and T. Kailath. Differential methods in inverse scattering. *SIAM Journal on Applied Mathematics*, pages 312–335, 1985.

[54] J. Skaar, L. Wang, and T. Erdogan. Synthesis of thick optical thin-film filters with a layer-peeling inverse-scattering algorithm. *Applied Optics*, 40(13):2183–2189, 2001.

[55] J. Skaar, L. Wang, and T. Erdogan. On the synthesis of fiber bragg gratings by layer peeling. *Quantum Electronics, IEEE Journal of*, 37(2):165–173, 2001.

[56] L. Poladian. Simple grating synthesis algorithm. *Optics Letters*, 25:787–789, 2000.

[57] MAG Laso, T. Lopetegi, MJ Erro, D. Benito, MJ Garde, MA Muriel, A. Sorolla, and M. Guglielmi. Chirped delay lines in microstrip technology. *IEEE Microwave and Wireless Components Letters*, 11(12):486–488, 2001.

[58] MAG Laso, T. Lopetegi, MJ Erro, M. Castillo, D. Benito, MJ Garde, MA Muriel, M. Sorolla, and M. Guglielmi. Real-time spectrum analysis in microstrip technology. In *European Microwave Conference, 2001. 31st*, pages 1–4, 2001.

[59] B.M. Oliver. Directional electromagnetic couplers. *Proceedings of the IRE*, 42(11): 1686–1692, 1954. ISSN 0096-8390. doi: 10.1109/JRPROC.1954.274664.

[60] Leo Young. The analytical equivalence of tem-mode directional couplers and transmission-line stepped-impedance filters. In *Proceedings of the Institution of Electrical Engineers*, volume 110, pages 275–281. IET, 1963.

[61] Alan V Oppenheim, Ronald W Schafer, John R Buck, et al. *Discrete-time signal processing*, volume 5. Prentice Hall Upper Saddle River, 1999.

[62] Athanasios Papoulis and S Unnikrishna Pillai. *Probability, random variables, and stochastic processes*. Tata McGraw-Hill Education, 2002.

[63] Ole Henrik Waagaard. *Inverse scattering and experimental characterization of optical grating filters*. PhD thesis, Norwegian University of Science and Technology, 2007.

[64] N. I. Akhiezer. *The classical moment problem: and some related questions in analysis*, volume 5. Oliver & Boyd Edinburgh, 1965.

[65] Sophocles J Orfanidis. Optimum signal processing: an introduction, 1985.

[66] E Folke Bolinder. An evaluation of an important advance in network synthesis theory. Technical report, DTIC Document, 1965.

[67] Otto Brune. *Synthesis of a finite two-terminal network whose driving-point impedance is a prescribed function of frequency*. PhD thesis, Massachusetts Institute of Technology, 1931.

[68] S Darlington. A survey of network realization techniques. *Circuit Theory, IRE Transactions on*, 2(4):291–297, 1955.

[69] N. Kinayman and I. Aksun. *Modern microwave circuits*. Artech House microwave library. Artech House, 2005. ISBN 9781580537254. URL `http://books.google.pt/books?id=AR1TAAAAMAAJ`.

[70] Emil Cauer, Wolfgang Mathis, and Rainer Pauli. Life and work of wilhelm cauer (1900-1945). In *Proceedings of the 14-th International Symposium on Mathematical Theory of Networks and Systems, Perpignan, France*, 2000.

[71] Farooq Mukhtar, Yury Kuznetsov, and Peter Russer. Network modelling with brune's synthesis. *Advances in Radio Science*, 9(6):91–94, 2011.

[72] J.O. Smith, Stanford University. Center for Computer Research in Music, Acoustics, Hertz Foundation, and Calif.) System Development Foundation (Palo Alto. *Techniques for digital filter design and system identification with application to the violin*. Number no. 14 in Report. CCRMA, Dept. of Music, Stanford University, 1983. URL `http://books.google.pt/books?id=8pAXAQAAIAAJ`.

[73] Te-Wen Pan and Ching-Wen Hsue. Modified transmission and reflection coefficients of nonuniform transmission lines and their applications. *Microwave Theory and Techniques, IEEE Transactions on*, 46(12):2092–2097, 1998.

[74] Te-Wen Pan, Ching-Wen Hsue, and Jhin-Fang Huang. Arbitrary filter design by using nonuniform transmission lines. *Microwave and Guided Wave Letters, IEEE*, 9(2):60–62, 1999.

[75] Thomas P Krauss, Loren Shure, and John N Little. *Signal Processing Toolbox for Use with MATLAB®: User's Guide*. The MathWorks, 1994.

[76] John G Proakis. *Digital Signal Processing: Principles, Algorithms, and Applications, 4/e*. Pearson Education India, 2007.

[77] Leo Young. Stepped-impedance transformers and filter prototypes. *Microwave Theory and Techniques, IRE Transactions on*, 10(5):339–359, 1962. ISSN 0097-2002. doi: 10.1109/TMTT.1962.1125523.

[78] R. Levy. Tables of element values for the distributed low-pass prototype filter. *Microwave Theory and Techniques, IEEE Transactions on*, 13(5):514–536, 1965. ISSN 0018-9480. doi: 10.1109/TMTT.1965.1126048.

[79] R.E. Collin. Theory and design of wide-band multisection quarter-wave transformers. *Proceedings of the IRE*, 43(2):179–185, 1955. ISSN 0096-8390. doi: 10.1109/JRPROC.1955.278076.

[80] H.J. Riblet. General synthesis of quarter-wave impedance transformers. *Microwave Theory and Techniques, IRE Transactions on*, 5(1):36–43, 1957. ISSN 0097-2002. doi: 10.1109/TMTT.1957.1125088.